UNIVERSITY OF BIRMINGHAM

UK Atomic Energy Authority

TUNGSTEN ALLOYS AND NANO-STRUCTURING FOR FUSION ENERGY

SCHOOL OF METALLURGY AND MATERIALS

N.M.Parkes (290090)

A thesis submitted to the University of Birmingham for the degree of DOCTOR OF PHILOSOPHY

Submission date: 31 September 2023

Viva date: 01 November 2023

Re-submission date:

Date: 30th April 2024

Word count: 49707

Project supervisors:

Dr Alexander Knowles (UoB) & Dr Chris Hardie (UKAEA)

Declaration

I declare that this thesis has not been submitted for a degree at this or any other university and is entirely my own work, except where specific reference is made in the text to the work of others performed in collaboration. This dissertation contains fewer than 50,000 words per the 2019-20 cohort University Regulations.

The following manuscripts were produced as a result of work conducted during this PhD:

Neal Parkes, Russel Dodds, Andy Watson, David Dye, Chris Hardie, Samuel A. Humphry-Baker, Alexander J. Knowles. Tungsten-based bcc-superalloys: Thermal stability and ageing behaviour. International Journal of Refractory Metals and Hard Materials Volume 113, June 2023, 106209

P.A. Ferreiros, S.O. von Tiedemann, **N. Parkes**, D. Gurah, D.J.M. King d, P. Norman, M.R. Gilbert, A.J. Knowles (2023) VNbCrMo refractory high-entropy alloy for nuclear application. International Journal of Refractory Metals and Hard Materials Volume 113, 106200

(Some of the work in the W-Ti-Fe in chapter 3 is presented in the above paper.)

The following three papers are in draft form and are in preparation for submission to Scripta Materialia

Neal M Parkes, Pedro Ferreiros, Luke Hewitt, Chris Hardie, Alexander J Knowles. Reduced-activation refractory high entropy alloys (RA-RHEAs) W-V-Cr-Ta(+Ti) for fusion energy The work in this paper was taken from Chapter 4.

Neal M Parkes, Kan Ma, Ben Poole, David Collins, Chris Hardie, Alexander J Knowles. Precipitation-induced recrystallisation (PIX) in a Ti-Fe-Mo bcc-superalloy The work in this paper was taken from Chapter 5.

Neal M Parkes, Chris Bearcroft, Luke Hewitt, Chris Hardie, Alexander J Knowles. Precipitation Induced Recrystallisation in Undeformed W-Cr alloys The work in this paper was taken from Chapter 6.

Abstract

Nuclear fusion offers a utopian vision for the sustained large-scale production of low-carbon energy. However, many technological challenges need to be overcome. The significant challenges relate to the properties of materials that can be used in such an extreme environment. Tungsten is a candidate material for the plasma-facing components (PFCs) in a nuclear fusion reactor because of its exceptional properties. It boasts a high melting point of 3420 °C, coupled with impressive thermal conductivity at 170 Wm^{-1} K^{-1}, and a dense structure with a density of 19.4 gcm^{-3}.

Nevertheless, there are challenges associated with the processing of tungsten. Its elevated melting point and lack of ductility characterized by a Ductile-Brittle Transition Temperature (DBTT) of approximately 400 °C, presents a hurdle to processing. One tungsten alloy that has been investigated in the literature is a binary alloy containing chromium. The addition of chromium has been shown to not only improve the mechanical properties but also to preferentially form a protective chromate layer instead of Tungsten trioxide. Furthermore, chromium can be used to nanostructure tungsten by utilising the miscibility gap that exists within the phase diagram. A W-28Cr wt% alloy was homogenised and aged within the miscibility gap to produce a two-phase microstructure that was observed to start at the prior parental grain boundaries and followed by a finer two-phase decomposition in the grain themselves. This was observed to produce substantial grain refinement and the production of a nanostructured alloy. An attempt to bulk manufacture the alloy through SPS and Hipping was carried out. However, considerable macrosegregation of elements and porosity ensued.

To investigate whether a nano-structured multi-phase tungsten alloy could be manufactured to improve its mechanical properties. A tungsten-based 'bcc-superalloy' within the W-Ti-Fe ternary system, consisting of W-TiFe, A2-B2 and β-β' nanostructures was explored. Alloys produced by arc melting were solution heat treated at 1250 °C, followed by ageing at 750 °C to control microstructure. It was demonstrated that a nano-scale B2

TiFe(W) forms within A2(W,Ti,Fe) in the W-Ti-Fe alloys, creating localised regions of the targeted A2-B2 (β-β') precipitate-reinforced structure.

Density functional theory (DTF) has shown that alloying tungsten with manganese can potentially improve the ductility of tungsten. To study this as a potential alloy a tungsten 50/50 atomic % alloy was manufactured and the mechanical and physical properties were investigated. Despite an increase in the density of low-angle grain boundaries being seen after various thermal treatments, considerable porosity ensued, rendering the alloy unsuitable for further testing.

WHAs offer very high density (approaching 19 g/cc) in combination with relatively high thermal conductivity, low thermal expansion, ambient corrosion resistance, and can be provided with mechanical properties comparable to many medium carbon steels.

Tungsten heavy alloys (WHAs) are manufactured by the addition of elements such as nickel and cobalt, they not only show high densities but demonstrate improved mechanical properties approaching that of medium carbon steels. With these improved mechanical properties in mind, a new W-30Ti at% alloy was manufactured through arc melting following homogenisation and by ageing at 1000 °C. Following rolling at 1000 °C, 3-point bending tests were performed at various temperatures in both the rolled and transverse directions. The results showed a DBTT at 200 and 175 °C, respectively. To examine how nanostructuring affected the mechanical properties, the W-Ti alloy was aged at 1000 °C to induce nanostructuring. Subsequent 3-point bending tests on the aged samples showed a reduction in DBTT to below 100 °C in both cases. Suggesting the ageing process is key to improving the mechanical properties of the nanostructured alloy.

High entropy alloys (HEAs) have the potential to possess many unique properties, including high ductility, wear resistance, strength, and corrosion resistance. To investigate whether a tungsten-based refractory alloy, has improved mechanical properties two RA-RHEAs were created; a W-V-Cr-Ta quaternary and a W-V-Cr-Ta-Ti quinary alloy. These alloys were produced through arc melting and subjected to thermal ageing at 1400°C to investigate their stable phases and compositions. The results revealed a microstructure

consisting of 2 bcc and a $TaCr_2$ C15 Laves phases. The quinary RA-RHEAs exhibited a single phase bcc and C15 Laves phase and a tertiary Ti A3 HCP phase. These alloys displayed elevated hardness values, with stable phases to at least 1400 °C.

Beta-Ti bcc-superalloys

In the Ti-Fe-Mo system, nano-scale B2 TiFe lamellar precipitation occurs following ageing at 750 °C, in contrast to cuboidal or spherical precipitates as in fcc-superalloys or other bcc-superalloys. This is suggested to be due to the differences in lattice parameters of the B2 and A2 phases, of 2.98 $\pm$ 0.01 Å and 3.18 $\pm$ 0.01 Å respectively, giving a misfit of -6.1% which is large compared to the misfits in fcc-superalloy of <1%. Interestingly, however, this grain refinement phenomena has not been studied in detail. Without any externally applied strain, a new recrystallization phenomenon was observed by the discontinuous precipitation of beta-Ti and beta-prime TiFe lamellar colonies originating from prior grain boundaries. The Ti+TiFe colonies were associated with significant internal grain misorientation, sub-grain formation, increased geometrically necessary dislocation density, and strain. This unique recrystallisation behaviour presents a new design tool for controlling grain structure, size, and texture in engineering alloys.

Dedication

To my mom for everything she does.

Acknowledgements

First and foremost I would like to thank my supervisor Dr. A. J. Knowles without him I wouldn't have had the opportunity to do this PhD. I would like to thank him for his continued support, guidance, and thoughts on the work that I have done. It has been an absolute pleasure to have worked with you.

To UKAEA/CCFE and in particular Dr Chris Hardie for their financial support and guidance provided through the CCFE-University of Birmingham doctoral research agreement. I would further like to take this opportunity to thank Dr Ben Poole and Dr Luke Hewitt for their help in collecting data.

To those who work at the University of Birmingham, I would like to give gratitude to T. Morris and Dr. L. Schneider at the CEM. To S. Cannon for his support and help with equipment. Also to Professor A. Mottura for his ever presence. To Dr. David Collins, and Prof. Yu-Lung Chiu for their guidance and pastoral support as mentors for the 4 years I was here.

And a special thanks to fellow PhD students Anastasia Vrettou and Paraic O'Kelly for their discussions and support.

I wish to acknowledge the support of the Henry Royce Institute for advanced materials for (NP) through the Student Equipment Access Scheme enabling access to AIP AIP8-45H and Fenn Rolling Mill facilities, as well as the SPS machine at The Royce Discovery Centre at the University of Sheffield; EPSRC Grant Number EP/R00661X/1 & EP/P02470X/1).

Contents

List of Figures

List of Tables

List of Abbreviations

ACI	Alloy Casting Institute
BCC	Body Centre Cubic
CCA	Complex Concentrated Alloys
CEIT	Centro Tecnológico Ceit
DBTT	Ductile to brittle transition temperature
EBSD	Electron Backscatter Diffraction
EDX	Energy-dispersive X-ray spectroscopy
FCC	Face Centre Cubic
HCP	Hexagonal Close Packed
HEA	High Entropy Alloy
MPEA	Multi-Principal Metal Alloy
OPS	Oxford Polishing Solution
PFM	Plasma facing Material
SEM	Secondary Electron Microscopy
SPS	Spark Plasma Sintering
TEM	Transmission electron microscopy
W-Cr	Tungsten Chromium
W-Mn	Tungsten Manganese
W-Ti	Tungsten Titanium

1 Introduction

The anticipated increase in the global population is projected to lead to a 48% increase in current energy consumption levels by 2040 (Administration 2023). Meeting future energy needs, particularly as non-fossil-fuel sources become increasingly essential, presents a challenge. Wind and solar power (and other renewable sources) are contingent on varying environmental conditions and are not a constant predictable supply. Additionally, there are technological hurdles in efficiently storing energy generated in this manner. Consequently, it is imperative to identify foreseeable and invariant energy sources to ensure a consistent energy supply and address unanticipated energy demands. Nuclear fusion holds the promise of being an efficient and reliable energy source that can address these concerns. Unlike fission, fusion does not grapple with issues related to the storage/processing of radioactive waste, and public perception.

However, before fusion reactors can become fully operational and economically viable, substantial research is required, particularly in the domains of plasma physics and reactor materials. The Joint European Torus (JET), currently the largest tokamak in operation, has demonstrated successful fusion reactor operation using a deuterium-tritium fuel mixture. Whilst JET primarily functions as a research platform to investigate plasma behaviour during fusion conditions, a new and ambitious fusion project known as ITER is currently under construction. ITER, boasting 10 times the volume of plasma of JET, is a collaborative effort involving multiple countries. ITER is set to commence power output in 2035 and is designed as the inaugural fusion reactor which will generate positive output of energy.

1.1 What is Nuclear Fusion?

Stars harness the power of nuclear fusion to convert matter (hydrogen and helium) into energy. Due to the extreme pressures and temperatures inside a star, hydrogen is stripped of its negatively charged electrons, leaving behind positively charged nuclei. This positive

charge will generally result in two atoms repelling each other. However, if the conditions are right (such as that of a star), the repulsion of the electrostatic force can be overcome if the distance between two nuclei is such that the attractive (nuclear) force prevails. The short-range or nuclear force is responsible for the binding protons and neutrons within the nucleus. In stars, due to the high pressures and temperatures, the kinetic energy of the hydrogen nuclei is such that they can travel at speeds sufficient to fuse nuclei, causing energy release. The gravitational forces of stars are sufficient to provide the necessary conditions for fusion; however, the lack of such forces on Earth means that to achieve the right conditions for the fusion of hydrogen (isotopes), extreme temperatures of approximately 150 million °C will need to be reached (Murphy 2021). This must be kept stable for prolonged periods under intense pressure to ensure the fusion of nuclei. Several hydrogen reactions occur in stars; however, the most feasible reaction that can be harnessed with current technology is deuterium (D) and tritium (T). At these elevated temperatures, the kinetic energy of both ions overcomes the electrostatic repulsion, and in so doing, they can fuse to produce helium and power in the form of heat, as shown in the equation below 1

$$ {}^{2}_{1}\mathrm{D} + {}^{3}_{1}\mathrm{T} \rightarrow {}^{4}_{2}\mathrm{H}e + {}^{1}_{0}\mathrm{n} + 17.6MeV \tag{1} $$

Unlike tritium, deuterium is very abundant and is found naturally in seawater. Tritium is only found in trace quantities naturally (although it can be made in conventional nuclear reactors); therefore, it must be produced as part of the reaction. The current proposed mechanism uses the neutrons produced as part of the reaction above to 'breed' tritium from a lithium blanket surrounding the reactor's core. The heat produced from the neutrons interacting with the breeder blanket can also heat a coolant around the blanket to generate electricity.

The fusion reaction outlined in Equation 1 produces 17.6 MeV of energy, divided across a neutron of 14.1 MeV and a helium nucleus (Bolt H 2004, ITER 2019*b*). Neutrons produced in this process are absorbed in a lithium blanket surrounding the reactor.

The blanket, often referred to as the "first wall," absorbs 85% of the energy produced from fusion. On absorbing a neutron, lithium is converted to tritium (Ley (May 2012), which is recycled as fuel for the reactor. A circulating coolant on the outside of the blanket captures the heat energy, enabling the production of electricity through conventional means. Impurities generated during the operation from erosion of the reactor components and most importantly helium (a waste product of the fusion reaction), must be purged to sustain the fusion reaction. The diverter, situated at the bottom of the vacuum vessel, is tasked with removing these unwanted ions (ITER 2019*a*), bearing the responsibility for exhausting approximately 15% of the power produced and potentially experiencing a thermal load of 10 – 20 MW/m $^{[2]}$ (Rieth 2013).

1.2 Experimental designs of reactors

At present, magnetic confinement and inertial confinement are the leading designs for a reactor. As the name suggests, magnetic confinement reactors employ Superconducting magnets to confine the plasma. The second, inertial confinement, compresses fuel as a pellet to smaller densities using lasers or particle beams.

The Tokamak reactor design is currently the leading prototype for magnetic confinement fusion (MCF) fusion reactors. This reactor employs toroidal magnetic fields, which constrain a plasma of temperatures up to 150 million Kelvin. The helium (and other particles that drift in the plasma) produced in this reaction must be removed. These particles will flow past the closed flux surface and into a region termed the scrape-off layer. The particles travel in an open flux until they reach the internal surface of the Tokamak (as shown in figure 1.1). In larger Tokamaks, a diverter plate collects the ash and the heat energy produced. The diverter plate, therefore, experiences extremely high-temperature fluxes. As a result, any material used to build a divertor plate is limited to those that can perform under extreme temperatures (high melting point) and have excellent thermal conductivity (Bolt H 2004).

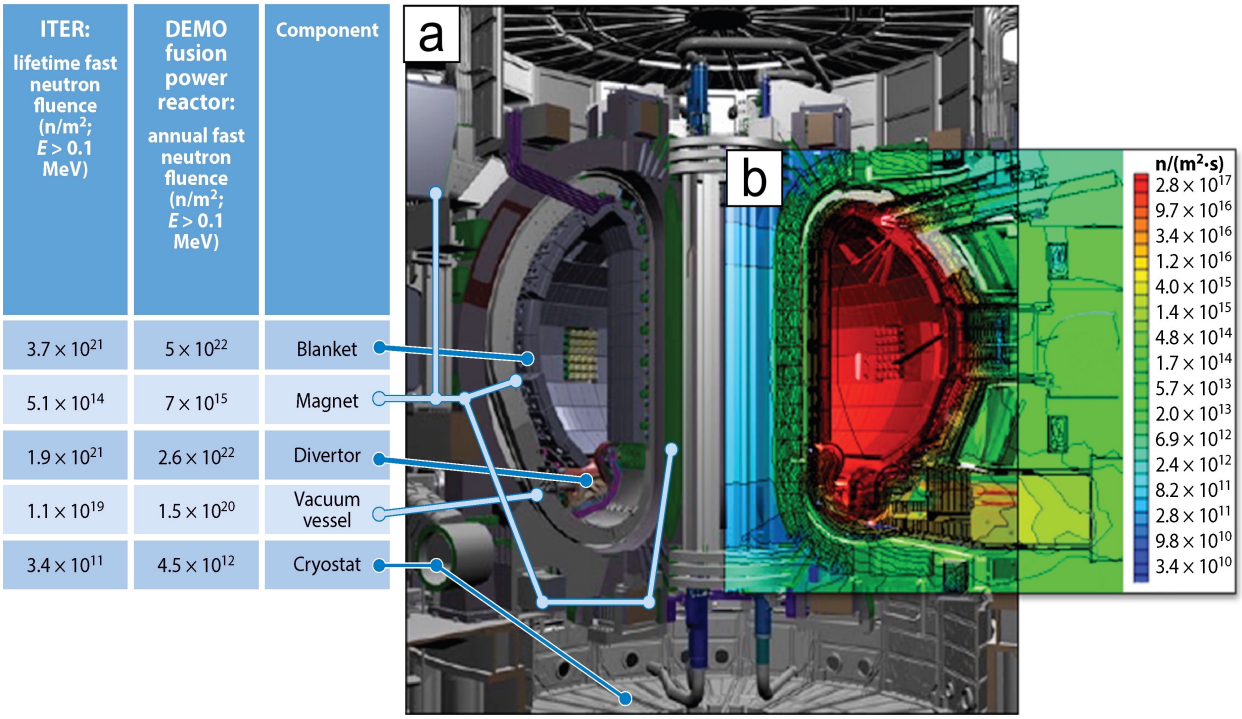

Figure 1.1: **Components of a fusion reactor with neutronics and cross-sections of the ITER tokamak.** Figure (a) shows a representation of the ITER tokamak, and inset figure (b) shows total neutron fluxes at certain positions in the reactor as based on calculations by R. Feder & M. Youssef. (Zinkle 2014)

Plasma-facing components will not only endure temperatures surpassing 900 °C but are also anticipated to bear substantial heat loads. Furthermore, high-energy neutrons will bombard any materials surrounding the plasma (Bolt H 2004). The interaction between neutrons and the crystal lattice results in the accumulation of defects due to the generation of a collision cascade (Yi 2013). This process may also induce transmutation, leading to the emergence of foreign elements such as rhenium, tantalum and osmium (Gilbert 2012, 2011). Surfaces which are exposed to a high fluence from the plasma will be permeated by helium and hydrogen (Gilbert 2012, 2011). At expected operating temperatures, the significant interstitial mobility of these gases enables them to migrate toward defects, cracks, or grain boundaries. Promoting both embrittlement and fortification (Broglie 2015). Plasma-facing components must exhibit particular key features to withstand the proposed operating conditions. Firstly, they should have a low activation to minimize the amount of radioactive waste (D 2019). It must also possess an operational

temperature range suitable for the specific reactor component. Thermal load, conductivity, and recrystallization determine the upper threshold. The brittleness (ductile to brittle transition), as well as response to irradiation damage, limits the lower end (Bolt H 2004). Tritium retention rate as well as the sputtering rate, (the pace at which plasma becomes tainted with worn-off materials) also influence the material choice. Ultimately, the material must demonstrate resilience and the ability to endure the impacts of radiation damage.

As well as damage caused by the heat flux, neutrons escaping the plasma will cause spluttering and subsequent erosion of the diverter plate. In addition, materials with higher atomic number (Z) will lose heat faster. To limit these losses and, therefore, the efficiency of the fusion reactor, either a low Z material (such as carbon) or a high sputtering energy material must be used.

With its high melting point, strength at elevated temperatures, and reduced sputtering yield (Bolt H 2004) tungsten emerges as a promising Plasma-facing material. However, it presents challenges due to an elevated brittle-to-ductile transition temperature (DBTT), low fracture toughness, and poor manufacturability (GUMBSCH 1998). The additional effects of neutrons and helium have the potential to limit the lifespan of tungsten as an armour material for fusion power (KL 1975)

Additional restrictions are placed on any material used by neutrons produced inside the fusion reactors (as shown in equation 1). Any neutrons produced are not held within the magnetic field. Therefore, they deposit some or even all of their energy into the structure of the reactor, displacing atoms and transmuting others. Therefore, any material used must have radiation resistance to reduce the chances of failure and legacy radioactive waste. The level to which an element (or elements) become activated depends on the isotope. Therefore, several elements are excluded from being used as a structural material. (Zinkle SJ 2009).

1.3 Materials currently considered for fusion reactors

Various structural materials have been explored; the leading candidates are presented in figure 1.2. The selection process involves evaluating their ability to endure high temperatures, neutron irradiation, and potential activation, seeking the most suitable candidates for fusion reactors. Figure 1.2 shows the operation temperature limits of each candidate material based on considerations of thermal creep as well as radiation damage. The dark horizontal bands represent the range of operating temperatures, while the lighter regions indicate the uncertainties in these limits.

For most materials, the temperature windows are wide ($\triangle$T=300–400 °C), allowing for the design of attractive blanket systems. However, CuNiBe is an exception due to its narrow operating temperature range close to room temperature. The specific functional temperature values must be combined with coolant compatibility data to assess potential reductions in the temperature window due to corrosion considerations.

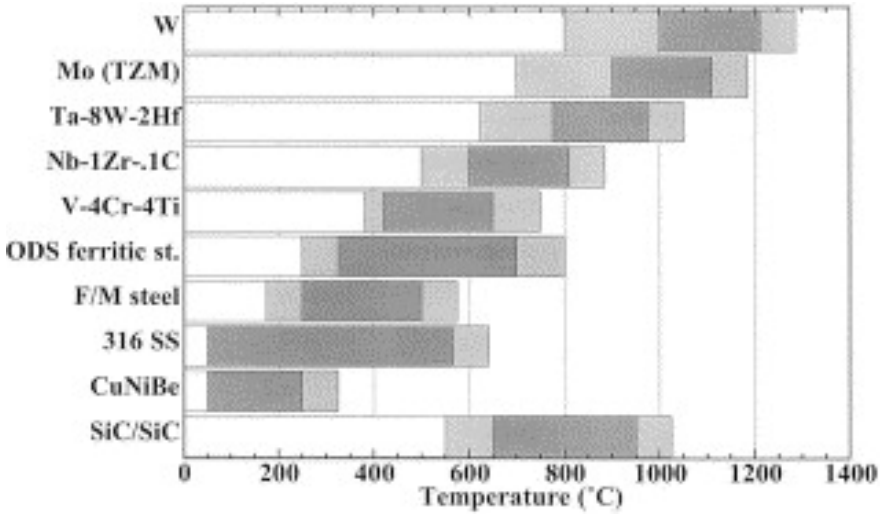

Figure 1.2: **Material selection.** Operating window of materials identified for fusion reactors (Zinkle 2000) (Light grey side bands represent uncertainties in the operating temperature)

Notably, the refractory alloys, such as Ta, Mo, and W alloys, have high minimum operating temperatures due to their inherent brittle nature (DBTT) at lower temperatures. This would mean that high-performance, materials such as Ni-based superalloys would

need to be used in certain parts of the reactor to bridge this gap. However, Nickel, unfortunately, not only has high thermal neutron absorption cross sections but long-lived radioactive isotopes, limiting its use in fusion reactors.

Certain factors, such as helium embrittlement and neutron irradiation, will dramatically affect the fracture toughness and induce radiation embrittlement, affecting these materials' upper and lower temperature limits. Further research and data are needed to establish more precise temperature limits, especially for some candidate materials' long-term and low-stress creep conditions.

Overall, understanding the operating temperature windows of these structural materials is crucial for designing effective fusion reactor systems while considering material properties, thermal creep, radiation damage, and coolant compatibility.

Although the D-T fusion reactors have been designed such that the neutrons produced in the fusion reaction will slow down and be deposited as heat in the first wall and blanket surrounding the plasma, these energetic neutrons will also cause extensive atomic displacements, leading to the degradation of material properties. The irradiation-induced microstructural changes can cause hardening and loss of tensile ductility. For fusion energy to be economically viable and safe, the design and production of materials that can perform at high temperatures and stress, high radiation resistance and reduced activation are needed.

Reduced-activation ferritic/martensitic (RAFM) steels are a proposed option, but their operating temperature limit is currently limited to around 550 ℃. Alternative materials such as Vanadium alloys and silicon Carbide composites are being explored to extend the temperature window. However, plasma-facing components pose additional challenges, as they must survive high heat and particle fluxes along with intense neutron irradiation. The materials selected for ITER, such as Be, carbon fibre composites, and W, are unsuitable for DEMO due to their irradiation instability and activation issues.

Due to limited testing facilities on offer, it is difficult to assess how these materials can perform. Generating experimental data in fusion reactors to mimic DEMO-relevant

conditions is crucial to advancing the production of suitable materials for future fusion reactors.

The microstructural evolution of irradiated materials depends on factors such as temperature, dose and damage rate, as well as the crystal structure and transmutant elements like hydrogen and helium. The temperature plays a crucial role in defining different microstructural regimes, and certain transition temperatures, known as stages I, III, and V, mark essential changes in defect behaviour.

Radiation-induced degradation induces rapid accumulation of defect clusters and leads to a reduction in mechanical properties due to embrittlement. Applying stress and transmutants can cause helium to collect at grain boundaries and cause intergranular embrittlement at high temperatures. At intermediate temperatures, void swelling, phase instabilities, and irradiation creep will define the operational window in which these materials can function.

Transmutant H and He gases can influence various degradation phenomena, and their generation affects material properties. However, quantifying their exact impact is challenging due to the constraints of modelling software and limited experimental facilities which can produce the operating conditions expected in a reactor.

1.4 Aims and Objectives

The principal aim of this thesis was to investigate the feasibility of bulk manufacturing tungsten-based alloys and to test their mechanical properties to replace current alloys used in the manufacture of diverter-type components. The following is a list of the objectives set out to be achieved in this thesis.

1. To determine the heat treatments needed to nanostructure a W-Cr through decomposition and explore the use of Spark plasma sintering to produce a bulk two-phase bcc W-Cr alloy.

2. To identify the decomposition mechanism behind the nanostructuring observed in the W-Cr.

3. A new recrystallization process is described in Ti-Fe-Mo through the formation of a (β + β') TiFe with considerable misfit to produce and characterise the alloy systems.

4. A series of W-TixFe alloys were produced to determine if a microstructure consisting of a tungsten matrix reinforced with TiFe (β + β') precipitates could be produced.

5. To produce a W-Ti alloy through decomposition into a two-phase bcc alloy and thermomechanical rolling. Then to test the DBTT of these alloys through 3-point bending.

6. To produce a single phase tungsten W-V-Cr-Ta quaternary or W-V-Cr-Ta-Ti quinary Refractory High entropy alloy through arc melting and subjected to thermal ageing at 1400 °C to investigate the stability of those phases.

1.5 Structure of the thesis

This thesis begins with a literature review (Chapter 2) of tungsten as a potential structural material for fusion reactors as a plasma-facing component and the environmental conditions that it will be exposed to. The review also covers the mechanical properties of tungsten and the methods that have been employed to improve its ductility. Chapter 3 covers the experimental methods employed to generate the results in this thesis. Chapter 4 addresses objective 1 and describes the work to design and manufacture a bulk sample of tungsten-chromium that has a two-phase nanostructure by exploiting the miscibility gap within the binary phase diagram. It covers several manufacturing methods including arc melting, powder manufacture, HIPping and spark plasma sintering. Chapter 5 investigates the physical phenomena behind this decomposition pathway (objective 2) that leads to the microstructure observed in Chapter 4. Following on from the work and methods used to gather the results in the previous chapter. Chapter 6 looks at the recrystallization process seen in a Ti-Fe-Mo BCC superalloy (objective 3) and uses a pseudo-insitu EBSD technique and SEM/TEM to explore the strain-induced mechanism behind the TiFe β' precipitates and the β molybdenum matrix (objective 3). Chapter 7 looks at the prospect

of using TiFe β' precipitates with a tungsten matrix as a reinforcing mechanism to improve the mechanical properties of tungsten (objective 4), it also explores the manufacture of a tungsten-heavy alloy with titanium and uses heat treatments and rolling to improve the ductility of this alloy (objective 5). High entropy alloys have been identified as having high strength, hardness, wear resistance, thermal stability, and corrosion resistance. Chapter 8 looks to produce two tungsten-based high entropy alloys; a quarterny WVCrTa and a quinternary WVCrTaTi. Following their manufacture thermal ageing of temperatures up to 1400 °C was used to investigate the stability of phases present within the alloys. The thesis then concludes with chapters 9 and future work chapter 10.

2 Literature Review

2.1 Tungsten's use as a plasma-facing component

Tungsten's proposed use as a plasma-facing component has many advantages over other materials. Specifically, having tungsten facing the plasma will enable any divertor plate constructed from this material to be directly cooled, reducing the need for cooling joints and extra support material. Additionally, conventional manufacturing methods, cold rolling and thin lamination are known to improve the DBTT property of tungsten (Gonderman S 2016). However, the downside to using tungsten as a structural material is its brittleness, which is attributed to reduced close-packed planes and poor grain boundary cohesion. Plastic deformation relies on $\frac{1}{2} < 111 >$ screw dislocations, causing significant Peirels stresses (Groger A 2008), limiting deformation and resulting in brittleness (Cheng W 2013). Intergranular fracture is the dominant failure mode (>95.9%) in pure tungsten, backed by computer models. Grain boundary impurities (oxygen, potassium, carbon, phosphorus) may worsen brittleness, but Gludovatz et al. found that high-purity tungsten also exhibits intergranular fracture without impurities. Tungsten's properties make it promising for fusion reactor applications, but further research is needed to understand its behaviour in extreme conditions, namely the reasons behind its ductile to brittle transition.

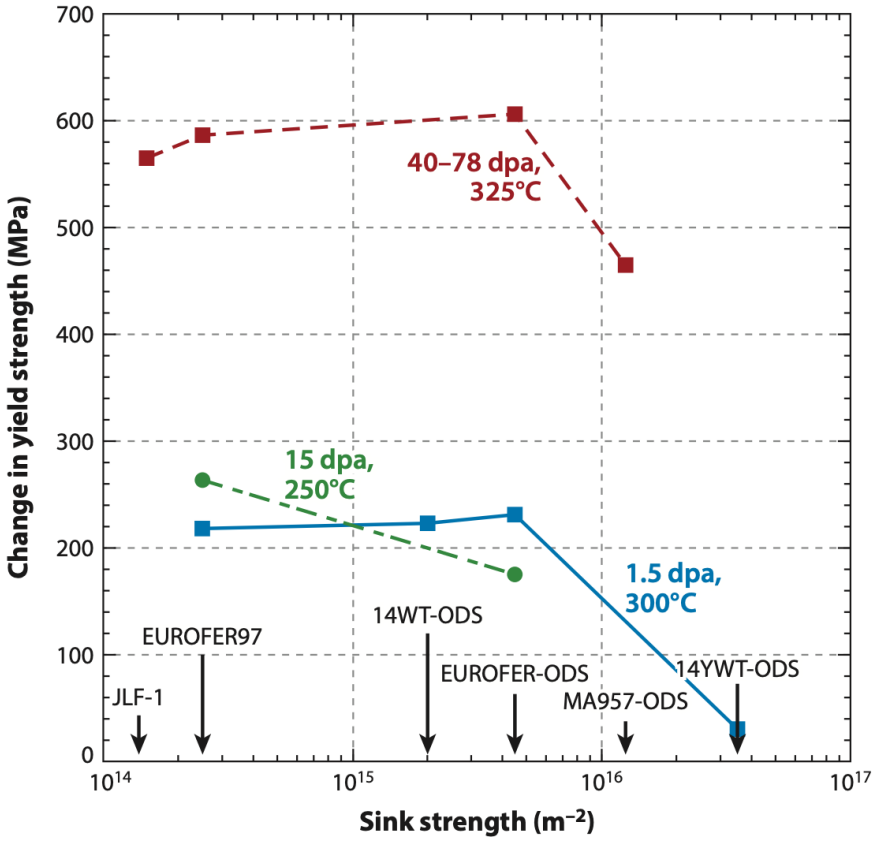

Figure 2.1: **Radiation hardening and initial sink strength.** The graph shows the change in yield strength of different steels at different temperatures following irradiation by fission neutrons with a displacement per atom (dpa) of between 1.5 to 78 following fission neutron irradiation. (Zinkle 2014)

2.2 Tungsten and the effect of Radiation Damage

2.3 Tungsten in a fusion environment

Tungsten is proposed as one of the candidate materials for a fusion reactor. In addition to the considerable heat flux inside a reactor, any tungsten present as a plasma-facing material (PFM) will have to perform in the presence of neutrons resulting from the fusion process (equation 1). These neutrons emerge from the plasma with energies in the region of 14.1 MeV since the magnetic field does not constrain them. When neutrons interact with any matter (whether tungsten or material, for that matter), they cause damage (displacement) and transmutation of elements. Each neutron that enters tungsten will pro-

duce a damaging cascade, leading to an excess production of interstitials and vacancies. The longer any component is near this neutron flux, the greater the number of interactions that will occur. This will result in greater displacements per at (termed dpa). Additionally, the damage caused by neutrons also produces transmutations in metals. Both events lead to microstructural changes, altering tungsten's mechanical and thermal properties.

2.3.1 Neutron transmutation of tungsten

Tungsten is transmuted mainly into three elements: rhenium, osmium, and tantalum (Gilbert MR 2011). In addition to these transmuted elements, there is a noted build-up of helium and hydrogen. The formation of rhenium helps improve tungsten's ductility (as discussed) (Leonhardt T 2009). However, if rhenium reaches concentrations of over 30 wt% before brittle phases, χ and σ form. Osmium lowers the formation energy of these two intermetallic phases. Therefore, any transmutation to osmium will lead to radiation-induced segregation in tungsten and increased production of brittle phases (Tanno T 2008*a*).

At the high temperatures experienced inside the reactor, helium can diffuse directly into tungsten (and any other metals present), as it enhances voids (bubbles) formation and eventual blistering of the surface (Yoshida N 1999).

2.3.2 The effects of Neutron Irradiation on Tungsten

In the 1950s, initial experiments on the impact of neutron irradiation on tungsten and other refractory metals were focused on assessing tungsten's electrical conductivity after irradiation in thermocouple devices used in fusion reactors (Keys LK 1970, Matolich J 1974, Williams RK 1983). The neutron energies in these early studies were considerably lower than those in fusion reactions.

Studies examined void formation, recovery stages, and phase precipitation in tungsten-rhenium alloys due to irradiation (Keys LK 1970, Matolich J 1974, Williams RK 1983). Radiation-induced segregation and the presence of χ intermetallic precipitates were observed (Williams RK 1983). However, the exact mechanisms remain uncertain, and recent

experiments have shown discrepancies in the results (Gleiter H 1981).

Neutron irradiation induced voids and dislocation loops in pure tungsten samples, with void size increasing linearly with temperature (Tanno T 2008*b*). Tungsten containing higher rhenium or osmium levels showed reduced void formation but more precipitates (Tanno T 2008*b*). The presence of rhenium suppresses void formation, but above a certain dose, the beneficial effects diminish (Tanno T 2008*b*, Hasegawa A 2011).

Irradiation affects tungsten's hardness, with significant hardening observed in both pure tungsten and tungsten-rhenium alloys at various temperatures and irradiation levels (He J 2006, Tanno T 2008*b*). Rhenium content and osmium presence significantly impact the hardening behaviour (Tanno T 2008*b*).

Tungsten becomes embrittled after neutron irradiation due to the loss of grain boundary strength (Tanno T 2007). The ductile-brittle transition temperature (DBTT) gets higher with irradiation, but results may be influenced by the testing method (Tanno T 2007).

Limited research exists on the effects of low fluence radiation on pure tungsten, with most studies conducted on tungsten-rhenium binary alloys (Steichen JM 1976, Krautwasser P 1995). Results show increased DBTT with neutron irradiation at various fluence levels and temperatures.

Overall, more research is needed to fully understand the effects of neutron irradiation on tungsten and optimize its use in fusion reactor applications.

2.3.3 Generation of defects in Tungsten

When exposed to particle bombardment, such as neutrons, the regular crystal lattice of a material undergoes disruption. These impacting particles displace atoms from their original positions, resulting in the formation of primary-knock-on atoms (PKAs). These PKAs, in turn, induce further displacements within the lattice, initiating a cascade of damage (as depicted in Figure 2.2). The space left vacant by the now-removed atom is termed a vacancy defect. Where the atom itself, now located in an interstitial space, is referred to as a self-interstitial atom (SIA). The displaced atom and the SIA are referred to as a Frenkel

Pair.

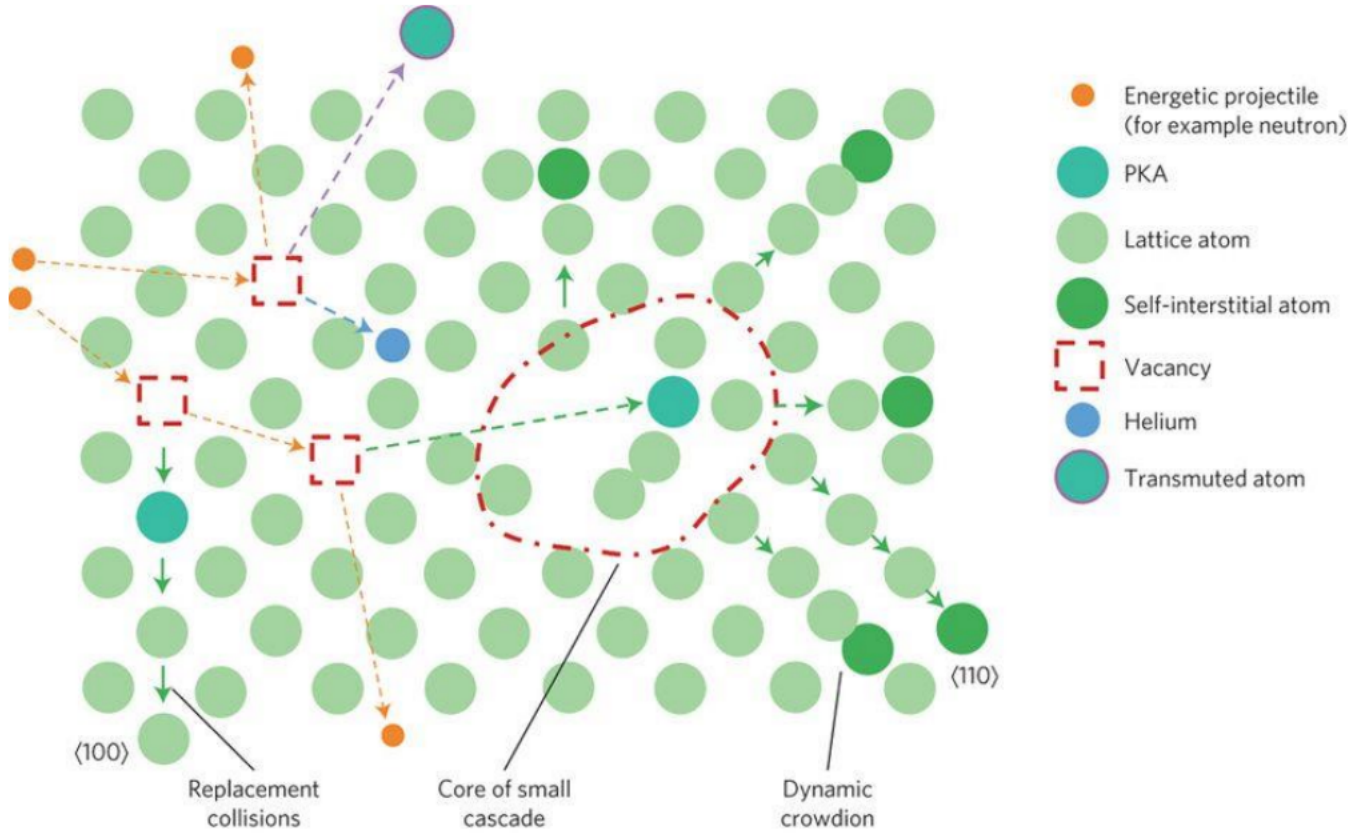

Figure 2.2: **The effects of irradiation damage** Schematic diagram of the effects of irradiation damage on the atoms which make up a lattice. (Williams RK 1983)

The quantification of radiation damage is commonly expressed as the number of displacements per atom (dpa). It's important to note that a significant portion of the atomic displacements tend to normalize over time, leaving only a fraction of them intact in the material. For example, in the case of helium implantation into a material, approximately 1% of the initial dpa remains long-term (Hofmann 2015*b*).

Inside a reactor, tungsten will primarily experience irradiation from both high-energy neutrons and helium coming from the plasma. Furthermore, gaseous elements generated through transmutation will interact with the defects induced by irradiation.

2.3.4 The effects of fusion neutrons on Tungsten

Apart from point defects, neutron irradiation triggers the creation of dislocations, disrupting the orderly alignment of atoms along a line. The destiny of these defects hinges on their density and mobility, leading to various potential outcomes: including annihilation at grain boundaries, absorption by defect clusters, annihilating each other, or enduring within the material. When these irradiation-induced defects persist, they serve as impediments for dislocations, causing an increase in the Brittle-to-Ductile Transition Temperature (BDTT). Vacancies can accumulate and give rise to voids, the size of which may fluctuate with dosage.

Troev et al. employed molecular dynamics simulations to estimate radiation damage resulting from displacement cascades in neutron-irradiated tungsten. For a neutron fluence of 2.5 × 10^{22}n/cm^2, they calculated a damage level of 2.85 displacements per atom (dpa) in tungsten per Full Power Year (FPY). In the early stages post-irradiation at energies below 100 keV, the volume of interstitial defects was twice as large as the vacancy volume. The defects included single and di-vacancies, interstitials, and interstitial clusters with more than three atoms. Given the fact that reproducing reactor conditions is currently impractical, alternative methods are needed to experimentally study the damage caused by fusion neutrons. Irradiation fission neutrons can be utilized to simulate fusion neutron damage, although compatibility issues between the spectrum energy and resulting microstructural damage between fission and fusion neutrons exist.

A comparison of several neutron irradiation facilities: IFMIF (intense stripping neutron), ESS and XADS (spallation sources), DEMO (prototype reactor), and HFR-8 and BOR60 (fission reactors). A comparison of neutron spectra from these facilities revealed that the only facility to match that of DEMO was the IFMIF spectrum closely resembled that of the (Figure 2.3a). HFR-8's spectrum matched well with that of the DEMO spectrum (Below 5 MeV) but was approximately a fifth of the value. However, above 5 MeV, the fusion spectrum did not match that of DEMO showing a lack of knock-on atoms (high-energy).

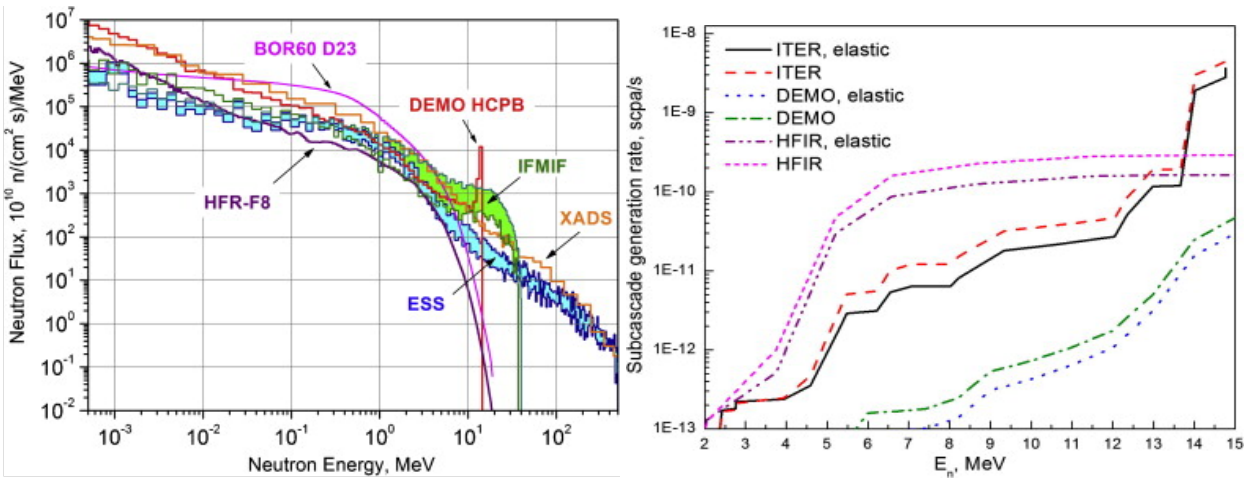

(a) (b)

Figure 2.3: **Neutron fluxes and their effects on tungsten**(a) A graph to show the neutron spectra for the blanket of a fusion DEMO reactor, from different neutron sources including IFMIF (Nemoto YY Hasegawa A Satou M Abe 2000) and (b) The calculated rates of sub-cascades for tungsten for elastic and inelastic nuclear channels (Dewald 2011)

The energy of primary-knock-on atoms (PKAs) plays a crucial role in shaping the morphology of cascade damage (Sekimura 1996). Once the PKA energy exceeds a certain threshold, cascades can bifurcate, leading to added complexity in the microstructure. The generation of sub-cascades is contingent on R (the radius) of the zone of damage caused by a secondary knock-on atom (SKA), which arises from elastic collisions (Ryazanov 2009). If the distance of two separate collisions when averaged (λ(E)) is more than the radius, a sub-cascade forms (Ryazanov 2009). Tungsten irradiated in HFIR, with neutron energies of less than 1 keV, the rate of sub-cascade generation is over twice that as seen in DEMO and ITER (Figure 2.3b) (Ryazanov 2011). A model based on the Monte Carlo binary collision approximation revealed that high-energy cascades primarily result in smaller defect clusters. Whilst a greater number of defects and defect clusters are seen in low-energy sub-cascades (Backer 2016). Consequently, an overestimation of the damage caused by fusion neutrons due to the high sub-cascade generation rate. Neutron irradiation also transmutes elements yielding gaseous elements. However, there are differences in the quantities of hydrogen and helium produced in tungsten when subjected to the same level of fluence in either fission or fusion environments. For a neutron fluence

of 10^{23}n/cm^2, in side HFIR fission neutrons generated only 0.0008 appm/dpa of helium. In contrast, 0.6 and 0.5 appm/dpa of helium were produced by magnetic confinement (MFE) and inertial confinement fusion (IFE) respectively (Sawan 2012). Similarly, the hydrogen production by fission neutron irradiation (0.003 appm/dpa for HFIR) was lower compared to that produced by MFE and IFE (1.8 and 1.2 appm/dpa respectively). Additionally, fission neutron irradiation renders materials radioactive, making them unsuitable for routine handling and laboratory experiments.

Transmission electron microscopy (TEM) of tungsten, which has been subjected to varying ion-irradiation damage levels, has yielded valuable knowledge of the way defects evolve as well as the number and characteristics of neutron-irradiated reactor components as a comparison of dosage (Yi 2013). Yi et al. investigated tungsten and W–5 wt.% rhenium following 150 keV tungsten-ion irradiation at 500 ℃, with fluences ranging from 10^{16} to 10^{18} W/m^2 and an irradiated layer approximately 25 nm thick. Primarily half vacancy loops appeared at below 0.01 dpa (Yi 2016). Then at doses of 0.1 - 1 dpa, migration of defect clusters with elastic loop interaction was seen, with loop density becoming saturated at around 10^{15} loops/m^2. In both pure tungsten and W-5 wt.%Re alloy, the majority of loops exhibited an a/2 Burgers' vector, with approximately 25% having a different Burgers' vector. Nano-indentation and micro-cantilever tests can be used to assess the impact these loops have on the mechanical properties of tungsten. At 300 ℃ tungsten implanted with 2 MeV ions, tested by nano-indentation demonstrated that above 0.4 dpa (0.8 GPa or 11% increase in hardness) the hardness saturates (Figure 2.4a) (Armstrong 2013*b*). Additionally, the density of the loop was observed to max out between 0.4 – 33 dpa (Armstrong 2013*b*). At higher temperatures, tungsten, implanted by self-ions shows an elevated hardness. Tungsten self-ion implated at 800 °C to 2 dpa, micro-cantilever bending tests (5 nm/s) (Figure 2.4b) showed an increase in hardness of approximately 20% (Gibson 2014). Transmutation of elements by fusion neutron irradiation is also observed with the production of rhenium, osmium, and tantalum (Gilbert 2011).

To investigate the transmutation effect that these elements have on tungsten, a tung-

sten alloy can be investigated under ion-irradiation and the cascade effects can be seen. Nano-indentation studies of tungsten at 300 °C show hardness saturation beyond 0.4 dpa. This is compared to self-ion implanted W-5wt.% rhenium samples showing an approximate 13% increase in hardness up to 1.2 dpa, followed by further increases of 20% at 13 dpa and 40% at 33 dpa (Figure 2.4a) (Armstrong 2013*b*). These significant hardness increases are believed to be induced by the formation of rhenium clusters, which could serve as initiation sites for the formation of sigma phase (Armstrong 2013*b*). Tungsten-5wt.% Ta alloy, however, shows a different hardness profile. At 0.07 dpa hardness is increased substantially by 21%, between 0.07 and 13 dpa hardness increases by less than 14% beyond 13 dpa the hardness saturates (Armstrong 2011). Additionally, pile-ups around Berkovich indents in these samples, have been observed for damage levels of 0.07 dpa and 1.2 dpa, in contrast with the significant pile-up seen around indents in un-implanted samples (Armstrong 2011). A plausible explanation for these observations is yet to be investigated. In summary, lattice defects in tungsten as a result of cascade damage lead to substantial increases in hardness, attributed to a microstructure dominated by loops. Alloying elements are found to exacerbate the effects of radiation damage.

However, the mechanisms governing the interaction of induced defects (primarily loops) with gliding dislocations, as a function of dose and temperature, warrant further investigation. Given the expense and time-consuming nature of neutron irradiation, ion irradiation presents a hindrance to studying damage cascades. Predictive data obtained from material irradiated with ions (or fission neutrons) cannot be extrapolated to give information on fusion.(Garner 1990). More information about the recoil spectrum of PKAs, transmutation, and displacement rates needs to be thoroughly analysed. Additionally, the effects of environmental parameters need to be considered if it is to be applied to the design of fusion devices.

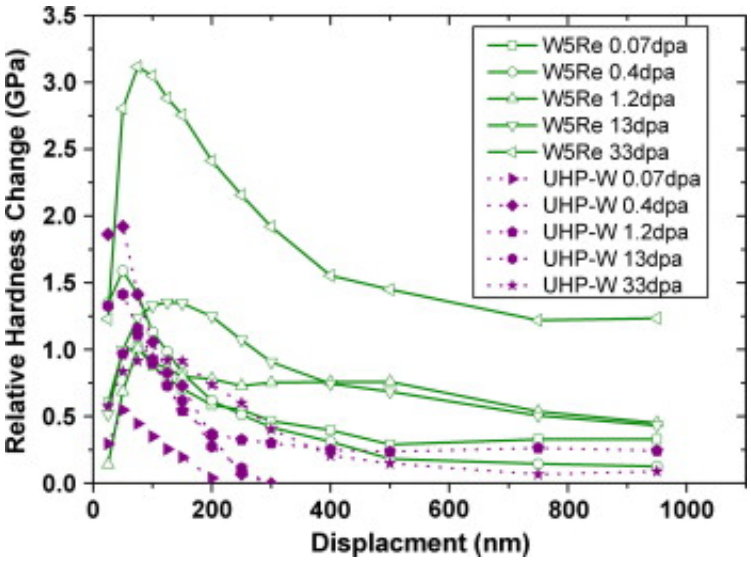

(a)

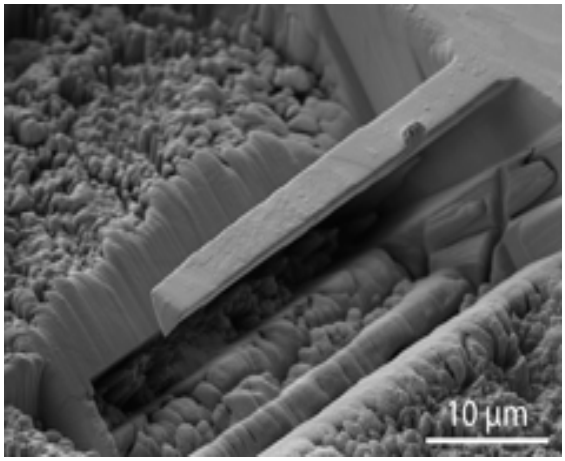

(b)

Figure 2.4: **Hardness increases in UHP-W and W-5% Re**(a) Graph shows the changes in relative hardness (GPa) compared to depth as a result of 0, 0.07, 0.4, 1.2, 13 and 33 dpa. (Armstrong 2013*b*)(b) A SEM image of the typical cantilever produced by FIB - Focussed ion beam used for mechanical testing of irradiated tungsten (Kuhn B 2011)

2.3.5 The effects of helium and hydrogen on tungsten

It is expected that after five years at full power, the amount of helium and hydrogen that evolved from the bombardment of tungsten with neutrons will be 34 and 76 appm, respectively (Gilbert MR 2011). Although this is a significant concern, the most worrying factor is the exposure of the tungsten surface to the plasma, which results in ion implantation of high-flux helium. This produces what is known as a tungsten fuzz (Baldwin MJ

2010). The impregnation of helium into the tungsten will ultimately interact with the radiation damage. Tungsten fuzz was first identified in 2006 (Takamura S 2006); it has been observed experimentally and in plasma devices on several different grades and alloys of tungsten (Baldwin MJ 2010). To form the fuzz required, the helium flux must exceed 10^{24} m^{-2}, and the temperature must be above 1000 K. TEM studies have observed the helium to accumulate in clusters and then grow and enlarge into bubbles. Those bubbles with proximity to the surface burst, causing the surface to look fuzzy (Miyamoto M 2014, Sefta F 2013). As mentioned earlier, the spluttering effect is a significant concern of fusion reactors. Observing fuzzing at the surface of tungsten could increase the amount of spluttering of tungsten and, therefore, more substantial plasma contamination. However, it has been observed that fuzzing reduces the effect of spluttering (Nishijima D 2011).

2.3.6 The effects of hydrogen from the plasma

Hydrogen retention (including isotopes) in tungsten is low, especially at doses below 10^{22}ions/m^2 (Iwakiri 2002). Experimental thermal desorption studies have indicated that most of the deuterium is released between 400 and 600 K (Iwakiri 2002). Density functional theory (DFT) modelling of the H-H bond, has predicted that it is unstable at small interatomic distances. Therefore for hydrogen to be retained in tungsten and form bubbles or blisters defects must be present (Becquart 2012).

Helium presence within defects in tungsten can influence the retention capacity of deuterium. Iwakiri et al. conducted an experiment where room temperature tungsten was first irradiated with 8 keV helium, then 8 keV deuterium at various temperatures (ranging from 300 to 673 K) (Iwakiri 2002). The study found that at 473 K, with a high dose of helium (2×10^{21}. ions/m^2.), a significant number of small helium bubbles formed effective trapping sites for deuterium. Consequently, deuterium trapping was three times higher compared to samples not pre-irradiated with helium.

The retention of deuterium undergoes alterations in the presence of defects induced by neutron irradiation. While the desorption spectra of deuterium (depicted in Figure 2.5)

revealed a single prominent peak at 550 K for pure tungsten, an additional peak emerged at 450 K in ion-irradiated tungsten (at 0.025 dpa). This is likely attributed to trapping of deuterium with different activation energies (Oya 2011). The author suggests that a third peak at 900 K is explained by the deuterium being trapped within the bulk of the material due to defects induced by neutron irradiation, as opposed to ion-irradiation defects being localized to the surface.

Trapped hydrogen can lead to a reduced pop-in load and an increase in hardness (with a maximum increase of 0.5 GPa), as observed in nano-indentation experiments on tungsten exposed to deuterium plasma at 443 K, with an incident ion energy of 35 eV and an accumulated fluence of 8.1 × 10^{25} ions/m^2 (Fang 2018). Similar findings of increased hardness were reported by Terentyev et al. (Terentyev 2016) and Zayachuk et al. (Zayachuk 2017) in tungsten exposed to deuterium plasma.

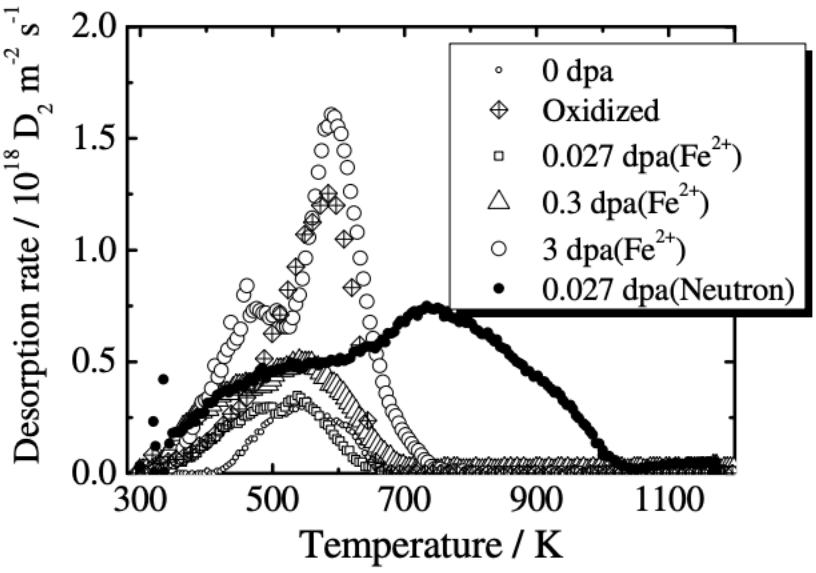

Figure 2.5: **The deuterium thermal desorption spectroscopy (TDS) of tungsten** Graph shows the deuterium desorption spectra of tungsten irradiated with Fe^{2+} (Oya 2011)

2.3.7 Helium and radiation damage in tungsten

It has been demonstrated via density functional theory (DFT) modelling that helium in tungsten interacts strongly with vacancies produced by radiation damage. The modelling

suggests that helium favours the formation of bubbles and voids. It must be noted that the evidence for this is, at present, limited. Tungsten irradiated to 13 dpa, then implanted with helium to 3000 appm at 573 K, demonstrated higher hardness due to helium embrittlement. However, there is a limit to the overall effect that helium has on hardness as the results suggest helium becomes encapsulated within the radiation damage, negating its contribution to further hardening (Armstrong DEJ 2013). Experiments at higher temperatures, 673 K and higher, significantly reduce the hardening effect of helium implantation (Gibson JSK 2015). At the time of writing this, no work has been carried out on the results of the irradiation of tungsten and its impact on the DBTT of tungsten.

2.3.8 The effects of Helium from the plasma

Helium formation through transmutation in tungsten is minimal, and it would take more than 300 years for any significant embrittlement due to transmuted helium (Gilbert 2012). Therefore, the primary source of helium will be from implantation during fusion plasma exposure. The damage induced by helium in tungsten is intricate and varies depending on fluence, implantation energy, temperature and amount of retained helium. Helium tends to be more effectively retained in polycrystalline tungsten compared to single crystals, as grain boundaries act as trapping sites, whereas the absence of these in single crystals allows for helium to diffuse during annealing (Hashimoto 2005).

At smaller separations, helium-helium binding is strong, enabled by pure elastic interaction, facilitating the formation of stable helium clusters in a crystal free from defects. As interstitial helium clusters grow, they displace metal atoms from their lattice positions to alleviate the pressure generated by the helium atoms. This process results in the formation of Frenkel pair defects, known as trap mutation. Helium also interacts strongly with other defects such as vacancies, vacancy clusters, and impurities, with the helium-vacancy bond being particularly robust (YANG 2009). DFT calculations have shown that mobile vacancy clusters, which disintegrate at fusion temperatures, are stabilized by helium atoms, reducing the vacancy emission rates (Becquart 2012). This helium-vacancy

bond not only immobilizes vacancies but also influences how voids form as a result of ion irradiation. Studies have found that in the presence of helium (0.25 keV at 10^{22} He+ /m^2) interstitial loops formed from Cu+ implantation in tungsten (at 2.4 MeV to 3 dpa) nearly vanish (Yoshida 2005). Below 873 K as a result of their low thermal migration, helium vacancy complexes form dense fine helium bubbles through the absorption of greater quantities of helium. As the quantity of helium bubbles grows, there is an increase in the lateral stresses. These stresses as a result of the stress build-up cause pressure to build up within the layer of bubbles. The bubbles may then fuse by a process called an inter-bubble fracture, leading to blister formation (Yoshida 2005, Evans 1977).

As the temperature rises to between 1073 K – 1273 K, helium bubbles and vacancies begin to migrate thermally, forming larger helium bubbles (Yoshida 2005). At these temperatures if helium fluence increases, 'nano-fuzz' structures can evolve from these larger bubbles (TAKAMURA 2006), (Baldwin 2008) (Figure 2.6).

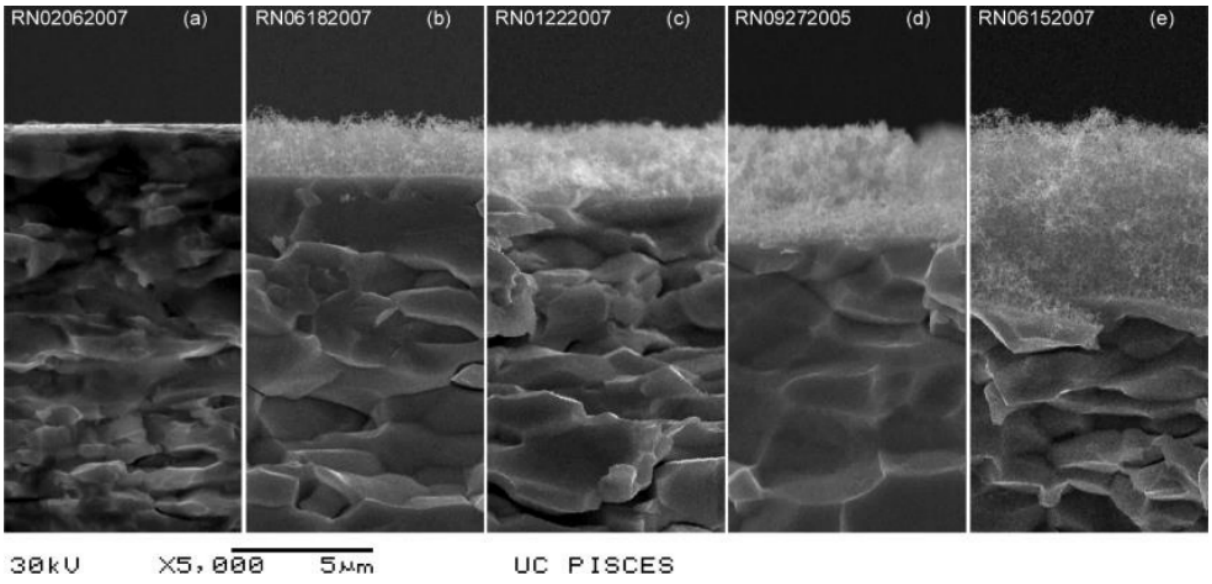

Figure 2.6: **The appearance of tungsten following exposure to Helium** SEM (Cross-section) images of tungsten samples exposed to pure He plasma for times of (a) 300s, (b) 2000s, (c) 4300s, (d) 9000s and (e) 22000s at a temperature of 1120 K. For changes in plasma properties please see original reference. (Baldwin 2008)

Changes in the surface of tungsten can result from even the implantation of low-energy helium ions. Surface pores have been observed in tungsten implanted with helium at

energy levels as low as 10 eV at 1600 °C and at 800 °C 19 keV helium has been shown to form large blisters (Sharafat 2009). Additionally, Sharafat et al. noted that between 730 °C and 1160 °C helium ions at fluences of 3 × 10^{22} m^{-2} and energy of 30 KeV, produced large helium bubbles and surface pores from prior vacancies (with lower densities at higher temperatures), ranging in diameter from 15-150 nm (with increasing diameter at higher temperatures) (Figure 2.7) in tungsten. At a fluence of approximately 10^{23} He/m^2 30 keV helium at temperatures ranging from 500-900 °C have also been shown to produce layers of subsurface semi-porous in polycrystalline tungsten, extending up to 1000 nm below the surface (Zenobia 2012).

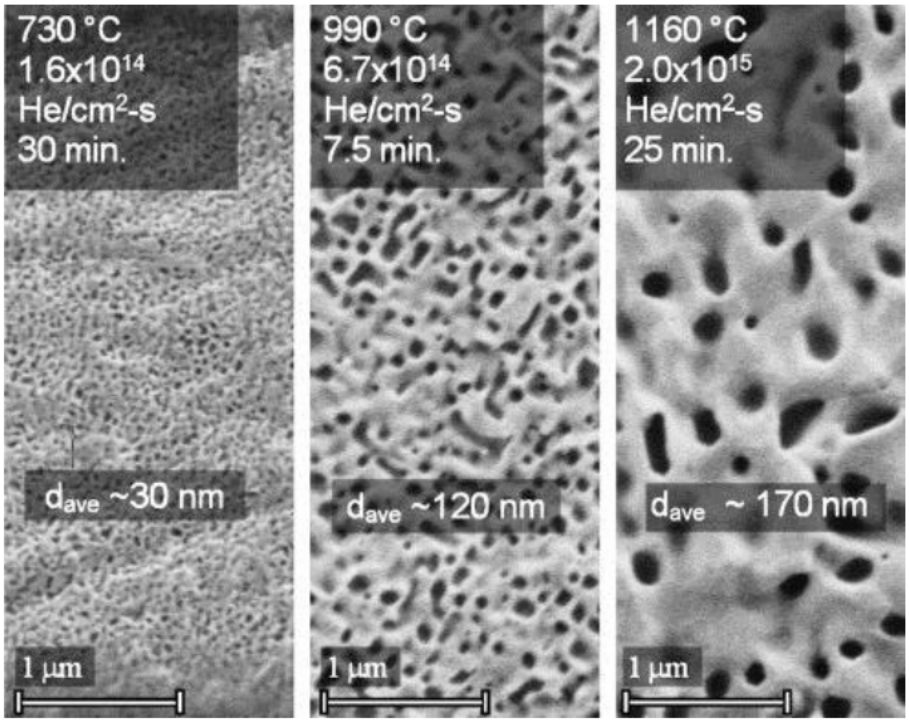

Figure 2.7: **The effects of Helium on the tungsten at varying temperatures** SEM images of the surface of tungsten following 30 keV He implantation at different temperatures. (Barton 2019)

The deformation behaviour of tungsten is significantly affected by the interaction of helium defects. Nano-indentation of tungsten that has been implanted with 600 appm of helium at 523 K demonstrated a hardness increase (150 and 400 nm average depth of penetration) of approximately 55%. However, a significant increase in hardness was observed above 700 K (Figure 2.8 (c)). At room temperature helium-induced defects

(few-atom-large V and SIA clusters), created even by low doses of 0.3 at. wt.% helium produces a significant increase in tungsten's hardness and embrittlement. At 300 K, 0.3 at.% has been shown to lead to a 30% increase in hardness (Hofmann 2015*a*). Furthermore, in contrast to the suppressed pile-up observed around indents in self-ion-implanted tungsten (Armstrong 2011), Berkovich nano-indents in W-0.3 at.% He (implanted at 300 K) showed a significant pile-up at depths around 250 nm (Figure 2.8 (a)-(b)) (Beck 2017). This suggests that the mechanism of how dislocations and helium defects interact at depths differs from that with defects induced by self-ion implantation. However, a comprehensive understanding of

how helium defects and glisile dislocations interact is still to be eluded. This is primarily because helium defects at room temperature, fall outside the sensitivity of transmission electron microscopy (TEM) (1.5 nm defects and smaller are not accurately detected) (Armstrong 2013*a*, Wenwang 2018). An alternative approach to investigate such defects is to determine the lattice strains they induce. Micro-Laue diffraction of W-1at.%Re implanted with 3110 appm helium at 573 K demonstrated significant lattice swelling of 1.5 $\times$ 10^{-3} (out-of-plane) strain (Hofmann 2015*c*). Increasing the temperature to 1473 K, led to lattice strain being measured beyond the implanted layer, suggesting that thermal activation increases the migration of helium defects further into tungsten (Broglie 2015).

2.3.9 Radiation sinks

Any material's ability to resist radiation depends on its ability to annihilate radiation damage. The rate theory model of radiation resistance states that sink strength is a measure of the efficiency of an interface to annihilate a defect (Millett PC 2009). Therefore, the greater the sink strength, the more defects produced by radiation damage will be eliminated. Figure 2.1 shows the change in yield strength of different steels following fission neutron irradiation. The graph shows that ODS steels have the greatest potential; therefore, nano-structuring offers advantages for operational use in a fusion reactor. One way of producing a nano-structured microstructure other than precipitation can be produced

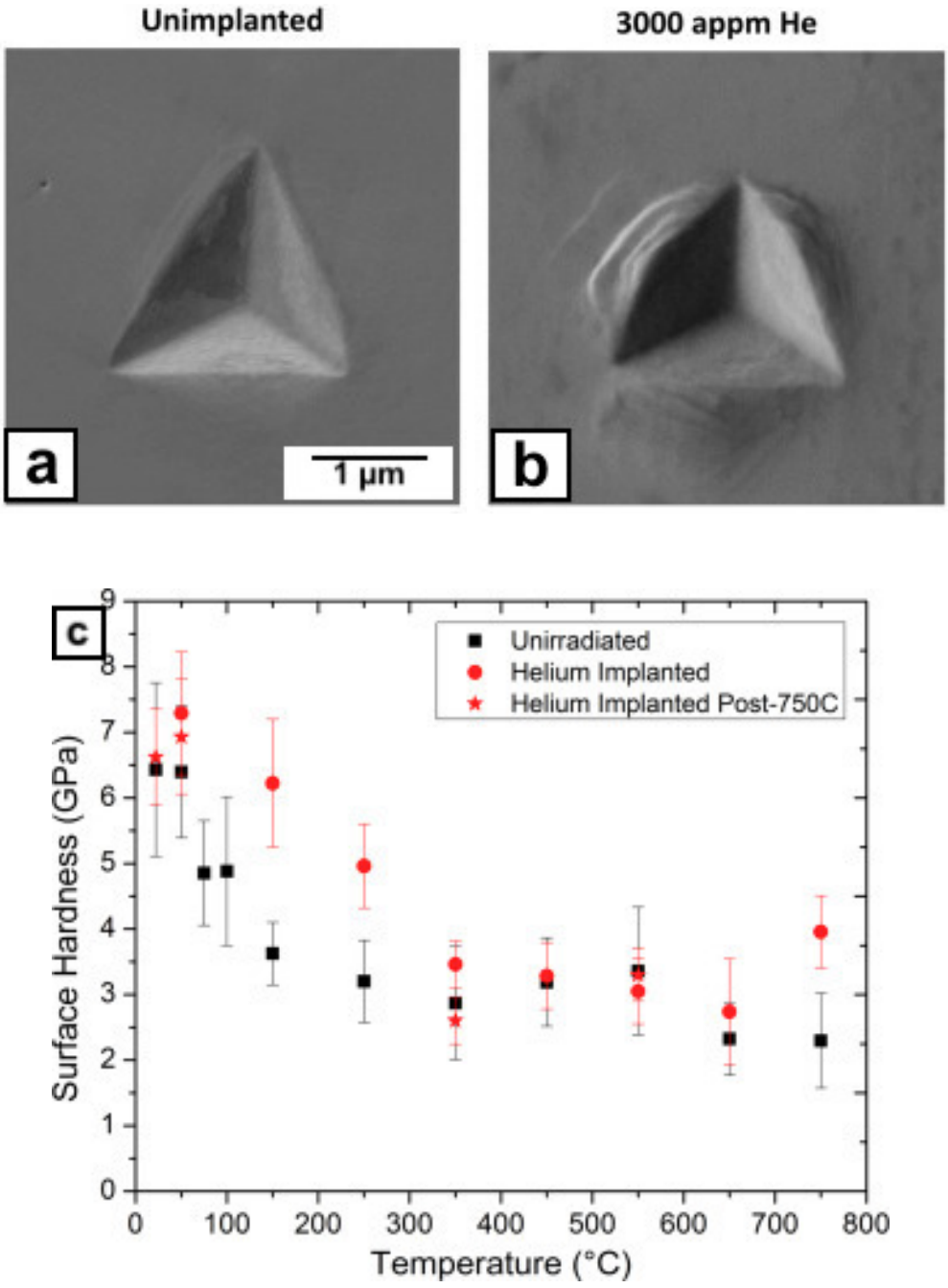

Figure 2.8: **Nano-indentation hardness tests of tungsten before and after exposure to helium** (a)-(b) SEM images of tungsten before and after Helium implantation following Nano-indentation to 250 nm. (Gibson JSK 2015) (c) Graph to show the changes in Nano-indentation hardness as a measure of temperature following exposure to helium. (Miyamoto M 2014)

due to exploiting the miscibility gap. For any nano-structured material, the sink strength of a grain boundary with that of its diameter has an inverse relationship. Grain boundaries have been shown to act as preferential absorbers of interstitials, leaving a vacancy-rich grain. This leads to a situation where vacancies near the grain boundary are preferentially annihilated in a process called interstitial emission (Bai 2010), and it leads to enhanced recovery by increasing the length over which grain boundaries and defects can interact.

2.4 Ductile to Brittle Transition Temperature (DBTT) of tungsten and BCC metals

As a refractory body-centred cubic (bcc) metal, tungsten exhibits distinct plasticity and deformation behaviour compared to face-centred cubic (fcc) or hexagonal close-packed (HCP) metals. Schmid's law is not strictly followed under stress and compression and, therefore, displays various non-Schmid behaviours, making specific slip plane identification challenging and stress-dependent (Raffo P 1969). An extensive understanding of the origins of brittleness in tungsten is paramount for enhancing its ductility. Two intrinsic properties of tungsten are widely acknowledged in this context: an inherent deficiency of close-packed planes and weak grain boundary continuity. As tungsten is a body-centred cubic (BCC) metal, manoeuvrability of non-planar $\frac{1}{2}$ <111> screw dislocations play an integral part in tungsten's plastic deformation (Li et al. 2012). On relaxing, the cores of a screw dislocation can extend into three 110 planes, increasing the Peierls stress (Ren et al. 2018, Gröger et al. 2008). The Peierls stress is the energy needed for dislocation to glide from one minimum to another across a row of atoms at 0 °K. When the core of the screw dislocation spreads into the 110 planes, it increases the subsequent Pierel's energy for the dislocation to glide (Gludovatz et al. 2011). This is the fundamental limitation of deformation in tungsten and is one of the primary causes of its brittleness. Furthermore, tungsten also grapples with poor grain boundary cohesion and the need for slip planes. Impurities have also been cited as a contributory factor in the fracture of tungsten, with intergranular fracture emerging as the predominant failure mode in tungsten. Empirical

observations are substantiated by theoretical simulations (Setyawan & Kurtz 2012). It is recognised that grain boundary impurities are detrimental and play a significant role in the intergranular fracture of tungsten. Notably, potassium, carbon, phosphorous and oxygen are prominent impurities (Funkenbusch et al. 1979, Joshi & Stein 1970, Liu & Shen 1982). The consensus is that grain boundary segregation of these elements subsequently weakens them, promoting intergranular fracture, and contributes to tungsten's embrittlement (Barbour et al. 1960, Tran-Huu-Loi et al. 1985, Gupta et al. 2007, Nieh 1984, Lee & Tomar 2013). It has, however, been shown that pure tungsten samples (>99.97%) show almost predominantly intergranular fracture (up to 95.9% of fracture surfaces) (Gludovatz et al. 2011). It has therefore been concluded that unless these contaminants reach significant levels, grain boundary cohesion often isn't the decisive factor; instead, reduced ductility is more likely a consequence of strain incompatibilities between neighbouring grains (Gludovatz et al. 2011). Therefore, the exact cause of this embrittlement is still yet to be determined. Dislocation nucleation and motion play a crucial role in plastic deformation (Hull D 2001, Giannattasio A 2007). At the crack-tip vicinity, dislocations are nucleated, and their subsequent movement leads to further nucleation of dislocations, reducing stress through shielding (Roberts S 1993, Tarleton E 2009). Continuous shielding can reduce stress intensity below the fracture threshold, causing crack-tip blunting and plastic flow-driven crack propagation. Conversely, hindered dislocation movement results in brittle fracture if fracture toughness is surpassed (Tarleton E 2009). Materials may exhibit a ductile to brittle transition (DBTT) as temperatures decrease, attributed to reduced dislocation movement near the crack-tip and increased applied load intensity (Giannattasio A 2007, Tarleton E 2009). Dynamic simulations and experiments confirm that dislocation movement controls brittle fracture onset, especially in bcc metals, where screw dislocation mobility determines metal plasticity (Giannattasio A 2010). Irradiation damage in tungsten increases DBTT, impeding dislocation movement rather than nucleation (Giannattasio A 2010).

Tungsten is generally considered brittle at room temperature, except for single crystal

rolled or heavily worked foils and rhenium alloys. Unlike other crystalline materials, tungsten's plastic behaviour is controlled by dislocations, exhibiting unique responses to strain rates, temperatures, and compositions. Unlike most metals that show lower strain for failure under extensive plastic deformation, Tungsten's ductility improves with cold working. Solid solution alloying also enhances its ductility and softens it at room temperature, contrasting with the typical hardening observed in other metals. Tungsten's plasticity is further complicated by its bcc crystal structure and associated defects, such as slip-on abnormal planes that defy Schmid's law by not presenting maximum resolved shear stress (MRSS) and a twinning anti-twinning asymmetry response to stress direction. Slip occurs on the $\langle 110 \rangle$ and $\langle 112 \rangle$ closest-packed planes, violating Schmid's law for bcc metals. Tungsten's unique plastic behaviour poses challenges for high-temperature applications, making it difficult to work.

2.5 Ductilisation of Tungsten

Several processing routes have been and are being explored to enhance the ductility of tungsten. These include solid solutionising or alloying, nanostructuring, composite material production, and thermomechanical processing.

2.5.1 Thermomechanical processing of tungsten

Nanocrystalline or ultra-fine grain structures in tungsten can be achieved through two approaches: the "top-down" method using thermomechanical processes like cold rolling, plastic deformation, or extrusion, and the "bottom-up" approach involving powder metallurgy with nano-sized powders compacted and sintered. The top-down approach has shown promise in lowering the DBTT of wrought tungsten. Limited data is available for the bottom-up approach, but further research is needed to explore its potential impact on tungsten's properties.

Thermomechanical refinement has effectively decreased the DBTT and improved the ductility of tungsten. Rolling tungsten below its recrystallization temperature can lower

the DBTT to around 300 °C (Shen T 2016). The increased number of dislocations and laminated microstructure are key factors contributing to improved ductility. However, any improvements in the ductility of tungsten gained from deformation are subsequently lost following annealing and recrystallization, differing from the behaviour of most metals. Tungsten foil also exhibits similar trends at room temperature, where annealing results in loss of texture and dislocation density (Reiser J 2012). Recrystallization at 1600 °C for an hour significantly reduces ultimate stress and strain (Terentyev D 2015). Cold working has been utilized to mitigate re-crystallisation effects to enhance tungsten's ductility. Cold working in tungsten is any deformed performed up to a temperature of 1400 °C due to its elevated recrystallization temperature (Yih S 1979). Recrystallization and subsequent grain growth are prevented at these temperatures, producing a finely laminated microstructure and increased dislocation density as compared to wrought tungsten. Cold rolling at 400 °C leads to tungsten with increased low-angle grain boundaries, more dislocations, lower DBTT, and improved strength compared to wrought tungsten (Wei Q 2008, Reiser J 2016). However, further research is needed to understand tungsten's microstructure and mechanical behaviour comprehensively.

When metals undergo plastic deformation, the number of dislocations increases, typically increasing strength at the cost of ductility - work hardening (Dieter G 1961). However, the effect of work hardening on tungsten is opposite to that of ordinary ductile metals. To enhance the ductility of tungsten, various thermomechanical techniques have been identified in the literature, including rolling and severe plastic deformation (SPD) such as swaging and forging (Shen T 2016, Rupp D 2010, Wei Q 2006).

Early studies in the 1960s investigated the impact of thermomechanical processing on tungsten (Bodine G 1963, Maykuth D 1964). Bending tests were performed on tungsten annealed at 1100 °C after rolling at temperatures between 1150 to 1450 °C. Results indicated that the DBTT of tungsten was reduced to the range of 149 to 104 °C, while the sample thickness decreased from 38% to 73%. The DBTT was further reduced by eliminating annealing to 82 °C (Bodine G 1963, Maykuth D 1964). Additional bending

tests were conducted on tungsten samples with up to 65% reduction and pre-cracked notches (Rupp D 2010). Samples rolled in radial or parallel directions exhibited intergranular fracture, whereas those in tangential directions showed transgranular cleavage. Transgranular specimens had higher toughness (20 Mpa.m$^{1/2}$) compared to 10 Mpa.m$^{1/2}$ (radial) and 13 Mpa.m$^{1/2}$ (parallel). Tangential specimens also had a lower DBTT below 275 °C, highlighting the significance of grain size and texture on tungsten's properties.

The orientation of grain structure after rolling significantly impacts tungsten's mechanical properties. Bending tests of rolled tungsten at 1450 °C tested in with a transverse grain orientation, to that of the applied stress improves the DBTT from 300 °C to 250 °C (Shen T 2016). Similarly, the DBTT in Charpy impact tests of cold-rolled samples improve further to 125 °C with different sample orientations (Reiser J 2016). Deformation and rolling temperature also affect tungsten's mechanical properties. At 1500 °C rolling temperature and below 40% reduction, grains break up and new grains nucleate. The growth of new grains increases with up to a 60 % reduction. At approximately 80% reduction, a delaminated microstructure forms if rolling occurs at lower temperatures. For the 60% reduced sample, Charpy impact testing shows a decrease from 350 to 577 fibrous microstructure for sintered tungsten. A further reduction to 90% lowers the DBTT by an additional 50 °C (Zhang X 2016). However, the DBTT of tungsten processed typically by thermomechanical means is somewhat higher, likely due to subsequent annealing at 1100 °C.

This demonstrates that the DBTT of tungsten is directly related to the degree to which the microstructure is deformed. The results suggest that as the thermomechanical temperature increases, so does the DBTT and grain size. This has also been confirmed by Wei et al. (Wei Q 2008). As shown in figure 2.9, as the temperature of further rolling processes is reduced, the ductility of tungsten also increases.

Wei et al. stated that the microstructure of tungsten rolled at lower temperatures leads to a finer laminated appearance. The thickness of which is directly related to temperature. Any additional tungsten rolling leads to further flattening of the microstructure. This

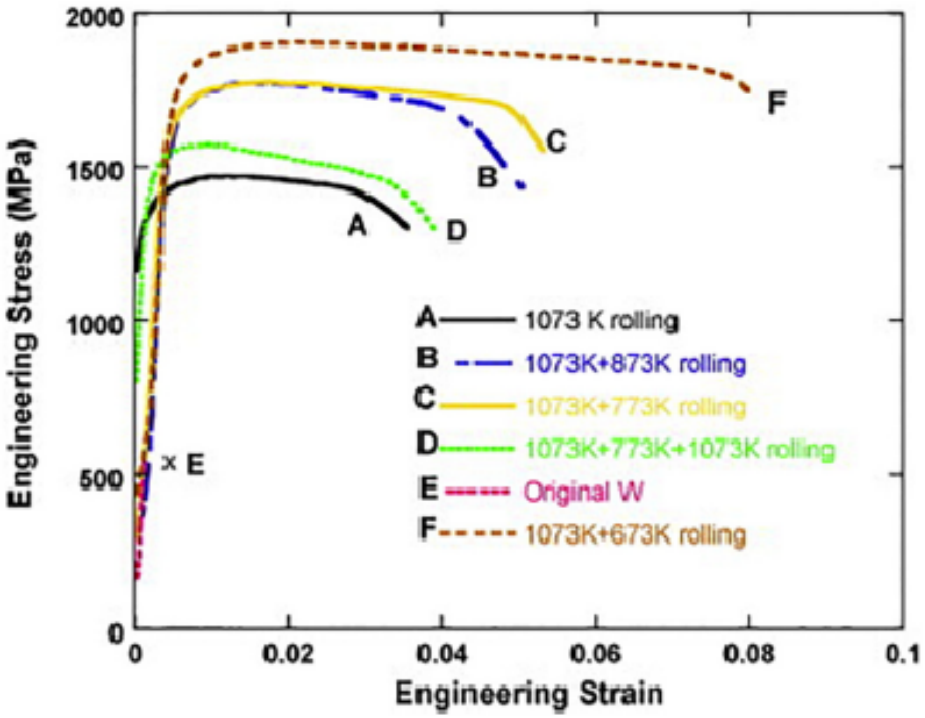

Figure 2.9: **Stress–strain curves for tungsten.** Engineering stress–strain curves for rolled tungsten which has been heat treated at various temperatures. (Wei Q 2008).

lamellar can precisely deform in a plastic manner before failure occurs (Wei Q 2008). Cold rolled tungsten, in addition to the presence of smaller grains, also contains a higher number of low-angle grain boundaries than wrought or hot rolled samples (Reiser J 2016). These have been shown elsewhere to act as dislocation sources (Hull 2011)

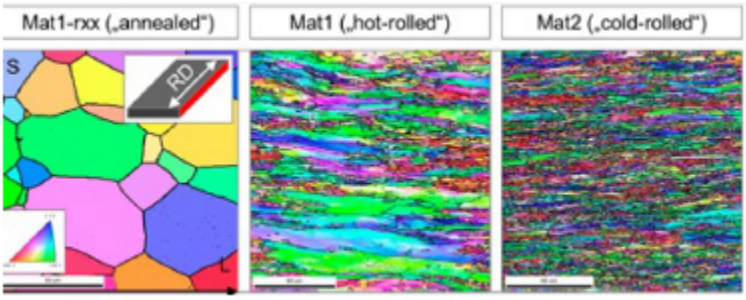

Figure 2.10: **EBSD of tungsten.** Three EBSD images/images of annealed, hot- and cold-rolled tungsten (L and S indicate Longitudinal or short Transverse Direction.) (Reiser J 2016)

EBSD images from Reiser et al. are shown in figure 2.10. They clearly show a difference in microstructure as a result of thermomechanical processing. The annealed sample shows significantly larger grains as compared to both of the rolled specimens. Moreover,

the grains also appear less ordered and show no directional bias compared to the rolled samples, which are elongated, deformed grains parallel to the direction of the applied rolling. As a result of the microstructure refinement, the images in the middle and on the right show a significantly more significant number of grain boundaries than the annealed sample. This refinement of the grains present after rolling lowered the DBTT from 675 °C to 125 °C for cold rolled tungsten as compared to 375 °C for high temperature rolling (Reiser J 2016). To date (excluding single crystal), the only form of tungsten with a DBTT near to that of room temperature is in the form of filaments or foils (Coolidge W 1910, Reiser J 2012), as demonstrated by Reiser et al. (100 μm foil).

In addition to cold rolling, Equal-channel angular pressing (ECAP) and forging have produced promising results. Shen et al. showed that tungsten forged at 1700 °C has a lower DBTT when compared to the same material rolled at 1650 °C (Shen et al. 2016). Further grain refinement of tungsten can be performed using equal-channel angular pressing (ECAP). ECAP can generate grains on the order of 0.3-2μm. Tungsten ECAP'ed at 800 °C and 950 °C had a reduced DBTT in Charpy impact testing, with the 950 °C having a lower DBTT than that of the 800 °C (322 and 386 °C respectively).

Due to this, the effects of annealing have been extensively researched. Annealing has been shown to reduce the length-to-width ratio of hot rolled tungsten at 1300 °C. From a ratio of 35 to 11 (Briant C 1989). Additionally, annealing has been shown to recrystallize the once deformed grains, thereby resulting in an increased DBTT to 675 °C, from 375 °C (Reiser J 2016). These studies indicate that some or even all of the improved properties gained by tungsten through thermomechanical working are reduced by annealing.

2.5.2 Tungsten wire

Tungsten wire is probably the most commonly produced tungsten product where series deformation is used to create the final nanostructured product.

Powder metallurgy is most often the starting point for tungsten products, including tungsten wire. The production of tungsten wires begins with several rounds of sifting

to separate particles and then blending and milling. The powder is then placed into a hydraulic press and formed into a bar. The pressed bar is then pre-sintered in a high-temperature furnace in a hydrogen atmosphere; the bar is then sintered with a high electric current within the furnace to produce a bar with a density in the region of 93%. As tungsten is brittle at room temperature, the bar is therefore heated repeatedly to ductilise it and swagged. At this stage, the tungsten grains are now elongated with a fibrous appearance. The final stage is the drawing of the swagged bar into a wire through tungsten carbide or diamond dies.

2.5.3 The addition of additives and their effect on thermomechanical processing

Several reports in the literature exist as to the use of additives in the manufacturing of tungsten. These have included (but not exclusively); ZrC, La_2O_3, TiC and TaC. Sintering, tungsten alloyed with 0.2 wt% TaC, which is then manufactured using SPS, decreases DBTT by 150 °C. Reductions in thickness of up to 70% have been seen by increasing TaC to 0.5 wt% following rolling (Wurster S 2011). Reductions in DBTT have also been shown for ZrC (Xie Z 2015), La_2O_3 (Yan q 2013) and TiC (Lang S 2016) and K (Faleschini M 2007).

2.5.4 Potassium doping

Potassium doping has strengthened tungsten filaments (Schade 2010, Snow 1979). Tungsten doped with potassium has nano-bubbles consisting of potassium atoms (in the ppm range) (Schade 2010). These bubbles are mainly distributed on grain boundaries. Volatilization of potassium during the sintering processes causes the formation of these nano-bubbles that act as pinning sites, preventing the movement of dislocations and grain boundaries (Snow 1979). This leads to strengthening and suppression of recrystallization (Bonnekoh C 2018). The prevention of grain motion results in a finer grain structure than pure tungsten, in addition to the strengthening and toughening produced by grain refinement. Many grain boundaries may improve neutron-irradiation-induced embrittlement due

to many sinks (Nogamia S 2020).

2.5.5 Using alloys to improve ductility

Rhenium is one of the only elements known to improve (lower) tungsten's DBTT. This process was first introduced in the 1950s (Geach G 1955). In this study, 35 at.% rhenium was alloyed with tungsten arc melted and rolled at room temperature to an 11%

The addition of alloys has been reported in the literature to reduce Peierls stresses by forming additional slip planes in tungsten 112. These extra planes result from solution softening (Garfinkle M 1966, Stephens J 1970). To date, only Rhenium has been shown to improve the ductility of tungsten through solid solution. However, the cost of this alloy for potential use in fusion reactors would make it too expensive. In addition, Rhenium increases the radiation embrittlement of tungsten. Work is currently progressing to replace Rhenium with either tantalum (Wurster S 2011), chromium (Dodds R 2018), vanadium (Wurster S 2011, Rieth M 2012) or titanium (Aguirre M 2010, 2009).

When Rhenium has been added to tungsten via arc- or electron-beam melting, it has been shown to refine the grain structure of the tungsten alloy. The most significant effect of Rhenium on tungsten can be seen when the weight percentage is above six wt% (Klopp W 1966). The overall properties of tungsten are determined by its grain size figure 2.11. This figure demonstrates how the grain size of tungsten and tungsten-rhenium alloy (arc melted) affects DBTT. These results were obtained by bending tests (Klopp W 1968). When tested at 327 °C, swaged tungsten alloyed with 20 at% rhenium (maximum) showed improved yield strength (Klopp W 1966, Raffo P 1969). The DBTT of the 3-point bending sample is both forged and sintered tungsten-rhenium alloys, improved to 800 °C (Gludovatz B 2010, Mutoh Y 1995). The increase in properties seen for tungsten via solid solution alloying (including molybdenum and chromium) by Rhenium in a BCC metal is known as the "rhenium effect" (Budagovskiy S 1973). Of the reports cited above, most of the results are reported under thermomechanical processing. Therefore, it should be noted that any change in the grain structure cannot only be attributed to the effects of

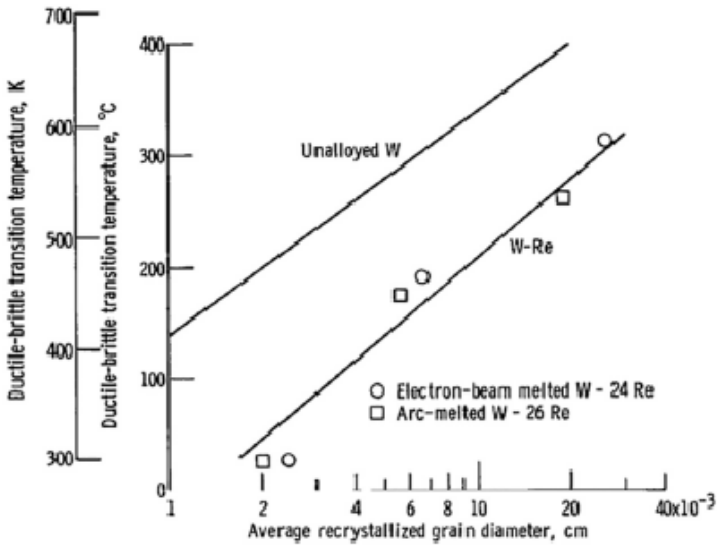

Figure 2.11: **The effect of Rhenium on the DBTT of tungsten.** DBTT changes for tungsten and tungsten-rhenium versus grain size diameter(Klopp W 1968).

Rhenium alone. In addition, any effects brought about by mechanical processing are comparatively short-lived and degraded by re-crystallisation. Annealing at 2000 °C of forged tungsten with 26wt% Rhenium showed a 58% reduction in fracture toughness (Wurster S 2010, Gilbert A 1966).

But despite the thermomechanical processing of tungsten-rhenium, there is a general tendency towards improved ductility compared to tungsten alone. Tungsten alloyed with increasing wt% Rhenium (up to 10 wt%) also shows improved fracture toughness (K_{IC}) in the absence of thermomechanical processing (Mutoh Y 1995). Sintered alloys of tungsten-rhenium have also been shown to have improved mechanical properties. A homogenous alloy has been shown to form up to 25wt% rhenium (Ramalingam M 1986). Comparisons made between sintered and arc-melted tungsten 25wt% rhenium, which has undergone rolling from 25.4 to 1.524 mm, showed differing results, with sintered alloy having a reduced rupture ductility at 1650 °C, whilst at the increased temperature of 2200 °C having improved the ductility, as compared to wrought tungsten(Stephenson R 1971).

Again, the effects of rhenium on sintered tungsten were tested under thermomechanical processing. Adding rhenium to sintered tungsten also gives beneficial mechanical

properties at room temperature. With the hardness of tungsten 16% (3.6 wt%), Rhenium alloy is significantly lower than pure tungsten. This further demonstrates the softening effects of rhenium on the tungsten alloy.

Aside from the cost complexities of building rhenium parts for fusion reactors, its use has additional drawbacks. Above 27% rhenium, the σ-phase metallic precipitates at room temperature; this brittle intermetallic dramatically reduces the mechanical properties of the tungsten-rhenium. Significantly for use in fusion reactors, rhenium under neutron bombardment transmutes into osmium. This will automatically affect the disposal of all tungsten components as high-level waste (HW) (El-Guebaly L 2011).

Despite the above issues, rhenium is currently the only alloying addition effectively known to ductilise tungsten on an industrial basis (Lassner E 1999). The exact means by which this occurs is still to be determined. Therefore, several mechanisms have been historically identified, including impinging of impurities (most notably oxygen) within the lattice and offsetting grain boundary segregation and embrittlement (Jaffee R 1958), directly improving the cohesion of grain boundaries (Setyawan W 2012) or changing mechanical responses (Muzyk M 2011). The best two mechanisms that explain the improvement of screw dislocation mobility at lower temperatures to date are solid solutionising (Gibala R 1973) or dislocation modification (Romaner L 2010).

2.5.6 Alloying elements other than rhenium

Considerable research has ensued to find rhenium substitutes. The two methods that have been employed are solid solutionising and composites. The purpose of adding the composites to tungsten is to form a final microstructure that contains second phases. The first approach is somewhat complicated because elements that form solid solutions with tungsten at room temperature are limited. Only vanadium, tantalum, molybdenum, and niobium are shown to have full miscibility in tungsten when phase diagrams are considered. Other elements are partly soluble in tungsten (titanium, technetium, and osmium). Tungsten can additionally form metastable alloys with other elements, such as copper.

However, its mechanical properties have not been investigated (but it has been shown to have a range of lattice parameters). It is suggested in the literature that this alloy is unlikely to offer any beneficial increases to the ductility of tungsten (Gaffet E 1991, Raghu T 2001). The solubility of titanium and rhenium are limited by the formation of intermetallics χ and σ, which occur at 12 wt% and 27 wt% respectively (Coenen J 2011, Loewenhoff T 2011). This is because when these intermetallic forms, there is usually a loss in ductility. Iridium has shown potential in arc-melted tungsten that is subsequently annealed. At wt%'s between 0.4 and 0.8 iridium, similar results were seen to that of the tungsten-rhenium alloy when tensile elongation tests were performed at room temperature. (Luo A 1991). But as iridium is once again a rare earth element, there are still the cost implications. In addition, there are also limited studies done on these elements, and what has been done is only one small concentration range. To reduce the limitation of these rare earth elements' concentration range, use one of the following alloys: vanadium, tantalum, molybdenum, niobium or titanium.

However, tungsten alloys of tantalum or vanadium have shown mixed results in reducing the DBTT. It has been shown up to and including 10wt% tantalum have no effect (Wurster S 2011). Yet this contrasts the results published by Reith et al., who showed that increasing the concentration of tantalum to 5wt% produced a marked reduction in the Charpy impact energy at 700 to 1100 °C (Rieth M 2012). Titanium, however, improves strength and toughness when tested through three-point bending. This has been the case for tungsten-titanium up to 4wt% Titanium (Aguirre M 2010). The improvement in the properties has been linked to how the fractures initiated in the tungsten grain (Aguirre M 2010). Despite these noted improvements (of the samples tested), there still was no notable change in the DBTT. This outcome is similar to the results obtained in molybdenum, which also do not show any appreciable improvement in the DBTT (up to 30wt%). There is little evidence from the literature as to solid solutionising offering a promise to reduce the ductilisation of tungsten. There is some evidence from simulations that adding elements that can lower the aforementioned Peierls stress may improve the ductility of tungsten.

Without thermal activation, the Peierls stress represents the critical stress that is needed for dislocation movement. Table 1 illustrates the Peierls energy values for several elements used in tungsten alloying (Hu YJ 2017). Elements with positive Peierls energy also exhibit positive interaction energy, raising both Peierls's stress and nucleation energy when no external energy is applied. Conversely, elements in groups V, VII, and VIII display negative values for Peierls and interaction energy. This suggests that 1/2 <111> screw dislocations are encouraged to move, facilitated by lattice sites within the alloy favouring double-kink nucleation (Hu YJ 2017). Incorporating these elements can promote tungsten ductility, but caution is needed as higher concentrations may lead to solute pinning of kink migration. Studies indicate that aluminium and manganese are predicted to have the most significant effect in reducing both Peierls and interaction energy. Table 2 presents the calculated atomic percentages of these solute elements to be added to Tungsten for improved ductility (Hu YJ 2017).

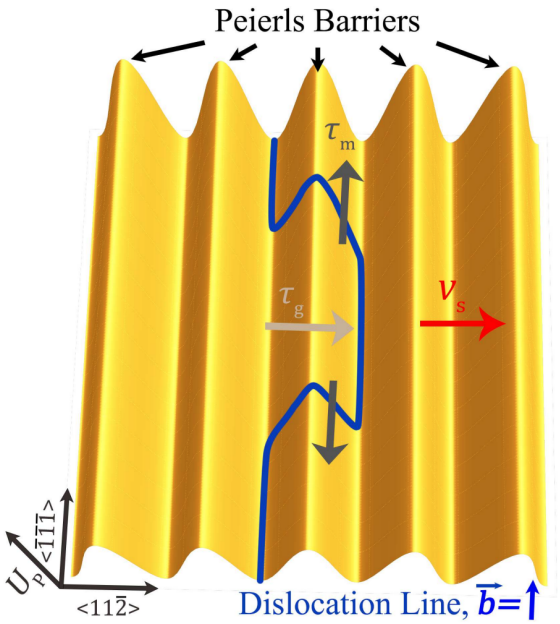

Figure 2.12: **Kink Pair formaiton.** Shows the formation of a kink and its subsequent migration (Hu YJ 2017)

Table 1: **Interaction energy and Peierls misfit** Shows the interaction energy and Peierls misfit as calculated for elements added to tungsten.(Hu YJ 2017)

Group	Element	interaction energy ($E_{int}{}^{0}$) (eV)	Peierls misfit (τ')
4	Ti	0.038	0.293
	Zr	0.032	0.310
	Hf	0.082	0.437
5	V	0.027	0.065
	Nb	0.048	0.211
	Ta	0.066	0.354
6	Cr	-0.138	-0.362
	Mo	-0.065	-0.114
	W	0.00	0.00
7	Mn	-0.429	-0.919
	Tc	-0.335	-0.243
	Re	-0.238	-0.440
8	Fe	-0.701	-0.701
	Ru	-0.717	-0.708
	Os	-0.634	-0.606
	Al	-0.408	-0.723

Table 2: **Weight percentage of elements to improve the ductility of Tungsten.** Predicted atomic wt% of elements needed to be added to Tungsten to improve its DBTT (Hu YJ 2017)

Element	Predicted atomic %
Mn	2.5 ± 0.2
Tc	3.9 ± 0.1
Re	7.4 ± 0.1
Fe	0.8 ± 0.1
Ru	0.7 ± 0.1
Os	1.0 ± 0.1
Al	2.7 ± 0.2

In summary, although much research focuses on the improvements in the DBTT of tungsten due to rhenium additions. In addition, most research on rhenium does not focus solely on rhenium but combines it with thermomechanical processing.

However, the mechanism behind this improvement is still not fully understood. Several suggestions have been put forward, these include;

- A solid solution softening effect, whereby the 1/2 {111} screw dislocations are more

mobile, reducing the required critical stress and the Peierls stress.

- promotion of extra slip planes with activation of the {112} plane. Thereby doubling the number of accessible slip planes to 12 (from the original six).

Overall, rhenium increases dislocation emissions from the crack tip, blunting it. This reduces the chance of brittle fracture and promotes plastic deformation. Rhenium's cost, transmutation to osmium and rarity are major stumbling blocks to its use in fusion reactors.

Both dynamic simulations and experimental studies demonstrate that dislocation movement and not nucleation at the crack tip control the onset of brittle fracture. In bcc metals of the two dislocations (screw and edge), the former is the slowest to move due to its inherently nonplanar shape. This observation shows that the ability of screw dislocations to move determines the plasticity of a metal Giannattasio A (2007). When stress is applied, a double-kink on a straight dislocation nucleates through thermal fluctuations Hu YJ (2017). This occurs by a dislocation "bowing" towards an adjacent lattice site, as shown in Figure 4(a). As seen in Figure 4(b), the now bowed kink migrates outwards following the direction of dislocation. Resulting in dislocation movement towards a position of minimum energy, a Peirel's valley Hu YJ (2017). When an element is alloyed with tungsten, the energy of both the migration and the nucleation of the kink will change Hu YJ (2017). Peierl's stress is related to the stress dependence of the kink nucleation and, therefore, the barrier to its migration. It is the critical stress required for dislocation movement to occur without thermal activation. These elements raise Peierl's stress and the nucleation energy when the energy applied is zero. However, those elements in groups V, VII, and VIII show that the Peierl's and interaction energy are negative. This means that 1/2 <111> screw dislocations are promoted to move by providing lattice sites within the alloy that favour the formation of double-kink nucleation Hu YJ (2017). Therefore, it could be stated that additions of these elements could promote the ductilisation of tungsten only at smaller concentrations. (It must be noted that increasing the concentration of these elements to any significant level can lead to solute pinning of the migration of the kinks). From these studies, aluminium and Manganese are predicted as the solute elements to have the most

significant effect of lowering both Peierl's and interaction energy. However, very little work has been carried out, and information on the manganese tungsten system is limited. It has been reported by Slyusarenko et al. that Manganese has a solubility of up to 8 at % at 953 °C. In addition, manganese is bcc above 1012 °C. Although the only available phase diagram for tungsten-manganese shows no intermetallics, several pieces of literature cite this binary of having such phases Atwani O El (2019). To this end, a 50:50 at.% binary alloy of tungsten manganese was created, and a primary characterization study was conducted to identify the feasibility of manufacturing components for fusion reactors.

2.6 Grain Refinement and nanocrystalline structuring of metal alloys

The 1980s began the era of using nanocrystalline techniques for improving the mechanical properties of metals. The method was initially used to develop nanocrystalline materials with particular mechanical, electrical, and thermal properties (Gleiter H 1981, Birringer R 1986). It wasn't until the 1990s that ultrafine-grained metals were produced (Valiev R 1990, 1991, Musalimov R 1992, Valiev R 1993), using deformative methods collectively termed severe plastic deformation (SPD) (Segal V 1977, 1995). It is accepted that aluminium alloys are deformed using ECAP at room temperature. As a result, Valiev et al. modified the grain size of the alloy from 10 μm to 200 nm and increased the elongation to 6% from an original 5%. The conclusion of this method showed tensile yield stress increased to 550 MPa from an original 330 (Valiev R 1993). Several SPD methods are now used to produce ultrafine-grained metals (Valiev R 1993). These include (but not exclusively); accumulative roll-bonding (Saito Y 1999, 1998), multi-directional forging (Salishchev G 1993, Valitov V 1994) and high-pressure torsion (HPT) (Zhilyaev A 2003, 2008, Smirnova N 1986, Valiev R 1988). In addition to aluminium, titanium (Stolyarov V 2001) and magnesium (Yamashita A 2001) have also shown significant improvements in tensile stresses and elongation to failure following ECAP.

2.6.1 Methods to produce ultra-fine grains in Tungsten

Due to the promising results that grain refinement has shown in other metals and their alloys, it is suggested that this method could be employed to try and improve the DBTT of tungsten (Nygren R 2011). From studies of BCC metals, the movement of screw dislocations appears slower than that of edge dislocations (Wei Q 2004, 2011, 2007). Structurally, tungsten and molybdenum are similar. Results obtained by Cheng et al. figure 2.13 showed that as grain size reduces the number of screw dislocations, the number of edge or mixed dislocations increases.

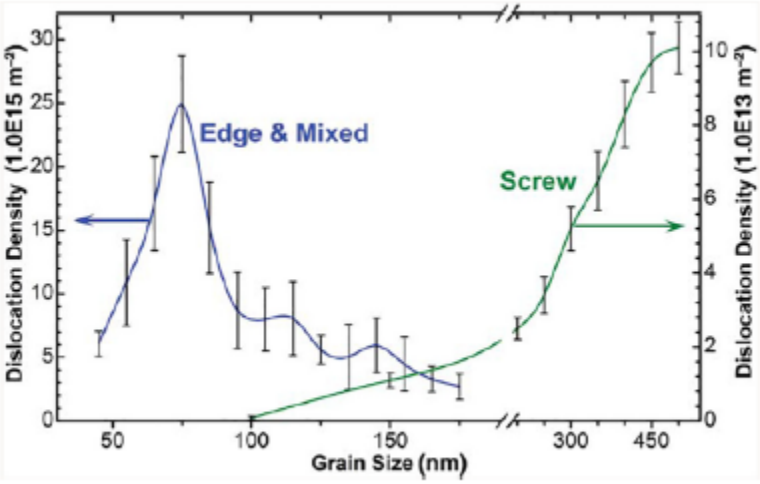

Figure 2.13: **Dislocation Density** Changes in ½<111>screw and edge + mixed, dislocation densities as a result of grain refinement in HPT molybdenum. The number of dislocations is counted using HRTEM (Cheng G 2013)

To produce ultrafine-grained tungsten, two methods are employed: the bottom-up and the top-down (Kevskes L 2007).

2.6.2 The bottom-up method

The bottom-up method uses nano-sized powder particles and advanced additive techniques such as hot isostatic pressing (HIPping), microwave sintering or spark plasma sintering (SPS) (Monge M 2009, Kim Y 2009, Liu R 2012, Piotter V 2008) to control grain structure. HIPping at 1700 °C produces 4.4 μm grain size at 92.7% density (Monge M

2009). SPS improves density to 96.9%, but grain size increases to 18.8 μm (Kim Y 2009). Microwave sintering shows promise, yielding nearly 97.0% Thermally stable particles, like yttrium oxide, are added during sintering to control grain growth. 1As a pure element, Yttrium removes oxygen from tungsten powder during milling (Wurster S 2013). Substituting Lanthanum oxide in microwave sintering improves grain size (1.4 μm); however, the final density is lowered by 1.9% (Liu R 2012). TiC, a thermally stable inhibitor, achieves 3 μm grain size and 98.6Despite improved grain size and density with additives (except TiC), scalability for fusion reactor samples is a concern. Further research is needed to optimize these methods for large-scale applications. Achieving ultrafine-grain range (less than 500 nm) of tungsten remains unexplored in the literature

As expected, the refinement of grains, as a result of these additions, improves the Vickers hardness by up to 37% for yttrium oxide (Liu R 2012). However, there is little other evidence in the literature to compare. Lanthanum oxide has been shown to improve tungsten's fracture toughness by up to 63% (Faleschini M 2007). Only one report looks at refining grains' effects on the DBTT of tungsten. It was reported that zirconium and zirconium carbide (less than 0.5%) reduced DBTT by up to a maximum of 200 and 100 °C, respectively. These additions are speculated to remove oxygen from grain boundaries and help pin dislocations. It must be noted that there were no indications in the paper itself as to the testing method used to obtain these results, nor was there any mention of the processing route.

Although sintering offers a means of producing a nanocrystalline material, a means of reducing the time for sintering is being pursued. One such example of this is what is termed accelerated sintering. (Park & Schuh 2015). As the name suggests, the process reduces the time and temperature needed to produce nanocrystalline alloys. By doing this, the alloys being manufactured have less time to undergo any microstructure evolution. It has been shown that if a tungsten alloy demonstrates a phase separation, as seen in the miscibility gap of tungsten chromium, a nanocrystalline structure can be achieved. Within this region, the alloy separates into two distinct nano-sized phases. Due

to the presence of this dual phase, the alloy can be induced to sinter faster (Park & Schuh 2015).

Powder Metallurgy

Powder metallurgy involves metal powder being used to produce materials or components. It allows for net-shaped or near-net-shaped products, reducing the need for final finishing, minimizing wastage, and lowering costs. It's beneficial for refractory metals, oxides, and cemented carbides. Powder metallurgy enables the production of materials with high melting points, like tungsten carbide (WC). Advanced techniques like spark plasma sintering (SPS), hot isostatic pressing (HIPping), and induction hot pressing have further improved powder manufacturing.

Ball milling

Ball milling produces fine particles from powder through mechanical procesding (Moosakazemi F (Aug. 2017). It involves a hollow cylindrical vessel with metal or ceramic balls that grind the powder as it rotates about its axis. The milling process reduces particle size, induces deformation in the crystalline structure, and modifies the surface and phases. Ball compression flattens powder particles initially, followed by fracturing and cold welding from ball collisions. Continued milling refines particle size and homogenizes microstructure. Chemical reactions can occur due to milling. The powder refinement depends on operational conditions like ball density, hardness, mass, milling time, vessel size, and rotation speed (Cerný R 2013, Ravnsbæk DB (Oct. 2013, Huot J (Jan. 01, 2013, Ley (May 2012, Ravnsbœk (Apr. 2012).

Mechanical alloying

Developed in the 1960s, mechanical alloying (MA), in response to the need to produce an alloy for use at higher temperatures. John Benjamin of INCO used MA to develop a nickel-based alloy with uniformly dispersed yttria (Y2O3) particles (Benjamin JS 1992). These

alloys are what are now categorized as oxide-dispersion strengthened (ODS) superalloys (Phaniraj 2009, Hirata A 2011, Miller 2013, Oono N 2016)

Powders, either in their elemental form or as pre-alloyed powders, are loaded into vessels alongside the grinding medium. The process is then a repeated cycle of cold welding and fracturing to reduce the size of the powder. The final powder size can, therefore, be specifically tailored by modifying the length of the welding and fracturing times or the number of repeated cycles.

Sintering

Sintering can be broken down into three distinct phases: initial, intermediate, and final (figure 2.14). The initial phase forms a neck between adjacent powder particles, stopping when the neck is about one-third the particle size. In the intermediate phase, pores between particles remain connected, and grain growth starts. When the neck size reaches half the particle size, this stage ends. The final stage begins with pore collapse, allowing unhindered grain growth after powder densification surpasses 92% (see Figure 1) (Rahaman 2010). Grains and pores coarsen during sintering, reducing the system's surface energy. Pore annihilation occurs through material diffusion from grain boundaries to low-curvature regions, driving grain centres together. For crystalline materials, material transport during sintering can occur via six principal methods, as seen in figure 2.15.

These mechanisms can be split into two categories: those promoting densification (grain boundary and lattice diffusion, plastic flow) and those promoting particle coarsening (vapour transport, surface, and lattice diffusion) (see graphs).

2.6.3 The Miscibility gap in binary phase diagrams.

The tungsten-chromium and Tungsten-titanium binary system is rare in that the phase diagram shows a simple miscibility gap where both of the resultant phases are bcc (bcc_A2 and bcc_A2) as shown in figure 2.16 and 7.42. A miscibility gap is a region of the phase diagram where at least two co-existing phases are present. The two phases form in two proposed methods: nucleation and growth or spinodal decomposition.

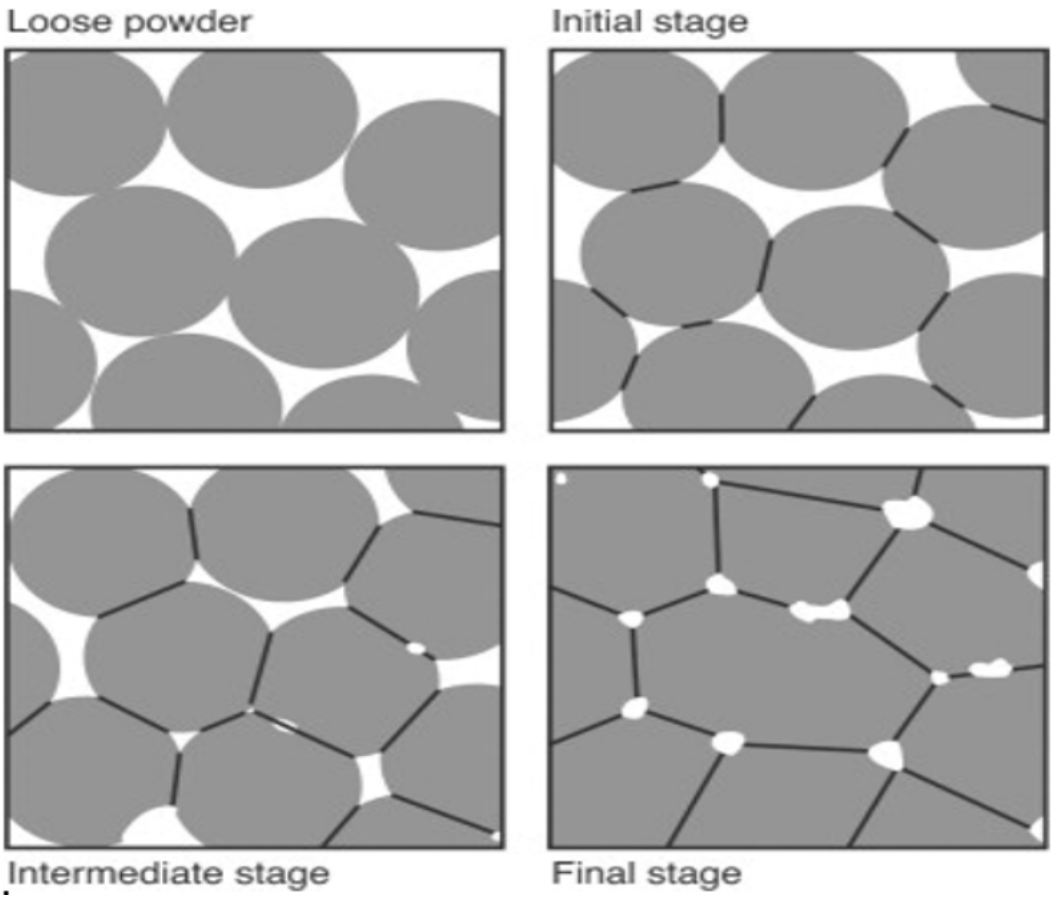

Figure 2.14: **A schematic diagram (adapted from the literature) of the idealized sintering process of powder particles.** (a) Powder particles initially loose, (b) initial stage, necking up to 0.2% of the diameter of the particles begin to form, density reaching 60-65%. (c) cylindrical channels at the edges begin to develop along three-grain edges, increasing the density to around 90% (d). The final stage is the elimination of pore channels and an increase in density to 95-99%.

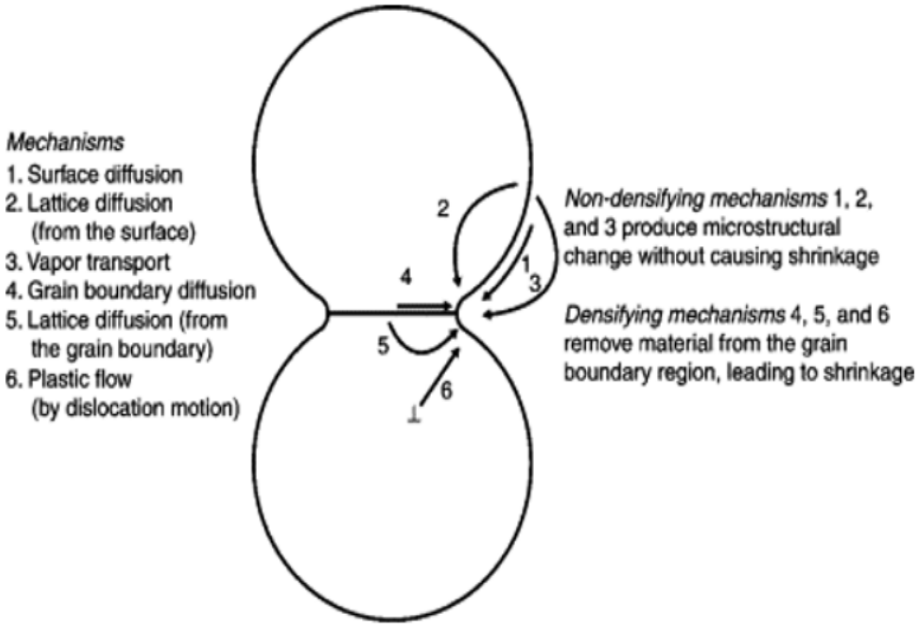

Figure 2.15: **Pathways for mass transportation**. The six main pathways for mass transportation of green mass between the contact area of two interconnected powder particles (German 2010).

2.6.4 Which mechanism does the Tungsten Chromium alloy decompose by?

As can be seen in the CALPHAD phase diagram for tungsten-chromium (figure 2.16). A miscibility gap is present at temperatures below 1655 °C; this indicates the decomposition route would be spinodal. In 1967, Porter DE identified three characteristics that an alloy should possess to be recognized as decomposing via spinodal means. These are as follows. (1) side bands on x-rays during the early stages of decomposition, (2) precipitates form randomly, and (3) characteristics of growth are simple. In this study, Porter concluded that all three were absent, and consequently, the decomposition process is nucleation and growth (Porter 1967). This lack of evidence, accompanied by the lamellar microstructure of the final product, led Porter to conclude that the system decomposes without spinodal decomposition (Porter 1967). However, since then, little research has been conducted on this alloy, and therefore, the decomposition mechanism has yet to be firmly concluded.

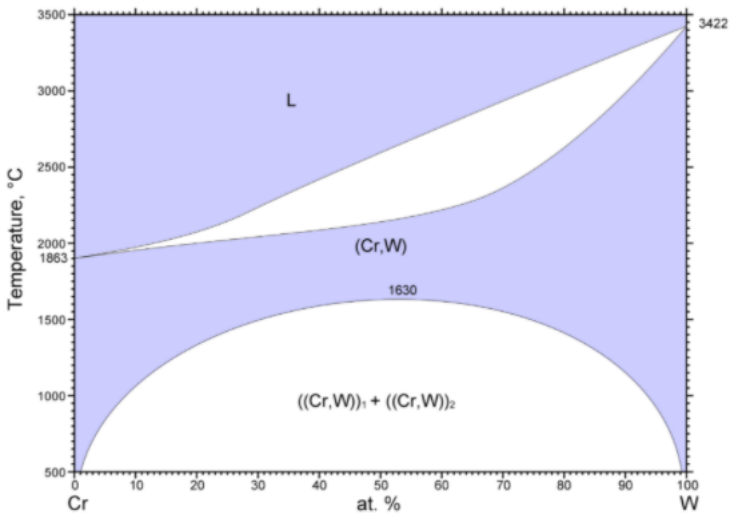

Figure 2.16: **Tungsten-chromium binary phase diagram.** WCr phase diagram showing miscibility gap in the binary alloy. (Naidu 1984)

2.6.5 Spinodal Decomposition

Spinodal Decomposition is a process in which a solution can be divided into two or more phases, each with unique physical properties and chemical compositions. This process, unlike nucleation, is uniform and occurs throughout the entirety of the material, not just at specific nucleation sites. The separation of the phases occurs when the material moves into a region on the phase diagram where it is unstable. Calculated through the mathematical equation (2):

$$\frac{d^2G}{dX_B^2} > 0 \tag{2}$$

This can be ascertained using the common tangent approach to a Gibbs free energy diagram. This is commonly described as the binodal or coexistence curve. Identifying the negative regions of the binodal curve shows where the spinodal region can be found. When the materials transition into this area of the phase diagram, the result can be a spinodal decomposition. Concerning figure 2.17a, an alloy with a composition X_o is lowered from a high-temperature T_1 to a final temperature of T_2, The free energy at this point is

termed (as indicated in the lower half of the diagram) G_o. Following this transition, slight variations in the composition of the alloy will produce regions rich in A- and B- components. These richer regions will ultimately lower the system's free energy (as referenced by S_1, S_2 on the free energy curve). Further diffusion of phases continues (by up-hill diffusion - as shown in figure 2.17b) until the compositions of each phase reach that of X_1 and X_2. Any changes in the density or the composition of a homogeneous solution within this spinodal region will become unstable. Therefore, no thermodynamic barrier exists, which would prevent the formation of new phases. Therefore, this process is fully controlled by diffusion.

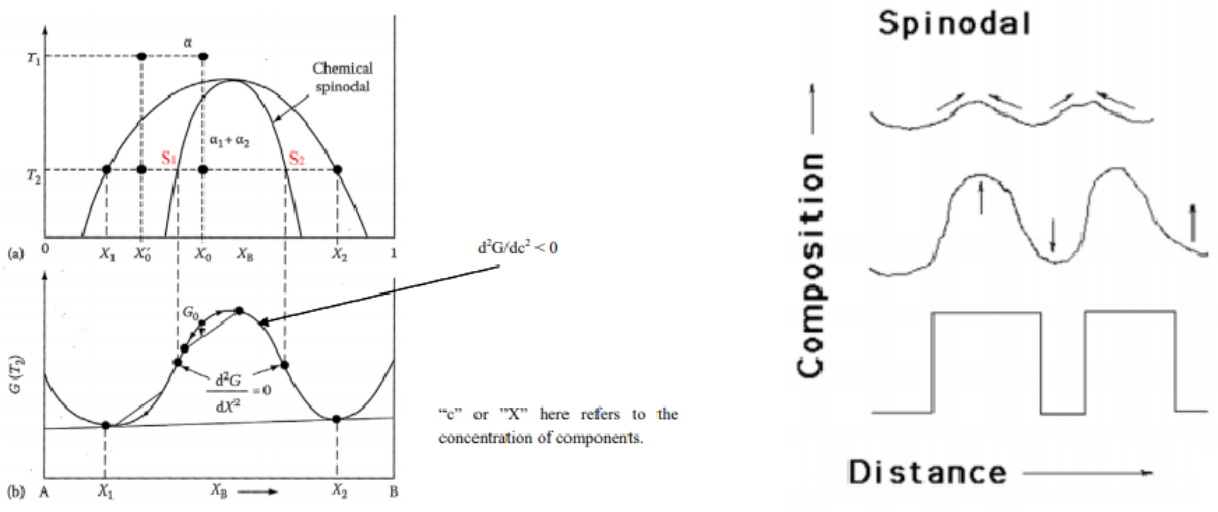

(a) (b)

Figure 2.17: **Spinodal decomposition**(a)The Free energy curve used to describe the theory behind the spinodal decomposition process (Zang L 2015), (b) Shows how composition changes during uphill diffusion (Zang L 2015).

If a homogenous alloy of composition X_0 initially undergoes a compositional fluctuation of wavelength λ with an amplitude of ΔX gives the Gibbs free energy as described by equation (3):

$$\Delta G = \frac{1}{2}\frac{d^2G}{dX^2}(\Delta X)^2 + K(\frac{\Delta X}{\lambda})^2 + \eta^2(\Delta X)^2 E' V_m \tag{3}$$

Concerning equation (3), as described earlier, the first term is always negative for

an alloy whose composition is in the spinodal region. The second part of the equation (3) describes the interfacial energy or surface tension ΔG_y, which is a gradient energy determined by the interface's chemical composition. K is a constant of proportionality that is affected by the bonding energy of atoms.

The last term accounts for the lattice parameter difference resulting from the phases' decomposition. η, is the differential of the lattice parameter a, V_m, the molar volume and E'= E/(1-v), (v is Poisson's ratio). This part of the equation leads to two conclusions: The first is that to reduce the Gibbs free energy, the wavelength of the composition modulations must be greater than that of $\lambda_critical$ described by equation 4:

$$\Delta G < 0 \Leftrightarrow \lambda > \lambda_c = \left[-2K / \left[\frac{d^2G}{dX^2} + 2\eta^{22} E' V_m \right] \right]^{\frac{1}{2}} \tag{4}$$

The second is that for a homogenous solution to become unstable and undergo spinodal decomposition from equation 4, the conditions can be described by equation 5:

$$-\frac{d^2G}{dX^2} > \frac{2K}{\lambda^2} + 2\eta^2 E' V_m \tag{5}$$

Assuming the boundary condition, λ=∞ for which spinodal decomposition is possible. Then the limits of temperature and composition are as follows (equation (6):

$$\frac{d^2G}{dX^2} = -2\eta^2 E' V_m \tag{6}$$

Figure 2.18 shows the region within the chemical spinodal region as described by equation 6. It is termed the coherent spinodal, and it can be deduced from equation 5 that the condition to describe the wavelength of modulations within the coherent spinodal must be represented by equation 7

$$\lambda^2 > -2K / \left[\frac{d^2G}{dX^2} + 2\eta^2 E' V_m \right] \tag{7}$$

The miscibility gap represented by most phase diagrams is the incoherent miscibility gap. The difference between this and the coherent spinodal is the magnitude of $|\eta|$. The

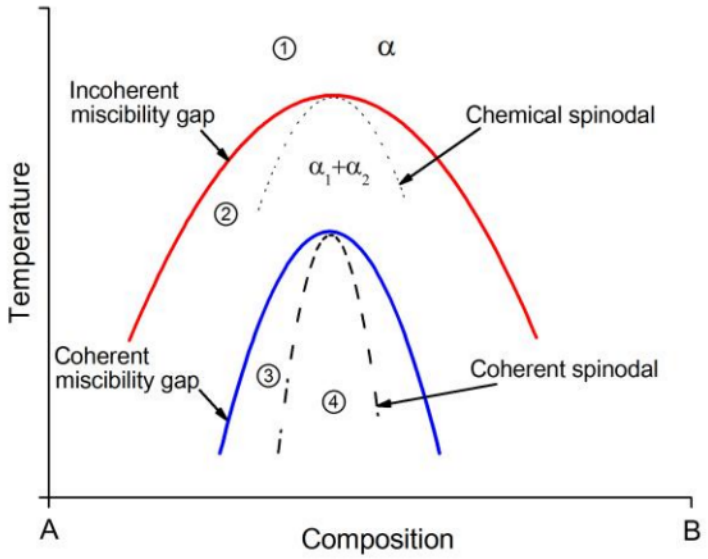

Figure 2.18: **Schematic diagram showing the components of a spinodal within a miscibility gap.** Schematic of the phase diagram showing Coherent region within the spinodal region as described by equation (6) (Iguchi Y 2017)

larger η is, the greater the under-cooling needed to mitigate the effects of the strain energy.

2.6.6 Spinodal Composition kinetics

Figure 2.17b shows that as the concentration of one of the elements increases (within the spinodal region), its chemical potential decreases. This means that diffusion in this region from lower to higher concentrations leads to an overall reduction in the system's free energy. Being spontaneous, uphill diffusion is given a minus sign to show the diffusive flux is against the chemical composition.

Fick's first law of diffusion is described in the following equation (8):

$$J = -D\frac{dc}{dx} \tag{8}$$

In a system with two atoms, A and B, if the molar fraction of B is described by the $\mathbf{c}$, then the molar fraction of atom A at any time can be described as (1-c).

Then the interdiffusion coefficient D in equation 8 is described as:

$$\tilde{D} = \frac{c(1-c)}{N_0} \{cM_A + (1-c)M_B\} \frac{\partial^2 g}{\partial c^2} \tag{9}$$

Where (N_0 is the Avogadro constant, k_B is the Boltzmann constant.)

If we define $Mas = [cM_A + (1-c)M_B] \cdot c \cdot (1-c)$

Where $\frac{D_A}{k_B T} = M_A$ and $\frac{D_B}{k_B T} = M_B$ and $\mathrm{M_A}$ and $\mathrm{M_B}$ are mobilities of A and B, respectively.

Then, Fick's first law can be modified as follows:

$$\tilde{D} = \frac{M}{N_0} \cdot \frac{\partial^2 g}{\partial c^2} \tag{10}$$

If we expand equation 10 and substitute this expansion into Fick's second law, we have the following equation:

$$\frac{\partial c}{\partial t} = -\frac{\partial J}{\partial x} = \frac{\partial}{\partial x}\left[\frac{M}{N_0} \cdot \frac{\partial}{\partial x} \cdot \left(\frac{\partial g}{\partial c}\right)\right] \tag{11}$$

Although M relies on changes in the composition if it is assumed for simplicity that it remains constant, equation 11 can be rewritten as:

$$-\frac{M}{N_0} \cdot \frac{\partial^2}{\partial x^2} \cdot \left(\frac{\partial g}{\partial c}\right) \tag{12}$$

If the Cahn-Hilliard equation is used to describe the free energy of a solid solution of concentration c, per unit volume, (equation (13) (Zang L 2004)):

$$G = A \int \left[g\left(c_0\right) + \left.\frac{\partial g}{\partial c}\right|_{c_0} \left(c - c_0\right) + \left.\frac{1}{2}\frac{\partial^2 g}{\partial c^2}\right|_{c_0} \left(c - c_0\right)^2 + \ldots\ldots\ldots + K\left(\frac{\partial c}{\partial x}\right)^2 \right] dx \tag{13}$$

If equation (13) is then integrated by parts, and the assumption is made that the compositional variations are approximately zero, (in the early stages) e.g. $\frac{dc}{dx} \approx 0$

$$\delta G(c) = \int_x \frac{\partial g}{\partial c}\delta c dx = \int_x \left[\left.\frac{\partial^2 g}{\partial c^2}\right|_{c_0} (c - c_0) - 2K\frac{d^2 c}{dx^2} \right] \delta c dx \tag{14}$$

That is $\frac{\partial g}{\partial c} = \left.\frac{\partial^2 g}{\partial c^2}\right|_{c_0} (c - c_0) - 2K\frac{d^2 c}{dx^2}$

As a result, Fick's second law is now described as follows:

$$\frac{\partial c}{\partial t} = -\frac{\partial J}{\partial x} = \frac{M}{N_0} \cdot \left\{ \left.\frac{\partial^2 g}{\partial c^2}\right|_0 \frac{\partial^2 c}{\partial x^2} - 2K\frac{\partial^4 c^2}{\partial x^4} \right\} \tag{15}$$

Equation 15 is called Cahn's diffusion equation. In addition to describing the spinodal decomposition of an alloy, this equation also includes the quasi-interfacial energy (the part of the equation containing K), which opposes the separation of the phases but simultaneously promotes the growth of the amplitude in spinodal decomposition.

2.6.7 Nucleation

Outside of this region, any chemical composition changes increase the Gibbs free energy, and the alloy becomes metastable. The Gibbs free energy can only be reduced if the composition of the nucleus is different from that of the matrix. Therefore, nucleation and growth are the only transformation methods outside the spinodal region. Unlike spinodal decomposition, nucleation results in the formation of thermodynamically distinct phases. There are two forms of nucleation: Heterogeneous and homogeneous. Of the two processes, heterogeneous is the more common. It occurs at grain boundaries or impurities (preferential sites) because the barrier for formation is lower (free energy of formation is lower). Solute atoms diffuse from the matrix into the nucleus by downhill diffusion (as shown in figure 2.19). The daughter and parental phases may have different structures; therefore, a sharp interface may occur.

2.7 High Entropy Alloys (HEAs) to ductilise tungsten?

Another alternative approach to alloying tungsten could be manufacturing tungsten-containing High Entropy Alloys (HEAs). HEAs compose several elements, each at a higher con-

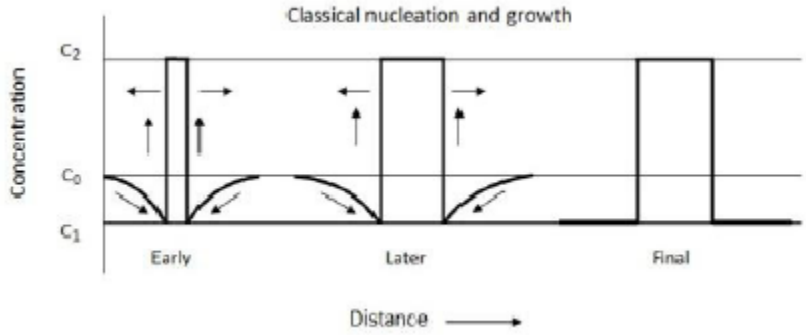

Figure 2.19: **Downhill diffusion.** Downhill diffusion as seen in classical nucleation (Zang L 2015)

centration than is typically seen in traditional alloys. These alloys are a crystalline solid solution of fcc, bcc, or HCP. As the elements within the alloy mix differently throughout, the environment surrounding each atom differs. This means that any defects resulting from the material are unique because of the compositional differences, and therefore, the energies of these defects will vary. Thus, how interstitials and vacancies combine will be different. One consequence of this is that these alloys have improved radiation resistance (Wang 2024).

HEAs can be divided into five main subfamilies depending on their chemical composition: (i) 3d transition metal, HEAs containing iron, nickel, cobalt, manganese, titanium and chromium (ii) refractory high entropy alloys (RHEAs) (iii) low-density HEAs, (iv) HEAs with at least 4 elements from the lanthanide series and (v) others. Of the five subfamilies, a tungsten-based refractory high entropy alloy (RHEAs) is the most important for fusion due to the high melting points of the consistent elements.

2.7.1 How to describe HEAs - The four Core effects

Since their conception, four terms have been used to describe HEAs' physical and mechanical properties. Three of the four effects are hypotheses and are based on the distortion of the lattice, diffusion, and High entropy effect of using several elements. The fourth, the cocktail effect, is more of a descriptive term; thus, it will not be mentioned further.

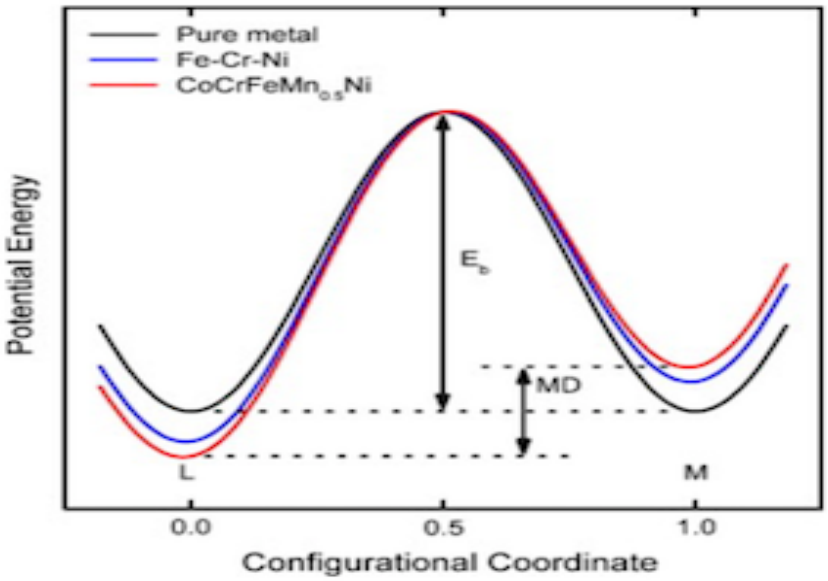

Figure 2.20: **lattice potential energy (LPE) and changes in the potential energy (MD) in different alloys** Diagram representing the LPE and MD changes between two lattice sites of pure metal, alloy, and HEA (Yeh JW 2004)

2.7.2 HEAs and sluggish diffusion

As HEAs are constructed from several elements, any atom undergoing diffusion from one position to its next will most likely find its new position utterly different from its last. Therefore, if that new site's lattice potential energy (LPE) is higher than the original, the atom will return to its original position.

The greater the variation in the LPE between two different sites, the greater its effect on diffusion. Atoms want to minimize their energy, and therefore, sites with the lowest LPE will produce a potential well for atoms, and any movement will require a greater activation energy to overcome the barrier for diffusion. If we look at two adjacent sites in a lattice (as represented by L and M) in figure 2.20. In a pure metal, both sites have the same energy potential wells; therefore, the amount of energy to move back and forth is the same. However, when comparing the energy potential of alloys (blue line), the potential wells are no longer the same.

The average difference (MD) in the potential energy of two sites in the HEA $CoCrFeMn_{0.5}Ni$ is 60.3 meV if a Boltzmann type expression is used to describe the transition of Ni atom

from site L to M, ($\exp^{-MD/k_BT}$). Therefore, at 1000 °C, an atom of Ni is 1.73 times more likely to be at site L than M.

So far, only one study, conducted by Tsai et al. and referenced as (Tsai 2013), has provided measured values for self-diffusion coefficients in High Entropy Alloys (HEAs). Their research focused on the diffusion of individual constituent elements within the equiatomic HEA CrMnFeCoNi. What they discovered was that the scaled activation energy, represented by the ratio of the activation energy (Q) to the alloy's melting point, was consistently higher in HEAs compared to selected face-centred cubic (fcc) binary alloys and austenitic steels. Notably, the values for this ratio (Q/Tm) in HEAs also exceeded those reported by Brown and Ashby ((Brown 1980) for fcc binary alloys.

For instance, Tsai et al. ((Tsai 2013) recorded a value of 0.1975 kJmol^{-1}K^{-1} for Ni diffusion in CrMnFeCoNi, while the maximum value reported by Brown and Ashby ((Brown 1980) was 0.1933 kJmol^{-1} K^{-1}, with an average of kJmol^{-1}K^{-1} for fcc binary alloys. Importantly, the diffusivity (D) is exponentially dependent on Q/Tm, meaning even slight variations in this ratio can lead to significant changes in D. However, it's essential to recognize that D is also influenced by the pre-exponential factor (A), which can vary significantly and more than compensate for changes in Q/Tm.

Apart from the direct measurements of diffusivities, there is substantial experimental evidence indicating that atomic movement in HEAs is not exceptionally slow. Notable observations include precipitation in many as-cast HEA samples, even those subjected to rapid cooling or high-temperature heat treatments. For instance, Ni–Al-based B2 precipitates were found to form during air cooling of the HEA Al CrFeCoNiCu from elevated temperatures. These findings challenge the notion that furnace cooling in HEAs can be equated to rapid quenching operations.

It's important to exercise caution when correlating precipitation rates with D values, as atomic fluxes are affected by D, concentration gradients, and chemical potential gradients. Nonetheless, in practical metallurgy, atomic fluxes are of primary concern, and the rapid precipitation observed in HEAs suggests that these fluxes are high. If we entertain the

idea that D values are unusually low in HEAs, rapid precipitation implies that chemical potential gradients are exceptionally pronounced, possibly confirming the fluctuations in lattice potential energy proposed by Yeh et al. ((Yeh 2014, Tsai 2014).

Furthermore, it has been suggested that the observed resistance to recrystallization in some HEAs provides evidence for sluggish diffusion kinetics. While slow atomic diffusion does impede recrystallization, the rates are also influenced by other factors, including dislocation concentrations, grain size, and the presence of secondary phases or inhomogeneities. Consequently, a careful examination is necessary before linking recrystallization kinetics to diffusion kinetics.

In conclusion, the accumulated evidence suggests that atomic diffusion in HEAs is unlikely to be unusually slow and certainly not universally sluggish across all HEAs.

2.7.3 Lattice distortion

HEAs frequently form a bcc or fcc crystal structure in a solid solution. As HEAs consist of multiple elements, these will all have different atomic sizes. Therefore, this difference in atomic size will have additional constraints on the unit cell formed. This will cause lattice strain as the elements push on each other (figure 2.21).

If the rule of mixtures is used to determine the hardness of a HEA, then MoNbTaVW has a hardness of 1,596 Mpa. This is compared to an experimentally measured value of 5,260 MPa. The difference is thought to be due to the distortion in the lattice producing a solid solution hardening effect (Miracle DB Senkov 2017). However, experimental evidence for this distortion is lacking. The only evidence to date is a decrease in the peak intensity as observed by XRD (Tsai 2009). But lattice distortion is not the only explanation for this (including fluorescence and crystallographic texture (Pickering 2016)), in addition, due to the lack of observation of these alloys in enough detail (SEM/TEM) the presence of fine precipitates could also be an explanation for the high hardness seen (Herbstein 1956).

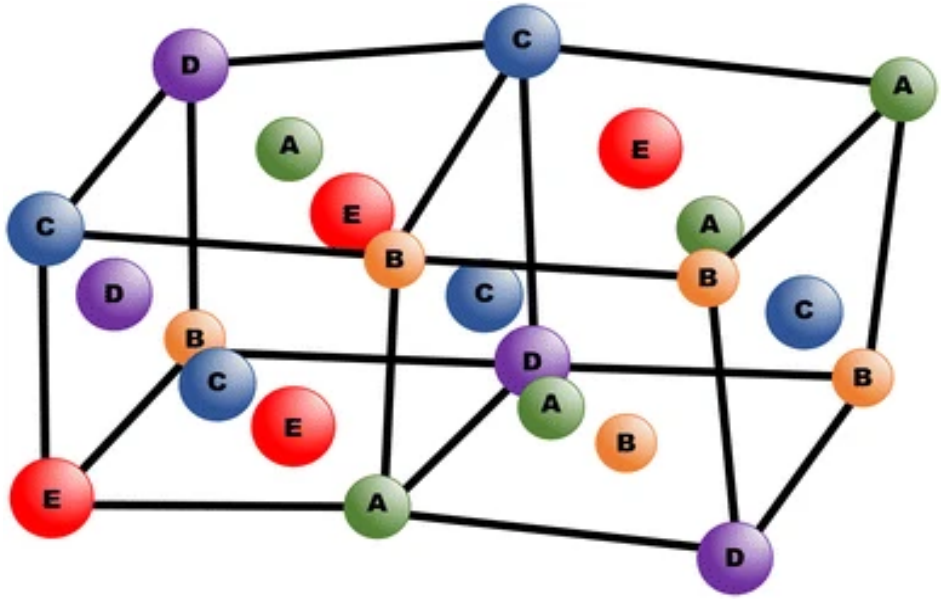

Figure 2.21: **Schematic representation of elements in a HEA** The possible random arrangements of elements A to E in a solid solution HEAs. Due to size mismatch in elements, a distorted fcc crystal structure is proposed to occur (Yeh JW 2006)

2.7.4 Entropic Stabilisation of HEAs

To determine if a solid solution will form in a HEA the Gibbs free energy must be considered. A problem arises in HEAs due to the inability to accurately determine ΔG at particular conditions. For Metallic glasses, this problem has been overcome by assuming that ΔG for a given composition is proportional to ΔG_{mix} of any liquid phase (Takeuchi A 2005).

Further assumptions have been made that ΔG_{mix} can be determined from the following equation 16

$$\Delta G_{mix} = \Delta H_{mix} - T\Delta S_{mix} \tag{16}$$

T is the absolute temperature, and ΔH_{mix} and ΔS_{mix} are the enthalpy and entropy of mixing, respectively.

The calculation of the enthalpy of mixing for a HEA can be simplified by adopting a regular solution model and determined using equation 17

$$\Delta H_{mix} = \sum_{i=1,1\neq j}^{n} \Omega_{ij} c_i c_j \tag{17}$$

Where Ω_{ij} = 4 Δ H_{AB}^{mix} is the regular solution interaction parameter C is the composition of each element found in the HEA, and Δ H_{AB}^{mix} is the enthalpy of mixing based on the Miedema model of elements. These values were taken from Tables 1 and 2 of Ref (Takeuchi A 2005).

The Entropy of a HEA can be calculated using a Boltzmann type expression for a multi-component alloy made up of n elements as expressed in equation 18

$$\Delta S_{mix} = -R \sum_{i=1}^{n} (c_i ln c_i) \tag{18}$$

Where R is the molar gas constant (8.314 Jk^{-1} mol^{-1}).

Enthalpy and entropy of mixing will both contribute to the overall appearance of the final HEA alloy. A negative ΔH_{mix} will promote intermetallic compounds and greater force of attraction between elements, whereas a positive ΔH_{mix} drives the separation of elements due to less miscibility. A ΔH_{mix} of nearer to zero will improve the chance a solid solution phase formation. As ΔS_{mix} for a HEA will always be positive and, as a result, will inherently encourage disorder in a multi-phase alloy. Therefore, a higher ΔS_{mix} will more likely result in a random solid solution and inhibit intermetallics formation. In addition, the value of the entropy will rise as temperature increases, and therefore, $T\Delta S_{mix}$ will promote a solid solution. To determine if a solid-solution forming as a posed to a multi-component system of intermetallics entropy-enthalpy factor Ω has been proposed (Yang X 2012) equation 19

$$\Omega = \frac{T_m \Delta S_{mix}}{|\Delta H_{mix}|} \tag{19}$$

Where T_m^{mix} is the sum of the melting points of all elements (T_m^{mix} =$\sum_{i=1}^{n}$ $c_i(T_m)_i$)

Therefore, a value of 1 for Ω is critical for forming a solid solution. Below this value, an intermetallic is formed due to ΔH_{mix} being the predominant force. Above 1 and $T\Delta S_{mix}$

is greater than ΔH_{mix} and a solid solution is formed.

This method, however, needs to consider the mismatch in the size of elements present in the HEA. Larger atoms will occupy more space within the lattice and, therefore, induce a local elastic strain due to misfit. As a result, this could increase the system's free energy and reduce solid solution formation. In addition, larger atoms could prevent the movement of other elements, promoting segregation. A δ factor was introduced to address this concern, as indicated in the below equation 20.

$$\delta = \sqrt{\sum_{i=1}^{n} c_i (1 - \frac{r_i}{\bar{r}_i})} \tag{20}$$

Where $\bar{r}$ is the average atomic radius of elements in the HEA mix as calculated by $\sum_{i=1}^{n} c_i r_i$.

A δ<5% value should facilitate forming a solid solution, however, recent reports have started to suggest that entropic stabilisation does not affect phase stability that is pertained to (Pickering 2016). Instead more experimental evidence suggests that HEAs are not single-solid solutions. Instead, the reported single-solid solution in the as-cast state is not always stable at all temperatures (up to melting point). In fact, at the time of writing, the only known HEA to be stable is that of the bcc equiatomic HEA, VNbMoTaW (Senkov 2010), Al_xCrFeCoNi (Wang WR Wang WL Wang SC Tsai YC Lai CH Yeh 2012) and TiV_xZrNbMo$_y$ (Wu 2015). The alloy known as the Cantor alloy thought once to be a solid solution has recently been shown to form σ phase rich in chromium at temperatures below 800 °C (He JY Zhu C Zhou DQ Liu WH Nieh TW Lu 2014).

Further, evidence of the lack of entropic stabilisation has been reported by Otto et al (Otto 2013). In their work elements within the CrMnFeCoNi HEA were substituted with elements of the same electronegativity size and crystal structure (Hume-Rothery 1969). Each substituted element favoured the formation of intermetallics, despite δ suggesting better stabilisation of the single phase. Senkov et al (Senkov 2015). and Troparevsky et al (Troparevsky 2015). both report that increasing the number of elements, which as the entropic stabilisation would suggest favours entropic stabilisation, does the opposite and

promotes the formation of several intermetallic phases.

2.7.5 Refractory metal HEAs - RHEA

For a HEA to be classified as refractory, it must first contain a minimum of four of the nine refractory elements. The first appearance of a true RHEA was that in MoNbTaW and quinary MoNbTaWV alloy created by Senkov et al. These two refractory HEAs demonstrated high strengths from RT to 1,600 °C. Table 3 shows the yield stress and Vickers hardness values for tungsten-based HEAs at room temperature.

Table 3: **Mechanical properties of tungsten Alloys.** Shows the Vickers hardness and yield strength for several tungsten RHEAs from the literature. ($\sigma_{0.2}$ - yield in compression)

HEA	State	HV	$\sigma_{0.2}$
MoNbTaVW	Cast	535	1246
MoNbTaW	Cast	454	1058
NbTaTiVW	Cast	447	1420
NbTaVW	Cast	493	1530
MoFeNiW	ELM	1682	1674
CoCr$_{2.5}$FeNi$_2$TiW$_{0.5}$	SLM	581	436.7

2.7.6 Microstructure of refractory HEAs

Of the reported microstructures for RHEAs in the as-cast conditions and for the limited data of those RHEAs annealed above 1000 °C. A single-phase bcc structure is the predominant microstructure reported. However, alloys with two-, three, and four-phases are identified in the literature. A breakdown of the phases found in RHEAs is shown in Table 4.

The C14 and C15 Laves phases are the most regularly reported of the second phase, with the presence of chromium being the most associated element. Conditional to the heat treatment percentage fraction, the Laves phase is present in either large or fine particles (or a combination of the two) in a bcc matrix. Laves phases within the alloy is appealing due to their strong oxidative resistance and high-temperature properties. However, they do demonstrate low ductility at room temperature. As shown in the above

Table 4: **Phases found in arc melted RHEAs.**Table to show the phases present in bcc alloyed RHEAs from the literature.

RHEA	Phases present	Year
MoNbTaW	bcc	2010
$MoNbTiV_{1.5}Zr$	2bcc	2012
$CrMo_{0.5}NbTa_{0.5}TiZr$	2bcc + Laves	2011
CrNbTiZr	bcc + Laves	2013
$Al_{0.3}NbTaTi_{1.4}Zr_{1.3}$	B2+ bcc	2014
$Al_{0.5}CrMoNbSi_{0.3}TiV$	bcc+ Laves+ M_5Si_3	2014
$HfNb_{0.18}Ta_{0.18}Ti_{1.27}Zr$	bcc + a"	2014
AlNbTiVZr0.5	B2+Al_3Zr_5 + Laves	2017
$AlMo_{0.5}NbTa_{0.5}TiZr_{0.5}$	B2	2018

BSE, the likely presence of a Laves phase at grain boundaries does offer a strengthening agent. In addition, several reports in the literature show Laves phases showcasing an improved creep resistance (although there are also contrary reports to this) and yield strength improvements. Laves phases are also known to be the initiation site for pinning dislocations and crack growth.

2.7.7 Mechanical properties of refractory metal HEAs

At present, for high-temperature applications, Nickel-based superalloys are usually selected. However, the γ' has an operating temperature limit of 950 °C. Above 980 °C, it becomes susceptible to environmental conditions due to the presence of constituent elements. Due to the significantly higher melting temperatures and specific strengths of RHEAs between 1000–1600 °C, these alloys could offer a solution for applications beyond the capability of Nickel-based superalloys.

Of the plethora of available refractory HEAs, only a few have been studied so far;

the existing data shows outstanding potential for nuclear applications. These include low neutron cross-section, reduced activation and improved strength at high temperatures. RHEAs also offer the possibility to design a microstructure specifically designed for nuclear reactors. These can include nanoscale layer particles, materials with denser dislocation fields, and fine precipitates.

One such example of this is the tungsten-based W-V-Cr-Ta alloy. $W_{38}Ta_{36}Cr_{15}V_{11}$ has excellent radiation resistance (Atwani O El 2019). This alloy also has a high nano hardness of 14GPa that shows a negligible increase following radiation up to 8dpa. This improved radiation resistance is likely due to the improved mobility of dislocations and the Vanadium chromium-rich precipitates. However, this alloy was only produced as a thin film. Unlike bulk-cast alloys, it does not suffer from issues of macrosegregation of elements seen in conventional manufacturing. Unlike fcc, bcc HEAs lack radiation hardening and improved ductility depending on the manufacturing route. However, an issue that remains is what phases are present in the alloy. The above authors report a single-phase bcc alloy. In contrast, others say a bcc and Laves C15 structure, with the significant difference being the manufacturing method (splutter vs. sintering).

Producing clean energy from fusion power is the ultimate goal. To reach this target, such reactors' components must have low activation levels. One such material is an alloy of vanadium, V-4Cr-4Ti. This family of alloys has an extremely low DBTT, and any subsequent rise in DBTT due to irradiation is slight, with DBTT as low as -200 C, showing no intergranular fracture at the fracture surface. Titanium additions to this alloy have been shown to reduce swelling and embrittlement from hydrogen, with the swelling of this alloy being lower than 0.3% at 30 dpa. At the same time, chromium has also been added for strengthening and corrosion resistance.

In addition, compared to tungsten, a W_xTaTiVCr HEA showed nearly a doubling in strength and hardness (Waseem O 2018). The Addition of Ti to two other HEAs, NbMoTaW and VNbMoTaW (20 at% and 16.6 at% Ti respectively), also increased the fracture strains from an initial 2.6% and 1.7% to 14.1% to 10.6%, respectively (Han ZD 2017).

2.7.8 The effects of radiation on HEAs

Although most of the focus had been on HEAs with an fcc crystal structure, it has nevertheless been demonstrated that the complexity of HEAs alters the properties (thermodynamic) of defects formed under irradiation that would otherwise cause microstructural changes in a material. Zhang et al. have shown that by altering the compositions of these certain alloys, the level of radiation-induced damage can be varied (Zhang 2022). Segregation and voids as a result of radiation are significantly lower (despite an increase in hardness) (Kumar et al. 2022). However, the evidence for bcc HEAs demonstrating the same tolerance level is somewhat limited. There are examples of HEA tungsten-based thin films showing excellent radiation resistance (Atwani O El 2019).

2.7.9 Recrystallisation

Recrystallization is one of the most common methods to control the microstructure of metals. This is mainly because this process can control the structure-sensitive properties of materials (McQueen 2004). Recrystallization can control not only the mechanical but also the physical properties of a alloy.

Recrystallization is the name given to a group of manufacturing techniques that alter the stress state to varying degrees in a deformed metal by reducing the levels of energy stored within it as a result of deformation when heat treated at an applicable temperature (McQueen 2004, Yamagata H 2001).

Recrystallization was first mentioned in 1885 (Yamagata H 2001). Since then, several significant advantages have been made by Cahn (Beer AG 2007, Cizek 2016)and Cottrell (Pierce DT 2015), to name a few. The history of the discovery of the process is covered in several historical reviews (McQueen 2004, Cram DG 2009, Galiyev A 2001).

As mentioned above, recrystallization is driven by the energy stored in a metal. This energy is stored due to the imperfections and strain in the lattice, driven into the material due to deformation. Of the total amount of energy placed into the material via deformation, only a small amount is stored in the material, with most energy dissipated as heat. The

stored energy, crystal imperfections such as point defects and dislocations (with the latter being the major contributor) make up the most significant proportion. An example of this is cold working, which has been shown to increase dislocation density from $10^{10-12}m^2$ to around 10^{16} in the deformed state. Each dislocation is associated with a strain in the crystal lattice, which results in an increased strain energy of the material (Smallman RE 2007).

The level of stored energy is proportional to the "complexity" of the deformation process. Less complex deformation processes have little or no friction and lower strain gradients. This has been confirmed regarding energy stored and deformation process (Bampton CC 1978, Ericsson 1966). In addition, dislocation density is also temperature dependant. The lower the temperature, the greater the level of work hardening. This is a result of suppressing the amount of energy released immediately after or during the deformation process. It has also been shown that "cryo-rolling" has more significant deformation than samples deformed at room temperature (Jones AR 1979). Stored energy has also been reported to be affected by grain orientation and size, alloy composition, melting point, and any second-phase particles present.

2.7.10 The Recrystallization mechanisms

If a sample is deformed at a temperature that is below 10 % of its absolute melting point, then the accumulation of defects should occur. As a result, stored energy increase (Takigawa Y 2008). This defect accumulation is unstable thermodynamically and will often result in changes in the material's physical properties (such as corrosion resistance) (Gil Sevillano J 1980). From a thermodynamic standpoint, the metal will want to minimize its stored energy. Returning to its pre-deformed state will require activating this stored energy to remove the defects produced by work hardening. To do this, an external heat process will be required. The activation energy determines the amount that the material relaxes. This relaxation in the metal's defect density is known as recovery and recrystallization.

Recovery consists of a two-step process; The first stage results in the removal (anni-

hilation) of point defects. The second is the reorganization or annihilation of a dislocation network caused by the dislocation glide during cold working (polygonization). Removing these dislocations is done either by creating new boundaries or the movement of existing low-angle boundaries (Doherty RD 1984, Nes 1998). Both of these steps result in some of the stored energy imparted by deformation being released.

Primary recrystallization is the term given to the process that can remove almost all remaining dislocations after recovery. It results in the creation and subsequent growth of distortion-free grains with the deformed matrix. High-angle grain boundaries (HAGB) mark the interface between the matrix and new grains (Wang K 2016). This second phase occurs in areas with high-stress fields around the dislocation fields and is driven by the "accumulated excess volume energy" (Derby B 1987). The energy required to drive the recrystallization process is higher than that needed for polygonization. However, this changes as more and more stored energy is consumed.

One prerequisite required for recrystallization is the need for a minimum level of deformation before any heating (Derby 1991). This critical level of deformation is thought to be needed to produce the right level of misorientation and distortion in the crystal lattice needed to create recrystallization nuclei that appear on heating. When recrystallization occurs after deformation at higher temperatures, the process is termed dynamic recrystallization.

Dynamic recrystallization is dependent on a multitude of different factors. These include non-inclusive deformation temperature, phase composition, temperature, and stacking fault energy (Urcola JJ 1987). Dynamic recrystallization necessitates the need for both strain hardening and softening to occur simultaneously. Therefore, the state of the factors mentioned above at the time of recrystallization determines the final structure. Dynamic recrystallization is classified into three classifications, each based on the mechanism used to create new grains. These are discontinuous-, continuous-, geometric dynamic recrystallization (GDRX) (the latter will not be discussed here.

2.7.11 Titanium alloys and recrystalisation

A superalloy "is an alloy developed for elevated-temperature service, usually based on group VIIIA elements, where relatively severe mechanical stressing is encountered, and where high surface stability is frequently required". (Sims 1923-)

Superalloys display excellent physical properties (including creep, corrosion-, oxidation-resistance, and strength, to name a few). These properties are maintained at elevated temperatures, even close to their melting point. Superalloys are split into three major classes; nickel-, cobalt- and iron-superalloys. All superalloys have a face-centred cubic (fcc) crystal arrangement. In particular, nickel superalloys have two phases: a continuous matrix of gamma (γ) austenitic fcc phase, which is strengthened through the presence of solid-solution elements and a gamma phase (Ni_3(Al,Ti)). These coherent precipitates are an ordered L_{12} fcc crystal, and due to their ductility, the γ' increase the strength of the alloy without reducing toughness.

Traditionally the properties of titanium alloys are improved through the precipitation of hcpα phases (10-25 nm) within a bccβ matrix. However, bcc superalloys are now being developed analogues to those created in fcc systems. For titanium, one example of this is an ordered β' B2 precipitate (size range of 50 nm) in a bccβ matrix (Knowles A 2017). A candidate for this could be a TiFe intermetallic in an A2 molybdenum and titanium matrix. This would produce a precipitation strengthening method similar to the length scale in fcc superalloys (Knowles A 2017), allowing improvements in strength but not at the expense of ductilisation. Although molybdenum has limited solubility in B2 TiFe, it has complete miscibility (bcc-A2) with Ti over a large region of the phase diagram (Franke P 2006).

Deforming a material results in an increase in the energy stored in the material. The energy is stored in the form of statically stored dislocations (SSD) and geometrically necessary dislocations (GND). This stored energy is thought to be the driving force for recrystallization. Due to the need to maintain material compatibility during any deformation process, GNDs form at grain boundaries. The density of SSDs and GNDs is directly proportional to the material's strain and properties, e.g., stacking faults and grain size. If

one assumes that dislocation density is not homogenous, then dislocation density is directly proportional to flow stress and stored energy. Established using data fitted through equations for flow stress and stored energy, with are described in equations 22 and 21

$$\tau = 0.5\mu bp^{0.5} \tag{21}$$

$$E_s = \alpha(\tau^2/\mu) \tag{22}$$

With b being the burgers vector, μ the shear modulus, ρ dislocation density and α constant. By combining equations 22 and 21, a formula to describe a direct relationship between stored energy and dislocation density can be written 23

$$E_s = \alpha\frac{(0.5\mu b\rho^{0.5})^2}{\mu} \tag{23}$$

The most popular method for automated measurement of dislocation density utilizes EBSD analysis in conjunction with Nye's dislocation density tensor. The Nye's dislocation density tensor relationship is shown in equation 24.

$$\alpha_{ij} = nb_i r_j \tag{24}$$

Where the b and r are the Burgers and unit vectors of each dislocation, and n represents the number of dislocations intersecting in the unit area. In defining the dislocation density tensor in this manner, only the net dislocation density for a unit volume is calculated. The net dislocation density calculated is linked to the curvature over that given point. Therefore, Nye's dislocation tensor only determines the GND for a given point. It does not, however, calculate the total dislocation density as statistically store dislocations (SSDS) are not described by curvature and have no net Burgers vector. Suppose we use the notation (dϕ_i) to identify a slight lattice rotation about one of the axes regarding a right-handed screw dislocation. This can be described by the use of a second rank tensor k_{ij} and dx_j, which identifies the curvature of that lattice of displacement as shown in equation

25.

$$d\phi_i = k_{ij} dx_j \tag{25}$$

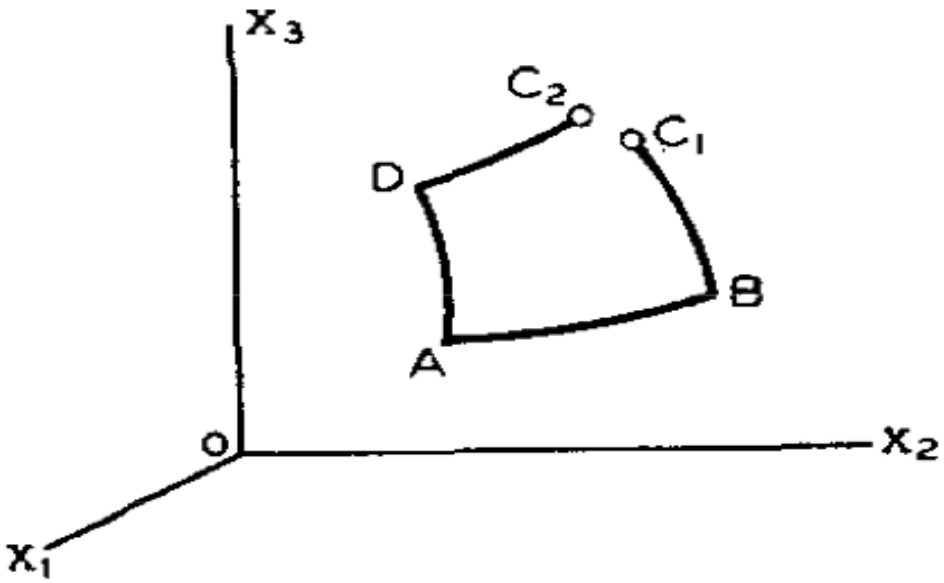

Figure 2.22: **Incomplete burgers circuit** shows an incomplete burgers circuit from C_1 to C_2 normal to the y axis. (Nye 1953)

The circuit shown in figure 2.22 can either described in terms of either a vector from C_a to C_b or in terms of the difference in the path (turns and rotations) needed to transverse from different nodes in the circuit. In his seminal paper, Nye shows that for such an example, the difference between the movements (described in terms of second-rank tensors k_{ij}) to close the circuit is as follows 26:

$$B_1 = -(k_{22} + k_{33}), B_2 = k_{12} and B_3 = k_{13} \tag{26}$$

Suppose a Burgers vector b finishes the circuit of dislocation and has a unit length of r. The number of n dislocations of this type crossing a unit vector l, normal to it, can be described as equation 27.

$$B_i = b_i(nr_j l_j) \tag{27}$$

It can be shown that this equation can be simplified by the use of α_{ij} (the dislocation tensor), then the Burgers vector can be written as 28.

$$B_i = \alpha_{ij} l_j \qquad Where(i, j = 1, 2, 3) \tag{28}$$

If this equation (28) is substituted into equation 26 and remembering this is for the (1,0,0) vector then equation (28) becomes:

$B_1 = \alpha_{11}$, $B_2 = \alpha_{21}$, $B_3 = \alpha_{31}$.

As a result,

α_{11} = -(k_{22} + k_{33}), α_{21} = k_{12}, α_{31} = k_{13}

Using the above approach, and instead using circuits normal to the other axis Ox_2 and Ox_3 six further relationships between α_{ij} and K_{ij} can be found;

$$\alpha_{12} = k_{21}$$
$$\alpha_{22} = -(k_{33} + k_{11})$$
$$\alpha_{32} = k_{23}$$
$$\alpha_{13} = k_{31}$$
$$\alpha_{23} = k_{32}$$
$$\alpha_{33} = -(k_{11} + k_{22})$$

This leads to the general description α_{ij} and k_{ij} to describe a curvature as;

α_{ij} = k_{ji} - $\delta_{ij} k_{kk}$) where (i,j,k = 1,2,3)

and

δ_{ij} = 1 when i=j but 0 for i $\neq$ j.

Substituting this relationship for α_{ij} into 25 the following equation can be obtained:

$$\frac{\partial k_{ij}}{\partial X_k} = \frac{\partial^2 \phi_j}{\partial X_j \partial X_k} = \frac{\partial K_{ik}}{\partial X_f}\frac{\partial \alpha_{ji}}{\partial X_k} - \frac{\partial \alpha_{ki}}{\partial X_f} = \frac{1}{2}(\delta_{ij}\frac{\partial \alpha_{ll}}{\partial X_k} - \delta_{ik}\frac{\partial \alpha_{ll}}{\partial X_j}) \tag{29}$$

Using the above equation and the 3 possible values for i, j, and k, 27 possible solutions can be found. Removing the solutions for j=k and identifying the symmetry in j and k, 9 independent results remain for α_{ij}. These are termed the "equilibrium equations". (Nye 1953) From the 2D EBSD data, six curvature components can be found, and from this information, 5 dislocation density tensors can be calculated as shown below:

$$\alpha_{12} = k_{21}$$

$$\alpha_{13} = k_{31}$$

$$\alpha_{21} = k_{12}$$

$$\alpha_{23} = k_{32}$$

$$\alpha_{33} = k_{11} - k_{22}$$

However, four elements of the tensor are missing, each requiring the k_{i3} and, therefore, a measurement in the Z-axis, which is not available from a 2D EBSD. Sun et al. (Sun S 2000) have suggested a solution to this problem. That is to assume that the variation along the z-axis is negligible and set the derivatives of this direction to zero.

The obvious shortcoming of analyzing GND density in this manner is that 3D information is obtained from a 2D measurement. However, Calcagnotto et al. (Calcagnotto M 2010) have reported that GND from a 2D data set gives a reasonable estimate. In addition to this, step size significantly influences the data quality collected. The Kikuchi images' quality is often only one order of magnitude different from the noise.

2.8 Conclusion of the Literature review

The literature clearly highlights that ductilising is an important factor in the need to produce tungsten alloys for high-temperature applications (especially if there is a need to cycle through its DBTT). Although improvements have been made to lower the DBTT of tungsten. The fundamentals controlling this ductilisation and the manufacturing routes able to produce ductile tungsten need further understanding and assessment. This will not only help to improve the manufacturability and the range of temperatures over which tungsten alloys can be used.

At present, the addition of rhenium is the only reliable method known to ductilise tungsten. Being a rare earth element, the cost and quantity of this element and the fact that it transmutes to osmium make its use in fusion reactors limited. computational modelling has shown that several other elements (Al, Mn and) could be a suitable alternative; however, there is limited data (if none existent) available on these alloying additions.

Without alloying, thermomechanical processing offers a repeatable method for producing ductile tungsten. Forging, rolling, and ECAP all produce a marked reduction in the DBTT of tungsten. Ultrafine-grained tungsten, along with the applied deformation, can produce ductile room-temperature tungsten. However, any improvement in the ductility is soon removed on subsequent thermal heat treatments, and recrystallization ensues.

Further to the above that shows ultrafine grain tungsten improves ductility has led to the idea that the so-called "bottom-up" process of creating ultrafine tungsten (and tungsten alloys) can be created from submicron powders that have been blended or mechanically alloyed together. Pinning agents such as potassium and yttrium have also been shown to reduce grain growth. Although it has been proposed that this technique would improve ductility, no data has yet been published that shows it actually improves ductility. In fact, the opposite has been demonstrated, with residual porosity and lack of grain boundary cohesion being predominant in samples created to date.

The goal of this PhD is, therefore, to identify alloying additions (other than rhenium) that can be manufactured in such a way as to control the grain structure to produce ultrafine microstructures that lead to ductile tungsten alloys at room temperature (or close to it). Little work has been done to assess the ductility of tungsten alloys that have been created through powder manufacturing. Therefore, more work needs to be done to investigate the properties of these alloys.

3 Experimental Methods

3.1 Manufacturing method for W-Cr

Previous work has shown that a tungsten Chromium 72/28 at.% alloy gave the best nanostructuring. A first attempt at creating a tungsten-chromium alloy was through conventional arc melting through vacuum arc melting on a water-cooled copper hearth in an environment of high-purity Argon gas via a 600 Amp current and tungsten electrode. A homogenous as-cast sample was difficult to produce due to the presence of unmelted tungsten in the ingot, the sample was rolled and remelted several times to improve the quality of the as-cast sample. However, due to the level of porosity, a sample of tungsten Chromium 72/28 at.% was purchased from ACI.

3.2 Powder for W-Cr

2Kgs of Irregular Chromium (Cr) Powder Purity> 99.5% with a mean particle Size, -325 mesh was purchased from Reade Advanced Materials. 1Kg of tungsten WM300 powder was purchased from Global Tungsten & Powders -325 mesh. A Cilas 1190 laser analyzer was used to perform a granulometric analysis of both metal powders. Fraunhofer diffraction was used with the wet path method. The powder size distribution was measured after sonication of the powder in water to ensure thorough dispersion of the powder. The overall size of the powder particles is determined based on the flow of the medium as it passes through a light source of wavelength 830 nm. Each of the powders in various stages of development was measured once and displayed graphically.

3.2.1 Preparation of Samples for Microscopy

All alloys were sectioned after homogenization and ageing heat treatments using a Kemet Miracut 151 cutting machine and diamond blade.

All samples were mounted in Bakelite using a MetPrepHA30 Mounting Press. Then

polished and ground to a 0.03μm finish as shown in table 5

Table 5: **Polishing method.** Table shows the polishing method used to prepare tungsten alloys for SEM/BSE and EBSD.

Grinding using Silicon Carbide				
Grid	**rpm**	**Force (N)**	**Time (min)**	
220	200	10	1	
800	200	10	1	
1200	200	10	2	
2400	200	10	2	
4000	200	10	3	
Polishing				
Cloth	**DP Suspension**	**rpm**	**Force**	**Time (min)**
DP-Chem	0.03 μm OP-S Activated Colloidal Silica	200	30	45

3.2.2 Homogenisation and Heat treatments

To homogenise W-28Cr at.% at 1700 °C W-28Cr at.%, samples were first wrapped in 99.9% pure 0.1 mm molybdenum foil and placed in an alumina cylinder. The cylinder was placed into a Thermal Technology LLC's Laboratory Furnace (Model 1100-2560-1/2) at Imperial College London. Once inside the lower chamber, the cylinder was backfilled with Argon to a pressure of 300 mbar following a thorough air evacuation. Following the evacuation and backfilling of the upper chamber with argon. The cylinder was moved to the upper shelf, which was then heated to 1700 °C from RT, at a rate of 10 °C/min. The furnace was then cooled at a rate of 100 °C/min and water quenched. The sample was left overnight to depressurize to room pressure before being removed.

The time to homogenize tungsten samples was calculated using a random walk calculation based upon the 3-D Einstein-Smoluchowski Equation (30).

$$x = \sqrt{6Dt} \tag{30}$$

where x=40μm due to the average grain size seen in the as-cast samples. D, the diffusion coefficient, as approximated from molecular dynamic calculations carried out by Park et

al. as 6.96x10^{-15} m^2/s (Park M 2014), this gives a diffusion timescale of 24,521 or 6.8 hours assuming an average diffusion distance of 32$\pm$3 μm taken from the as-cast sample.

To age the sample at 1250 °C, the samples, again wrapped in molybdenum, were placed into a quartz tube of 14mm in diameter. The foil was used to prevent the sample from coming into contact with the quartz tubing and as an oxygen "getter". The tube was evacuated several times, backfilled with Argon at a pressure of 0.808 psi, and sealed. The quartz tube was then placed into a preheated furnace. All furnaces were checked before heating cycles with a K-type thermocouple, and temperatures were adjusted appropriately. At the end of the ageing period, the sample was removed from the furnace, and water quenched before breaking from the glass.

3.2.3 Preparation of Samples for Microscopy

All alloys were sectioned after homogenization and ageing heat treatments using a Kemet Miracut 151 cutting machine and diamond blade.

All samples were mounted in Bakelite using a MetPrepHA30 Mounting Press. Then polished and ground to a 0.03μm finish as shown in table 6

Table 6: **Polishing method.** Table shows the polishing method used to prepare tungsten alloys for SEM/BSE and EBSD.

Grinding using Silicon Carbide				
Grid	**rpm**	**Force (N)**	**Time (min)**	
220	200	10	1	
800	200	10	1	
1200	200	10	2	
2400	200	10	2	
4000	200	10	3	
Polishing				
Cloth	**DP Suspension**	**rpm**	**Force**	**Time (min)**
DP-Chem	0.03 μm OP-S Activated Colloidal Silica	200	30	45

3.2.4 Microscopy

All scanning electronic microscopy (SEM) and energy dispersive x-ray (EDX) analysis was performed on a JEOL 7000F FEG, with a 30.0 KV and size 14 probe current. EBSD (Electron Back Scattering Diffraction) maps were obtained using 20 kV, with a 10 mm working distance and step size of 2.0 μm with a 583 µm by 487 µm grid. All data were then processed using INCA software, and MTEX software was employed to post-analyze the data. Due to the significant variation in grain size, a statistical approach was used to measure the average using equation (31) (Enqvist H 2003).

$$d_{4,3} = \frac{\Sigma d^4}{\Sigma d^3} \tag{31}$$

Where d is the grain diameter

3.2.5 Vickers Hardness Tests

Vickers hardness values were collected, with 2 kg weight and a dwell time of 5s. A minimum of 10 indents were performed, and the values were then averaged. As mentioned above, indents were performed on areas with similar microstructures and compositions to avoid recording being affected by the segregation of the alloy. SEM had previously identified these areas.

3.2.6 X-ray diffraction

X-ray diffraction (XRD) was performed using a Proto AXRD diffractometer utilizing a Cu Kα radiation source operated at 30kV and 20mA with a receiving slit of 1mm. Diffraction spectra were collected in the 2θ range of 20-150 $^\circ$ with a dwell time of 5 seconds, step size of 0.05 $^\circ$, and a total collection time of 13 hours

3.2.7 Density calculations

Theoretical density was calculated using the following equation 32.

$$\rho = \frac{\rho_W \, \rho_{Cr}}{x\%\rho_W + (1 - x\%)\rho_{Cr}} \tag{32}$$

3.2.8 3-Point Bending

1mm x 1mm x 15mm match stick samples were tested using a 3-point bending test rig. Electrical discharge machining (EDM) was used to cut samples from the rolled sheet in both the rolled and transverse direction as defined by ASTM standard E399. Samples were then ground to a 4000-grit finish. The bending tests were performed on an Instron 5000 with a strain rate of 0.40 mm/min to a maximum force of 1x10^{-3} KN at room temperature or a hot blower to control temperature. The temperature of the sample was assessed using two thermocouples attached to the rear of the by-welding. The samples were kept at temperature for 5 minutes prior to testing to ensure thorough heating.

3.3 Experimental methods W-Ti-Fe, W-Mn and W-Ti

3.3.1 Manufacture of W-Ti-Fe, W-Mn and W-Ti

To investigate the tungsten-titanium-iron (W-Ti-Fe) ternary as a potential system to produce a tungsten-based bcc superalloy. It was decided that the iron content of the alloys would be kept constant at 20 at % as it gave the best opportunity of producing the B2 precipitate (Knowles et al. 2021). The titanium content was varied from 20-60 at%, with the balance being tungsten.

The alloy was manufactured at Imperial College London via vacuum arc melting from elements with a purity greater than 99.9%. With a 600 Amp current and tungsten electrode. A homogenous as-cast sample was difficult to produce due to the presence of unmelted tungsten in the ingot, the sample was rolled and remelted several times to improve the quality of the as-cast sample.

A bar measuring 50 mm x 25 mm x 25 mm of W-Mn 50/50 at% and W-30Ti wt% were purchased from ACI and Testbounre respectively. Each sample was manufactured by arc melting 99.9% pure elements with a tungsten electrode. Due to the difference in melting temperature between tungsten and manganese, it was felt that having a 50/50 alloy would maximise the amount of manganese in the final alloy, but would still be identified as a tungsten-based alloy.

W-30Ti wt% was chosen as it is the composition on the phase diagram where the peak of the miscibility gap is. This should provide the greatest scope for spinodal decomposition to occur.

3.3.2 W-Ti-Fe, W-Mn and W-Ti Preparation

All samples were mounted in Bakelite using a MetPrepHA30 Mounting Press. All samples were polished and ground to a 0.03μm finish as shown in table 7

Table 7: **Polishing and grinding method.** Table shows the polishing method to prepare Ti-Fe-Mo for SEM/BSE and the final polishing method for EBSD

Grinding using Silicon Carbide				
Grid	**rpm**	**Force (N)**	**Time (min)**	
220	200	10	1	
800	200	10	1	
1200	200	10	2	
2400	200	10	2	
4000	200	10	3	
Polycrystalline diamond solution polishing				
Cloth	**DP Suspension**	**rpm**	**Force**	**Time (min)**
DP-Chem	0.03 μm OP-S Activated Colloidal Silica	200	30	45

3.3.3 Homogenisation and Heat treatments of alloys

Before any heat treatment was conducted, all alloys were encapsulated in a quartz tube that was evacuated and backfilled with argon several times before sealing. All W-Ti-Fe (except W-Ti-60Fe) alloys were homogenised at 1250 °C for 100h to remove micro segregation from the casting process. W-Ti-60Fe was instead solution heat treated at

1100 °C as prior tests had shown that it melted at 1250 °C.

All homogenised W-Ti-Fe alloys were then aged at 750 °C for 80 h to induce the formation of the TiFe intermetallic phase. After each treatment, the quartz tubes were immediately water quenched upon removing them from the furnace.

Samples of W-Mn were subject to the same encapsulation and quenching as W-Ti-Fe. However, the homogenisation and ageing treatments were varied due to issues with manganese loss from the samples. The actual temperature at which the alloy was heat treated is described in the results instead of the method section.

3.3.4 SEM observation of Alloys

All microstructural assessment of the alloys was performed using scanning electron microscopy (SEM), using a JEOL 7000, for BSE imaging and energy dispersive x-ray (EDX) analysis. EBSD was conducted at 30KV using a step size of 0.5 with a 30KV beam current.

3.3.5 Hardness indentation

Vickers hardness measurements were conducted using a 2 kg load with a 10 s dwell for ten indents, which were averaged. Due to alloys not being truly homogenised, all indents were assessed to ensure the same regions of the samples were measured.

3.3.6 xrd

X-ray diffraction (XRD) was carried out with a Proto AXRD diffractometer using CuKα radiation at 30.0KV 20mA with a 1mm slit. All scans were conducted with a 2θ of 20-120 ° with a 0.05 ° step size.

3.4 Experimental Methods - HEAs

3.4.1 Alloy manufacture

In order to maximise the entropic stabilisation equiatomic concentrations of each of the two alloys were selected. The equiatomic RA-RHEAs W-V-Cr-Ta (25at.% each) & W-V-Cr-Ta-Ti (20at.% each) alloys were produced using arc melting from raw elements with purity > 99.95%, by ACI alloys.

Sections of the 50 g ingots were glass encapsulated in quartz ampoules evacuated and backfilled with argon, which was then heat treated at 1400 °C for 100h. Secondary ageing was then made at 750 and 1000 °C for seven days, each followed by water quenching.

3.4.2 HEA Preparation

All samples were mounted in Bakelite using a MetPrepHA30 Mounting Press. All samples were polished and ground to a 0.03μm finish as shown in table 8

Table 8: **Polishing and grinding method.** Table shows the polishing method to prepare Ti-Fe-Mo for SEM/BSE and the final polishing method for EBSD

Grinding using Silicon Carbide				
Grid	**rpm**	**Force (N)**	**Time (min)**	
220	200	10	1	
800	200	10	1	
1200	200	10	2	
2400	200	10	2	
4000	200	10	3	
Polycrystalline diamond solution polishing				
Cloth	**DP Suspension**	**rpm**	**Force**	**Time (min)**
DP-Chem	0.03 μm OP-S Activated Colloidal Silica	200	30	45

3.4.3 Secondary electron microscope (SEM) observation

Characterization by Scanning Electron Microscopy (SEM) was conducted on a Joel 7000, with Oxford instruments with Energy-dispersive X-ray (EDX) and Electron Backscatter

Diffraction (EBSD) detectors, following mechanical polishing to 4000 grit SiC paper and finished with a final polish of OPS. A 20 keV beam energy and a probe current of 13 A were used to collect EDX and EBSD maps were captured using a step size of 0.5 with a 30KV beam current using a JOEL 7000 microscope equipped with INCA software. Subsequent analysis was performed using MTEX software. EDX data were quantified as at.% using Aztec software from Oxford instruments.

3.4.4 XRD analysis

X-ray diffraction (XRD) was performed using a Proto AXRD diffractometer utilizing a Cu Kα radiation source operated at 30kV and 20mA with a receiving slit of 1mm. Diffraction spectra were collected in the 2θ range of 20-150 $^\circ$ with a dwell time of 5 seconds, step size of 0.05 $^\circ$, and a total collection time of 13 hours

3.4.5 Hardness measurements

The properties of the alloys were first measured via Vickers hardness indentation, which was performed at room temperature with a 2Kg load for 5s. Ten indents were performed on a polished surface, and an average value and standard deviation (S.D.) were obtained. Nano-indentation arrays were used to find the properties of the multi-phase microstructure, carried out on a KLA iMicro-Indenter. The indentation array covered an area of between 70 and 105 µm^2 with a maximum grid of 400 indents. The target load for each cut was 5 mN. Each indentation was performed with an oscillation amplitude of 5 nm and a target frequency of 110 Hz. To a specified depth of 200 nm and a spacing of 3 µm between indents. With a Maximum load hold time of less than 1 second and surface approach velocity of 100 nms^{-1}.

3.5 Experimental methods - W-Cr72 at% - A Ex-situ Recrystallisation

For early observation of the decomposition process, the homogenised sample was indented to act as fiducial markers. The same sample was then encapsulated and back-

filled with argon and was aged at 1250 °C for 1hr, 10hrs and 100hrs inclusive. Following each heat treatment, the sample was polished and observed under SEM.

3.5.1 "Ex-situ BSE"

SEM BSE was performed on a TF Apreo 2S HiVac at 20Kv and beam current of 13 nA. After homogenisation at 1700 °C, the sample was encapsulated and backfilled with argon and aged at 1250 °C for increments of 1hr, 10hrs and 100hrs.

3.5.2 "Ex-situ EBSD"

EBSD analysis of the four ageing conditions: homogenised 8h 1700 °C, 1hr 1250 °C, 10hr 1250 °C and 100hr 1250 °C, ex-situ) were performed using a TF Apreo 2S HiVac with an Oxford Instruments Symmetry S3 detector with a voltage of 20KV and stepsize of 0.25. Grain size data was analysed using AZtecHKL. The grain size data presented is an average of 5 EBSD maps of 200 μm^2 and is an average of all phases present.

3.5.3 polishing of SEM samples

All samples were mounted in Bakelite using a MetPrepHA30 Mounting Press. All samples were polished and ground to a 0.03μm finish as shown in table 9

Table 9: **Polishing and grinding method.** Table shows the polishing method to prepare Ti-Fe-Mo for SEM/BSE and the final polishing method for EBSD

Grinding using Silicon Carbide				
Grid	**rpm**	**Force (N)**	**Time (min)**	
220	200	10	1	
800	200	10	1	
1200	200	10	2	
2400	200	10	2	
4000	200	10	3	
Polycrystalline diamond solution polishing				
Cloth	**DP Suspension**	**rpm**	**Force**	**Time (min)**
DP-Chem	0.03 μm OP-S Activated Colloidal Silica	200	30	45

3.6 Experimental Details - Ti-Fe-Mo

3.6.1 Ti-Fe-Mo Preparation

All samples were mounted in Bakelite using a MetPrepHA30 Mounting Press. All samples were polished and ground to a 0.03μm finish as shown in table 10

Table 10: **Polishing and grinding method.** Table shows the polishing method to prepare Ti-Fe-Mo for SEM/BSE and the final polishing method for EBSD

Grinding using Silicon Carbide				
Grid	**rpm**	**Force (N)**	**Time (min)**	
220	200	10	1	
800	200	10	1	
1200	200	10	2	
2400	200	10	2	
4000	200	10	3	
Polycrystalline diamond solution polishing				
Cloth	**DP Suspension**	**rpm**	**Force**	**Time (min)**
DP-Chem	0.03 μm OP-S Activated Colloidal Silica	200	30	45

3.6.2 Heat treatments

The Ti-Fe-Mo alloy was heat treated in a quartz ampule that had been evacuated and then filled with argon at 1170 °C for 16 hours. Then soft quenched in water. The sample was again encapsulated, backfilled with argon gas and aged at 750 °C for up to 80 hours. The sample was quenched, removed from the ampule, and polished as in table 6.

3.6.3 SEM Analysis

A 3 g sample of 56Ti-22Fe-22Mo (at.%) was manufactured by arc melting pure (>99.9%) elements under Ar gas. The ingot was turned and remelted four times to ensure homogeneity. A section of the as-cast sample was ground and polished with colloidal silica Oxford Polishing Solution (OPS). Scanning electron microscopy (SEM), observations were made using a JOEL 7000 Microscope coupled with Oxford INCA energy-dispersive X-ray spectrometry (EDS). The composition of the alloy was found to be (56.90$\pm$0.89)Ti

– (21.28±4.76)Fe – (21.84±5.00)Mo (at.%). The as-cast sample was encapsulated in a quartz ampule backfilled with argon and a 'homogenizing' heat treatment made at 1170 °C for 16 hours, followed by soft quenched in water.

3.6.4 Ti-Fe-Mo EBSD

A "quasi-in-situ" EBSD method was utilized to track recrystallization during heat treatment. After homogenization, several regions of interest (ROI) were identified for subsequent examination after ageing. The homogenized sample was encapsulated again and sequentially aged at 750℃ for 24, the samples were repolished for 20 minutes using OPS to remove the surface oxide layer (shown pictorially in figure 3.1). EBSD analysis, including grain size measurement, was then conducted on the identified ROIs to monitor texture evolution, enabling a "quasi-in-situ" analysis described in (Guan L 2019, Zeng ZR 2016). The above procedure was repeated in intervals of 24 hours as shown in figure 3.1) up to a total ageing time of 72 hours.

Electron Backscatter Diffraction (EBSD) mappings were generated on XY sections of Ti-Fe-Mo samples. Maps were captured using a step size of 0.5 with a 30KV beam current using a JOEL 7000 microscope equipped with INCA software. Subsequent analysis was performed using MTEX software.

3.6.5 XRD

XRD was performed using a Proto AXRD diffractometer utilizing a Cu source to determine lattice parameters and misfits. Diffraction spectra were collected in the 2θ range of 20-150° with a dwell time of 5 seconds, step size of 0.05 °, and a total collection time of 13 hours.

3.6.6 TEM

Transmission electron microscope (TEM) samples were prepared using a Focused Ion Beam (FIB) on an FEI Quanta 3D dual-beam SEM. A Tecnai F20 TEM microscope at a

voltage of 200 kV equipped with an Oxford INCA EDS instrument was used to perform TEM (STEM)/ED. The selected area diffraction patterns of the zone axis in the matrix and precipitate were indexed automatically using the auto-index function in the software SingleCrystal software based on the A2 β Ti structure.

3.6.7 Vicker's Hardness

Vickers hardness was measured by averaging ten indentations of 0.3 kg load after each heat treatment. Indents were performed on regions of the sample that had similar microstructure to represent values of homogenised material.

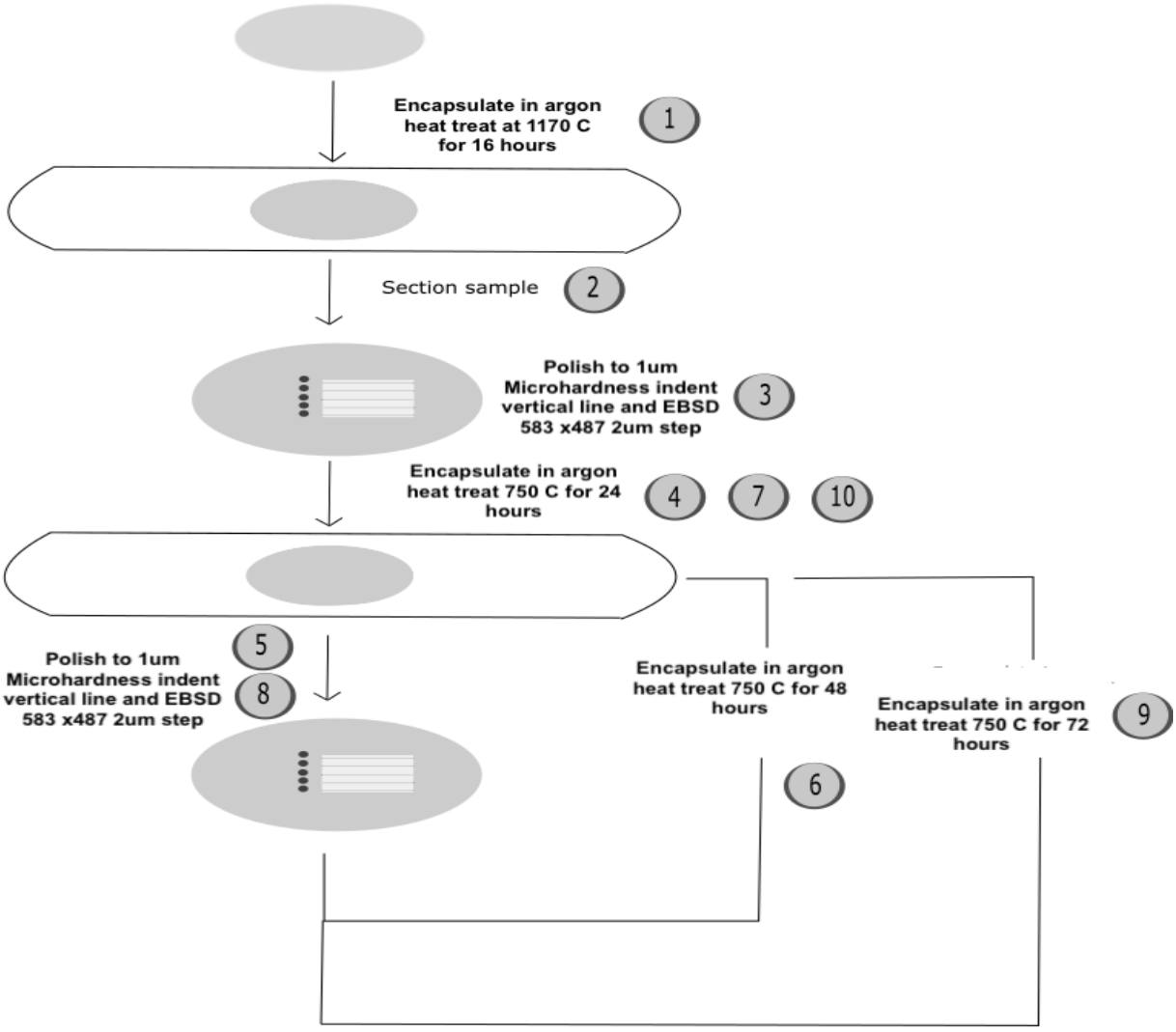

Figure 3.1: **Flow chart to show the method used for capturing pseudo-in situ re-crystallization of Ti-Fe-Mo.** Following Homengisation, the sample indentation marks were placed in a line on the sample to create a fiducial marker for SEM/EBSD analysis. The sample was then re-encapsulated and aged for 24 periods (in argon), and following a light polish in OPS, the area marked before ageing was reobserved. Numbers in circles indicate progressive steps in the process.

4 W-Cr - Design of nano-structured tungsten alloys

4.1 Introduction

The demands of fusion energy require a high-temperature material that can survive contact with plasma. Tungsten's high melting point and low sputtering yield means it is an ideal candidate material for fusion reactors. However, inherently brittle at room temperature as its DBTT is above 400 °C; being so high, the operational usage of tungsten is limited to above its DBTT; otherwise, it fails by catastrophic brittle fracture. In addition, the harsh environmental conditions of the fusion reactor will further raise its DBTT, reducing its operational effectiveness. To harness tungsten's superior mechanical properties, first, the DBTT must be reduced to lower temperatures. One of the methods that has shown promise is nanocrystalline or ultrafine-grained tungsten. This has been done through top-down and bottom-up manufacturing methods. Like "cold" working and thermomechanical processing, the top-down approach employs rolling, extrusion, and severe plastic deformation to refine grains. Ultrafine-grain tungsten produced in this manner exhibits improved ductility (Nygren et al. 2011). As the name suggests, the bottom-up process involves using nanosized powder particles, which are refined and sintered to produce near (to fully) dense bulk alloys of tungsten to manufacture ultrafine grain tungsten. The observation that ultrafine grain tungsten improves DBTT is a tempting prospect. One method not considered for the nanostructuring of a tungsten alloy is the exploitation of the miscibility gap. Any alloy system containing such a region in the phase diagram could potentially be used for decomposing it into a nanostructured structure. Such a fine structure could mimic that seen in a mechanically processed alloy of ultra-refined grains and increased dislocation network. The tungsten-chromium (W-Cr) binary alloy contains such a system. Porter et al. have investigated the system previously to show that within the miscibility gap, a solid solution decomposition takes place (Porter 1967).

With this in mind, this first chapter exploits the miscibility gap within the tungsten-chromium binary system to create a nanostructured two-phase alloy. As well as combining

this with several manufacturing methods with the purpose of creating bulk samples of two-phase tungsten allow for a nanostructured microstructure. In addition, the self-passivating nature of chromium which forms a chromate layer will act as a layer of protection for the tungsten giving it the title of a "Smart alloy". This will act as an extra layer of safety in the reactor in the event of oxygen ingress into the reactor.

4.2 W-28Cr at% - Arc melted

4.2.1 W-28Cr at% - As-Received

As-received W-28Cr at% figure 4.1a shows variations in solute concentration due to the coring of the dendrite structure. EDX analysis (figure 4.1a) of the sample shows that the lighter areas are tungsten and the darker ones are chromium (figure 4.1b). The cored dendrites structure results from the cooling method used in the casting process. The rapid removal of heat prevents significant solid-state diffusion producing a cored structure.

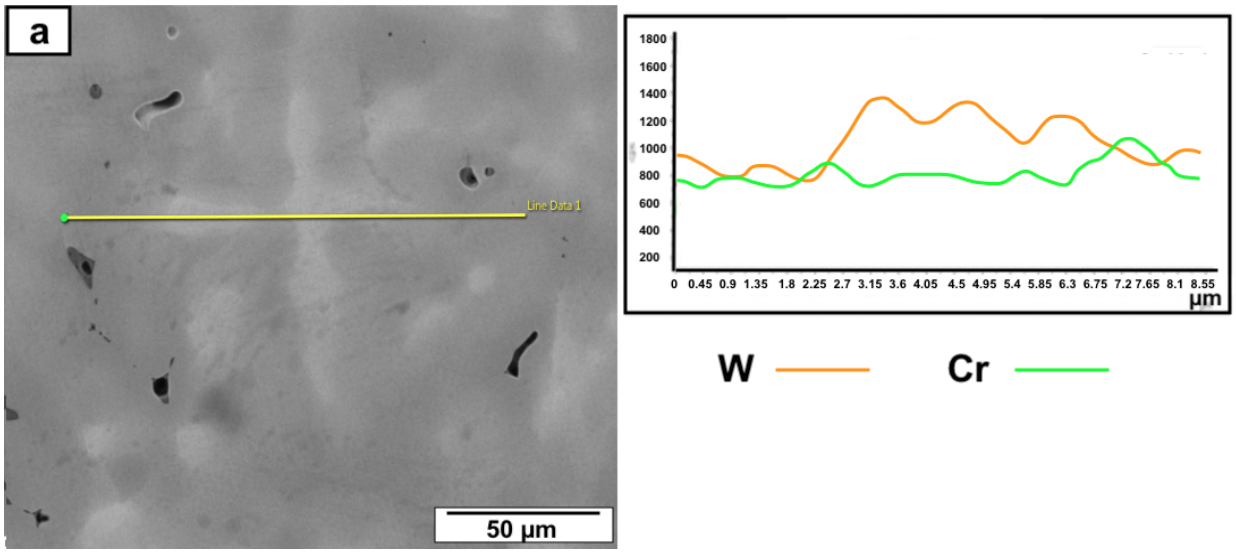

Figure 4.1: **Microstructer of W-28Cr at% in the as-received condition** (a) BSE and (b) line scan profile of yellow line seen in (a) of W-28Cr at% in the as-received condition.

4.2.2 W-28Cr at% - Solution heat treated

Due to the limitations of encapsulation, with a maximum heat treatment being 1400 °C. This would have meant homogenizing the alloy within the miscibility gap and inducing

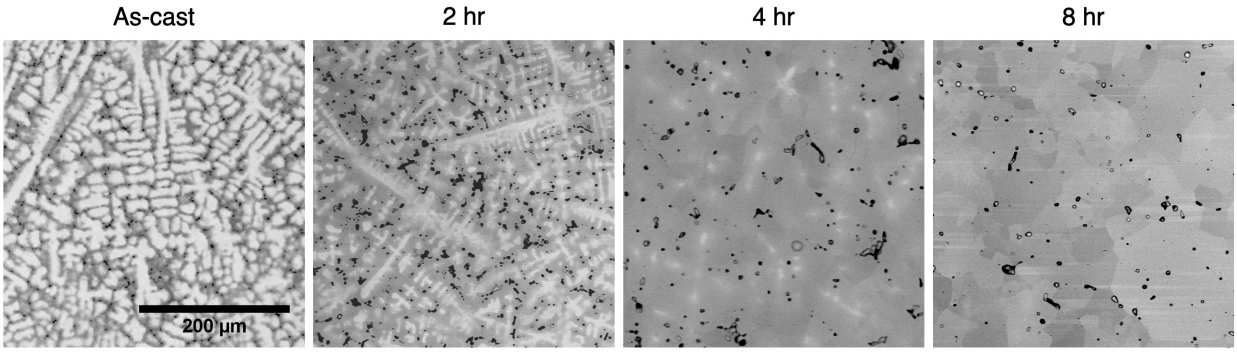

Figure 4.2: **Homgenisation experiment of WCr at 1700 °C** Micrographs showing the microstructure of WCr after homogenization from 2 till 8 hours Black areas indicate regions of porosity.(images taken by Spencer Cheung MEng thesis.)

decomposition on cooling. Therefore, the samples were homogenized at the Centre for Advanced Ceramics (CASC), Imperial College London. To determine the optimum time for homogenisation, the as-received sample was solution heat treated for up to 8 hours (as indicated by the diffusion equation 30). The results of which are shown in figure 4.2. Despite the sample being homogenous there is considerable porosity in the samples (as evidenced by the black areas in figures 4.1 and 4.1). On homogenising the samples a purple discolouring of the inner surface of the furnace was observed. This indicates that chromium was lost from the sample.

The sample was homogenized at 1700 °C for 8 hours. However, the structure of the furnace meant that quenching could not be done, and only furnace cooling was permissible. Figure 4.3a and b shows BSE and EDX line scan (respectively) of the microstructure after 8 hours of solution heat treating, demonstrating a homogenised microstructure.

4.2.3 W-28Cr at% - Aged

Following homogenisation samples were Aged at 1250 °C for 100 hours brought it within the miscibility gap and produced a fine lamellar structure (figure 4.5a). Two different lamellar structures can be observed a finer and much thicker (coarser) lamellar.

Figure 4.5b shows an EDX line scan of W-28Cr at% solution heat treated and aged for 100h at 1250 °C, the microstructure is a nanostructured two-phase lamellar precipitation of chromium-rich and tungsten-rich phases. The lighter (brighter) regions are due to the

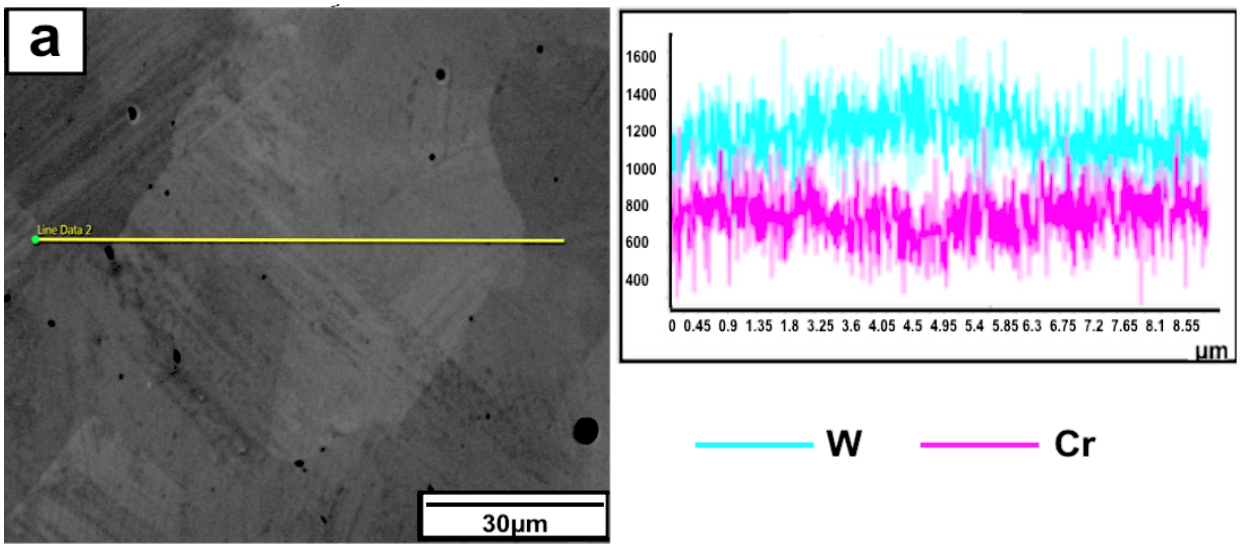

Figure 4.3: **W-28Cr at% 1700 °C homogenization** (a) BSE and (b) line scan profile of yellow line seen. in(a) for W-28Cr at% solution homogenized for 8h at 1700 °C. Black areas indicate regions of porosity

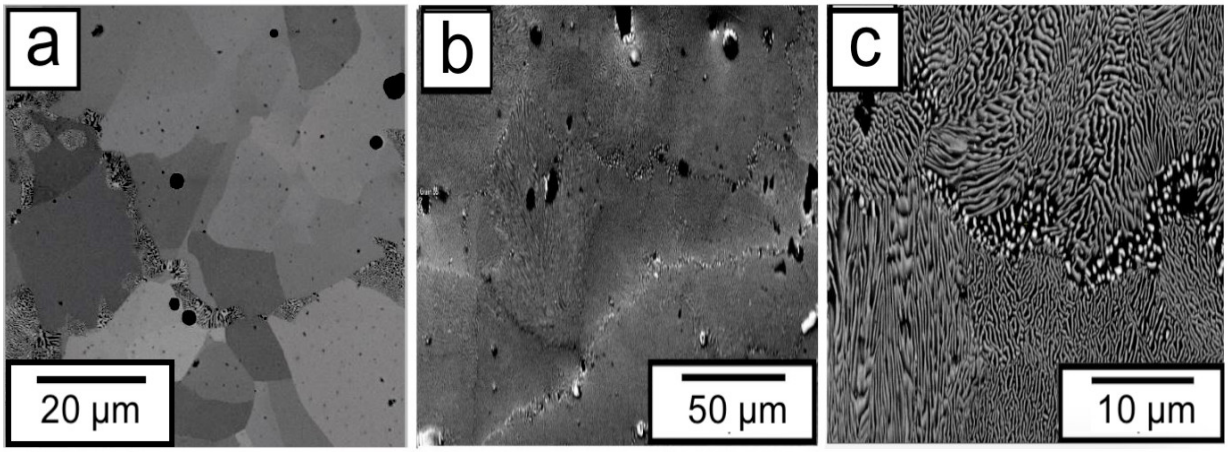

Figure 4.4: **W-28Cr at% 1250 °C ageing 1-10h** (a) BSE of W-28Cr at% aged for aged for 1hr at 1250 °C (b) BSE of W-28Cr at% aged for 10hr at 1250 °C (c) Zoomed in BSE of W-28Cr at% aged for 10hr at 1250 °C

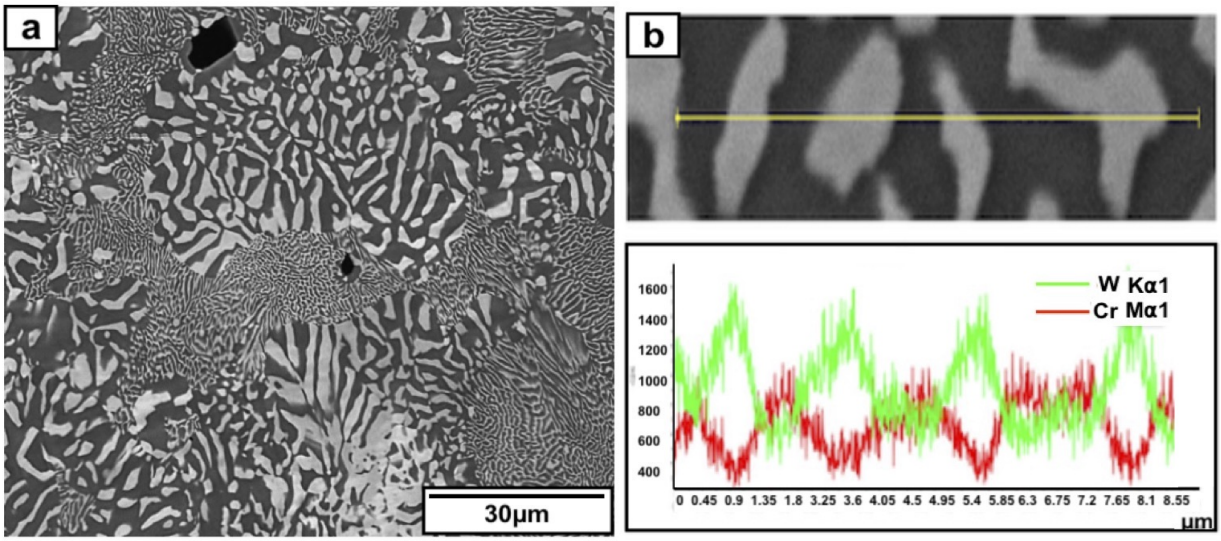

Figure 4.5: **W-28Cr at% 1250 °C ageing 100h** (a) BSE and (b) line scan profile (yellow line) and BSE of W-28Cr at% solution heat treated at 1700 °C for 8hrs and aged for 100h at 1250 °C.

presence of an element with a high atomic Z number (tungsten), and the darker areas have a lower nuclear Z number (chromium). As can be observed in figures 4.5, there appears to be a duel phase lamellar precipitation: The first has a much coarser grain size of approximately 580 ±42 nm in width, the second a much finer grain size of about 135 ± 31 nm. The finer precipitates are richer in chromium than the coarser precipitates, which are rich in tungsten. Although not shown, there are regions of the homogenized structure that show decomposition following homogenization of the alloy at 1700 ◦C; these are probably due to slow cooling in the furnace. The origin of this two-phase structure may, therefore, be due to the coarsening of the already present decomposed structure as a result of the homogenization. The second much finer chromium-rich phase precipitates due to ageing the alloy within the miscibility gap. The two-phase structure may also be due to the inherent nature of the miscibility gap, producing a tungsten-rich phase (with a composition matching the right-hand side) and a chromium-rich (matching the left-hand composition) of the binodal curve. At present, the reason behind this two-phase structure is still unexplained.

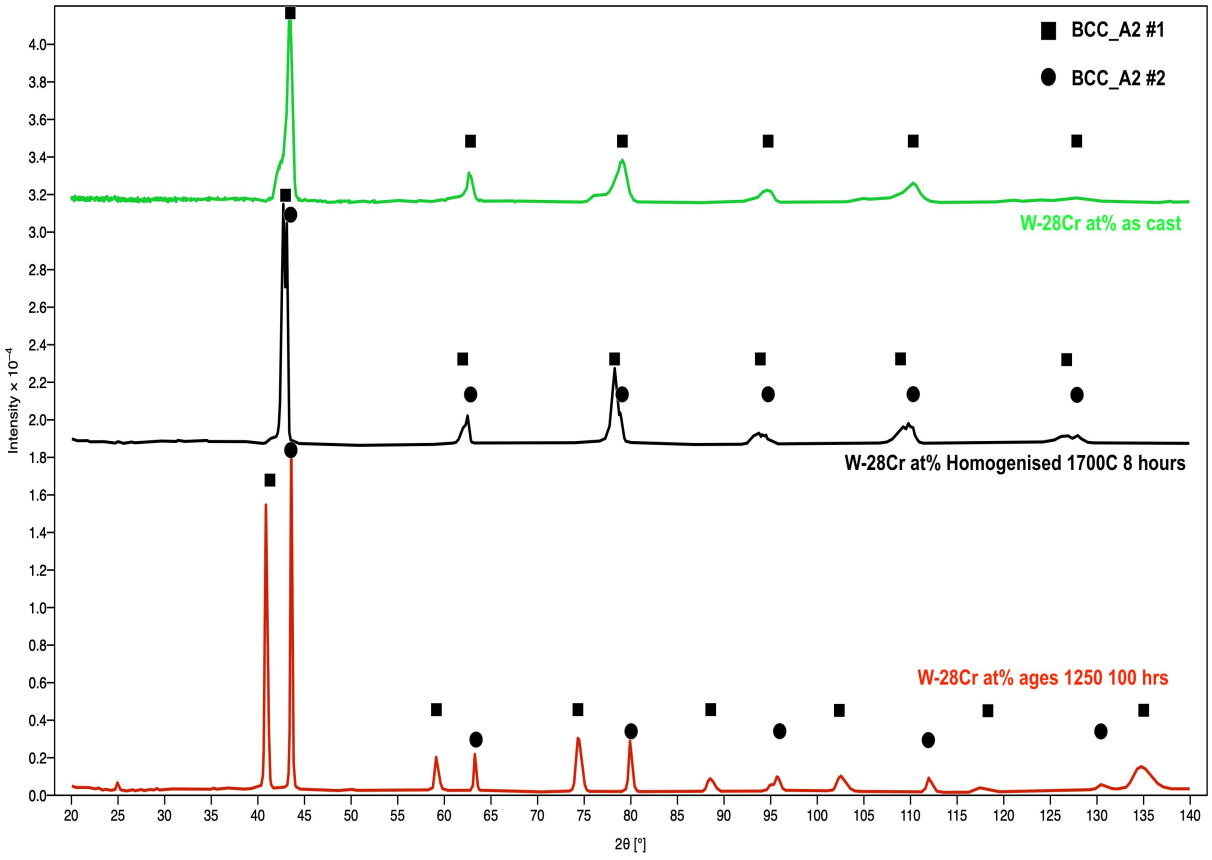

Figure 4.6: **W-28Cr% wt Xray diffraction** Identification of the phases present by XRD for W-28Cr% wt after varying heat treatments as indicated in the graph.

4.2.4 W-28Cr at% - XRD

Figure 4.6 shows XRD analysis of as-cast W-28Cr at% (red line), homogenized (black line), and homogenized and aged 100h (green line). Comparing the two lines for homogenized and as-cast samples. Analysis of aged W-28Cr at% confirms the presence of two phases of Im-3m WCr in 0.254 and 0.746 proportions. This confirms the conclusion seen from the SEM imaging of the presence of two different lamellar thicknesses. The larger 0.746 fractions in the aged sample are also in the heat-treated sample. The lattice parameters (Table 12) for the two im-3m phases of W-28Cr at% in the aged sample are 3.12 $\pm$ 0.01 and 2.83 $\pm$ 0.01. This is compared to the lattice parameter seen in the as-cast sample of 2.91 $\pm$ 0.007. The presence of the two lattice peaks in the aged sample confirms the spinodal decomposition of the W-28Cr at% sample with the 3.12 $\pm$ 0.01 peaks of the tungsten-rich phase and 2.87 $\pm$ 0.01 peaks of the chromium-rich phase.

Table 11: **W-28Cr at% XRD analysis** Crystal structure of W-28Cr at% (cast) as analyzed by XRD

Sample	2 θ angle	θ angle	d= λ/2sin(θ)	1/d^2	M= (H^2+K^2+L^2)	H	K	L	Lattice parameter (Å)
W-28Cr at% as cast	42.80	21.70	2.23	0.20	1.77	1	1	0	2.91$\pm$0.01
	62.68	31.84	1.48	0.46	4.02	2	0	0	
	77.13	38.57	1.21	0.68	6.02	2	1	1	
	93.52	46.76	1.05	0.91	8.01	2	2	0	
	110.24	55.12	0.94	1.13	9.99	2	2	1	
	128.11	64.06	0.86	1.36	12.00	2	2	2	

Table 12: **W-28Cr at%** Lattice parameter measurements of W-28Cr at% as analysed by XRD

Sample	Crystal structure	2 θ angle	θ angle	d= λ/2sin(θ)	1/d^2	H	K	L	Lattice parameter (Å)
W-28Cr at% Heat Treated 4 hours 1700 ° C aged 100 hours 1250 ° C		24.02	12.01	3.70	0.07				
	bcc$_1$	40.90	20.45	2.21	0.21	1	1	0	3.12±0.01
		59.62	28.81	1.56	0.41	2	0	0	
		74.43	37.22	1.27	0.62	2	1	1	
		88.53	44.26	1.10	0.82	2	2	0	
		103.52	51.26	0.99	1.03	3	1	0	
		118.66	58.83	0.90	1.23	2	2	2	
		136.72	67.36	0.84	1.44	3	2	1	
	bcc$_2$	43.58	21.79	2.08	0.23	1	1	0	2.83±0.01
		63.54	31.77	1.49	0.45	2	0	0	
		79.91	39.96	1.20	0.70	2	1	1	
		95.78	47.89	1.04	0.93	2	2	0	
		112.08	56.04	0.93	1.16	3	1	0	
		130.44	65.22	0.85	1.40	2	2	2	

4.2.5 W-28Cr at% - Hardness indenting

To determine the effects of ageing, the Vickers microhardness of W-28Cr at% alloy in each heat-treated condition was tested using a 2 kg load. The results from each test are shown graphically in figure 4.7. Heating W-28Cr at% to 1700 °C allows the as-cast structure to homogenize. The homogenization process removes the solute segregation of elements. After 1hr of ageing at 1250 °C, there is a slight increase in the hardness of the alloy. This can be explained by the presence of the fine lamellar precipitate, which can be seen to extend from the grain boundaries into the bulk of the grains when the alloy is aged within the miscibility gap. On ageing the alloy for 10 and 100h, there is a continuous decrease in the overall hardness of the alloy. A much coarser lamellar structure replaces this fine lamellar structure. This periodization of the finer lamellar structures reduces precipitation hardening and softens the alloy, as can be seen in figure 4.7

The work in this first section has demonstrated that a two-phase nanostructured W-Cr alloy can be produced through arc melting. Although this shows great promise, there are issues with manufacturing a sample in this way, namely the loss of chromium, segregation and overall porosity. The next step is to take this initial idea and produce greater quantities

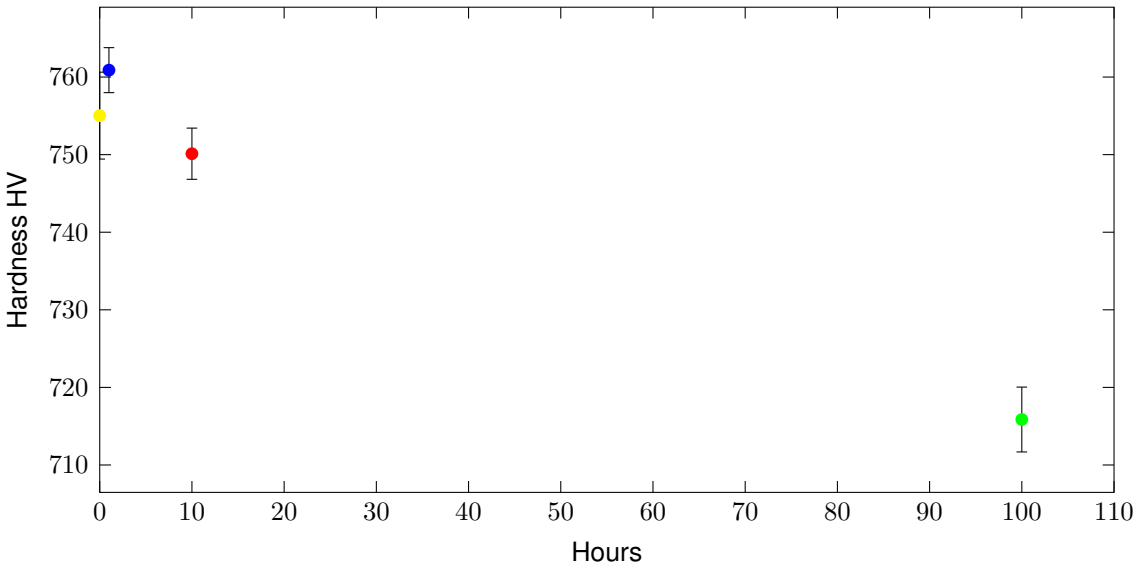

Figure 4.7: **W-28Cr at% hardness comparison** A comparison of the Vicker's hardness values following different heat treatments. Homogenisation at 1700 °C 8hrs, and 1, 10 and 100 hrs at 1250 °C.

of material that have less porosity; to this end, preparation and manufacturing techniques were explored further in section 4.3.

4.3 50/50 W-Cr alloy through powder metallurgy

4.3.1 Introduction

It has been demonstrated in this thesis and elsewhere that a W-Cr alloy is promising as a potential alloy for fusion reactors. However, there are obvious issues in manufacturing by conventional arc melting, as shown in figure 4.8. With this in mind, the following chapter explores using powders (blended and mechanically alloyed) for manufacturing bulk W-Cr samples.

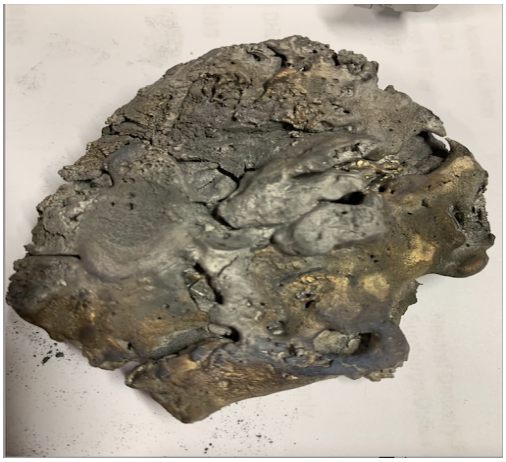

Figure 4.8: **Arc melted W-28Cr at% alloy** Example of an Arc melted tungsten chromium sample produced in the lab. Notice the presence of large segments of unmelted tungsten. What is not shown in the photograph is a large amount of chromium lost from the sample during the melting process.

4.3.2 A new tungsten chromium alloy from powders.

The first attempt was to make a new W-Cr alloy from tungsten and chromium powder via blending due to the relative simplicity of the procedure. 156.0 g of Tungsten and 44g of Cr (particle size -323 Mesh) were blended by planetary milling for 8 hours to break up agglomerates and to form a thoroughly mixed W-28Cr at% powder (figure 4.9 and 4.10). The powder was then die compacted into -12.7mm X 12.7mm pellets. The die set has a diameter of .509” (12.92mm). All sets were pressed at a 6000 pound (29,486 lb./in^2) load (some blow-off was observed during pressing). The pre-sintered pellets were characterized as follows:

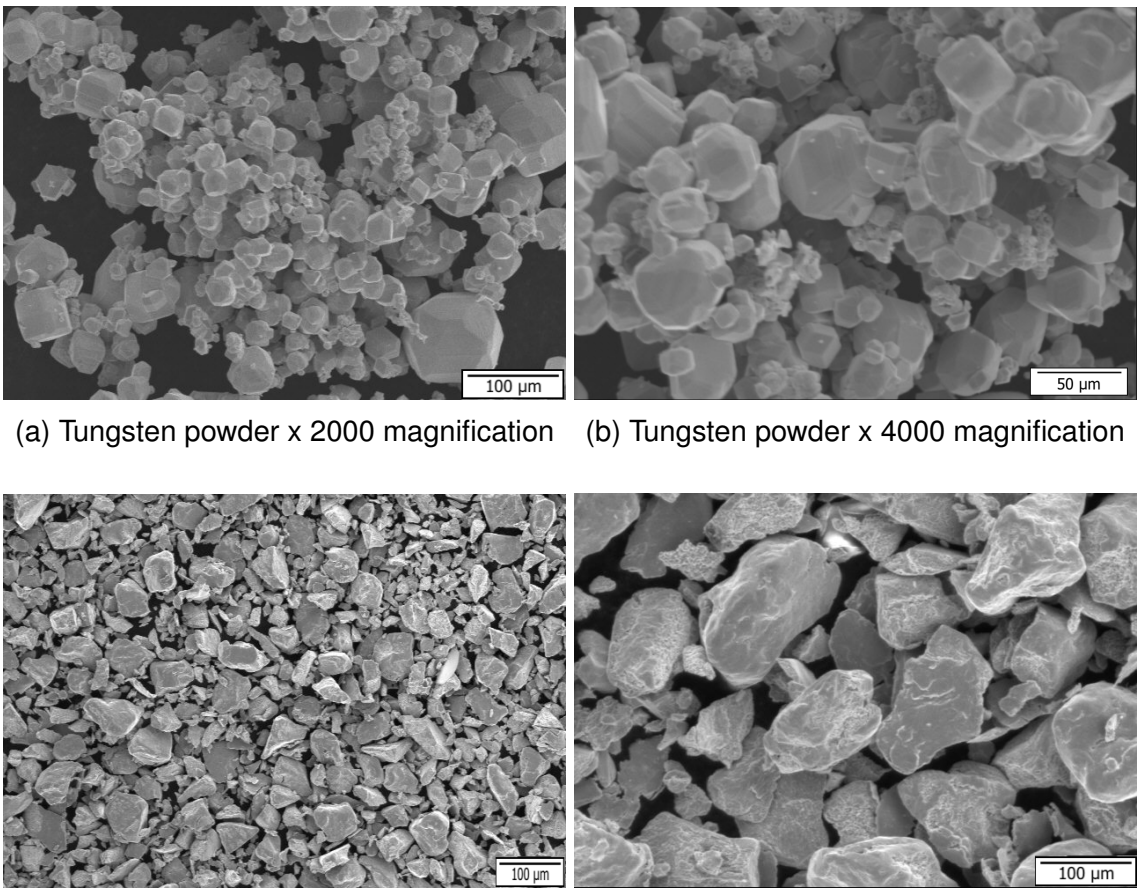

(a) Tungsten powder x 2000 magnification (b) Tungsten powder x 4000 magnification

(c) Chromium powder x 250 magnification (d) Chromium powder x 1000 magnification

Figure 4.9: **SEM of chromium and tungsten powders** SEM images of varying magnification of chromium and tungsten powders as purchased for manufacture of the W-28Cr at% alloy.

- 10.2 wt 9.1g .240” tall X .5130”
- 10.4 wt 9.4g .247” tall X .5130”
- 15.8 wt 15.5g .4125” tall X .5130”
- TD calculation = .2066in^2 X .4125” = 0.08526in^3 X .6990 = .0595 lb X 453.6 = 27.03g
- 15.5/27.03 = 57.34% dense

4.3.3 Batch 1 - Blending of a new tungsten chromium alloy from powders.

The above pellets were placed on a tungsten slab and pushed to the edge of the hot zone to burn off the die wall lub for 5 min. The pellets were then pre-sintered for 30 minutes

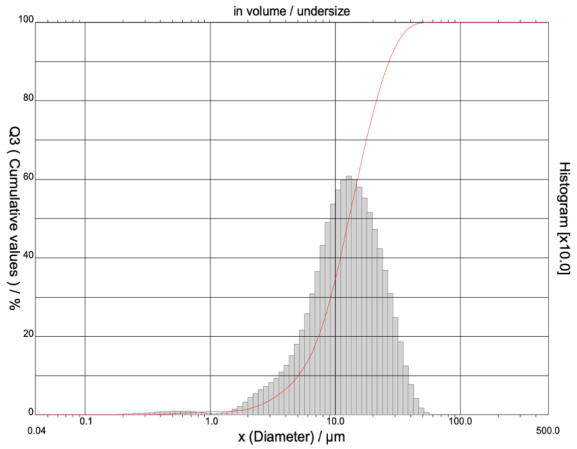

(a) Tungsten powder profile analysis

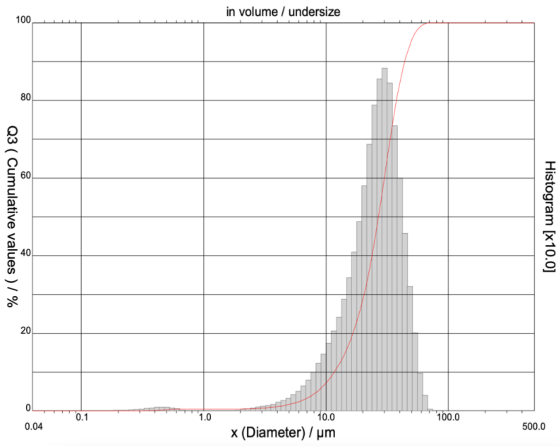

(b) Chromium powder profile analysis

Figure 4.10: **Profiles of powders used in the manufacture of W-28Cr at%** The size of the powder particles were measured by a Particle Size Analyzer, CILAS 1190 at Rhenium Alloys

in a 100% hydrogen atmosphere. After 30 min at temperature, the tungsten slab was pushed into the cold zone and cooled under a hydrogen atmosphere. The pellets were placed on a tungsten sheet inside a Spectra-Mat furnace for 1 hour at 1800 °C and 5 hours at 2000 °C. Following removal from the furnace, the samples were characterized for weight, size, and microstructure. The three tungsten pellets weighed 10.4, 10.2, and 15.8 grams. The pellets have a “dome shape with curved sides”. The three tungsten pellets, however, are not curved and appear more cylindrical. Their weights are similar to the powder pressed; 10.4 grams .3840” tall with a diameter on the bottom of 0.4885” and top 0.4515”. The theoretical weight of the W-Cr pellets should be 15.39 g, so the manufactured pellets have a theoretical density of 67.5%. ImageJ analysis of the etched samples shows a porosity of approximately 25.6 $\pm$ 2.85 % (as shown in figure 4.11 (c)).)

Due to the high degree of porosity and low density, it was felt that the issue in the manufacturing process lay in the large and irregularly shaped Chromium powder. It was, therefore, decided that the Chromium powder should be ball-milled using a tungsten carbide jar and balls. A chemistry check on the powder would need to be carried out to identify what contamination level this would have on any manufactured pellets. The sintering cycle would also be slowed down to increase diffusion time.

Table 13: **Blended Powder characteristics.** Diameter of powder particles with 325 Mesh as a percentage of sieved powder

	Tungsten 325 Mesh (μm)	Chromium 325 Mesh (μm)
Blended Powder PDS		
Diameter at 10 %	5.23 $\pm$ 0.15	10.59 $\pm$ 0.77
Diameter at 50 %	13.03 $\pm$ 0.18	24.81 $\pm$ 1.48
Diameter at 90 %	27.57 $\pm$ 0.49	42.24 $\pm$ 1.35
After blending PDS		
Diameter at 10 %	2.99 $\pm$ 0.12	
Diameter at 50 %	9.44 $\pm$ 0.31	
Diameter at 90 %	19.96 $\pm$ 0.27	

4.3.4 Batch 2: Ball Milling

Due to the high porosity in the initial samples, it was thought that ball-milling the powder would reduce the overall powder size and, subsequently, the porosity. With this in mind Eighty-two grams of blended W-28Cr at% powder from the initial pellet manufacturing process was blended with 200g of new W-28Cr at% powder. This powder was then milled at 400 rpm for 4 hours with WC jars and balls (10mm large and 4.69mm small). 141g of powder was placed in each jar (figure 4.11). Following milling, 259.8g of -200 mesh W-28Cr at% powder was collected in the pan, giving a 92% yield. Figure 4.12 shows the powder distribution spread after ball milling. If a comparison is now made to the blended powder before milling (figure 4.10), we can see that the profile of the chromium powder is shifted to the left, showing a considerable reduction in the mean size of the particles. Six pellets (12 grams each) were die compacted with a 5000-pound load with a 0.509" diameter ram. Two sintering runs were conducted. The first was a long pre-sintering where three samples were placed in the furnace at 800 °C and ramped slowly to 1600 °C to diffuse all the chromium for 8 hours at a positive pressure hydrogen atmosphere to slow pre-sinter and then held at this temperature. The second was a much shorter pre-sintering run of 1000℃ 10-30min. All of this was conducted positively under a positive-pressure hydrogen atmosphere.

All six samples were then sintered together by ramping to 1800 °C and hed for 1 hour, then ramped to 2000 °C for 5 hours.

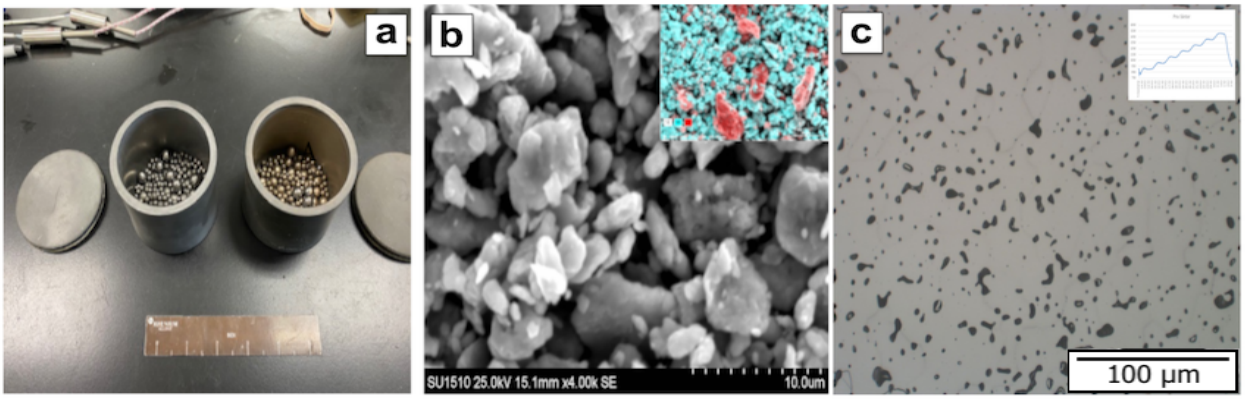

Figure 4.11: **W-28Cr at% alloy created from blended powder and long term sintering** (a) WC ball mills used to blend powder, (b) SEI and EDX image (inset) of ball milled powder and (c) BSE of long-term sintered manufactured W-28Cr at% alloy (inset shows timing ramp for long-term sintering)

On the characterization of the sample, microstructure necking was observed in the long pre-sintered microstructure (figure 4.13). The long-term pre-sintered ball mill pellets achieved a theoretical density of 77-84%, and short pre-sinter ball milling achieved only 66-75% density. Chromium, however, evaporated during sintering from the short pre-sintering samples. The long pre-sintered/sintered microstructure has both porosities at grain boundaries and porosity in the grains (figure 4.16).

In the last experiment, long pre-sintering and sintered pellets had less porosity and high hardness (522VHN), indicating good alloying. Based on this observation, a long-term pre-sintering was conducted from 800 °C to 1600-1625 °C with an 8-hour slow ramp rate to promote diffusion without evaporating the chromium. The powder was held for 8 hours at 1625 °C.

4.3.5 Batch 3: Ball Milling and cold isostatic pressing (CIPping)

Compared to previous experiments, the observation of less porosity in these samples demonstrates that finer chromium powder gives a better result. To improve further on the porosity issue, it was felt that further milling of the powder and using a CIPping step before sintering might help to improve the density. The chromium powder was ball milled for a further 8 hours. The batch was 1000g, 220g Cr, and 780g of GTP M55 grade

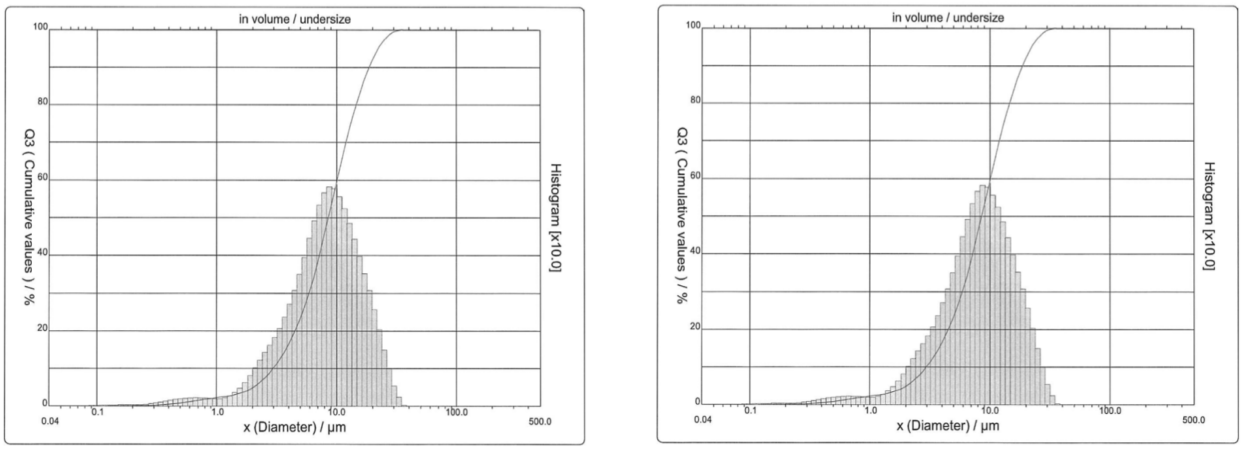

(a) (b)

Figure 4.12: **PDS of tungsten and chromium powders after ball milling. The size of the powder particles was measured by a Particle Size Analyzer, CILAS 1190 at RHenium Alloys** (a) Powder distribution spread (PDS) of tungsten powder profile analysis after ball milling (b) Powder distribution spread (PDS) of chromium powder profile analysis after ball milling

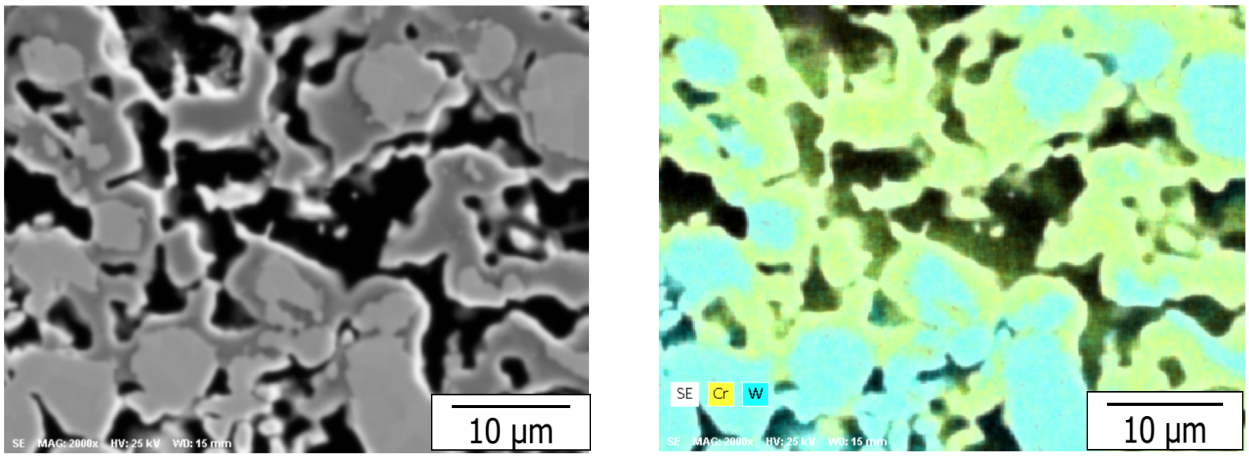

(a) SEI image of long-term sintered ball milled powder

(b) EDX image of long-term sintered ball milled powder

Figure 4.13: **EDX analysis of ball milled powder**

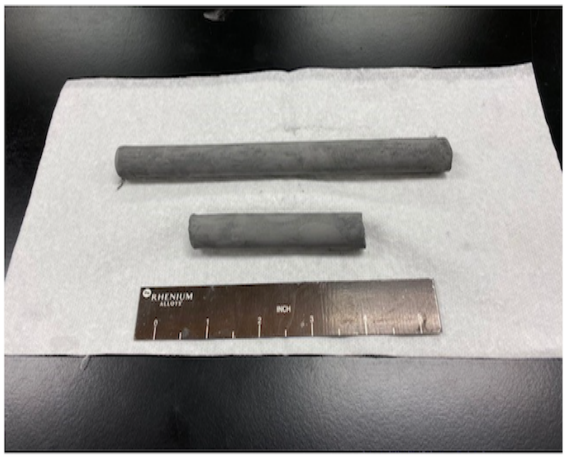

Figure 4.14: **CIPped W-28Cr at% bars** 2 bars of W-28Cr at% after slow CIPping and prior to the pre-sintering phase.

tungsten was blended. 584g of W-28Cr at% powder was used to pack a 0.850" CIP bag. In addition to what had been done previously, it was thought that CIPping the powder before sintering could aid diffusion and promote better alloy bonding. The CIPped was operated at a pressure of 58KSI in a 10 X 24 chamber. The resulting CIP rod was broken into two pieces (figure 4.14). The CIP W-28Cr at% (ball milled Cr only) was pre-sintered for three days up to 1600 °C. On day one, the CIP rod was placed in a small molybdenum boat in the tube furnace for pre-sintering with positive-pressure hydrogen. At a starting temperature of 350 °C and slowly ramped to 1500 °C with a step of 100 °C and held for 45 min and then ramped up an additional 100 °C to 1600 °C. It was held at 1600 °C for 2.5 days. The rod was then pulled into the cool zone (water-cooled/hydrogen atmosphere) and cooled to room temperature (figure 4.15). The average diameter of the rod was 0.652", with a length of 3.3", a weight of 194.6 grams, and a theoretical density of 76.4%. The larger CIP rod was sintered for 8 hours at 2000 °C.

Chemical composition on the small Pre-sintered CIP rod was conducted. The larger CIP rod was then sintered for 8 hours at 2000 °C. The sample is shown in figure 4.16.

Hardness values for the six samples produced from the first three manufacturing methods described above are shown in table 14. In addition to these values, porosity and grain diameter (table 15) are also presented.

(a) W30Cr (wt.%) after slow ramped pre-sintering phase.

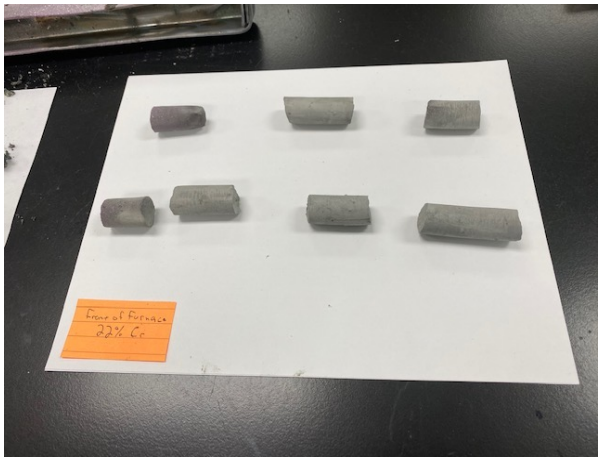

(b) W-28Cr at% after slow ramped pre-sintering phase

Figure 4.15: **W-28Cr at.% and W30-Cr (wt.%) after slow ramp rate pre-sintering to 1650 °C.** The temperature was ramped from 500-1650 °C over 5 days and then held at 1650 °C for two days

Table 14: **Hardness measurements for W-28Cr at%.** Hardness measurements for W-28Cr at% produced by different manufacturing methods described above.

Sample	Hardness Measurements (2Kg)					Average Measurement
Blended W, with extra	342.9	310.0	326.5	344.3	321.8	**329.4 ± 13.2**
blended Cr Powder	305.1	336.2	343.6	327.2	336.4	
Ball Milling	458.8	447.2	474.2	458.1	477.4	**471.0 ± 16.2**
CIPping Short Sinter time	502.5	461.3	488.2	458.7	483.7	
Ball Milling/CIPping	437.7	462.4	472.9	387.4	450.3	**446.7 ± 25.9**
8 hours Sintering time	447.9	420.8	451.7	484.6	451.4	
Ball Milling/CIPping	429.2	405.9	345.8	350.2	415.3	**392.1 ± 33.7**
Short Pre-Sintering time	428.2	416.6	361.3	349.7	418.3	
Ball Milling/CIPping	383.5	351.5	410.9	388.3	441.0	**399.0 ± 33.3**
8 hours Sintering time	366.2	393.2	423.2	462.4	370.0	

Table 15: **W-28Cr at% Porosity and grain size measurements.** Porosity and grain diameter measurements for W-28Cr at% produced by different the first three manufacturing methods described above.

manufacture method	Porosity %	Grain Diameter μm
Blended W, Cr Powder	-	-
Blended W, with extra blended Cr Powder	20.29± 13.2	20.4 ± 0.8
Ball Milling/CIPping Short Sinter time	13.99 ± 16.2	18.7 ± 0.3
Ball Milling/CIPping 8 hours Sintering time	18.90 ± 25.9	10.2± 0.2
Ball Milling/CIPping Short Pre-Sintering time	23.01 ± 1.57	3.0 ± 0.5
Ball Milling/CIPping 8 hours Sintering time	16.71 ± 1.39	4.3 ± 0.9

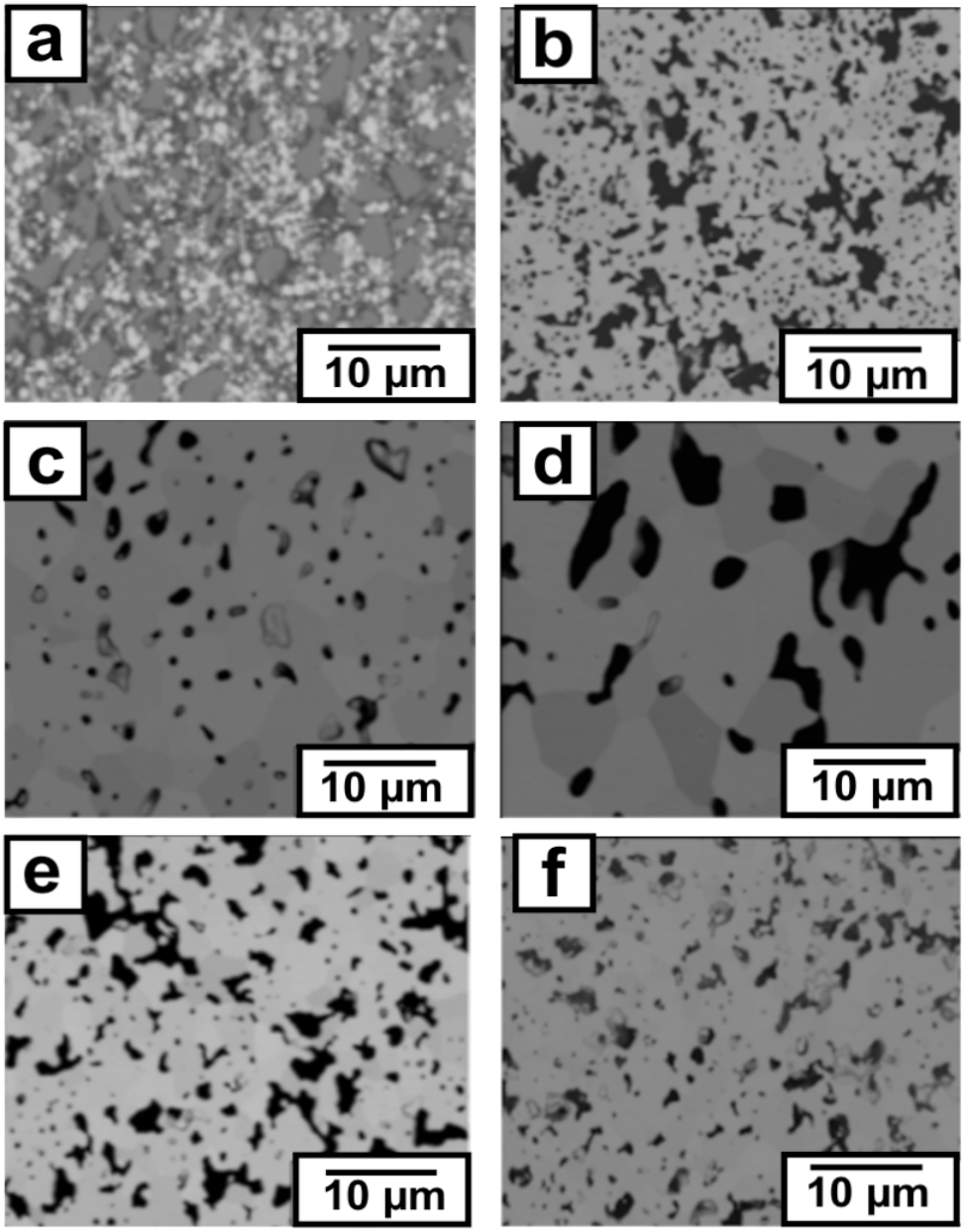

Figure 4.16: **BSE images of each W-28Cr at% sample manufactured in experiments 1 through 3.** (a) Blended W and Cr powder p-933, (b) Blended W, with extra blended Cr Powder p-934, (c) Ball Milling CIPping Short Sinter time p-970, (d) Ball Milling/CIPping 8 hours Sintering time p-971, (e) Ball Milling/CIPping Short Pre-Sintering time p-019 and (f) Ball Milling/CIPping 8 hours Sintering time p-021

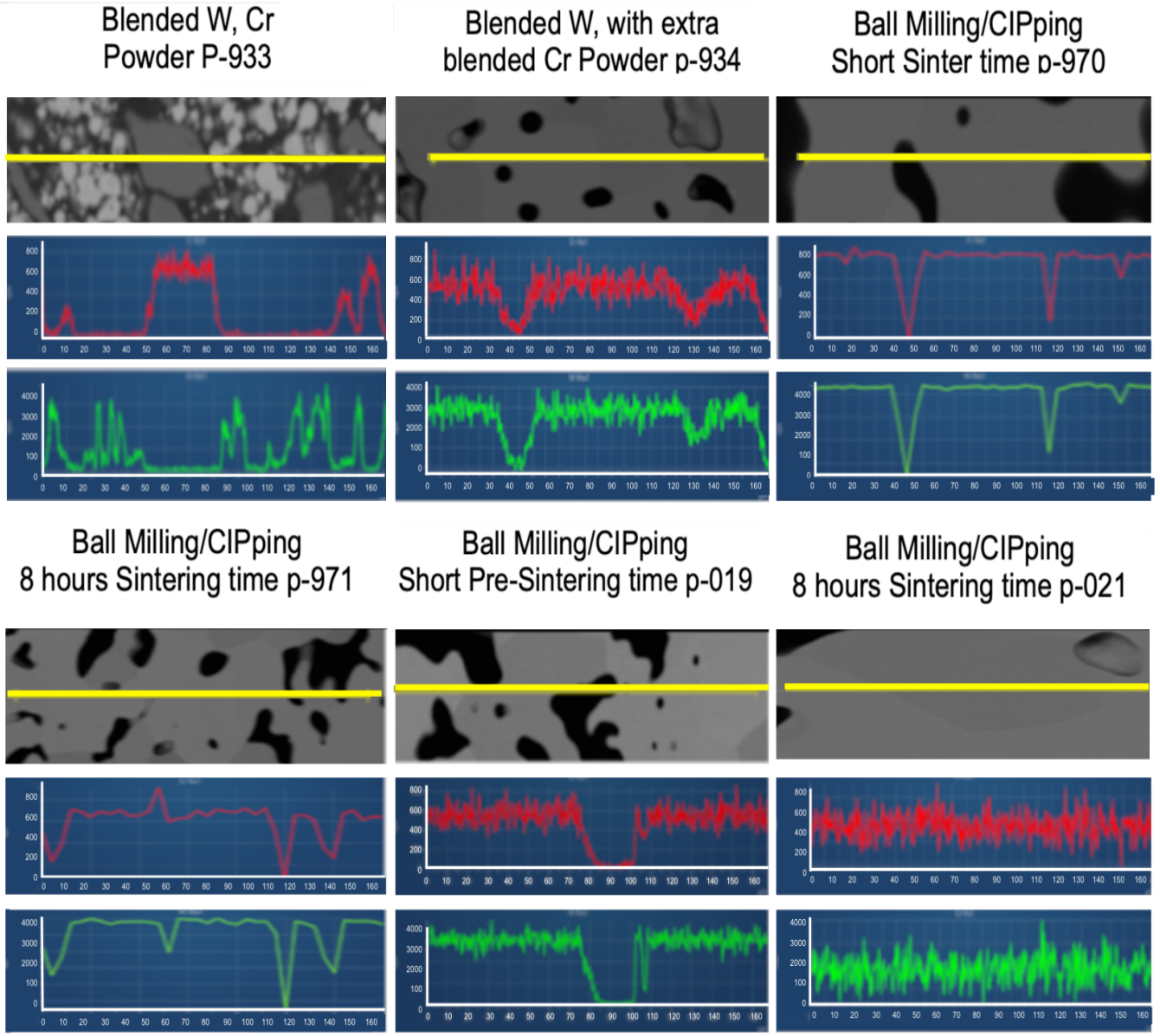

Figure 4.17: **BSE images and EDX line scans of each W-28Cr at% sample manufactured in experiments 1 through 3.** Each sample is identified by the number above or below the images. (Red - tungsten, Green - chromium.

4.3.6 Batch 4: Blending, CIPping, Sintering, HIPping and Swagging and a little extra chromium

Both (figure 4.16) CIPped samples had an extensive area of approximately 1 to 1.5 mm on the exterior of the cast sample that is devoid of chromium (image not shown). To mitigate some of the losses from the surface, in addition to W-28Cr at% that was manufactured in the previous three iterations. W-30Cr was made by blending W-28Cr at% with extra ball-milled chromium, and then the blended powder re-ball milled to alloy the W and Cr mechanically.

Figure 4.18: **Sintered bars of W-28Cr at% alloy** W-28Cr at% samples after sintering in molybdenum cans for 8 hours at 2000 °C

The CIPped bars were pre-sintered in a hydrogen furnace for nine days. Initially, the powder used for CIPping was ramped slowly from 750 °C to 1625 °C for 7.3 days and then held at 1650 °C for a further two days. At this stage, the compact produced broke into small pieces on removal from the furnace. Figure 4.15 the new W-28Cr at% and W-30Cr at% after pre-sintering. The samples were replaced into the furnace for extra-long sintering, with a slow ramp rate pre-sintering to 1650 °C. The temperature was ramped from 500-1650 °C over five days, then held at 1650 °C for two days. Figure 4.15b shows the W-28Cr at% samples after this stage. The W-28Cr at%, and W-30Cr at% compact was then sealed in a molybdenum tube for sintering to 2000 °C for 8 hours to prevent loss of chromium during the high-temperature sintering process. After sintering, both cans

developed holes (probably due to the vitalization of chromium), one on the side and the other a hole on the bottom, as can be seen in figure 4.18.

Samples were then HIPped at 2000 °C for 8 hours in a 0.020" (.508mm) niobium sheet and 0.125" (3.175mm) OD niobium tubing cans. However, the damage was evident when removing both samples from the HIP chamber. This suggested that the pressure of the argon gas inside the can became too high during the manufacturing process and caused rupturing. When the sample was removed from the can and observed under a light microscope, considerable porosity was seen. Therefore, further experimental work on this sample was halted.

4.4 W-28Cr .at% spark plasma sintered (SPS), blended powder

4.4.1 Introduction

The previous section shows that a W-Cr alloy of sufficient density was not produced despite the manufacturing method used. Therefore, a second approach to manufacturing this alloy was investigated using spark plasma sintering (SPS) or field-assisted sintering technique (FAST). Two approaches to SPS were investigated; the first was to use the blended powder created previously, and the second, the mechanically alloyed powder, was used to manufacture a W-28Cr at% alloy.

4.4.2 Blended Powder with Spark Plasma Sintering

In the first approach, 600g of blended powder created from the CIPping process above was processed into 3 200g SPS pucks of approximately 40 mm diameter and 10 mm thick. Three 0.05 mm wide graphite tabs were placed above and below the powder to help prevent the melting of the powder to the die. Graphs showing the loading pressure, processing temperature, holding time, and average relative piston height from its starting position are presented for each sample produced in figure 4.19.

The first sample was processed at 1800 °C for an hour. However, on removing the puck from the dye, a small lump of metal was observed on the outside of the carbon tab.

Table 16: **Tungsten phase composition in SPS samples manufactured from blended powder.** Table to show the tungsten composition (.at%) of each phase present in the as-received SPS alloys as measured by EDX analysis average of 10 point measurements for each sample.

Sint. Temp. (°C)	Time at max temp (mins)	Average Composition .at%	Tungsten Rich Region .at%	Mixed Region .at%	Chromium Rich Region .at%
		W	W	W	W
1500	60	45.88 ± 2.56	87.93 ± 1.82	47.84 ± 2.37	6.16 ± 0.84
1650	10	48.90 ± 0.19	84.93 ± 2.65	46.60 ± 1.48	3.17 ± 2.86
1800	60	49.80 ± 1.67	74.86 ± 1.84	52.00 ± 2.62	2.04 ± 0.63

EDX analysis of the lump gave an average composition of 92.4 ± 2.2 at.% chromium. Suggesting some of the material (mainly chromium) had escaped during the sintering process. A second and third puck from the same powder was processed at 1500 °C and 1650 °C, respectively, each for ten minutes. Despite the reduction in temperature, metal was seen on the outside of the dyes.

4.4.3 SEM and EDX of Blended SPS alloys

SEM images and EDX analysis of the three blended samples in the as-received condition are shown in figure 4.20. Figure 4.20 shows regions of segregation, with the darker grains richer in chromium. This is due to the sintering temperature being below the homogenization temperature reported in the literature between 1630 and 1677 °C. Table 16 shows the measured compositions of the different phases in the as-received condition. The porosity of the sample was estimated to be 16.4 ± 2.4% (image J). Comparing this to the sample processed at 1650 °C (Figure 4.20b), SEM and EDX show greater homogeneity between the tungsten and chromium in addition, the porosity of the sample was measured to be 8.6 ± 1.7% (image J). Although the final sample processed at 1800 °C for 1hr (Figure 4.20c) has remarkedly less porosity (5.2 ± 0.8% (image J)), EDX analysis shows a considerable loss of chromium (as mentioned earlier). SEM and EDX of the outer regions of the sample confirm significant losses of chromium. As seen in figure 4.21, tungsten precipitation is formed in the darker chromium-rich phase. These decomposition regions

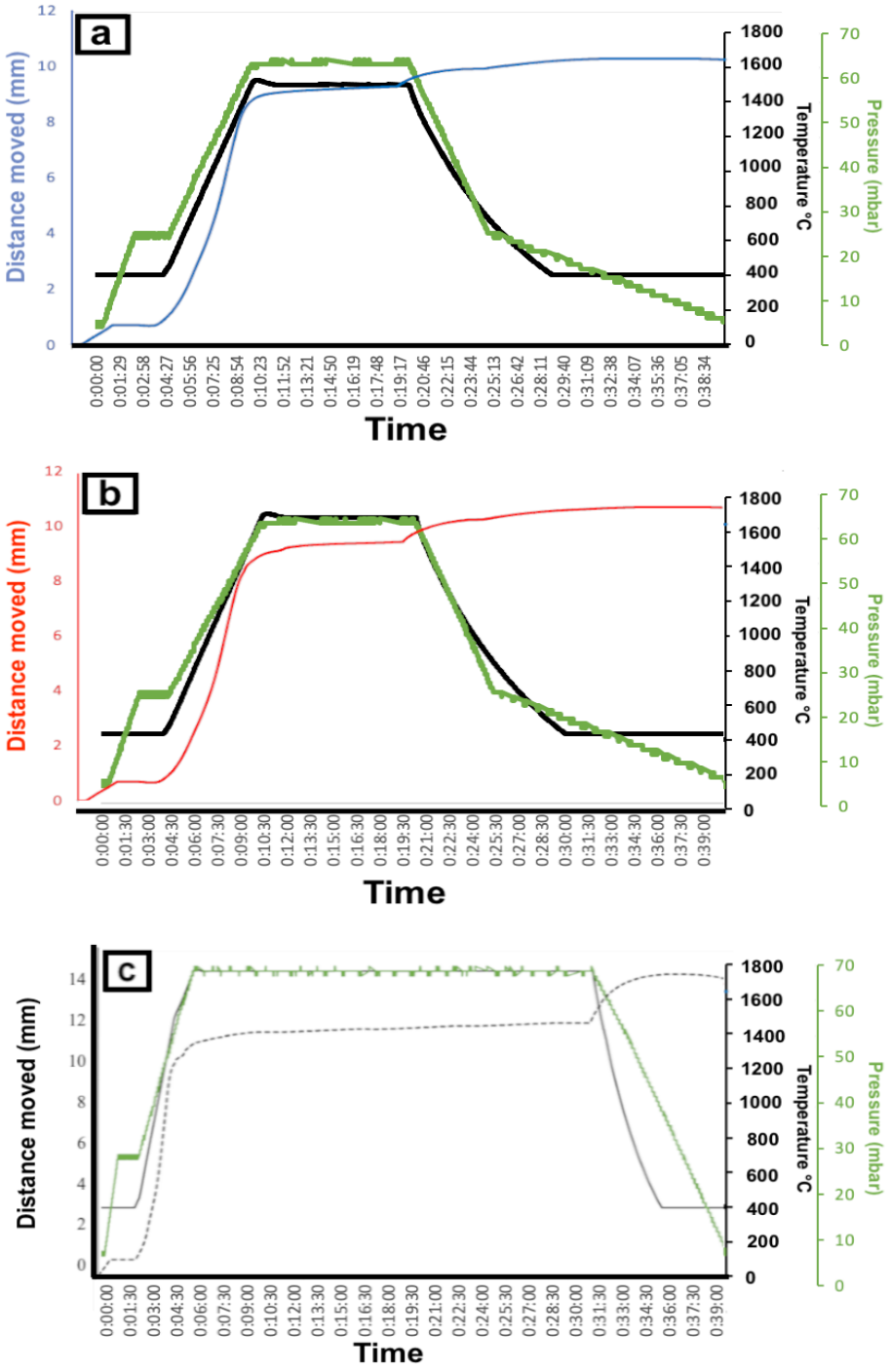

Figure 4.19: **Spark plasma sintering (SPS) machine cycle parameters used to create the three samples from the blended powder.** Each graph shows the pressure (black) and temperature (green). Blue, red, and black (dotted) represent the reduction in the sample thickness as the dye moves downwards as the powder is sintered for blended powder at 1500 °C for 10 mins, 1650 °C for 10 mins and 1800°C 1hr.

result from manufacturing the two samples within the miscibility gap of the phase diagram. The presence of the decomposed phases explains the peaks observed in the XRD analysis mentioned earlier.

Figure 4.22 shows the three blended alloys in their homogenized condition (After 8 hours at 1700 °C). Each of the three alloys shows regions rich in tungsten (light grey) and chromium (black). Of the three samples, the 1800 °C manufactured sample shows the greatest homogeneity, with fewer chromium-rich regions (bright green areas, EDX analysis). This could, however, be due to the loss of chromium from the sample seen in the manufacturing stage. EDX maps (figure 4.22 inset) show that the chromium-rich areas (green) have small areas of tungsten (orange) present. It has been stated that the homogenization of a W-Cr alloy is determined by the diffusion of tungsten into the chromium phase (Oliver Cc 2021).

On ageing the samples at 1250 °C for 100 hours, each of the three samples appears as a partially decomposed structure of alternating layers of tungsten and chromium (figure 4.23). EDX and line scan data (figure 4.23) further confirm the decomposition of the homogenized samples into a two-phase microstructure. The 1800 °C manufactured sample shows the finest decomposed structure of the three blended samples. It suggests that although there is a significant loss of chromium from the sample in the manufacturing stage, the initial temperature determines greater powder diffusion in the as-received sample. This leads to a more consistent and finer decomposition structure in the final aged sample.

Figure 4.20: **SEM observation of the 3 SPS W-28Cr at% alloys manufactured from Blended powder after in their as received condition**(IPF map, SEI, and EDX analysis (tungsten orange, chromium green) (a) 1500 °C 10 mins (b) 1650 °C 10 mins and (c) 1800 °C 1 hour.

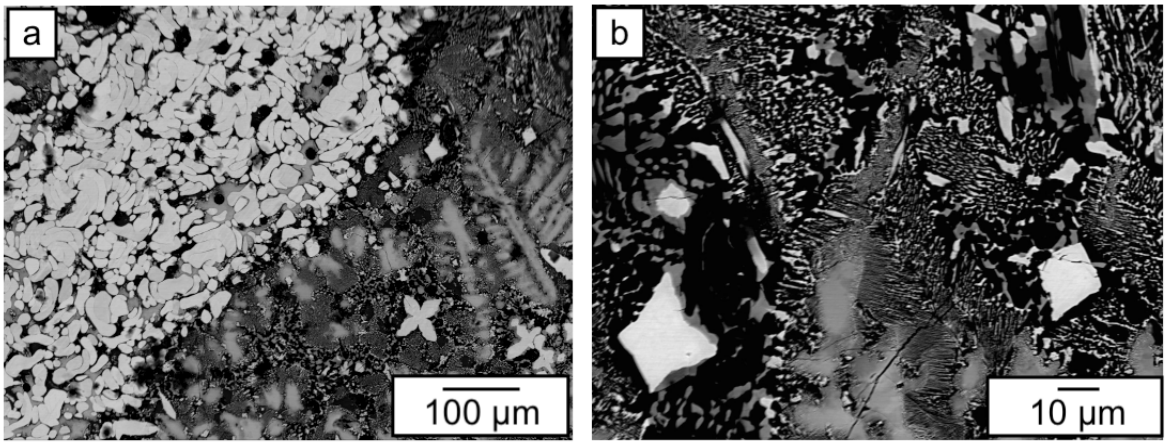

Figure 4.21: **SEM showing regions of decomposition of the as-received SPS sample manufactured at 1800°C for 1hr.** (a) low magnification SEM image (b) zoomed-in image of the selected area of (a) showing the decomposition of the alloy into two distinct regions as indicated by the white (tungsten) and black (chromium) rich regions as a result of rapid cooling.

Figure 4.22: **SEM observation of the 3 SPS W-28Cr at% alloys manufactured from Blended powder after homogenization at 1700 °C.** IPF map, SEI, and EDX analysis (tungsten orange, chromium green) of the 3 SPS Blended powder W-28Cr at% alloys manufactured by SPS (a) 1500 °C 10 mins (b) 1650 °C 10 mins and (c) 1800 °C 1 hour

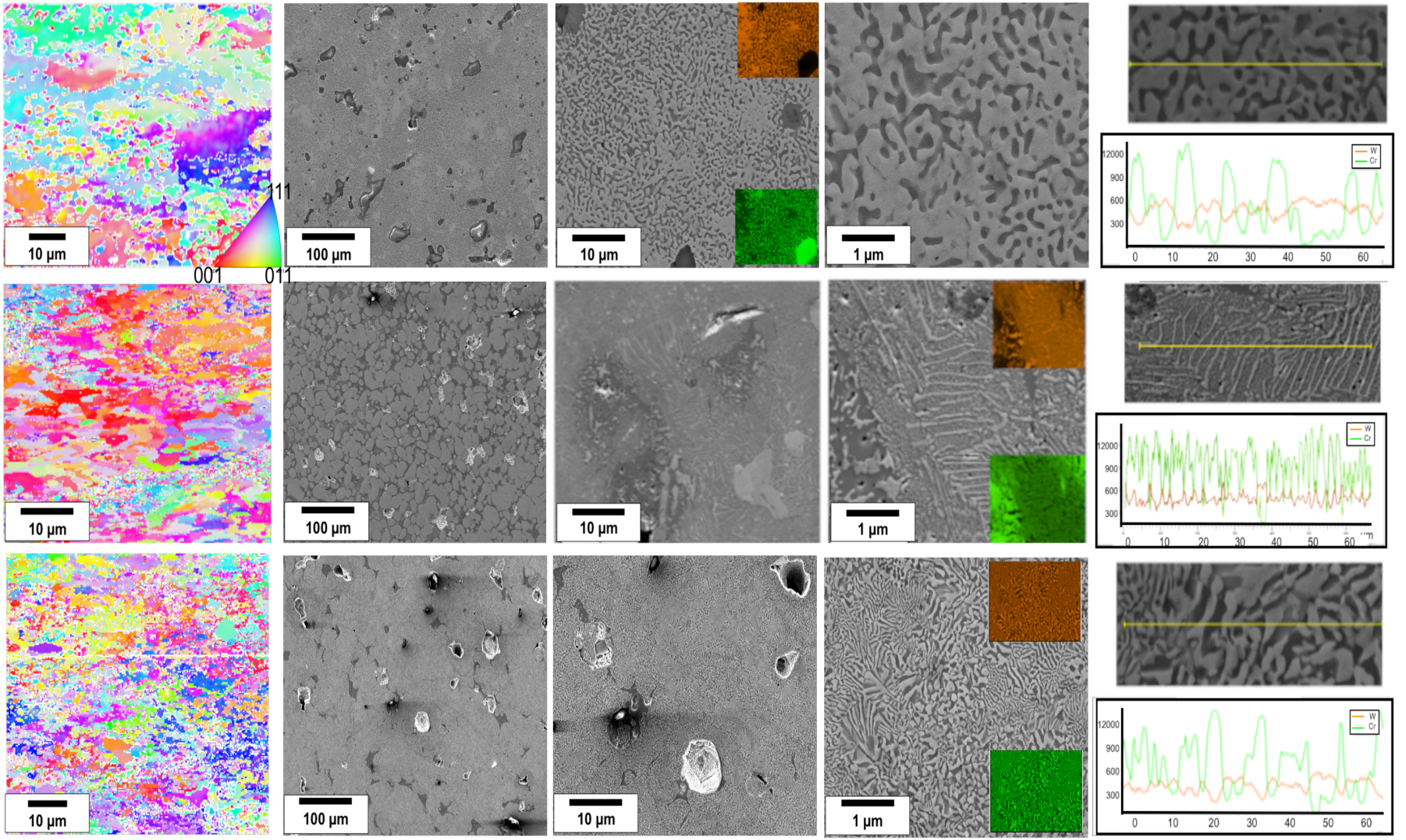

Figure 4.23: **SEM observation of the 3 SPS W-28Cr at% alloys manufactured from Blended powder after ageing for 100 h at 1250 °C.** IPF map, SEI, and EDX (insets) and line scan analysis (tungsten orange, chromium green) (a) 1500 °C 10 mins (b) 1650 °C 10 mins and (c) 1800 °C 1 hour.)

4.4.4 XRD of Blended SPS alloys

XRD analysis of the three as received blended samples are presented in figure 4.24. Each pattern has five central alpha Body body-centred cubic (bcc) crystal structure peaks. All samples show double diffraction peaks at each of the five peaks, which may indicate the phase decomposition into two bcc A2 phases. These decomposed phases result from the manufacturing temperature being in the miscibility region of the tungsten chromium phase diagram. The presence of double peaks in the sample manufactured at 1800 °C is interesting as this is outside of the miscibility gap and should not produce a two-phase alloy. It could indicate that the decomposition is due to the alloy cooling within the miscibility gap.

The varying chemical composition of the finished alloy will, therefore, result in a broadening of the diffraction peaks. As seen in figures 4.24b and c, magnified images of the (110) and (200) peaks from the as-received samples show a shift in both of the peaks (as indicated by the black arrow) for the 1500 °C sample (blue); this is due to the higher content of chromium (approximately 4%) in the sample which lowers the lattice parameter of the alloy. The 1650 and 1800 °C, which lost chromium during manufacturing, show increased lattice parameters due to the tungsten content. This demonstrates that manufacturing the alloy at lower temperatures improves the amount of chromium in the final alloy.

Lattice parameters for the three alloys produced from the blended powder (Table 17) in the as-received condition are similar to those found in the literature for W-Cr alloys. Those portions of the alloy rich in chromium have a lower lattice parameter than the tungsten-rich regions.

Following Homogenisation at 1700 °C for 8 hours, XRD analysis of the blended samples is shown in figure 4.24d. All samples show some degree of double please and not the expected single bcc peaks. Therefore, this suggested that the homogenisation procedure was not sufficient or again, the manner in which they cooled allowed the alloys to sit in the miscibility gap too long

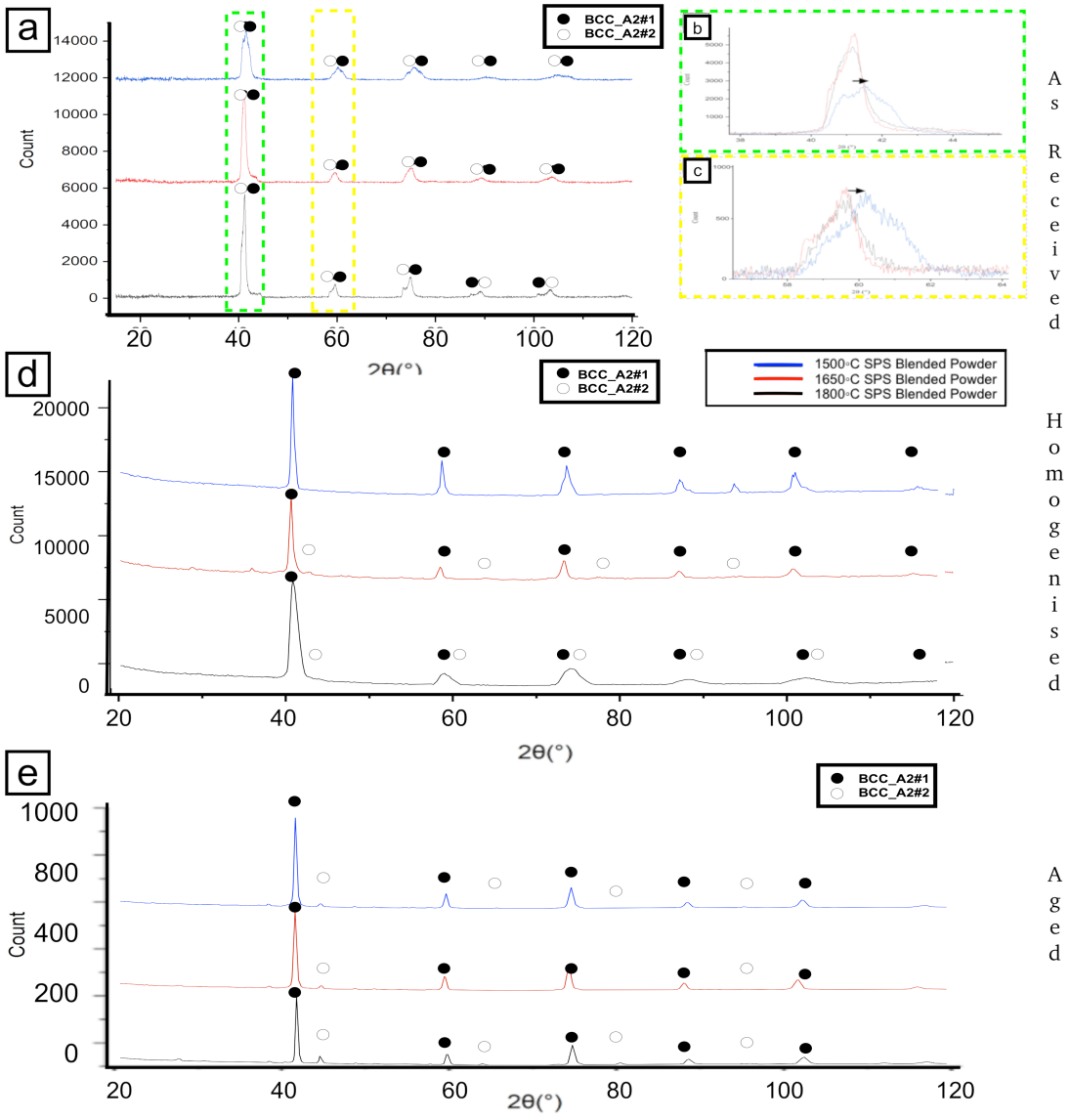

Figure 4.24: **XRD analysis of the 3 SPS samples manufactured from blended powder in the as-received condition, homogenised at 1700 °C 8 hours and aged at 1250 °C for 100 hours.** (a) XRD patterns of SPS sintered samples in the as-received condition; black dots represent tungsten bcc crystal structure peaks. (b, c, and d) Stacked and magnified images of peaks seen at 42 ° and 60 ° show shift due to chromium content. (e) XRD patterns of SPS after homogenised at 1700°C 8 hours. (f) XRD patterns of SPS sintered samples after ageing for 100 hours at 1250 °C. (g) Magnified images of peaks seen at 42 °, 60 ° and 71 ° show shift due to chromium content. Manufacturing temperatures represented as 1500 °C 10 mins (blue), 1650 °C 10 mins (red) and 1800 °C 1 hour (black).

Table 17: **Table to show the results of Relative density, Porosity, and lattice parameters for SPS manufactured samples.** Relative density, Porosity, and lattice parameters results for SPS manufactured samples with different powders and processing routes in the as-received condition.

Heat treatment	Manufacturing Method	Relative Density (%)	Porosity (%)	Lattice Parameter (nm)
As Received	Blended Powder			
	1500℃	86.94	13.06	3.07 3.11
	1650℃	97.81	12.19	3.10 3.15
	1800℃	99.71	0.29	3.13
	Mechanically Alloyed Powder			
	1500℃	99.95	0.05	3.08 2.95
	1575℃	98.44	1.56	3.09 2.95
	1650℃ 5 mins	98.83	1.17	3.07 2.94
	1650℃ 15 mins	97.93	2.07	3.08 2.94
Homogenised 1700°C 8 hours	Blended Powder			
	1500℃	87.01	12.99	3.12 3.09
	1650℃	98.23	1.77	3.13 2.95
	1800℃	99.72	0.28	3.10
	Mechanically Alloyed Powder			
	1500℃	99.95	0.05	3.12
	1575℃	98.76	1.24	3.13
	1650℃ 5 mins	98.92	1.08	3.12
	1650℃ 15 mins	98.13	1.87	3.08
Aged 1250°C 100 hours	Blended Powder			
	1500℃	87.01	12.99	3.10 2.82
	1650℃	98.23	1.77	3.12 2.83
	1800℃	99.71	0.29	3.09 2.82
	Mechanically Alloyed Powder			
	1500℃	99.94	0.06	3.14
	1575℃	98.77	1.23	3.15
	1650℃ 5 mins	98.94	1.06	3.15
	1650℃ 15 mins	98.13	1.87	3.14

XRD results are shown in figure 4.24e for the three blended samples after ageing at 1250 °C for 100 hours. Each of the three alloys shows two sets of bcc peaks, one belonging to a tungsten-rich phase and the second to the chromium-rich phase (as shown later). The peaks show slight differences in the measured diffraction angles, indicating a compositional difference in the decomposed phases. This is probably due to the chromium lost during the initial manufacturing stage.

4.4.5 Porosity and Archimedes density of SPS manufactured samples.

Table 17 presents the porosity and Archimedes density of SPS manufactured samples. When comparing the two powders, the Mechanically alloyed powder produces samples that improved density, a much finer grain structure, and reduced porosity.

4.4.6 EBSD of Blended SPS alloys

EBSD analysis of the three samples in the as-received condition is shown in figure 4.20. The mean grain size for each alloy is plotted in figure 4.25. As can be seen from the plot, the sample processed at 1500 °C has the largest average grain size of the three samples manufactured by SPS from blended powder, with the sample manufactured at 1800 °C having the smallest average grain size (this grain trend is later confirmed by the hardness data.) EBSD analysis of the blended samples following homogenization at 1700 °C for 8 hours (figure 4.22) show an increase in grain size as compared to that of the as-received samples. The increase in grain size matches with the initial trend of the as-received samples, with the 1500 °C having the largest grain size of the three samples. On ageing, all of the samples show are marked decrease in grain size (as can be seen in the SEM images demonstrating decomposition) with the 1800 °C having the smallest grain size measurement of 1.65 μm^2. Grain area measurements for the three alloys are 3.07, 3.01, and 1.65 μm^2. Excluding temperature and length of manufacture is the only difference in the alloys.

Recrystallisation is observed by the reduction in HAGBs (and subsequent by the in-

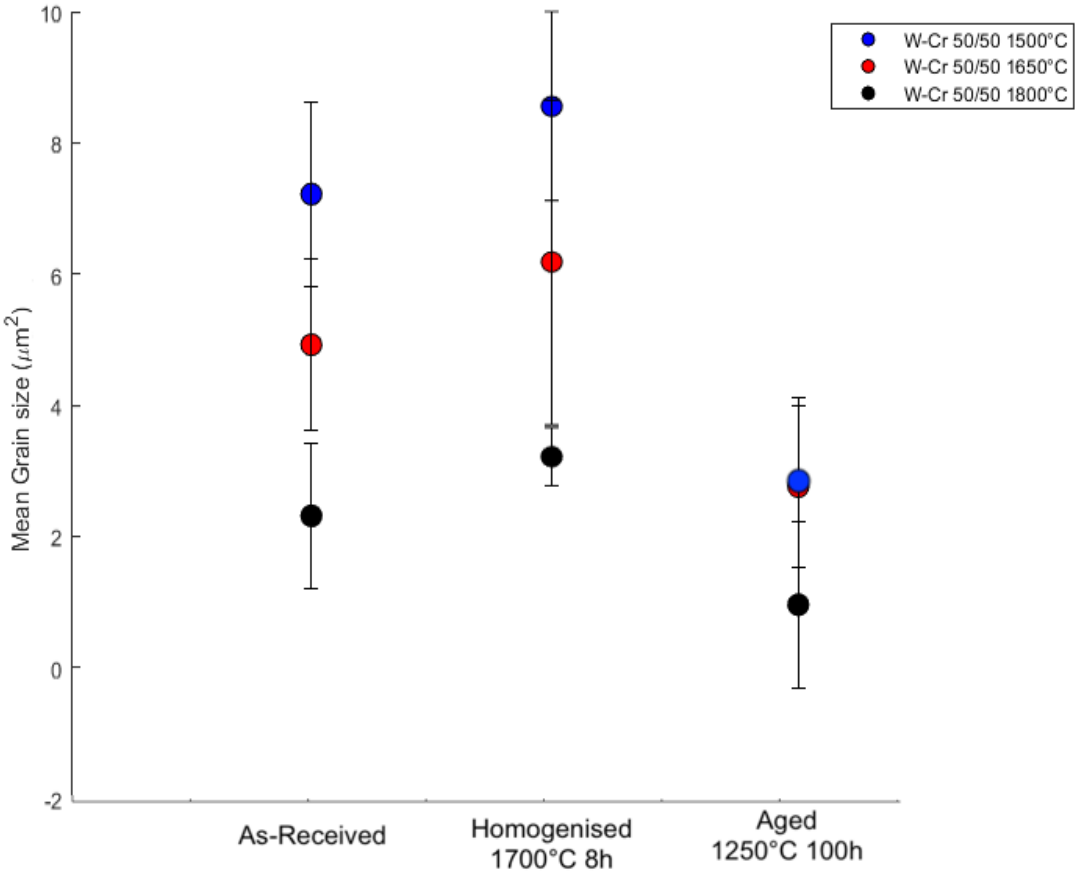

Figure 4.25: **Grain size plot for W-28Cr at% alloys manufactured by SPS blended powder** Mean grain size data obtained from EBSD analysis for 1500 °C 10 mins (blue) 1650 °C 10 mins (red) 1800 °C 1 hour (black) for different heat treatments as indicated on the graph (represents an average of 5 ebsd's taken at random over the sample.

crease in LAGB) as shown in figure 4.26.

In addition, the deformation metrics of the grains were determined using mean Kernal Average Misorientation (KAM). KAM takes the central pixel and compares its mean orientation to that of its eight nearest neighbours (Brewer L 2009, Bingert JF & Cerreta 2009). As the recrystallization of tungsten begins with the sub-grain coalescence, KAM is an effective way to determine the degree to which it has occurred. KAM data for the blended alloys in the as-received, homogenized, and aged samples are shown in figure 4.27. As tungsten recrystallization occurs by a mechanism known as sub-grain coalescence, KAM can be very useful in studying the level of recrystallization state. In the as-received condition, the average KAM values for the two samples (1500 °C, 1650 °C) have similar mean KAM values for the are probably a result of the cooling rate for each of the alloys. However, the 1800 °C has a significantly lower mean KAM value than the other samples. This is probably a result of the sintering temperature being above the miscibility and driving the homogenization of the alloy and, hence, larger grain size. The higher values of KAM in the 1500 °C and 1650 °C samples are a result of manufacturing temperature being present in the miscibility gap and (peak of the miscibility gap) and the appearance of decomposition seen earlier. On annealing, the samples at 1700 °C, both the 1500 °C, 1650 °C show a reduction in both KAM and a reduction in the proportion of HAGB figure 4.26. There is no statistical difference in the number of HAGB present in the samples manufactured at 1800 °C in the as-received and annealed conditions. The grain boundary data also shows the ratio of HAGB/LAGB of the 1500 °C and 1650 °C samples converge to that of the 1800 °C. On ageing the samples at 1250 °C for 100 hours, the three samples have very similar grain boundary characteristics to that of the as-received samples. The largest proportion of grain boundaries being greater than 15 ° (figure 4.28).

Following ageing, at 1250 °C for 100 hours grains show a dramatic reduction due to heat treating the alloy. This suggests the decomposing the alloy within the spinodal region leads to the refinement of the grain size. The single-phase alloy decomposes into a two-phase structure of tungsten and chromium-rich regions. As seen in figure 4.26, the

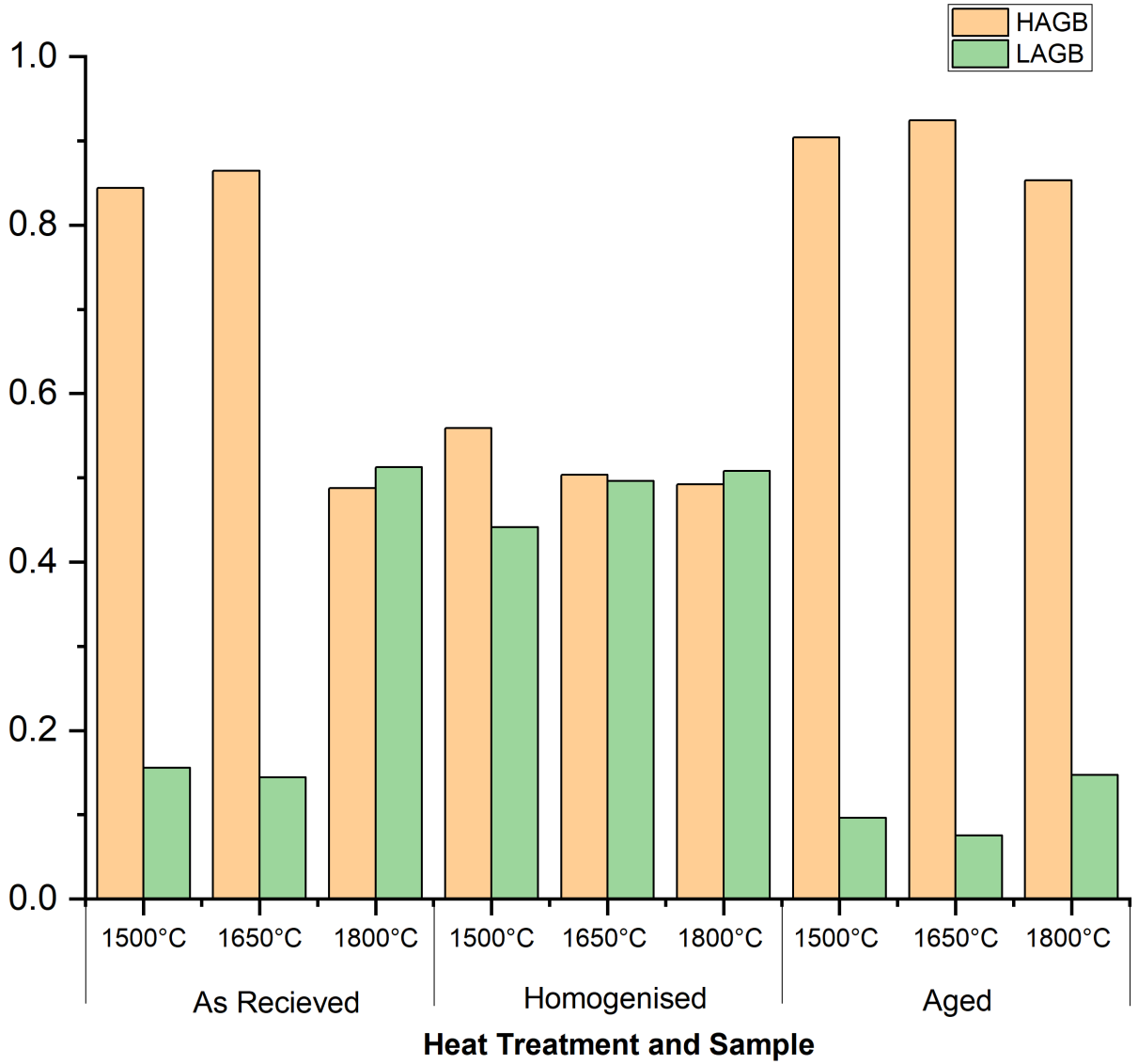

Figure 4.26: **Graph to show the proportion of High- and low-angle grain boundaries (threshold set at 15°) of the three samples manufactured from blended powder and SPS as measured by EBSD.** Frequency of low and high angle grain boundaries as measured from the 3 SPS samples made from blended powder in their (a) As-received (b) homogenisation at 1700 °C for 8 hours (c) after ageing 1t 1250 °C for 100h conditions. (High angle grain boundaries are those measured as being greater than 15 °) by MTEX software following EBSD analysis

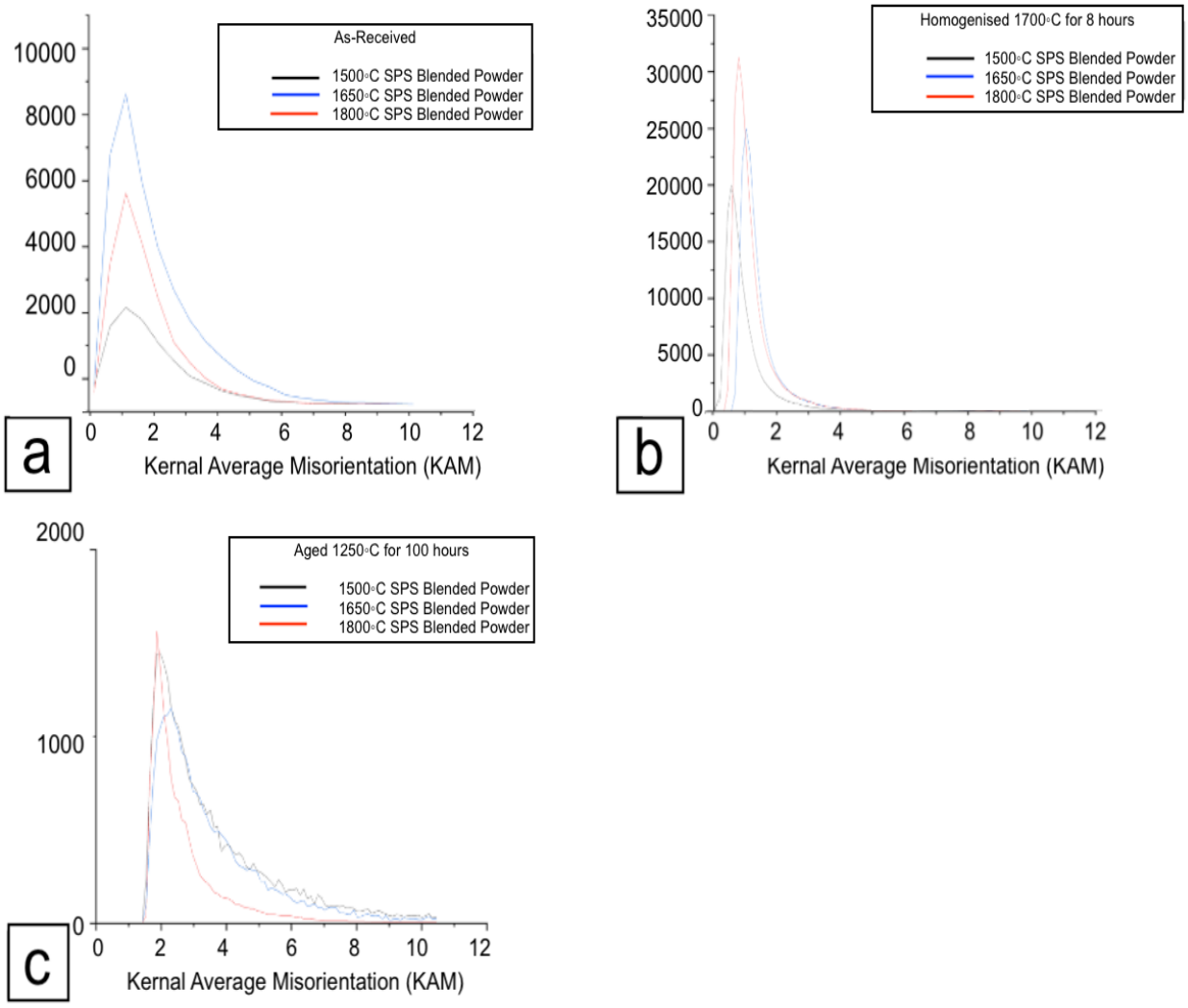

Figure 4.27: **Kernel average misorientation measured by MTEX of the 3 SPS samples manufactured from blended powder.** (a) As-received (b) after homogenisation at 1700 °C for 8 hours (c) after ageing 1t 1250 °C for 100h.

proportion of LAGB seen in the aged samples is similar to that of the as-received samples. The strain to failure % values for the aged samples also match the as-received samples, suggesting similar ductility levels.

One of the main methods to improve the ductility of tungsten is plastic deformation, either by rolling or forging. This results in an increase in the density of dislocations and the formation of a network of low-angle grain boundaries (LAGB) (Yin C 2021). In bcc metals, dislocation movement is paramount to plastic deformation. LAGBs are a source for mixed and edge dislocations (Hull Oxford (2001). This is especially important at temperatures below the critical temperature for forming kink pairs and screw dislocation movement (Yin C 2021). The decrease in LAGB observed in the aged samples may be the reason why these alloys are so hard and brittle.

4.4.7 Hardness of Blended SPS Alloys

Vickers hardness measurements for the samples manufactured from Blended powder in the as-received condition are shown graphically in figure 4.29. A literature search shows that the hardness of pure tungsten is approximately 410–430 HV (Yu 2020). All of the alloys manufactured show hardness values that exceed that of pure tungsten. This is not surprising as the nanostructuring of an alloy is known to increase hardness. The Vickers hardness of a stoichiometric W-Cr alloy manufactured by high-gravity combustion synthesis is similar to those presented here (Liu 2016). Having the smallest grain size, the sample processed at 1800 °C also had the highest measured Vicker's Hardness, 1035 ±49. This has the highest concentration of tungsten present within the sample 49.8 ± 1.69% compared to 46.6 ± 2.42% and 45.88 ± 2.56% for the 1650 °C and 1500 °C samples respectively which might go some way to explain the trend in hardness with sintering temperature in addition to the porosity above. By comparison, the hardness of the 1650 °C and 1500 °C processed samples were measured at 825 ± 19 and 634 ± 18, respectively. The higher hardness values of the Blended powder samples (as compared to that of the samples made from the mechanically alloyed powder) are due to insufficient

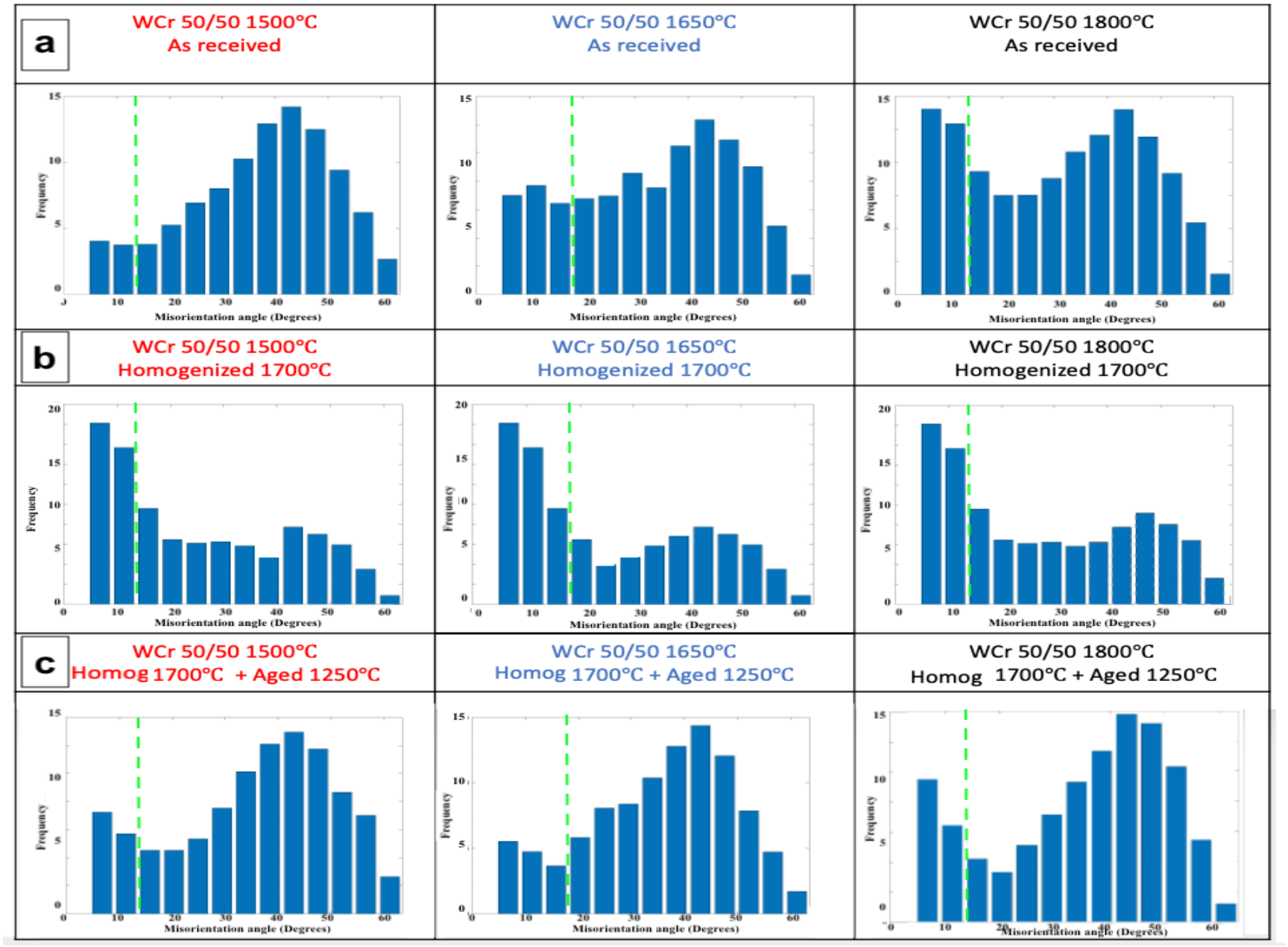

Figure 4.28: **Grain boundary misorientation as measured by MTEX of THE 3 SPS samples manufactured from blended powder.** (a) As-received (b) after homogenization at 1700 °C for 8 hours (c) after aging at 1250 °C for 100h. (Vertical green dotted line represents the threshold for high/low angle boundaries set at 15°.

mixing of the powders and loss of chromium from the sample, which was seen on the sides of the press. Large pieces of chromium (approximately 5mm) were seen protruding from the press when the 1800 °C was removed. (Compared to the mechanically alloyed samples, only a thin layer of chromium was seen on the sides of the press).

On homogenizing at 1700 °C, there is a marked reduction in the measured hardness of each of the blended alloys (figure 4.30a). If a comparison is made of the grain size of the homogenized alloys, (EBSD data figure 4.24c) shows that the alloy manufactured at 1500 °C 1650 °C has the smallest grain size in addition to this the alloy also show the decomposition of tungsten into the chromium-rich region. Decomposition is also seen in the 1650 °C sample. The grain size of the 1800 °C and homogenized have the largest of the three samples. The alloys manufactured at 1500 and 1800 °C show a similar microstructure and have Vicker's hardness of 645.6 ± 28.6 and 656.2 ± 52.8, respectively. In the 1650 °C manufactured sample, there are, however, regions identified by EDX scans to be tungsten rich (figure 4.31c). This would result in the higher hardness of the alloy measured at 725.4 ± 18.5.

Ageing the samples within the miscibility gap (1250 °C) results in decomposing the single phase to a dual phase of alternating layers of tungsten and chromium. EBSD data shows that there has been considerable nanostructuring of grain size (figure 4.24c) and SEM (figure 4.23a, b, and c). Hardness measurements of the three alloys are shown in figure 4.31a.

4.4.8 Mechanical testing of blended alloys

Three-point bending of the samples at room temperature showed exclusive brittle fracture. The hardest of the three samples (1800 °C) showed the greatest flexural strain of 1.22%. SEM images of the fracture surface (figure 4.29b) show what can be described as a dendritic tree-like structure covering much of the inner surface of the cleavage site. The samples processed at 1500 °C and 1650 °C have a flexural strain of 0.59 and 0.31 %, respectively. The fracture surface of the sample processed at 1500 °C shows large

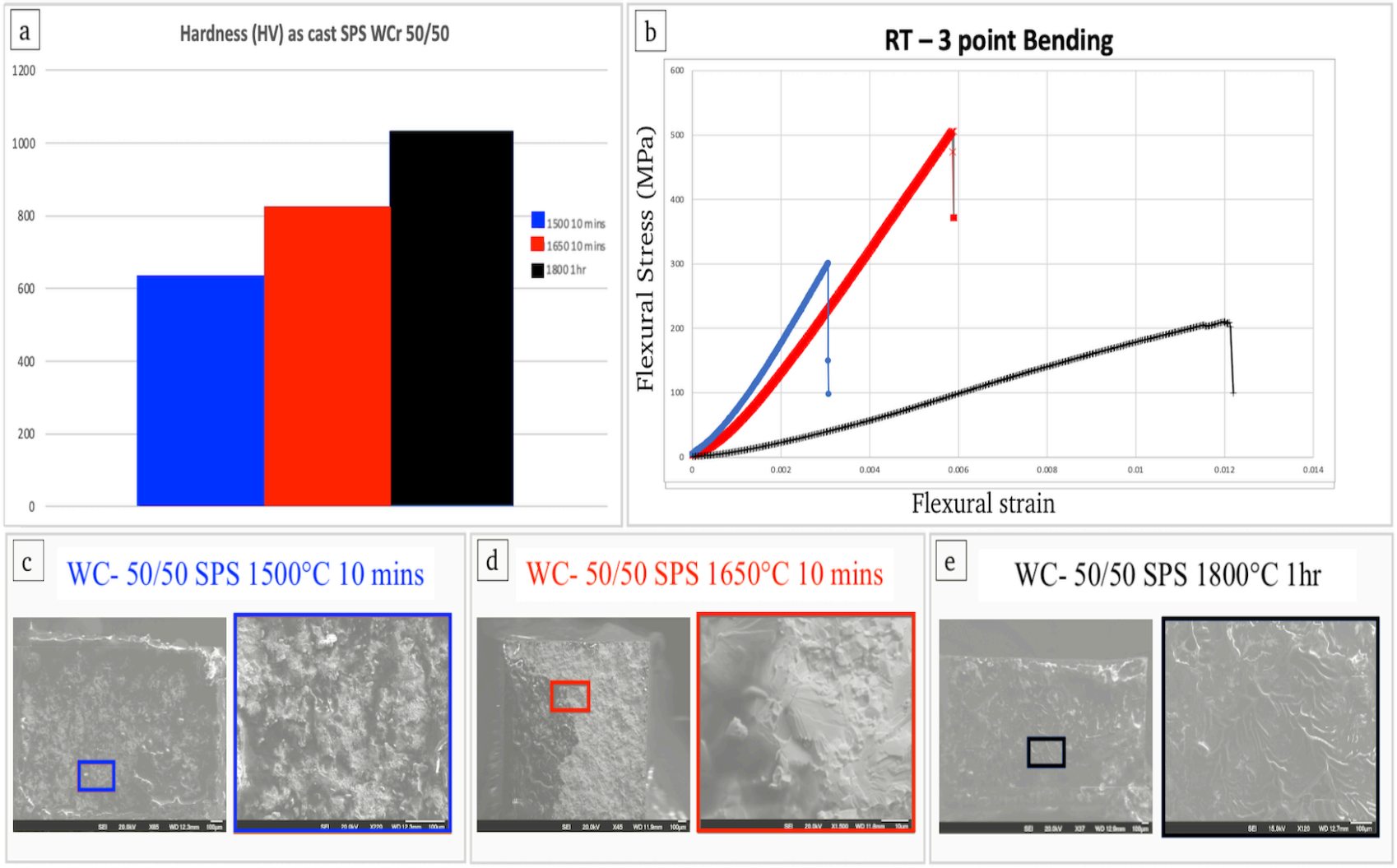

Figure 4.29: **Mechanical and fracture surface analysis of the bending of as-received blended SPS W-Cr manufactured at 1500 °C 10 mins (blue), 1650 °C 10 mins (red) and 1800 °C 1 hour (black).** (a) Vickers Hardness (b) 3-point flexural stress-strain diagram (c, d, and e) SEI fracture surface images.

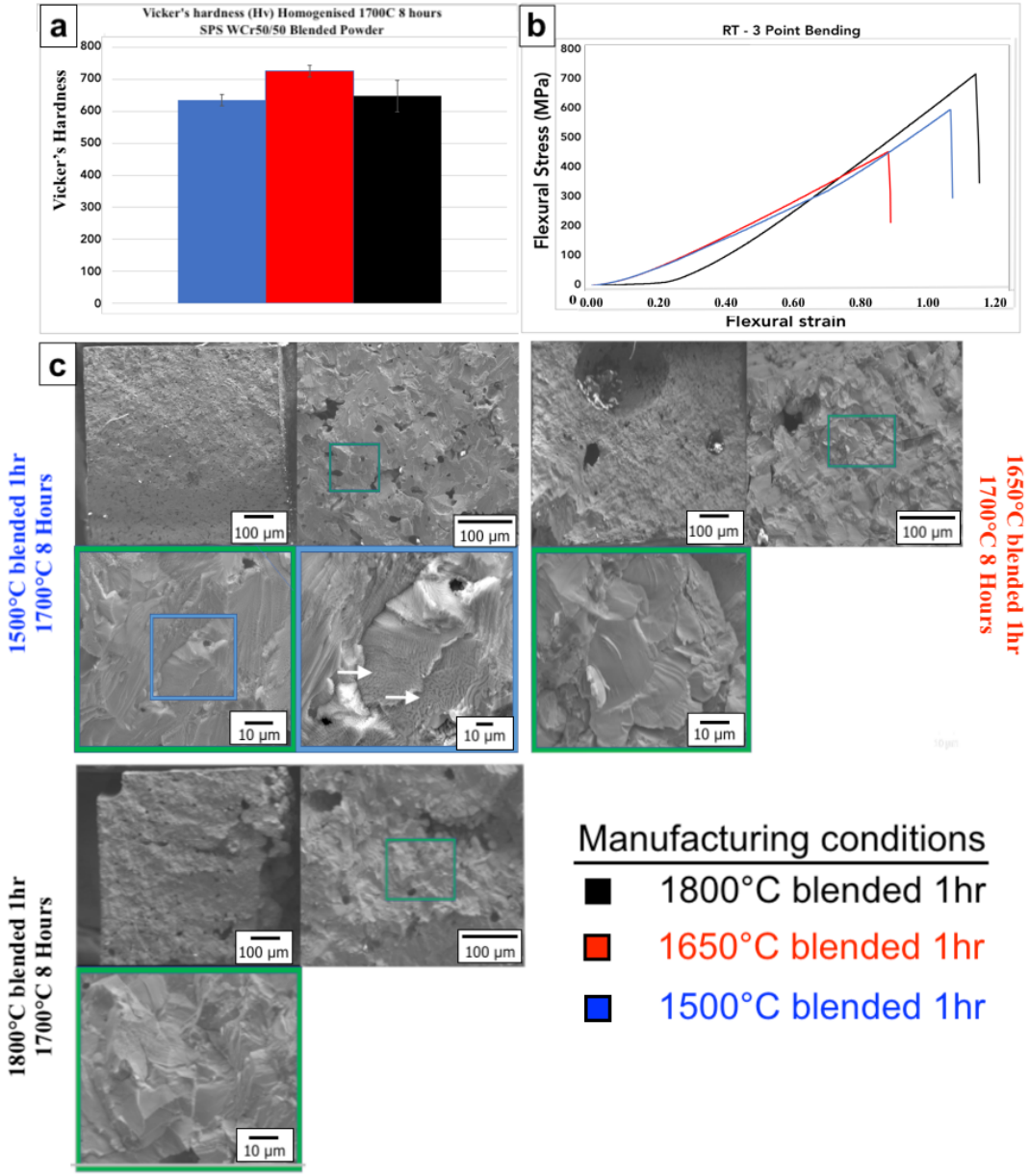

Figure 4.30: **Mechincal properties of the 3 SPS samples manufactured from blended powder after homogenization at 1700 °C for 8 hours.** 1500 °C 10 mins (blue), 1650 °C 10 mins (red) and 1800 °C 1 hour (black) (a) Vickers Hardness, (b) 3 point bending flexural stress-strain diagram and (c) SEM fracture surface images following 3-point bending (The white arrows show regions of decomposition of the alloy into a two-phase structure observed after homogenisation suggesting problems with the process)

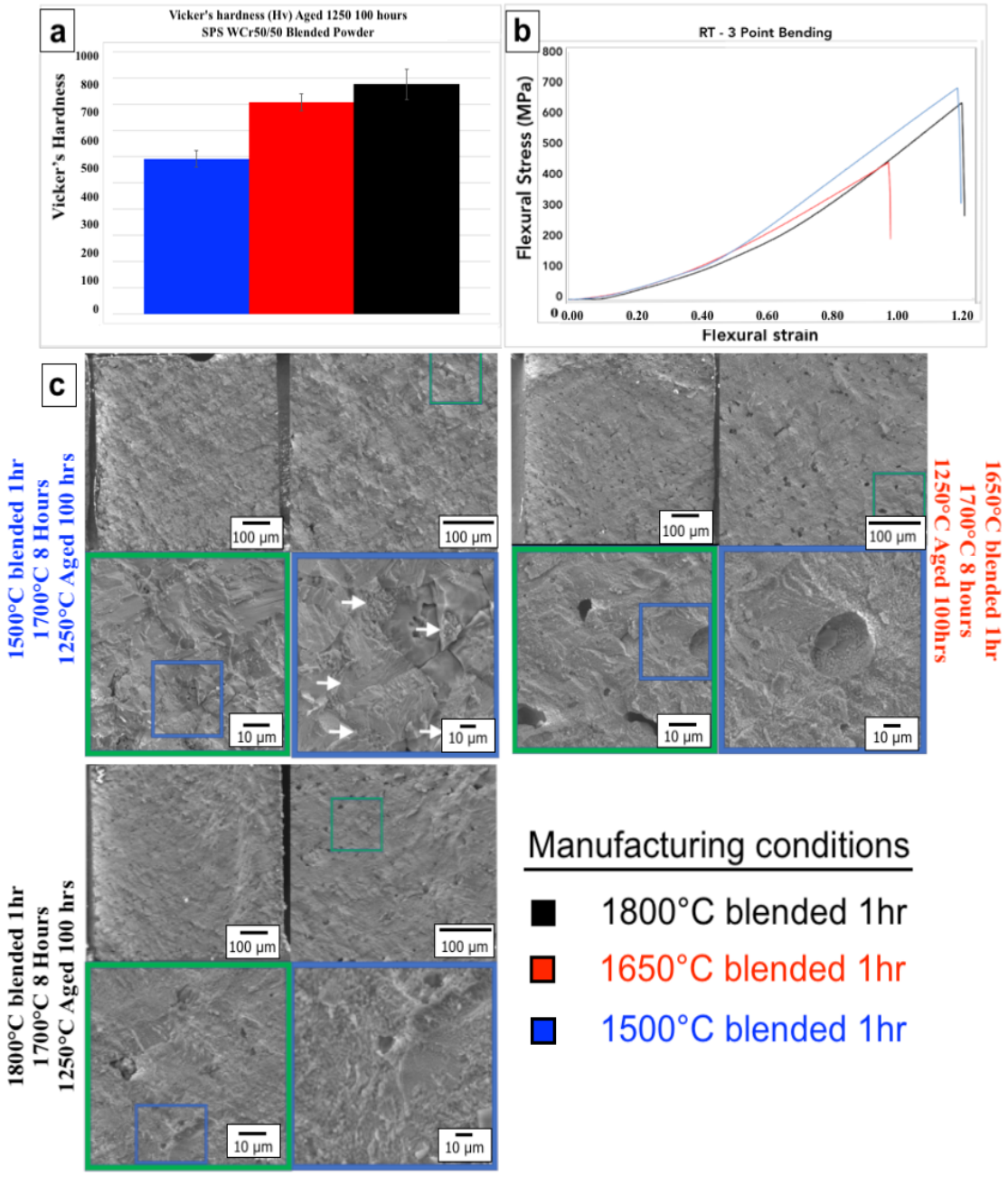

Figure 4.31: **Mechanical properties of the 3 SPS samples manufactured from blended powder after ageing at 1250 °C for 100 hours.** 1500 °C 10 mins (blue), 1650 °C 10 mins (red) and 1800 °C 1 hour (black) (a) Vickers Hardness, (b) 3 point bending flexural stress-strain diagram and (c) SEM fracture surface images following 3 point bending (The white arrows show regions of decomposition of the alloy into a two-phase structure observed after homogenisation suggesting problems with the process)

pores and intergranular fracture. In addition to the intergranular fracture seen at lower processing temperatures, the 1650 °C sample also shows transgranular brittle fracture. The presence of pores in the 1500 °C sample could explain the premature failure of the alloy as compared to that of the 1650 °C.

SEM of the fracture surface of 3-point blended samples shows a mixed mode of fracture with intergranular and transgranular fracture present, both of which indicate brittle fracture at room temperature. The early failure of the 1500 °C is probably a result of the porosity seen in both SEM and EBSD. The sample manufactured at 1800 °C varies significantly from that of the others; there is a significant reduction in flexural stress (UTS) of 210.4 MPa as compared to 302.3 and 506.0 for 1500 °C and 1650 °C respectively. However, the strain to failure is twice that of the sample manufactured at 1650 °C. The fracture surface of the 1800 °C sample (presented in figure 4.29c), in addition to the river patterns seen in the other two blended alloys, has what can only be described as "veins" over an area of approximately 30% of the fracture surface. This vein-like structure observed here is similar to that seen in most metallic glasses. The vein is formed when the high elastic energy released during fracture melts or softens within the shear bands (Lowhaphandu P 1999, Wright WJ 2001, Donovan 1989, Liu CT 1998). The melted or softened alloy within these shear bands then "flows" to form these vein-like features. As the samples were tested, the presence of these veins must be associated with the temperature at which the samples were manufactured. This phenomenon must be further investigated (Liu CT 1998, Wright WJ 2001).

Fracture surface analysis of the homogenized samples at room temperature showed river patterns (figure 4.30c), demonstrating cleavage. Therefore, all samples underwent brittle fracture. In addition to the signs of brittle fracture, the alloy manufactured at 1500 °C showed the presence of decomposition (as indicated by the white arrows). This further suggests that the homogenization time was not long enough to remove the microstructure produced from manufacturing. The 1500 °C and 1650 °C show improved strain to failure compared to the as-received samples with values of 1.14 and 0.88%. However, there is a

reduction for the 1800 °C compared to a value of 1.06%.

Compared to the as-received and homogenized samples, there is a clear difference in the visual appearance of the fracture surface of the aged samples (figure 4.31c). The fracture surface has a greater area covered by the decomposed phases. In addition, there is a clear absence of river patterns 1650 °C. and 1800 °C as compared to that of the 1500 °C sample. This suggests cleavage fracture is no longer the main failure mechanism; intergranular fracture is the predominant mechanism for brittle fracture. All Three samples show improvements in their strain to failure compared to the homogenized and the as-received conditions. Only the 1800 °C sample shows a strain to failure similar to that in the as-received condition.

4.5 W-28Cr .at% spark plasma sintered (SPS), Mechanically alloyed (MA) Powder

The mechanically alloyed powder was produced by processing W-28Cr at% blended powder compacts through a crusher and then through a 12-hour ball milling operation. The W-28Cr at% powder compact was heat treated at around 100 °C for 2 hours to promote diffusion. The powder cakes (figure 4.32) underwent a second crushing and a further 2-hour ball milling operation.

Figure 4.32: **Powder cake** W-28Cr at% powder for SPS in cake form.

With the knowledge of the previous SPS experience of the blended powder, it was

thought that heating the powder above 1650 °C would result in leakage of chromium, as seen above. Therefore, four samples were processed using the same parameters as before. This time, the heating temperature and times were as follows: 1500 °C and 1575 °C for 30 minutes and 1650 °C for 5 and 15 minutes. Graphs showing the loading pressure, processing temperature, holding time, and average relative piston height from its starting position are presented for each sample produced in figure 4.33.

The Chemical composition of the alloy in the as-received condition is shown in table 18.

Table 18: **Composition of W-28Cr at% of SPS alloys in their as-received condition.** Table to show the chemical composition of W-28Cr at% in the as-received condition alloys manufactured from Mechanically alloyed powder via SPS at different tempoeratures

Alloy	Composition			
	% weight		% Atomic	
	W	Cr	W	Cr
1500°C 30 mins	90.1 ± 0.3	9.9 ± 0.5	72.1 ± 0.2	27.9 ± 0.3
1575°C 30 minutes	92.7 ± 0.5	7.3 ± 0.3	78.1 ± 0.7	21.9 ± 0.6
1650°C 5 mins	91.3 ± 0.8	8.7 ± 0.4	74.8 ± 0.6	25.2 ± 0.6
1650°C 15 mins	91.9 ± 0.3	8.1 ± 0.7	76.2 ± 0.4	23.8 ± 0.5

4.5.1 SEM and EDX of Mechanically alloyed samples

SEM and EDX analysis of the as-received samples for the mechanically alloyed powder is shown in figure 4.34. Each of the four samples shows three distinct chemical regions; the first is tungsten-rich, the second a chromium-richer tungsten region, and a chromium-rich region. The different contrasts of the SEM micrographs show the three separate regions, with the black regions being almost pure chromium (Dine S 2021). The segregation of elements is due to the extremes in temperature; on rapid cooling, tungsten partitions into the solid phase, where chromium enriches the liquid phase. On further cooling, the liquid phase becomes further enriched by chromium until the final solidification of an almost pure chromium phase. As seen by the three-phase contrast in the SEM images.

In the homogenised condition, each of the four alloys has a similar appearance (figure 4.35). A lighter tungsten-rich phase (indicated by orange in the EDX images inset and

line scans) and a much smaller chromium-rich phase (indicated by green in the EDX images inset and line scans). Zoomed-in on the darker chromium-rich regions shows small lamellar regions of a tungsten decomposition as seen in the blended alloy.

SEM of the aged samples (figure 4.36) does not show the level of decomposition as seen in the blended samples. Decomposition is only seen in the dark chromium regions of the samples and the tungsten grains bordering those regions. Unlike the blended samples, there is little diffusion of chromium into the tungsten-rich areas during the homogenisation process; therefore, decomposition does not occur to the same extent. In addition, the areas where decomposition occurs do not result in the same level of nanostructuring as seen in the blended samples.

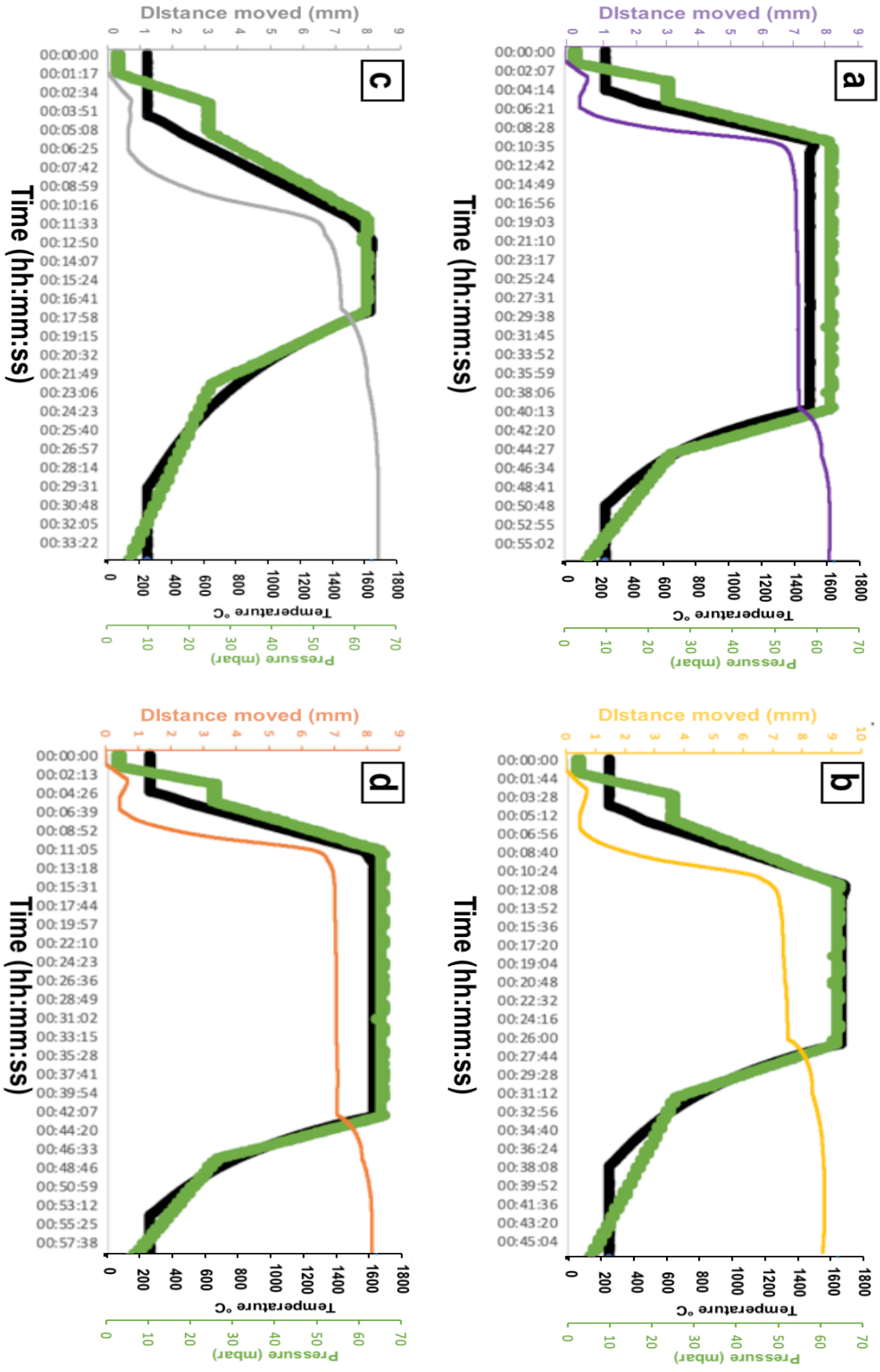

Figure 4.33: **Spark plasma sintering (SPS) machine cycle parameters used to create the four samples from the Mechanically Alloyed (MA) powder.** Each graph shows the pressure (black) and temperature (green). Purple 1500°C 30 mins, orange 1575°C 30 minutes, grey 1650°C 5 mins and yellow 1650°C 15 mins represent the reduction in the sample thickness as the dye moves downwards as the powder is sintered.

Figure 4.34: **IPF map, SEM, and EDX analysis (tungsten orange, chromium green) of the 4 SPS Mechanically alloyed (MA) powder W-28Cr at% alloys manufactured by SPS in the as-received condition** (a) 1500°C 30 mins, (b) 1575°C 30 minutes, (c) 1650°C 5 mins and (d) 1650°C 15 mins.

Figure 4.35: **IPF map, SEM, and EDX analysis (tungsten orange, chromium green) of the 4 SPS Mechanically alloyed (MA) powder W-28Cr at% alloys manufactured by SPS after homogenisation at 1700 °C for eight h** (a) 1500°C 30 mins, (b) 1575°C 30 minutes, (c) 1650°C 5 mins and (d) 1650°C 15 mins.

Figure 4.36: **IPF map, SEM, and EDX analysis (tungsten orange, chromium green) of the 4 SPS Mechanically alloyed (MA) powder W-28Cr at% alloys manufactured by SPS after homogenisation at 1700 °C for 8h and ageing at 1250 °C for 100h** (a) 1500°C 30 mins, (b) 1575°C 30 minutes, (c) 1650°C 5 mins and (d) 1650°C 15 mins.

4.5.2 XRD of Mechanically alloyed SPS samples

XRD of the 4 SPS samples in the as-received condition is shown in figure 4.37a. As each alloy was manufactured at temperatures within the reported miscibility gap for tungsten chromium, it is unsurprising that each of the four XRD traces shows two sets of peaks, each corresponding to a bcc structure. As the manufacturing temperature rises, there is an increased splitting of the two peaks associated with each bcc peak, suggesting a more significant decomposition of the alloy into the two phases, as shown by changing the lattice parameter. This is demonstrated in the difference of the lattice parameters identified in the as-received alloy (Table 17). The presence of several phases in the alloys is seen in the SEM and EDX of the samples. Therefore, each mechanically alloyed sample in the as-received condition is a mixture of two phases: a tungsten-rich and chromium-rich phase.

After homogenising the four received alloys (figure 4.37b), XRD analysis reveals the presence of 2 sets of peaks; the first two sets identified in all alloys match that of a bcc phase. With the exclusion of the alloy manufactured at 1650 °C for 15 minutes, the second phase matching that of Cr_2WO_6 is also present in the spectrum. This could have been caused by the contamination during the homogenisation process.

XRD analysis of the aged Mechanically alloyed samples is shown in figure 4.37c. All major peaks show double peaks, indicating the complete decomposition of the single bcc W-Cr alloy into two single bcc-A2 phases, one rich in tungsten and the other in chromium.

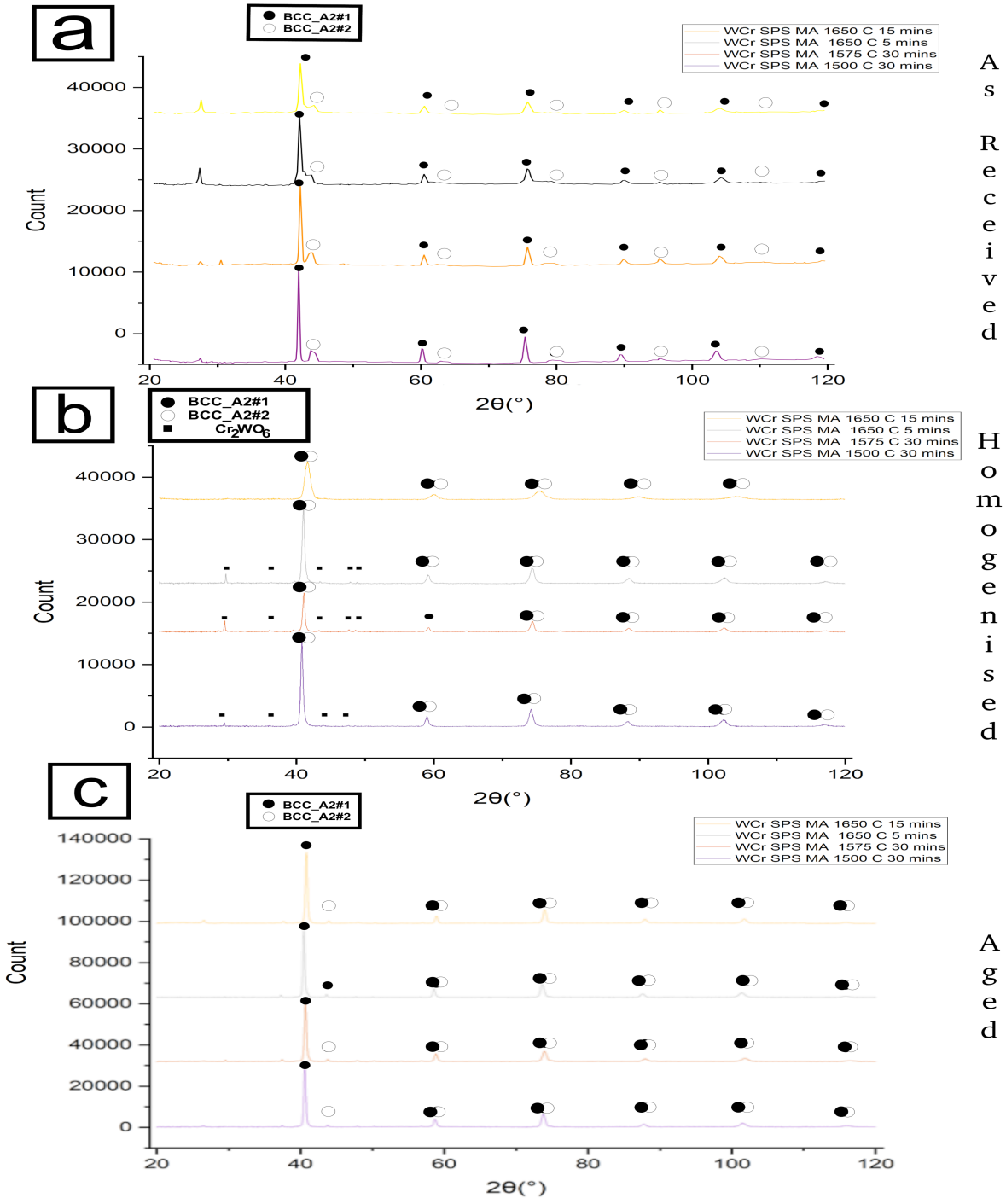

Figure 4.37: **XRD analysis of the 4 SPS samples manufactured from Mechanically alloyed (MA) powder after varies heat treatments** 1650 °C 15 mins (Orange), 1650 °C 5 mins (black), 1575 °C 30 mins (red) and 1500 °C 30 mins (purple). Black dots represent peaks for tungsten and chromium bcc crystal structures. XRD patterns of SPS samples manufactured from Mechanically alloyed (MA) powder (a) In the as-received condition (b) After homogenisation at 1700 °C 8 hours (c) Aged at 1250 °C for 100h.

4.5.3 EBSD and grain analysis of Mechanically alloyed samples

EBSD analysis of the as-received Mechanically alloyed samples (figure 4.34a-d) shows the presence of unindexable areas. BSE (not shown) did not show any difference in the microstructure. Therefore, EDX analysis was performed to determine these areas' composition. However, impurities were not observed, and instead, they were seen to be enriched with chromium. Figure 4.38 shows the mean grain size for each of the four MA SPS samples. The sample manufactured at 1575 °C for 30 mins has the largest average grain size with a value of 17.32 μm^2. The sample with the smallest grain size is the one manufactured at 1500 °C for 30 mins at 14.37 μm^2. The samples manufactured at 1650 °C for 5 and 15 mins have almost the same mean grain size.

On homogenizing (figure 4.35), the area not indexed by EBSD increases. Unfortunately, on receiving the homogenized samples, it was suggested that the furnace had become contaminated, leading to an alteration in the samples (although no contamination was seen in the samples following EDX observation). This may be explained by the presence of Cr_2WO_6 observed in XRD analysis of homogenised samples. Analysis of the indexed grains shows an increase in mean grain size for all four manufactured samples (figure 4.38). The MA samples manufactured at the lower temperatures (1500 °C and 1575 °C) have the largest grain sizes following homogenisation. This suggests that the mean grain size is somewhat affected by the amount of chromium present in the alloy after manufacture. It appears that manufacturing the alloys at higher temperatures for longer times results in the loss of more chromium from the samples, resulting in a reduction in grain refinement. The samples manufactured at 1650 °C display this trend. This would indicate that a temperature-to-time ratio should be investigated.

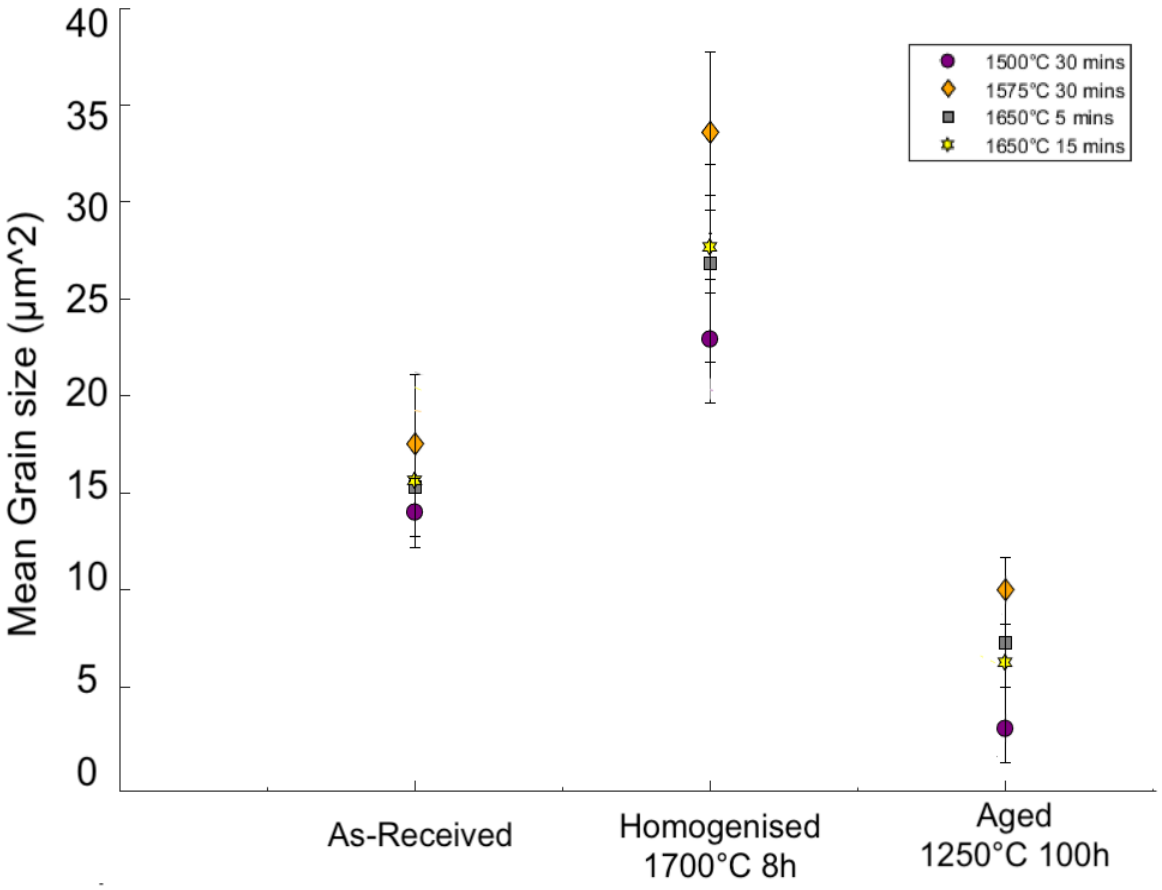

Figure 4.38: **Grain size plot for W-28Cr at% alloys manufactured by SP Mechanically alloyed (MA) powder** Mean grain size data obtained from EBSD analysis for (purple - circle) 1500°C 30 mins, (orange - diamond) 1575°C 30 minutes, (grey - square) 1650°C 5 mins and (yellow - decagon) 1650°C 15 mins for different heat treatments as indicated on the graph

Ageing the alloys at 1250 °C causes a reduction in the grain size of all of the alloys due to the decomposition of the two phases (figure 4.36). The mean grain size of the aged samples follows the same trend as that of the as-received and homogenised samples. With the 1500 °C sample having the most significant refinement with a mean grain size of 0.4 μm^2

KAM data for the mechanically alloyed samples are shown in figure 4.40 along with grain-boundary information in the form of HAGB/LAGB ratios and as misorientation data (figures 4.39 and 4.41 respectively). In the as-received condition, the mean KAM is directly related to the proportion of HAGB. The 1500 °C sample has the lowest HAGB and mean KAM values. The other three alloys both show similar HAGB and mean KAM values.

Again, as seen in the blended alloys on annealing the alloys at 1700 °C, there is a reduction in the proportion of HAGB in all four of the alloys, with both of the alloys manufactured at 1650 °C having more LAGB than HAGB. A reduction sees this shift in misorientation in the KAM values for all alloys. Each annealed alloy shows not only a reduction in the mean KAM but also a reduction in the spread of the KAM. On ageing the alloys at 1250 °C for 100 hours, the proportion of HAGB approaches that of the as-received condition. With the sample manufactured at 1650 °C, 15 minutes had the highest proportion of HAGB. This is reflected in the KAM data, with the highest mean value. The mean KAM value is near that of the as-received samples.

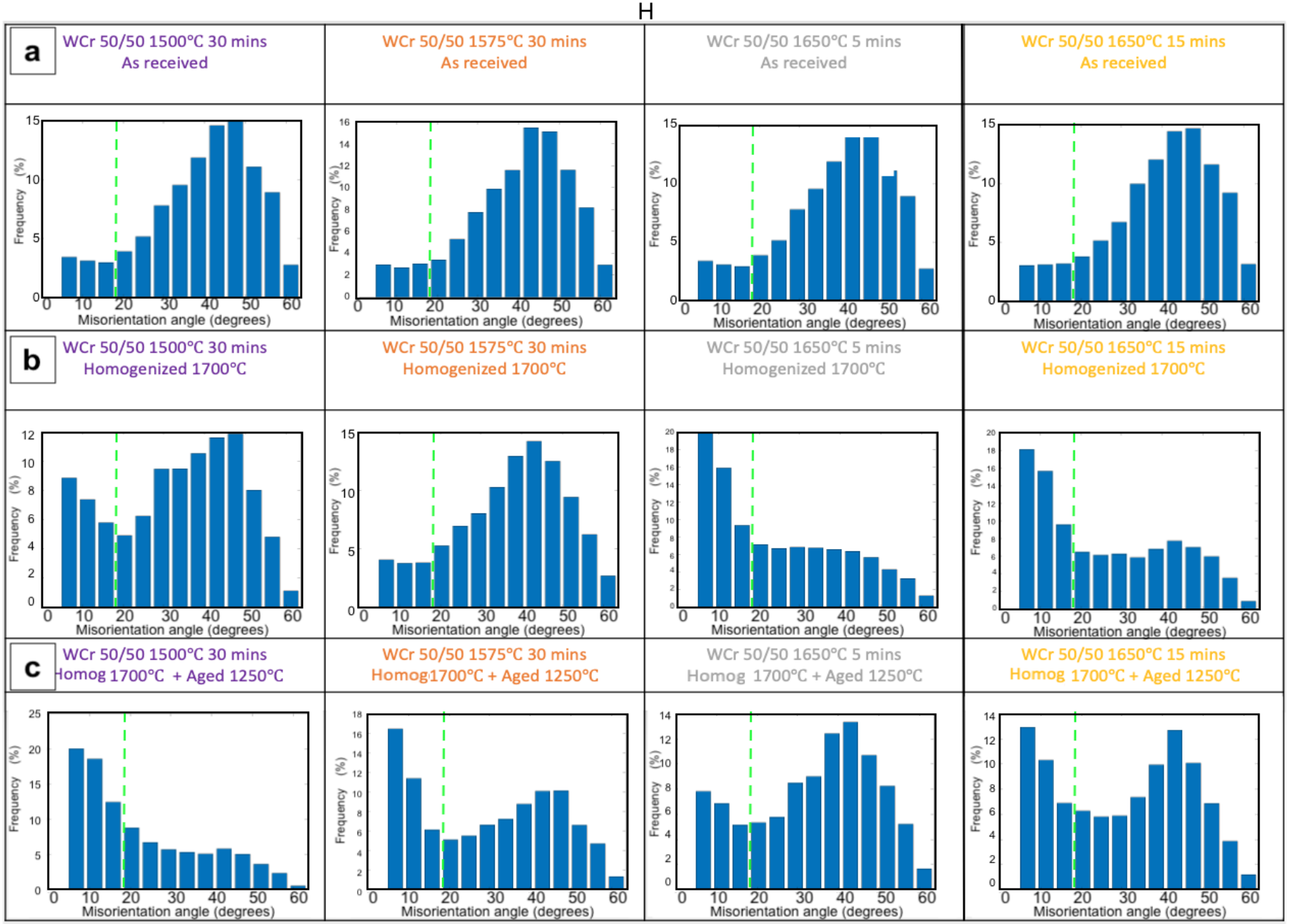

Figure 4.39: **Kernel average misorientation as measured by MTEX of the 4 SPS samples manufactured from Mechanically alloyed (MA) powder** in their (a) As-received (b) after homogenization at 1700 °C for 8 hours (c) after ageing 1t 1250 °C for 100h.

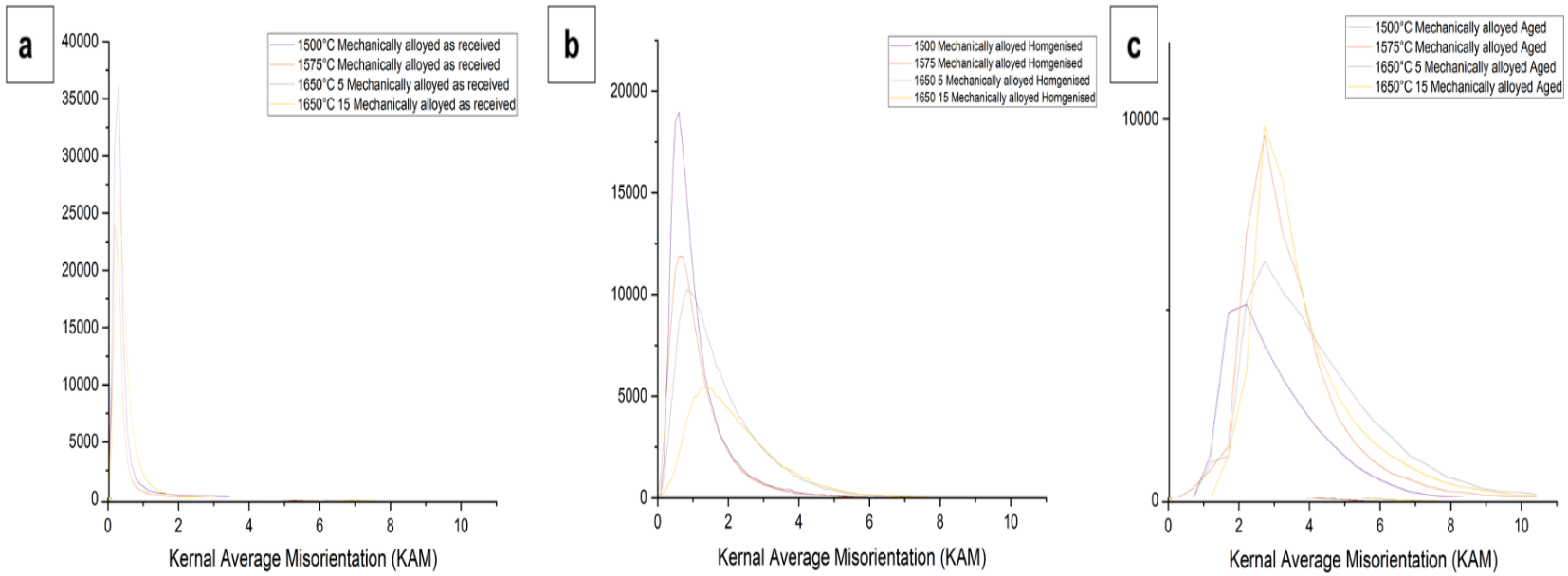

Figure 4.40: **Grain boundary misorientation as measured by MTEX of the 4 SPS samples manufactured from Mechanically alloyed (MA)** in their (a) As-received (b) after homogenization at 1700 °C for 8 hours (c) after ageing 1t 1250 °C for 100h. (Vertical green dotted line represents the threshold for high/low angle boundaries set at 15°.

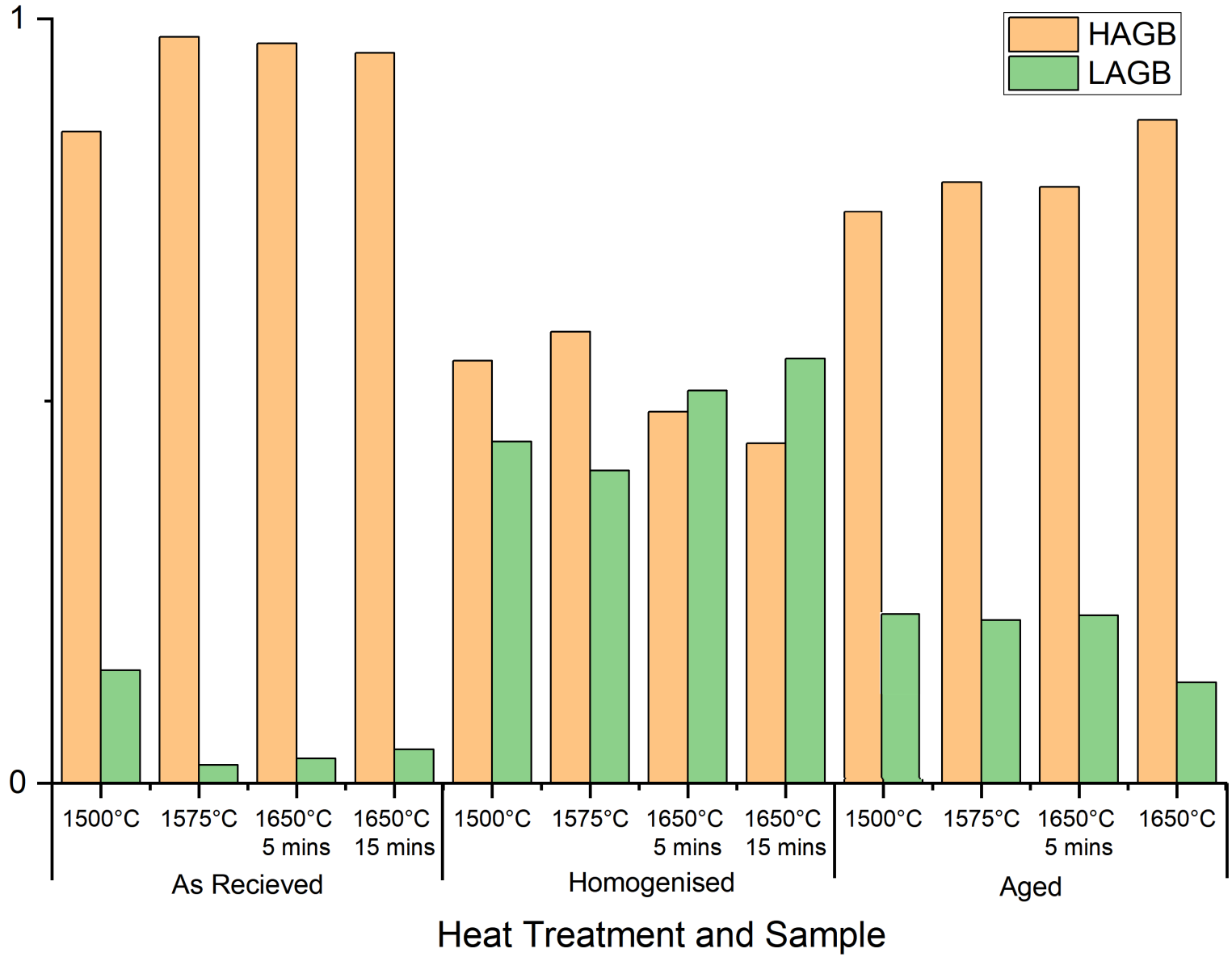

Figure 4.41: **Graph to show the proportion of High- and low-angle grain boundaries (threshold set at 15°) of the 4 SPS samples manufactured from Mechanically alloyed (MA) powder.** In their (a) As-received (b) after homogenization at 1700°C for 8 hours (c) after ageing 1t 1250°C for 100h.

4.5.4 hardness of mechanically alloyed samples

The hardness of the mechanically alloyed samples is more consistent than that of the Blended ones. The refining of the powder could explain this as compared to the blended. It gives a better-mixed starting powder that melts more homogeneously. The ability to nanostructure tungsten and tungsten alloys through heat treatments offers a means of producing an alloy with exceptional hardness. It has been reported in the literature that polycrystalline tungsten follows a Hall Petch relationship ($H = H_o + Kd^{-\frac{1}{2}}$). Where polycrystalline tungsten values for H_o and K are 3.5 Gpa, and 0.1 GPa $mm^{\frac{1}{2}}$) (Vashi 1970). Plotting the same graph for the received mechanically alloyed powder gives a linear relationship with the values obtained from the trend line as 5.76 Gpa and 2.82 GPa $mm^{\frac{1}{2}}$ for H_o and K respectively (figure 4.42). This is not the first study to show the potential for W-28Cr at% alloys to produce nanoscale-sized grains and improved hardness compared to tungsten. Results from 3-point bending show similar flexural strengths and strain values. It is worth noting that the two alloys with the smallest average grain sizes (1500 °C and 1575 °C) have the highest flexural strength. This is analogous to rolled and deformed tungsten, where smaller grains produce better mechanical properties. As viewed under SEM, all four fracture surfaces are shown in figure 4.43. Each shows a granular-like structure with clear evidence of river patterns, indicating a transgranular fracture's dominant cause for failure.

Figure 4.44a shows the hardness data measured in the homogenized condition. On homogenizing, all samples show an increase in hardness compared to the as-received samples. On EBSD of all samples, the area fraction of the sample not indexed increases. This is due to decomposition in the chromium-rich phase (as shown by the EDX data and SEM images). The formation of this phase is due to the migration of tungsten from the tungsten-rich regions, as explained by the Kirkendall effect (described later). EBSD data (figure 4.35) also indicates a refinement of the grain structure. The presence of this phase and that of globular tungsten-rich domains is probably responsible for the increase in hardness seen in the homogenized samples.

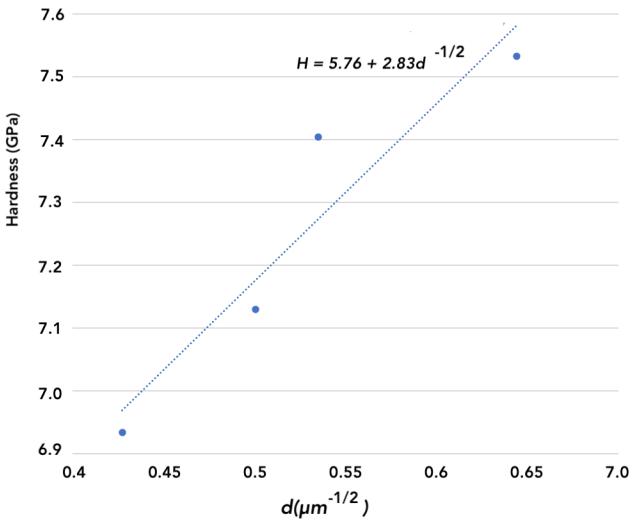

Figure 4.42: **Hall-Petch relationship.** A plot to show the HallPetch relationship between grain diameter and hardness for the as-received sample in the as-received sample for four samples manufactured from Mechanically alloyed powder.

On ageing the samples within the miscibility gap (1250 °C), all alloys show an increase in hardness compared to that of the homogenized samples. This is due to the samples' refinement and the alloy's decomposition into two phases. This is shown in the EDX and EBSD data presented in figures 4.36 and 4.37c. The grain refinement of the MA alloys (although not as extensive as the blended alloys) is responsible for the increase in hardness.

4.5.5 Mechanical testing of Mechanically alloyed alloys

Figure 4.43c shows the results of three-point bending of the MA samples in the as-received condition at room temperature. SEM of the fracture surface shows exclusive brittle fracture. All samples show a very granular appearance. With increased casting temperature, a more significant proportion of the fracture surface comprises river plates, with the samples cast at 1650 °C showing the essential proportion of river patterns. This suggests insufficient melting of powder particles at lower temperatures, which could explain why the overall mechanical properties of the alloys are poor in 3-point bending tests.

Figures 4.44 and 4.45 show the fracture surfaces of the four alloys in the homogenized and aged samples, respectively. In both conditions, SEM images show the presence of

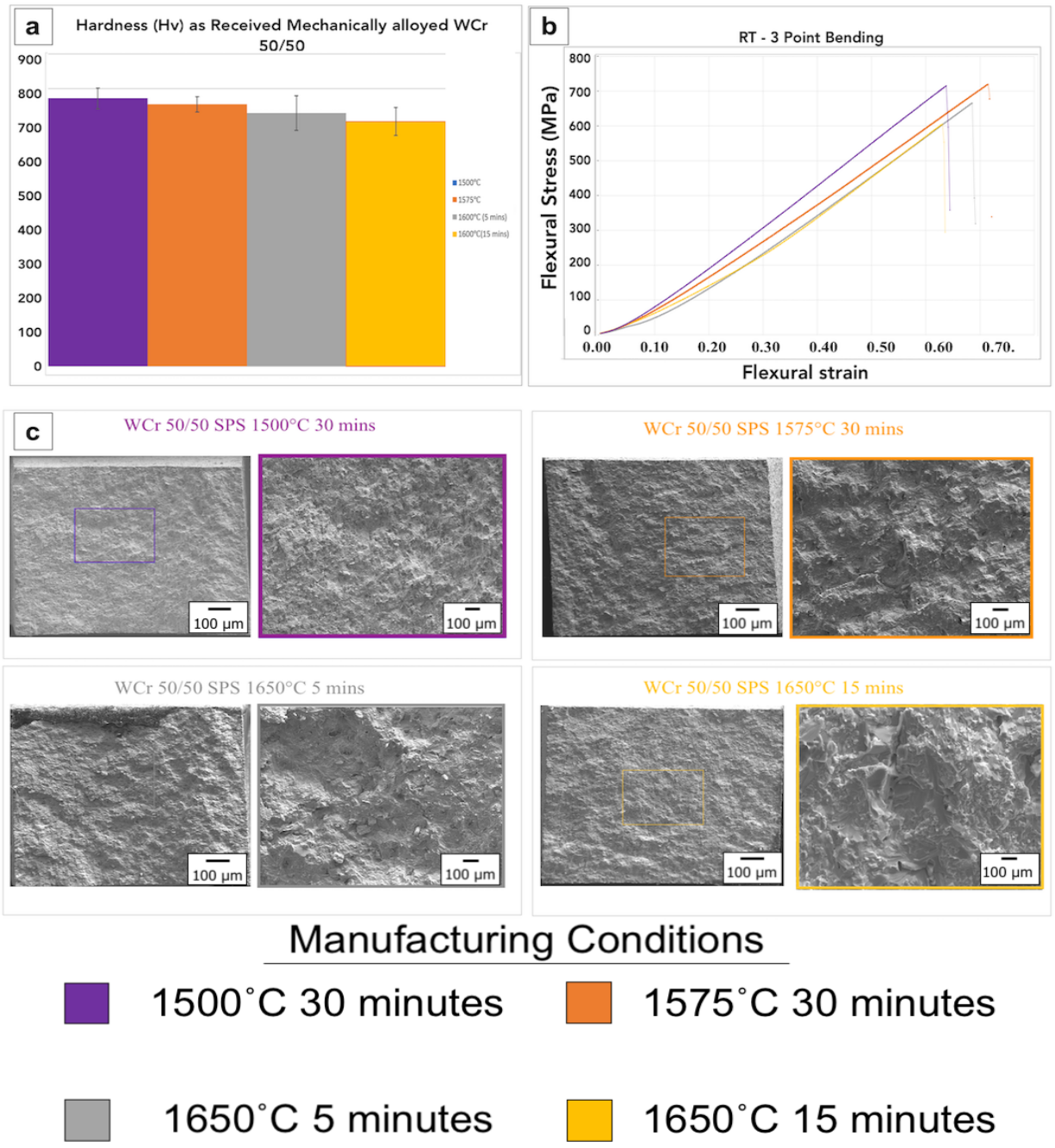

Figure 4.43: **Hardness and fracture surface analysis of three-point bending of as-received manufactured from mechanically alloyed (MA) SPS samples** Manufactured at 1500°C 30 mins (purple) 1575°C 30 minutes (orange) 1650°C 5 mins (grey) 1650°C 15 mins (yellow) (a) Vickers Hardness (b) 3-point flexural stress-strain diagram (c) SEM fracture surface images of each alloy (colours as indicated above.

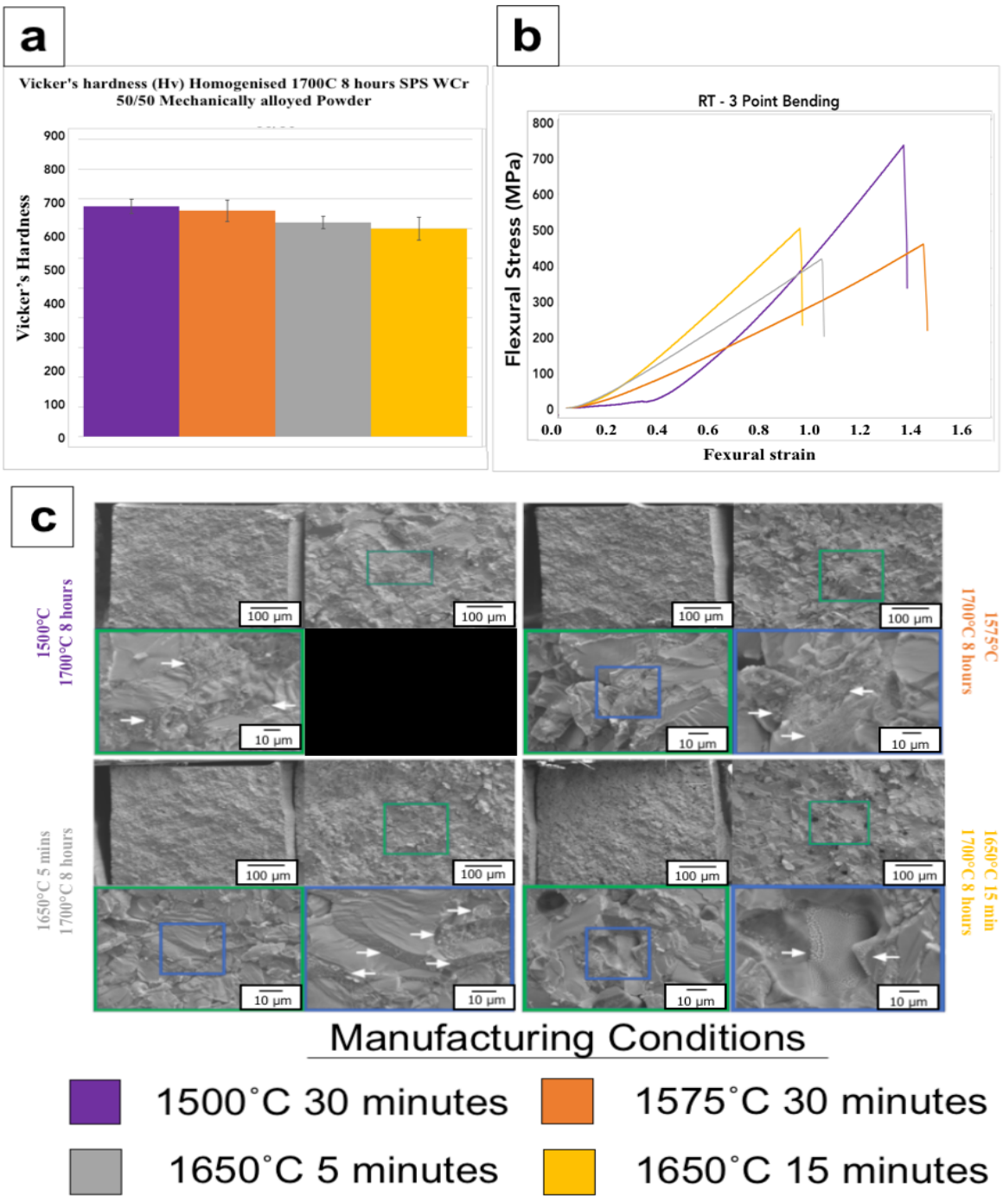

Figure 4.44: **Hardness and fracture surface analysis of three-point bending of samples homogenization at 1700°C for 8 hours manufactured from mechanically alloyed (MA) powder and SPS.** 1500°C 30 mins (purple) 1575°C 30 minutes (orange) 1650°C 5 mins (grey) 1650°C 15 mins (yellow) (a) Vickers Hardness, (b) 3 point bending flexural stress-strain diagram and (c) SEM fracture surface images following 3 point bending.

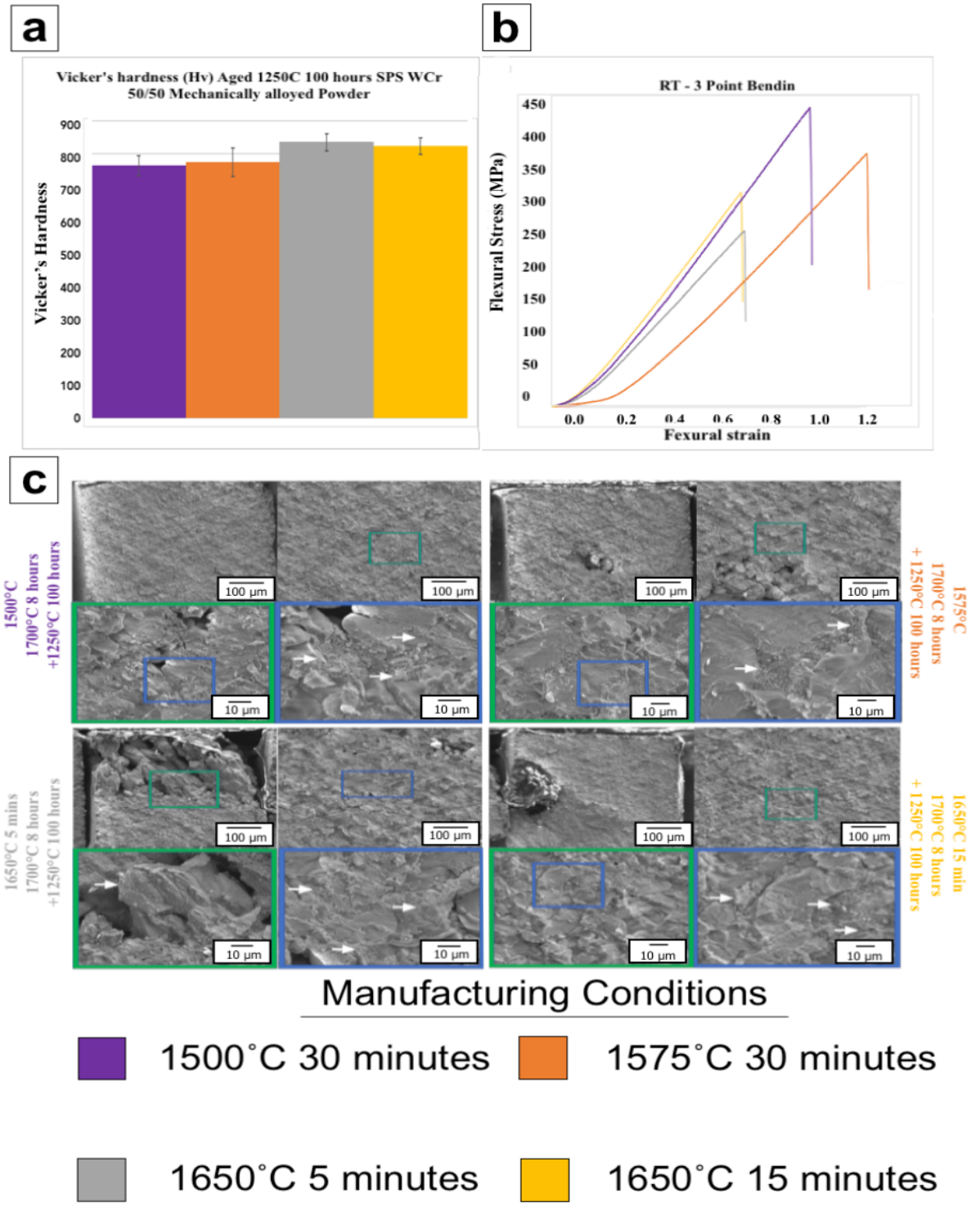

Figure 4.45: **Hardness and fracture surface analysis of three-point bending of samples homogenization at 1700°C for 8 hours and ageing at 1250°C for 100h manufactured from mechanically alloyed (MA) powder and SPS** 1500°C 30 mins (purple) 1575°C 30 minutes (orange) 1650°C 5 mins (grey) 1650°C 15 mins (yellow) (a) Vickers Hardness, (b) 3 point bending flexural stress-strain diagram and (c) SEM fracture surface images following 3-point bending.

the decomposed two-phase alloy (as indicated by the white arrows). However, the aged samples show a more significant proportion of the decomposed sample on the fracture surface than the homogenized samples. The presence of this decomposed phase adds weight to the incomplete homogenization of the sample. The decomposed phase is seen (in both samples) to be present on the edges of the river plates or, in the case of the aged samples, the absence of river plates. Suggesting the decomposed phase arrests or deflects the progression of crack growth.

4.6 Comparison of W-28Cr at% samples made via SPS blended vs MA

A comparison of the mechanical properties of all of the homogenized and aged data obtained for the blended and Mechanically alloyed powders are shown in figures 4.46 and 4.47, respectively. Table 19 displays the values of the previous two figures. The results demonstrate that the samples made from mechanically alloyed powder have better mechanical properties than those made from blended powder if a direct comparison is made for the samples manufactured at 1500 °C and 1650 °C. All three heat treatments (including as cast), Young's modulus, UTS and strain to failure, are larger for the samples manufactured from mechanically alloyed powder. One explanation for this is the lower levels of porosity seen in the mechanically alloyed samples.

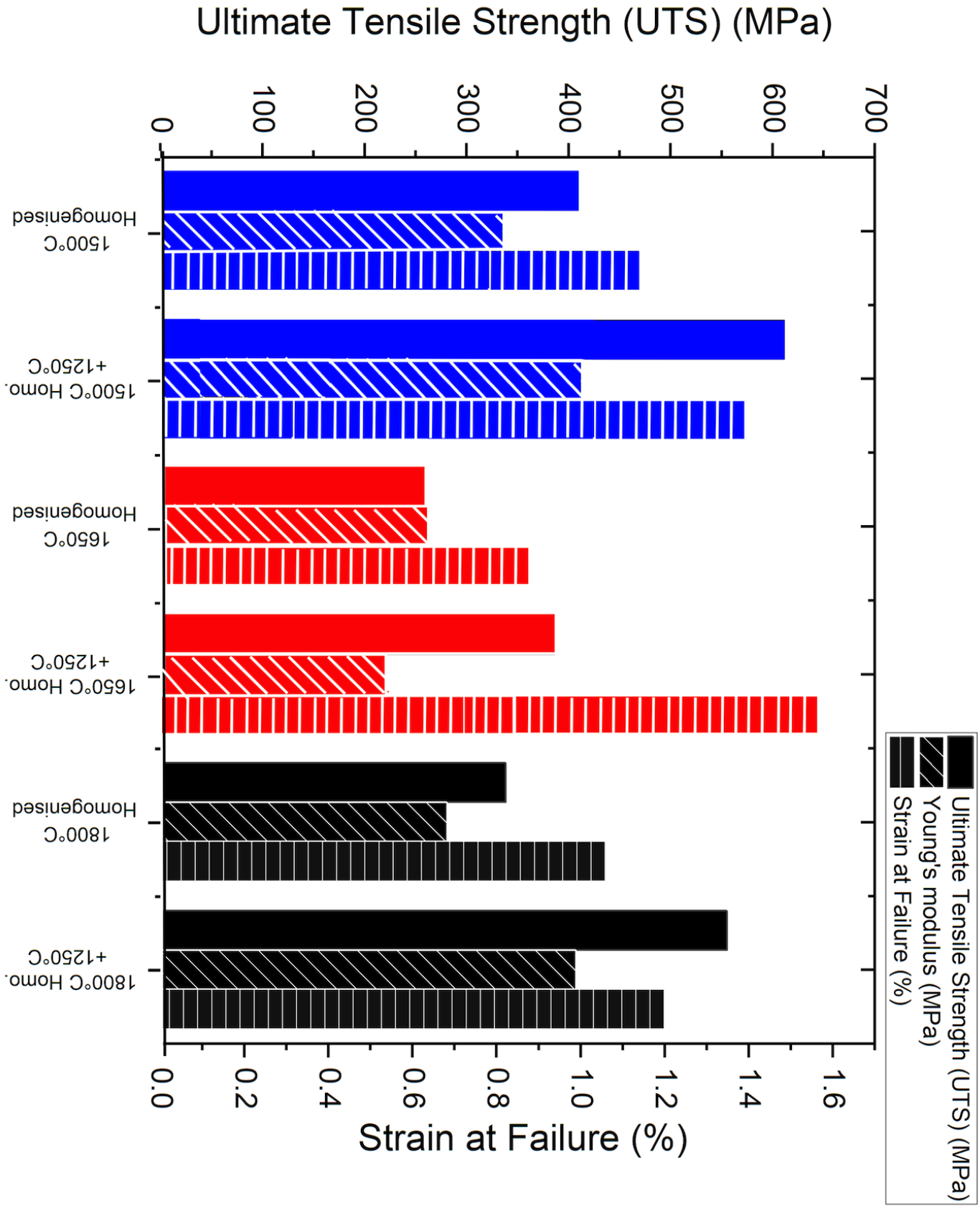

Figure 4.46: **Comparison of the mechanical properties for homogenized and aged samples of the three blended samples manufactured by SPS.** Graph displays Ultimate tensile strength (UTS), young modulus, and strain to failure for blended SPS samples manufactured at 1500 °C (blue), 1650 °C (red) 1800 °C (black) in a homogenized and aged condition.

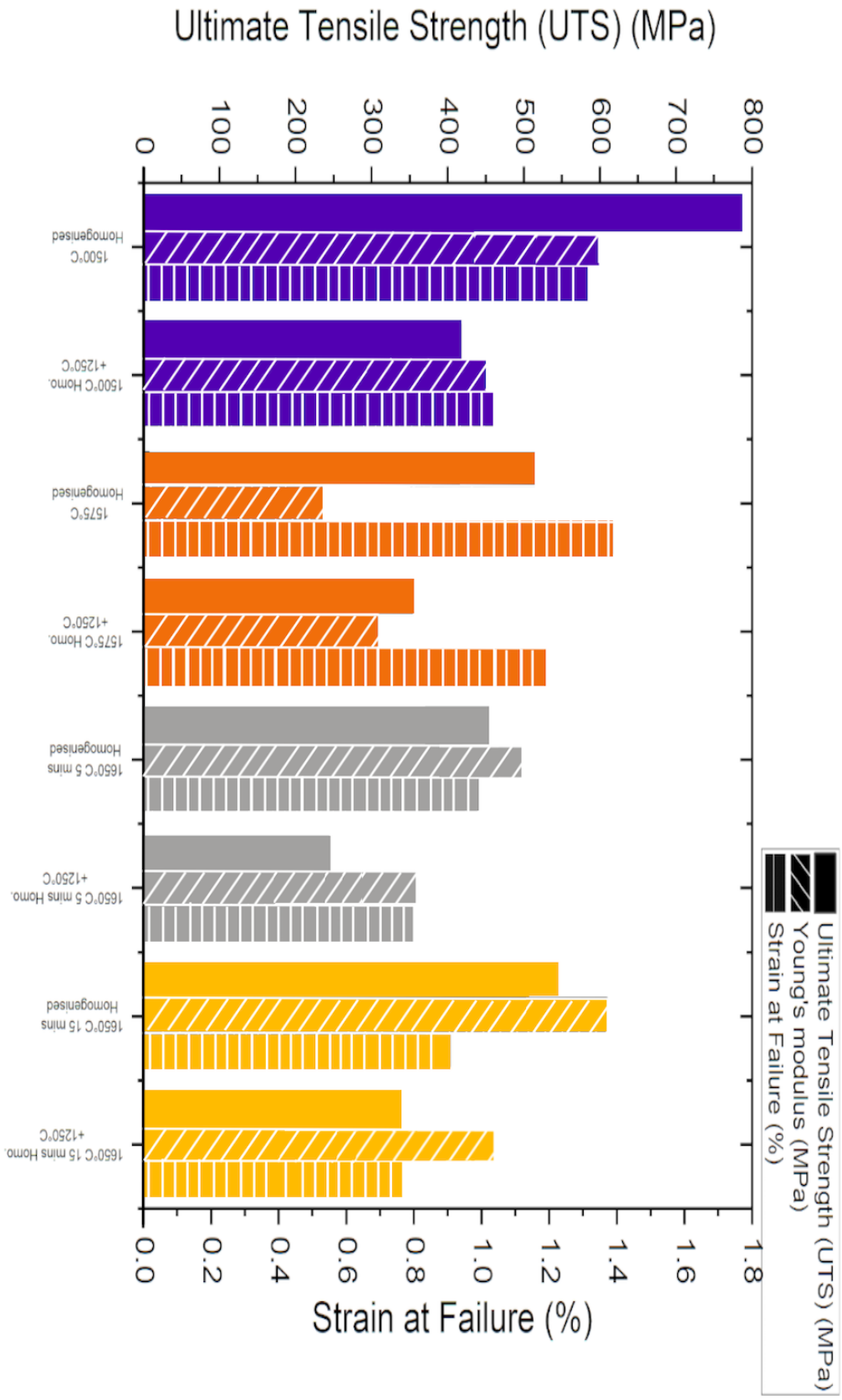

Figure 4.47: **Comparison of the mechanical properties for homogenized and aged samples of the 4 Mechanically (MA) samples manufactured by SPS.** Graph displays Ultimate tensile strength (UTS), young modulus, and strain to failure for Mechanically alloyed SPS samples manufactured at 1500 °C (purple), 1575 °C (orange) 1650 °C 5 minutes (grey) and 1650 °C 15 minutes (yellow) in a homogenized and aged condition

Table 19: **Mechanical test data of SPS alloys.** Table to show mechanical properties from bending tests for homogenized and aged SPS alloys

Heat treatment	Manufacturing Method	Ultimate tensile stress (MPa)	Strain at failure (%)	Young's modulus (GPa)
As Received	Blended Powder			
	1500℃	301.27	0.31	821.34
	1650℃	505.96	0.59	842.58
	1800℃	210.35	1.22	194.73
	Mechanically Alloyed Powder			
	1500℃	719.42	0.72	908.12
	1575℃	665.84	0.69	897.6
	1650℃ 5 mins	715.86	0.64	1017.5
	1650℃ 15 mins	605.43	0.63	953.46
Homogenised 1700℃ 8 hours	Blended Powder			
	1500℃	407.51	1.14	336.02
	1650℃	257.22	0.8	263.07
	1800℃	338.39	1.06	280.93
	Mechanically Alloyed Powder			
	1500℃	787.5	1.31	600.49
	1575℃	515.39	1.39	237.50
	1650℃ 5 mins	478.85	0.99	482.23
	1650℃ 15 mins	565.25	0.91	620.25
Aged 1250℃ 100 Hours	Blended Powder			
	1500℃	611.16	0.39	413.30
	1650℃	386.14	0.57	221.35
	1800℃	555.12	1.20	407.09
	Mechanically Alloyed Powder			
	1500℃	416.79	0.98	437.16
	1575℃	383.44	1.19	308.83
	1650℃ 5 mins	264.69	0.75	352.17
	1650℃ 15 mins	336.89	0.74	454.68

4.6.1 Pathway for decomposition of phases in W-Cr SPS alloys

To observe the decomposition pathway in the SPS alloys, figure 4.48 shows time-interrupted ageing for six homogenized 1800°C samples. After one hour of ageing, a lighter grey phase (tungsten) is seen to precipitate from the much darker chromium-rich phase. At around 2 to 4 hours, a W(Cr) rich decomposition is seen at the grain boundaries. The fine tungsten-rich lamellar precipitates begin to grow into the chromium-rich grains. On further ageing, these primary lamellae begin to increase in thickness, and around 8-16 hours, a finer lamellar begins to appear in the central portion of the tungsten region. After 24 hours, the finer lamellar has been consumed by the much larger lamellae seen in the early stages of decomposition. Figure 4.49 shows a schematic illustration of the process. They show the alloy's significant changes during the first 24 hours of ageing.

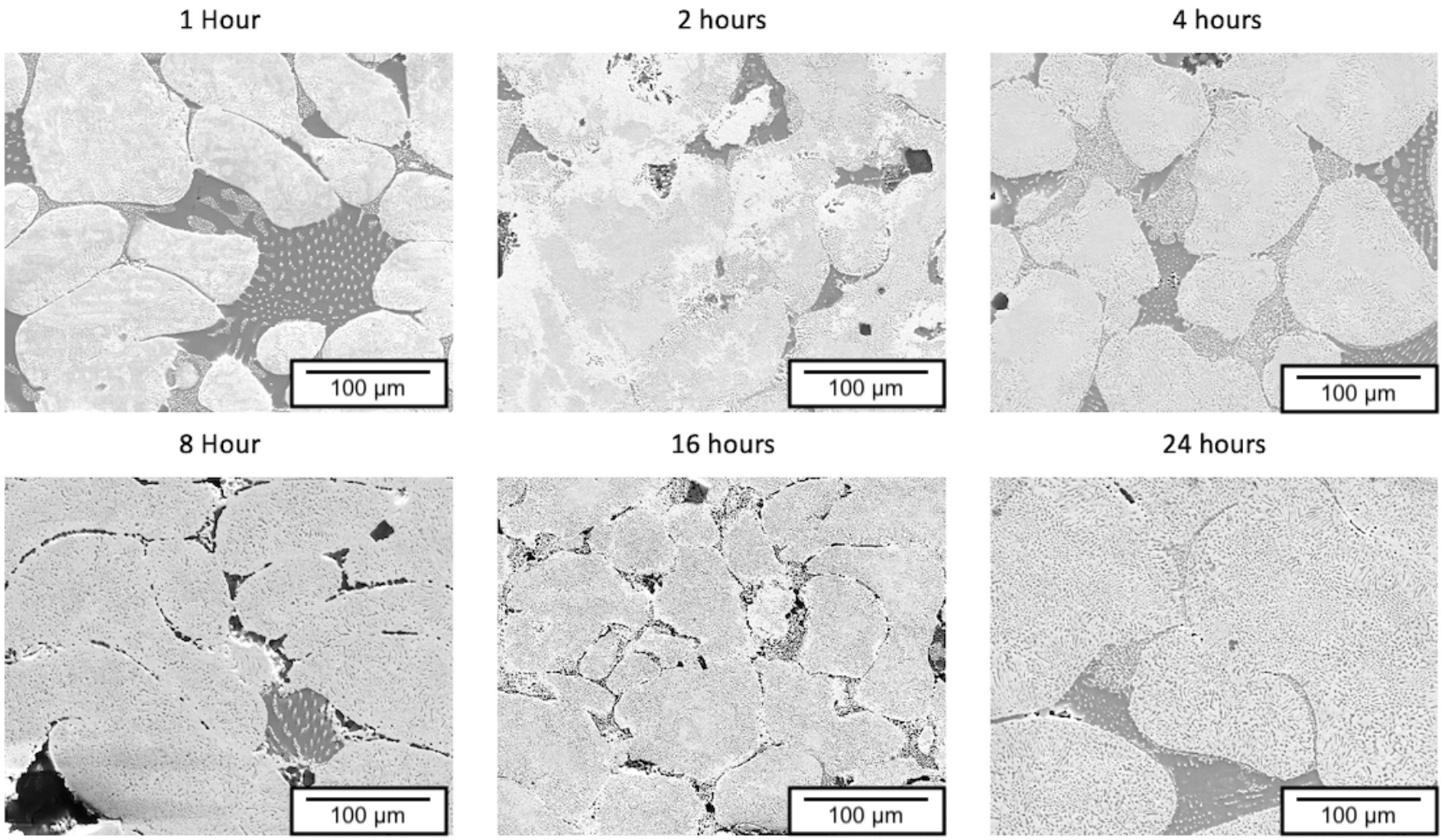

Figure 4.48: **BSE of time-inte]rrupted ageing for six homogenized 1800°C samples** Bse show the progression of the decomposition of the W-Cr alloy into bcc tungsten and chromium following ageing at 1250 °C from 1 to 24 hours

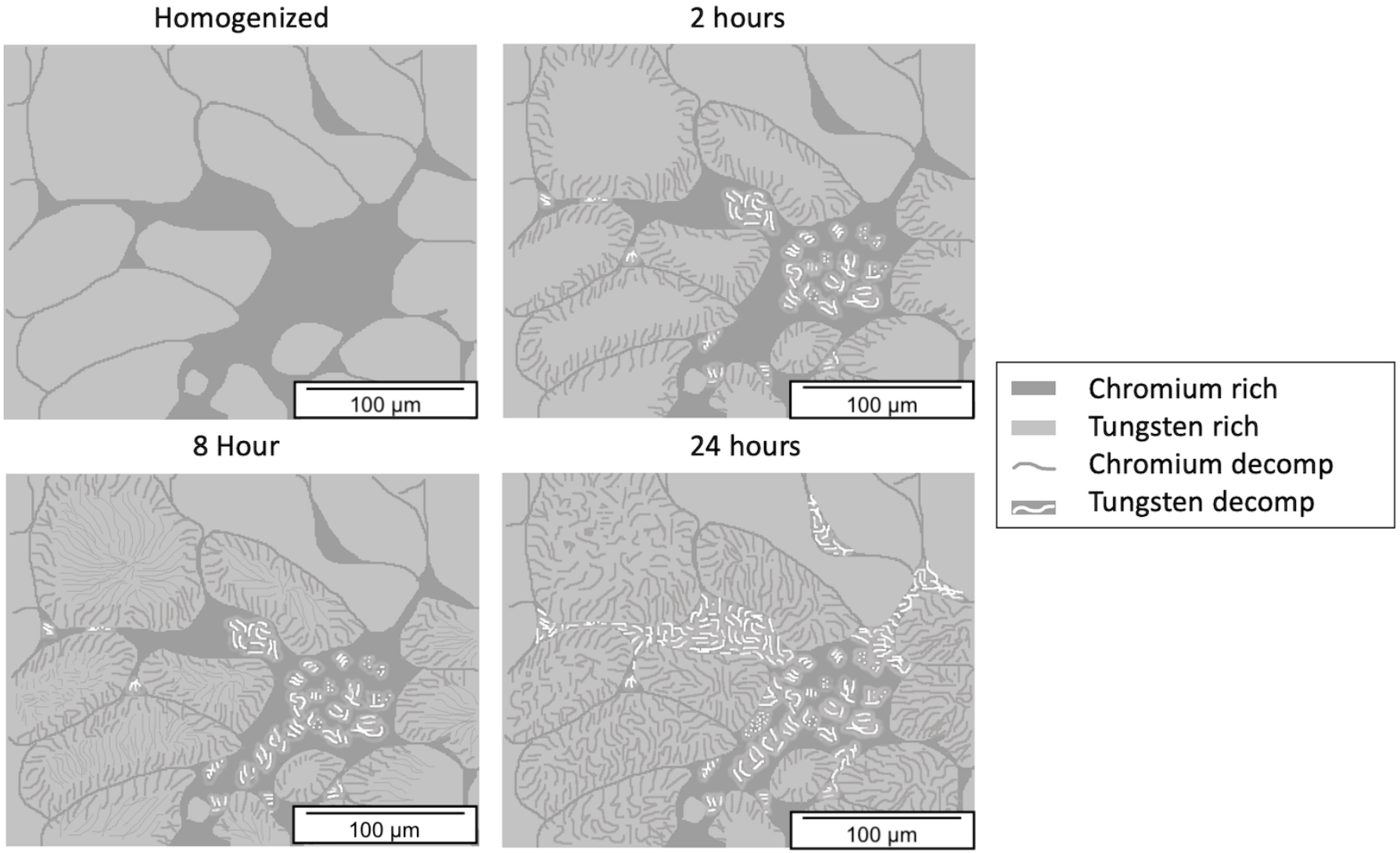

Figure 4.49: **BSE of time-interrupted ageing for six homogenized 1800°C samples** Schematic diagram of the major morphological changes in the microstructure as seen under SEM when a homogenized 1800°C W-Cr sample created by SPS undergoes decomposition at 1250°C for a total time of 24 hours.

4.7 Hot Isostatic Pressed (HIPed) W-28Cr-0.5Zr-0.5Y, MA Powder, manufactured by CEIT

4.7.1 The loss of chromium

As we can see from the above experiments, the main problem is the loss of chromium. Pure chromium has a melting point of 1,857 °C. However, we have seen that in both the alloys manufactured by arc melted and SPS. Chromium is seen to volatilize from the surface. Even at relatively low temperatures, the vapour pressure of chromium is high. At 1157 °C, chromium has a vapour pressure of 10^{-4} (Lesker 2022). In addition, chromium has been shown not to melt when arc melted and instead will sublime. These two factors alone may describe why the production of a tungsten chromium alloy has been challenging to manufacture. To consider an alternative to the manufacturing root, HIPping was further investigated; instead, this time, a lower chromium content was investigated.

It has been suggested (as indicated in the introduction) that the presence of oxygen (and other impurities) at the grain boundaries is a source of embrittlement in tungsten. A sample of HIPped W-28Cr-0.5Zr-0.5Y at.% was obtained from CEIT to explore further methods for improving tungsten's ductility. It has already been shown that adding zirconium to tungsten removes oxygen and improves mechanical properties. Additionally, zirconium in the form of Zirconium Carbide (ZrC) has improved tungsten's ductility and strength. It was observed that the ZrC dispersoids form a coherence phase within the tungsten matrix and scavenge both carbon and oxygen at the grain boundaries (Xie 2015). Grain refining is one method that can be used to improve tungsten's mechanical properties. This can be done by adding elements or compounds that will not only scavenge impurities but will pin grains and retard their growth. One such example is the addition of yttrium, which absorbs oxygen forming Y_2O_3, which subsequently pins the movement of grain boundaries (Zhang D 2020).

The alloy was manufactured by hipping mechanically alloyed powder at 1250 °C, 140MPa for 2 hours, followed by thermal heat treatment of 1555 °C for 1.5 h, then cooled

at 60 °C/min (Sal 2023). Figure 4.50 details the alloy's microstructure in the as-received condition. Initial BSE images at low magnification show a refined grain structure with dark and light grains. Figure 4.50b shows a zoomed-in BSE image of the microstructure. Two black regions can be seen; first, the more significant black regions are indexed as chromium-rich. The second, much smaller, finer precipitates seen at the grain boundaries and within the matrix are yttrium-rich precipitates. With some of the chromium-rich (larger dark precipitates), a decomposed tungsten-rich lamellar phase is observed (figure 4.50d) and EDX maps figure 4.50e and f.

The microstructure observed in the chromium-rich regions results from the Kirkendall effect (Broeder FJA 1972). When comparing the vacancies in both tungsten and chromium at 1250 °C. It is calculated that the number of vacancies in tungsten, compared to chromium, is 1 in 10,000,000. Therefore, it can be reasonable to suggest that the number of vacancies in tungsten is almost negligible. As a result, tungsten atoms will diffuse into the chromium-rich regions if a vacancy reaches the interface between the two elements. However, The chromium atoms will not diffuse out of the chromium-rich areas due to the lack of vacancies in the tungsten phase.

An EBSD and corresponding IPF map are shown in figure 4.50c of the homogenized sample. A histogram and cumulative frequency plot of the grain length data are shown in figure 4.54. The vertical yellow line indicates the mean grain size at 0.67 μm.

To further nanostructure the alloy, samples were heat treated at 800 °C (figure 4.51), 1000 °C (figure 4.52) and 1250 °C (figure 4.53) to induce decomposition. However, unlike the original W-Cr alloys presented earlier, although there is grain refinement, the production of the tungsten-chromium lamellar (as seen in arc melted and SPS samples) is not present following ageing (at the three temperatures). Therefore, it is evident that adding either zirconium or yttrium (or both) prevents the decomposition to the lamellar phase.

Figure 4.55 displaces the results of the XRD analysis of the four alloys after their subsequent heating conditions. The graph shows that as the ageing temperature reduces from 1250 °C to 800 °C, there is a general reduction in the lattice parameter from 3.1205

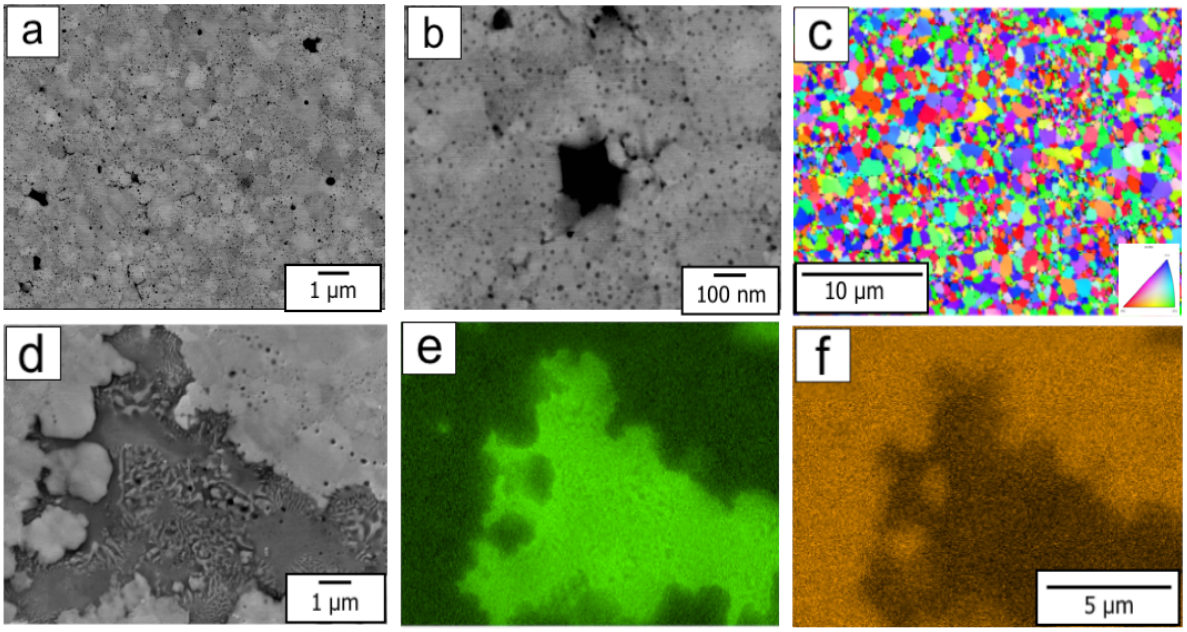

Figure 4.50: **W-28Cr-0.5Zr-0.5Y at% HIPped sample heat treated in the as-received condition.** (a) BSE image, (b) BSE image of the large dark region and smaller precipitates, (c) EBSD and IPF-X Map, (d) zoomed-in BSE of large dark precipitates, (e and f) EDX map to show tungsten (orange) and Chromium (green) rich regions.

at 1250 °C to 3.0924 at 800 °C. However, the lattice parameter of the as-received (3.1022) sample compared to the sample aged at 1250 °C is lower but more significant than the other two heat treatments. Any reduction in the lattice parameter will result from an increased concentration of the elements with lower lattice parameters in the matrix phase present. It would suggest that the amount of Zr and or Cr in the tungsten (matrix) phase is more significant than at 1250 °C.

The effect of Zr (seen above) on the disruption of the two-phase decomposition that is observed in the binary W-Cr alloy is similar to that of CoCrNi- and CoCrFeNi-based alloys (He JY 2016, Zhao YL 2017). In these alloys, alternating layers of an L12 ordered $\gamma\prime$-Ni_3(Al, Ti) precipitates in a γ matrix, growing behind an inward moving grain boundary (Williams 1981) are observed. However, the addition of even a small amount of 0.8at.% Nb disrupts the discontinous precipitation of the Ni_3(Al,Ti). In these alloys, Nb was seen to segregate to the grain boundaries. In so doing, not only is the precipitation at the grain boundaries stopped, but additionally, the migration of the boundaries is halted via solute drag and energy reduction (Fan L 2020). It is thought that the addition of Zr in these alloys

acts similarly to that of Nb.

Figure 4.54 shows the grain profiles of the three alloys aged for 100 hours at 800 °C, 10,00 °C and 1250 °C. The mean grain lengths are marked on each graph with a yellow line (as measured by EBSD). The grain sizes of the aged samples are similar to that of the homogenized sample. This suggests there has been no movement of prior grain boundaries despite ageing. This adds weight to the idea that adding Zr or Y (or both) significantly inhibits decomposition and grain boundary movement.

Specifically, in the W-Cr system itself, alloying with either Ta or Hf has been shown via first principle calculations and experimental observations to inhibit discontinuous precipitation during annealing at 1000 °C. The results showed that additions of only 2% Ta can reduce the temperature of the miscibility gap by 35%. It was demonstrated that Ta reduces the decomposition kinetics due to its affinity for chromium, which promotes the clustering of the two elements. This directly affects the formation of the chromium-rich phase (Veverka J 2023). Creates a diffusion barrier that prevents W-Cr decomposition into two separate phases.

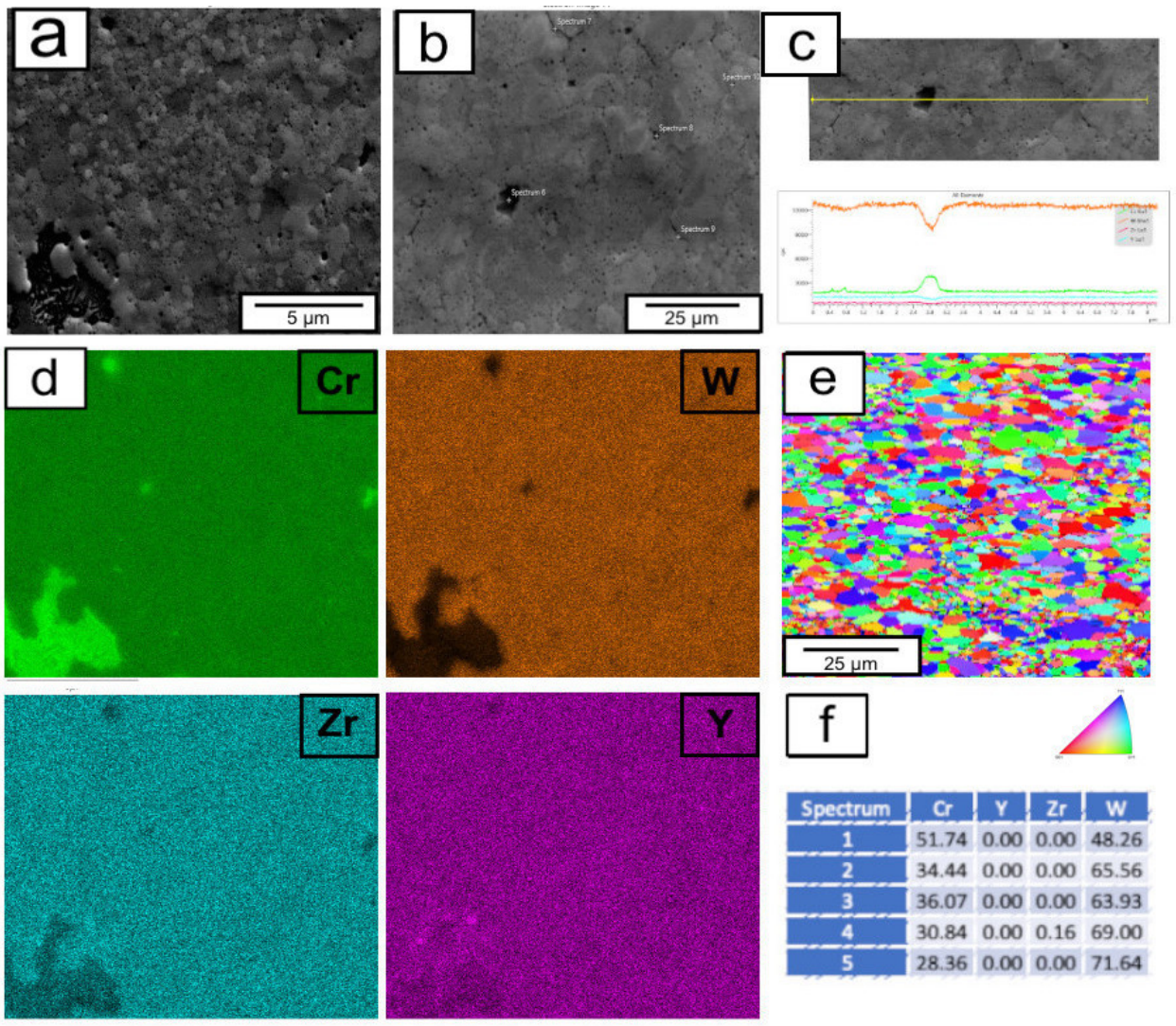

Spectrum	Cr	Y	Zr	W
1	51.74	0.00	0.00	48.26
2	34.44	0.00	0.00	65.56
3	36.07	0.00	0.00	63.93
4	30.84	0.00	0.16	69.00
5	28.36	0.00	0.00	71.64

Figure 4.51: **W-Cr-Z-Y HIPped sample heat treated at 800 °C for 100 hours** (a) Hi magnification image showing Chromium-rich regions, (b) Low magnification BSE, (c) EDX line to show the distribution of elements to determine the composition of smaller precipitates (d) EDX map (tungsten (orange) and chromium (green), yttrium (pink) and Zirconium (blue)) (e) EBSD IPF-X map (f) Point scan data. (atomic %).

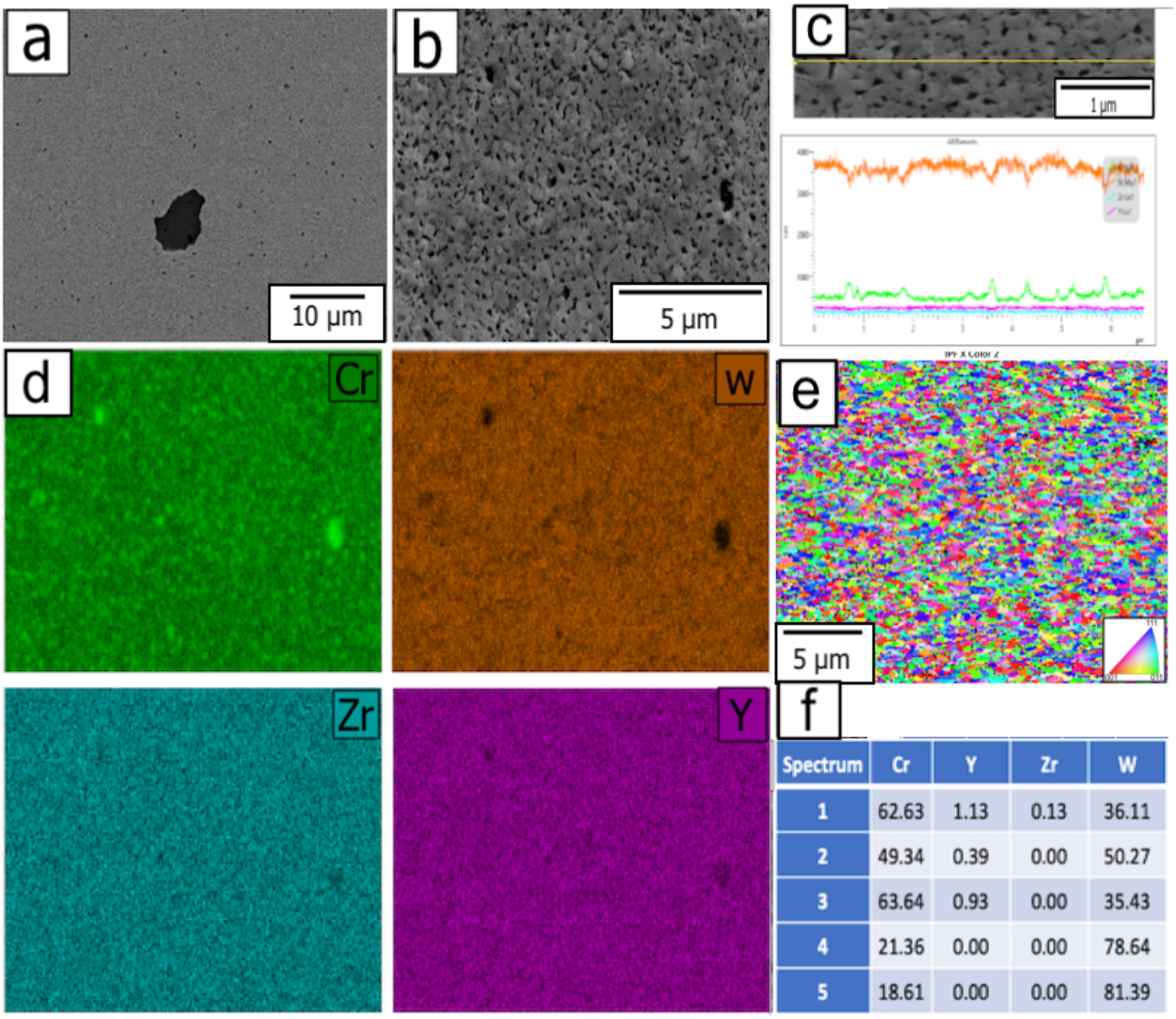

Spectrum	Cr	Y	Zr	W
1	62.63	1.13	0.13	36.11
2	49.34	0.39	0.00	50.27
3	63.64	0.93	0.00	35.43
4	21.36	0.00	0.00	78.64
5	18.61	0.00	0.00	81.39

Figure 4.52: **W-Cr-Z-Y HIPped sample heat treated at 1000 °C for 100 hours.** (a) Hi magnification image showing Chromium-rich regions, (b) Low magnification BSE, (c) EDX line to show the distribution of elements to determine the composition of smaller precipitates (d) EDX map (tungsten (orange) and chromium (green), yttrium (pink) and Zirconium (blue)) (e) EBSD IPF-X map (f) Point scan data. (atomic %)

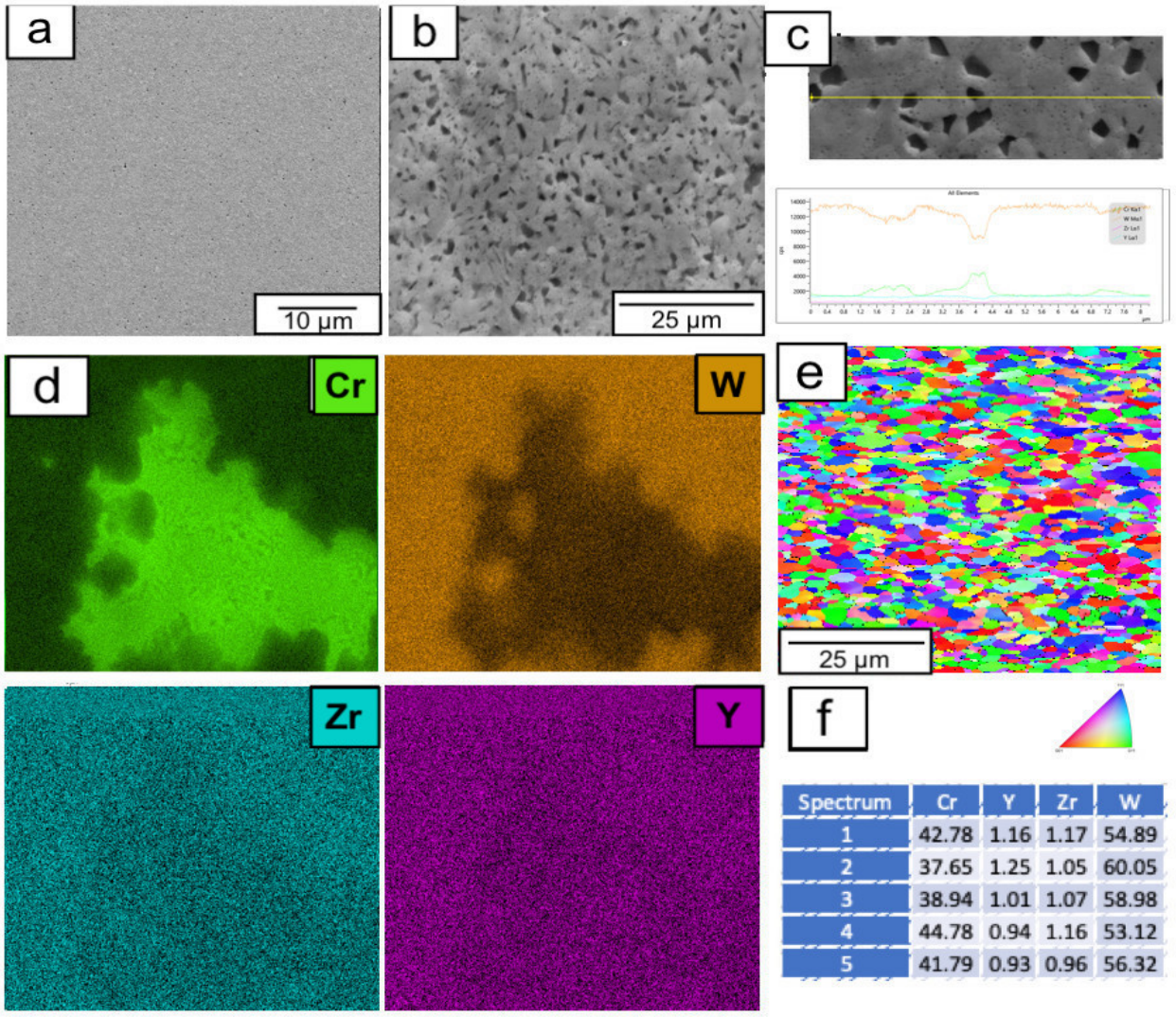

Spectrum	Cr	Y	Zr	W
1	42.78	1.16	1.17	54.89
2	37.65	1.25	1.05	60.05
3	38.94	1.01	1.07	58.98
4	44.78	0.94	1.16	53.12
5	41.79	0.93	0.96	56.32

Figure 4.53: **W-Cr-Z-Y HIPped sample heat treated at 1250 °C for 100 hours.** (a)Low magnification BSE, (b) Hi magnification image showing Chromium-rich regions, (c) EDX line to show the distribution of elements to determine the composition of smaller precipitates and (d) EDX map (tungsten (orange) and chromium (green), yttrium (pink) and Zirconium (blue)) (e) EBSD IPF-X map (f) Point scan data. (atomic %)

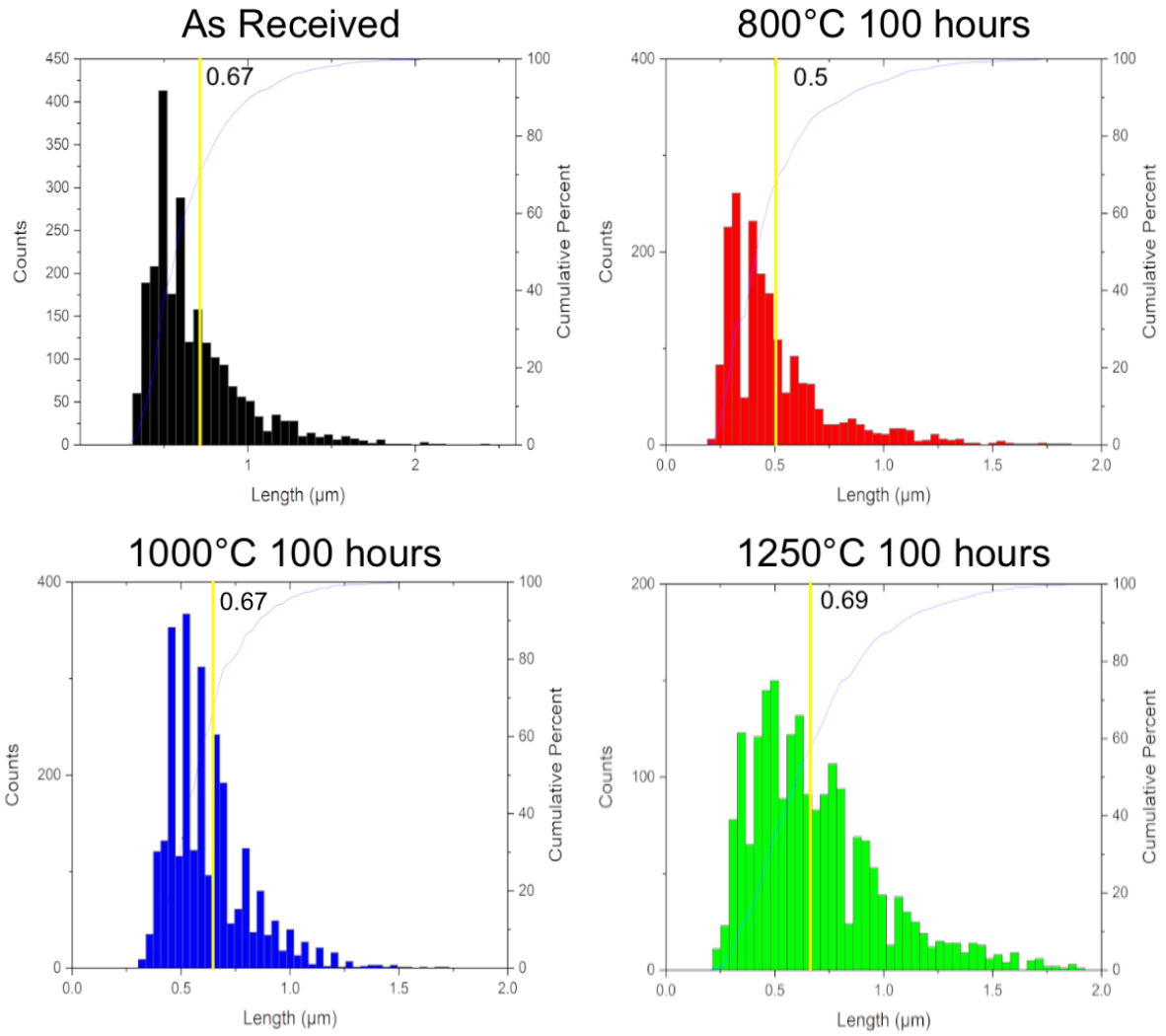

Figure 4.54: **Grain length (μm) histograms** Representing data obtained from EBSD maps of each sample in the as received (black), 800 °C (red), 1000 °C (blue), 1250 °C (green). Yellow vertical lines indicate the mean grain size in μm, and the thin blue line represents cumulative frequency.

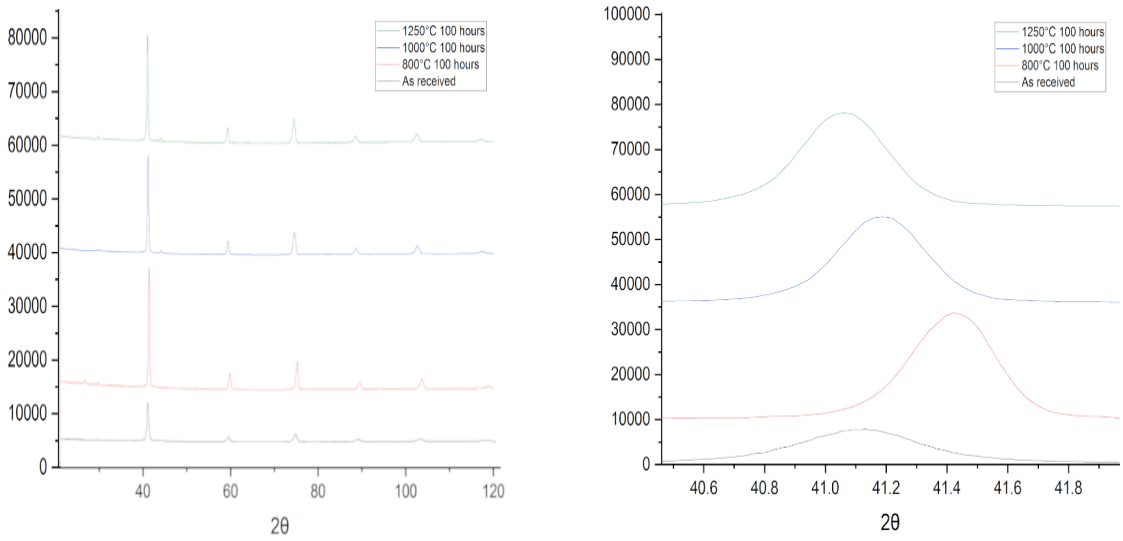

Figure 4.55: **XRD analysis of HIPped W-28Cr-0.5Zr-0.5 at% samples in the as-received condition.**(a) XRD plots for homogenized received (black) and heat treated 800 °C (red), 1000 °C (blue), 1250 °C (green). (b)zoomed-in image of the first peak observed at 41° on the XRD pattern to show a shift in peaks.

4.8 Conclusion

This study aimed to try and bulk manufacture an alloy of W-28Cr at%. It was shown that in conventional arc melted W-28Cr at% a two-phase BCC alloy could be produced by harnessing the miscibility gap in the tungsten-chromium phase diagram. However, due to the high melting point of tungsten, there was considerable macrosegregation, and porosity, which was suspected due to chromium loss. Several sintering methods were used to not only produce a bulk sample but also to improve the homogeneity and porosity. These included powder manufacture, SPS and HIPping.

- W-28Cr at% can be manufactured by conventional arc melting. Following homogenisation at 1700 °C and then ageing at 1250 °C for 100h a fine two-phase lamellar structure can be produced. However, the sample shows considerable porosity and there are regions of macrosegregation.

- SPS has shown some promise; W-28Cr at% alloys of and were manufactured in bulk at different temperatures and times. However, despite varying heat treatments, a homogenized structure was never obtained. Ageing of the alloy within the miscibility gap did produce decomposition of the fine lamellar structure that we saw earlier in the ACI alloy. However, the lack of homogenization was probably to blame for the absence of complete nanostructuring, as there were large areas of single-phase chromium in all of the samples manufactured by SPS. Due to the lack of homogenization of the alloys manufactured by SPS, no mechanical testing was performed on the aged samples.

- The HIPped samples produced by CEIT showed the most promise. However, they did not have the fine lamellar structure we could make in the ACI alloy. Ageing at 1250, 1000, and 800 °C all produced a nanostructuring. The lack of lamellar precipitates in the CEIT sample results from zirconium and yttrium additions, as yttrium is known to diffuse to grain boundaries and act as a pinner. It is thought that

adding Zirconium to the alloy inhibits the diffusion of chromium from the tungsten phase, preventing the formation of lamellar precipitates.

5 W-Cr72 at% - A Ex-situ Recrystallisation

5.1 Introduction

From the work conducted in Chapter 5, the recrystallization process was investigated further in W-Cr using the techniques learned. First, an "ex-situ" electron backscatter diffraction (EBSD) method was used to investigate the phenomenon behind the recrystallisation process. Ex-situ EBSD refers to the EBSD analysis of several different samples that have undergone various heat treatments. Here, several regions of interest (ROI) after homogenization were identified for observation after ageing at different time periods within the miscibility gap.

5.2 Results and Discussion

5.2.1 "Ex-situ EBSD"

Figure 5.1 shows SEM BSE images of the typical microstructure of W-72%Cr following homogenisation at 1700 °C for 8h (a) and subsequent ageing at 1250 °C for 1, 10 and 100h. EBSD of the same areas presented in Figure 5.1 are shown in figure 5.2. Along with grain size histograms as measured by AZTEC software. By ageing a tungsten chromium alloy inside the miscibility gap, the grain size can be reduced from 184.48 $\pm$ 17.62 μm^2 on homogenization to 3.87 $\pm$ 2.39 μm^2 at 100h of ageing (figure 5.2). This clearly demonstrates that the miscibility gap can be harnessed to reduce the overall grain size and lead to nanostructuring. Producing a two-phase microstructure of alternate layers of tungsten and chromium as shown in figure 4.5.

Based on this evidence, the miscibility gap can be used to control the size of the grains of this alloy; more investigation must be carried out for ageing times around the 100-hour mark. This should determine the optimum ageing time to produce the finest grain structure in this alloy. The gradient of the graph between 1h and 10h demonstrates that ageing for less than 10h would not result in a finer grain structure, and there is potential for further

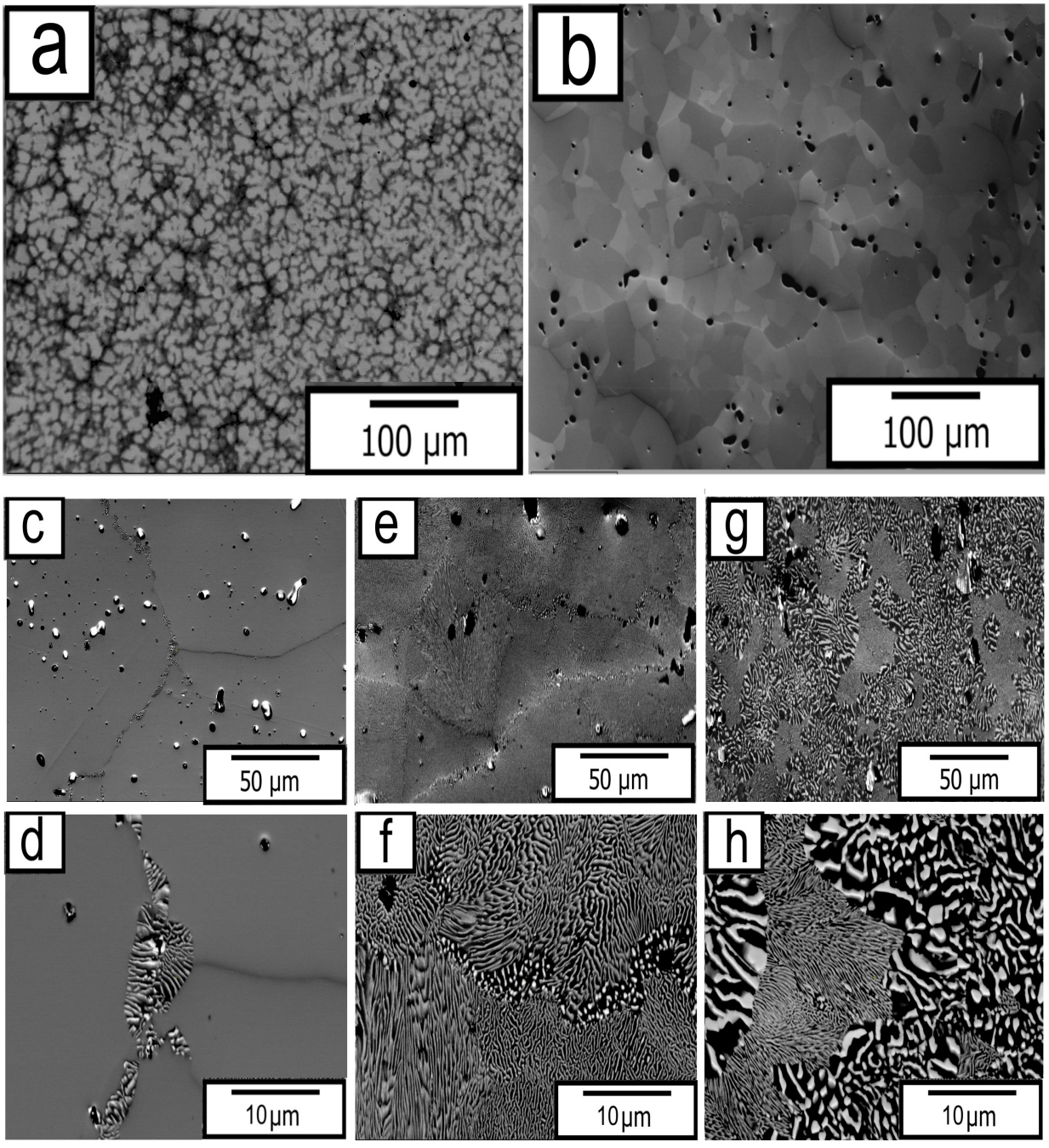

Figure 5.1: **BSE images of WCr after varies heat treatments** (a) As cast (b) Homogenised 1700 °C 8hrs (c) 1hr 1250 °C (d) zoomed in 1hr 1250 °C (d) 10hr 1250 °C (e) 10hr 1250 °C (f) Zoomed in 10hr 1250 °C (g) 100hr 1250 °C (h) Zoomed in 100hr 1250 °C

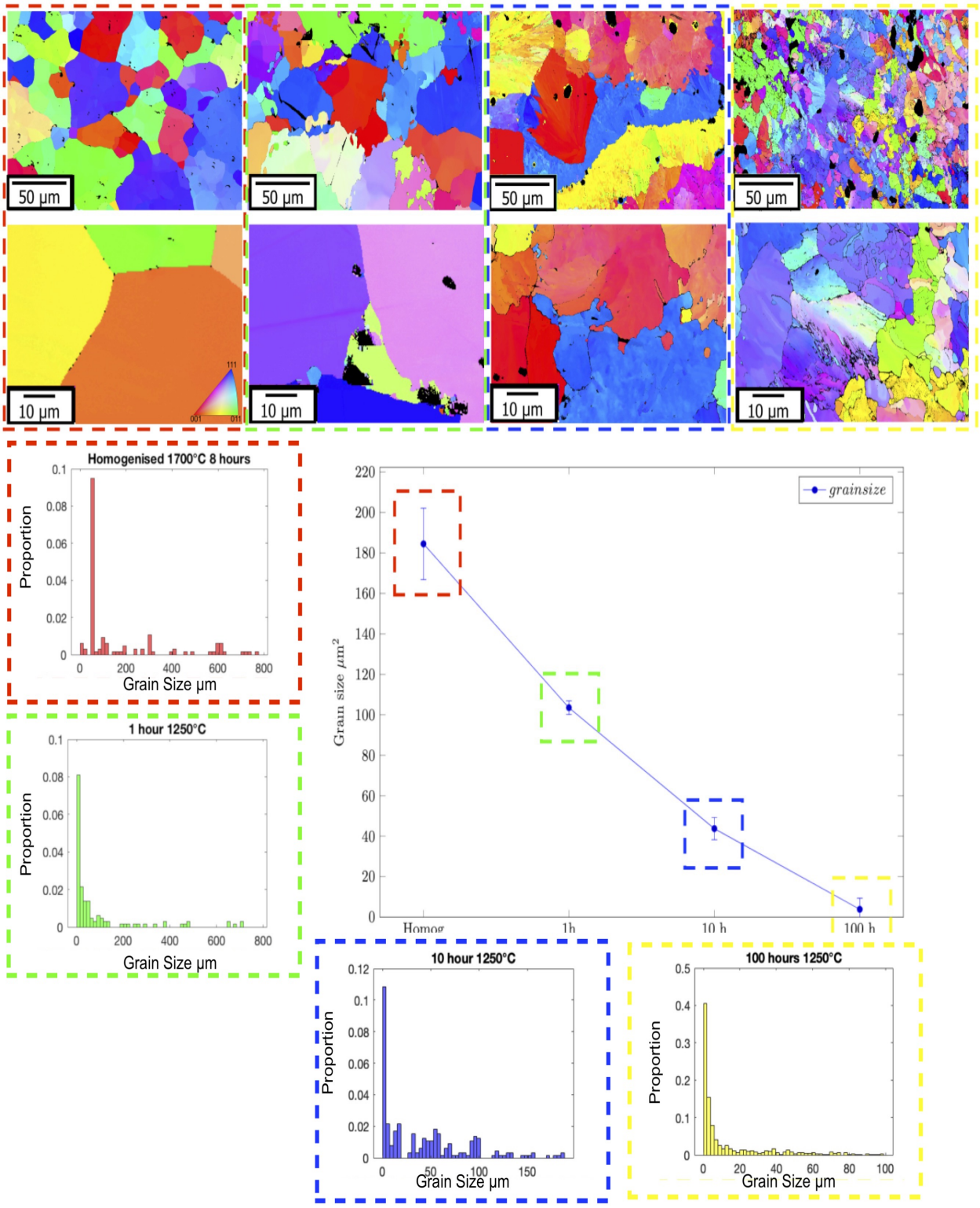

Figure 5.2: **Recrystallisation of W-Cr** (a) Homogenised 8h 1700 °C (b) 1hr 1250 °C (c) 10hr 1250 °C (d) 100hr 1250 °C.(The top row of EBSD images are of the same area as shown in figure 5.1.) (e) A graph to show Grain size distribution from EBSD data from each condition above

refinement by ageing the sample for more than 100h.

The above has demonstrated a grain refinement and, more interestingly, a decomposition of the single phase bcc_A2 into two separate bcc_A2 phases on ageing within the miscibility gap. However, the actual phenomenon behind the recrystallization process of this alloy still needs to be eluded.

5.2.2 W-Cr72 at% - analysis of early stage nucleation & growth of fine-scale lamellae

.

The previous section has shown that on ageing the alloy in the miscibility gap (at 1250 °C), the alloy undergoes a grain refinement to form a two-phase (A2-A2) bcc structure. What follows is a look at the experimental evidence collected and assesses it against the literature to determine the decomposition mechanism in this alloy.

Figure 5.3 catalogues the decomposition of the alloy from a homogenised condition through to the first 2 hours of heat treatment at 1250 °C following interrupted heat treatments. In the homogenised conditions (a and b), large uniaxed grains are observed with the addition of pores (black regions). All grain boundaries (and boundaries) are free of precipitates. However, at approximately 30 minutes of ageing at 1250 °C, a two-phase (dark and light) lamellar can be observed at grain boundaries and around defects in the sample (pores). There is no evidence (at least in the samples observed here) of the presence of the fine lamellar structure on the interior of the grains that can be seen at 10hrs (figure 5.1). After 1hr of ageing, the lamellar precipitates continue to grow inwards into the centre of the grains. The overall volume fraction of the precipitates is seen to increase. Again, after 2 hours of ageing at 1250 °C, the precipitates have grown almost to cover the entire region under observation.

As can be seen from the images of the early stages of this process. The decomposition of single-phase bcc into two separate phases seems to occur at grain boundaries or defects (pores) from the homogenised phase. The additional observation that this decom-

position is not homogenous after the initial stages of the ageing process would suggest that spinodal decomposition is not the decomposition mechanism.

Classical discontinuous decomposition and discontinuous spinodal decomposition are two distinct processes observed in materials science, each exhibiting unique characteristics in specific alloy systems. In classical discontinuous decomposition, the lamellae consist of the precipitate phase, and the formation occurs through a discontinuous growth mechanism. On the other hand, discontinuous spinodal decomposition involves the formation of coherent lamellae due to sinusoidal waves with increasing amplitude.

The study conducted by Gorsse et al. (Gorsse 2011). focused on spinodal decomposition in an alloy of Pb0.36Ge0.64Te. During this process, the original (Pb,Ge)Te parental phase separated into two distinct phases - darker PbTe(Pb) and lighter GeTe(Pb) phases - forming coherent lamellar structures. The interlamellar spacing in spinodal decomposition was smaller than in classical discontinuous precipitation.

To better understand the decomposition mechanism in the early stages, a FIB lift out of a decomposed region was removed after 1hr of ageing at 1250 °C. As shown in Figure 5.4a. Figure 5.4b shows a more detailed view of the decomposed front before any visual interpretation of the decomposed phase was conducted to determine if the elements present had been given enough time to diffuse.

$$X = \sqrt{6Dt} \tag{33}$$

If the value of 2.59x10^{-16}m2/s is used for D (inter diffusivity constant of tungsten) (as calculated from Park et al. (Park M 2014)) is used in the equation 33 for a random work. T (time) is calculated at 4 hours for a temperature of 1523K. Therefore, the lamellar precipitates produced were considered in an equilibrium condition based on the diffusion rate. Measuring the width of the light and dark phases presents the average widths are 0.41 $\pm$ 0.12 μm 107 $\pm$ 18 nm. Both of which are larger than the typical microstructure seen in a spinodially decomposed alloy. In addition, most of the decomposed phases show directionality to the growing front of the growing phase.

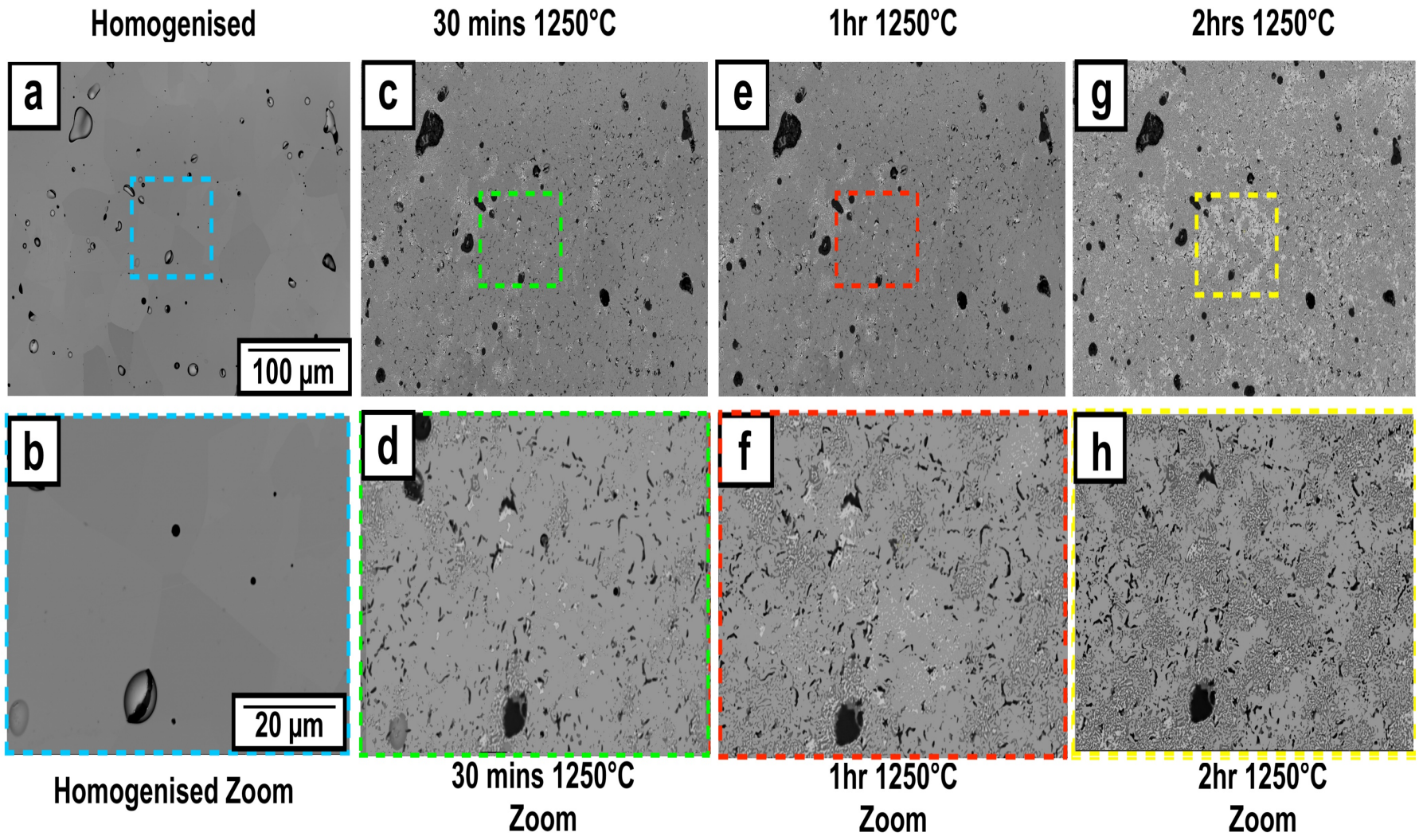

Figure 5.3: **WCr72 at% Early stage growth of decomposition following ageing at 1250 °C** SEM BSE images showing pseudo-insitu WCr72 at% precipitate growth for the same area after Homgenisation 8 hours 1700 °C (a and b), then aged at at 1250 °C for; 30 minutes (c and d), 1 hour (e and f) and 2 hours (g and h)

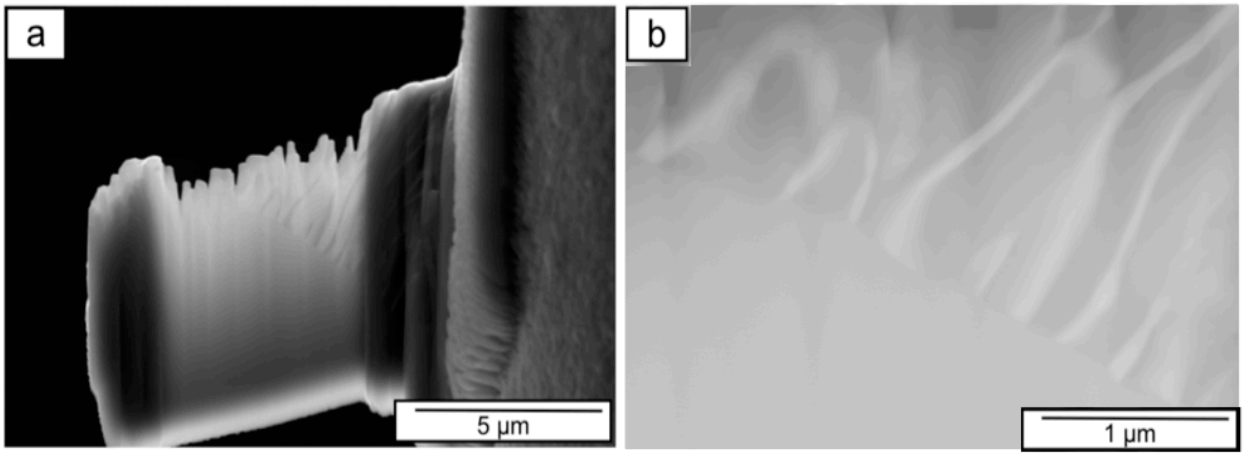

Figure 5.4: **WCr72 at% after 24 hours ageing at 1250 °C** SEM image of FIB lift-out showing WCr72 at% precipitate under observation in the top left-hand corner and (b) Magnified BSE image of precipitate in (a).

To further investigate the decomposition mechanism, Porter identified a list of characteristics that are observed in a spinodal decomposition (Porter 1967) as follows :

1. Presence of bands on the sides of X-ray peaks during the early stages of decomposition.

2. Characteristics of simple growth.

3. Precipitation of phases in a random manner. Analyzing the experimental findings related to these characteristics of the alloy being studied:

The following makes a comparison of the above characteristics to those observed here;

1. X-ray Patterns: During the early stages of decomposition, no side bands are present in the XRD patterns for both classically manufactured samples (figure 4.6) and those produced by SPS (Spark Plasma Sintering) (figures 4.24 and 4.37) or HIPping (Hot Isostatic Pressing) figure 4.55. Side bands on X-ray peaks are not observed, suggesting that the first characteristic of spinodal decomposition is absent.

2. Location of Precipitated Phase: The precipitation of the decomposed phase is solely located at the grain boundaries, and there is no evidence of the decomposition happening within the matrix. The lamellar precipitation of tungsten chromium has a

similar appearance to that of pearlite (FeC). This indicates that the growth of the two-phase alloy is solely the result of nucleation and growth, implying that the second characteristic of straightforward development is observed.

3. Appearance of the Decomposed Phase: The laminar (decomposed) phase appears to cover the matrix only after 8-12 hours. This indicates that the precipitation occurs gradually and does not show a random distribution. This suggests that the third characteristic of spinodal decomposition, which involves spontaneous precipitation of phases, is not observed.

In summary, based on the experimental observations, it appears that the alloy's decomposition does not follow the characteristics of spinodal decomposition, as none of the three main features proposed by Porter are present. Using the critical temperature (T_c), equation (34), combined with Young's modulus for the 50/50 wt

$$T_c = \frac{\eta^2 E}{2(1-\nu)KN_\nu} \tag{34}$$

Poisson's ratio (ν), Boltzmann's constant (k), number of atoms per unit volume N_ν and linear expansion per unit composition change η, a value of 0.093 was used for W-Cr72 at%.

To determine if an alloy will undergo spinodal decomposition and the amount of supercooling needed, Cahn identified that at the apex of the miscibility gap, the double differential of Gibbs' free energy is zero. Therefore, the critical temperature can be calculated from equation (34). Using the Young's Modulus values for SPS samples aged at 1250 °C (Table 19), the critical temperatures calculated for the maximum and minimum Young's Modulus values would be between 3005 and 6172 °C. However, these values exceed the miscibility gap temperature and the under-cooling used experimentally (1225 °C). As a result, the conclusion is that W-Cr72 at% does not undergo spinodal decomposition, and any microstructure seen from quenching within the miscibility gap results from a different decomposition process, not spinodal.

FFT and radial distribution function

A fast Fourier transform (FFT) was applied to the backscattered electron (BSE) data of W-Cr72 atThe FFT formula for a 2D image is given by equation 35, where f(k_1k_2) is defined for any number of N x N pixels (as long as N is a power of 2 and is commonly an integer greater than 1024). The variables f(k_1k_2) are defined as any integer between 0 and N-1.

$$\sum_{K_{2=0}}^{N-1}\sum_{K_{1=0}}^{N-1} exp(2\pi i k_1 n_1/N) f(k_1 k_2) \tag{35}$$

Figure 5.5 shows the 2D FFTs in row (b) of the images above (row (a)). Each image in row (a) represents a W-28%Cr sample in its homogenized condition and at various stages of the ageing process. The zero frequency has been shifted to the centre of the image. In addition, to compare the results obtained here to that of the literature, a screenshot of a computerized spinodal decomposition is included, as well as its 2D FFT ((Wang 2020)). A radial average of each alloy and computerized spinodal is presented as a graph, in row (c), for each of the FFTs computed and presented as normalized intensity vs distance from the centre in pixels. Red arrows indicate the measured first maximum peak of each of the samples.

To determine if the results obtained were accurate, a comparison was made to that of the internet. The 2D FFT from ((Wang 2020)) was first converted in a radial plot, and the number of pixels was identified for the first maximum peak. Using ImageJ, the number of pixels was converted into a measurement, and the wavelength was determined by inverting the value (Fujita 2008). The calculated wavelengths of the W-Cr72 at% sample and that of the exemplar are shown in table 20.

Table 20: **Table to show wavelengths calculated by FFT.** Wavelength measurements of W-Cr72 at% decomposed phase at different ageing times compared to a known spinodal micrograph as calculated by FFT and inverse characteristic length.

	Homgenised 1700 °C 8 hours	**Aged 1 hour 1250 °C**	**Aged 10 hours 1250 °C**	**Aged 100 hours 750 °C**	**Spinodal decomposition Computer generated**
Wavelength	0	1.252 μm	0.713 μm 1.301 μm	0.443 μm 1.329 μm	190 nm

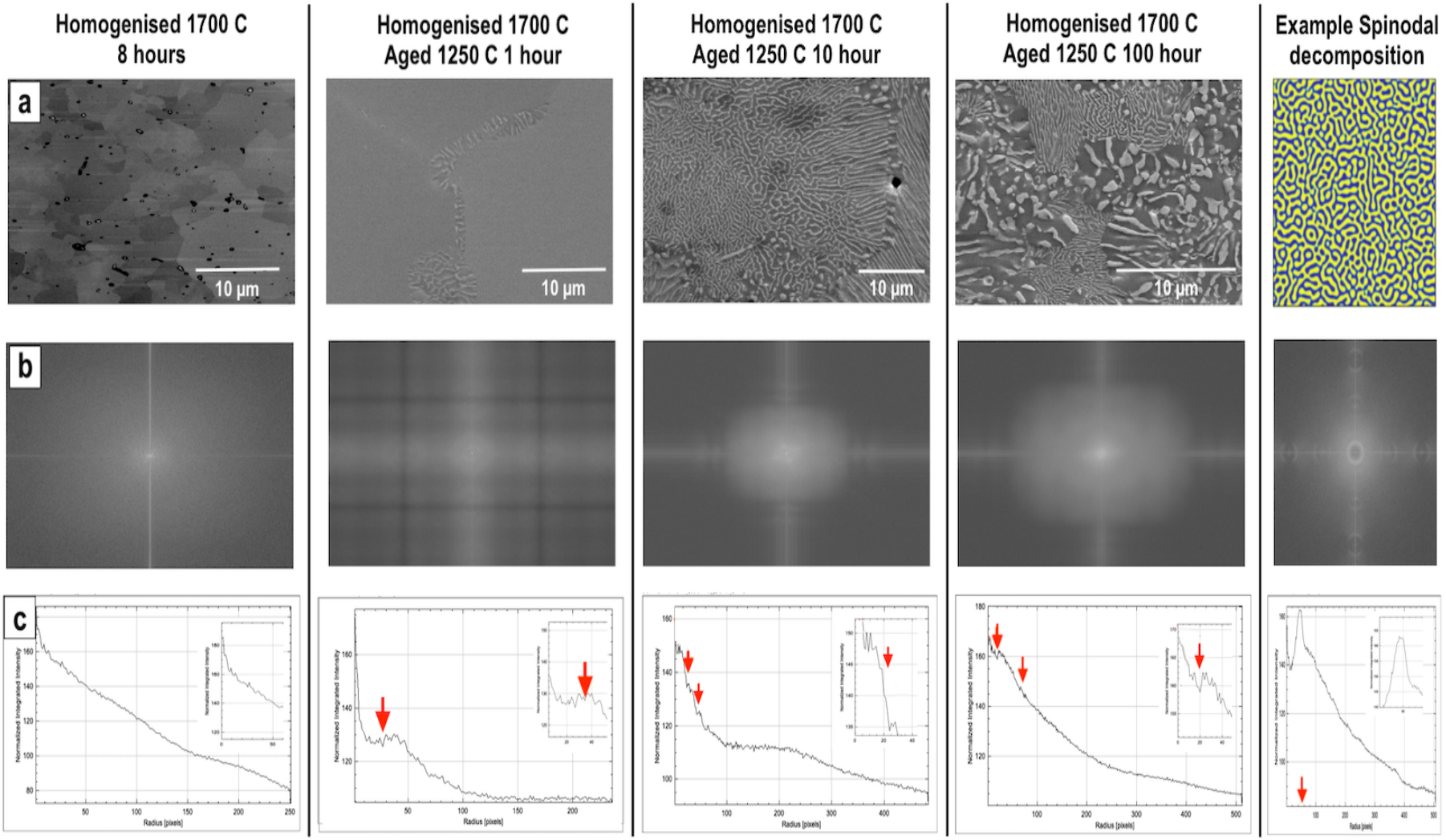

Figure 5.5: **FFT of Tungsten chromium 72/28 wt% alloy** (a) BSE images of Tungsten chromium alloy after homogenization at 1700 °C for 8 hours, followed by typical microstructure after 1, 10 and 100 hours of ageing at 1250 °C. (b) Corresponding FFT images of typical images above. (c) radial plot showing maximal peaks.

5.3 Conclusion

In conclusion, classical discontinuous decomposition and discontinuous spinodal decomposition are distinct mechanisms contributing to the formation of lamellar structures in different alloy systems. The example provided by Gorsse et al. (Gorsse 2011). sheds light on the characteristic features of spinodal decomposition. Still, the W-28Cr at% sample displayed unique lamellar behaviour that deviated from the conventional patterns of spinodal decomposition. The ageing experiment on W-28Cr at% has illuminated unique composition wavelength and phase formation aspects. The observed behaviour challenges conventional expectations and points to the potential involvement of Oswald ripening instead of the more commonly studied spinodal decomposition. The second phase adds complexity to the decomposition process and warrants further investigation to gain deeper insights into its origin and influence on the overall system.

- The ageing experiment conducted on W-Cr72 at% has provided fascinating insights into the decomposition process, particularly concerning composition wavelength and phase formation. While prior research (Forouhi and de Fontaine, 1987) suggested that increasing ageing time would lead to an increase in composition wavelength during decomposition, the current experiment showed a significant departure from this expectation, with the measured wavelength from FFT being notably more significant than previous reports.

- In this study, two distinct stages with remarkably different wavelengths were observed. The initial phase, characterized by a larger wavelength, initiated at grain boundaries and gradually expanded into the matrix. Conversely, with a finer wavelength, the second phase emerged approximately 10 hours into the ageing process and consumed the available matrix. Notably, the phase with the larger wavelength exhibited continuous growth. Still, the growth rate differed significantly between the first 10 hours and the subsequent 10 to 100 hours, indicating a potential cessation in development and possible stabilization.

- One limitation of the experiment lies in its relatively short duration, only spanning up to 100 hours. Consequently, uncertainty remains regarding the longer-term behaviour of the wavelength and the more significant phase. Further investigation is needed to ascertain whether these aspects continue to grow, stabilize, or diminish beyond the 100-hour mark.

- The second, finer phase represents a novel finding not previously reported in the literature. The presence of this phase suggests the possibility of decomposition involving two separate phases due to compositional changes in the matrix.

6 Pseudo-in-situ recrystallisation in the Ti-Fe-Mo system

6.1 Introduction

Unpublished results from Dr A Knowles figure(6.1) show that on heat treating and ageing TiFeMo at 750 °C for 72 hours. It undergoes what appears to be a "strain" induced recrystallization (figure 6.1b). One explanation for the "strain" seen in the EBSD image may be due to the misfit seen in bcc Ti to A2 TiFe.

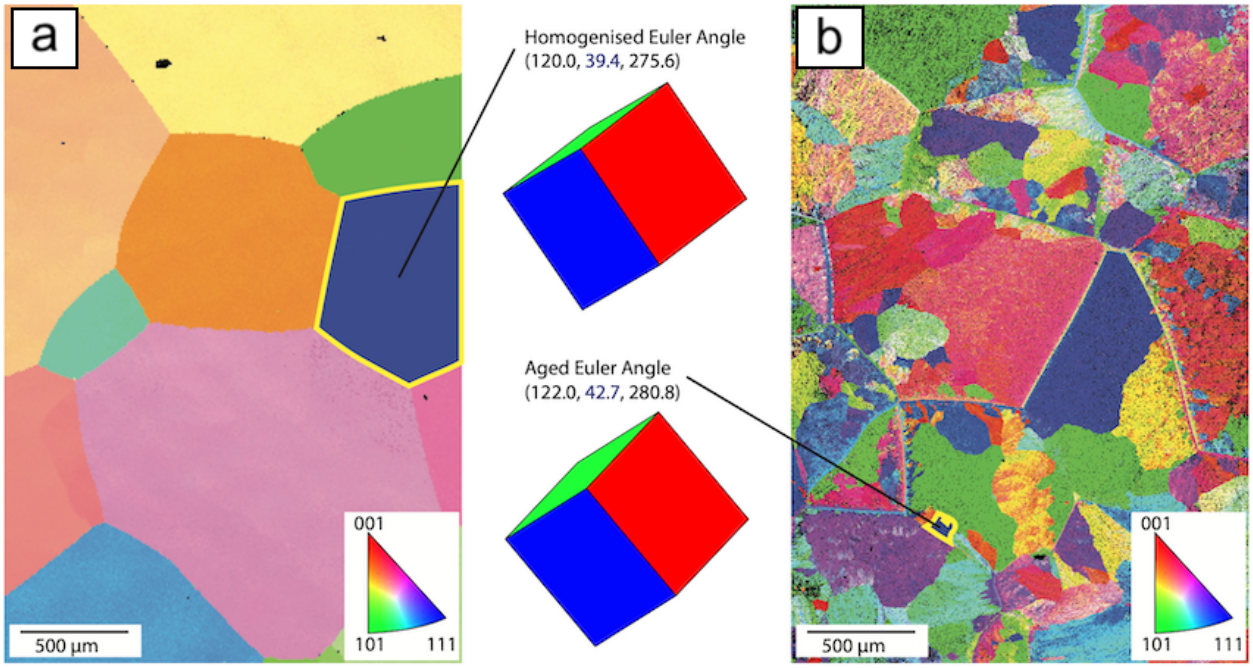

Figure 6.1: **EBSD image of TiFeMo** (a) EBSD analysis of a TiFeMo following homogenized at 1170 °C for 16 hours (b) EBSD analysis of a TiFeMo following ageing at 750 °C for 72 hours. Unpublished research by Dr A Knowles

Following ageing, XRD analysis measurements show the lattice parameters of the B2 and A2 phases to be 2.98 $\pm$ 0.01 Å and 3.18 $\pm$ 0.01 Å (Knowles A 2017). This gives an approximate misfit of -6.1% between the two phases. If this misfit % is compared to that of the traditional (γ)/(γ') superalloy, of approximately $\pm$1% there is a considerable difference in the coherency of the precipitates with the matrix seen in this alloy. These precipitates are approximately 40 nm and of a lamellar structure. The presence of fine particles in an alloy has been extensively shown to not only restrict the movement of grain boundaries

but also prevent dislocation re-arrangement. Both alter the slow nucleation and, therefore, recrystallization of new grains. Closely packed particles have a dual effect; not only do they increase stored energy by creating a complex dislocation network. But also their presence may accelerate recrystallization via a process known as particle-stimulated nucleation. The result depends on particle volume fraction, size, and distribution. As a result of deformation, a strain gradient builds up around the second phase particle. Only when the misorientation is high enough around the particle that it produces a high angle boundary (θ > 10-15°)with the matrix does it nucleate, despite research that has shown that the particle must be >1 μm, it has been reported that a "cluster of particles" could have the same effect. However, it has also been concluded that nucleation would only result if particles were between 1 and 2 μm's. Therefore, the need to improve the understanding of this process is needed.

The aim of this chapter is to track the evolution of this developing structure by "a quasi-in-situ electron backscatter diffraction (EBSD)" (Guan L 2019). Quasi-in-situ EBSD has been used to track the texture evolution of several cold-rolled magnesium samples effectively. It can be used to collect data from an area of 1.4 mm^2, for repeated annealing times from 135s to 68 hours (Zeng ZR 2016). By tracking the evolution of the microstructure the phenomenon behind the recrystallization process observed by Dr Knowles can be eluded.

6.2 Results and Discussion - TiFeMo

6.2.1 Iron iteration

Following the ageing of the Ti-Fe-Mo sample, BSE images were taken to observe precipitate formation. However, the amount of precipitation in the aged sample (and, therefore, the subsequent recrystallization) was limited. ImageJ measured the percentage area covered by the precipitates in 10 20µm^2 BSE images (similar to that shown in figure 6.2c) to be approximately 13.72 $\pm$1.57 %. The Fe content of this sample was measured as 11.64 at.%. This was considerably below that of the expected concentration of approximately 15.4 at.%. Three alloy compositions of 18, 20, and 25 at.% iron where chosen to try

Table 21: **Composition versus Precipitate percentage** Table shows the atomic percentage of elements in the aged Ti-Fe-Mo sample and the relative percentage area covered by precipitates as calculated by imageJ

Atomic percentage		**Precipitate percentage**	**Atomic percentage**		**Precipitate percentage**
Fe	11.64		**Fe**	14.42	
Mo	25.03	**13.72 ±1.57**	**Mo**	24.11	**62.85 ±2.14**
Ti	62.58		**Ti**	61.47	
Atomic percentage		**Precipitate percentage**	**Atomic percentage**		**Precipitate percentage**
Fe	18.38		**Fe**	19.23	
Mo	15.76	**86.94 ±3.28**	**Mo**	19.17	**88.61 ±1.83**
Ti	65.26		**Ti**	61.60	

and improve the final composition. Following their manufacture, the samples were homogenized and aged. BSE and ImageJ measured the percentage area covered by the precipitate. The final composition of the alloys and the precipitate percentage area covered by the precipitate are shown in table 21. Following this observation, the alloy used to observe the recrystallization process was manufactured with a starting iron at.% of 25%.

6.2.2 The Ti-Fe-Mo alloy

As cast Ti-Fe-Mo (figure 6.2a) shows the classic dendritic tree-like structure observed from the cooling of molten metals. XRD analysis of the as-cast Ti-Fe-Mo sample (table 45) shows the presence of two phases, A2 and B2. EDX analysis of the as-cast alloy (figure 6.3) confirms the presence of two separate phases; one rich in molybdenum and the other rich in titanium and iron. The lattice parameters of the two phases were 3.167±0.002 and 3.324±0.002, respectively. A single peak at 42.71° can also be seen, suggesting the presence of an omega phase (Knowles A 2016).

Figure 6.2b is a BSE micrograph of the alloy following homogenization at 1170 °C for 16 hours. The image shows the presence of a two-phase structure of lighter tungsten-rich regions and the second a much darker titanium-iron-rich region. This suggests that at this homogenizing temperature, a two-phase region exists (Dodds R 2018). The presence of a two-phase microstructure is confirmed by EDX analysis (figure 6.3). EDX does show the

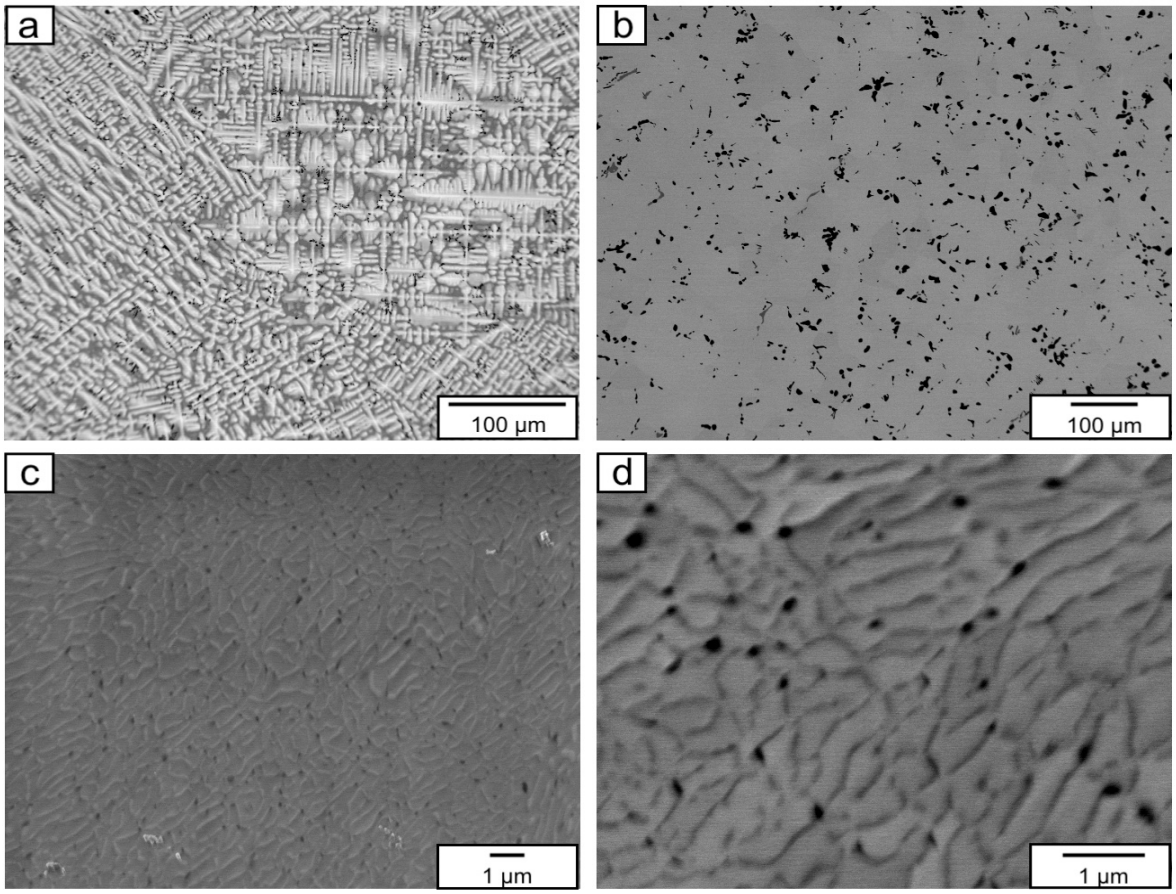

Figure 6.2: **SEM BSE images of Ti-Fe-Mo** At (a) as cast, (b) homogenized 1170 °C and (c and d) low and high magnification images after 72h ageing at 750 °C

presence of a third phase Omega which is not observed in any of the SEM images taken. After heat treatment and ageing of the sample at 750 °C for 72 hours, a fine lamellar structure of approximately 36 $\pm$ 1.2 nm in width.

Grain size has significantly reduced in the aged sample with almost a 9-fold (8.85) reduction in the average grain size (figure 6.4). This is also confirmed by the Aspect and PARIS ratio, which all demonstrate the presence of much smaller grains in the aged sample. The high proportion of HAGBs, from the EBSD data, identifies that a recrystallization event is occurring.

EBSD can be used to determine the level of plastic deformation. As a result of slip from deformation, grains develop with different orientations. This produces subdivision and grain fragmentation, which can be viewed in situ analysis with EBSD (Yvell K 2018), where these appear as a mosaic of colours within an individual grain. EBSD analysis of

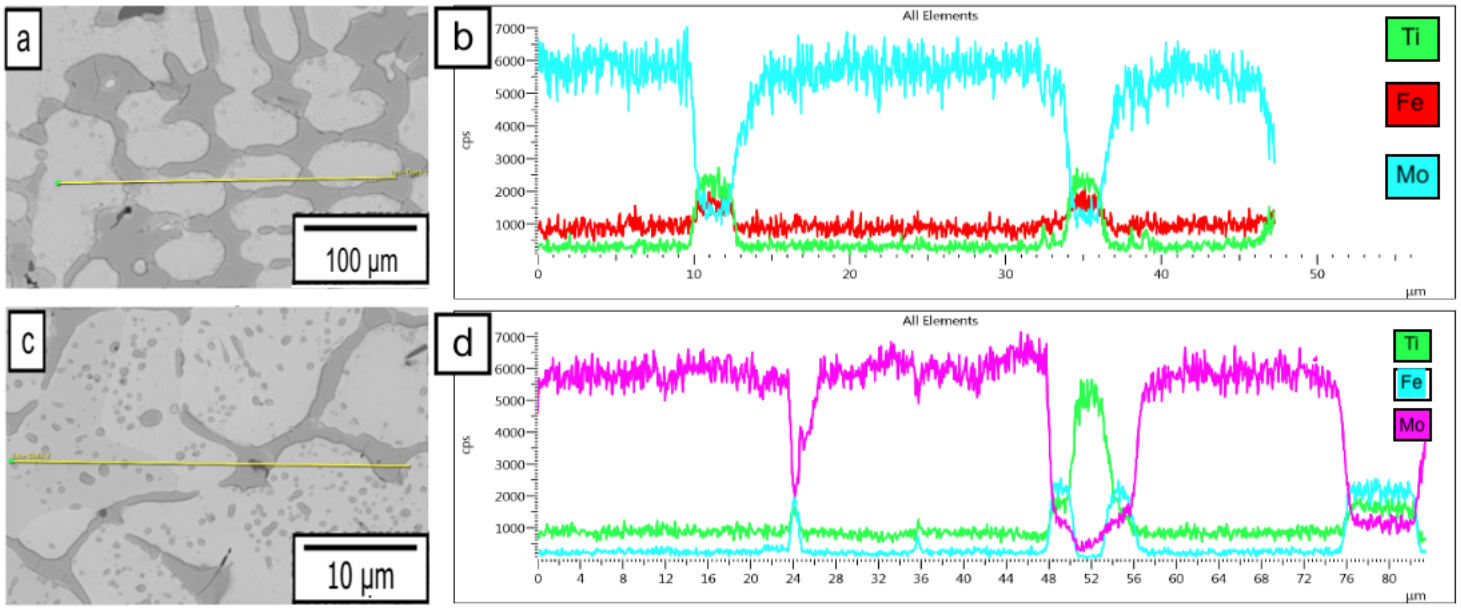

Figure 6.3: **SEM image and EDX analysis of as cast and homogenized Ti-Fe-Mo** (a) Ti-Fe-Mo in the as-cast condition and (b) corresponding line profile (yellow line in (a)). (c) Ti-Fe-Mo following homogenization at 1170 °C for 16 hours and (d) corresponding line profile (yellow line in (c)

.

Table 22: **EBSD analysis of Ti-Fe-Mo** Grain data obtained for Ti-Fe-Mo from EBSD analysis at different heating and ageing conditions

State		Grain Size (μm^2)	GOS (°)	KAM	Aspect Ratio	PARIS (%)	LAGB/HAGB (%)
Homog.	Max	1.98x10^5	4.99	0.08	20.50	1649.8	16.67 / 83.33
	Avg	664.12	0.07	5.38x10^{-4}	1.77	45.84	
Homog. Aged	Max	252.63	16.99	16.35	11.07	157.14	8.95 / 91.05
	Avg	29.56	2.08	0.86	1.88	26.23	

the homogenized alloy is shown in figure 6.5. The grain characteristics obtained from the EBSD are shown in table 22. Using this analysis, KAM, GOS, and grain misorientation line profile of the most prominent grain are presented in figures 6.5b, 6.5c and 6.5e respectively. Both the GOS and KAM data presented in table 22 show grains with relatively minor plastic deformation and low levels of dislocations. This is confirmed by the line profile, which shows the misorientation across the most prominent grain to be a maximum of 3° (figure 6.5f).

When the homogenized sample is aged at 750 °C for 72h and analyzed using EBSD (figure 6.6), the resulting map shows plastic deformation in most of the grains sampled. The high degree of plastic deformation is also confirmed by the KAM and GOS data presented in table 22 and figure 6.7. A GND map (figure 6.6) produced from the EBSD data also shows grains with a high density of dislocations, confirming the extent of deformation in the aged sample.

A high-resolution EBSD map of single grain in the aged Ti-Fe-Mo sample is shown in figure 6.8 along with GOS, KAM, and line misorientation plot. The misorientation plot shows regions within the grain having a difference of up to 48 ° demonstrating a high degree of subdivision and grain fragmentation in a single grain. One explanation for the difference in the level of deformation in the homogenized as compared to the aged sample is the formation of the TiFe (β') precipitate seen in the BSE images (figure 6.2 and XRD analysis (figure 6.9).

BSE images of 24-hour interrupted Pseudo in situ recrystallization observations of Ti-Fe-Mo samples aged at 750 °C for a total of 72 hours are shown in figure 6.10(a).

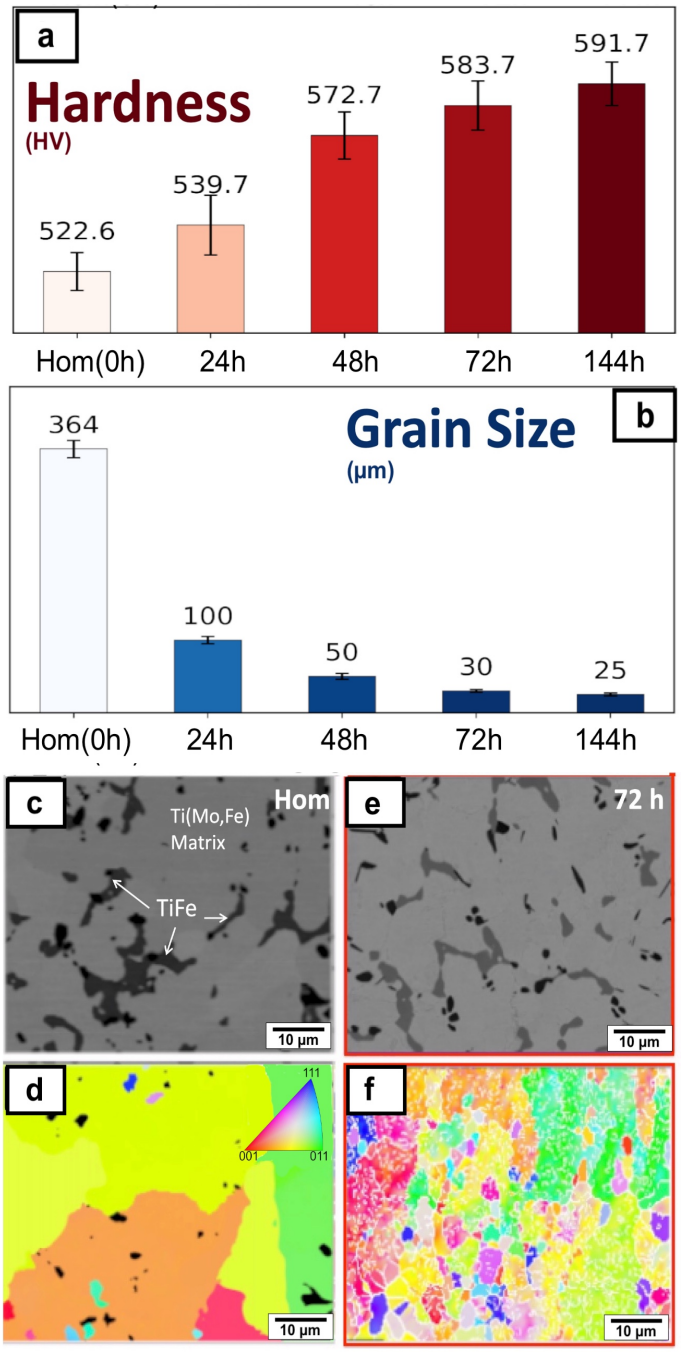

Figure 6.4: **Recrystallisation of Ti-Fe-Mo.** Grain refinement in Ti-Fe-Mo by ageing without external strain. (a) Grain size evolution as a function of the ageing time as measured for all phases in the alloy. (b) Hardness changes as a function of ageing time. (c) BSE image with (d) EBSD IPF-x map showing the general microstructure of the alloy after homogenization at 1170 °C. (e) BSE image with (f) EBSD IPF-x maps after ageing at 750 °C for 72h.

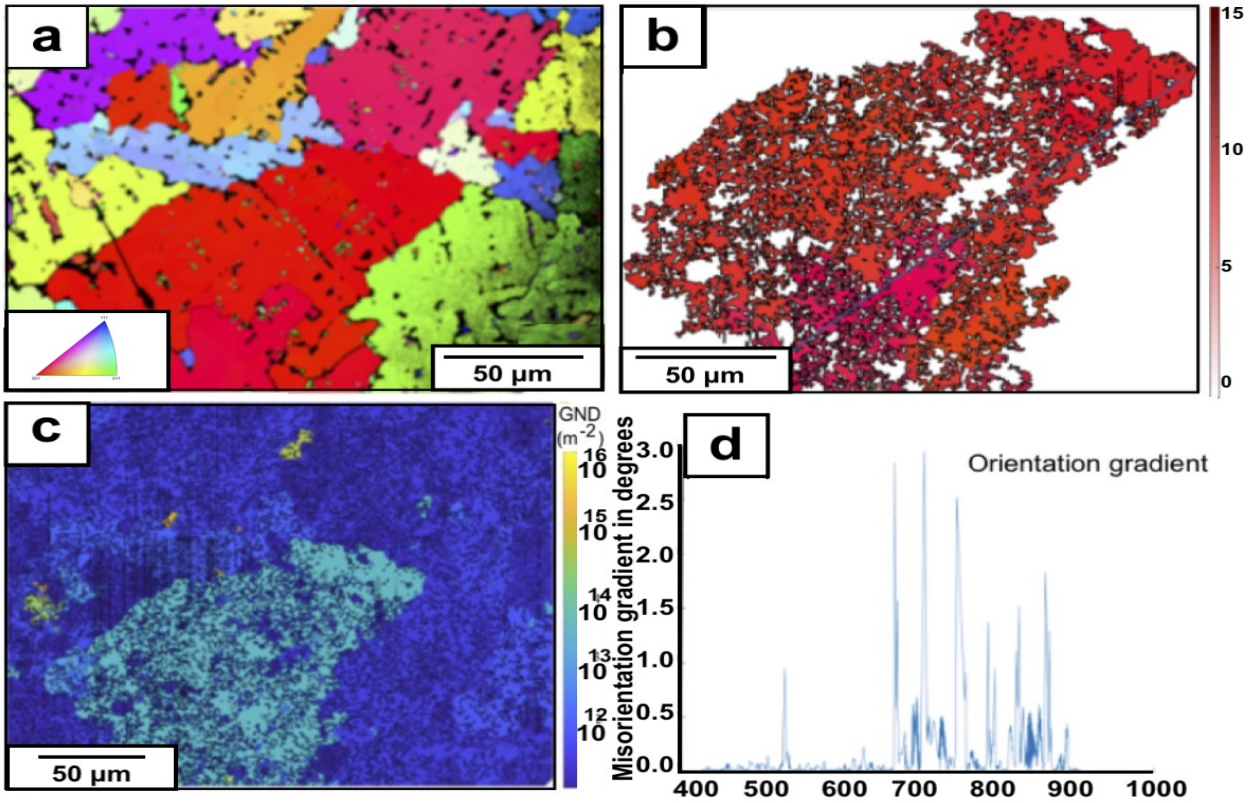

Figure 6.5: **EBSD analysis of typical grains observed for Ti-Fe-Mo after homogenization at 1170 °C for 16 hours.** (a) IPF map (b) KAM, (c) GOS, (d) misorientation profile of a typical homogenised grain

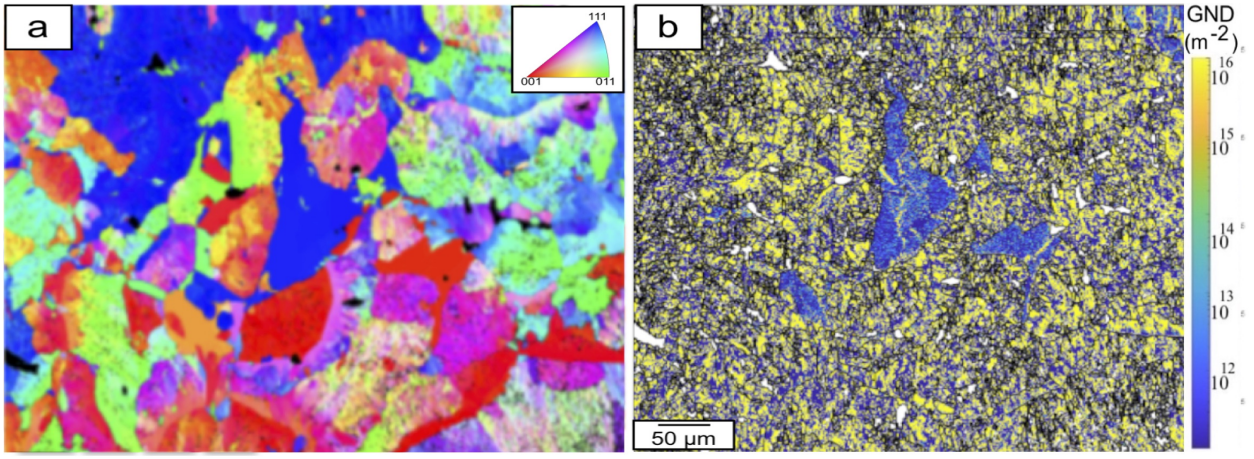

Figure 6.6: **EBSD analysis of typical grains observed for Ti-Fe-Mo after ageing at 750 °C for 72 hours.** (a) IPF map and (b) corresponding GND map of Ti-Fe-Mo aged for 72h aged at 750 °C

An area (marked by a blue circle) was observed under higher magnification (as seen in figure 6.10(b). Over the 72h ageing time, nano-sized precipitates are seen to grow from the pre-existing B2 phase. As the ageing time progresses, the area of the image covered is increased. Demonstrating a gradual growth of the precipitate into the matrix.

BSE images of typical grain boundary morphology at 24h, 48 hours, and 72h ageing are shown in figures 6.10(c),(d), and (e), respectively. At 48h of ageing, SEM observation of grain boundaries showed tiny, almost spherical precipitates of TiFe of less than 100 nm in diameter (figure 6.10(c)) (Lee 2017). In addition to the fine precipitates at the grain boundaries, further precipitates grow from the significant B2 phases in the matrix. Previously TiFe precipitates have been shown to nucleate within the grain matrix; however, no preferential nucleation sites were observed. Therefore, the precipitation of a fine lamellar TiFe precipitate mainly occurs at defects in the microstructure, such as grain boundaries and interphase boundaries which act as nucleation sites (Sharma G 1999, Dong R 2018). At 24 hours, the grain boundary precipitates appear round in shape. However, those precipitates inside the grains as the B2 phase appear to be finer and more lamellar in structure. Following a further 24h of ageing, lamellar precipitate forms from the grain boundaries containing spherical precipitates at 24h of ageing. In figure 6.10d, a grain boundary can be seen, which is both populated with the prior spherical precipitates from which a finer lamellar precipitate is growing in the grain matrix. The lower figure shows lamellar precipitates contacting both the grain boundaries and the B2 phase within the matrix. Suggesting it takes less energy for the precipitate to grow towards the B2 phase from the grain boundary or vice versa than to grow into the matrix. After 24h, the precipitates form waves that now span several grains. One such wavefront is shown in figure 6.10e, a magnified area marked by the blue box is displayed with the lamellar precipitates growing over the prior grains. Further BSE images show precipitates forming as 'islands' ahead of the progressing precipitate front. Unlike earlier images, these precipitate 'islands' do need grain boundaries or the B2 phase to grow. To further the understanding of the precipitates, EBSD was conducted on the area shown in figure 6.10(a,

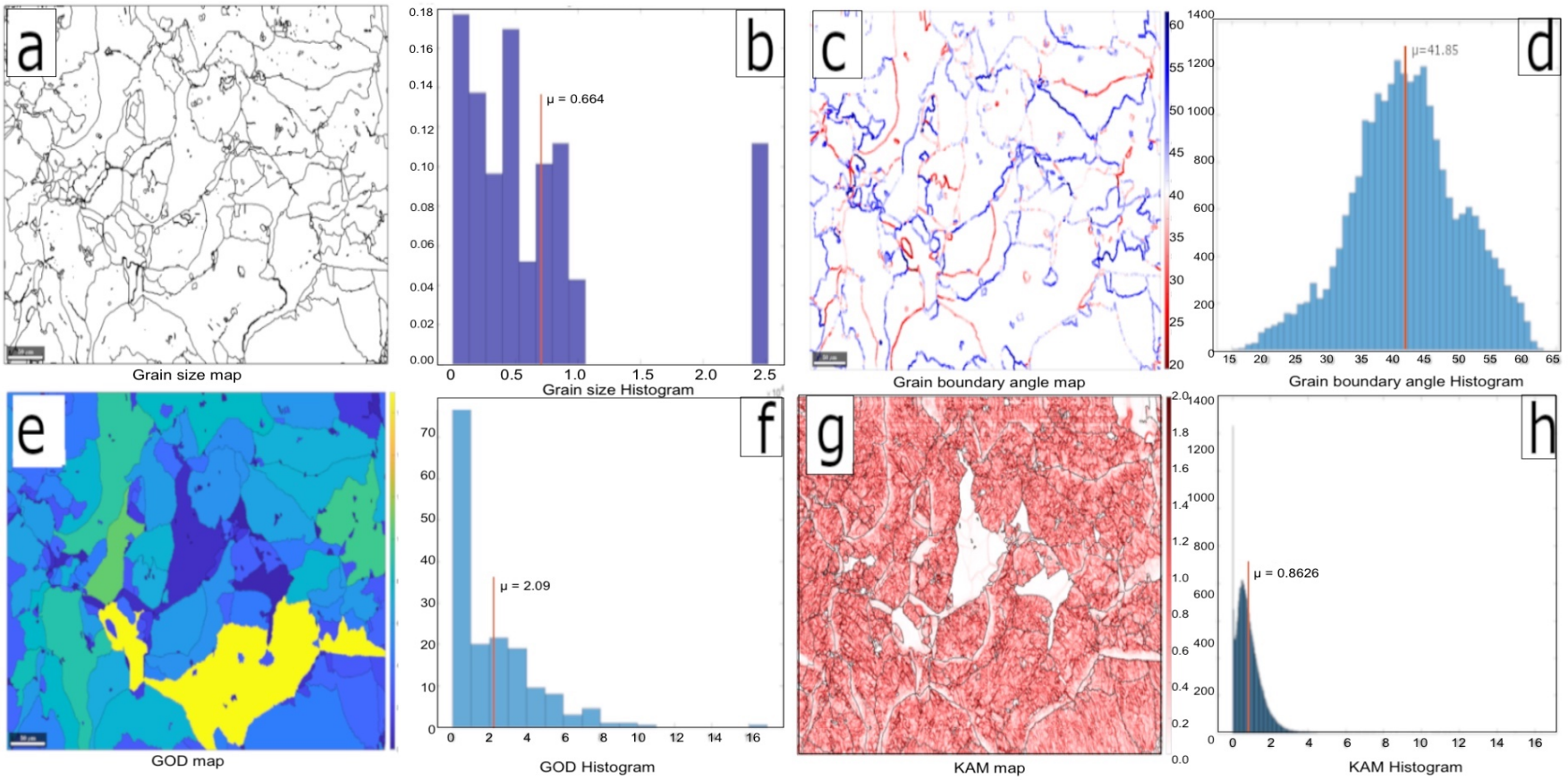

Figure 6.7: **EBSD analysis of the data presented in figure 6.6 to determine the level of deformation in a typical aged sample** of the homogenised alloy. (a and b) Grain size area map and histogram. (c and d) Misorientation grain boundary map and histogram. (e and f) GOS map and histogram. (g and h) KAM map and histogram.

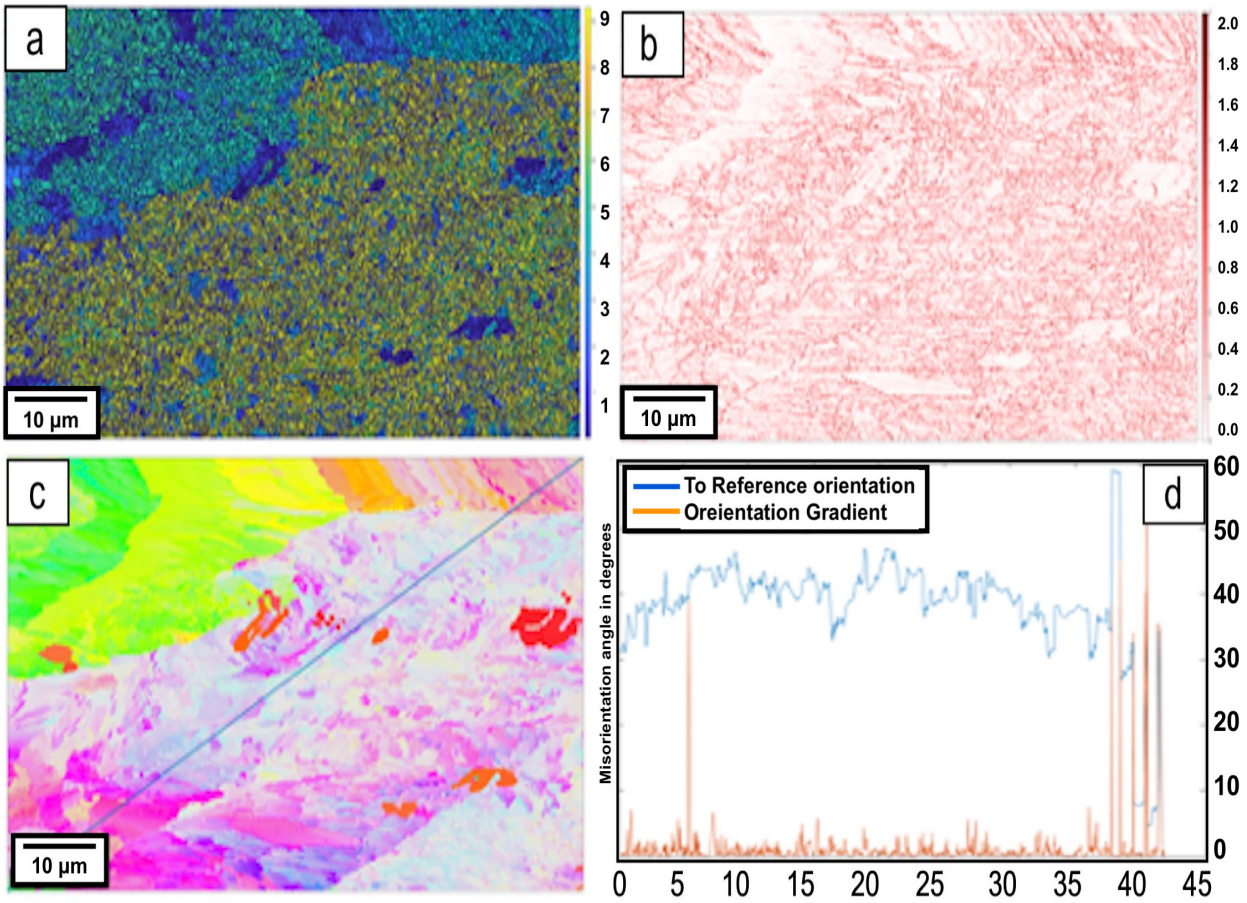

Figure 6.8: **High-resolution EBSD map of single grain in Ti-Fe-Mo sample aged for 72 hours at 750 °C.** (a) GOS, (b) KAM (c) IPF colour map (d) Grain orientation profile of line plotted in (c).

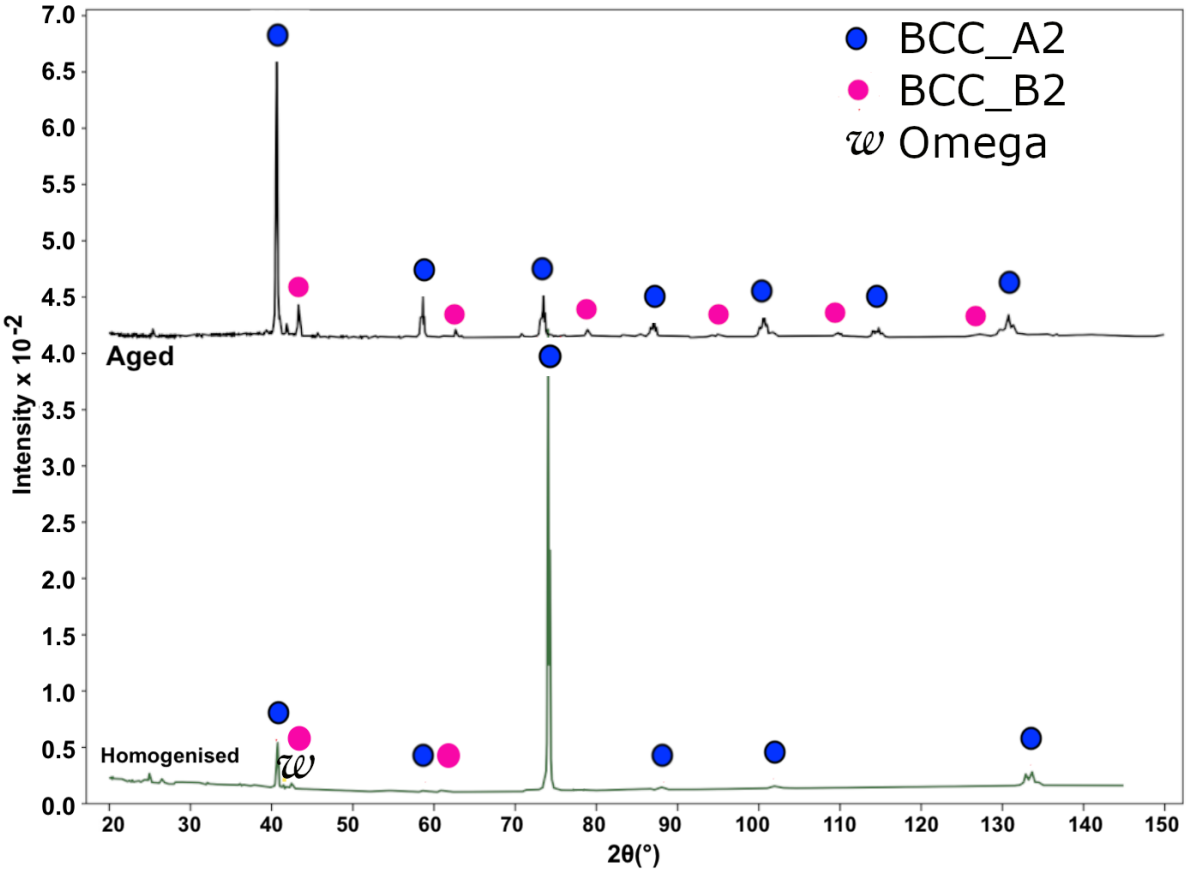

Figure 6.9: **XRD analysis of solution treated and Ti-Fe-Mo aged 72 hours at 750 °C.** Identified phases found in both homogenized and aged samples by XRD, a key is shown top righthand for clarification (CuKα)

b, and c). IPF Y map, as well as GOS, KAM, and misorientation plots, are shown. The KAM and GOS maps demonstrate the presence of highly plastically deformed lamellar structures with high misorientation profiles with the prior grain structure (which appear devoid of any deformation, as shown by their lower KAM and GOS profiles). Figure 6.13a shows a BSE image of a small area after homogenization along with its accompanying EBSD (figure 6.13c). The same area is shown in 6.13b and d following 72h of ageing. The EBSD image of the same area clearly shows highly deformed grains (as evidenced by the change in colour over a single grain). Additionally, several new grains are seen in the aged sample developed from the parent grains in figure c. A magnified image of the area in the blue box is also shown. Visible are the lamellar precipitates identified early. If figure 6.13b is carefully examined, the points at which the different precipitates meet the colony front. This is where the new grain boundaries are seen in the EBSD image at 72h. Grain size histograms are presented for the homogenized and aged samples. As can be seen, the grains in the homogenized sample are much larger than those of the aged sample.

Table 23 shows the Vickers hardness HV of the alloy following different heating treatments. The initial material in the as-cast condition had an HV of 549.9 $\pm$7.8. Which reduced to 522.6 $\pm$7.5 on homogenizing. However, ageing the sample for 72h increased to 583.7 $\pm$9.0. However, unlike other reports in the literature ((Choe HJ 2018)), ageing the sample for an extended period (144h). The hardness did not rapidly reduce. Instead, it increased (although slightly) to 591.7 $\pm$7.6.

BSE images of the precipitate structure at 144h are shown in figures 6.11a and b. When these images are compared to that of the 72h ageing treatment, the low mag image 6.11a (as compared to figure 6.2c) clearly shows a greater density of precipitates. It also shows that the size of the precipitates has increased as they are more visible at 144h despite similar magnifications. Ten separate high mag (x16,000) images of the 72h and 144h ageing were analyzed via threshold maps in ImageJ. The results showed that the area covered by the TiFe precipitates in the 72h was 19.05 $\pm$ 0.25 % compared to

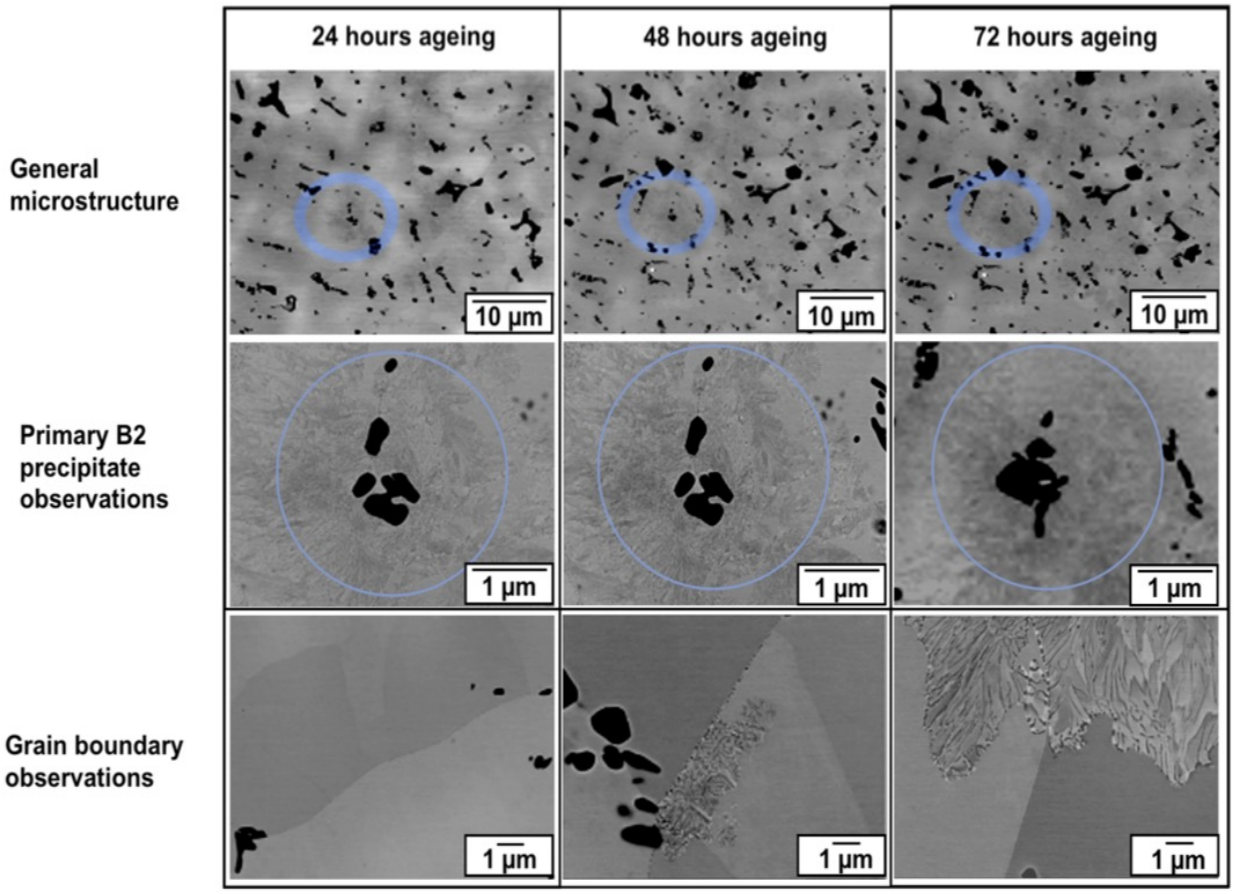

Figure 6.10: **Pseudo in situ recrystallization of Ti-Fe-Mo SEM BSE** Pseudo in-situ observations of the colony growth. General microstructure of a specific area in Ti-Fe-Mo aged for (Column 1) 24 hours, (Column 2) 48 hours, and (Column 3) 72 hours showing the colony growth. The blue circle shows a typical primary B2-TiFe precipitate development over a 72-hour heat treatment. BSE images of grain boundary morphology are shown over the same period to elucidate the growth of colonies further.

Table 23: **Vicker's hardness values of Ti-Fe-Mo** Hardness measurements for Ti-Fe-Mo under different heat treatments

Ti-Fe-Mo	Hardness Measurements (2Kg)					Average Measurement
As Cast	569.0	539.5	555.7	552.1	546.4	**549.9 ± 7.8**
	549.1	547.4	545.8	542.7	551.7	
Homogenised	505.2	529.7	520.9	515.6	532.4	**522.6 ±7.5**
	521.6	527.6	524.8	520.6	527.5	
Homogenised and 24h aged	530.1	551.8	537.6	542.7	593.4	**539.6 ±10.8**
	540.4	538.7	548.9	542.7	514.7	
Homogenised and 72h aged	566.8	575.8	584.4	596.4	593.4	**583.7 ±9.0**
	570.4	587.6	592.3	582.0	587.4	
Homogenised and 144h aged	581.9	604.0	592.2	577.4	591.0	**591.7 ±7.6**
	589.4	595.8	600.9	595.5	588.6	

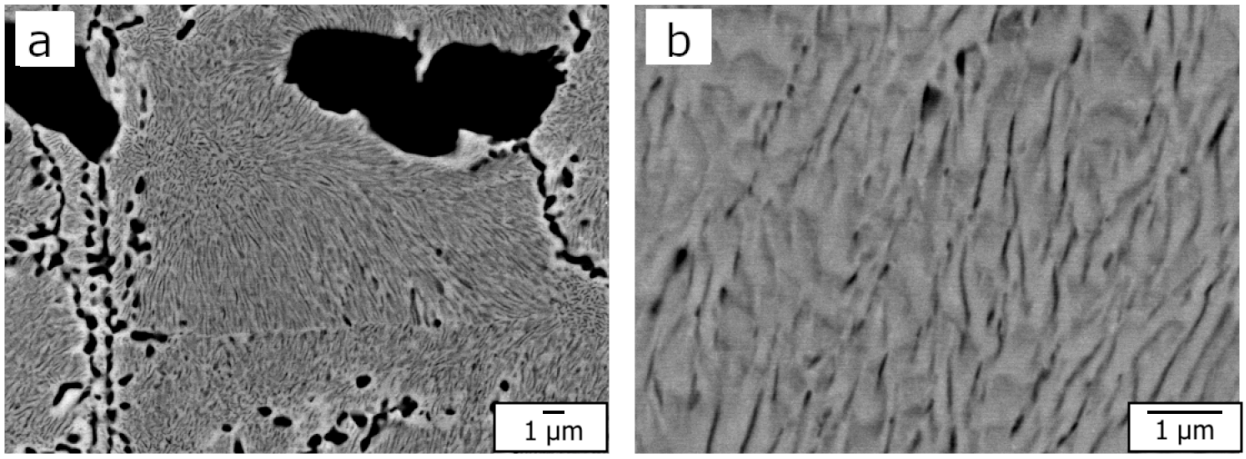

Figure 6.11: **BSE images of precipitate structures** (a) low and (b) high magnification of Ti-Fe-Mo following ageing at 750 °C for 144hs.

144h, which was 31.48 $\pm$ 0.38 %.

To track the apparent grain refinement during ageing, Fig. 6.13(a-d) presents the "quasi in-situ" evolution of microstructure and texture in a specific region. After ageing for 72 hours, while the parent grain can be identified, its orientation has changed. Several new grains have formed, and a strong misorientation exists within all grains, as evidenced by the change in colour and orientation over a single grain. Further observations in Fig 6.12 revealed a heterogeneous precipitation of colonies and their growth from prior grain boundaries or macroscopic TiFe grains.

When the XRD patterns are considered from earlier Fig. 6.9 reveals that the homogenized sample has a mostly A2 structure, except for a small peak at 42.5° attributed to the ω phase (Dodds R 2018). After the 72 hour ageing, the microstructure is dominated by lamellar precipitates (Fig. 6.13(e)), and XRD analysis shows two sets of peaks, one related to the A2 matrix seen in the solution heat-treated sample and a separate set from the B2 precipitates (Fig. 6.13(f)). The lattice parameters of the A2 structure were measured to be 3.141 $\pm$ 0.002 Å in the homogenised sample and 3.150 $\pm$ 0.001 Å in the aged sample. The lattice parameters of the B2 precipitates in the aged sample is 2.980 $\pm$ 0.086 Å . Using equation 36, the lattice misfit in the aged sample is -5.4 %.

$$\delta = (a_{precipitate} - a_{matrix})/a_{matrix} \tag{36}$$

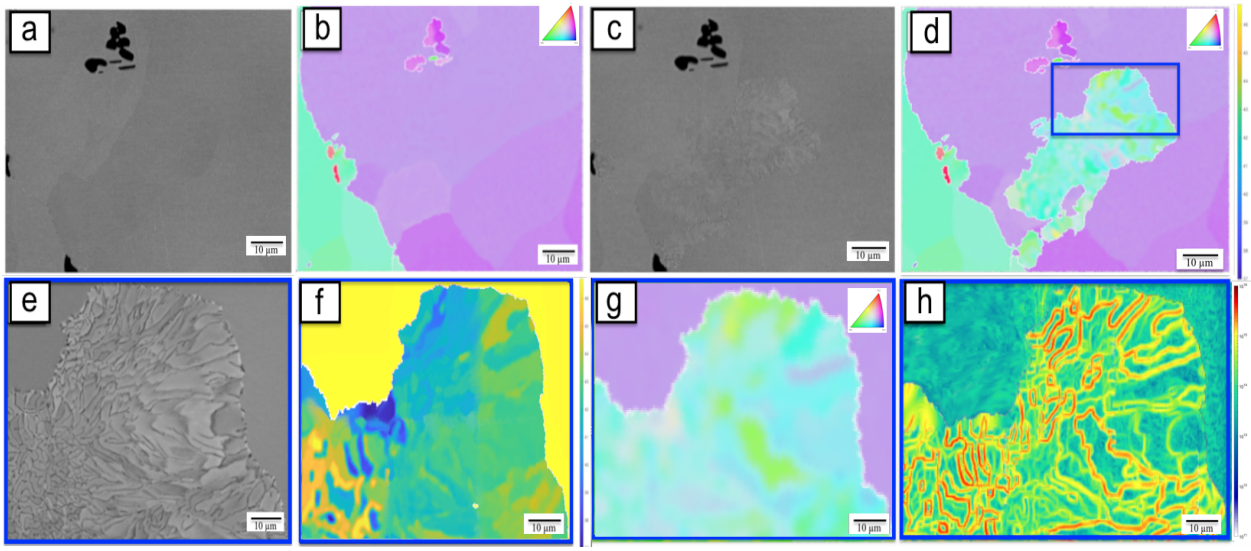

Figure 6.12: **Precipitation of Ti-Fe-Mo at 24 hours**. Comparison of a pseudo-in-situ grain boundary in the homogenized and aged at 750 °C for 24hs conditions. (a) BSE and (b) IPF map of grain boundary in homogenized condition, (c) BSE and (d) IPF map of grain boundary in aged at 750 °C for 24hs condition. (e) BSE (f) IPF, (g) Misorientation, and (h) GND Maps of the zoomed-in area of precipitate as shown by the blue box in (d).

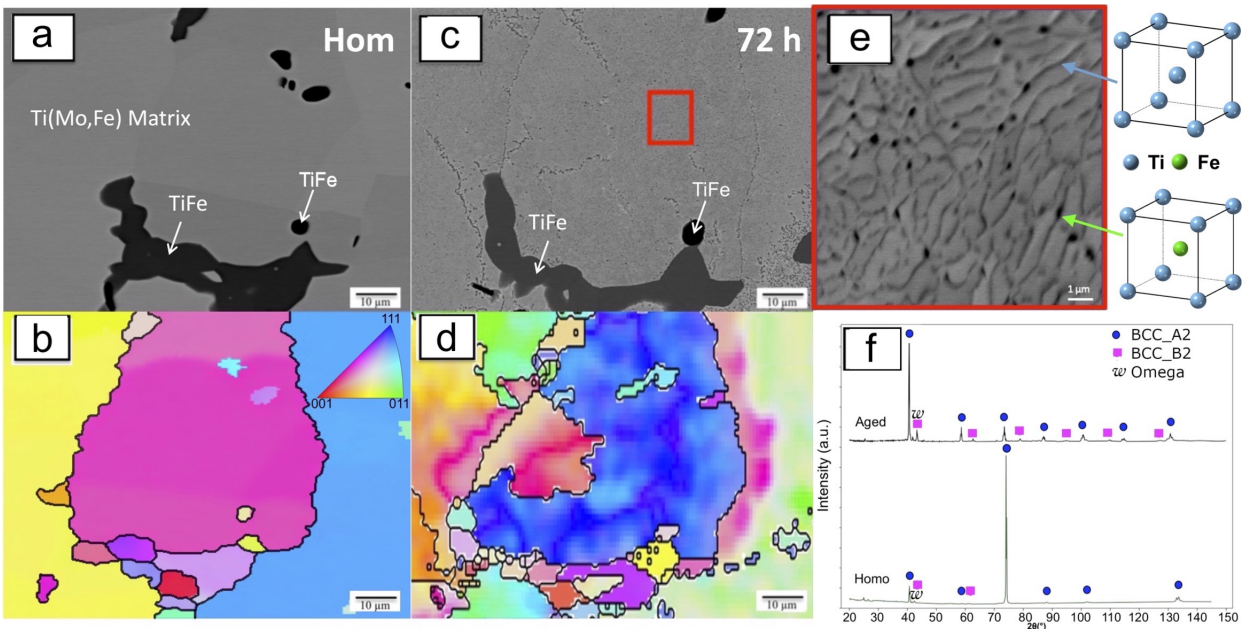

Figure 6.13: **Pseudo in-situ recrystallisation of Ti-Fe-Mo**. (a) and (b) BSE image and EBSD IPF map of the same area after homogenization at 1170 °C (c) BSE image and (d) EBSD IPF maps of (a) and (b) after ageing for 72h at 750 °C. (e) High magnification BSE of the area marked by the red square in (c) showing TiFe B2 precipitates, (f) XRD of homogenised and aged for 72h at 750 °C samples.

This misfit is consistent with the value in the Ti-Fe binary system (Murray 1981). Such a misfit value suggests that precipitates are unlikely to be fully coherent with the matrix, as a cohesive precipitate should have a misfit preferably lower than 0.1 % (Ghosh G 2007). Therefore, a complex semi-coherent interfacial dislocation network could accommodate the lattice misfit and induce a considerable misfit strain at the interface. The presence of strain may accelerate recrystallization via a process known as particle-stimulated nucleation, of which the result is dependent on particle volume fraction, size, and distribution (Humphreys FJ Pergamon UK). It is suggested that, due to the lattice misfit, a strain gradient builds up around the second-phase particles and induces recrystallization (grain refinement). It is thus necessary to investigate the precipitate growth process to improve the understanding of the correlation between precipitation and recrystallization.

The microstructure in a sample aged for an intermediate time (24 h) is shown in Fig. 6.15(a), whereby a precipitate colony is growing into the matrix. Before ageing, there was only a matrix with similar orientated grains as seen in the unconsumed matrix (area outside the colonies in Fig. 6.15(a)). Three phases are observed inside these colonies, as shown in Fig. 6.15(b,c). One is the colony phase rich in (Ti, Mo). The other two are lamella-like colony precipitates: one is rich in (Ti, Fe) and one is rich in Ti. The SEM image analysis based on the backscattering electron contrast grey value in Fig. 6.15(b,c) results in about 13$\pm$2% (Ti, Fe) phase and lower than 2% Ti-rich phase. The IPF map in Fig. 6.15(d) shows a different orientation of the growing precipitate colony from the matrix. Across both precipitate colonies, orientation changes suggest a high strain level within the colonies. To further investigate the level of strain and deformation within the precipitate, high resolution (HR)-EBSD was conducted to measure geometrically necessary dislocations (GND) and strain. Following the acquisition of EBSD patterns, strain and GND maps were determined using the CrossCourt software (Karamched 2011, Zhang 2017) and presented in Fig. 6.15(e). There are large regions of the colony front with values of GND exceeding 1x10^{16} m^{-2} (as indicated by the areas coloured in bright yellow) with the average GND measured to be 2.3x10^{14} m^{-2}.

The areas showing the greatest density of dislocations are located at the interface between the matrix and the growing colony, which is the recrystallization front. In addition, a high level of GND density is also observed at the interface between the colonies. The misorientation between these two colonies 'grains' was measured to be a minimum of 45°, suggesting a high-angle grain boundary. A strain map for ϵ_{11} in Fig. 6.15(d) and strain maps for all directions are shown in Fig. 6.14) shows a high level of strain at the interface of precipitate-matrix and precipitate-precipitates, consistent with the dislocation density mapping. It is worth noting that high dislocation density and strain are detected at the lamella-lamella interfaces within the precipitate colony. Stresses associated with the strain field levels around these interfaces due to precipitation can be as high as 1 GPa, which could be an additional driving force for the grain boundary movement leading to the recrystallization.

This complex precipitation was further investigated using TEM. A TEM sample was lifted out from the region in Fig. 6.15(a). Fig. 6.16(a) shows the STEM/EDS mapping. In the colonies, sub-grains rich in (Ti and Mo) are observed with twisted lamellar or rod-like precipitates at the boundaries of sub-grains. Consistent with the SEM observation in Fig. 6.15(b), two types of lamellar precipitates, TiFe-based and Ti-rich phases, are detected. Fig. 6.16(e-g) show the selected area diffraction (SAD) patterns on the different phases to identify their structure. In Fig. 6.16(e), the (Ti, Mo)-rich matrix within the colony is evidenced to have a β A2 structure. At the same time, the TiFe precipitates have a β' B2 structure with a slight rotation 1.1° to the A2 matrix and with a misfit of $\sim$ -6% consistent with the XRD results. The Ti-rich precipitates are indexed as αTi with an HCP structure. The diffraction patterns in Fig. 6.16g show that $(0001)_\alpha \parallel (011)_\beta$ and $[11\bar{2}0]_\alpha \parallel [1\bar{1}1]_\beta$. This is a typical Burgers orientation relationship between α and β of (Burgers 1934). Other weak spots close to the αTi spots could be related to the doubled diffraction (Williams et al. 1996, Knowles et al. 2021).

Fig. 6.17(a,b) present a STEM bright field image showing the overall view of the cross-section compromising a matrix region and two precipitate colonies with the misorientation

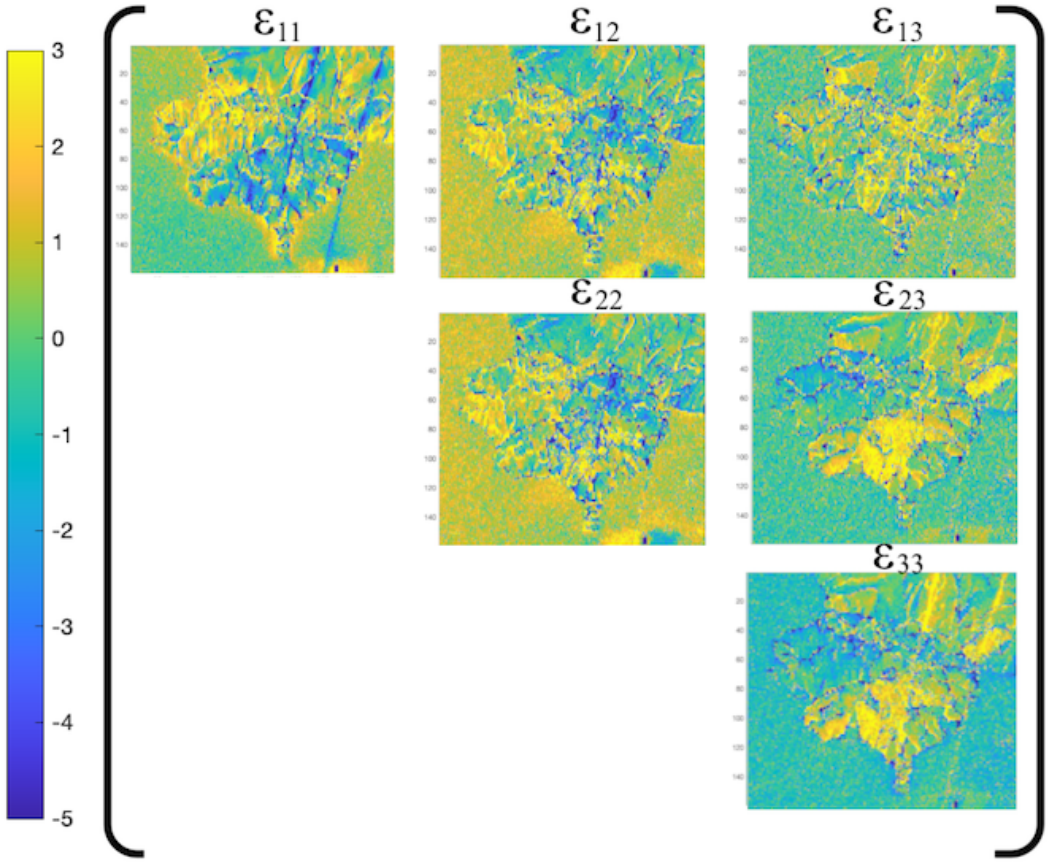

Figure 6.14: **Strain maps** Strain maps showing the degree of strain observed in the precipitate analyzed by HREBSD as shown in figure 6.15

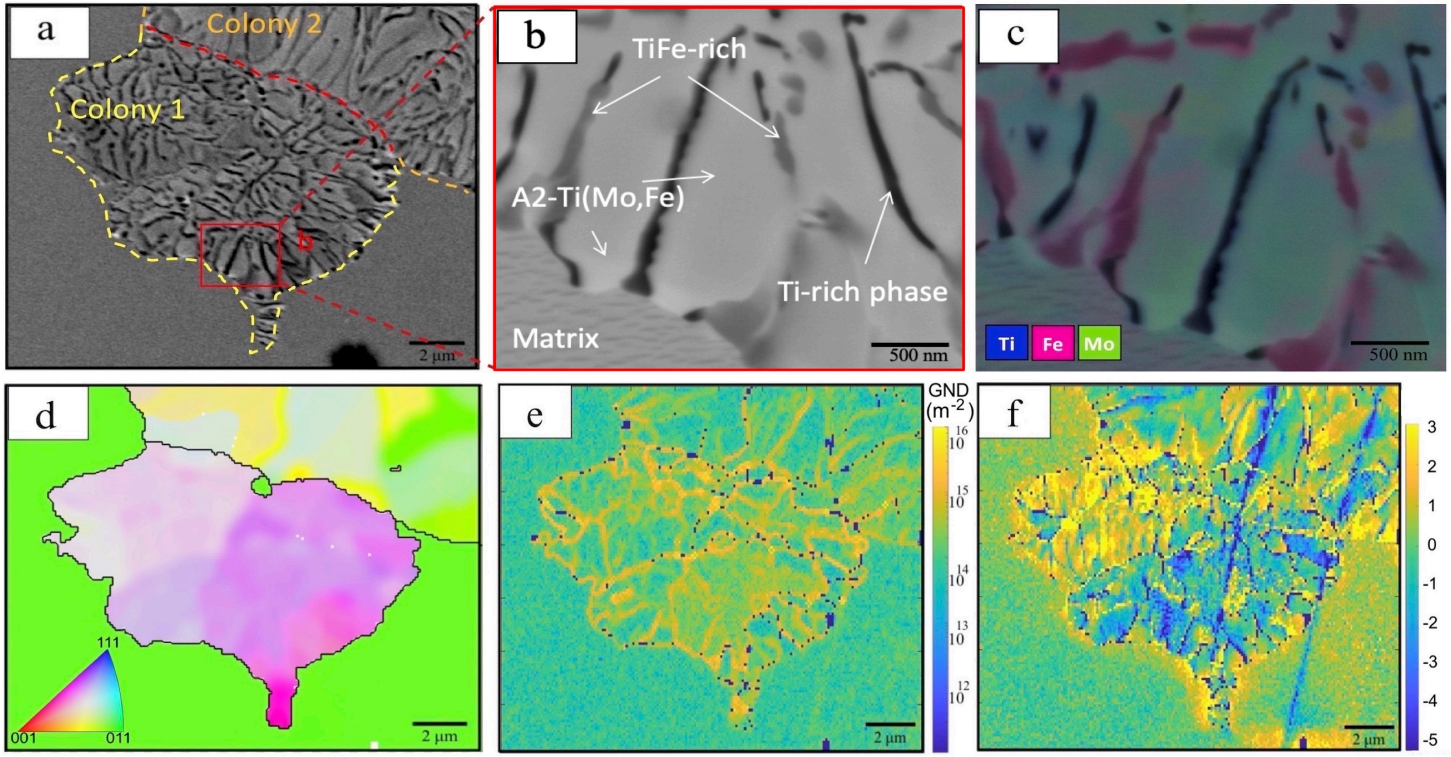

Figure 6.15: **Microstructure of typical colonies in a Ti-Fe-Mo alloy aged at 750 °C for an intermediate ageing time 24 hours** (a) SEM back-scattering electron image showing the matrix-colonies microstructure. The yellow and orange dashed lines indicate matrix-colony boundaries; the colony-colony boundary is the red dashed line. (b) A zoomed-in observation in a colony with (c) element mapping by SEM/EDS showing precipitates inside the colony. EBSD characterization in the same area as (a) showing the misorientation by (d) the IPF-X map and dislocation density by (e) GND map and internal strain by (f) ϵ_{11} strain map. The colour scale shows log(GND density in dislocations m^{-2}) in (e) and strain in GPa in (f). (Images b and c taken by Dr Kan Ma, University of Birmingham.)

of the matrix and sub-grains of colonies. The misorientation between the matrix and colonies varies from 7° to 33°. The sub-grains (2 to 3 in Fig. 6.17(a) and 1 to 2 in Fig. 6.14(a)) have misorientation angles of 30° and 17°. At 24 hours, a clear phase separation can be seen within the growing colony. As shown in Fig. 6.16(a), regions of A2 - Ti(Mo, Fe) are separated by B2-TiFe-rich precipitates. The misorientation between subgrains 1 and 2 have been verified at three different tilts angles (Fig. 6.18), which show similar values around 17° suggesting the B2-TiFe-rich precipitate acts as a means to pin the growing A2 - Ti(Mo, Fe) phase. Most grain boundaries are, therefore, HABs, and within the precipitates, the HABs are accommodated by the lamellar precipitates. A STEM bright field (BF) image in Fig. 6.16(h) shows a high density of interfacial dislocation network at the sub-precipitate interfaces. Close to these precipitates, dislocations in the precipitate sub-grains are frequently observed, suggesting that these precipitates with highly strained interfaces induce a high-level deformation of the precipitate. Outside the advancing colonies, a large number of plate-like nano-scale precipitates were observed in the matrix as shown in the bottom left-hand corner of Fig. 6.15(b) and bottom right-hand of Fig. 6.16(a). They have widths of approximately $\sim$ 10 nm and length $\sim$ 100 nm and are homogeneously distributed within the matrix. A HAADF-STEM image of the matrix precipitates is shown in Fig. 6.17(c). TEM analysis using SAD, dark-filed imaging, and STEM/EDS in Fig. 6.17(d-h) suggests that these fine precipitates are β' B2-TiFe. The orientation relationship between the matrix and the precipitates is <100>$_{\beta'}$||<100>$_{\beta}$, $\{100\}_{\beta'} \parallel \{100\}_{\beta}$. Based on the SAD patterns and the precipitate morphology, these precipitates grow preferentially on the 011 planes. These B2 precipitates should induce another source of strengthening on the matrix. Unlike the precipitates seen in the colonies, those observed in the matrix have a particular orientation. This adds credence to the idea of a high incoherency of the precipitate with the grain boundary front. In addition, the formation of αTi precipitate may be related to oxygen impurity, but their role in the recrystallization needs further investigation.

The new colonies and sub-grain boundaries reduce the overall grain size. For grains

at this scale (>100 nm), the reduction of grain size will not only increase tensile strength but will also improve ductility based on the Hall-Petch strengthening (Morris DG 2011). Reducing the overall grain size should lead to more grains with aligned slip planes for dislocations to progress from one grain to the next (Larrouy B 2015), leading to better dislocation motility in a strained alloy. Here we have shown a way to improve the strength of material through the precipitation of a TiFe precipitate. The increase in hardness in this alloy is directly related to the growth of the TiFe colonies as the colony migrates from the previous grain boundaries; the growing precipitates behind the colony front drive recrystallization and the development of fresh new grains behind it.

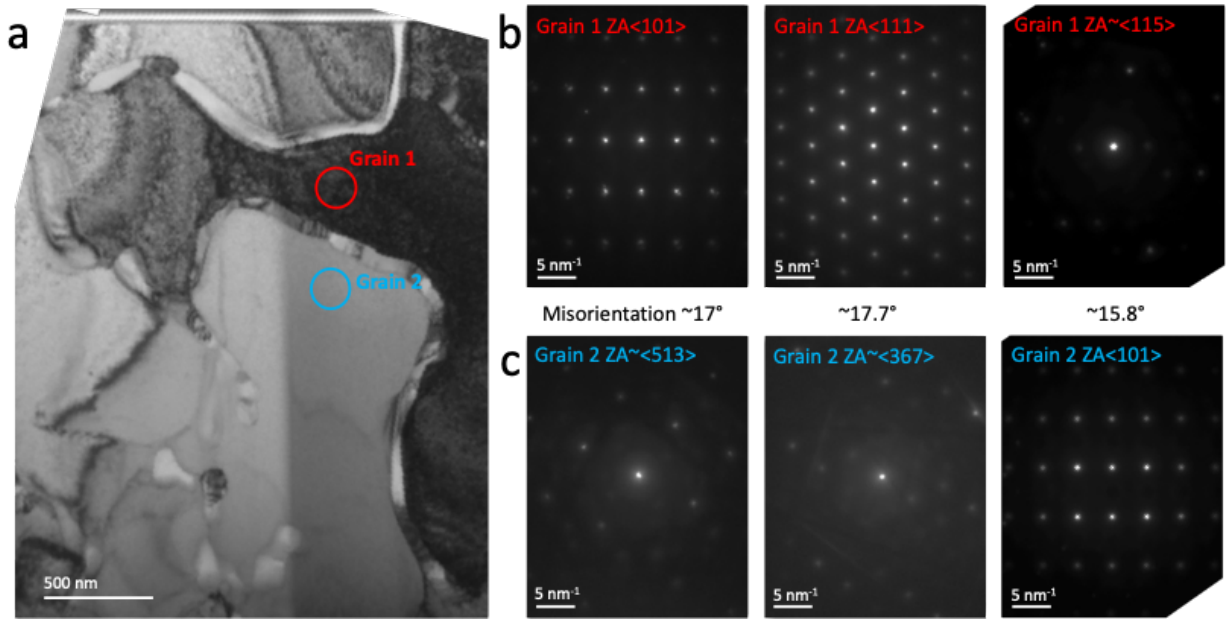

Figure 6.18: **STEM** (a) Bright-field TEM image of a TEM lamella from Ti-Fe-Mo (750 ^{circ}C, 24 h) showing the misorientation of two sub-grains in a colony. Diffraction patterns of both sub-grains are given in (b) and (c) for three tilt angles, suggesting similar misorientation angles. (Image taken by Dr Kan Ma, University of Birmingham.)

6.3 Conclusion

A Ti-Fe-Mo bcc-superalloy comprising a bcc A2 β-Ti matrix reinforced by ordered-bcc B2 TiFe β' intermetallic precipitates has been studied, which exhibits an unusual recrystallisation phenomenon, whereby ageing with no externally applied deformation results in

substantial grain refinement, with the following conclusions:

- Ageing of the Ti-Fe-Mo alloy results in a grain size refinement from 364 $\pm$ 12 μm when homogenised, to 30 $\pm$ 2 μm after a 72 hour ageing. This is correlated with the formation of TiFe intermetallic precipitates, which have a high misfit of -5.4%.

- Pseudo-in-situ EBSD observations revealed heterogeneous precipitation and growth of colonies from prior grain boundaries, with accumulation of strain and dislocations at the colony growth front, and between the A2 and B2 lamellea.

- TEM study within the colonies found the A2 - Ti(Mo, Fe) colony matrix is separated mainly by B2-TiFe-rich precipitates, the high degree of misorientation between the sub-grains and high interfacial dislocation density suggests the B2-TiFe-rich precipitates act to pin the A2 - Ti(Mo, Fe) matrix, leading to the high dislocation density and strains is observed at the matrix-colony fronts and within the colonies by EBSD.

- The precipitation-induced recrystallisation and grain refinement led to an increase in the Vicker's hardness of the alloy, offering a new method for improving the mechanical properties of the alloy without the need for thermomechanical processing.

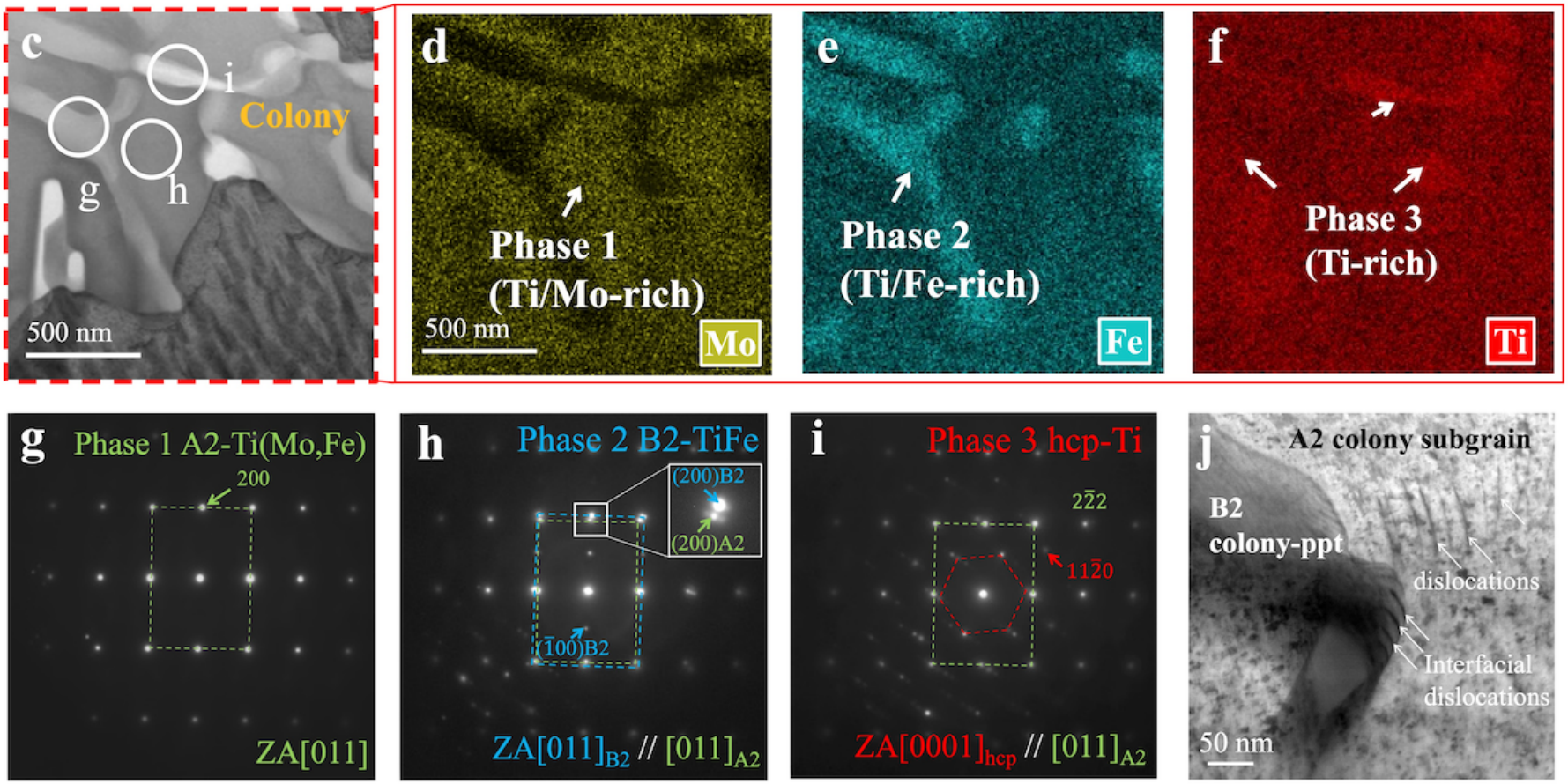

Figure 6.16: **HAADF-STEM image showing the microstructure within the matrix and colonies lifted out from the area in Fig. 6.15** in (a) Ti-Mo-Fe alloy aged at 750 °C for 24 hours. STEM/EDS element mappings in (b) Titanium, (c) Iron and (d) Molybdenum, (e,f,g) Diffraction patterns using selected area diffraction showing the structure of colonies and precipitates (ppt) identified in (a) showing B2 superlattice reflection from the matrix along zone axis <011> and a TEM dark field image using a superlattice spot. (h) Bright-field STEM images showing the interfacial dislocations between the colony and precipitates and dislocations in the colonies. (Image taken by Dr Kan Ma, University of Birmingham.)

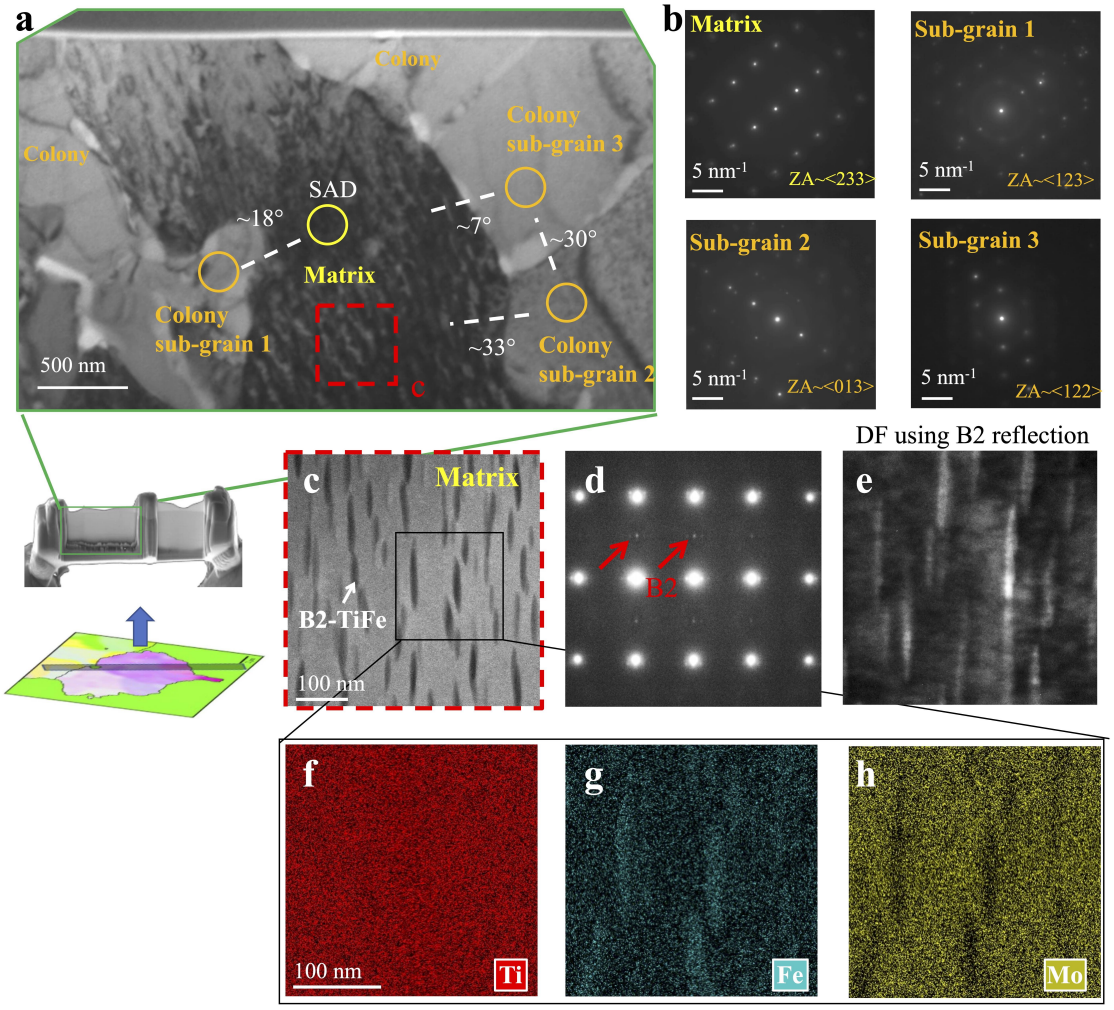

Figure 6.17: **Misorientation between the matrix and sub-grains in the colonies.** (a,b) Bright-field TEM images using two-beam conditions with corresponding selected area diffraction patterns in the matrix and three different sub-grains. (c) HAADF-STEM image showing the microstructure within the matrix. (d) Diffraction patterns using selected area diffraction of (c) showing A2, B2 microstructure. (e) Dark Field image using B2 reflection. STEM/EDS element mappings in (f) Titanium, (g) Iron, and (h) Molybdenum (of the area indicated in (c)) (Image taken by Dr Kan Ma University of Birmingham.)

7 Alternative nano-structuring Tungsten alloy systems - W-TixFe, W-Mn 50/50 wt%, W-Ti 50/50 wt% and W-Ti 70/30 wt%.

ODS tungsten is one of the methods that has been investigated to improve tungsten's ductility and mechanical properties (Zhi D 2021). However, due to manufacturing issues associated with these alloys, an alternative may be to produce a tungsten alloy that is strengthened through the precipitation of an intermetallic phase. This could be achieved by an analogy to the γ-γ' system where an ordered γ' precipitate is used to strengthen a disordered γ matrix - the basis of nickel-based superalloys. One way to do this in tungsten could be through the B2, L21, or $D0_3$ precipitate.

The 'bcc-superalloy' microstructure concept is possible within beta-titanium superalloys and tungsten-based bcc-superalloys. These use alloying additions of Ti and Fe to produce nanostructured tungsten, exploiting the phase equilibria in the W-Ti-Fe ternary phase diagram. These bcc-superalloys are intended to increase the strength of tungsten and irradiation damage tolerance, whilst further work is needed to understand the effect on DBTT and ductility. Careful selection of alloying additions can promote the formation of secondary reinforcing phases with a bcc matrix, namely the B2 intermetallic phase, forming a 'bcc-superalloy' microstructure of fine precipitates with semi-coherent interfaces, which can potentially act as internal sinks for irradiation damage, prolonging the operational life of the tungsten alloys in the fusion first wall. Interface sinks can allow the trapping of vacancies, enhancing the recombination with self-interstitial atoms, and trap He, suppressing bubble formation on grain boundaries. Furthermore, these second phases also strengthen and may improve the creep resistance of the alloys. The purpose of this work is to build on our first demonstration of a bcc tungsten superalloy in ref. [9] by investigating a different preparation route and the effect of secondary heat treatments to further optimise the microstructure.

In addition, the literature has identified several elements as possible ductilisers for tungsten and an alternative to rhenium. Two that stand out from the literature are manganese and titanium. Titanium has been selected due to its low activation level as well as it being identified as a structural material for some of the components of the reactor. In addition, it allows comparisons to be made to that of the W-Ti-Fe alloys being created in this chapter.

Excluding tungsten-heavy alloys (a composite of nickel, iron, and tungsten), rhenium is one of a few known alloying additions which improve the ductility of tungsten.

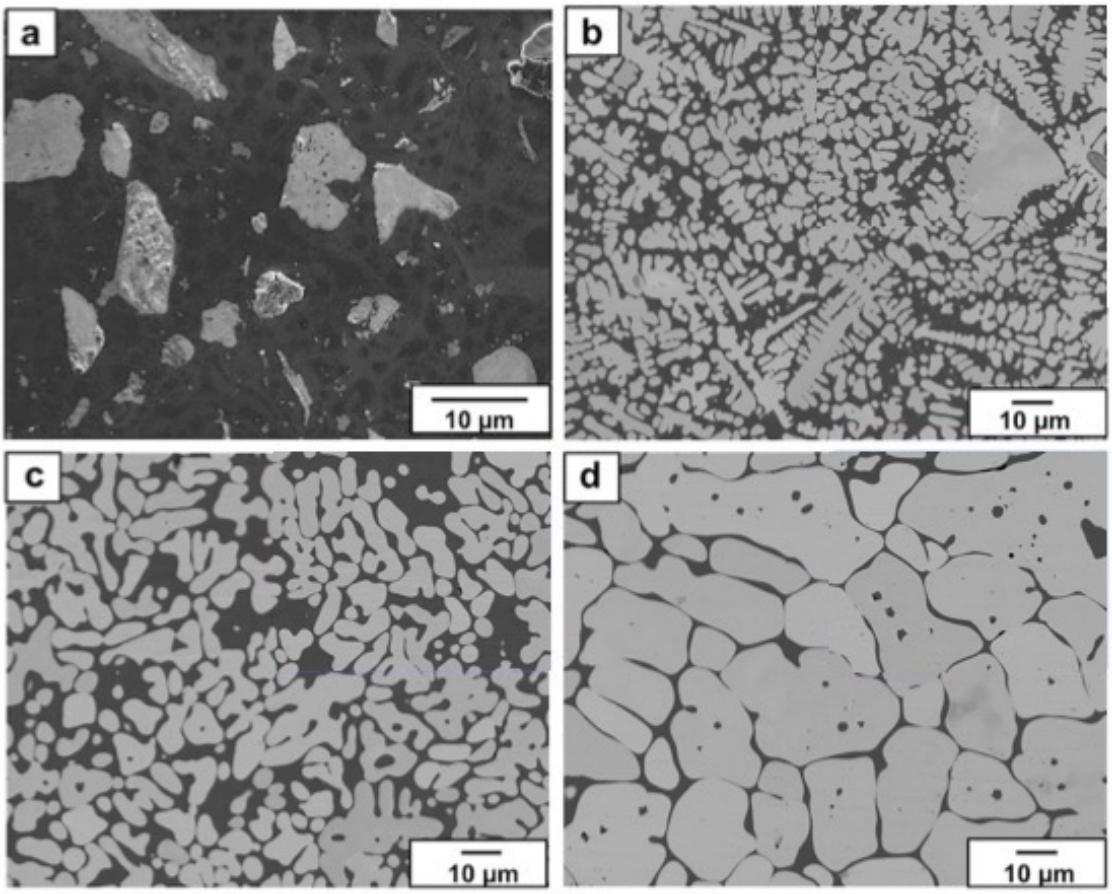

Figure 7.1: **Microstructural changes in WTiFe in the as-received condition due to titanium concentration.** (a)WT60F, (b) WT40F, (c) WT30F and (d) WT20F in the as-received condition

7.1 Results and Discussion - W-Ti-xFe

7.1.1 As cast W-Ti-xFe

To determine the microstructural changes in the alloys, backscatter images were taken of WFTixFe in the as-cast condition (figures 7.1(a-d)). The Fe content was kept constant for each alloy, whilst the W content was increased in place of Ti. The alloys are subsequently referred to as WTxF in which x is the target concentration of Ti, Fe held constant at 20This chapter aims to design and create alloys of tungsten that could potentially modify the mechanical properties of tungsten improving its DBTT. Either through the production of precipitates or through the decomposition of the alloy into different phases.

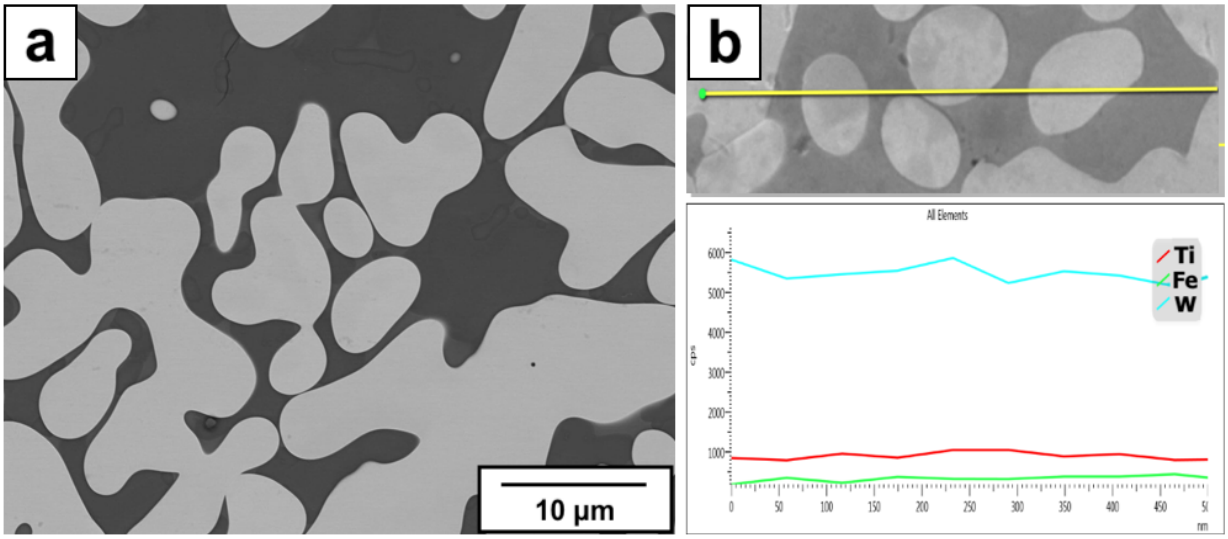

Figure 7.2: **WT40F Microstructural changes in the as-received condition** (a) BSE and (b) line scan profile of WT40F in the as-received condition

7.1.2 Solution heat treated W-Ti-xFe

Following a heat treatment of 1250 °C for 100h (when WT60F was heat treated at 1250 °C, significant melting of the sample occurred; therefore, the homogenising temperature was lowered to 1100 °C). BSE of the Solution heat-treated alloys is shown in figure 7.3(a-d) and EDX line scan figure 7.4. Magnified images of each alloy (see insets) are also shown to observe the microstructure better. These magnified images show the presence of small black precipitates within the lighter tungsten-rich phase of WT30F and WT20F. The composition of this phase was later confirmed by STEM-EDX (Parkes N 2023). This extra phase was unexpected (not seen in the phase diagram). Therefore, it is likely to be present due to either the initial segregation of the elements during the manufacturing process or the inability to homogenize the alloy at higher temperatures. This was limited by the thickness of the glass encapsulation tubes used during homogenization, not being sufficient to withstand higher temperatures.

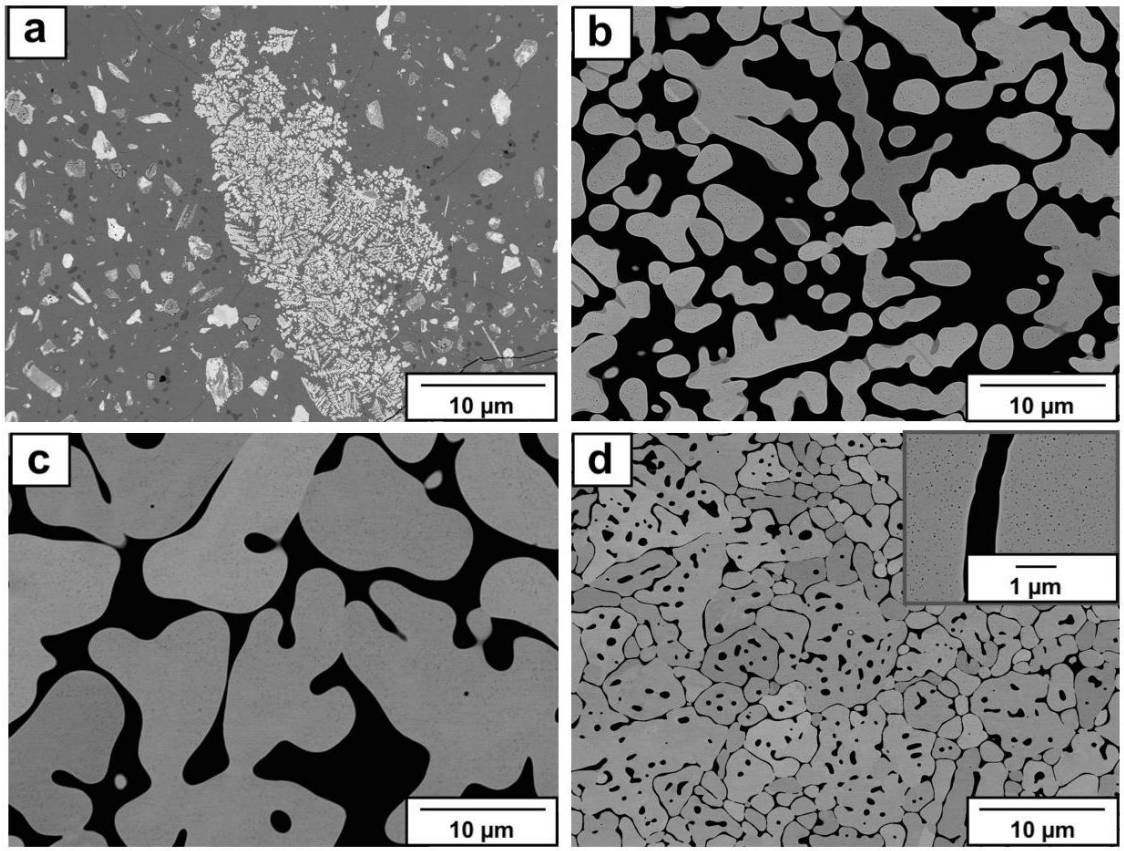

Figure 7.3: **WTxF Microstructural changes following solution heat treatment due to titanium concentration.** (a)WT60F, (b) WT40F, (c) WT30F and (d) WT20F (zoomed-in image to show TiFe precipitates within the matrix). Solution heat treated for 100h at 1250 °C.

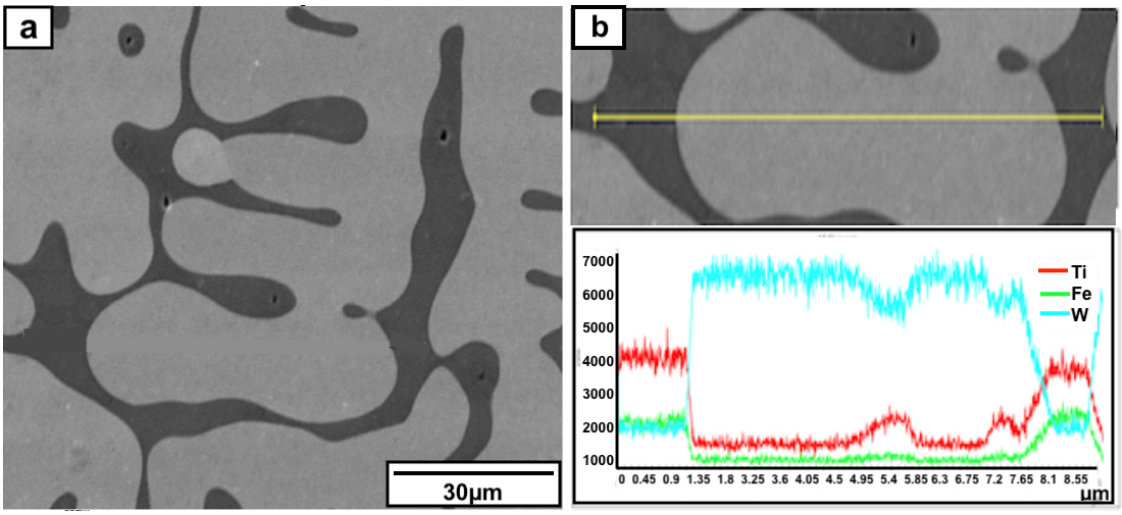

Figure 7.4: **WT40F Microstructural changes following aging.** (a) BSE and (b) line scan profile of WT40F homogenization for 100h at 1250 °C.

7.1.3 Aging of W-Ti-xFe

Following solution heat treatment, the samples were aged at 750 °C for 80 hours and BSE images of the resulting microstructure are shown in figures 7.6(a-d) along with an EDX line scan of WT40F (figure 7.7). On observing the microstructure by BSE, all four alloys show the presence of a third phase that was not present after solution heat treatment. This is a fine lamellar structure within the titanium-rich phase. Due to the fine structure of these lamellar-like precipitates in the titanium-rich matrix, the composition of these phases could not be confirmed by EDX. Study of this phase by STEM-EDX in the titanium-rich regions ((Parkes N 2023)) shows a possible transformation of the A2(Ti, W,Fe) phase to an A2(Ti, W,Fe) and A3Ti(Fe,W) (figure 7.5) (Parkes N 2023).

7.1.4 Microhardness Testing

Each of the samples for WTiFe where tested using a 2Kgf load. The results obtained for WT40F are shown graphically in table 24. The data shows only a slight increase of 36.77 Hv in hardness of the homogenized WT40F as compared to that of the cast sample. Following ageing, there is a slight reduction (however, not to the hardness observed in the as-received alloys). Due to the degree of macro segregation in all four alloys, the results presented here for hardness can only be used as speculation of the final properties of the alloy. Only once a truly homogenized alloy can be created can the mechanical properties be honestly commented upon. It can be inferred that due to the lack of cracks at the indent corners, this alloy has some promise in reducing the brittleness of tungsten at room temperature.

7.1.5 X-ray diffraction (XRD) of the WT40F

X-ray diffraction (XRD) of the WT40F samples (figure 7.8) shows the presence of three phases; FeTi, tungsten, and titanium. Comparison of the lattice parameters (Table 25) for the as-received and aged samples show a reduction in both Ti and W phases from 3.157 $\pm$ 0.004 to 3.13 $\pm$ 0.01, whilst the FeTi intermetallic phase has a lattice parameter of 2.97

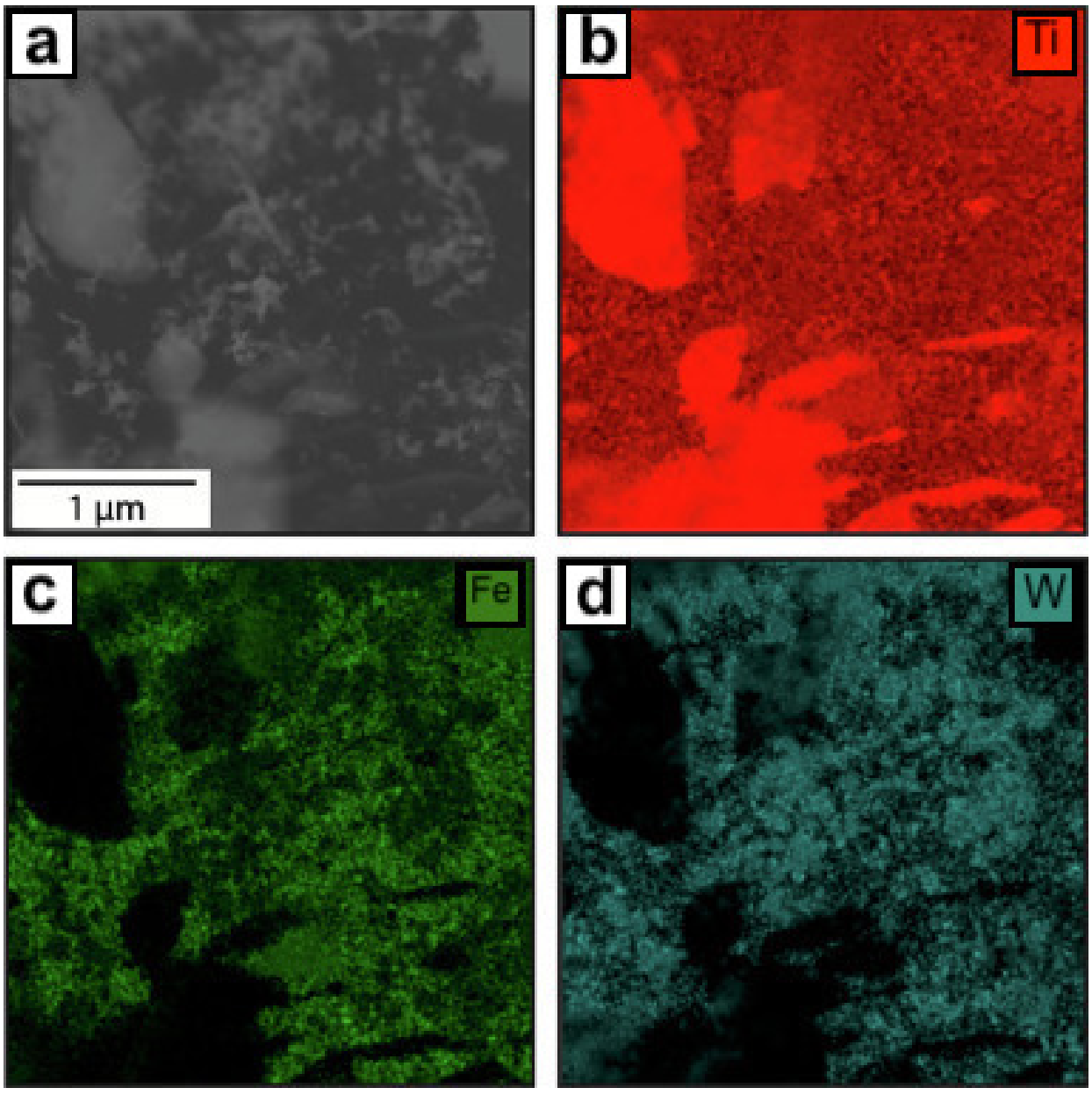

Figure 7.5: **WT60F solution treated and aged** (a) HAADF-STEM micrograph, followed by EDX elemental maps for (b) Ti, (c) Fe and (d) W. following ageing for 80h at 750 °C.

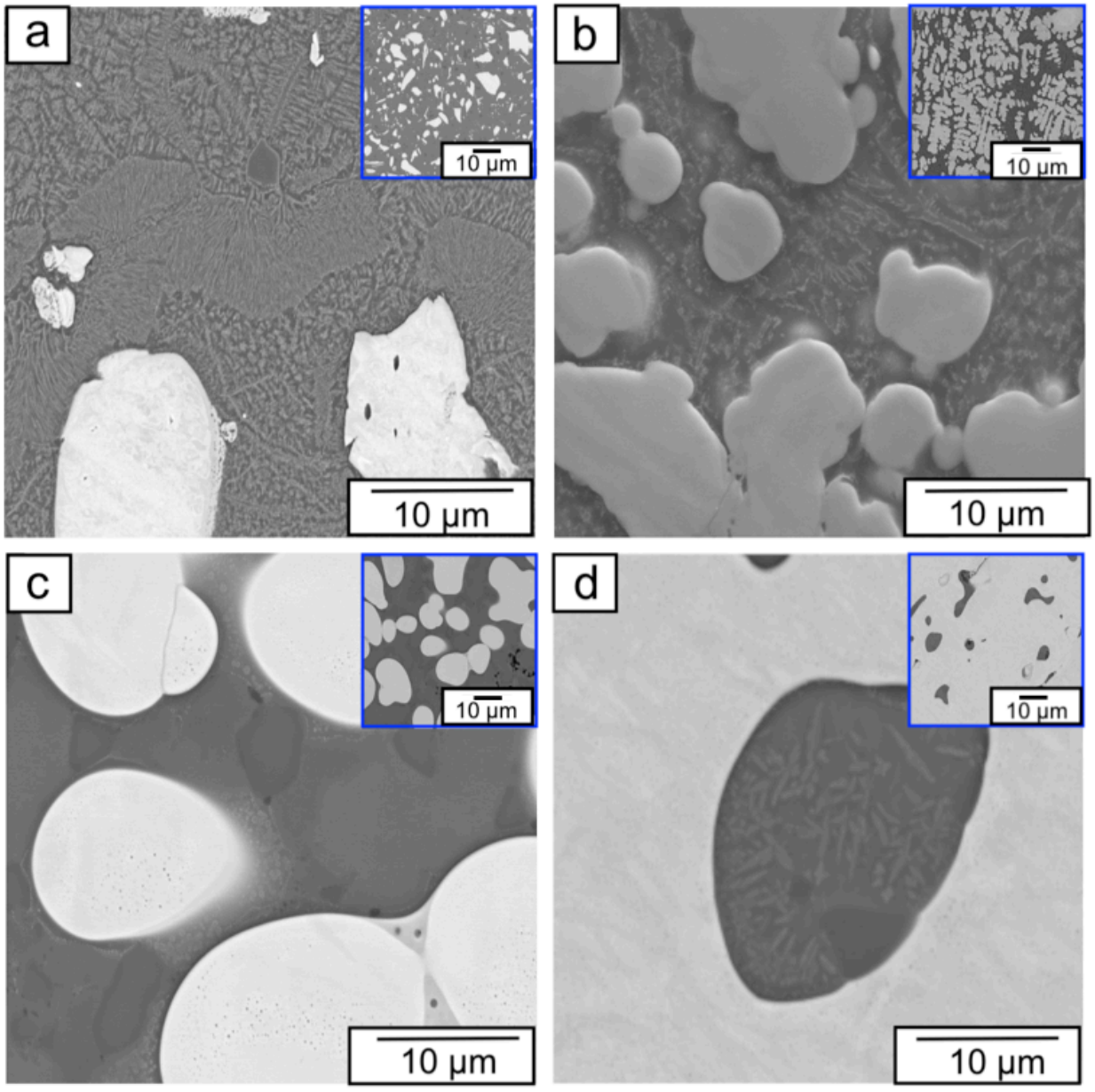

Figure 7.6: **WTxF Microstructural changes following ageing.** (a)WT60F, (b) WT40F, (c) WT30F and (d) WT20F following aging for 80h at 750 °C.

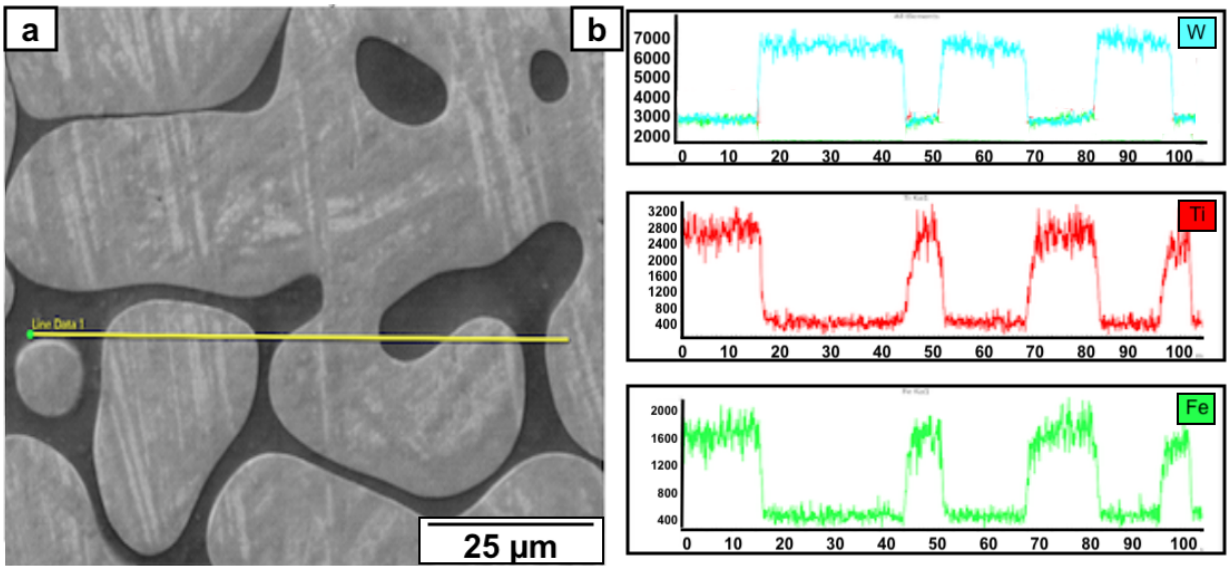

Figure 7.7: **WTxF Microstructural changes following ageing.** (a) BSE and (b) line scan profiles of WT40F ageing for 80h at 750 °C.

± 0.01. The identification from XRD analysis of a nanoscale precipitate within the alloy following ageing confirms what is observed in the aged samples. Figure 7.7(c) shows the TiFe phase's presence within the tungsten-rich phase, which is not observed in the XRD data. This could be explained by its size or lack of homogeneity across the sample. The lack of observation of this phase in the other samples may also be due to its segregation as opposed to its absence.

Table 24: **Vickers hardness testing of TiFeW** Table shows Vicker's hardness values for a 2kg load for WT40F after varying heat treatments.

Sample	Vickers Hardness					Av. Hardness
TiFeW as cast	587.9	562.5	571.4	580.4	576.4	575.6
	571.4	581.7	582.5	579.6	562.3	
TiFeW Heat treated	688.0	649.5	712.5	672.3	678.9	612.4
	692.5	673.5	682.9	689.5	684.2	
TiFeW Heat treated aged	578.2	634.9	601.5	567.7	623.2	600.4
	687.6	571.8	573.6	583.5	572.8	

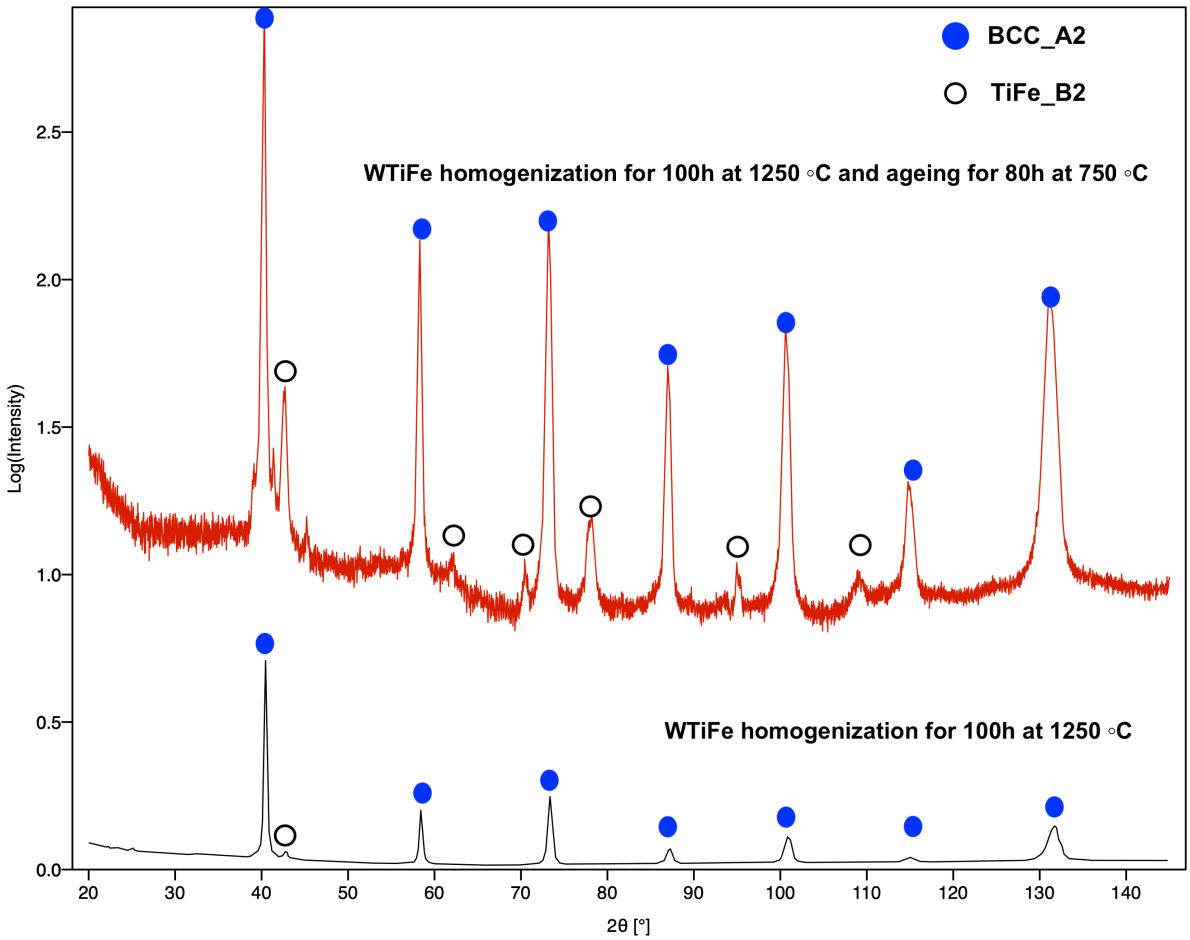

Figure 7.8: **X-ray diffraction of analysis W-Ti-Fe alloy** Diffraction profiles for TiFeW after homogenization (black) and ageing (red).

Table 25: **X-ray diffraction of TiFeW** Crystal structure of TiFeW as analyzed by XRD for as received and TiFeW heat treated aged 750 °C 80 hours

Sample	2 θ angle	θ angle	d= λ/2sin(θ)	1/d^2	H	K	L	Lattice parameter
TiFeW as cast	40.50	20.25	2.23	0.20	0	1	1	3.16$\pm$0.004
	42.85	21.43	2.11	0.23	1	0	1	
	58.46	29.23	1.58	0.40	0	0	2	
	73.40	36.70	1.29	0.60	1	1	2	
	87.23	43.62	1.11	0.80	0	2	2	
	100.94	50.47	1.00	1.00	0	1	3	
	115.15	57.57	0.91	1.20	2	2	2	
	131.83	65.91	0.84	1.41	0	1	3	
	42.85	21.43	2.11	0.23	1	0	1	2.92
TiFeW heat treated aged 750 °C 80 hours	40.71	20.36	2.22	0.20	1	1	0	3.13$\pm$0.001
	58.83	29.41	1.57	0.41	2	0	0	
	73.60	36.80	1.29	0.61	1	1	2	
	87.35	43.68	1.12	0.80	2	2	0	
	101.04	50.52	1.00	1.00	3	1	0	
	115.17	57.59	0.91	1.20	2	2	2	
	131.49	65.74	0.85	1.40	3	2	1	
	43.05	21.53	2.10	0.23	2	0	0	2.97$\pm$0.001
	62.73	31.37	1.48	0.46	2	2	0	
	70.91	35.45	1.33	0.57	2	1	0	
	78.77	39.38	1.21	0.68	2	1	1	
	95.41	47.70	1.04	0.92	2	2	0	
	110.06	55.03	0.94	1.13	3	1	0	

7.2 W-Mn 50/50 wt% - Results and Discussion

7.2.1 Microstructure and relative density of W-Mn 50/50 at%

Figure 7.11 shows a BSE, EDX map, and line scan for the 50:50 at.% alloy as cast by ACI. The BSE images show small (approximately 6.4 $\pm$ 0.3 µm) spherical powder particles of tungsten in a manganese matrix.

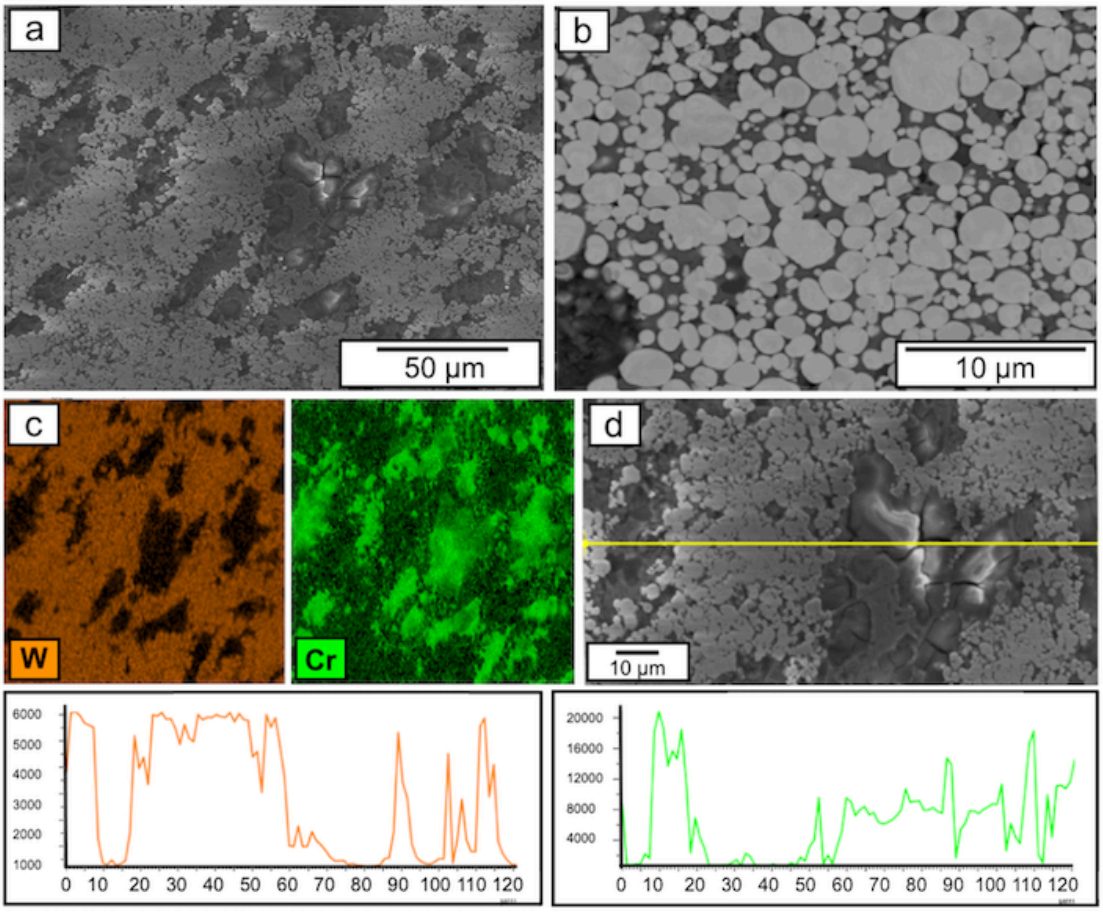

Figure 7.11: **W-Mn 50/50 at% Characterisation in the as-received condition** (a) SEM image of the typical as cast microstructure (b) BSE image (c) EDX map tungsten (orange) chromium (green), and, (d) Line scan data for the two different elements.

As the melting temperature of manganese 1246 °C, a sintering temperature of 1225 °C was used to melt the manganese powder around the tungsten thoroughly. Previous work has shown that a sintering time of 60 minutes 1225 °C produced a homogenised microstructure. However, after heat treating the alloy for 1h at 1225 °C, the microstruc-

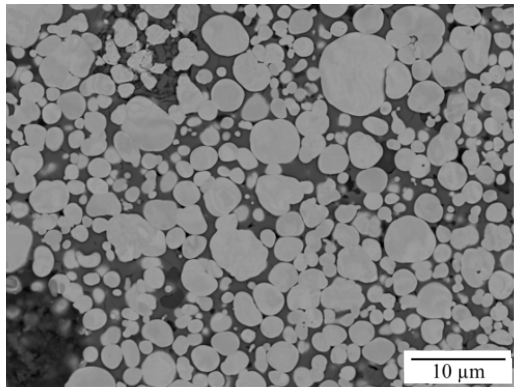

(a) 1225 °C 1hr

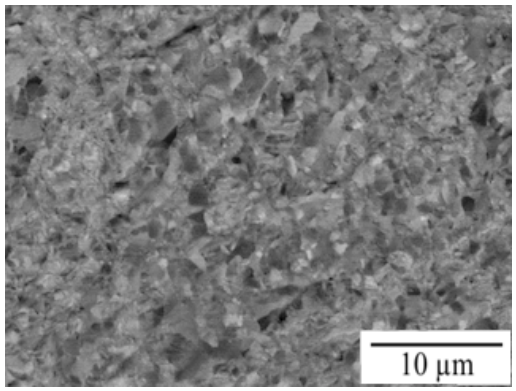

(b) 1225 °C 24hr

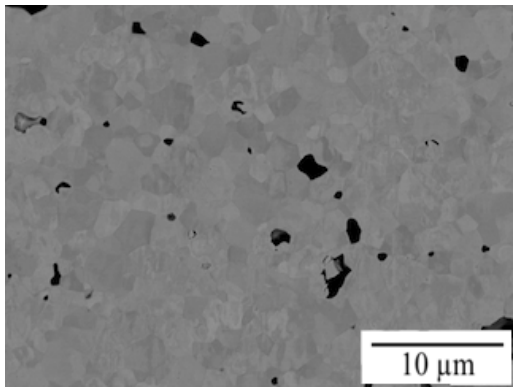

(c) 1225 °C 72hr

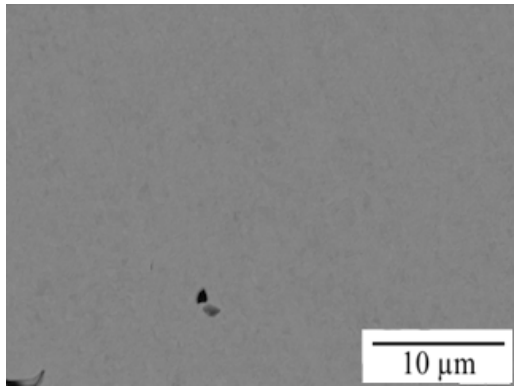

(d) 1225 °C 72hrs plus 750 °C 100h

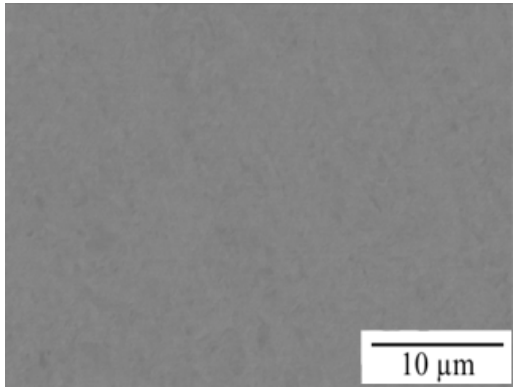

(e) 1225 °C 72hrs plus 1000 °C ageing 100hrs

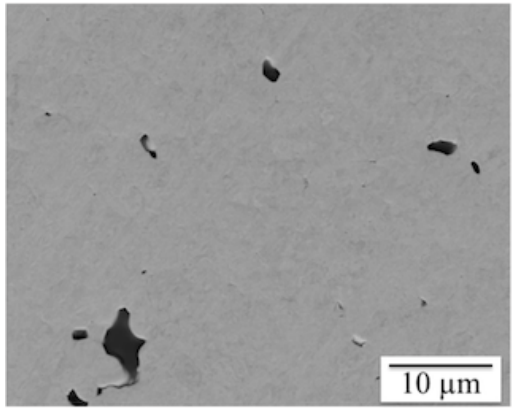

(f) 1200 °C 100hr

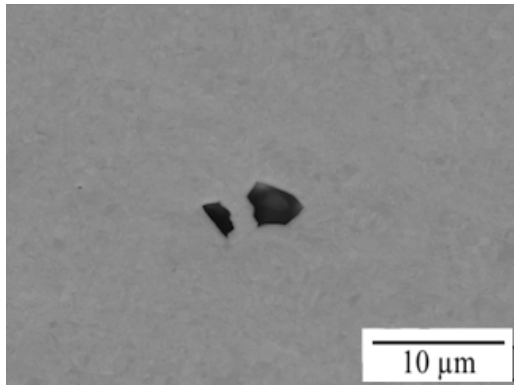

(g) 1200 °C 72hrs and 750 °C 100hrs

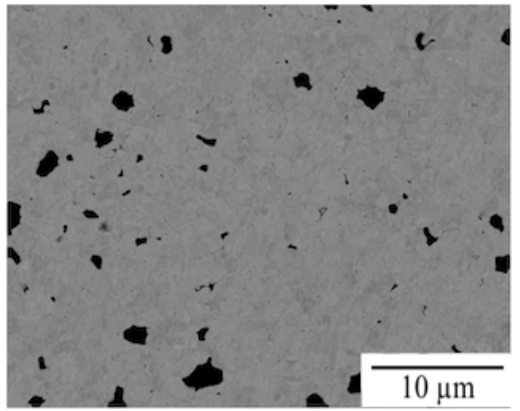

(h) 1200 °C 100hr

Figure 7.9: **W-Mn 50/50 at% SEM BSE images** BSE images of W-Mn 50/50 at% alloy following varying heat treatments.

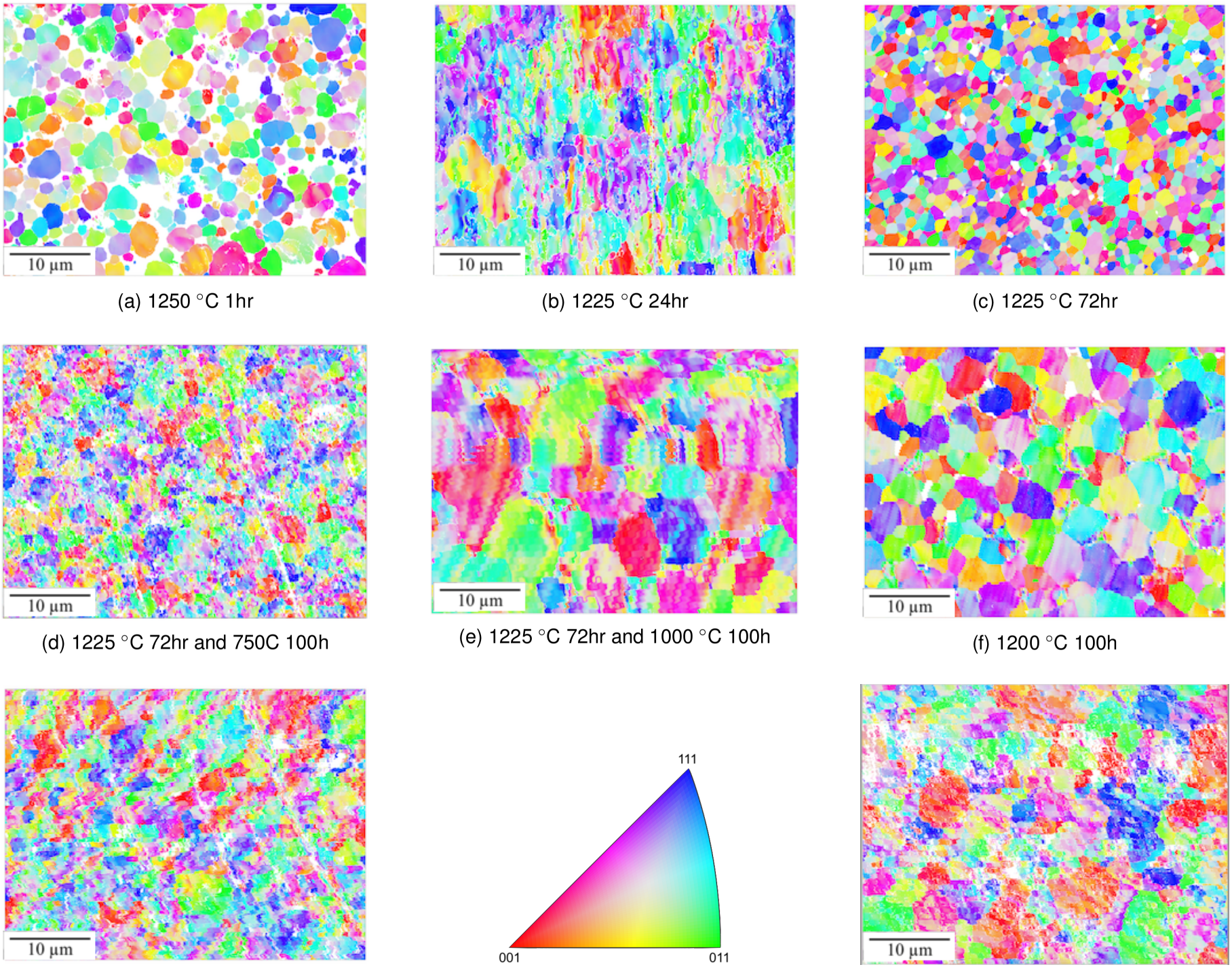

(a) 1250 °C 1hr

(b) 1225 °C 24hr

(c) 1225 °C 72hr

(d) 1225 °C 72hr and 750C 100h

(e) 1225 °C 72hr and 1000 °C 100h

(f) 1200 °C 100h

(g) 1200 °C 100h and 750 °C 100h

(h) 1200 °C 100h and 1000 °C 100h

Figure 7.10: **W-Mn 50/50 at% EBSD analysis** EBSD maps and IPF Key of W-Mn 50/50 at% alloy following varying heat treatments.

ture of the alloy shows remarkable similarity to that of the compacted alloy (figure 7.9a). The BSE images show small (approximately 6.4 $\pm$ 0.3 μm) spherical powder particles of tungsten interconnected with smaller manganese powder particles. To produce a more homogenised alloy, an as-cast sample was solution heat treated at 1225 °C for 24h. Figure 7.9b shows a highly disordered microstructure of relatively small grains of varying contrasts. The sample still contains regions of unmelted manganese (black spots). Increasing the homogenisation time to 72 hrs (figure 7.9c) improved the texture. Leading to larger, more equiaxed grains. BSE images of the homogenized 1225 °C for 72h aged for 4 days at 750 °C and 1000 °C (figure 7.9d and 7.9e). As compared to the 72hr 1225 °C homogenised sample, the grain size of the aged for four days at 750 °C and 1000 °C is more refined. To try and improve the quantity of manganese in the final sample, the homogenising temperature was reduced to 1200 °C. The microstructure of the homogenised and aged for four days at 750 °C and 1000 °C is shown in figures 7.9f, 7.9g and 7.9h respectively. The pattern of grain morphology matches that of the previous heat treatment. The homogenised grains are larger than the aged samples, and the sample added at 1000 °C has a larger grain size than that of the sample aged at 750 °C. Ageing the sample at 750 and 1000 °C should produce a β phase (cubic lattice structure) W-Mn alloy Elsebaie O (2018). Manganese transforms to a β structure at 720 °C. The δ phase (body-centred cubic - bcc) is stable below 1244 °C. The reduction in grain size seen during the sample's ageing may be due to the transformation of the cubic phase to that of the bcc to cubic phase.

7.2.2 Grain Size of W-Mn 50/50 at%

The W-Mn binary alloy was homogenised and aged at different temperatures to determine manganese's effect on tungsten characteristics. The primary grain properties are shown in table 26 as analysed by MTEX software.

EBSD analysis images are shown in figures 7.10b. Grain statistics for this heat treatment are shown in table 26. The KAM and GOS data demonstrate that the grain in this

sample is highly deformed, with average values of 0.51 and 2.38, respectively. This shows grains are still undergoing recrystallisation. Therefore, a more extended homogenising treatment is needed. The average grain diameter of 1.02 μm is comparable to the literature (Elsebaie O 2018).

Solution heat treating the alloy for 72h at 1225 °C leads to a more prominent average grain diameter of 3.47 μm. EBSD analysis (figure 7.10c) shows both the KAM and GOS values (table 26) have reduced, indicating a reduction in the plastic deformation. Demonstrating the recrystallisation event observed at 24h of homogenisation has progressed.

δ-manganese at 1140 °C has a lattice parameter of 3.01 Å Basinski ZS (1954) and that of pure tungsten is 3.17 Å. Therefore, manganese should lower the lattice parameter of tungsten. XRD analysis of the 12h and 24h specimens (figures 7.12) gives a lattice parameter of 3.16 Å for both; this is similar to the 3.1628 $\pm$ 0.0005 given in the literature Elsebaie O (2018). The XRD data for the homogenised alloy does not show the presence of intermetallics (at least in a quantity that can be detected). This is also confirmed by SEM and BSE imaging.

Point scan analysis of the alloy homogenisation at 1200 °C showed an average manganese concentration of 3.15% $\pm$ 0.42 manganese. This is significantly improved from the 1225 °C homogenisation, where the level of manganese was undetectable. EBSD analysis (figure 7.10f) showed an average grain diameter of 2.58 μm (linear intercept method). Ageing of the sample at 750 °C reduced the average grain diameter by more than 50% and the grain area by a tenth. Ageing at 1000 °C also reduced the grain diameter and size by almost 50%. The grain area was significantly reduced compared to the homogenised sample but was nearly double that of the sample aged at 750 °C.

7.2.3 W-Mn 50/50 at% GOS, KAM and grain Misorientation

In addition to grain size (figure 7.13), EBSD was used to obtain grain orientation spread (GOS) maps to identify the presence of both deformed grains as well as those which are deformed. Typically, a recrystallised grain has a GOS value of $\leq$2 °, compared to a

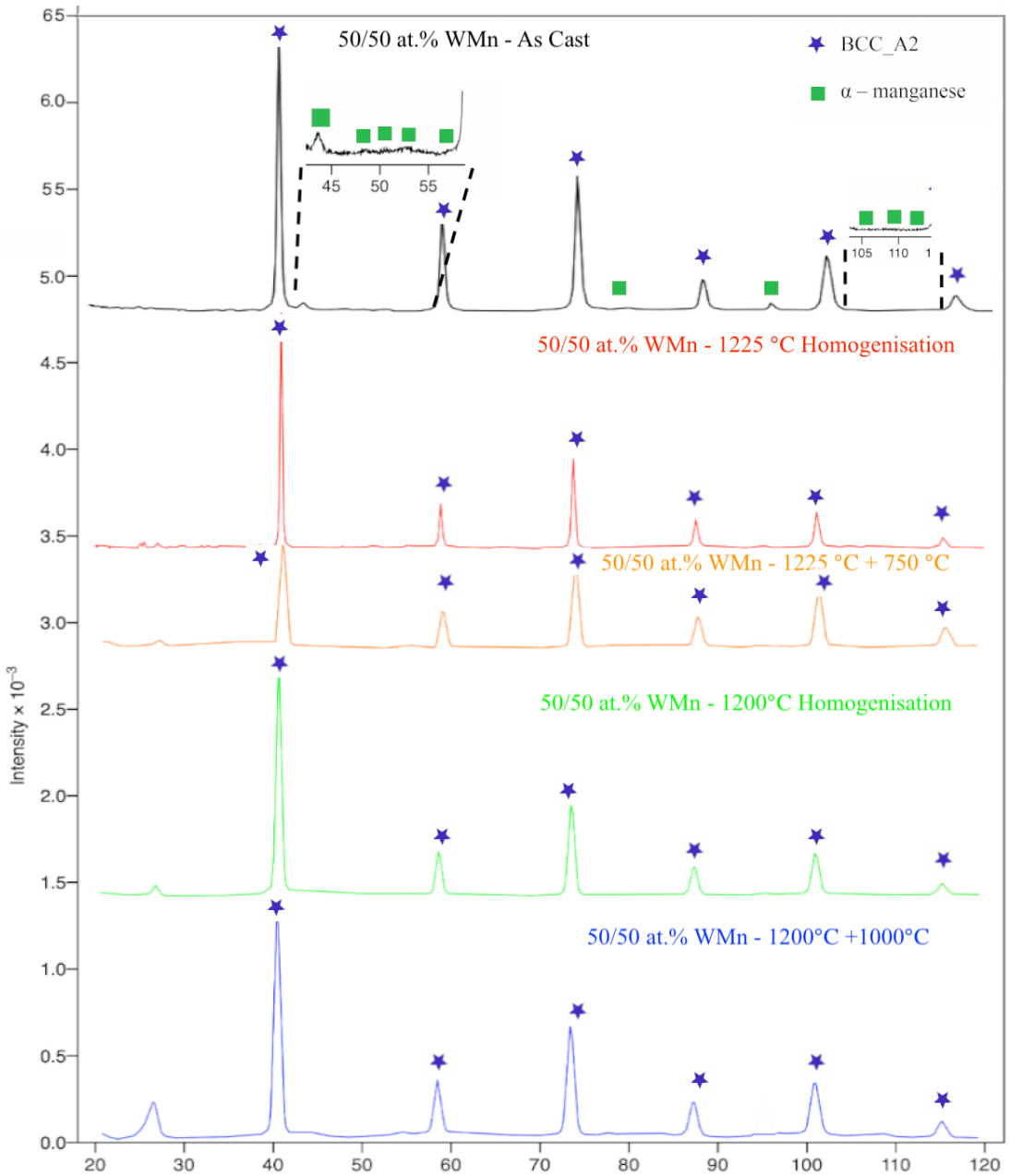

Figure 7.12: **W-Mn 50/50 at% X-ray diffraction patterns** The graph shows the different phases identified by XRD in the W-Mn alloy following various heat treatments.

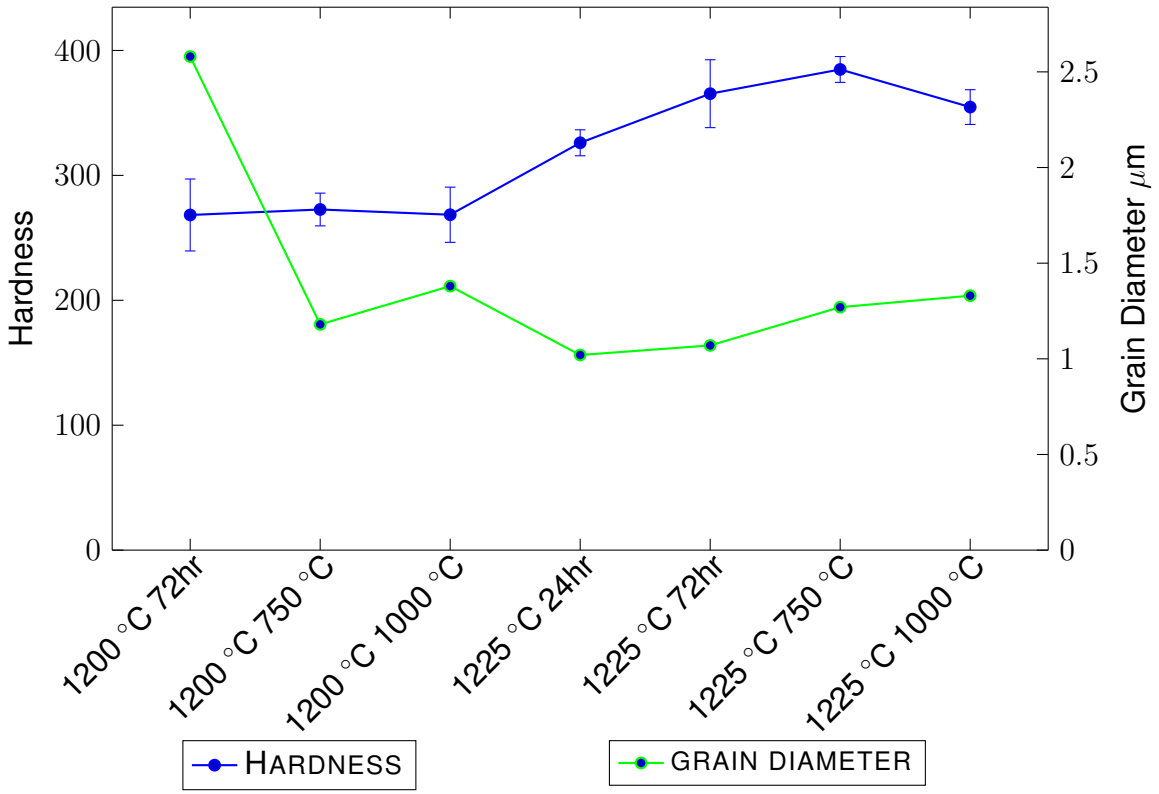

Figure 7.13: **W-Mn 50/50 at% Grain size and hardness**. Shows grain size and hardness change for different ageing treatments of W-Mn 50/50 at% alloy.

deformed grain with a value $>$ 3 °. Kernel average misorientation (KAM) measures the misorientation of a point in relation to its neighbours. A value of $\leq$2.5 ° is considered recrystallized, whereas a value of $>$2.5 ° is considered deformed. KAM and GOS values are shown in table 26 for each homogenised and aged sample. The data for the two parameters suggests that homogenising the alloy at 1225 and 1200 °C, a highly recrystallised structure is formed with minor levels of deformation. However, on ageing both samples at lower temperatures, the degree of deformation in the grains increases. This is indicated by the average GOS values for both the 1000 °C aged samples and the 750°C aged 1200 °C homogenised samples being over 3°. KAM values also show an increase in the level of local plastic deformation in the aged samples compared to that of the homogenised. The level of deformation in the samples is also supported by the Low-angle grain boundaries (LAGB) percentage.

7.2.4 W-Mn 50/50 at% Vickers Hardness

Homogenising the alloy at 1200 °C as compared to 1225 °C produced a reduction in hardness measurements (Table 27). Despite the changes in the deformation of the grains in aged samples, there is only a slight increase in hardness for the samples aged at 1000 °C. However, the samples aged at 750 °C showed almost no change in hardness (1200 °C homogenised) and a slight reduction in hardness for the 1225 °C sample.

As the melting temperature of manganese is 1246 °C a sintering temperature of 1250 °C was used to thoroughly melt the manganese powder around the tungsten. Previous work has shown that a sintering time of 60 minutes 1225 °C produced a homogenised microstructure. However, after sintering for 1h at 1250 °C, the alloy's microstructure shows remarkable similarity to that of the compacted alloy (as shown by EBSD analysis). I am therefore uncertain how the above study could have produced BSE images of an almost fully dense structure. They do not state at what pressure the consolidated powder was sintered, and therefore it cannot be accessed how they made such an alloy at this temperature.

To further assess whether a W-Mn alloy could be created at this temperature, 1cm ^{2} sections of the as-cast ACI sample were solution heat treated at 1250 °C for 24h. EBSD analysis and XRD and BSE images are shown in figures 7.12 and 7.14, respectively. Grain statistics for this heat treatment are shown in table 26. The KAM and GOS data demonstrate that the grain in this sample is highly deformed, with average values of 1.49 and 2.22, respectively. This shows grains are still undergoing recrystallisation. Therefore, a more extended homogenising treatment is needed. The average grain size of 1 µm is comparable to the literature (Elsebaie O 2018).

Solution heat treating the alloy for 72h at 1250 °C leads to a larger grain average grain size of 3.93 µm. EBSD analysis shows both the KAM and GOS values (table 26) have reduced, indicating a reduction in the plastic deformation. Demonstrating the recrystallisation event observed at 24h of homogenisation has progressed.

Comparing δ-manganese at 1140 °C which has a lattice parameter of 3.02 Å (Basin-

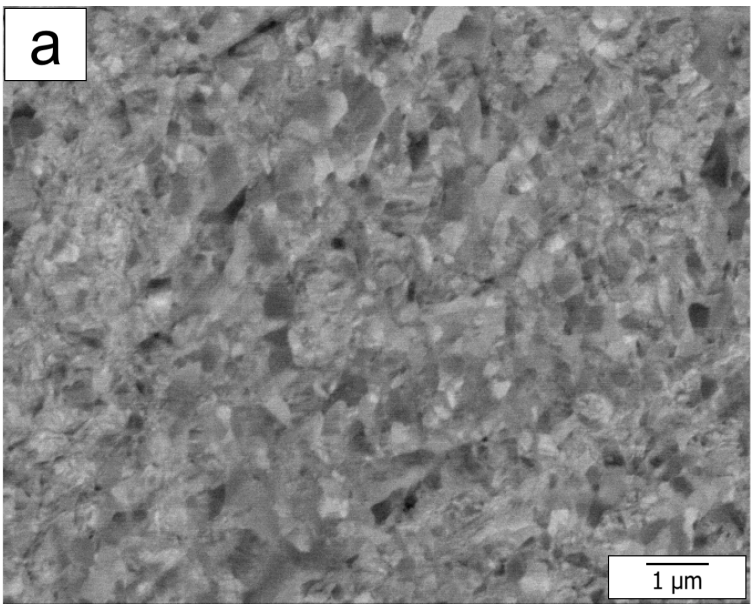

Figure 7.14: **BSE image of W-Mn homogenized at 1250 °C for 24h**

ski ZS 1954) and that of pure tungsten is 3.17 Å. Therefore, any addition of manganese to tungsten should reduce the lattice parameter. XRD analysis of the 12h and 24h specimens (figure 7.12 gives a lattice parameter of 3.16 Å for both; this is similar to the 3.16 $\pm$ 0.05 given in the literature (Elsebaie O 2018).

Although the hardness values obtained for alloy homogenised at 1250 °C show a significant reduction in comparison to pure tungsten (410–430 HV) and a change in the lattice parameter observed, it was difficult to ascertain if there was manganese present, in the sample after an incubation period of 72h at 1250 °C (figure 7.15). Therefore, it was decided to reduce the temperature for the homogenisation to 1200 °C. BSE image and XRD data of W-Mn and line scans are shown in figures 7.16a and 7.16c, respectively. Point scan analysis showed an average manganese concentration of 3.15% $\pm$ 0.42 manganese (as shown in figure 7.16c). This is significantly improved from the 1250 °C homogenisation, where the level of manganese was undetectable. Hardness measurements showed a further reduction (Table 27) in hardness as compared to 1250 °C. EBSD analysis showed an average grain size of 3.5 μm (linear intercept method).

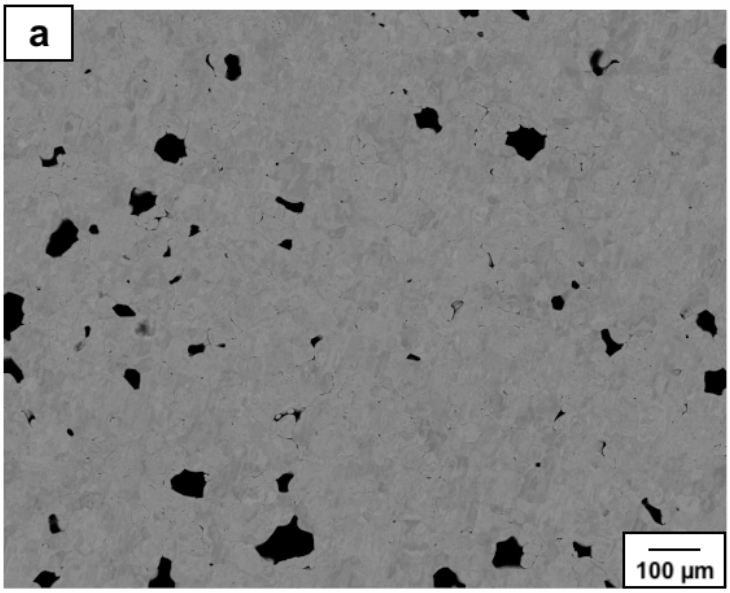

Figure 7.15: **W-Mn 50/50 at% SEM BSE after homogenisation at 1250 °C for 72h and aged for 100h at 1000 °C**. (a) BSE image of the typical microstructure after homogenisation at 1250 °C for 72h and aged for 100h at 1000 °C

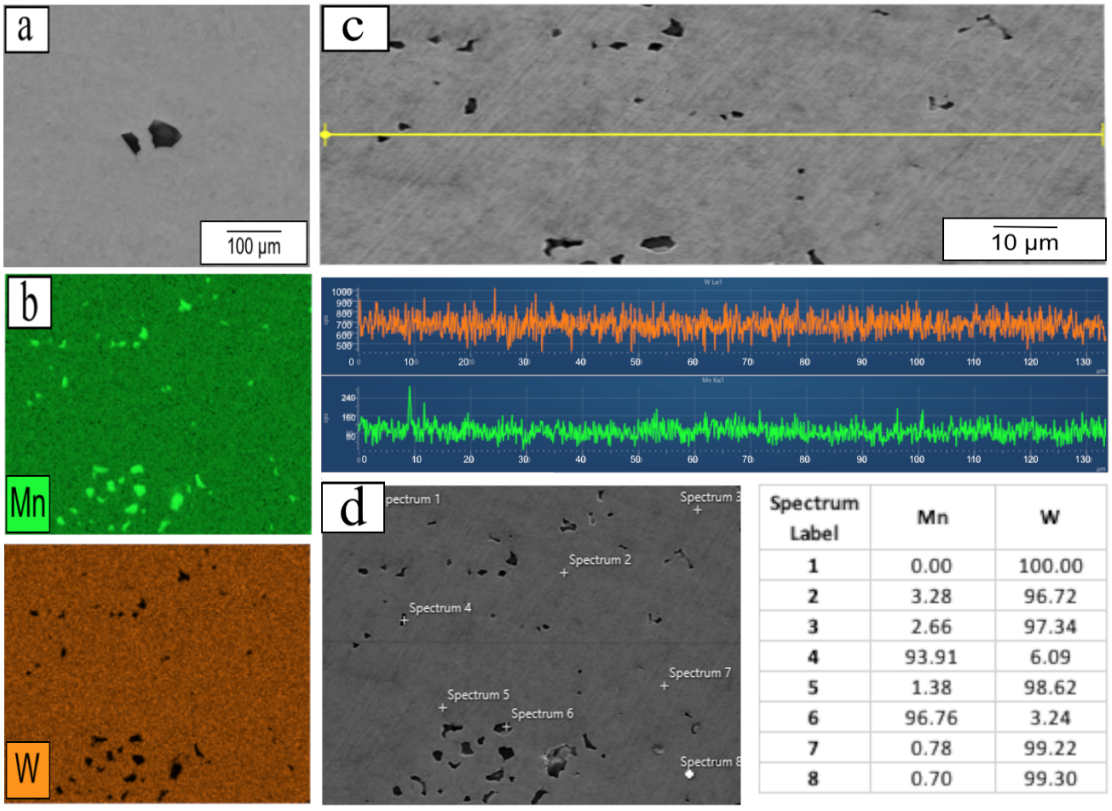

Spectrum Label	Mn	W
1	0.00	100.00
2	3.28	96.72
3	2.66	97.34
4	93.91	6.09
5	1.38	98.62
6	96.76	3.24
7	0.78	99.22
8	0.70	99.30

Figure 7.16: **W-Mn 50/50 at% Characterisation after homogenisation at 1200 °C for 100h** (a) SEM image showing manganese-rich particles (b) EDX map, Manganese (green) and tungsten (orange) (c) SEM and line scan profiles and (d) Point scans and corresponding table showing values in atomic %

7.2.5 W-Mn 50/50 at% Grain boundary density

LAGBs have been shown computationally to better cope with and resist strain effects and prevent fracture Cheng Y (2008), Lim LC (1990), Watanabe T (2004). In particular, bi-crystals with LAGBs perform better under 3-point bending tests and are less affected by the presence of impurities Smiti E (1984*a*). In addition, ultrafine grain tungsten provides sources of dislocations needed to improve plasticity Smiti E (1984*b*). Recrystallised grains are usually identified as grains free of subgrains and surrounded by HAGBs. As expected, both homogenised samples have the lowest percentage of LAGBs, increasing the sample's ageing. It can be seen that lowering the homogenisation temperature to 1200 °C increased the number of LAGBs as compared to that of homogenisation temperature of 1225 °C. In addition, ageing the sample at 1000 °C produced a more significant proportion of LAGBs as compared to that of 750 °C.

7.2.6 W-Mn 50/50 at% Low angle grain boundaries

Compared to manufactured tungsten, deformed tungsten shows improved mechanical properties, especially if it is cold-rolled. Tungsten, when rolled at 400 °C, demonstrates improved strength, increased density of dislocations, and a greater proportion of low-angle grain boundaries (Wei Q 2008, Reiser J 2016). It has already been observed that adding magnesium reduces the grain size of tungsten following various heat treatments. Despite the grain reduction, macroscopically, the alloy was very porous due to the inability to homogenise the sample properly. Therefore, the potential to conduct mechanical (3-point bending) tests on the alloy was impossible. Instead, It was decided to characterise the nature of the grain boundaries obtained from EBSD (figure 7.10). Each EBSD captured a cut-off limit of 15 ° to distinguish between high- and low-angle grain boundaries. Figure 7.17a shows the total number of grain boundaries identified as either. LAGB or HAGB after various heat treatments. The orange segment represents those grain boundaries with an angle of less than 15 °, whereas the blue bar shows those grains with an angle greater than 15 °. To better determine the proportion of the number of LAGB. The

Table 26: **W-Mn 50/50 at% EBSD results.** Grain characteristics for W-Mn alloy heat treated at 1250 °C for different holding times

W-Mn		Grain Size μm	GOS (°)	KAM	Aspect Ratio	PARIS %	Misorientation (°)
1h	Max Average	Still Powder Particles					
24h	Max Average	16.68 1.02	35.9 2.22	57.89 1.49	9.35 1.86	281.26 17.45	24.56/75.44
72h	Max Average	35.49 3.93	20.81 1.38	32.63 0.33	5.26 1.52	104.39 39.47	32.68/67.32

Table 27: **W-Mn 50/50 at% Vicker's hardness measurements.** Hardness measurements of W-Mn 50/50 at% in homogenised condition with 2kg load on samples homogenised for 72h

Homogenisation Temperature	Hardness Measurements (2Kg)					Average Measurement
1200	259.3 235.0	208.6 310.8	254.8 287.1	263.8 279.2	295.4 286.7	**268.0 ± 28.8**
1250	396.3 384.6	385.0 320.0	398.6 364.6	354.7 310.2	373.6 371.7	**365.9 ± 27.2**

percentage of grain boundaries is shown as an overall proportion of the total number of grain boundaries identified in figure 7.17b. Figure 7.18 shows the grain boundary misorientation angle found at varying heat treatments of the W-Mn alloy. In terms of engineering, a more significant number of low-angle grain boundaries. The data tells us that the lower homogenisation temperature of 1200 °C produces a more significant proportion of LAGB than homogenising at 1225 °C. In fact, from EDX point scans, the greatest concentration of magnesium seen in the alloy was identified after homogenising at 1200 °C (Figure 7.16d of 3.28 at %). Additionally, ageing the alloy at the lower temperature of 750 °C for increased time periods helps to improve the overall number of LAGB compared to HAGB. Despite the improvement in the ratio of LAGB to HAGB, the overall porosity of the sample (being large tungsten particles loosely held together by a manganese-rich matrix) makes the viability of this allow extremely low using as-received samples. Any attempt to homogenise the sample resulted in significant manganese losses, creating greater porosity than the as-received sample.

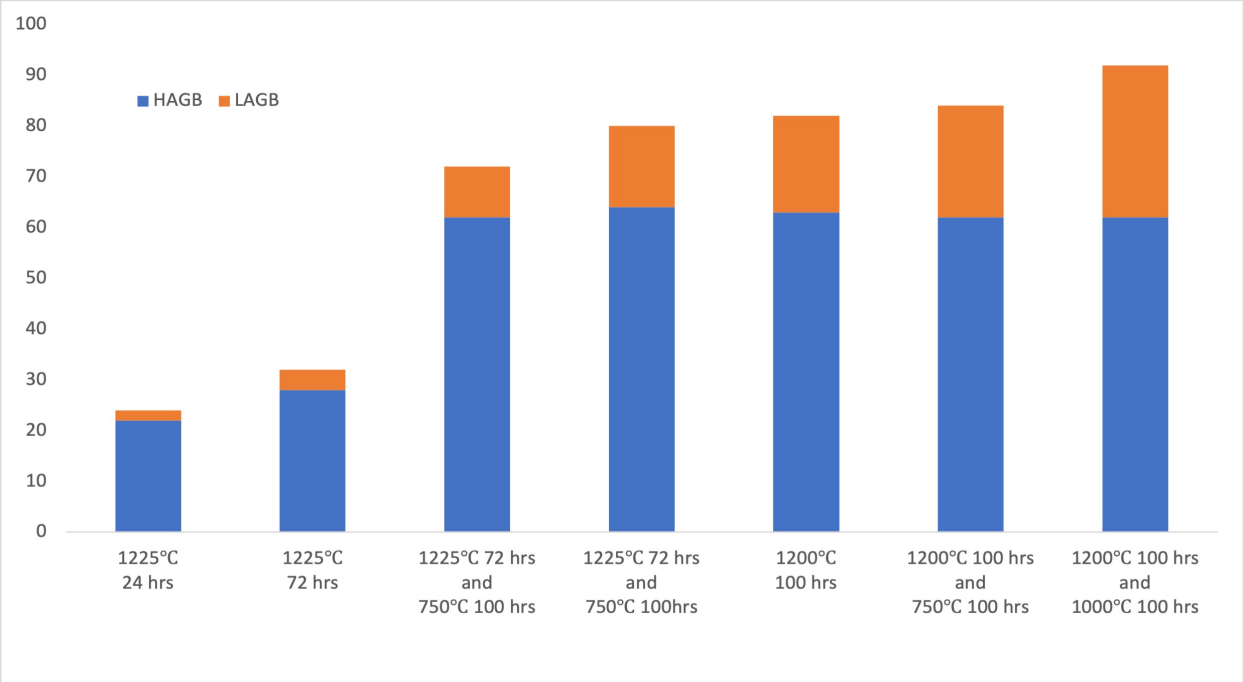

(a)

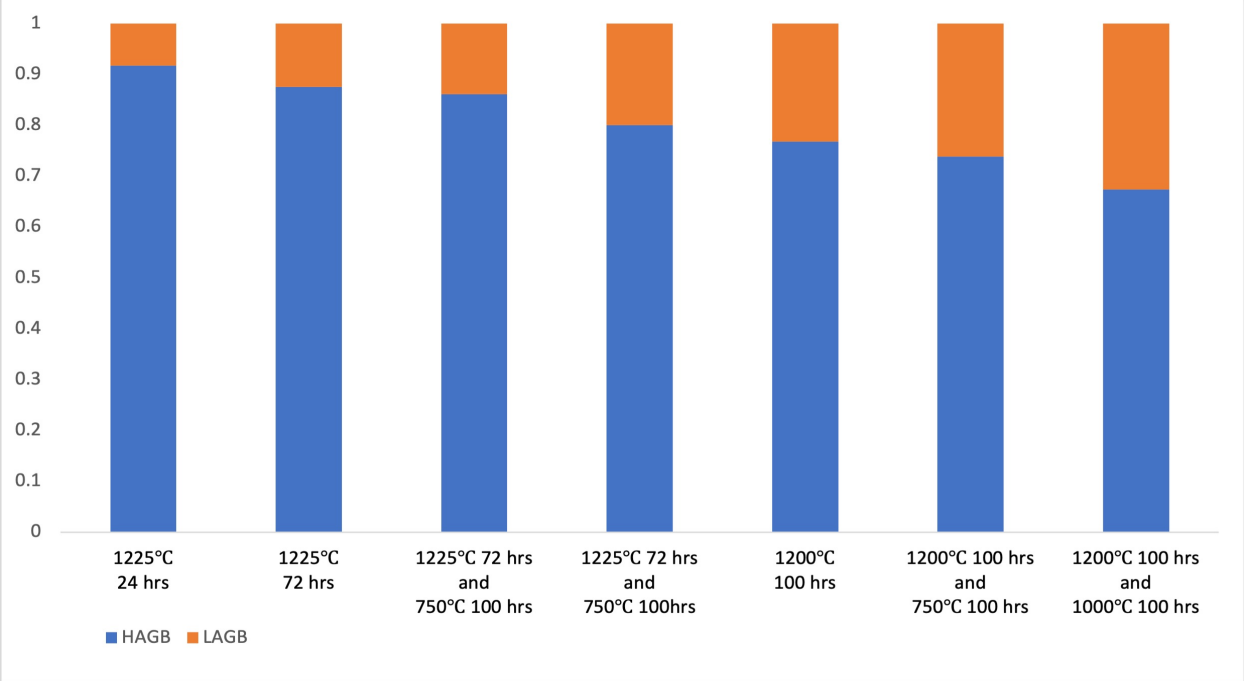

(b)

Figure 7.17: **W-Mn 50/50 at% Grain boundary analysis** (a) Total number of grain boundaries identified as either LAGB or HAGB after various heat treatments (b) Percentage fraction of grain boundaries identified as either LAGB or HAGB after various heat treatments.

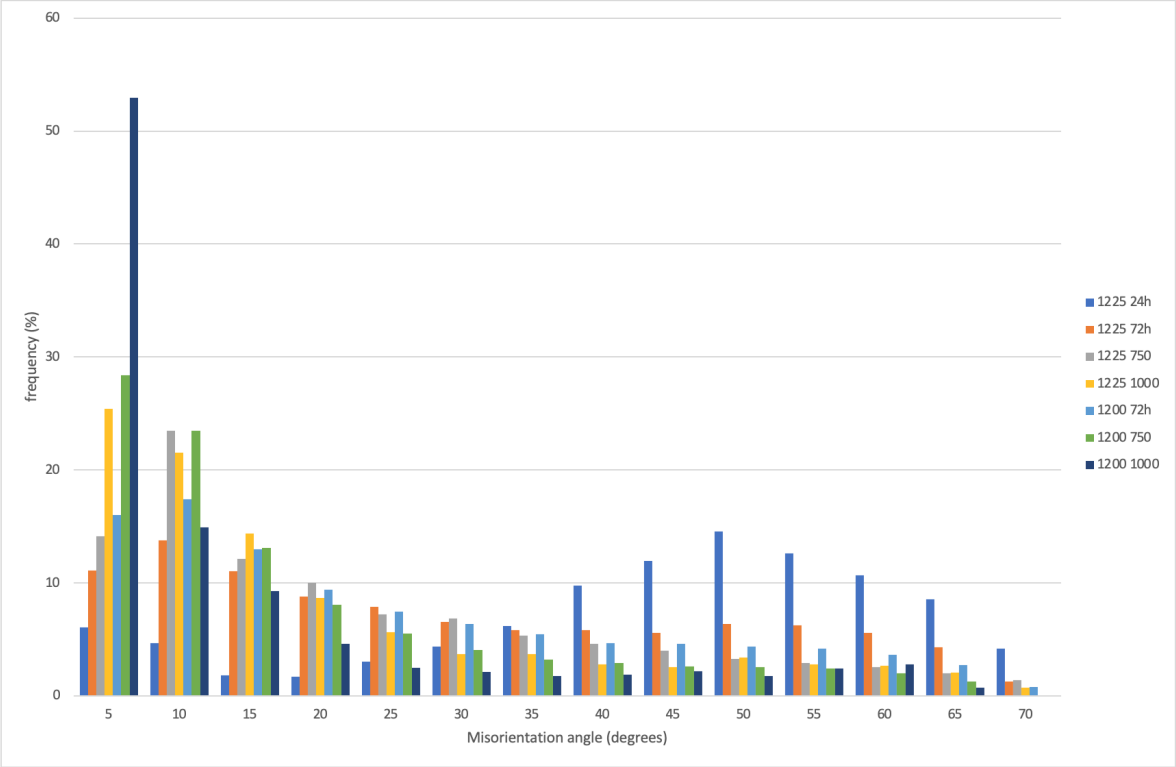

Figure 7.18: Grain Boundary misorientation at varying heat treatments of the W-Mn. The graph shows the misorientation angle of grain boundaries found at varying heat treatments of the W-Mn alloy.

7.3 Results and Discussion - W-Ti alloys

To improve the DBTT of tungsten (and, in general, bcc metals), the literature focuses on three routes; mechanical processing, either rolling or forging, and alloying; the best candidate for tungsten is rhenium, however, being a rare earth element; this has other concerns. The final method is either refining or strengthening grain boundaries. Deforming tungsten mechanically leads to an increase in the number of low-angle grain boundaries (LAGB). Tungsten alloys engineered to be ultra-fine or nanostructured grain show better mechanical properties, higher strengths with increasing temperatures, and, more importantly, improved ductility at lower temperatures than their coarser-grained alloys.

To this end, the W-Ti binary system was investigated by annealing the alloy in the proposed miscibility gap of the phase diagram (approximately 15 to 65 % tungsten). To engineer a nanostructured binary alloy that would have improved mechanical properties and the physical microstructure to aid self-annealing during radiation damage. In addition, the presence of titanium should also help to strengthen ductility as well as being able to allow better weld-ability to structural components. To this two alloys of composition, W-Ti 50/50 wt% and W-Ti 70/30 wt% were purchased and assessed for their mechanical properties following various heat treatments.

7.3.1 Arc melted W-Ti 50/50 wt% ACI

Table 28: **W-Ti 50/50 wt% and W-Ti 70/30 wt% compositional analysis.** Compositional analysis of W-Ti 50/50 wt% and W-Ti 70/30 in the as-received condition.

Alloy	Composition			
	% weight		% Atomic	
	W	Ti	W	Ti
W-50/50 wt% Ti	49.2 $\pm$ 0.8	50.8 $\pm$ 0.7	20.1 $\pm$ 0.8	79.9 $\pm$ 0.7
W-70/30 wt% Ti	69.8 $\pm$ 0.2	30.2 $\pm$ 0.3	37.6 $\pm$ 0.2	62.4 $\pm$ 0.3
W-70/30 wt% Ti- Rolled	69.5 $\pm$ 0.3	30.5 $\pm$ 0.2	37.0 $\pm$ 0.3	63.0 $\pm$ 0.4

Table 28 shows the compositional analysis of the as-received alloy. Figure 7.19 shows the as-received alloy as manufactured by ACI from arc-melted powder; as seen from the

BSE, there is macrosegregation of the tungsten and titanium. The manufactured alloy consists of what appear to be macro-segregated tungsten particles with isolated regions of titanium. Comparing the as-cast alloy to the sample homogenized for 24h at 1400 °C (figure 7.19), there are extensive regions demonstrating homogenization. However, there are still regions showing segregated segregation of titanium (however, not to the extent of the as-cast sample).

EBSD analysis (figure 7.20a) of the homogenized regions of the sample show an average grain size of 4.38 μm (this matches well to the grain size as measured by the linear intercept method, an average of 226 grains of 4.15 μm). A histogram plot of the data obtained in the EBSD is presented in figure 7.20b.

Tungsten is a well-established β eutectoid-forming stabilizing element for titanium. The ability of different elements to stabilise the β-phase of Ti alloys is encompassed by the molybdenum equivalent equation 37 Lutjering G (2007)

$$\begin{aligned} Mo_{eq} = [Mo] + 0.2[Ta] + 0.28[Nb] + 0.4[W] + 0.67[V] \\ +1.25[Cr] + 1.25[Ni] + 1.7[Mn] + 1.7[Co] + 2.5[Fe] \\ (wt\%) \end{aligned} \tag{37}$$

When Mo_{eqs} is greater than 10 wt.%, rapid quenching can result in a microstructure that contains β-Ti phase (Cotton et al. 2015). At 882.5 °C, titanium undergoes a phase transition. Below this temperature, titanium is a closed-packed hexagonal crystal structure (hcp) commonly termed α phase. Above this temperature, an allotropic phase transformation occurs to a body-centred cubic crystal structure, β stage. The purity of the metal heavily influences this phase transformation. The alloy was aged at 1000 °C to avoid this phase transition and achieve maximum nanostructure of the alloy by spinodal decomposition due to the differences in composition and lack of homogenization. BSE images (figures 7.19), EDX map, line scans (figure 7.21), and points scans (figure 7.22) show the classical two-phase decomposition associated with spinodal decomposition. The re-

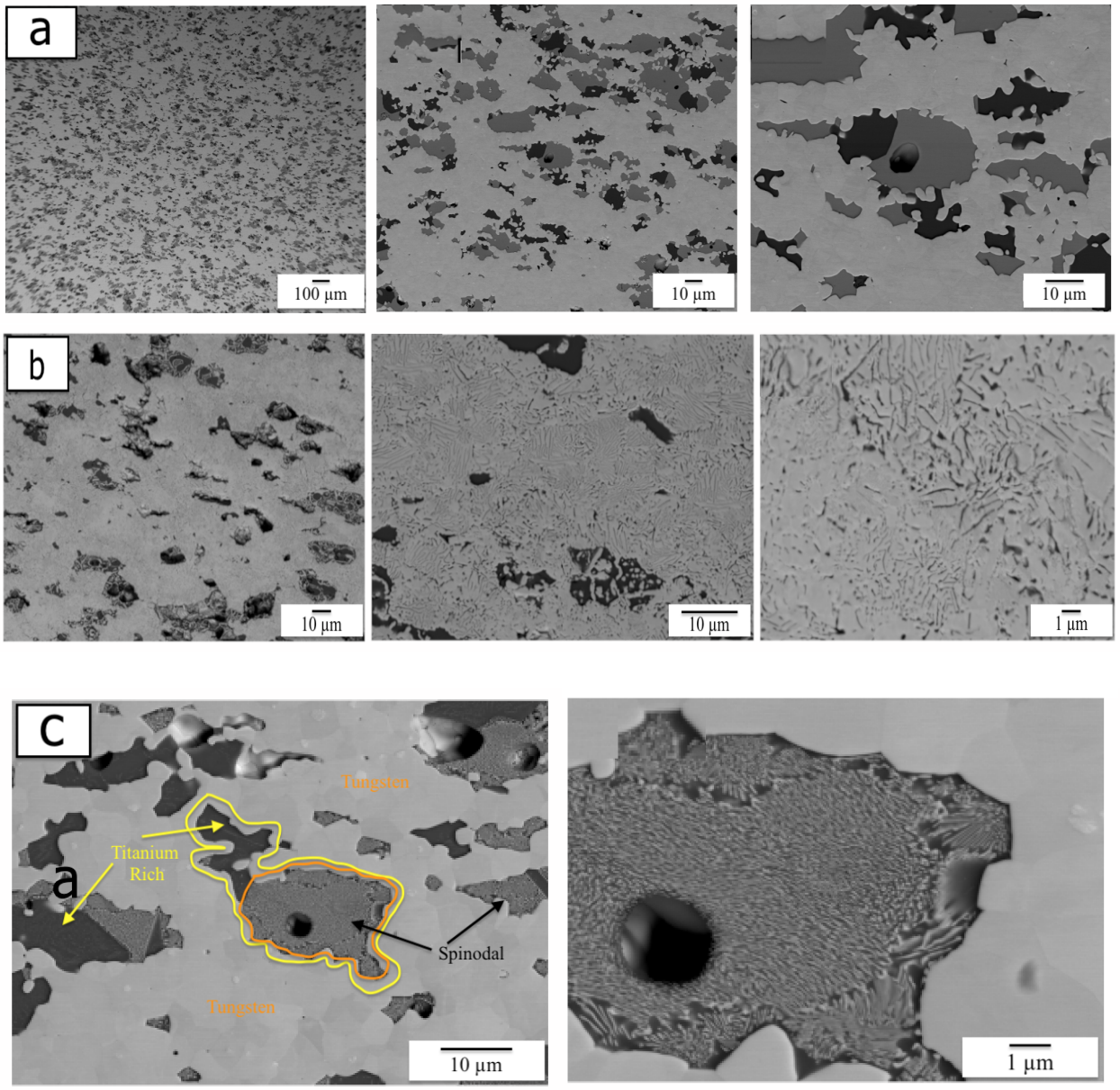

Figure 7.19: **W-Ti 50/50 wt% SEM BSE images** (a) show SEM images of the ACI alloy after homogenization at 1400 °C for 100h. (b) SEM images of the typical microstructure after homogenization at 1400 °C for 100h and ageing at 1000 °C for 100h. (c) Zoomed-in images of the decomposed regions identified in the titanium-rich regions.

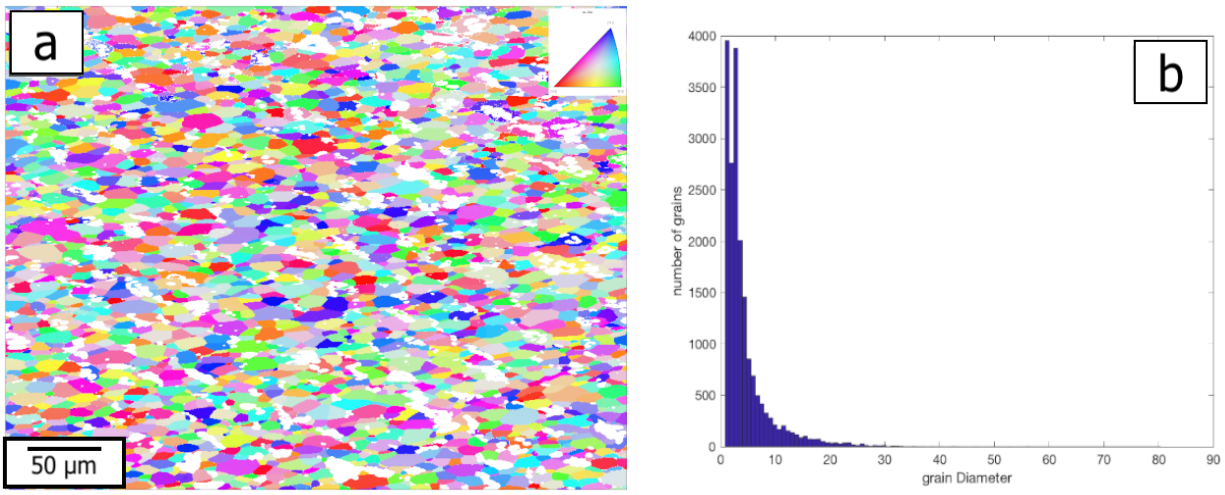

Figure 7.20: **W-Ti 50/50 wt% EBSD analysis after homogenized at 1400 °C for 24h** EBsd map and IPF key (b) Histogram showing grain size data.

sults of ageing experiments show two different nanostructured morphologies: The first is present in the tungsten-rich regions of the sample (59.67 $\pm$ 3.48 at% tungsten), with an average grain size of approximately 8.39 $\pm$ 2.65 μm. The second is a much finer microstructure with an average grain size of less than 0.05μm present in titanium-rich regions with a tungsten concentration of 14.59 $\pm$ 4.15 at% (figure 7.19 and figure 7.22).

To determine the effects of heat treatments on the overall hardness of the material. Vickers Hardness tests were carried out after homogenization and varying ageing temperatures. The results are shown in table 29. Compared to the cast sample, homogenization of the alloy at 1400 °C showed almost a doubling of the hardness from 261 $\pm$ 11.7 to 524.6$\pm$ 18.7. This could be explained by the fact that homogenizing at this temperature helps to reduce the porosity of the alloy and helps to combine the tungsten particles with the titanium matrix. The slight increase in hardness after ageing at 1000 °C and 900 °C can be explained by the decomposition seen in figure 7.19, which leads to grain refinement and nanostructuring.

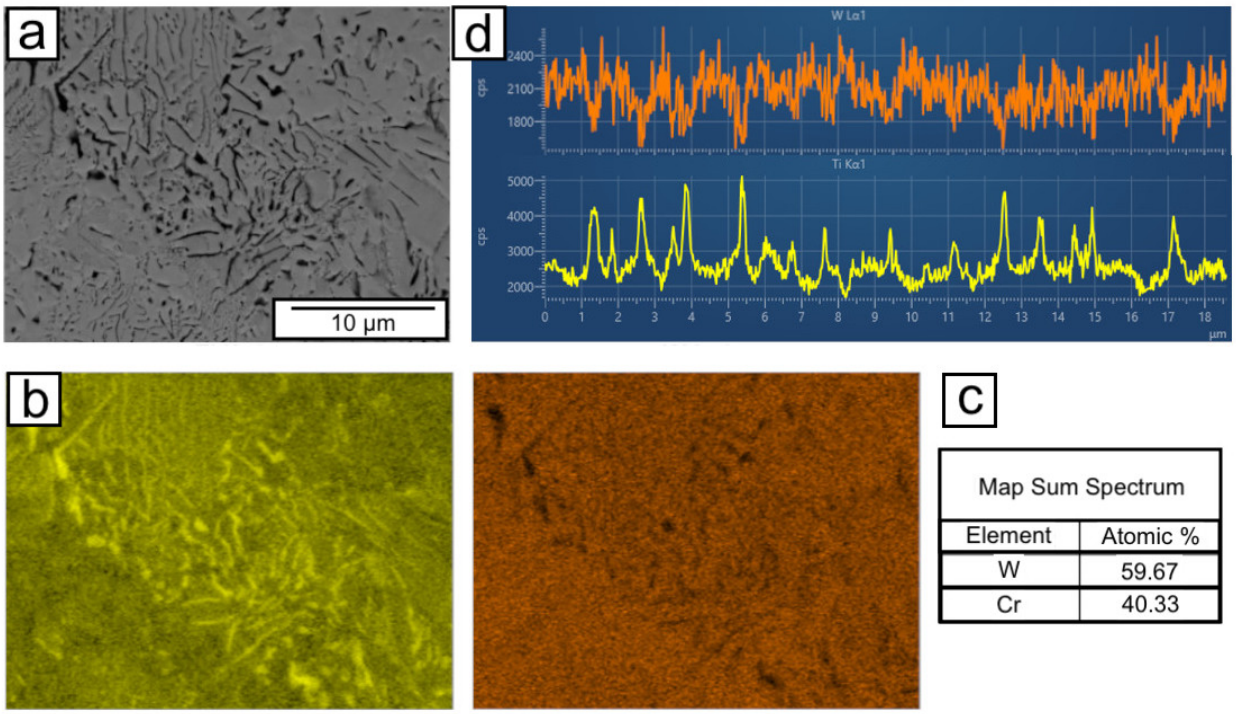

Figure 7.21: **W-Ti 50/50 wt% Analysis of the decomposition.** (a) BSE image (b) EDX map (c) composition (d) line scans of the tungsten-rich regions. Titanium is shown in yellow, and tungsten in orange.

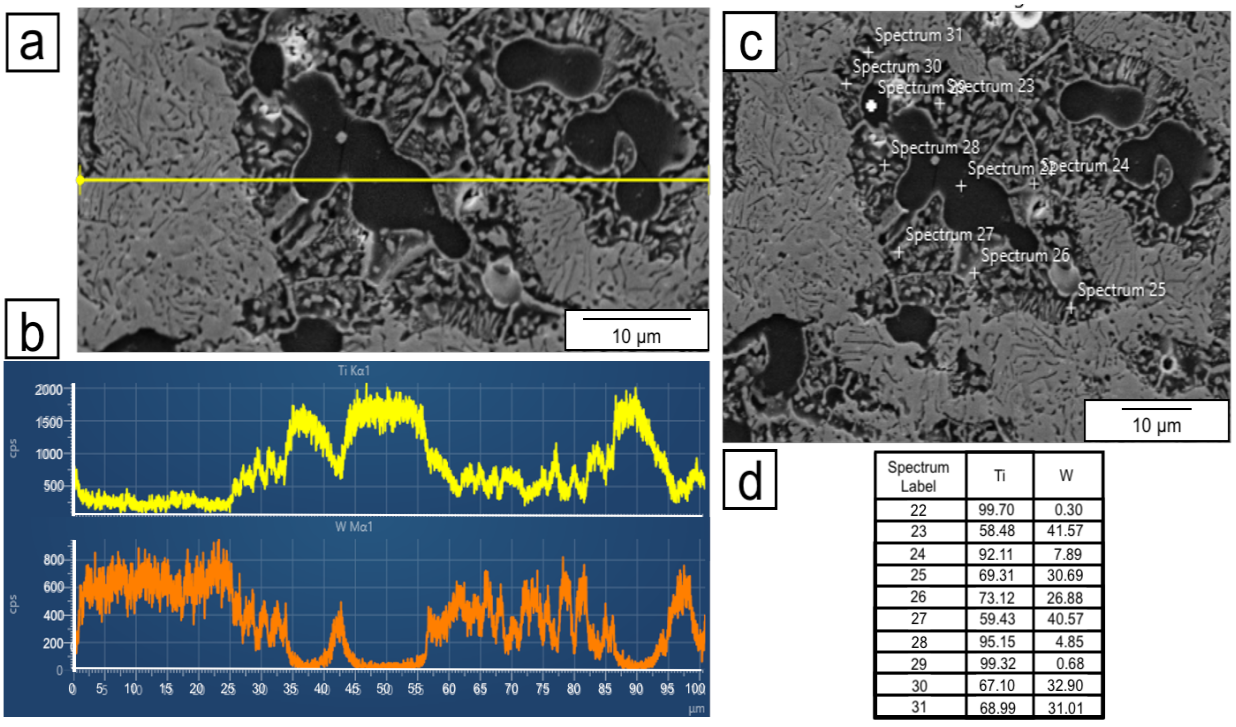

Figure 7.22: **W-Ti 50/50 wt% Analysis of spinodal decomposition** (a) line scan, (b) line scan data, (c) point scans, and (d) point values of the titanium-rich regions.

Table 29: **Hardness measurements of W-Ti 50/50 wt%** Hardness measurements for W-Ti alloy in different conditions with 2kg load

Heat Treatment	Hardness Measurements (2Kg)					Average Measurement
As Cast	253.8	260.1	236.2	271.4	252.6	**261.7 ± 11.7**
	265.4	253.8	266.9	277.2	273.6	
1400 °C Homogenisation	558.7	569.2	533.6	511.9	538.6	**542.6 ± 18.7**
	563.4	541.3	523.5	542.9	542.6	
1400 °C Homogenisation + ageing at 1000 °C for 100h	676.9	556.9	557.3	603.3	620.6	**598.2 ± 44.2**
	586.0	527.2	573.2	633.0	647.2	
1400 °C Homogenisation + ageing at 900 °C for 100h	530.6	580.1	608.2	608.1	607.5	**586.6 ± 30.0**
	593.7	527.2	600.6	604.6	609.4	

XRD analysis was conducted on each sample to determine phases present within the homogenized and aged samples. The data for the alloy in the varying ageing temperatures are shown in figure 7.23. The XRD spectrum for the as-received samples shows peaks for α and β titanium and bcc tungsten. This is confirmed by the lath structure in figure 7.25. After the homogenization of the alloy at 1400 °C, XRD of the sample still shows peaks for tungsten and for α and β titanium; this is surprising as the transus temperature for titanium is 882 °C. This would suggest that certain alloy parts were not immediately quenched and cooled more slowly than the rest. Following the ageing of the sample at both 1000 °C, the peaks for β titanium are no longer present and only peaks for bcc tungsten and α titanium are observed.

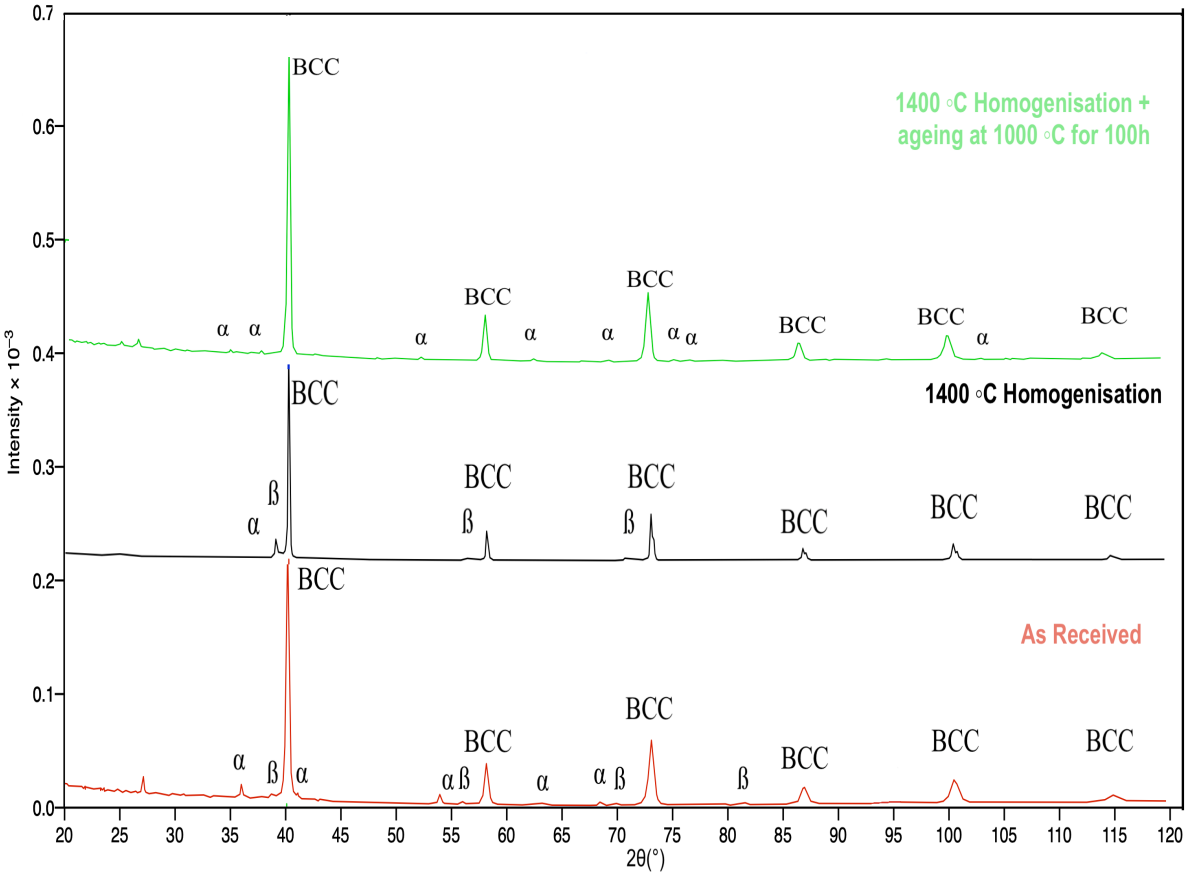

Figure 7.23: **W-Ti 50/50 wt% X-ray diffraction data.** X-ray diffraction profiles for phases present during various heat treatments. key: bcc - bcc Tungsten, α-HCP Titanium, β-bcc Titanium

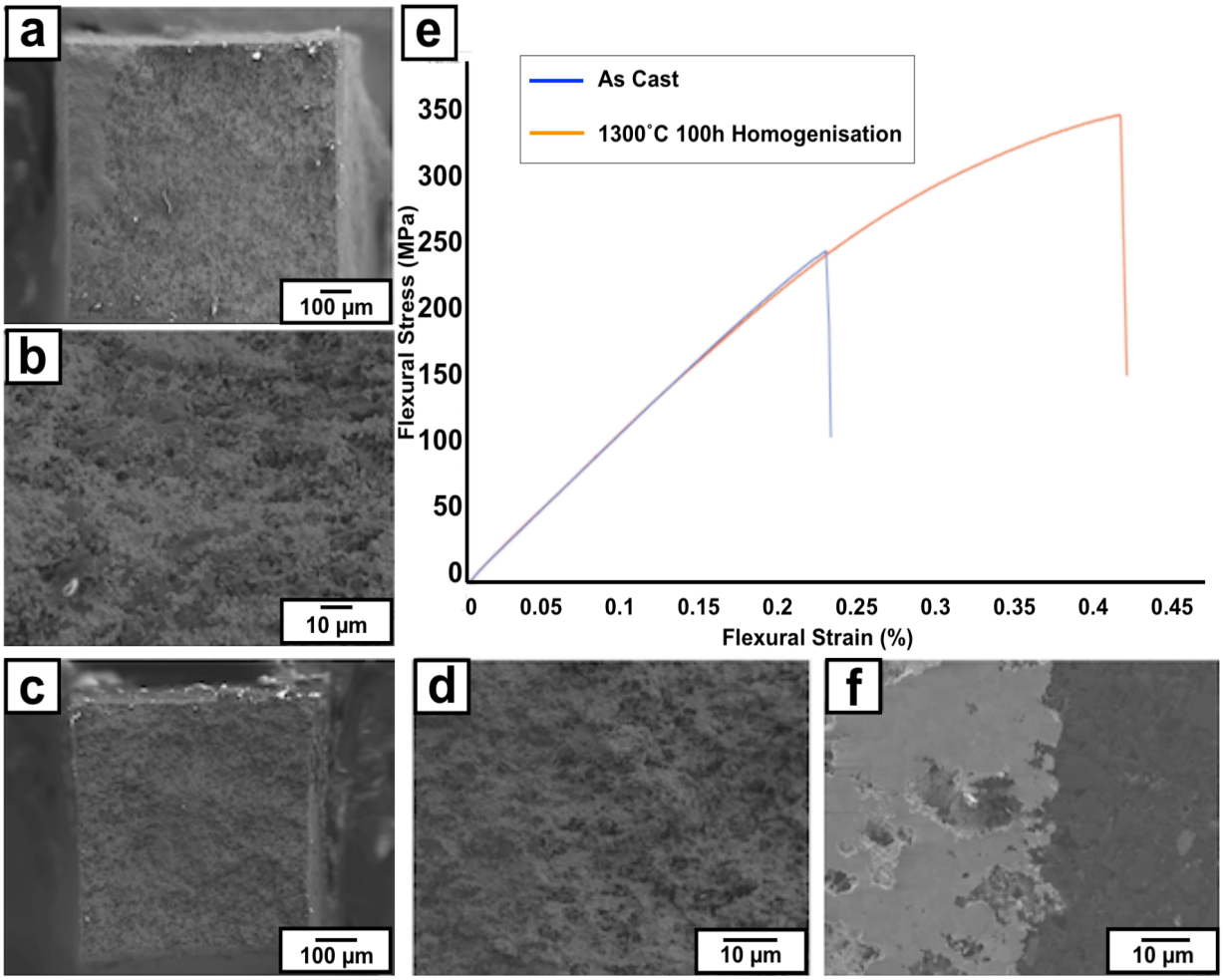

Figure 7.24: **W-Ti 50/50 wt% 3-point bending and fracture surface.** (a) Fracture surface as received, (b) High magnification SEM image of (a), (c) Fracture surface after homogenization at 1300 °C, (c) High magnification SEM image of (d), (e) Graph of the flexural stress-strain of as received and homogenized samples shown in a-d, and (f) Side profile of the fracture surface in the homogenized condition.

7.3.2 Mechanical testing of arc melted W-Ti 50/50 wt% (ACI)

The ACI alloy demonstrates complete brittle fracture. Fracture surfaces of the as-received and homogenized alloy at 1300 °C are shown in figures 7.24(a,b) and (d,e), respectively. This is further evidenced by the flexural stress-strain graph (figure 7.24c), which shows no ductile behaviour and sudden fracture of the alloy before yielding. A side profile of the homogenized alloy after fracture (figure 7.24f) shows that cleavage during 3-point bending occurs around the sintered powder particles. This suggests that the alloy's porosity and lack of density are the reasons for the premature failure of the alloy at room temperature.

7.3.3 Arc melted W-Ti 70/30 wt% (Testbourne)

With the nanostructure structuring observed in figures 7.19 and 7.21, a new tungsten 70/30 titanium Wt% alloy was purchased from Testbourne Ltd. Figure 7.25 Shows SEM micrographs as well as EDX analysis of the as-received sample. As was expected, the alloy consists of tungsten particles (light grey and orange) within a titanium matrix. Unlike the previous sample from ACI, no powder particles are present, and the sample shows almost 100% density. Figure 7.25e shows the titanium matrix consists of a two-phase microstructure of primary α and β lamellar structure with α grain boundaries. The β phase is present because tungsten is a known β titanium stabiliser. Preventing the transformation of β to α during the high cooling rate of arc melting. EDX characterization of the alloy (Table 32) shows three distinct regions. One is a tungsten-rich region consisting of unmelted tungsten particles. The second region consists of almost pure titanium, seen as bright yellow lamellar and at the grain boundary edges (figure 7.25b) on the EDX images, and a third region, rich in titanium, but with a slightly richer composition of tungsten. The differing lamellar strips represent the α and β titanium phases, with the α phase characterised by the brighter titanium-rich phase and the β phase represented by the duller titanium tungsten richer phase. The presence of several phases confirms the lack of homogenization of the alloy due to the difference in the melting points. Table 30 shows the Vicker's hardness of the as-received alloy to be 360.5 $\pm$ 19.9, which is significantly higher (+100) than that of the ACI alloys, further confirming the density of the alloy as compared to that of the powder-based alloyed manufactured by ACI.

To further study the potential of W-Ti in the as-received alloy, mechanical testing was carried out using 3-point bending at room temperature. Compared to the results obtained from the previous alloy, it demonstrates more of a ductile behaviour as seen from the 3-point bending curve in figure 7.26b. Although low magnification images (figures 7.26c-d) show classic brittle failure. A high magnification image of the fracture surface (figure 7.27) shows voids nucleated by the loss of powder particles. Apparent dimples, otherwise known as 'equiaxed dimples', are seen in the SEM image in addition to river plates

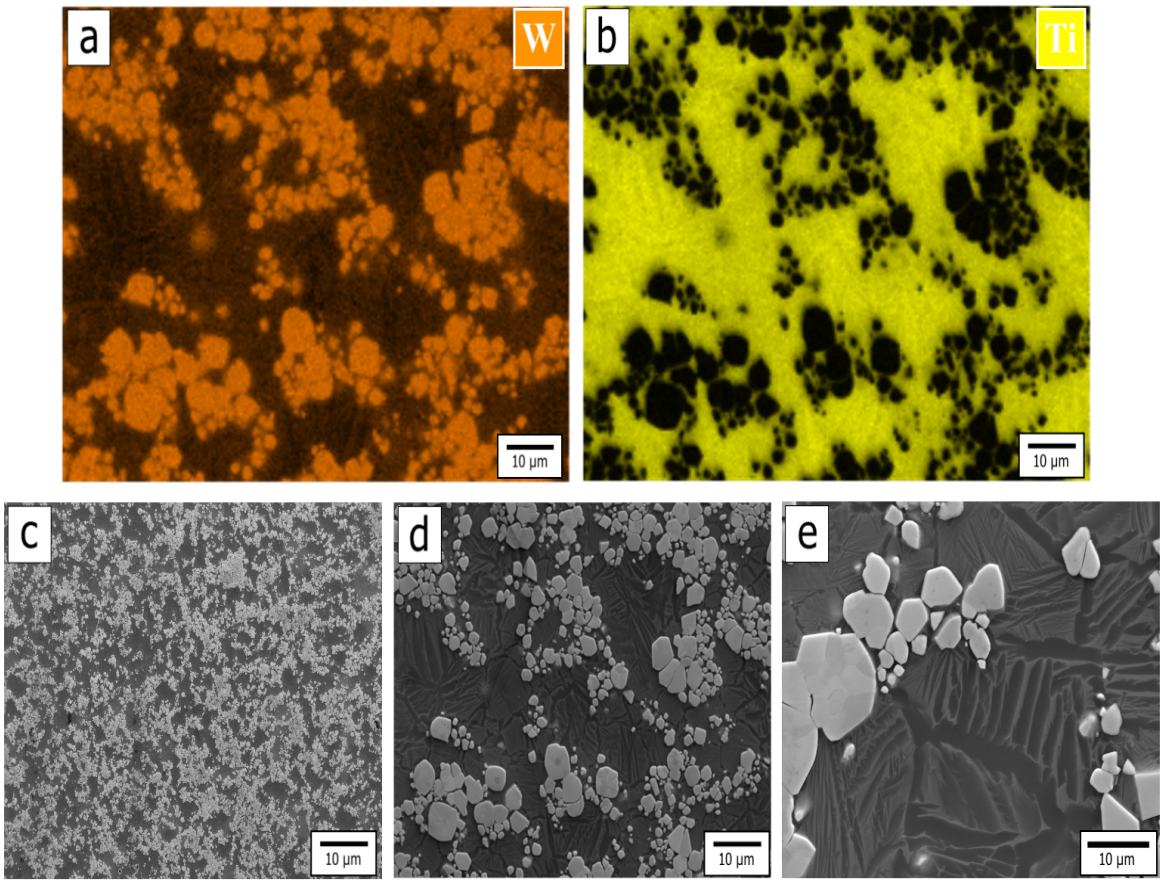

Figure 7.25: **W-Ti 70/30 wt% EDX and BSE analysis in the as received coniditon** EDX maps of (a) Tungsten (b) Titanium (c-d) BSE images at increasing magnifications (e) Shows α and β laths of titanium as seen in XRD analysis along with unmelted tungsten particles

demonstrating transgranular fracture. This would suggest that the titanium-rich regions in the sample are undergoing ductile failure with the loss of tungsten powder particles.

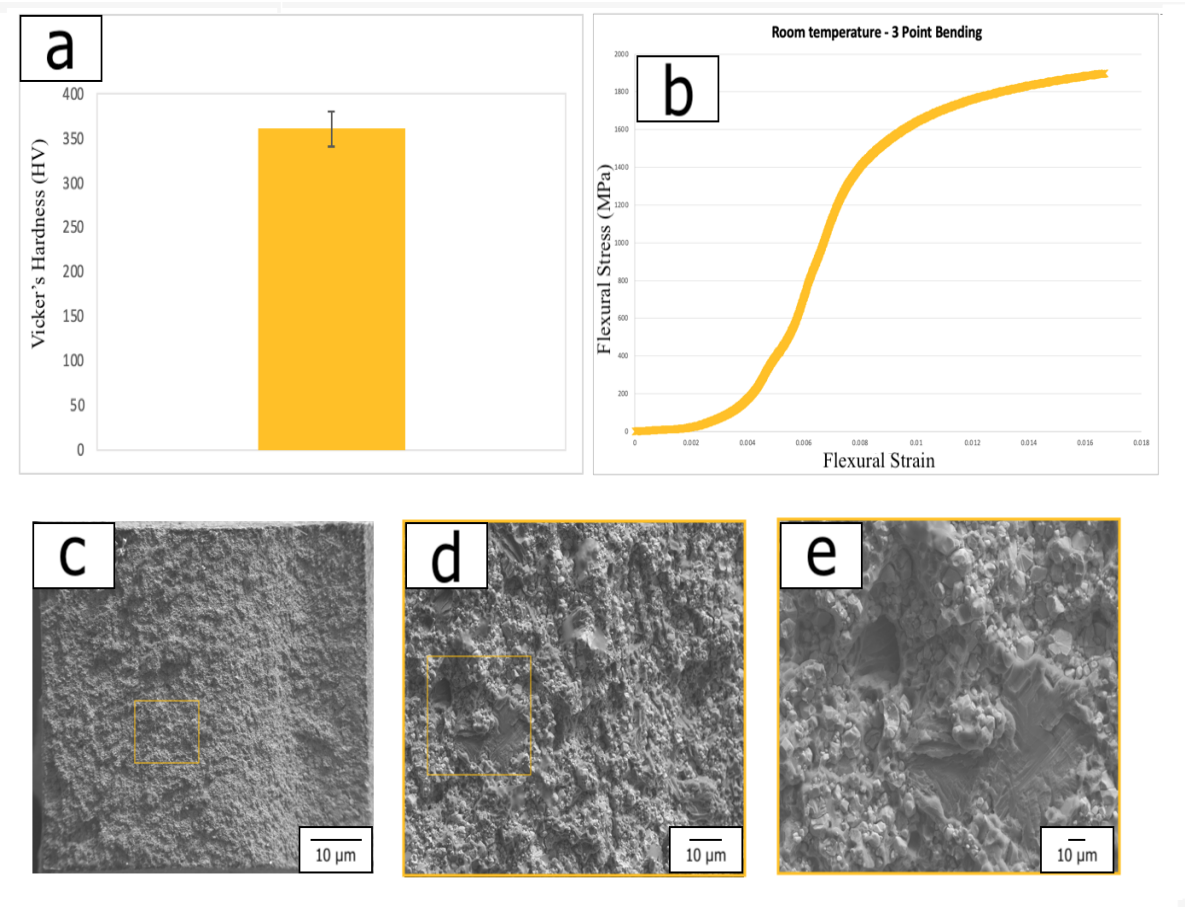

Figure 7.26: **W-Ti 70/30 wt% mechanical 3-point bending in the as-received condition** (a) Vickers hardness measurement (b) Graph of the flexural stress-strain of as-received alloy (c-e) BSE images of the fracture surface at increasing magnifications.

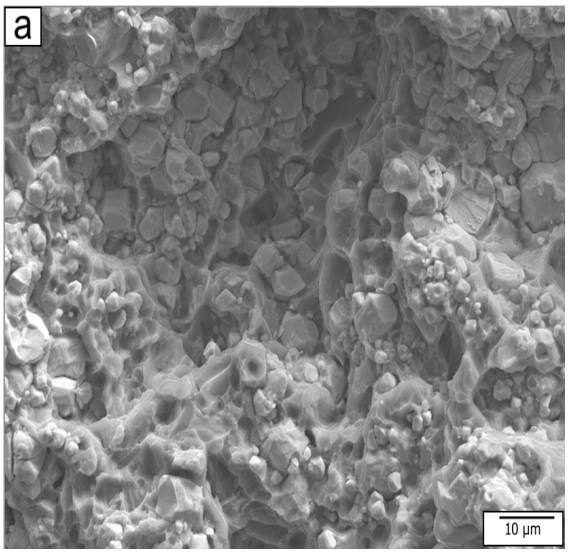

Figure 7.27: **W-Ti 70/30 wt% evidence of ductile fracture in the as-received alloy after 3-point bending at room temperature** BSE image of the fracture surface showing evidence of microvoids probably from the residual powder particles.

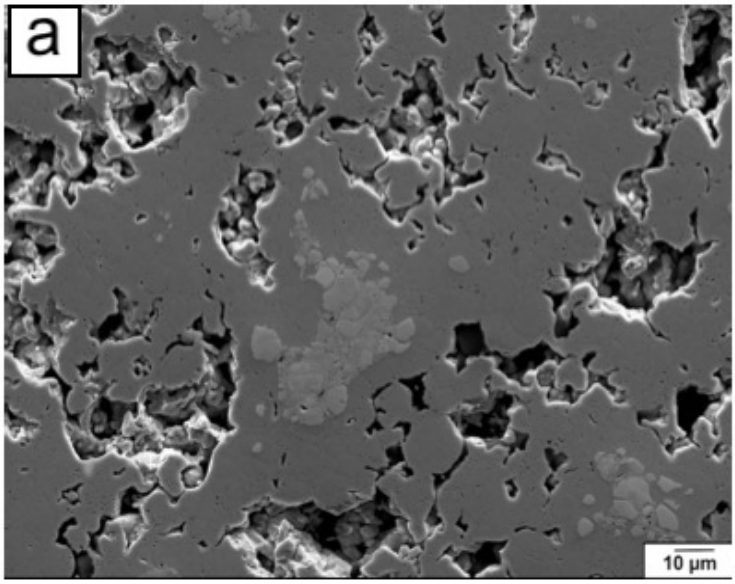

Figure 7.28: **W-Ti 70/30 wt% homogenized at 1400 °C.** (a) BSE image W-30Ti wt% homogenized at 1400 °C for 100h.

7.3.4 Homogenisation and aging of W-Ti 70/30 wt% alloy

To determine if a homogenous microstructure of the new alloy can be created, the as-received alloy was heat treated at 1400 °C for 100h. The resulting microstructure is shown in figure 7.28. From The BSE, we can still see large clusters of unmelted tungsten particles (a light grey area in the middle of the image). There are also large areas where voids can be seen from the loss of powder particles (most likely tungsten) from the sample during the heat treatment. To determine if the microstructure could be further controlled through ageing, the sample was held at 1000 °C for 100h. The resulting microstructure is shown in figure 7.29. Following this ageing process, the EDX scans and BSE show a fine lamellar structure composed of tungsten (orange) within a titanium-rich matrix. This confirms that at 1000 °C, there is a miscibility gap in the Tungsten-Titanium binary system. Despite attempts at homogenization and different ageing times, there were still large particles of unmelted tungsten within the sample. In addition, the lack of sintering in either the manufacturing stage or the homogenizing phase resulted in the loss of tungsten. These voids could be sites for initiating cracks and stresses during mechanical testing.

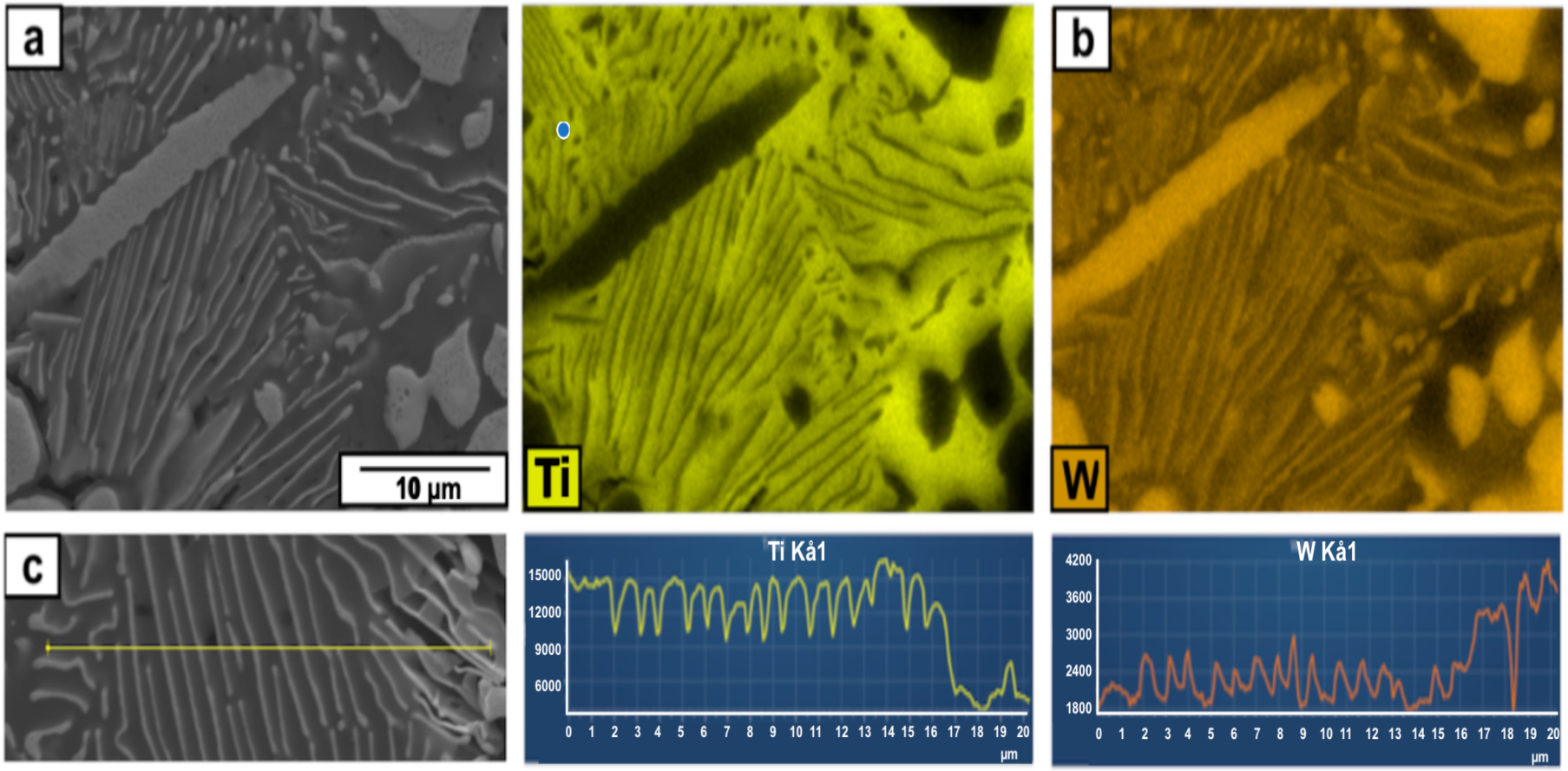

Figure 7.29: **W-Ti 70/30 wt% aged at 1000 °C for 100h** (a) BSE image (b) EDX map tungsten (orange) titanium (yellow) (c) line scan data, for W-Ti homogenized at 1400 °C 100h and aged at 1000 °C for 100h.

Table 30: **Hardness measurements of W-Ti 70/30 wt%.** Vicker's Hardness measurements for W-Ti alloy after different heat treatments with 2kg load

Heat Treatment	**Hardness Measurements (2Kg)**					**Average Measurement**
As Cast	395.9	352.6	356.9	348.3	379.3	**360.5 $\pm$ 19.9**
	381.3	361.2	334.2	336.2	359.5	
1400 $^{\circ}$C Homogenisation	396.5	402.8	368.3	393.8	414.8	**383.5 $\pm$20.1**
	361.9	351.8	368.6	391.5	381.5	
10% Rolled at Room temperature	420.8	419.6	418.4	427.2	426.0	**421.4$\pm$3.6**
	414.8	423.6	422.4	421.4	420	
80.1% Rolled 1000 $^{\circ}$C	449.8	449.6	449.4	449.2	449.0	**448.4$\pm$2.5**
	448.0	442.2	446.6	451.6	448.8	

7.3.5 Rolling of W-Ti 70/30 wt%

The alloy was rolled at 1000 °C to improve alloy density and mechanical properties through work hardening. A sample of W-Ti 70/30 wt% measuring 49.99 x 17.19 x 12.35 (mm) was initially heated to 1000 °C for 30 minutes. It was then rolled with 1mm reductions at a speed of 5 metres per minute, with 5-minute reheats at 1000 °C between passes, to a final thickness of 2.84 mm, giving an absolute reduction of 80.1%.

7.3.6 Texture and Rolling of W-Ti 70/30 wt%.

The $\phi 2$ = 45 ° section can be used to illustrate the texture of a bcc alloy following rolling. The $\phi 2$ = 45 ° has two main fibres; the αfibre which runs from the 001<110> with 111<110> which describes the <110>||Rolling Direction. The second is the γ fiber which begins from 111<110> direction to the 111<112> equivalent to <111>||Normal direction (Figure 7.30i).

To determine the texture evolution of this alloy following rolling. EBSD of the tungsten phase was conducted on a sample of the alloy rolled at room temperature to 10% and to 80.1% (at 1000 °C) (as shown in figure 7.30 d and h respectively. From this data, a Grain Reference Orientation Deviation (GROD) map (Figure 7.30c and g) for each rolled sample was constructed along with the ODF $\phi 2$ = 45 ° maps (Figure 7.30a and e) respectively. At 10% reduction, there is a weak intensity of twice that of a random orientation for the α bcc fibre. There is also a weak (2.2) intensity for the ϵ fibre. In the 80.1% rolled sample, there is no intensity shown for the fibres, instead only a weak maximum (2.4) near 112 <110> rotated cube position. The lack of intensity changes, or for the tungsten phase to deform along fibres, suggests that the deformation induced in this alloy is with the titanium matrix. GROD data also confirms the lack of misorientation and deformation within the tungsten particles. The average GROD for the 10% rolled sample is 1.92 compared to 2.53 for the 80.1% sample.

EBSD patterns of the side profiles of the sample rolled to 80.1% were conducted for the tungsten phase in figure 7.31 and the titanium phase in figure 7.32. The phases were separated to identify which alloy phase had the most deformation. Both the ODF,

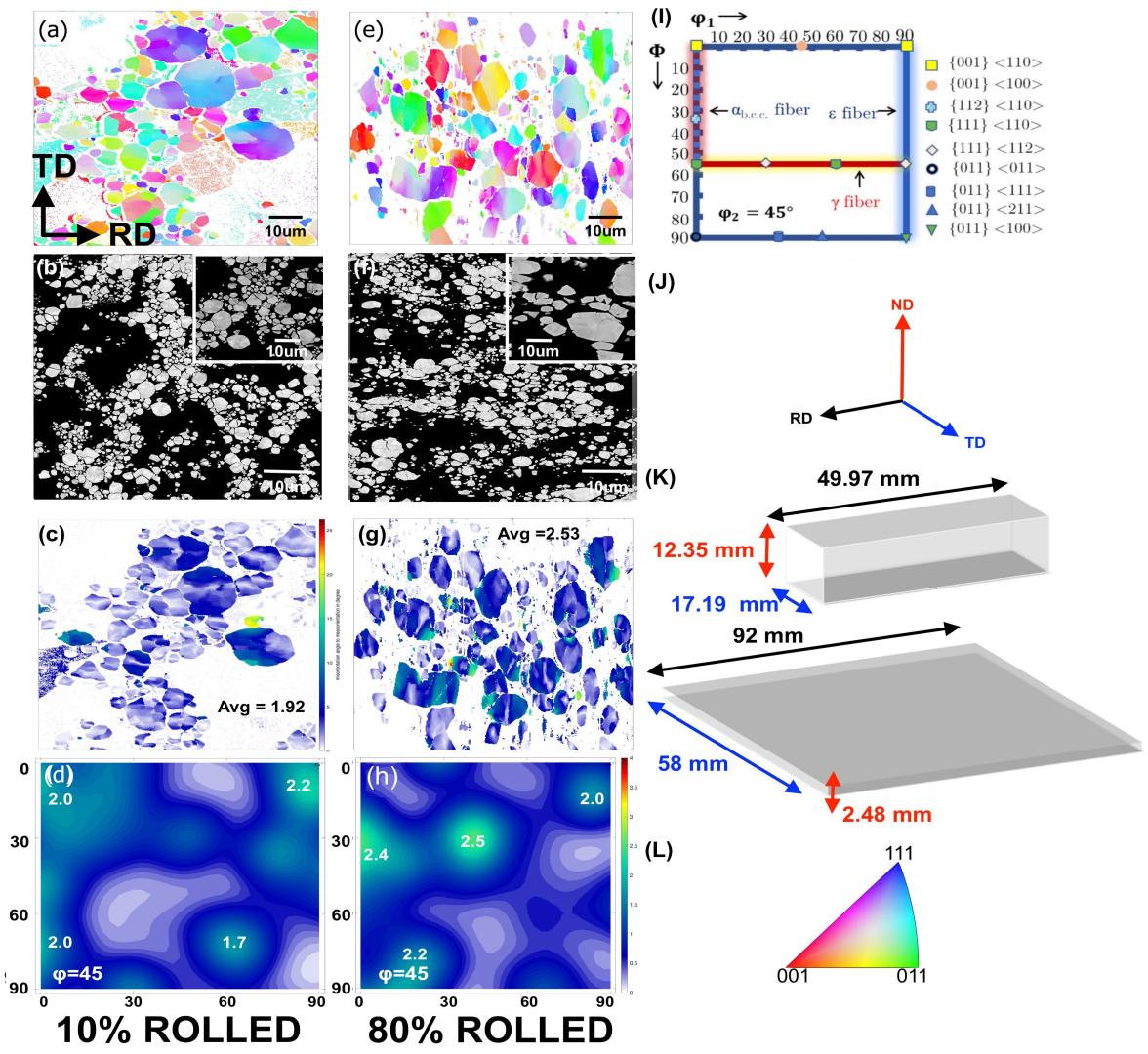

Figure 7.30: **W-Ti 70/30 wt% rolled at 1000 °C EBSD comparison of the texture profile of the tungsten particles following deformation of 10% and 80.1%.** (a) EBSD map, (b) BSE image, (c) GROD map, (d) ϕ=45 ODF map, (e) EBSD map, (f) BSE image, (g) GROD map, (h) ϕ=45 ODF map (i) Fibre texture taken from (Kumar 2022), (j) Orientation figure, (k) schematic diagrams of sample before and after 80.1% deformation and (l) IPF key.

$\phi 2$ = 45 $^\circ$ map (figure 7.31c) and the IPF maps (figure 7.31d) show a slight texture to that of the 001 plain however with a 1.8 and MUD value of 1.63 for the ODF and IPFs respectively there is little significance which can be placed on this. It, therefore, suggests that the tungsten particles show any texture following rolling. However, on the EBSD of the titanium matrix phase, there is evidence of texture following the rolling of the sample. Figure 7.32a shows pole figures for the HCP titanium phase indexed in from the side profile. Although the 1010 and 1011 poles show no real intensity, the 0001 pole shows a region of 8.1 intensity compared to the background. Using stereographic projections from the literature suggests that the basal pole is directed towards the $(1\bar{1}15)$ direction on deformation. If a comparison is also made between the GROD maps of the tungsten and titanium phases, orientation distribution is greater in the titanium phase than in the tungsten particles. Giving further argument to the titanium phase undergoing greater deformation.

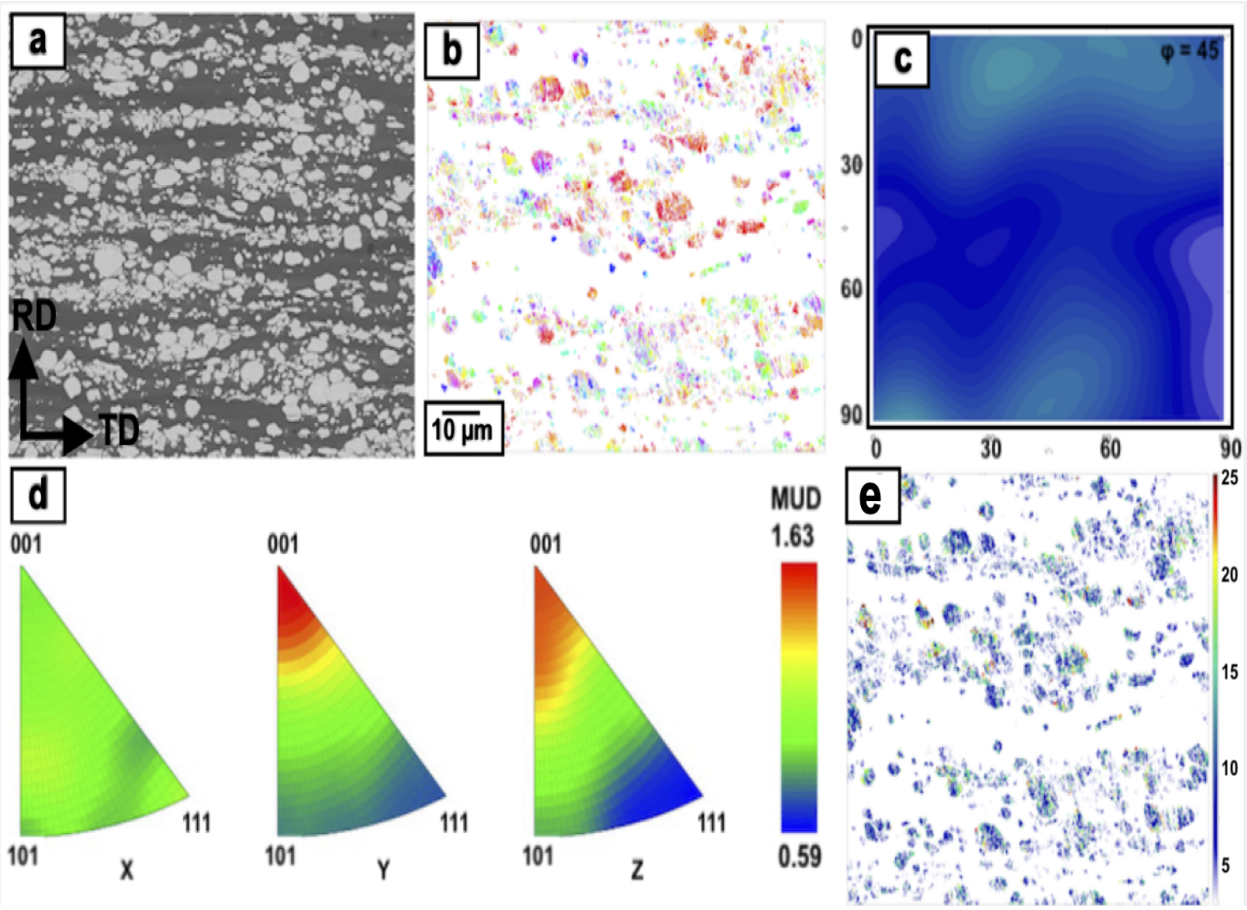

Figure 7.31: **W-Ti 70/30 wt% EBSD analysis of the tungsten phase in the side profile of rolled W-Ti rolled at 1000 °C with deformation of 80.1%.** (a) Band contrast map, (b) EBSD map, (c) ϕ = 45 ODF map, (d) inverse pole figures, and (e) GROD map

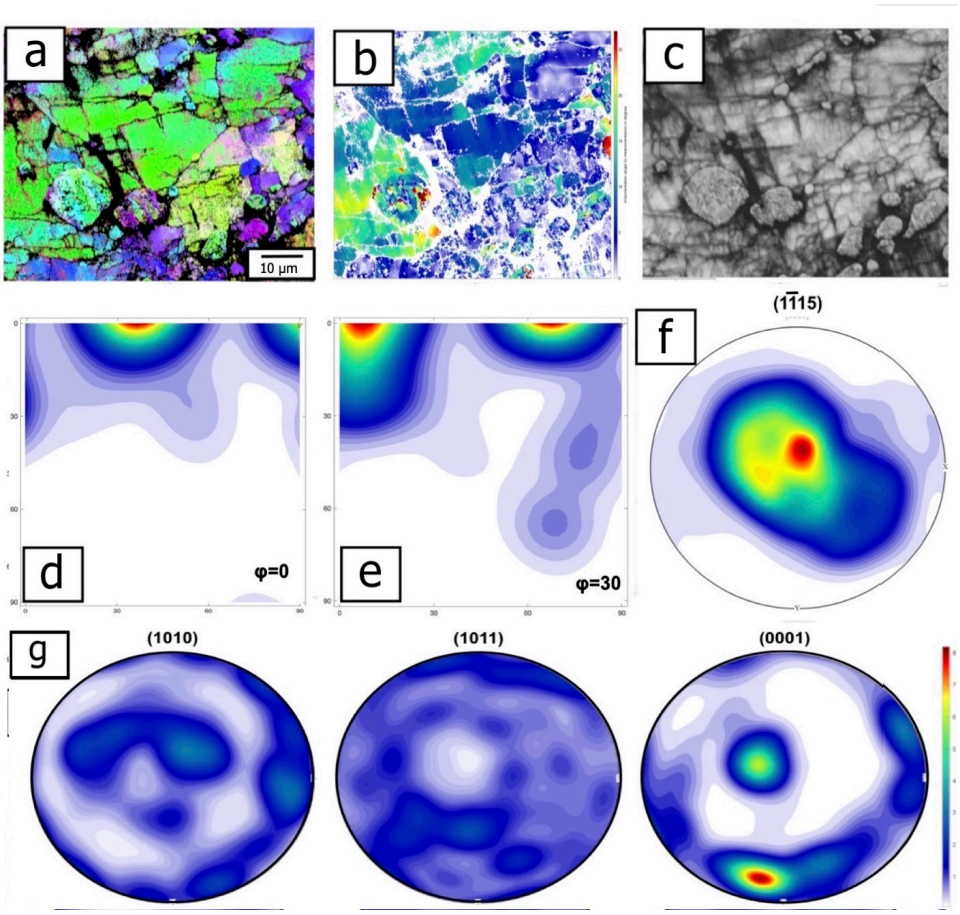

Figure 7.32: **W-Ti 70/30 wt% rolled at 1000 °C EBSD analysis of the Titanium phase in the side profile of rolled W-Ti rolled at 1000 °C with deformation of 80.1%.** (a) EBSD map (b) GROD map (c) band contrast map (d and e) ϕ= 0 and 30 ODF maps, (f) (1-115) pole figure (g) Pole figures (1010), (1011), and (0001).

7.3.7 Bending Tests of W-Ti 70/30 wt%

12mm x 2mm x 2mm bars were cut from the rolled sample of W-Ti. As shown in Figure 7.30 j-k, either in the transverse direction (TD) or rolling direction (RD). 3-point bend tests were then conducted on the above samples at varying temperatures from room temperature (RT) up to 250 °C. Figure 7.33a and b show the three-point bending stress-strain curves diagrams for the samples cut in the transverse and rolled directions, respectively. Mechanical data obtained from the three-point bending is presented in Table 31. The DBTT of the as-rolled samples was observed to be in the range of 200-225 °C and 150-175 °C transverse and rolled directions, respectively. The samples were then annealed at 1000 °C for 100h to determine what effect this would have on the alloy's mechanical properties. Figure 7.33c and d show the three-point bending stress-strain curves diagrams for the samples cut in the transverse and rolled directions, respectively. Mechanical data obtained from the three-point bending is presented in Table 33. The DBTT of the annealed samples were observed to be in the range of RT-100 °C and 50-100 °C transverse and rolled directions, respectively. Except for the samples cut in the rolling direction and annealed at 1000 °C, the stress-strain curves are almost horizontal once the elastic limit has been reached. This demonstrates that no strain hardening is occurring in the materials. Contrary to this, the samples cut in the rolling direction and annealed at 1000 °C show strain hardening for bending temperatures over 100 °C.

7.3.8 3 – point bending tests of W-Ti 70/30 wt%

For each of the 3 – point bending tests, in the as rolled condition and following annealing at 1000 °C for 100h. BSE images of the typical fracture surfaces were captured for the end on fracture surface (figures 7.34 and 7.36) and side profile views (figures 7.35a and 7.35b) for the samples cut parallel to the rolling direction.

In the as-rolled sample, the fracture surface of the sample bent at 150 °C figure 7.34a (left) shows two distinct regions; the top of the 55% of the sample is heavily populated with large dark regions (figure 7.34a (middle)). These dark regions (depressions) can be seen

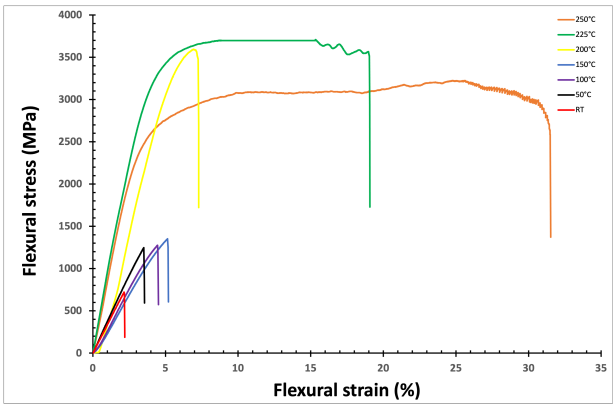

(a) As rolled, Rolling Direction

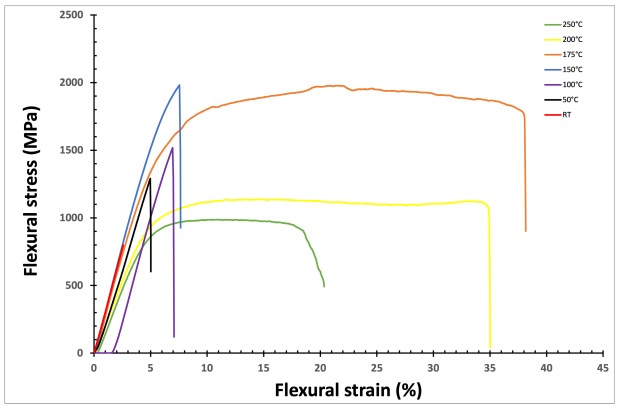

(b) As rolled, Transverse Direction

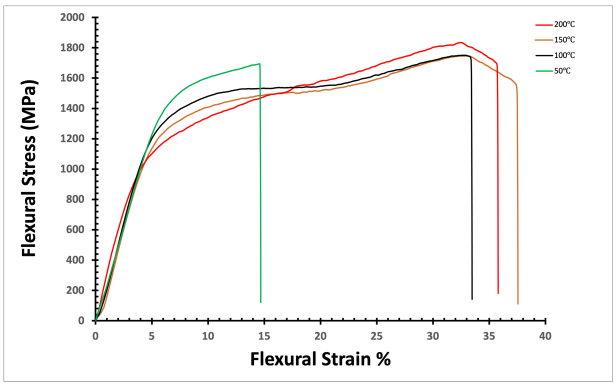

(c) Rolling Direction 1000 °C 100h

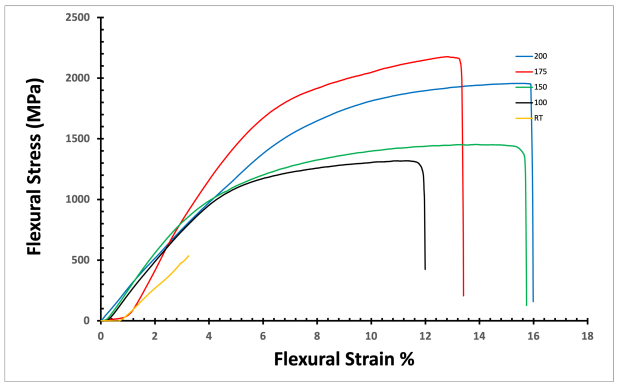

(d) Transverse Direction 1000 °C 100h

Figure 7.33: **W-Ti 70/30 wt% rolled at 1000 °C Flexural Stress-Strain diagrams from 3-point bending tests.** (a) As rolled, Rolling Direction, (b) As rolled, Transverse Direction,(c) Rolling Direction 1000 °C 100h and (d) Transverse Direction 1000 °C 100h.

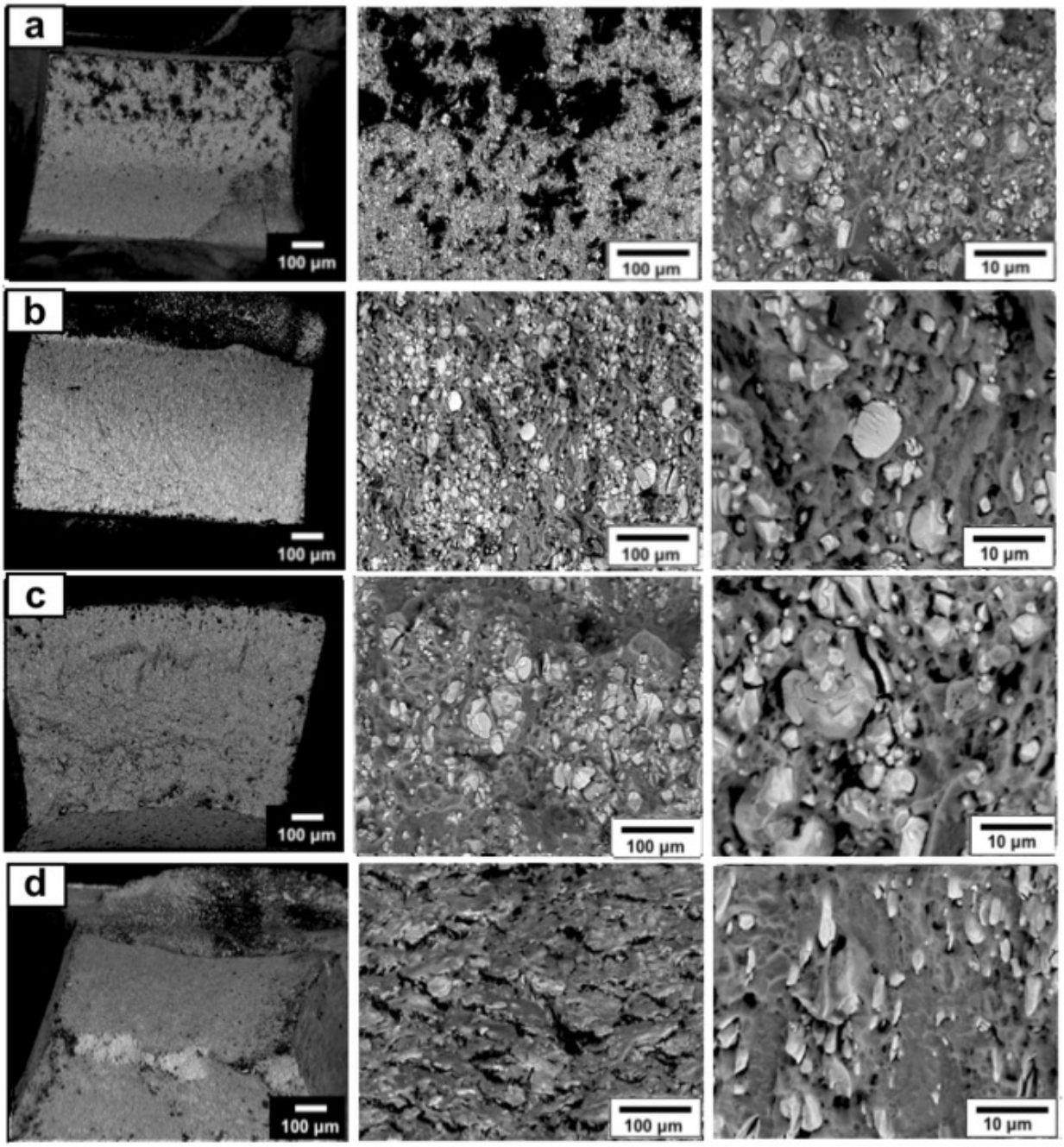

Figure 7.34: **W-Ti 70/30 wt% rolled at 1000 °C SEM BSE image of fracture surfaces after 3-point bending at different temperatures.** 3-point bending fracture surfaces after testing at (a) 150 °C, (b) 200 °C (c) 225 °C and (d) 250 °C of W-Ti in the as-rolled direction.

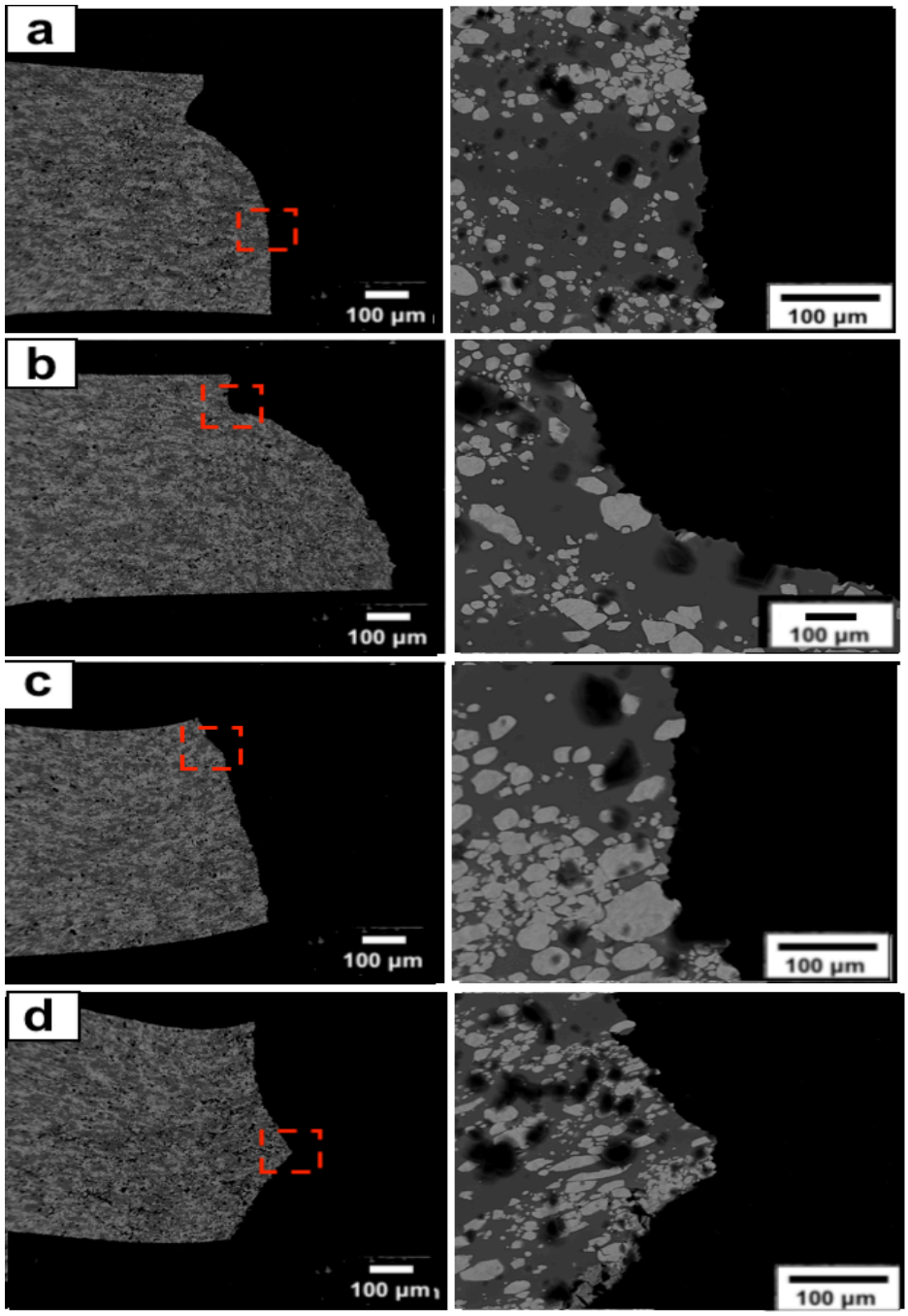

Figure 7.35: **W-Ti 70/30 wt% rolled at 1000 °C SEM BSE image of the side profile of fracture surfaces after 3-point bending at different temperatures** 3-point bending fracture surfaces after testing at (a) 150 °C, (b) 200 °C (c) 225 °C and (d) 250 °C of W-Ti in the as-rolled direction.

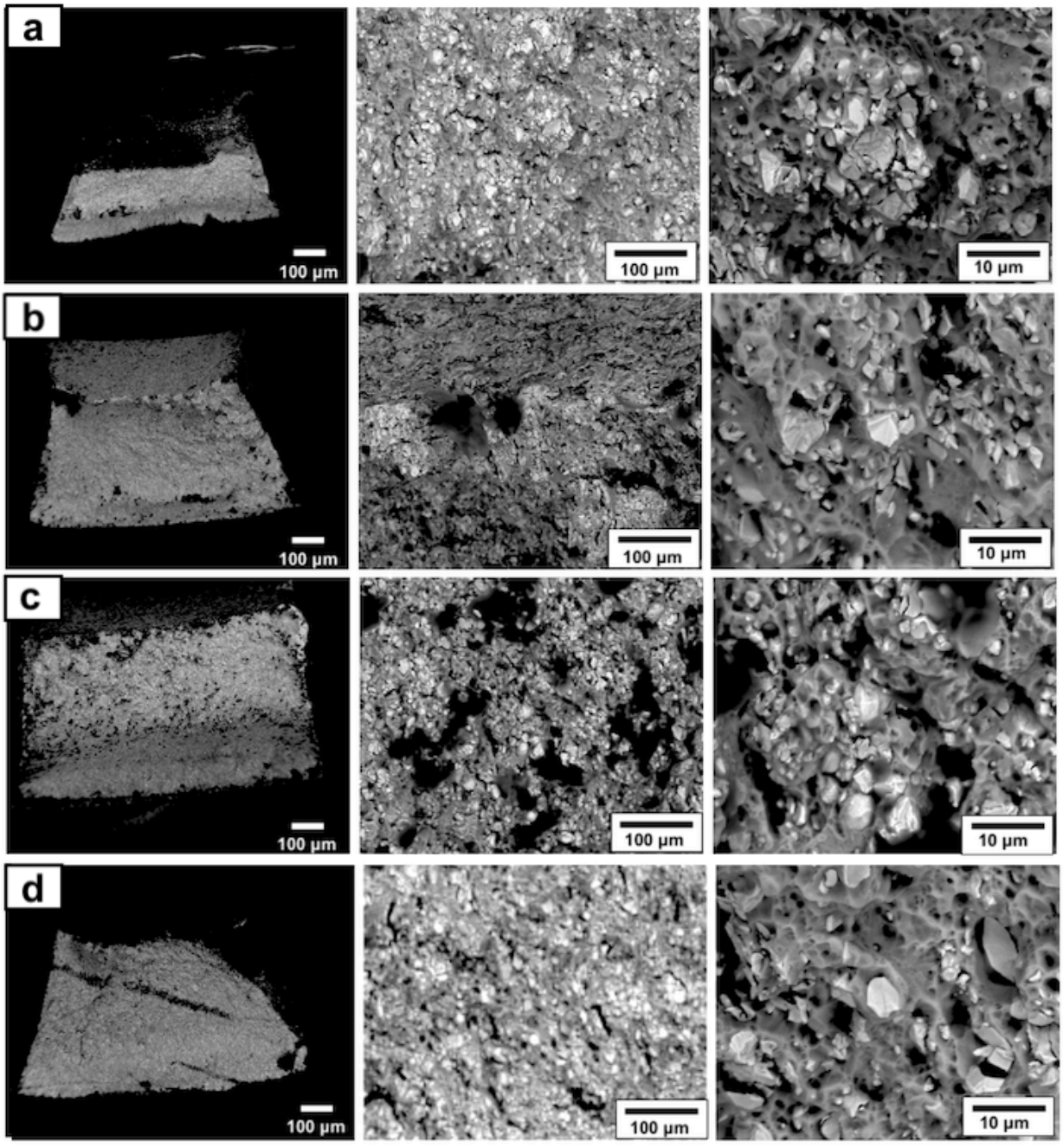

Figure 7.36: **W-Ti 70/30 wt% rolled at 1000 °C SEM BSE image of fracture surfaces after 3-point bending at different temperatures.** 3-point bending fracture surfaces after testing at (a) 150 °C, (b) 200 °C (c) 225 °C and (d) 250 °C of W-Ti in the as-rolled direction after aging at 1000 °C for 100h.

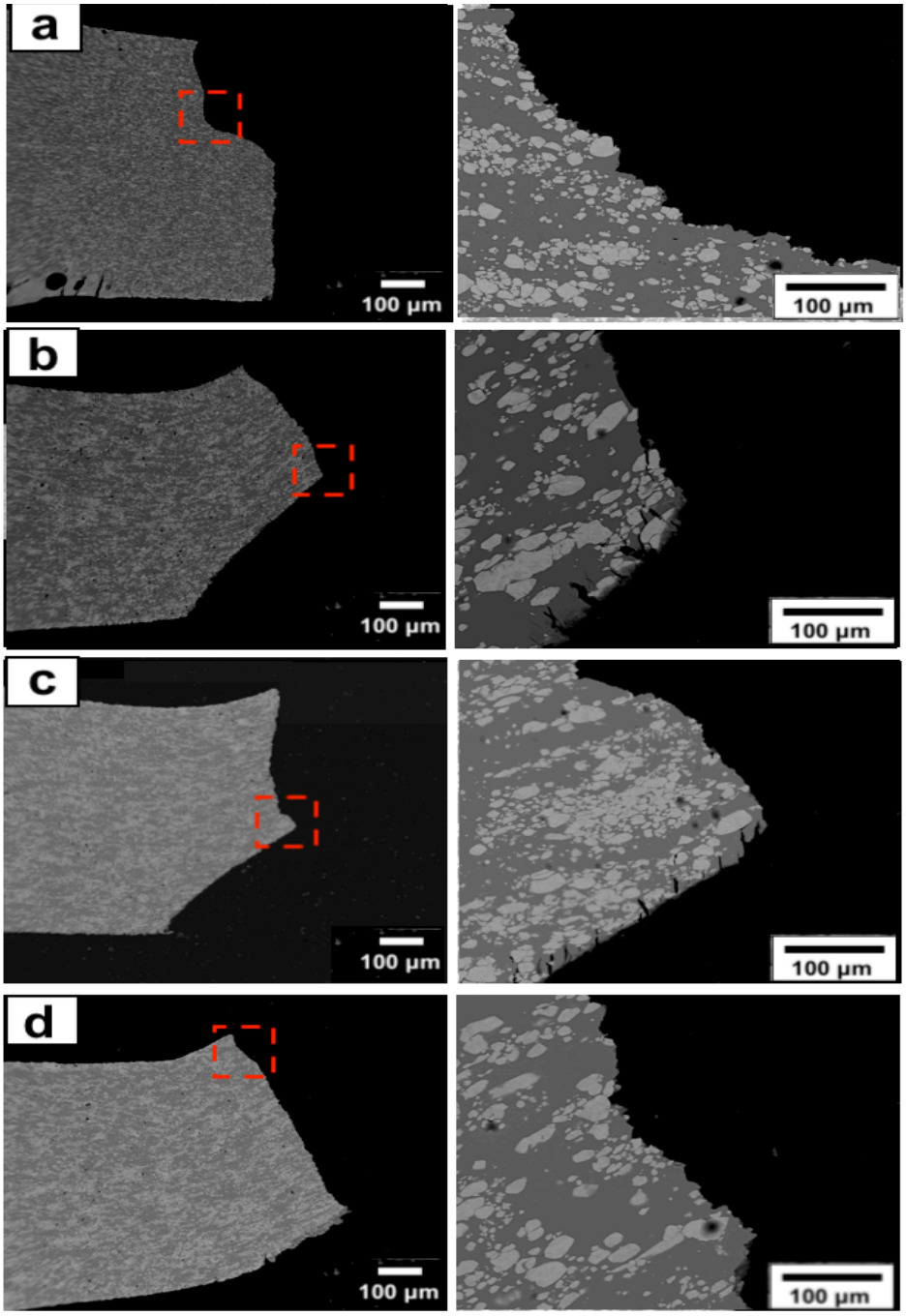

Figure 7.37: **W-Ti 70/30 wt% rolled at 1000 °C SEM BSE image of the side profile of fracture surfaces after 3-point bending at different temperatures** 3-point bending fracture surfaces after testing at (a) 150 °C, (b) 200 °C (c) 225 °C and (d) 250 °C of W-Ti in the as-rolled direction after ageing at 1000 °C for 100h.

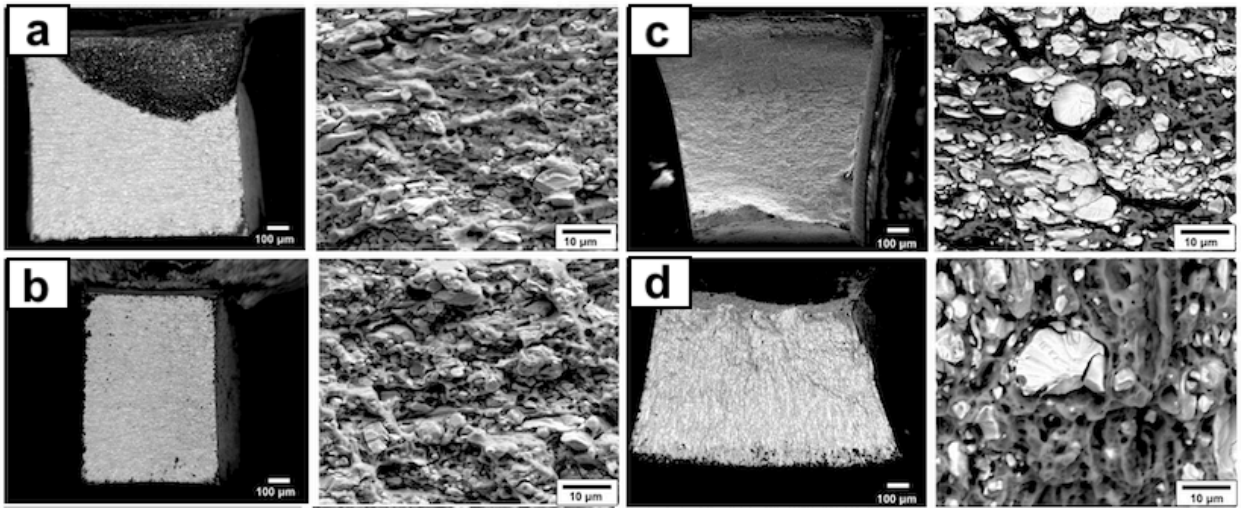

Figure 7.38: **W-Ti 70/30 wt% rolled at 1000 °C SEM BSE image of the fracture surfaces after 3-point bending at different temperatures** 3-point bending fracture surfaces after testing at (a) 22 °C, (b) 50 °C (c) 175 °C and (d) 200 °C of W-Ti in the transverse direction.

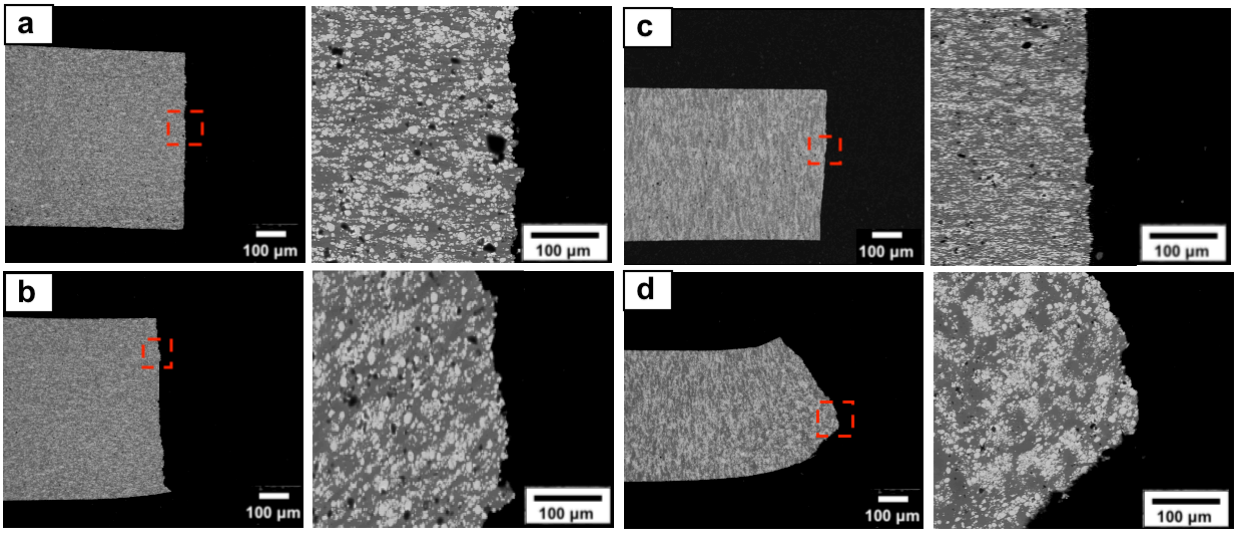

Figure 7.39: **W-Ti 70/30 wt% rolled at 1000 °C SEM BSE image of the side profile of fracture surfaces after 3-point bending at different temperatures** 3-point bending fracture surfaces after testing at (a) 22 °C, (b) 50 °C (c) 175 °C and (d) 200 °C of W-Ti in the transverse direction.

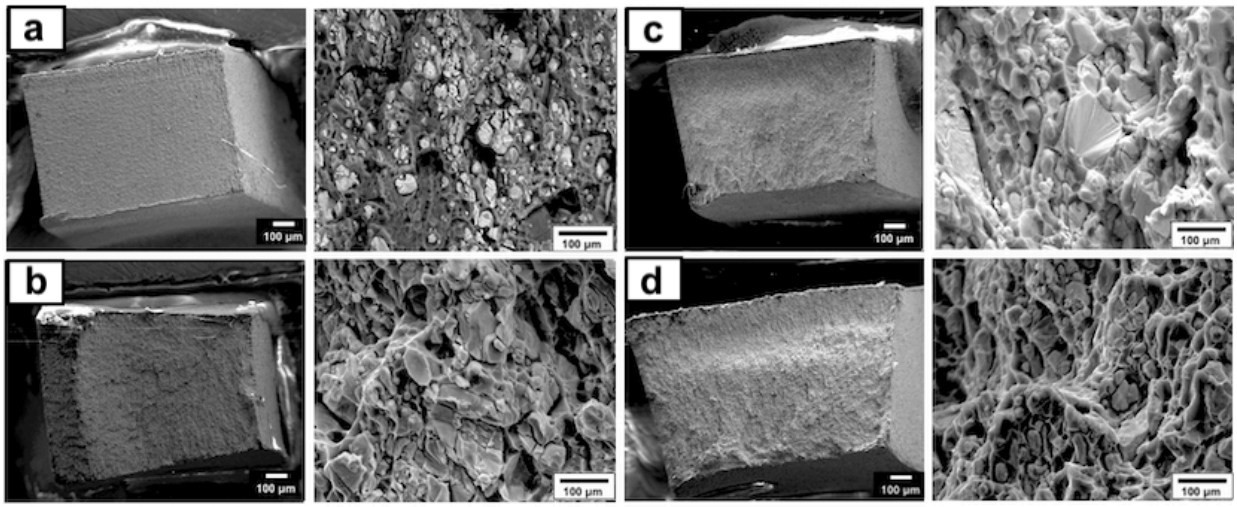

.

Figure 7.40: **W-Ti 70/30 wt% rolled at 1000 °C SEM BSE image of the fracture surfaces after 3-point bending at different temperatures** 3-point bending fracture surfaces after testing at (a) 22 °C, (b) 50 °C (c) 175 °C and (d) 200 °C of W-Ti in the transverse direction following ageing at 1000 °C for 100h.

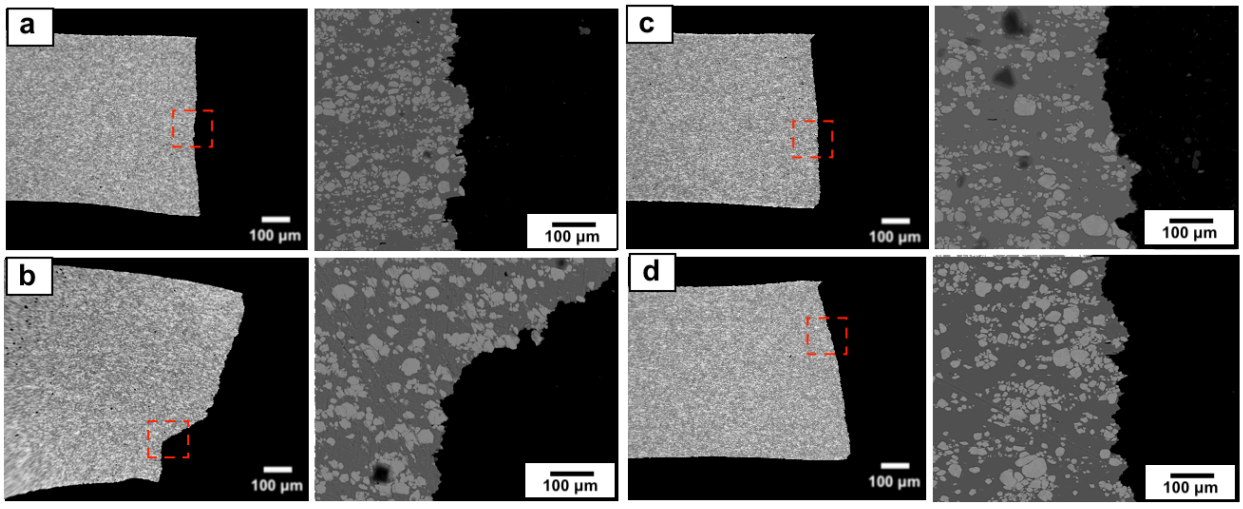

Figure 7.41: **W-Ti 70/30 wt% rolled at 1000 °C SEM BSE image of the side profile of fracture surfaces after 3-point bending at different temperatures** 3-point bending fracture surfaces after testing at (a) 22 °C, (b) 50 °C (c) 175 °C and (d) 200 °C of W-Ti in the transverse direction following ageing at 1000 °C for 100h.

Table 31: **Mechanical properties of of W-Ti 70/30 wt% rolled at 1000 °C**

	Temperature (°C)	Young's Modulus MPa	Fracture Stress MPa	Ultimate tensile strength (UTS)	Yield Strength MPa	Uniform Elongation %	Total Elongation %
	Room Temp. (RT)	261.23	708.72	-		-	2.19
L	**50**	284.74	1246.10	-	-	-	3.55
o	**100**	284.55	1276.72	-	-	-	4.51
n	**150**	139.31	1351.71	-		-	5.21
g	**200**	194.95	1352.33	-	-	-	11.23
	225	877.53	3506.94	3696.46	3669.5	11.83	19.08
	250	806.14	2715.93	3215.78	3089.55	13.12	31.52
	Room Temp. (RT)	273.95	799.2	-	-	-	5.14
T	**50**	307.83	1518.98	-	-	-	5.46
r	**100**	218.4	1513.85	-	-	-	6.91
a	**150**	311.07	1979.87	-	-	-	7.67
n	**175**	190.63	898.91	986.17	980.137	8.89	20.04
s	**200**	204.33	1039.84	1135.64	1130.61	11.37	34.91
	250	259.17	1735.16	1767.82	1818.75	10.96	38.16

Table 32: **Composiiton of W-Ti alloy** Table compares the different compositions of the phases present within the alloy from EDX maps.

	Overall Composition		Tungsten Rich Phase		Titanium Rich Phase	
	W	**Ti**	**W**	**Ti**	**W**	**Ti**
As received	18.35 ± 1.38	81.65 ± 1.38	97.50 ± 0.31	2.50 ± 0.31	3.69 ± 1.20	97.32 ± 1.2
As Rolled	18.32 ± 1.38	81.68 ± 1.32	97.28 ± 0.28	2.72 ± 0.31	3.69 ± 1.20	97.32 ± 1.2
Aged 100h 1000 °C	19.25 ± 1.38	80.75 ± 1.38	95.42 ± 0.29	4.58 ± 0.65	3.63 ± 1.16	96.37 ± 1.40

Table 33: **Mechanical properties of W-Ti rolled at 1000 °C after 100h of ageing at 1000 °C**

	Temperature (°C)	Young's Modulus MPa	Fracture Stress MPa	Ultimate tensile strength (UTS)	Yield Strength MPa	Uniform Elongation %	Total Elongation %
Long	**50**	294.99	1663.71	-	1608.51	14.60	14.60
	100	259.78	1709.60	1748.99	1522.67	32.95	33.39
	150	261.63	1675.43	1818.73	1396.03	32.93	35.71
	200	226.88	1536.93	1818.73	1458.71	32.95	37.54
Trans	**Room Temp. (RT)**	164.74	534.52	-	-	2.43	2.43
	100	239.10	1103.35	1317.53	1058.17	11.54	11.54
	150	265.16	1192.28	1449.82	1253.15	15.42	15.42
	175	291.32	853.88	2171.97	1887.21	12.50	12.50
	200	234.95	1163.92	1954.27	1754.5	15.63	15.63

in the fracture surface, indicating brittle fracture and material removal from the fracture surface. However, in the lower proportion of the fracture surface (figure 7.34a (right)), a granular-like appearance can be seen indicating.

At 200 °C figure 7.34b (left) displays brittle fracture. Brittle fracture is seen on both the tungsten particles (figure 7.34b (right)), with the presence of river plates on their surfaces. In addition, the presence of dark voids indicates intergranular fracture.

At higher temperatures 225 °C, the surface predominantly demonstrates ductile failure (figure 7.34c (right)). However, transgranular fracture of the tungsten particles is seen (figure 7.34c (right)), as indicated by the presence of river plates over the majority of the surface.

At 250 °C (figure 7.34d (left)) shows a unique fracture surface as compared to the others. On one half of the fracture surface, deformed tungsten particles can be seen protruding (figure 7.34d (middle)). On the other surface (figure 7.34d (right)), fractured tungsten particles are scattered within a titanium matrix, showing dimples and microvoids indicating ductile fracture. Figure 7.35d shows the side profile of the fracture surface at 250 °C. The lower region of the fractured sample (the section under tension) shows dark

fracture lines at almost 90° to that of the fracture. Indicating delamination of the tungsten particles. At the same time, the top surface (under compression) shows no indication of this delamination event. It could be suggested at this temperature, the tungsten particles become detached from the titanium matrix under tension. Indicating intergranular fracture (predominantly interfacial fracture). However, ductile fracture is observed in the region under compression, largely matrix failure. Suggesting that the deformed tungsten powder particles become dethatched from the matrix at higher temperatures under tension. The reduction in UTS of the sample tested at 250 °C compared to that of the sample tested at 225 °C could be explained by the delamination of the tungsten powder particles. In addition, at 250 °C, the aforementioned tungsten particles show a greater proportion of brittle fracture than seen in the samples tested at 225 °C.

Following annealing at 1000 °C for 100h, the samples cut in the rolling direction were tested for their mechanical properties to compare to the as-rolled samples. The end on fracture surface and side profiles are shown in figures 7.36 a-d and 7.37 a-d, respectively.

At a test temperature of 50 °C post-annealing, the fracture surface is similar to the as-rolled sample. The top section shows a large area of cleavage as indicated but the presence of dark voids (figure 7.36a (left)). A zoomed-in image of the lower proportion of the fracture surface (figure 7.36a (right)) shows signs of intragranular fracture. In addition, a river pattern can be identified on all the tungsten particles. Figure 7.36c shows microvoids and, therefore, ductile fracture in the lower part of the fracture surface. This is shown in the side profile of the fracture surface (figure 7.37a). As indicated by the change in the direction of the fracture profile. Samples tested at 150 and 200 °C show the same fracture as that seen in the sample tested at 225 °C for the rolled sample. Again, samples show different fracture modes, depending upon whether the region is under compression or tension. In the regions under tension, brittle fracture is seen in the dark regions, indicating intergranular fracture and removal of material from the sample (Figure 7.36b and c (middle) respectively). At a testing temperature of 200 °C, the double fracture mode does not occur (as seen in the rolled samples). This suggests either greater adhesion of the

tungsten particles to each other or to the matrix. It may also indicate that matrix failure has become the dominant fracture mode. Fracture by cleavage is the most common failure mode in alloys made from alloys containing small tungsten grains Manikandan R (2022). As the new interface is formed, a large amount of energy is released as it is formed. As a result, transgranular rupture occurs in the formation of the straight fracture surface.

Figure 7.38(a-d) shows the fracture surface for the W-Ti samples tested in the transverse direction. The sample tested at 22 °C shows a large area to the top right that has undergone complete failure. Closure examination of the fracture surface shows transgranular brittle fracture (figure 7.38a (right)). Analysis of the fracture surface from 50 °C, 175 °C, and finally 200 °C show a transition from brittle fracture to largely ductile fracture at higher temperatures fracture (figures 7.38(b-d) (right)). Figure 7.39(a-d) shows side profiles. Following ageing at 1000 °C for 100 hrs showed no differences in the fracture surfaces (as shown in figures 7.40(a-d) and side profiles figures 7.41(a-d)) as compared to that of the just rolled samples. Unlike the samples tested in the as-rolled direction, no difference was seen in the apparent fracture mode because of compression or tension.

7.4 Expansion of the Tungsten Titanium phase diagram.

Figure 7.42 shows a typical tungsten-titanium phase diagram. The red lines represent previous assessments from thermodynamic principles. Added to the is diagram are further point calculations of the predicted phases at specific calculations as conducted by Angqvist M (2019) (circles). The empty circles show compositions that were calculated to be single-phase; those filled-in circles are two-phase. In this thesis, two main temperatures (1000 °C and 1400 °C) were investigated. EDX was used to access the composition of the different spinodal-like regions observed in the aged and homogenised samples. The compositions were then plotted as points (blue) on the W-Ti phase diagram taken from Angqvist M (2019). The compositions of the two phases above identified at 1000 °C extended the bcc_Ti and bcc_W miscibility gap in the original phase diagram. But match well with the simulated data of Jin ZP (1993) Jonsson S (1996) at 1000 °C. The com-

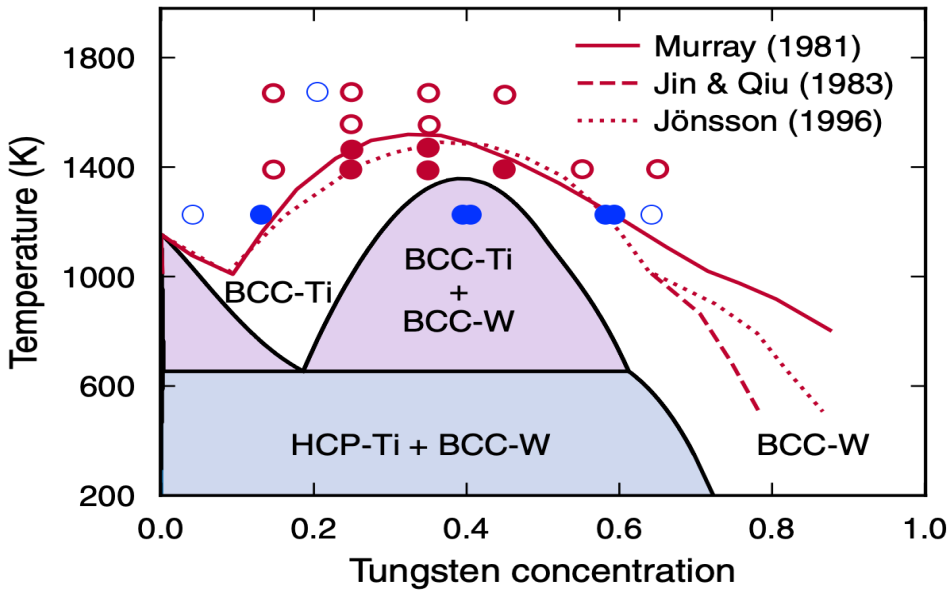

Figure 7.42: **Phase Diagram of W-Ti adapted from Angqvist M (2019)** showing both experimental and simulation-based data, overlaid with blue circles representing data obtained in this study.

position and the number of phases are shown in blue circles (again, filled-in circles are two-phase). The new data presented here match extremely well with that predicted by Murray et al. It shows that at 1273K (1000 °C), the two-phase (bcc-Ti and bcc-W) miscibility gap is much larger than what is presented. Extending the miscibility gap to 63.32 wt% from 14.69 wt% tungsten.

7.5 Conclusion

The purpose of this section was to create a nanostructured tungsten alloy, using several binary and ternary alloys through arc melting techniques, with the premise of using thermal heat treatments to modify the microstructure using their respective phase diagrams.

- W-Ti-Fe alloys have shown promise despite the obvious macrosegregation of tungsten from the titanium iron-rich matrix. SEM and TEM revealed nano-scale B2 TiFe(W) precipitates within the homogenised and aged alloys' tungsten-rich A2(W, Ti,Fe). They are suggesting the potential for the formation of β-β' superalloy. Despite solution heat treatment and ageing reducing the hardness of the alloys, no mechanical testing was performed due to the complexity involved in creating the

alloys via arc melting. This study has shown that intermetallic B2 precipitates of TiFe can be used to reinforce tungsten-rich matrix. The presence of this intermetallic phase offers a route for designing strengthened tungsten for high-temperature applications.

- SEM observation of the as-received tungsten manganese alloy, large areas of unmelted tungsten grains were seen. In addition, large voids were seen in the sample where powder particles had become dislodged. Or there were areas where the powder particles had not been appropriately sintered during manufacturing.

- Despite several solution heat treatments at different temperatures and durations, a fully dense alloy was never created. Additionally, despite ageing (again over several temperatures and times), the sintering problem still existed. Many of the samples observed had areas of either pure tungsten or manganese, and producing a homogenous alloy was never achieved.

- Despite the lack of homogeneity in the samples, EDX analysis of selected regions in the aged (and solution heat-treated) samples showed that up to a maximum of 3.1% manganese could be dissolved into the tungsten. Despite the lack of consistency in the composition of the alloy, EBSD data showed that the ratio of LAGB to HAGB in both the solution heat treating and aged samples was altered to favour LAGB with prolonged ageing times. However, mechanical testing via 3-point bending only showed brittle fractures at room temperature.

- Fracture surfaces showed the crack pack to follow that of the unmelted tungsten particles, suggesting they (and the voids formed around them during casting) are the sites for crack growth and initiation. The inability to make a fully dense (or near dense alloy) is probably due to the extreme difference in melting points of the two elements.

- Conventional arc melting of W-Mn is potentially tricky, and thus, to create an alloy, these alloys probably require an additive manufacturing process such as HIPping,

where higher pressure can be used to compact the powders and aid sintering at lower temperatures.

- A new 72/28 WCr alloy was cast, and microstructural characterization was performed following solution heat treatment and ageing.

- Clear macrosegregation of A2 W and Cr-rich phases could be observed on the as-received microstructure. Following solution heat treating at 1700 °C for 8 hours, a single-phase A2 W-Cr alloy was produced.

- Despite the lack of access to such high-temperature facilities, it does show that a single-phase tungsten binary alloy can be made. Therefore, compared to the others presented here, this is the only alloy with a genuinely homogenous single-phase alloy. The homogenized alloy did not have the voids and macro defects shown in the other systems.

- On ageing the W-Cr alloy at 1250 °C for 100 hours, a two-phase nanostructured lamellar precipitation was formed of a tungsten-rich A2 W(Cr) and a chromium-rich A2 Cr(W) composition. This decomposition demonstrated the potential use of the miscibility gap to nanostructure a tungsten-based alloy for high-temperature applications.

- The lamellar could be characterized into two different length scales. The first was of a much coarser scale of approximately 580 $\pm$ 42 nm in thickness. Notably, this phase was seen to occur at prior grain boundaries and grows towards the centre of the previous parent grain. The second much finer lamellar phase has a thickness of approximately 135 $\pm$ 31 nm. This finer phase grew within the centre of the grain, growing outwards towards the larger lamellar phase. The thicker of the two lamellar phases was present within the microstructure following homogenization (it must be noted that it was only seen on a few grain boundaries and could not be described as a common occurrence). Therefore, not only may it be due to the cooling rate in the

furnace, but it may also be due to the compositional difference in the alloy following homogenization.

- A bulk-phase nano-scaled A2 W(Cr) and A2 Cr(W) alloy can be manufactured with a semi-coherent interface, which could provide potential radiation sinks, reducing radiation embrittlement. On the ageing of this alloy, the Vicker's hardness reductions show the potential to reduce its ductile-to-brittle-transition-temperature. However, due to the casting issues, no mechanical tests could be conducted on the samples due to their size.

- The Tungsten Titanium alloy had similar casting issues to the tungsten chromium alloy. However, it showed promise. Even though several heat treatments were employed, the solution heat-treated sample had large areas of porosity. Where unmelted and unsintered tungsten particles could be observed, this suggested that tungsten powder particles were lost from the samples or lack of sintering on heat treatment.

- Following ageing for 100 hours at 1400 °C BSE images showed regions of unmelted tungsten in a titanium matrix. Despite the porosity of the sample, the as-received sample showed ductile fracture during 3-point bending tests. The sample was then rolled at room temperature (to induce deformation) to a final reduction of 10%. However, considerable cracking of the sample prevented any mechanical testing from being carried out.

- On "cold-rolling" at 1000 °C (to a final reduction of 80.1%), the sample showed up to 32.95% uniform elongation. Even after ageing at 1000 °C for 100h, the same material showed a uniform elongation of 15.63%. The alloy showed ductility at 100 °C, despite the presence of voids in the sample.

- In addition to the improved mechanical properties seen with the rolling of W-Ti. Ageing of the sample at 1000 °C also induced a decomposition in the alloy into lamellae

rich in tungsten. Again, this lamellar offers the potential for radiation sinks due to their semi-coherent interfaces.

- The W-Ti alloy has the most potential of the three alloys produced due to its low DBTT. However, EBSD observation of the rolled samples showed that the deformation in the sample was within the tungsten matrix. As stated, the alloy looks similar to that of a WHA. However, unlike conventional WHAs, the tungsten particles have little to no deformation. It is reasonable to conclude that should more tungsten be dissolved into the titanium-rich phase, the ductility may be reduced significantly and, therefore, warrants further investigation.

8 Tungsten based BCC - Reduced activation refractory high entropy alloys (RA-HEA)

A literature search for the tungsten-based RA-HEA reveals only thin films, powder sintering, and no bulk casting. Therefore, an assessment has yet to be done on bulk alloy production through conventional arc melting techniques of a tungsten-based RA-HEA. Due to the promise of high entropy alloys having many of the properties that are desired in a tungsten alloy (high -strength, -toughness, -temperature performance), an investigation was carried out to assess the potential for the production of a 4- and 5- element RA-HEA. When samples are made by arc melting, the alloys are evaluated only in their as-cast condition. Little has been done to assess the stable phases present after homogenisation and ageing. With this in mind, two bulk reduced-activation refractory high entropy alloys (RA-RHEAs) of W-V-Cr-Ta quaternary & W-V-Cr-Ta-Ti quinary were designed based on high melting point, combined with low activation. Both alloys were selected due to calculations suggesting their propensity to form single or multiple body-centred-cubic phases The alloys were experimentally produced by arc melting and solution heat treated at 1400 °C to demonstrate the stable phases and their compositions. The purpose of this study is to investigate and manufacture a bulk casting a high melting point reduced activation refractory high entropy alloy (RA-RHEA), with advantageous mechanical properties and stability for application in fusion energy. Through the manufacture of a tungsten-based refractory HEA, containing intermetallic phases for improved high-temperature mechanical properties. Through the use of Empirical models and thermocalc databases to guide the design of the alloy.

8.1 Results and Discussion

8.1.1 Bcc modelling with thermocalc - Entropy, Enthalpy, and Gibb's free energy

HEA alloys were designed on the following basis: (1) Low activation (2) High temperature (3) Propensity to form a majority body-centred-cubic phase, with the potential to be strengthened by second-phase intermetallic(s). (4) Contain the element tungsten

The two principal characteristics in designing a new tungsten-based RA-RHEA alloy for fusion reactors are that they can not only withstand the high temperatures of a fusion reactor but are also low activation. To this end, FISPACT-II software (Fleming 2018) was employed to determine the level of activity and decay times of elements to reach low-level waste (Gilbert 2019). This led to down selection to a design pallet of 15 low activation elements being chosen as identified by Gilbert et al. (Gilbert 2017) as low activation (less than 100 years) (in addition to that of tungsten).

Following the identification of the elements that could be used to create such an alloy. A potential RAHEA candidate was assessed through empirical calculations.

Empirical calculations offer an automated way of identifying the physical properties and phase structure of HEAs based on their constituent elements. Using equations (2)-(6), the values for ΔS_{mix}, ΔH_{mix}, T_{mix}, Ω and δ where calculated (all equations used to calculate values are shown in table 35). For all combinations of the elements listed above for both quaternary and quintary HEAs, a plot comparing average melting point vs Hmix vs Omega Ω is shown in figure 8.1a.

Zoomed-in images of the highest melting point RHEAs for each of the alloys are shown for clarity in Figures 8.1b). Both the quaternary and quintenary alloys with the highest melting points contain Hafnium (TiTaHfWCr) or rhenium (WRhTaCr); the price of these elements excludes them from any practical applications. In addition, it has been predicted that Hf containing HEAs decompose into an Hf-rich hexagonal close-packed structure (HCP) below 1298K (Chena 2021).

To determine the actual phases that may be present in the equiatomic alloys. thermo-

calc diagrams were produced using TCHEA5 (figure 8.1) to access the predicted phases of the final alloys. Although both diagrams show the potential for the formation of precipitates (σ, μ and leaves). Both diagrams show large temperature regions where a single-phase (or two-phase) BCC structure could exist. As both the thermocalc database and empirical calculations predicted the propensity to produce single-phase BCC alloys an arc-melted sample of each was manufactured.

The calculated values of Ω, δH_{mix}, and VEC are presented in Table 34 and plotted in comparison to known phases of multi-component alloys (Figure 8.1 (Yang X 2012)). It has also been suggested by Jiang et al. (Jiang 2016) additionally a δ value of $<$ 4.27% facilitates the formation of single phase bcc HEA. Values of 4.958 and 5.616 for WVCrTa and WVCrTaTi, respectively. Both values predict the formation of a solid solution plus intermetallic. However, both the VEC values of 5.50 and 5.20, respectively being lower than $<$6.87, an enthalpy of mixing between $-$7.27 kJ mol^{-1} and four kJ mol^{-1} (Calvo-Dahlborg 2017) predict a solid solution bcc formation.

In the formation of any HEA, the enthalpy of mixing and entropy of mixing will both compete and contribute to the overall formation of the final alloy. A negative ΔH_{mix} will promote the formation of intermetallic compounds and greater force of attraction between elements, whereas a positive ΔH_{mix} with drive the separation of elements due to less miscibility. The closer ΔH_{mix} is to zero, the more chance a solid solution phase can occur. However, ΔS_{mix} for a HEA will always be positive and, as a result, will inherently encourage disorder in a multi-phase alloy. Therefore, a higher ΔS_{mix} will more likely result in a random solid solution and inhibit the formation of intermetallics. In addition, the entropy of a mixture will increase with temperature and therefore, $T\Delta S_{mix}$ will drive the formation of a solid solution.

The stability of phases in any cast, homogenized, or aged sample is determined by the system's Gibbs free energy (ΔG_{mix}). Gibbs free energy is calculated by subtracting the entropy of mixing (ΔS_{mix}) from the enthalpy of mixing (ΔH_{mix}).

Due to the number of elements in a HEA, the common solubility between these ele-

Table 34: Calculated values for an additional method for identifying the stability of solid solution HEAs

	Element				
	W	**Cr**	**V**	**Ta**	**Ti**
r[Å]	0.1367	0.1316	0.1249	0.1430	0.1462
T_m [K]	3695	2183	2180	3290	1941
	δH_{AB}^{mix} [KJ/mol]				
W	-	-	-	-	-
Cr	1	-	-	-	-
V	-1	-2	-	-	-
Ta	-7	-7	-1	-	-
Mo	0	0	0	-	-
Ti	-6	-7	-2	-1	-
	HEA				
	WCrVTa		**WCrVTaTi**		
Atomic %	0.250		0.200		
$\bar{r}$ [Å]	0.134		0.136		
δ %	4.958		5.616		
Ω	7.694		5.18		
T_{mix} [K]	2837		2657.8		
δS_{mix} [J/K/mol]	11.526		13.381		
δH_{mix} [KJ/mol]	-4.25		-6.56		
VEC	5.50		5.20		

Table 35: **Calcualted changes of temperature for HEA state.** Calculated values of T_{liq}, T_{sol} and T_{dec} for tungsten-based HEA alloys

HEA	**T_{liq} [K]**	**T_{sol} [K]**	**T_{dec} [K]**
WVCrMo	2739.58	2444.65	1195.91
WVCrTa	2802.33	2331.70	1644.58
WVCrTaTi	2636.04	2096.39	1500.25

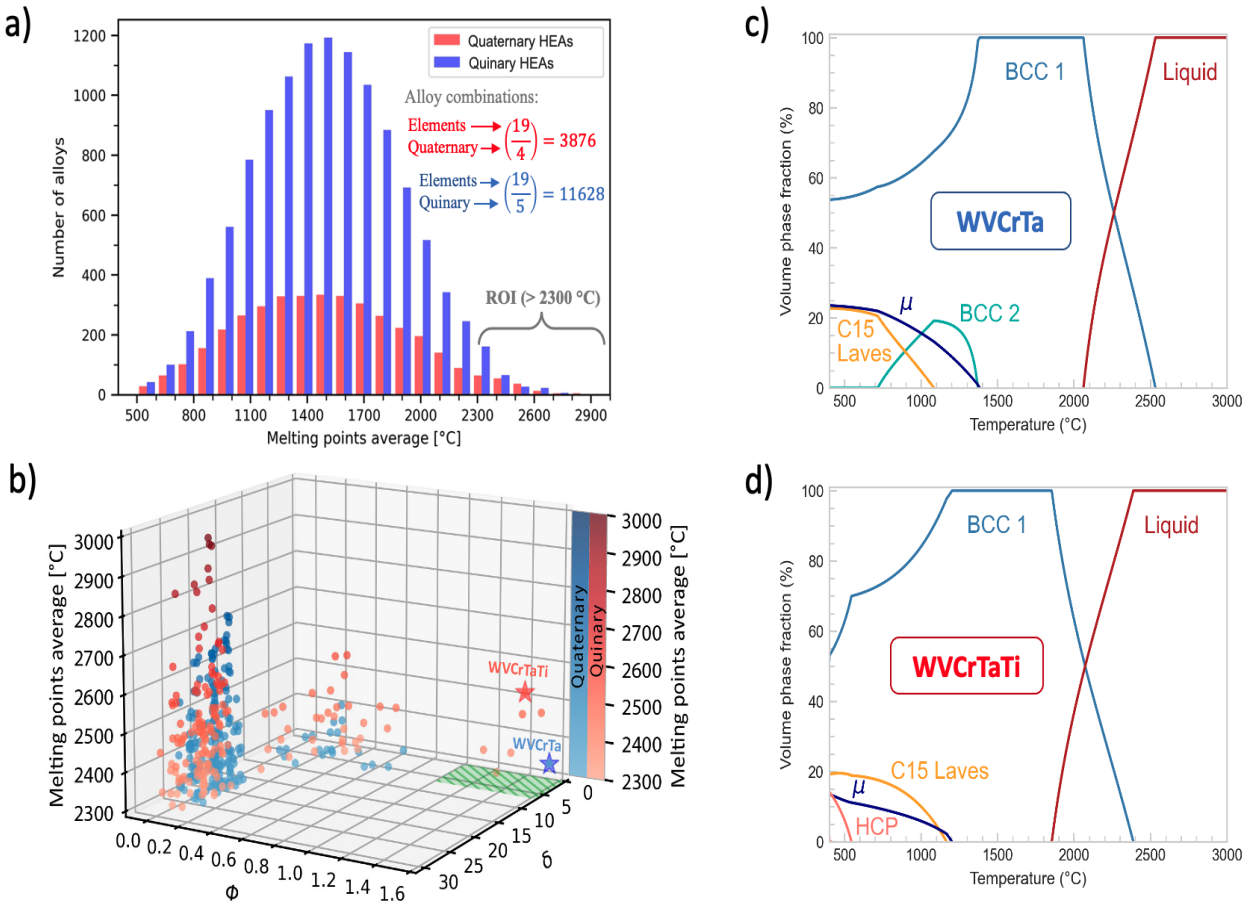

Figure 8.1: **Theoretical analysis of potential RARHEAs**.(a) Melting temperature vs H_{mix} vs Omega for tungsten-containing 4 (blue) and 5 (red) RARHEAs. (b) Zoomed-in area showing 4 RARHEAs with the highest melting point indicating chosen RARHEAs in dark blue. (c) thermocalc diagrams of chosen 4 RARHEAs from plots b. (d) Plot adapted from Yang X et al. indicating predicted microstructure of two chosen RARHEAs. (e) Zoomed-in area showing 5 RARHEAs with highest melting point, indicating chosen RARHEAs in dark red. (e) thermocalc diagrams of chosen 5 RARHEAs from plots e. thermocalc diagrams were produced using TCHEA5

ments should promote the formation of a single phase. According to Gibb's free energy equation, the entropy (from this enhanced solubility) should help improve this phase solubility, assuming the temperature is high enough. This is analogous to the phenomenon of melting. Where a liquid state has a higher entropy compared to that of the solid state promotes the formation of the liquid phase (Richard's rule). Therefore, those states with higher entropy should be stabilized by increasing the temperature of the solid state. In a solid solution, intermetallic compounds have lower mixing entropy than terminal and intermediate solids. Therefore, in a metal such as a HEA, the entropy of a solid solution should be inherently larger than that of any intermetallic phase due to the number of elements within it.

The phase stability of an alloy cannot be explained solely by configurational entropy. Otto et al. (Otto F 2013) and others have challenged this idea and shown that maximizing the configurational entropy of an alloy does not guarantee a solid solution (Laurent-Brocq 2016, Ma D 2015, Bracq G 2017)

Instead, the stability of any phase is controlled by Gibb's energy. The stable phase has the lowest Gibb's free energy at any temperature. However, when trying to generate a solid solution from Gibb's free energy equation, the mixing entropy is not the only parameter that can be considered. The mixing enthalpy also plays a significant factor in the final alloy. The enthalpy of mixing will compete with the entropy. It will also determine the chemical interaction of the elements in the alloy. It will determine how atoms mix and surround themselves with other atoms. Therefore, to have the maximum randomization of mixing between all elements, the enthalpy of mixing of all potential phases needs to be as low as possible.

8.1.2 New ACI HEA tungsten alloys

8.1.3 As cast HEAs

The BSE and EDX maps show that each alloy cast has large unmelted tungsten sections. Therefore, it was decided to outsource the manufacture of these alloys to ACI metals. The

BSE and EDX analysis of the as-cast WVCrTa and WVCrTaTi alloys as manufactured by ACI are shown in figures 8.2 and 8.4, respectively.

BSE images of the 4HEA show three separate phases as distinguished by contrast (figure 8.3(a)). EDX line scan (figure 8.3(b)) and point (figure 8.3(c)) scanning of these areas indicate that the lightest of the phases is rich in both tungsten and tantalum. This phase is interspersed with two distinct regions: a dark grey phase rich in vanadium, chromium, and tantalum and a darker phase rich in vanadium and chromium.

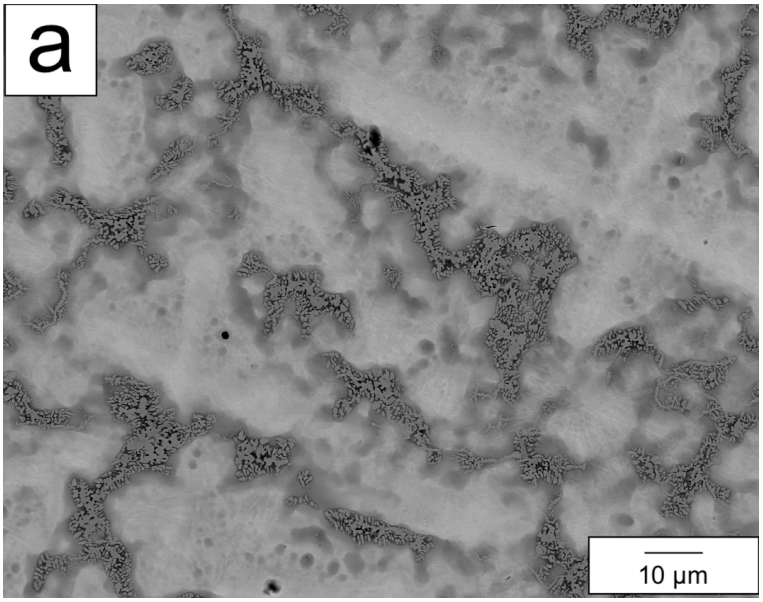

Figure 8.2: **BSE images of the as-cast WVCrTa HEA**. BSE micrograph showing dendritic segregation of tungsten and tantalum due to high melting points

W-V-Cr-Ta-Ti consists of a three-phase microstructure as shown in figure 8.5(a). The BSE images show a lighter phase interspersed with a darker grey phase and small black regions. Line (figure 8.5(b)) and point (figure 8.5(c))) scan analysis shows that the lighter regions are tungsten and tantalum-rich. The grey phase is rich in titanium, chromium and vanadium. The smaller black regions are almost exclusively titanium (EDX maps are not shown). XRD analysis of the quarternary HEA (figure 8.6a) in the as-cast state showed the presence of two phases: a bcc_A2 phase and a Laves C15. Due to the high negative values of the enthalpy of mixing, transition metals have a tendency to form intermetallic structures Sobieraj D (2020).

In order to identify any potential C15 (AB_2) Laves phase found via XRD analysis of

both HEAs, lattice parameters for several candidates are shown in Table 36. It is worth noting that the lattice parameters may vary as a result of temperature.

The presence of Laves phases in an alloy can be appealing due to their strong oxidative resistance and high-temperature properties Kuhn B (2011). However, they do demonstrate low ductility at room temperature. As shown in the above BSE, the presence of a Laves phase at grain boundaries could be an explanation for the increased hardness in these alloys. In addition, several reports in the literature show Laves phases imparting improved creep resistance Yamamoto Y (2007) (however, there are contrary reports to this) as well as yield strength improvements Zeumert B (1997). Laves phase is also known to be an initiation site for the pinning of dislocations and crack growth Schirra JJ (1991).

A Mu phase is predicted to be stable up to 1227 °C (figure 8.1e); however, this phase was not present in any of the as-cast samples.

The microstructure of as-cast WVCrTa is a mixture of a bcc_A2 phase a=b=c 0.312 nm and a Laves cubic a=b=c 0.697 nm phases which from EDX map data and Table 36 would indicate a Laves C15 type $TaCr_2$ phase. DFT calculations for the enthalpy of mixing of the C15 Laves phase for $TaCr_2$ gives a value of -148 meV as compared to that of the bcc binary of -80 meV Sobieraj D (2020). It is reasonable to suggest that the Laves phase would form at the expense of the single-phase bcc. BSE images of WVCrTa homogenized at 1400 °C show the presence of a three-phase microstructure. EDX analysis of these phases shows tungsten, tantalum-rich phase. This phase makes up the bulk of the sample and results from the prior tungsten-rich dendrites seen in the as-cast sample. The lack of mobility of tungsten at this temperature will also be a factor in any phases present. XRD of the same sample gives a lattice parameter of 0.316 nm, which matches well with the literature value for a TaW bcc unit cell (Volodin 2014). Within these tungsten-rich areas is what appears to be a decomposing region of two separate phases. BSE/SEM observation of this region confirms the presence of two phases. EDX analysis of the area further confirms this observation. The first phase in this region is a

vanadium and tantalum-rich phase, which is lower in tungsten (approx 7at.%) than that of the bulk. The second observed phase within this region is a tantalum and chromium-rich phase, which is low in tungsten (approx 1/5 of the at.%) of that of the bulk. The composition of this phase from EDX matches well with that of a Laves-type phase, with a ratio of 2:1 in favour of tantalum. Lattice parameters of the Laves phase, where a = b = c = 0.703 nm from data presented in Table 36 and the EDX data, it is most likely that the Laves phase is a C15#$MgCu_2$ type $TaCr_2$. As compared to the as-cast structure, the Laves phase now covers a much larger area than that seen in the as-cast sample, which would suggest the formation of a hypoeutectic lamellar Laves phase in a bcc matrix. The microstructure of this solution heat-treated alloy is similar to that of other eutectic HEAs seen in the literature, where a Fe_2Nb type Laves phase forms in an FCC matrix through the addition of Nb to a $CrFeNi_2$ HEA. The EDX data would suggest that Cr instead of Nb is the main component of the Laves phase.

XRD analysis of the WVCrTaTi sample in the as-cast condition is shown in Figure 8.6a. The presence of a bcc_A2 phases with lattice parameters of 0.312 nm, similar to the published value for TaW and the second for TiCrV, can be observed.

Table 36: **lattice parameters of various Laves phases.** Laves phases and their lattice parameters from the literature of suspected C15 phases present in WCrTaTiV HEA.

Laves Cubic Phase C15 #$MgCu_2$	**Lattice Parameter (nm)**
$CrCr_2$	0.658[a]
$CrTa_2$	0.748[a]
$TaCr_2$	0.697[b], 0.691[a], 0.700[a]
$TaTa_2$	0.764[c], 0.769[a]
TaV_2	0.709[c], 0.712 - 0.716[d,d,e,c,e], 0.7118[d], 0.722[d]
$TiCr_2$	0.686[f], 0.69[g], 0.694 [h]
TiV_2	0.712[e]
Ti(Cr or V)$_2$	0.694-0.696[i]
VTa_2	0.753[c]
VV_2	0.688[c]

[a] (Pavlu J 2009) [b](Kuo 1953) [c](Pavlu J 2011) (Charifi Z 2009) [e](Danon CA 2004) [f](Chen X 2005) (Ghosh C 2015) [h](Chen KC 1997) [i](Chen KC 1998)

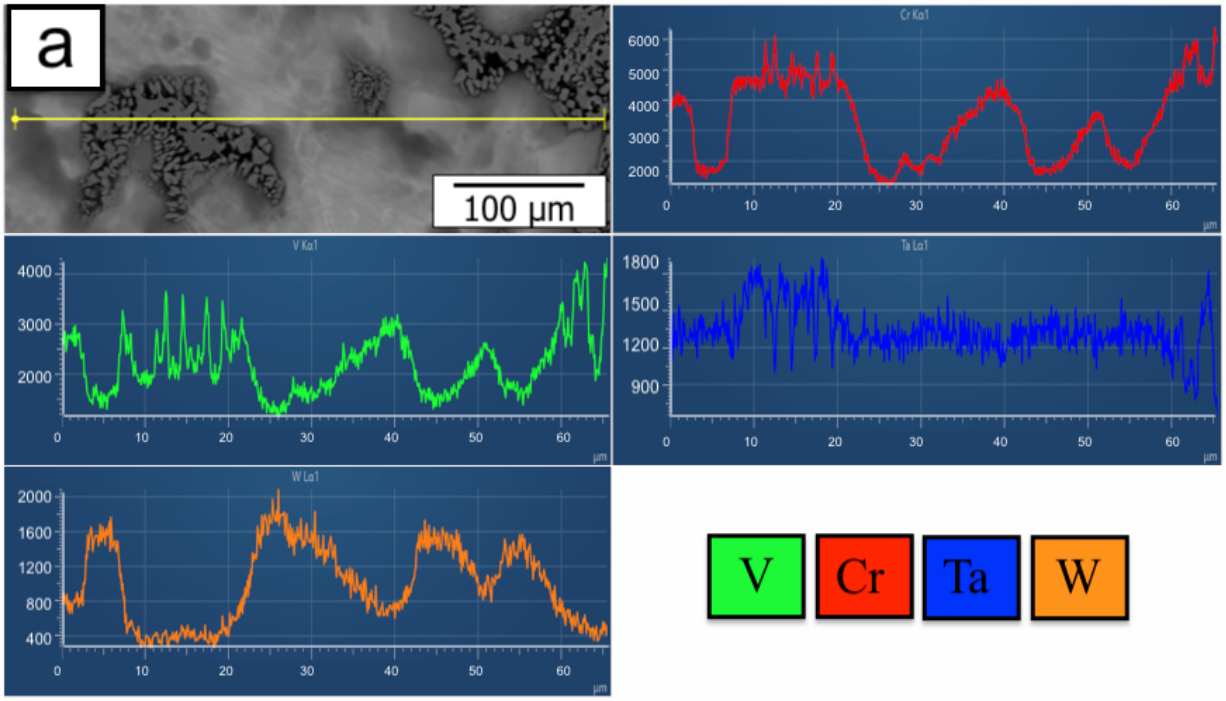

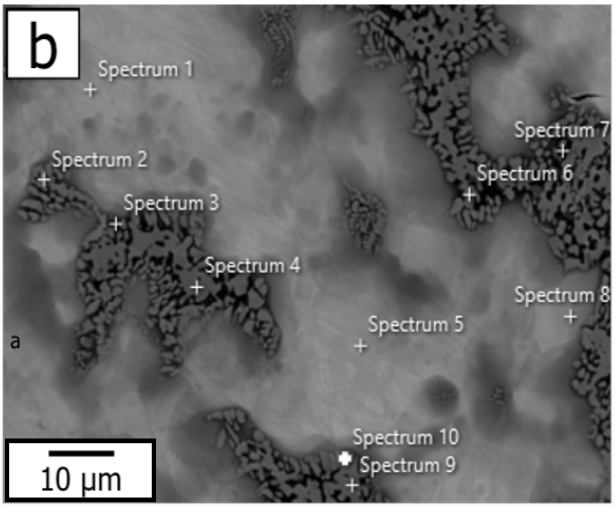

Spectrum Label	V	Cr	Ta	W
1	14.72	14.83	26.93	43.52
2	22.47	47.46	23.87	6.20
3	31.28	47.28	14.32	7.12
4	17.71	50.02	29.79	2.48
5	14.90	14.69	27.38	43.03
6	18.28	50.21	29.07	2.44
7	34.69	51.85	8.60	4.87
8	22.40	28.49	24.34	24.76
9	18.15	49.96	29.73	2.16
10	32.59	46.68	12.78	7.95

Figure 8.3: **Analysis of the as-cast 4HEA WCrVTa as produced by ACI** (a)BSE images EDX line scan, and (b) Point scan data showing composition values

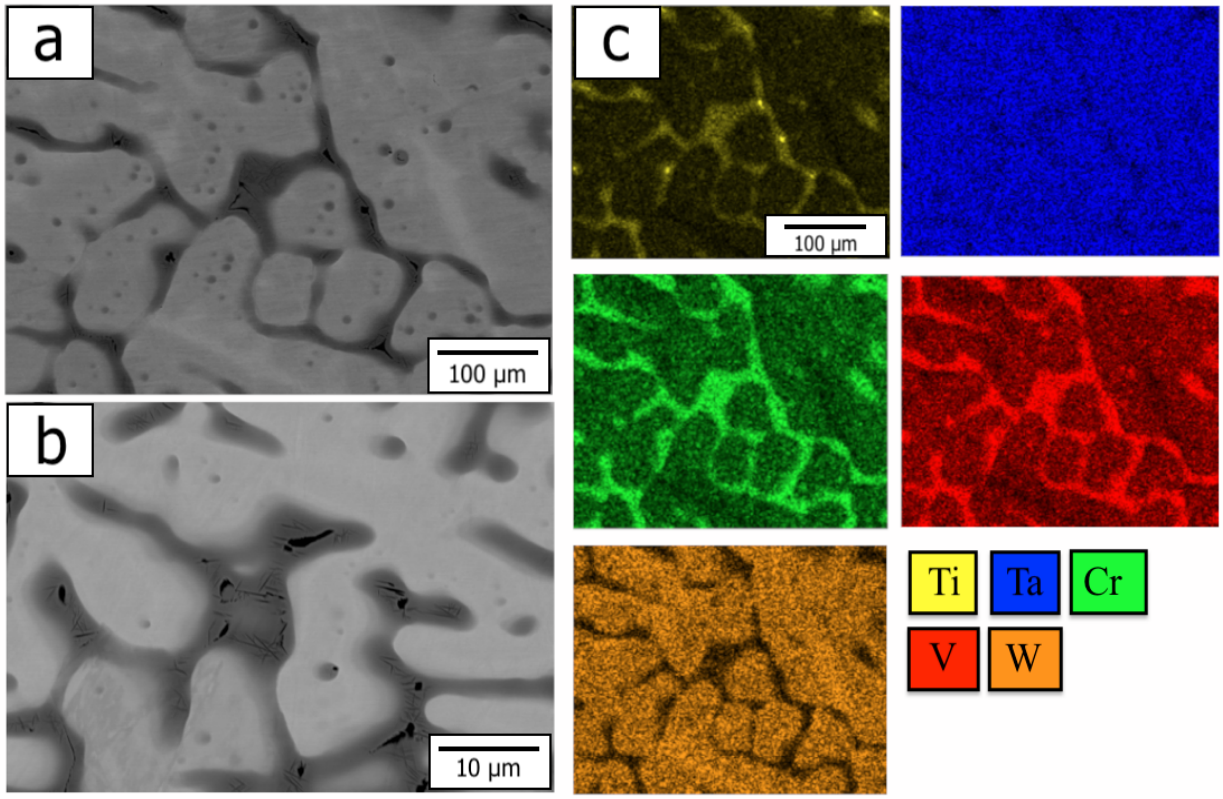

Figure 8.4: **SEM and EDX of as-cast WVCrTaTi HEA.** (a) SEM and (b) BSE images of the as-cast WVCrTaTi HEA showing dendritic segregation of tungsten and tantalum due to high melting points. (c) EDX map showing elemental segregation due to varying melting points.

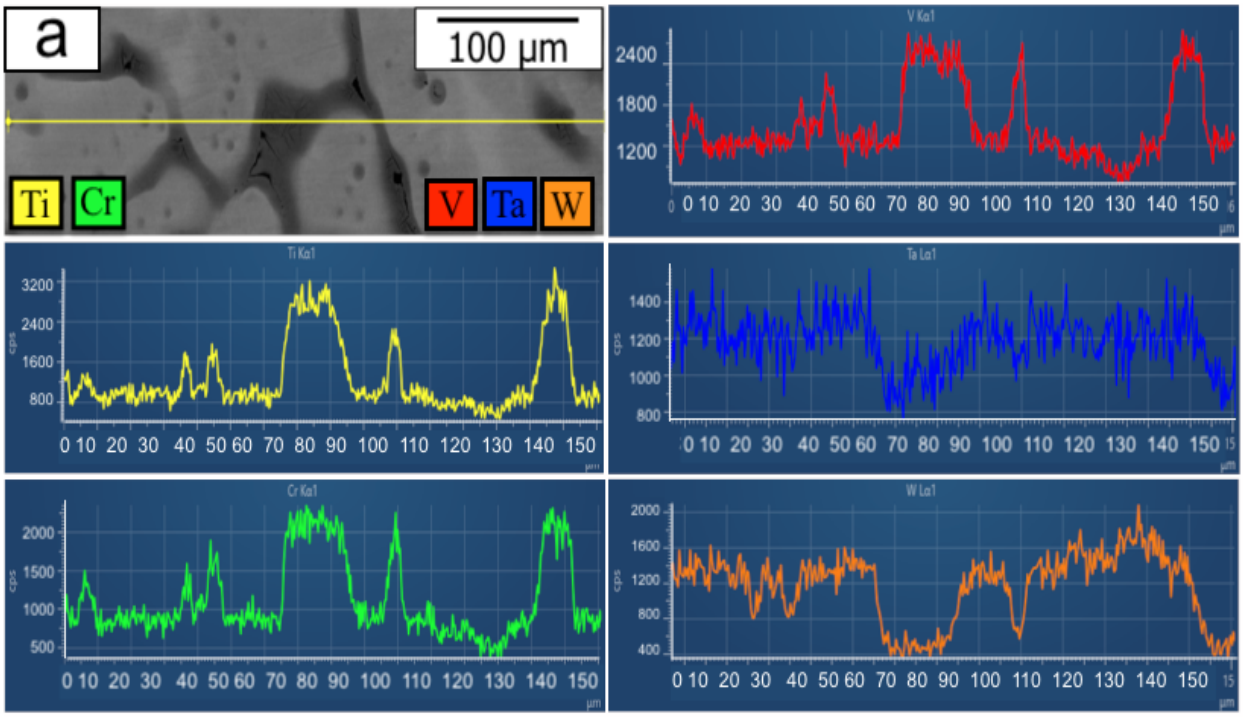

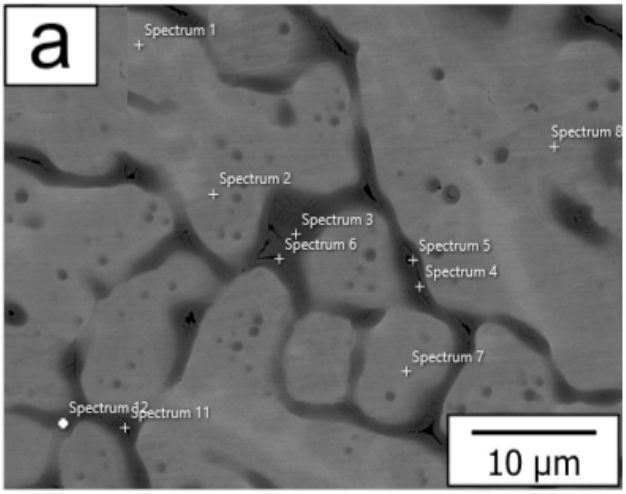

Spectrum Label	Ti	V	Cr	Ta	W
1	10.88	13.80	6.87	28.73	39.71
2	15.99	19.68	11.14	25.96	27.22
3	33.07	25.00	22.68	13.77	5.48
4	29.50	26.01	24.41	14.31	5.77
5	68.11	12.16	10.79	6.59	2.35
6	43.67	20.74	18.11	12.60	4.89
7	15.07	19.02	10.78	25.43	29.70
8	14.95	19.10	10.95	25.70	29.31
11	38.44	23.40	22.22	11.89	4.05
12	28.87	26.02	22.54	15.45	7.12

Figure 8.5: **Analysis of the as-cast 5HEA WCrVTaTi as produced by ACI** (a) BSE images EDX line scan, and (b) Point scan data showing composition values.

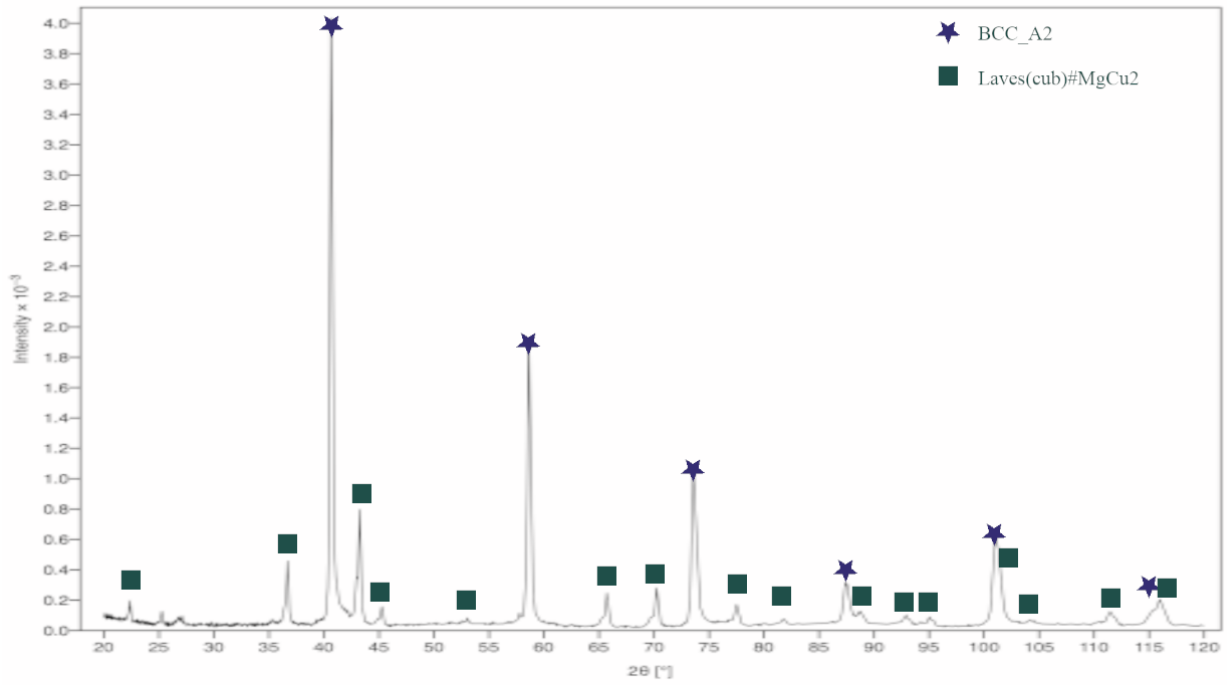

(a)

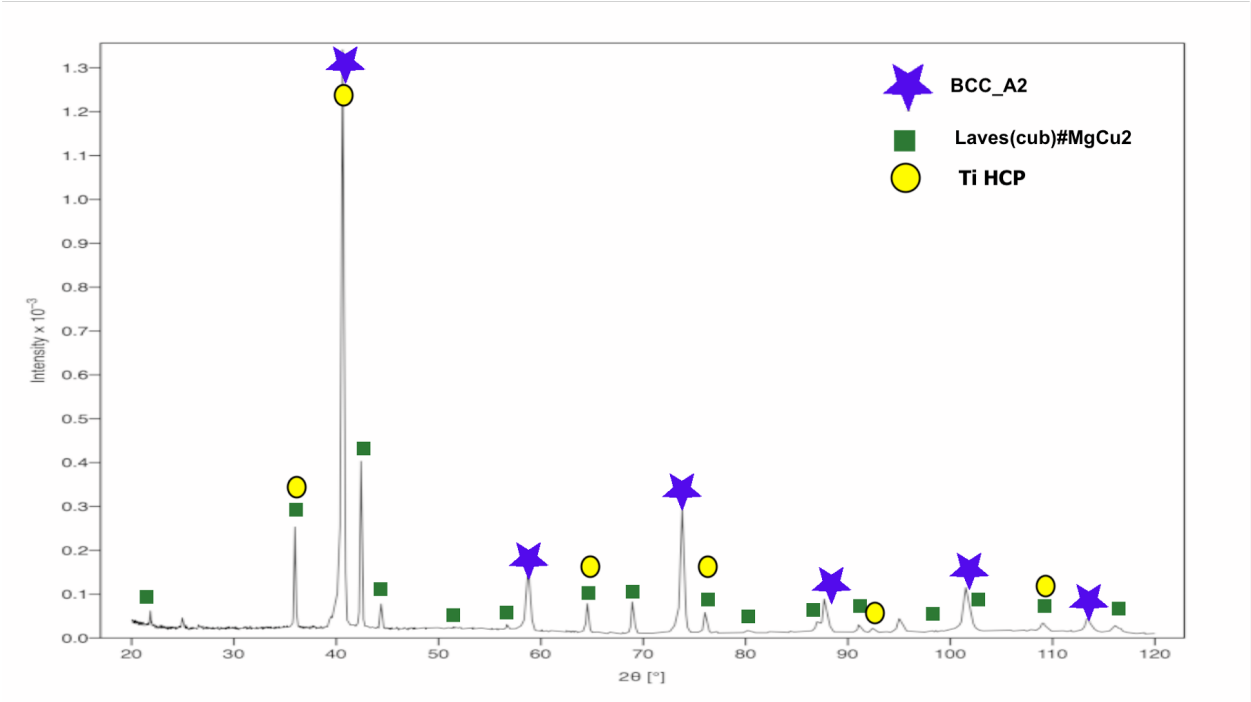

(b)

Figure 8.6: **XRD patterns of as-cast HEAs as produced by ACI** (a) WCrVTa and (b) WCrVTaTi.

8.1.4 Solution heat treating HEAs

Solution heat treating WVCrTa up to 1400 °C for 100 hours (as shown in figure 8.7a) did not produce a single bcc_A2 phase, as Atwani et al. (Atwani O El 2019) reported. This result may be due to the compositional differences in the alloys and the manufacturing technique. Using magnetron sputtering deposition would have ensured all elements in the alloy would have been melted and mixed as opposed to the cast alloy we present here. A homogenization temperature of 1400 °C is well below the melting temperature of the elements used. BSE images of WVCrTa homogenized at 1400 °C show the presence of a three-phase microstructure. EDX analysis of these phases shows tungsten, tantalum-rich phase. This phase makes up the bulk of the sample and results from the prior tungsten-rich dendrites seen in the as-cast sample. The lack of mobility of tungsten at this temperature will also be a factor in any phases present. XRD (figure 8.9a) of the same sample gives a lattice parameter of 0.316 nm consistent with the results found above. Within these tungsten-rich areas is what appears to be a decomposing region of two separate phases. BSE/SEM observation of this region confirms the presence of two phases. EDX analysis of the area further confirms this observation. The first phase in this region is a vanadium and tantalum-rich phase, which is lower in tungsten (approx 7at.%) than that of the bulk. The second observed phase within this region is a tantalum and chromium-rich phase low in tungsten (approximately 1/5 of the at.%) of the bulk. The composition of this phase from EDX matches well with that of a Laves-type phase, with a ratio of 2:1 in favour of tantalum. Lattice parameters of the Laves phase, where a = b = c = 0.703 nm from data presented in Table 36 and the EDX data, it is most likely that the Laves phase is a C15#$MgCu_2$ type $TaCr_2$. Compared to the as-cast structure, the Laves phase now covers a much larger area than that seen in the as-cast sample, suggesting the formation of a hypoeutectic lamellar Laves phase in a bcc matrix. The microstructure of this solution heat-treated alloy is similar to that of other eutectic HEAs seen in the literature, where a Fe_2Nb type Laves phase forms in an FCC matrix through the addition of Nb to a $CrFeNi_2$ HEA. The EDX data would suggest that Cr instead of Nb is the main

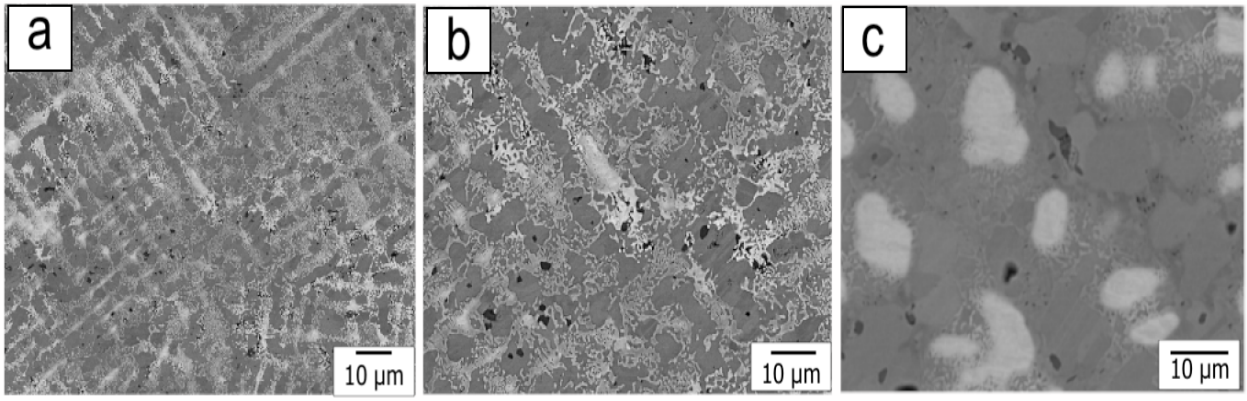

(a) BSE images

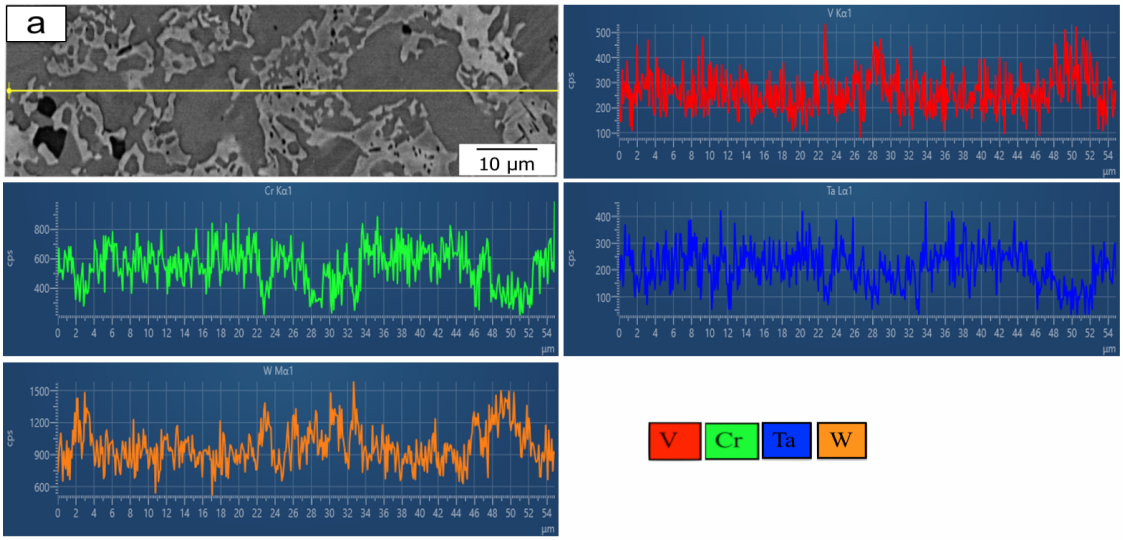

(b) Line Scan

Figure 8.7: **EDX and SEM analysis of WVCrTa** (a) BSE images, (b) EDX line scan of 4HEA WCrVTa homogenised at 1400 °C as produced by ACI

component of the Laves phase.

BSE images (figure 8.8a) show a microstructure similar to the as-cast. XRD analysis of the WVCrTaTi sample homogenized at 1400 °C (figure 8.9b) reveals a bcc_A2 phase with lattice parameters of 0.312 nm, similar to the published value for TaW and the second for TiCrV, can be observed. EDX area scans of WVCrTaTi homogenized at 1400 °C. From the spectrums obtained, the data reveals three different phases: a near pure titanium phase, chromium and tantalum-rich but tungsten and titanium-poor phase, and a third almost equiatomic phase except for chromium and tantalum, which the previous phase has depleted. XRD analysis of the homogenized condition (not shown) confirms the evidence

from the point scan (not shown) with a bcc_A2 phase with lattice parameters of 0.312 nm. Also present is a titanium HCP phase a=b = 0.2950 nm and c= $\frac{c}{a}$=1.588 nm phase. However, the manufacturing route used here differs from the literature. A single phase 5 HEA TixWTaVCr alloy (Waseem O 2018) has been produced at 1500 °C. However, the manufacture of this alloy did not use conventional arc melting and instead used sintered powder. In addition, the alloy was not truly equiatomic and only contained a maximum of 7 at% Ti (along with almost equiatomic concentrations of the other elements). Homogenizing the alloy at higher temperatures would produce a single-phase bcc_A2 alloy. The formation of a single bcc_A2 alloy in the Waseem et al. paper was attributed to "Ti-Cr and Ti-Cr-V", which above 1400 °C melt (Waseem O 2018). As the homogenization did not exceed the minimum temperature for the melting of these alloys, it may explain the segregation of elements and the formation of the laves phase. Further investigations with a higher homogenization temperature will demonstrate if a single phase bcc_A2 can be formed through arc melting.

Once again, XRD analysis of the HEAs solution heat treated at 1400 °C showed a similar appearance to that of the as-cast samples with both alloys containing bcc_A2 and Laves phases (figures 8.9a and 8.9b). A single bcc_A2 phase should be at this temperature should have been seen at this temperature according to the phase diagram. It would suggest that these phases are thermodynamically stable in the alloys (at least up to 1400) in cast samples.

8.1.5 Ageing Alloys

To determine the stability of the phases observed in the solution heat-treated samples, both HEAs were aged for 100 hours at 750 °C as can be seen from figures 8.10a and 8.12a.

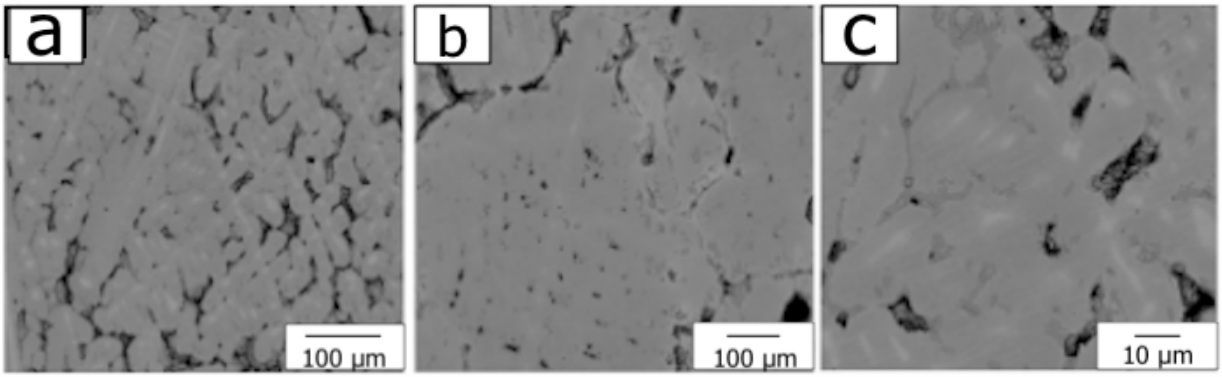

(a) BSE images

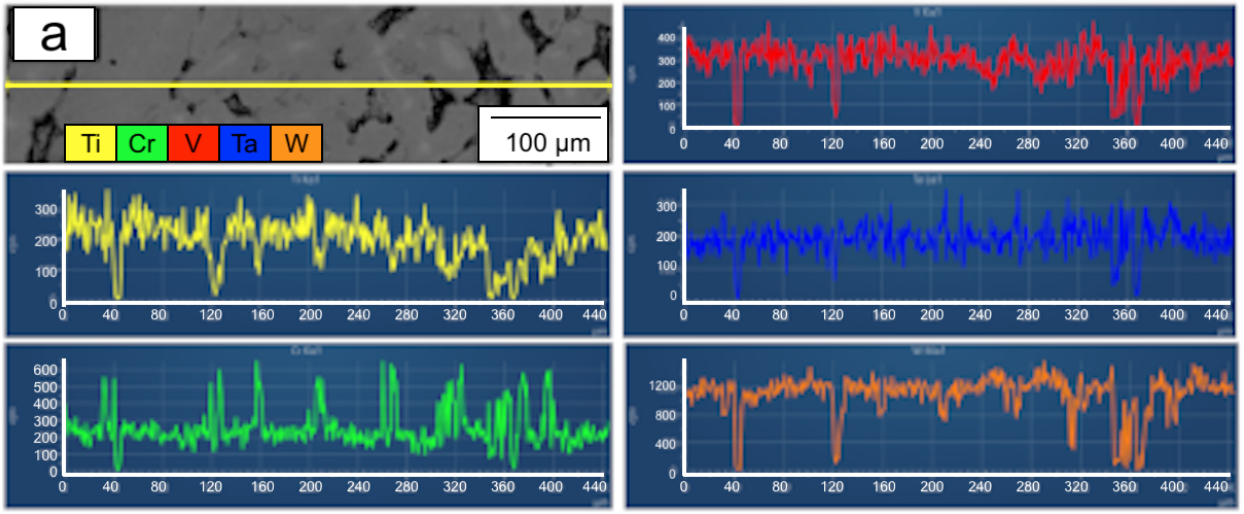

(b) Line Scan

Figure 8.8: **EDX and SEM analysis of WVCrTaTi** (a) BSE images (a-c) increase magnification, black areas are regions of porosity (b) EDX line scan of 5HEA WCrVTaTi homogenised at 1400 °C as produced by ACI

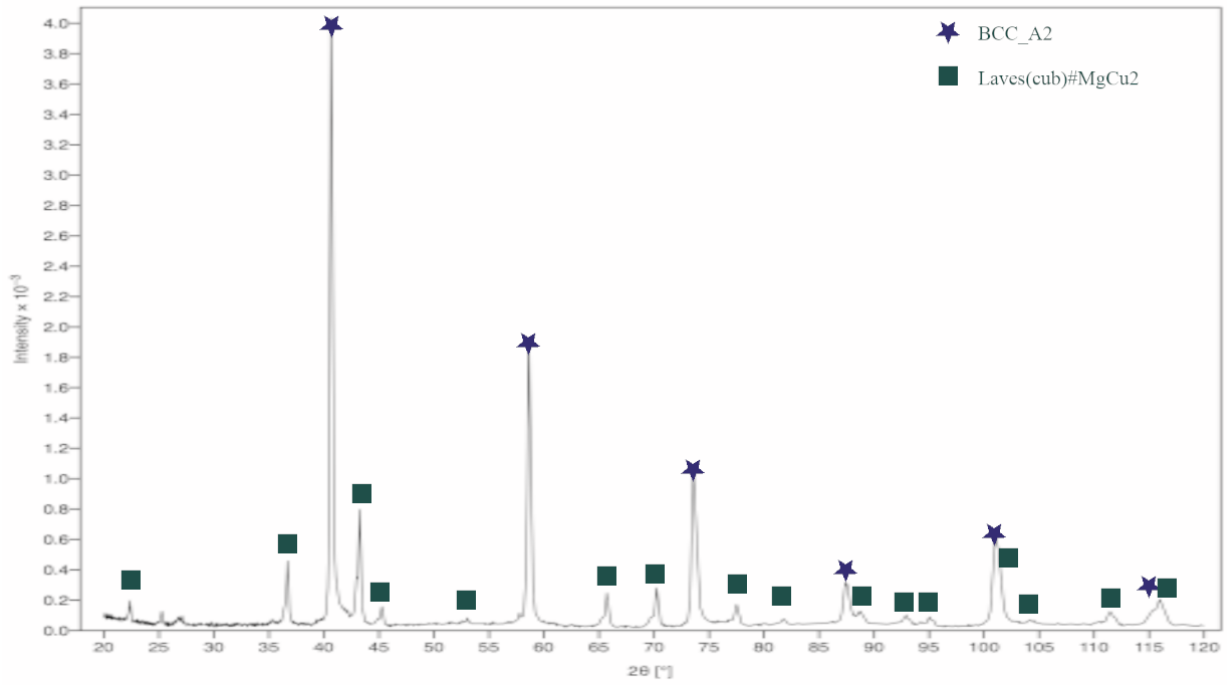

(a)

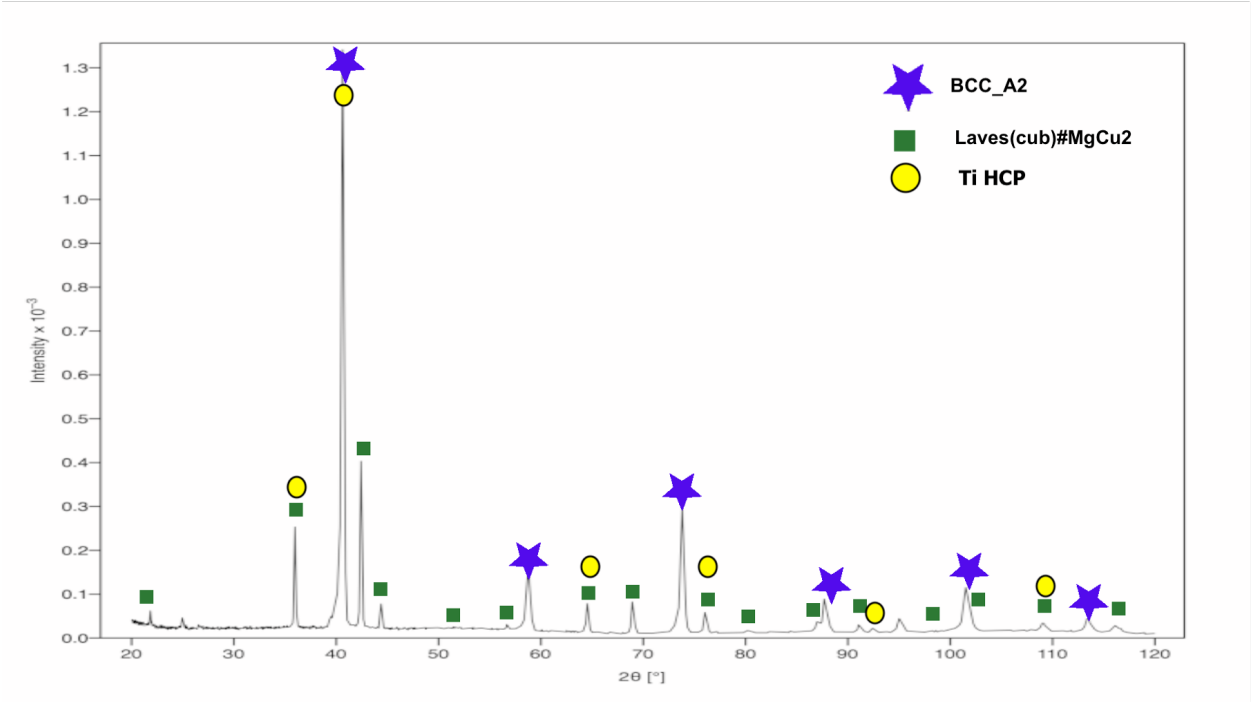

(b)

Figure 8.9: **XRD patterns of both HEAs produced by ACI following homogenization at 1400 °C for 100 hours.** (a) WCrVTa and (b) WCrVTaTi.

8.1.6 Thermocalc as a method for predicting phases in HEAs

XRD analysis of both the 4 and 5 HEAs (figures 8.10 and 8.12), respectively, show both alloys having a bcc_A2 phase and a Laves(cub)#$MgCu_2$ phases in the as-cast state. This particular C15 Laves phase possesses a cubic symmetry. DFT and ab-initio-based Cluster Expansion (CE) Hamiltonian calculations for WCrVTa show a possibility of 682 bcc structures in the 5HEA (and approximately 270 for the 4HEA) (Sobieraj D 2020). Of the possible binary systems present, Cr-Ta, the CrTa structure gives several binaries having both positive enthalpy of mixing, ranging from 142 meV ($Pm\bar{3}m$) (Sobieraj D 2020). To negative enthalpies of -39 meV per atom ($Fd\bar{3}m$). Like the above binary system, CrTi has positive and negative values (Sobieraj D 2020). The lowest of which Cr_2Ti_7 has a enthalpy of mixing of -67 meV (Sobieraj D 2020). In contrast, the CrV binary has only negative values; the most negative is -100 meV (Sobieraj D 2020). While WCr, TaTi, and TaV only have positive values. Due to the high negative values of the enthalpy of mixing, transition metals tend to form intermetallic structures (Sobieraj D 2020). The expected Laves phases in both alloys are shown in table 36 along with their lattice parameters. From the XRD data, the likely phase is a C15 (AB_2).

In addition to the phases identified, thermocalc predicts a sigma phase up to 1227 °C. However, no such phase was identified.

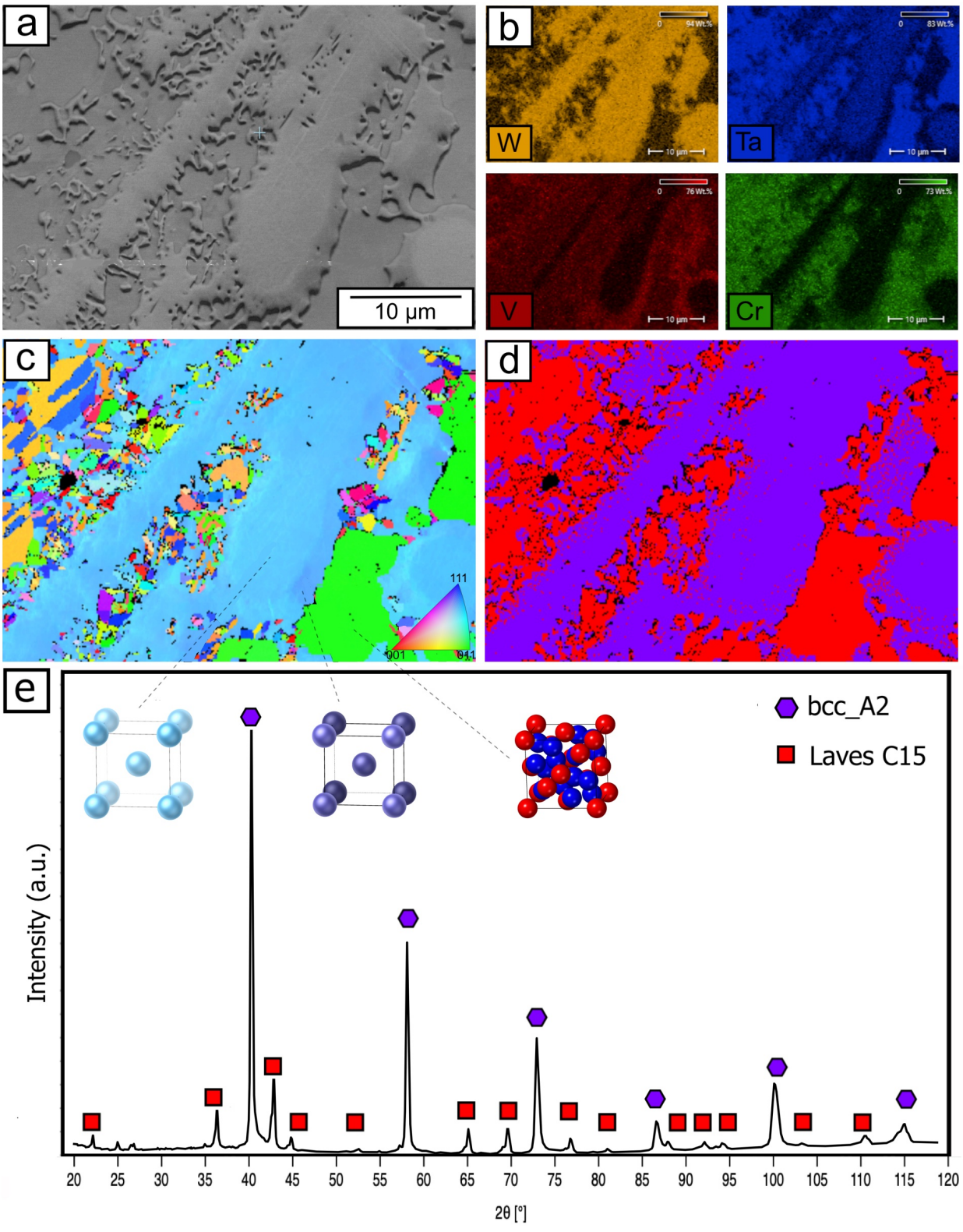

Figure 8.10: **EBSD and EDX analysis of WVCrTa at high magnification** (a) BSE image of general microstructure (b) EDX maps of elements, showing elemental segregation due to difference in melting temp. (c) EBSD map and (d) Phase map (e) XRD map

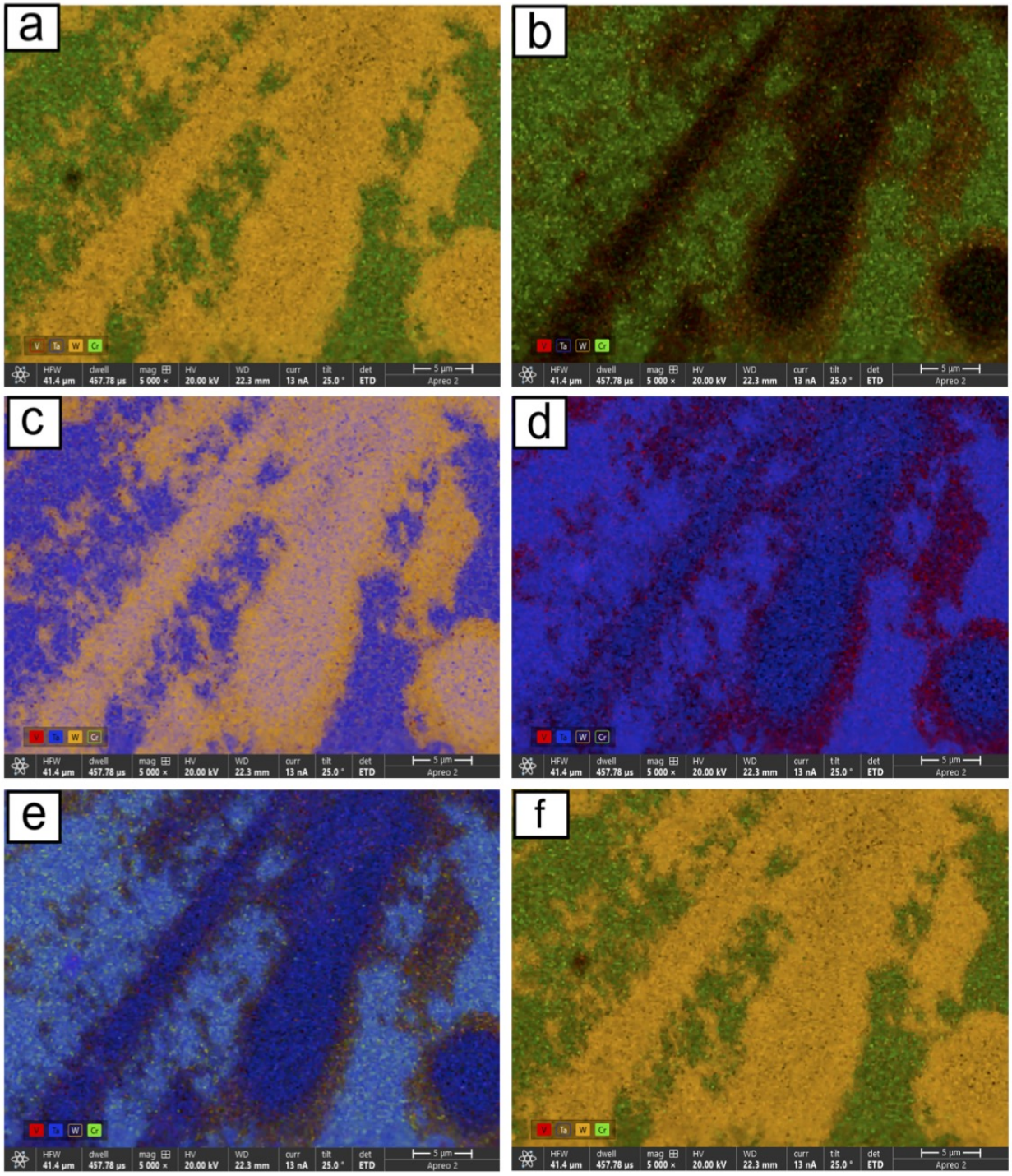

Figure 8.11: **EDX maps of WVCrTa at high magnification of area shown in figure 8.10a** (a) Map showing Tungsten and Chromium (b) Vanadium and Chromium (c) Vanadium, Tantalum, and Tungsten (d) Vanadium and Tantalum (e) Vanadium, Tantalum, and Chromium and (f) Vanadium, Tungsten, and Chromium

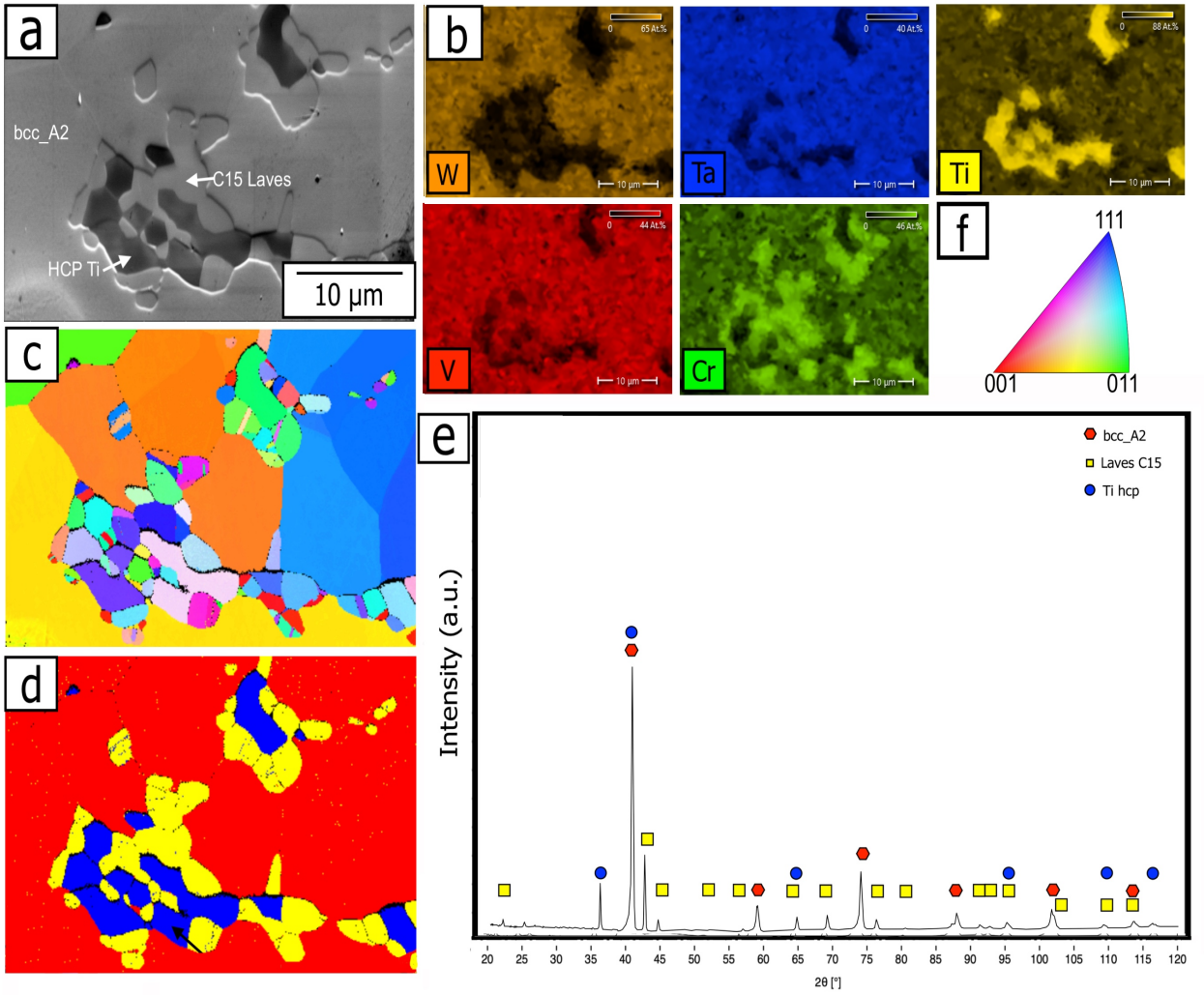

Figure 8.12: **EBSD and EDX analysis of WVCrTa at high magnification** (a) BSE image of general microstructure (b) EDX maps of elements, showing elemental segregation due to difference in melting temp. (c) EBSD map and (d) Phase map (e) XRD map (f) IPF map

Laves phases, however demonstrate brittle behaviour at room temperature. As shown in the above BSE, the likely presence of a Laves phase at grain boundaries could offer a strengthening behaviour. In addition, several reports in the literature show Laves phases imparting improved creep resistance (Yamamoto Y 2007) (however, there are contrary reports to this) as well as yield strength improvements (Zeumert B 1997). Laves phase is also the initiation site for pinning dislocations and crack growth (Schirra JJ 1991). The presence of this phase was not predicted by thermocalc analysis.

8.1.7 WVCrTa - Further phase analysis

Following homogenization and ageing of WVCrTa BSE image reveal a two-phase microstructure: a dendritic bcc phase within a secondary Laves phase. This is consistent with the XRD data presented here. However, a third phase between the dendritic and matrix phases seems to be present in a more detailed inspection of the alloy. To determine the composition of this phase and with the information of lattice parameters from the XRD data. A high-resolution EBSD and corresponding EDX maps were performed as shown in figure 8.10(a-d). The EBSD and phase map (figures 8.10(c-d)) indicate only the presence of two phases: a bcc and cubic C14 Laves phases. The first is the lighter blue, which is consistent with the EDX map for those areas that are rich in tungsten, but more specifically, those regions that overlap with tantalum (as indicated by the darker blue areas of 8.11(b)). The darker blue (purple) regions in the EBSD indicate a different orientation from the previous bcc phase. In addition to this, they appear to match the areas indicated as devoid of tantalum and rich in both Vanadium and Chromium (see EDX map).

To further establish the composition of the phases in the third phase, the elements displayed in the EDX maps were altered and are shown in figure 8.11. Figure 8.11(a) shows the EDX map for tungsten-chromium. A lighter region on the edge of the tungsten-rich dendrite can be observed. This indicates that both chromium and tungsten are localized to this phase. Map (b) shows the colocalization of Vanadium and Chromium to the third phase. This time, the edge of the dendrites is the only area on the map where vanadium is present. Additionally, the presence of chromium is confirmed by the orange colour. Figures c-f show EDX maps for different combinations of elements in this HEA and further confirm the presence of the three elements in this bcc phase. Therefore, the XRD data has only identified two phases in this alloy (one bcc and one Laves). EBSD and SEM/EDX have confirmed the presence of a second bcc phase.

The proportion of each phase identified in the WVCrTa and WVCrTaTi alloys are shown in Table 37. Comparing the two phases present in the solution heat treated (1400°C) and aged (750°C) WVCrTa alloy, there is little difference between the proportion

of phases present at the two temperatures. The aged sample has approximately 3.0% more laves phase as compared to the solution-treated sample. This demonstrates the stability of the Laves phase over various temperatures. In the WVCrTaTi alloy, a similar pattern emerges with Laves phase again being stable at all temperatures and again an increase in the percentage of Laves phase in the aged sample of 7.60% as compared to the solution heat-treated sample.

Despite thermocalc predicting a single phase bcc HEA to form at 1400°C in both alloys, the observation herein suggests otherwise; the purpose of using equiatomic concentrations was to maximize entropic stabilization as the dominant factor in alloy development. However, it has been shown that this is not the case, and in fact, intermetallic formation may be more influential in determining HEA microstructure. Table 37 shows the average at.% of elements in each phase as identified from point scan analysis seen in each phase of the two HEAs. As predicted, the bcc phase present in the WVCrTa alloy is composed of tungsten and tantalum. The amount of chromium present in the bcc phase at solution heat treatment, as compared to ageing, remains constant. However, there is a marked difference in the amount of vanadium seen. This could suggest that at lower ageing temperatures, vanadium is moving from the bcc phase to that of the Laves phase. The Laves phase has almost constant levels of chromium and tantalum between the two ageing temperatures, further demonstrating the stability of the phase. As tantalum is closest to the stoichiometric ratio (33.3 at.%), the Laves formed are of a tantalum nature. If the lattice parameter (and the elemental composition are taken into comparison), the Laves phase present is $TaCr_2$ in the solution heat-treated sample, and a mixture of $TaCr_2$ and TaV_2 in the aged sample. This would explain the increase in lattice parameters seen in the two alloys. The movement of vanadium from the bcc to Laves phases would also explain the slight increase in the fraction of Laves phase seen in the aged sample as compared to the solution heat treated.

The phase composition of the WVCrTaTi alloy is shown in Table 37. The amount of tantalum and tungsten present in the bcc phase after ageing (750°C) as compared to that

Table 37: Proportion of elements in HCP, Laves and bcc phases found in homogenised and aged samples as identified by BSE imaging

	thermocalc predicted Amount of phase (%)				Amount of phase (%) Experimental			
Heat treatment and Alloy	**HCP Phase**	**Laves Cubic Phase**	**Mu Phase**	**BCC Phases**	**HCP Phase**	**Laves Cubic Phase**	**Mu Phase**	**BCC Phases**
WVCrTa 1400°C 100h	-	0.0	0.0	100.0	-	65.8±4.8	0.0	34.2±2.6
WVCrTa 1400°C 750°C 72h	-	0.0	0.0	100.0	-	68.9±4.5	0.0	31.1±3.3
WVCrTaTi 1400°C 100h	0.0	0.0	0.0	100.0	9.2±2.1	23.1± 1.6	0.0	67.1±4.6
WVCrTaTi 1400°C 750°C 72h	0.0	0.0	38.3	61.7	7.6±1.7	30.7±2.9	0.0	62.7±3.8

of the solution heat treated has increased, whilst chromium remains the same vanadium concentration is reduced by 50%. As seen above, tantalum is close to the stoichiometric ratio (33.3 at.%), with chromium having a similar concentration to the Laves phase in WVCrTa.

It has been suggested in the literature that vanadium acts to increase the configurational entropy of both Laves and bcc phases (Carruthers 2021). This is thought to occur by modifying the composition of the phases to equiatomic. It is interesting to note that the concentrations of vanadium in both phases of each HEA are similar. Suggesting that it has reached an equilibrium point of maximum stabilization.

8.1.8 Mechanical Properties of HEAs

The hardness of the as-cast, homogenized, and aged samples was assessed using a macro indenter. A minimum of ten indentations were taken of each sample, and their value averaged. The hardness values for the WCrTaVTi HEA homogenized at a range of temperatures are shown in table 38. Table 39 shows the subsequent hardness after ageing each homogenization at either 750 and 1000 °C for 7 days. All of the Hardness values

Table 38: **Vickers hardness of WVCrTaTi HEA.** Hardness measurements for WCrTaVTi HEA alloy in homogenized at different temperatures with 2kg load

Homogenisation temperature	Hardness Measurements (2Kg)					Average Measurement
As cast	605.0	618.2	608.0	600.5	602.8	**608.5 ± 5.6**
	604.2	611.3	610.5	607.1	617.4	
750 C	717.4	710.4	699.2	680.5	674.1	**699.8 ±18.6**
	671.7	690.9	722.1	707.9	723.8	
1050 C	754.3	717.4	770.8	686.1	677.6	**725.6 ± 40.6**
	644.8	764.4	765.1	729.4	725.9	
1150 C	1974	1866	1763	1758	1938	**1879.3 ± 67.55**
	1941	1939	1902	1842	1870	
1250 C	689.5	670.0	731.6	695.4	685.2	**690.6 ± 19.3**
	656.5	686.7	677.0	710.4	704.0	
1350 C	630.9	637.9	601.0	579.4	603.8	**608.4 ± 16.4**
	613.9	600.9	592.8	608.4	614.7	
1400 C	529.4	545.6	554.6	589.4	551.0	**548.9 ± 21.3**
	554.0	562.2	568.6	529.6	504.9	

for the WCrTaVTi HEA are displayed graphically in figure 8.13. Comparing the results obtained here for the cast, homogenized, and aged samples to that of the literature (table 3). Only the MoFeNiW has a higher Vickers hardness for an as-cast sample. Notably, the sample homogenized at 1400 °C has the lowest Vickers hardness compared to the other homogenization temperatures and the as-cast sample. This could indicate (as suggested earlier) that raising the temperature of this alloy to above 1400 °C melts the phases that form the laves phases in the alloy. Reducing the amount of these phases would result in a softening and a reduction in the hardness.

Increasing the homogenization temperature on the WCrTaVTi HEA had little effect on the overall properties of the alloy. Grain size for this HEA (calculated by the linear intercept method) only varied slightly between homogenization treatments (table 40). This could be explained by the Laves phase's pining effect on the migration of sub- and grain-boundaries (Lu HH 2020). Except for the WCrTaVTi HEA alloy homogenized at 1150 °C, each homogenization temperature has similar Vickers hardness. XRD analysis of the alloy at 1150 °C showed the presence of several other phases, including a possible Heusler and L21 phase, which were not observed in any of the other homogenizations. Only

Table 39: **Vickers hardness of WVCrTaTi HEA.** Hardness measurements for WVCrTaTi HEA alloy after various ageing conditions with 2kg load

Homogenisation treatment	Ageing condition	Hardness Measurements (2Kg)					Average Measurement
1150 C	**1000 C**	1911	1982	1890	1963	1938	**1891.4**
	7 days	1933	1893	1816	1773	1815	± **65.7**
	750 C	1768	1834	1900	1917	1720	**1875.7**
	7 days	1970	1856	2003	1932	1857	± **83.0**
1250 C	**1000 C**	695.2	670.9	681.2	669.8	668.6	**673.3**
	7 days	679.9	659.6	685.9	656.4	665.1	± **11.5**
	750 C	720.3	680.7	727.7	705.8	725.5	**715.2**
	7 days	766.5	677.1	716.5	696.1	736.2	± **25.4**
1350 C	**1000 C**	631.5	686.3	643.3	640.0	735.6	**688.3**
	7 days	696.9	663.8	742.1	740.9	702.7	± **40.5**
	750 C	604.7	531.0	522.7	658.3	582.6	**603.9**
	7 days	640.7	511.2	654.1	670.8	662.6	± **59.8**
1400 C	**1000 C**	815.1	814.1	754.2	832.7	747.9	**794.5**
	7 days	801.5	828.8	784.2	777.5	788.5	± **27.8**
	750 C	715.3	773.8	734.8	754.6	694.3	**725.4**
	7 days	785.1	709.5	722.3	685.0	679.7	± **34.5**

Figure 8.13: **Hardness measurement of WCrVTaTi.** Graph to show Vicker's hardness measurements as measured with a 2 kg load of the as-cast and after various heat treatments.

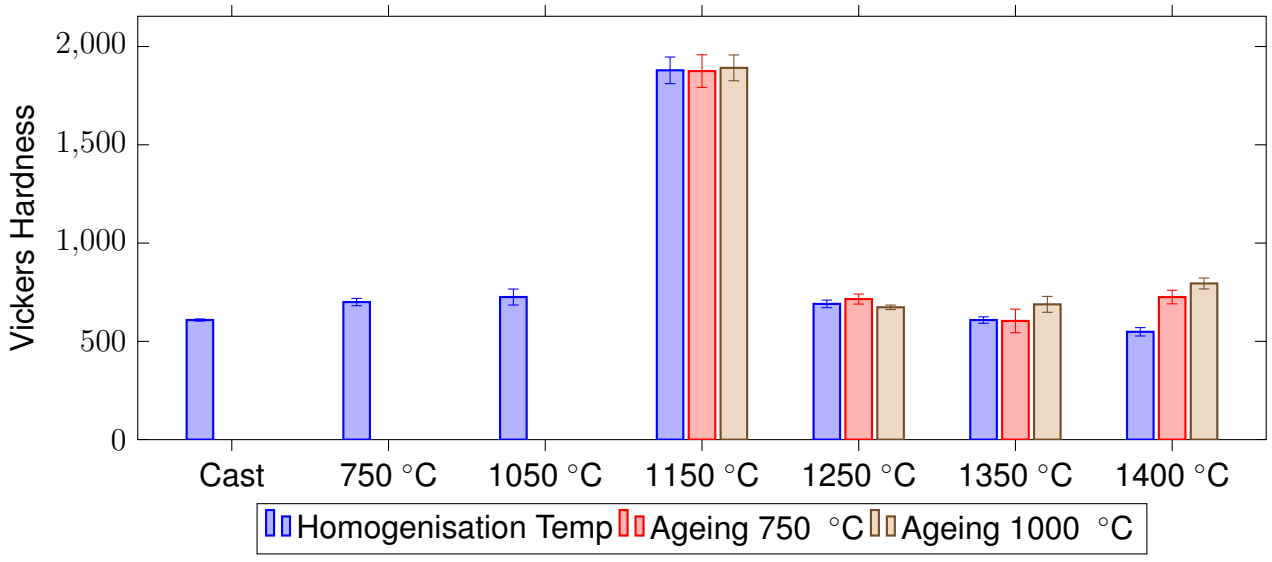

Table 40: **Grain size measurements of the WVCrTaTi HEA.** Grain size measurements for WCrTaVTi HEA alloy in homogenized and aged conditions - grain size reflects all phases present in the microstructure

Homogenisation treatment	Ageing Condition	Grain Diameter μm
750 °C	Homog.	37.2 ± 10.6
1050 °C	Homog.	39.3 ± 11.5
1150 °C	Homog.	63.3 ± 11.2
	750 °C	64.7 ± 8.6
	1000 °C	65.8 ± 9.3
1250 °C	Homog.	36.1 ± 13.7
	750 °C	43.5 ± 7.4
	1000 °C	38.9 ± 9.2
1350 °C	Homog.	35.1 ± 10.4
	750 °C	37.3 ± 11.6
	1000 °C	39.7 ± 9.0
1400 °C	Homog.	10.27 ± 4.0
	750 °C	23.4 ± 4.7
	1000 °C	27.8 ± 9.2

at the homogenization temperature of 1400 °C was a significant decrease in grain size seen. Vickers hardness of this homogenization temperature was also the lowest (of all of the homogenization temperatures and the as-cast sample), giving further weight to the suggestion of the melting of the leaves phases at this temperature, promoting hardness in this alloy.

This contrasts with WCrTaV HEA, which showed an increase in hardness with homogenization temperature as opposed to the observed phenomena of grain size increasing with homogenization temperature (figure 8.14) and Table 43. The results demonstrate a grain size reduction as homogenization temperature increases (Table 43). Therefore, one explanation for the increase in hardness could be the Hall-Petch relationship with grain size. Like the WCrTaVTi alloy, increasing the temperature would reduce the presence of Laves phases. This would promote greater homogenization between elements and nanostructuring of the alloy.

Table 39 shows the subsequent hardness after ageing each homogenization at either 750 and 1000 °C for 7 days, comparing the results obtained here for the cast, homoge-

Figure 8.14: **Hardness measurement of WCrVTa.** Graph to show Vicker's hardness measurements as measured with a 2Kg load of the as-cast and after various heat treatments.

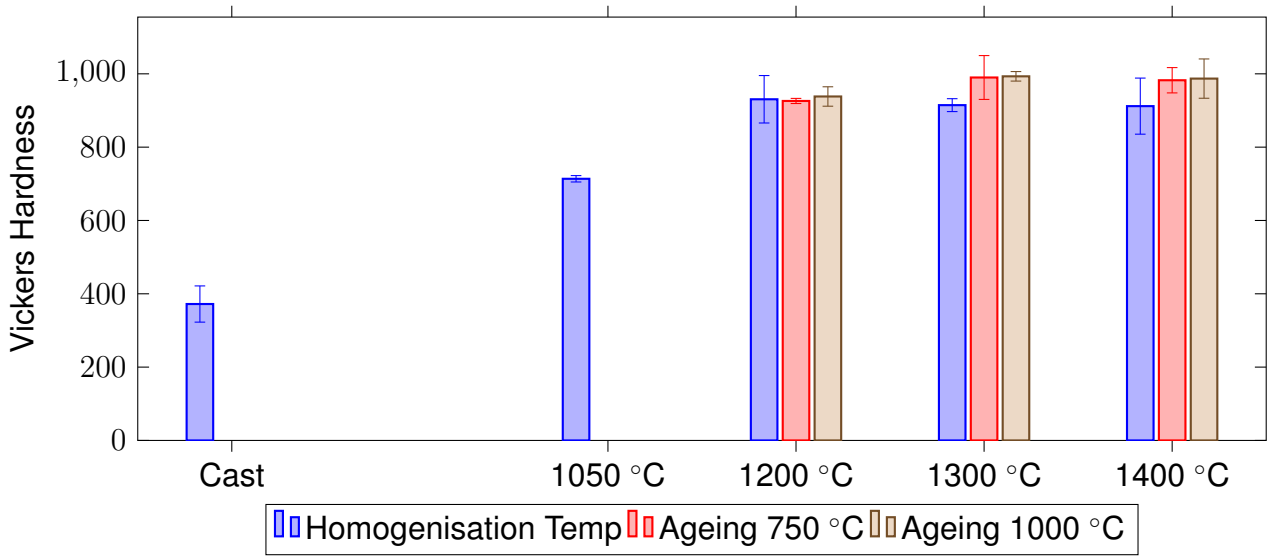

Table 41: **Vickers hardness of WVCrTa HEA.** Hardness measurements for WCrTaV HEA alloys in cast and homogenized conditions with 2kg load

Condition	Hardness Measurements (2Kg)					Average Measurement
As Cast	322.7	315.2	391.2	317.8	319.2	**372.1± 49.4**
	362.4	436.8	439.6	450.6	365.4	
1050 C	698.2	726.3	706.7	709.3	706.8	**713.7 ± 8.7**
	725.3	718.4	709.2	721.7	714.8	
1200 C	878.3	906.6	925.5	937.6	963.7	**930.6 ± 64.7**
	931.4	925.7	971.8	923.7	941.2	
1300 C	922.5	907.3	931.7	905.4	902.6	**914.6± 17.6**
	872.6	917.5	927.5	936.1	922.7	
1400 C	986.2	1053.0	988.8	892.2	925.7	**911.9 ± 76.5**
	804.2	842.6	801.9	867.6	956.8	

Table 42: **Vickers hardness of WCrTaV HEA.** Hardness measurements for WCrTaV HEA alloy after different thermal ageing conditions with a 2kg load

Homogenisation treatment	Ageing condition	Hardness Measurements (2Kg)					Average Measurement
1200 C	**1000 C**	969.6	963.6	973.9	958.2	948.6	**938.2 ± 26.5**
	7 days	922.4	907.1	930.4	906.5	901.5	
	750 C	911.4	921.8	935.6	919.3	928.8	**926.0±7.0**
	7 days	933.7	932.7	923.8	927.4	925.3	
1300 C	**1000 C**	1011	998.2	1008.5	977.2	988.7	**993.2 ±13.0**
	7 days	983.9	1009.5	993.8	989.6	971.5	
	750 C	997.5	973.8	993.7	983.7	992.6	**990.0 ±7.8**
	7 days	999.5	994.7	984.3	996.3	983.7	
1400 C	**1000 C**	956.2	1042.3	1004.2	1007.1	993.7	**987.0 ± 47.1**
	7 days	929.3	1054.2	961.3	1022.2	899.6	
	750 C	995.2	998.2	963.2	931.6	925.4	**982.6 ± 53.6**
	7 days	972.5	910.8	1029	997.2	1103.0	

Table 43: **WCrTaV grain size measurements.** Grain size measurements for WCrTaV HEA alloy in homogenized and aged conditions

Homogenisation treatment	Ageing Condition	Grain Diameter μm
750 °C	Homog.	54.9 ± 12.5
1050 °C	Homog.	56.5 ± 22.1
1200 °C	Homog.	42.7 ± 13.4
	750 °C	46.2 ± 11.9
	1000 °C	57.3 ± 9.6
1300 °C	Homog.	27.7 ± 12.6
	750 °C	33.9 ± 16.3
	1000 °C	37.3 ± 11.7
1400 °C	Homog.	9.08 ± 4.6
	750 °C	41.69 ± 22.2
	1000 °C	38.2 ± 15.7

nized and aged samples to that of the literature (Table 3). Only the MoFeNiW has a higher Vickers hardness for an as-cast sample. Notably, the sample homogenized at 1400 °C has the lowest Vickers hardness compared to the other homogenization temperatures and the as-cast sample. This could again suggest that raising the temperature of this alloy to above 1400 °C melts the phases that form the laves phases in the alloy. Reducing the amount of these phases would result in a softening, which would reduce the hardness.

The C14 Laves is the second most reported phase observed in RHEAs (Miracle DB Senkov (2017)). The presence of this phase is mainly associated with the three elements Cr, Zr, and Al. In the following systems "Cr–Zr–Me, Mo–Zr–Me, and V–Zr–Me" Miracle DB Senkov (2017), the Laves phase seems to be stable in regions where the Me (either Nb or Ti) is low.

8.2 Nano Indentation

To further analyse the phases present and the contribution made to the overall hardness of the alloys. Each aged sample was subjected to nano-indentation, and the subsequent area was analysed by EDX mapping and point scanning (Figures 8.15a and e). Images of the typical indents for each phase identified in the samples are shown in Figures 8.15b and f). Hardness maps (Figures 8.15c and g) as produced by the NanoBlitz 3D modelling software. Plots for each indented area are included (Figures 8.15d and h) to demonstrate the variation in hardnesses seen in the samples. To better understand the contribution of each phase in the respective alloys to the overall mechanical properties of the alloy. The data from the EDX/point scanning for each indent was collected (data not shown), and indents were grouped in terms of alloy composition. The data for each aged sample is displayed as hardness vs. modulus in Figures 8.15i and j. The compositional ranges and mechanical properties (hardness and modules) for each of the phases identified are shown in Table 44 along with number N, points measured. Nanoindentation of the 4-HEA reveals the hardness of the two phases identified earlier to be extremely hard, with mean Vickers harnesses of 2587.42 $\pm$ 378.92 and 1441.89 $\pm$ 284.21 for the Ta_2 and $TaCr_2$(VW)

Table 44: Compositional analysis by EDX point scan, Vickers hardness and Modulus measurements for phases identified by nano-indentation in the 4-HEA after ageing at 750 ∘C for 72h.

Alloy	Phase	N	Hardness HV		Modulus GPa	
			Mean	SD	Mean	SD
WVTaCr	Ta_2W	625	2587	378	415	43
	$TaCr_2$(VW)	402	1441	284	296	26
	WVCr(Ta)	17	775	218	204	49

Phase	Composition							
	W		V		Ta		Cr	
	Mean	SD	Mean	SD	Mean	SD	Mean	SD
bcc1 (Ta_2W)	23.53	1.12	9.95	0.35	57.93	2.80	8.59	3.58
Laves ($TaCr_2$(VW))	9.38	2.50	19.41	2.34	22.76	3.23	48.55	1.69
bcc2 (WVCr(Ta))	47.97	6.69	26.03	4.50	11.61	6.70	14.39	7.67

respectively. However, further analysis revealed a third phase (WVCr), which was not seen in the earlier experiments. On wider SEM observation of the sample, the presence of this phase was only seen in a small proportion of the alloy. The measured Vickers hardness of the third WVCr-rich phase was calculated to be 775.92 $\pm$ 218.05. EDX and Nanoindentation of the 5-HEA reveals three phases with varying hardness. The first is an almost equiatomic WVTaCrTi composition with a mean Vickers hardness of 945.01 $\pm$ 246.04. The second is a TaCrV-rich phase with a Vickers hardness of 3380 $\pm$ 274.97. The third and final phase is a titanium-rich phase with a Vickers hardness of 379.02 $\pm$ 133.99. Identifying a third phase in the 4-HEA further demonstrates the plethora of phases that can exist in a HEA. Adding further weight to the lack of stability on some HEAs that are calculated to be a solid solution plus intermetallic phase.

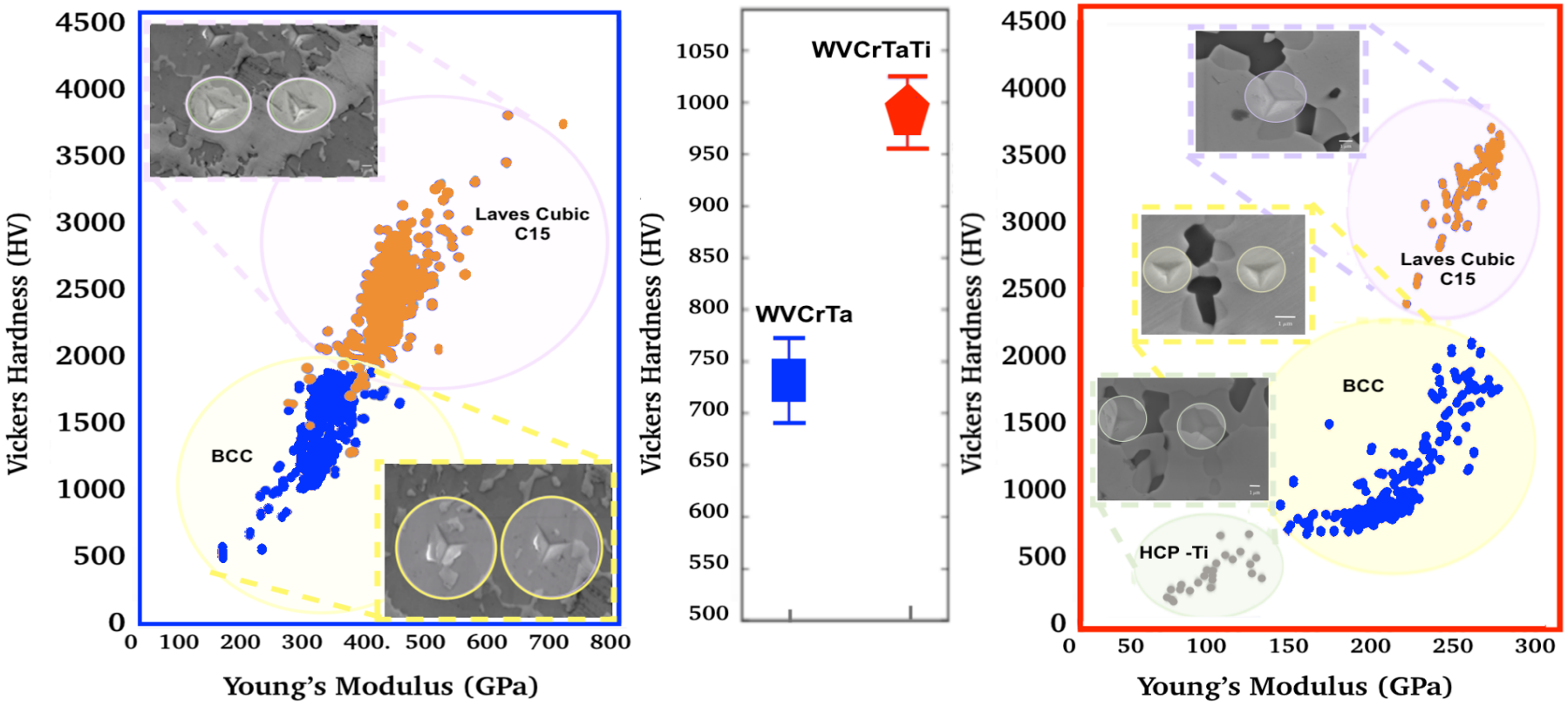

Figure 8.15: **RA-RHEA homogenized 1400 °C 100h + aged 750°C 7 days Nano and macrohardness**(a) Nanohardness of phases present in 4 RAHEA WVCrTa, complete with SEM images showing indents in respective Laves C15 and BCC_A2 phases (inset). (b) Macrohardness of the same RAHEAs for 4 (blue) and 5 (red) alloys, respectively. (c) Nanohardness of phases present in 5 RAHEA WVCrTaTi, complete with SEM images showing indents in respective Laves C15, BCC_A2 and titanium phases (inset). (colour key: Orange - C15 Laves Blue - bcc, Grey - HCP titanium.

8.2.1 Tungsten Chromium decomposition in a HEA - WCrVTa

As we have seen in the previous chapter, alloying tungsten with either chromium or titanium and subsequently ageing the binary alloy within the miscibility gap leads to a decomposition of the alloy into a two-phase microstructure. Figure 8.16 shows regions of decomposition in the WCrVTa alloy following homogenization at 1400 °C and then ageing for 7 days at 750 °C. EDX analysis of the decomposed region (figure 8.17) shows it to be due to the separation of tungsten and chromium.

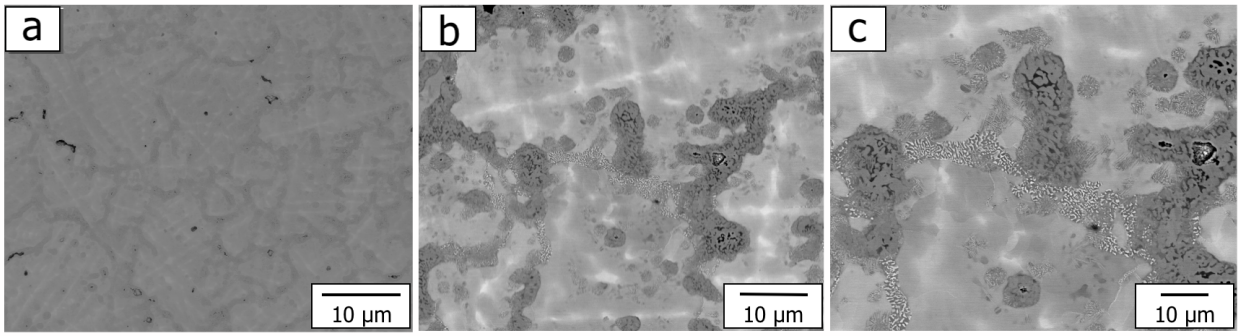

Figure 8.16: **BSE images of decomposed region of WCrVTa alloy**. (a-c) Low to a high magnification of the WCrVTa alloy showing regions of decomposition, following homogenization at 1400 °C and then ageing for 7 days at 750 °C .

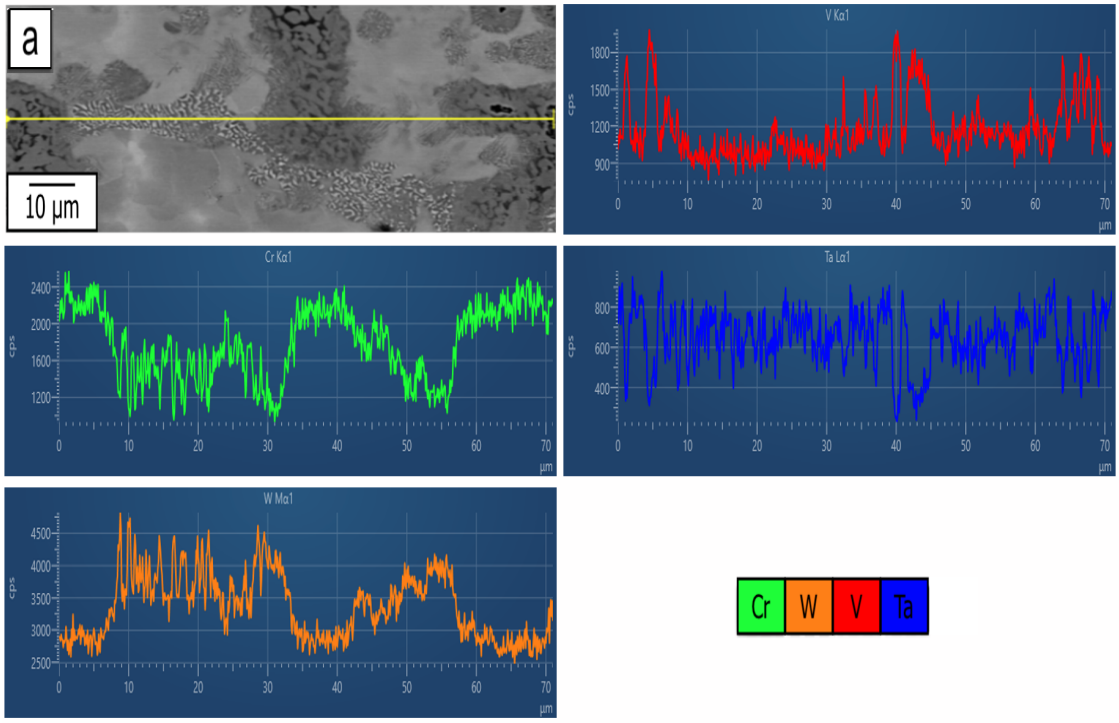

Figure 8.17: **Compositional analysis of the phases present in the decomposed region of WCrVTa alloy heat treated at 1400 °C and then aged for 7 days at 750 °C.** EDX line scan and profile maps for the elements found in the alloy.

8.2.2 Final compositions?

Analysis of both samples on a macroscopic basis reveals three potential phases in each alloy. Although compositions vary over the samples (due to the inhomogeneity from manufacture), figures 8.18 and 8.19 give compositions of the final stable phases (at least in this alloy) seen in each alloy after solution heat treating and ageing. Although the holy grail equiatomic single-phase HEA was not seen in the aged sample. BSE and SEM show that compositions will form a single bcc phase (although not equiatomic) and can be manufactured by arc melting and heat treatments.

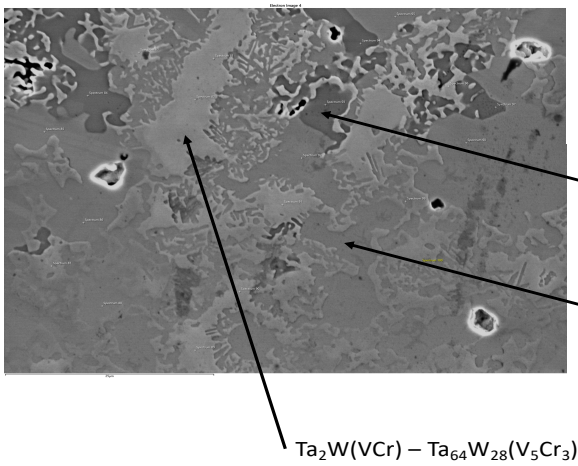

Alloy	Phase	N	Hardness HV		Modulus GPa	
			Mean	SD	Mean	SD
WVTaCr	Ta_2W	625	**2587.42**	378.92	**415.12**	43.79
	$TaCr_2$(VW)	402	**1441.89**	284.21	**296.64**	26.57
	WVCr	17	**775.92**	218.05	**204.11**	49.49

Phase	Composition							
	W		V		Ta		Cr	
	Mean	SD	Mean	SD	Mean	SD	Mean	SD
Ta_2W	**28.20**	1.12	**4.84**	0.35	**64.35**	2.80	**2.61**	3.58
$TaCr_2$(VW)	**10.77**	2.50	**16.16**	2.34	**27.17**	3.23	**45.91**	1.69
WVCr	**31.95**	6.69	**26.44**	4.50	**11.96**	6.70	**29.65**	7.67

Figure 8.18: **BSE image of the typical microstructure of WVTaCrV after homogenisation and ageing.** Identified in the image are the three main phases found in the aged sample, along with corresponding average compositions as observed by EDX.

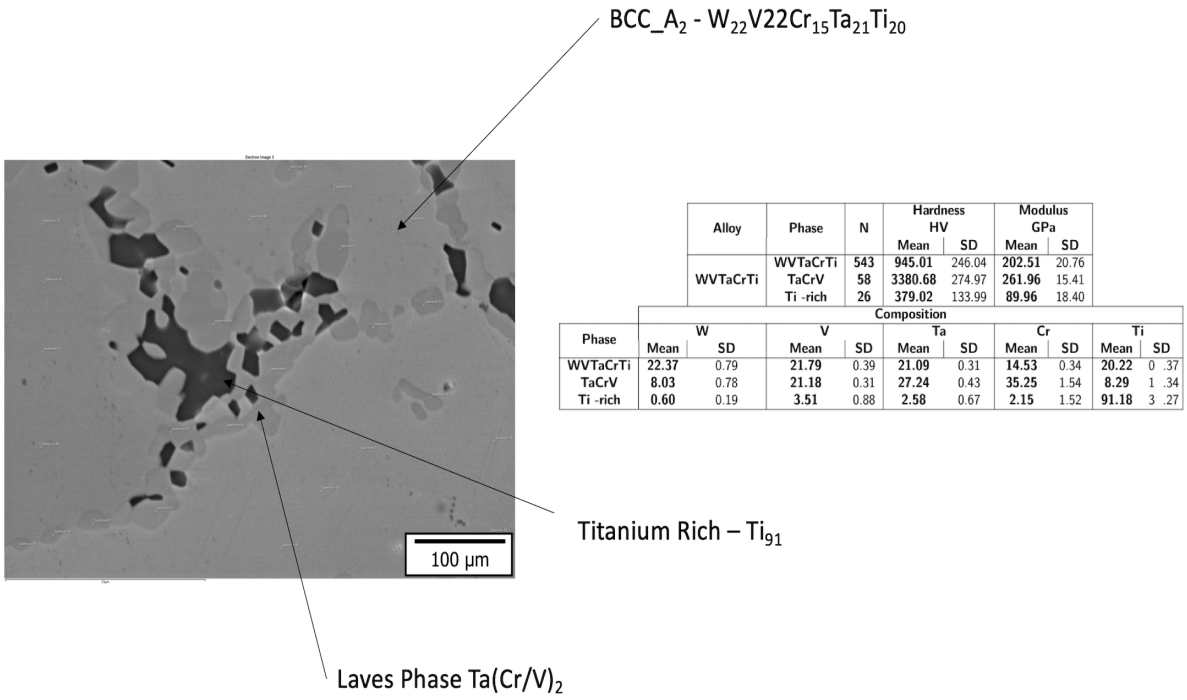

Alloy	Phase	N	Hardness HV		Modulus GPa	
			Mean	SD	Mean	SD
WVTaCrTi	WVTaCrTi	543	945.01	246.04	202.51	20.76
	TaCrV	58	3380.68	274.97	261.96	15.41
	Ti -rich	26	379.02	133.99	89.96	18.40

Phase	Composition									
	W		V		Ta		Cr		Ti	
	Mean	SD	Mean	SD	Mean	SD	Mean	SD	Mean	SD
WVTaCrTi	22.37	0.79	21.79	0.39	21.09	0.31	14.53	0.34	20.22	0 .37
TaCrV	8.03	0.78	21.18	0.31	27.24	0.43	35.25	1.54	8.29	1 .34
Ti -rich	0.60	0.19	3.51	0.88	2.58	0.67	2.15	1.52	91.18	3 .27

Figure 8.19: **BSE image of the typical microstructure of WVTaCrVTi after homogenisation and ageing.** Identified in the image are the three main phases found in the aged sample, along with corresponding average compositions as observed by EDX.

8.3 Conclusion

- WVCrTa and WVCrTaTi RA-RHEA alloys were selected by the use of empirical calculations to predict melting temperature, activation, and propensity to form a bcc solution plus intermetallic strengthening phase as candidate materials for fusion. From these calculations, two tungsten alloys were selected.
- Bulk casting of two new tungsten-based RA-HEAs was assessed experimentally and the microstructure of WVCrTa and WVCrTaTi alloys after solution heat treating at 1400°C for 100h, and after ageing of the alloys at 750°C for 7 days.
- Two phases dominate in the solution heat treated, a bcc solid solution rich in tantalum and tungsten, as well as a C15 Laves phase rich in chromium and tantalum. The same two phases are present in the samples ged at 1400°C however, a third HCP phase rich in Ti was present in WVCrTaTi alloy
- The experimental findings were compared to thermocalc predictions using the TCHEA5 database. Whilst bcc is correctly identified as the majority phase by thermocalc, a C15 Laves phase was found to be stable up to 1400 °C for both RA-HEAs. Despite only being predicted for WVCrTaTi. No Mu phase was identified in the WVCrTaTi despite it being predicted.
- Nanohardess measurements of the two RA-HEAs show distinct measurements for the individual phases. With the WVCrTa alloy showing Young's modulus values over twice that of the WVCrTaTi alloy.
- Compositions of both single-phase bcc hEAs can be observed in the allow. However, melting these compositions will likely result in an alloy containing macrosegregation of tungsten as seen above. With the current setup, it is impossible to arc melt a tungsten-based HEA with sufficient homogenisation. If a true tungsten-based HEA is desired that does not contain macrosegregation then other methods will need to be explored such as HIPping.

9 Final Conclusion

This project aimed to design and create novel tungsten-based alloys for high-temperature applications, particularly as a structural material within a fusion power plant. This explored the concept of nanostructured tungsten alloys, whereby alloying additions that induce a second phase(s) can be used to control the microstructure, and so improve the strength and ductility. Additionally, nano-scale interfaces will act as sinks for irradiation damage. In Chapter 3, there is a focus on what is termed a "smart" tungsten alloy, where adding chromium to the tungsten gives it a self-passivating nature as an extra layer of safety. With this in mind, the W-Cr binary system (as well as others) was investigated not only to improve the manufacturing methods but also to try and elucidate the recrystallization phenomenon behind this alloy. Of the several manufacturing methods explored in this thesis, multiple attempts were made to arc melt a binary alloy (both internally and externally). However, the loss of chromium was severe; attempts were made to account for the loss, but still, the "Hedgehog" type sample prevailed. This comes from the high difference in melting points of the elements (over 1000 °C in the case of tungsten and chromium), however, despite the problems with manufacturing an alloy. Considerable strives were made to produce fine-scaled lamellar nano-scaled precipitates, which showed some evidence of improved mechanical properties. This led to the reasoning that a powder-based method via blending or mechanical alloying powder would improve the diffusion of elements and, therefore, on melting, a fully dense homogenised alloy would be produced. However, the problem of the vaporisation of the chromium from the alloy still prevailed. Several iterations of this using extra chromium still lead to the production of very porous (and therefore extremely brittle) alloy. An attempt was made to manufacture a HIPped sample from the powder; however, the choice to do so under argon was ultimately wrong and led to the catastrophic failure of the can. A HIPped W-Cr-Z-Y manufactured by CEIT showed the best prospect for bulk manufacturing a W-Cr-type alloy. However, it did not show the fine lamellar precipitation in the W-Cr samples manufactured by arc melting

and SPS. Despite this, it does show that a W-Cr-based alloy can be manufactured under HIPping. Further attempts at creating a 50/50 W-Cr alloy should be investigated using a bottom-up approach and HIPping. In Chapter 4, three other tungsten alloy systems W-Ti-xFe, W-Mn and W-Ti alloys, were investigated. W-Mn exhibited the same problems seen with W-Cr. The obvious difference in melting points leads to the excessive loss of manganese from the binary alloy, leaving a very porous and brittle alloy. Although examination of the alloy did show a promising increase in the number of LAGBs, the ability to produce a homogenised single alloy was not achieved. In the W-Ti-xFe tertiary alloy system, as predicted, nano-scale B2 TiFe(W) precipitates were seen to form within an A2(W,Ti,Fe) matrix. However, despite various compositions and ageing treatments, the formation of an alloy with evenly distributed precipitates was not achieved. The formation of an alloy with an A2-B2 (γ-γ') precipitate-reinforced 'Tungsten-superalloy' does show promise. With the difficulty in producing an ODS tungsten alloy, this demonstrates a viable alternative. However, work still needs to be done to validate such a system and optimise the mechanical properties. Of the alloys investigated, W-Ti has shown considerable promise. However, the final microstructure was akin to that of a tungsten-heavy alloy (WHA). The alloy demonstrated ductility at room temperature with a reduction in thickness of 10% on rolling. But 3-point bending on samples rolled at 1000 °C showed considerable ductility at temperatures as low as 150 °C. Further refinement of the composition of the alloy and rolling temperatures should help to reduce the DBTT to even lower temperatures. This should allow heat treatments to produce a nano-structured two-phase alloy, as seen in the W-Cr system, that may help improve the overall mechanical and irradiation properties. In Chapter 5, the potential of producing tungsten-based reduced activation high entropy alloys (RA-HEAs) for fusion was investigated. Again, during the production of both RA-HEAs, there was a loss of chromium on arc melting. Despite master alloys of melted binary elements to try and reduce the melting point of tungsten (Tungsten-Tantalum) on trying to melt these binary alloys with the lower melting point elements (chromium and vanadium), there was immediate vaporisation of the later elements. This led to a lack of

homogeneity in the as-cast/as-received samples meant that solution heat treatments of both alloys did not produce the single-phase alloy that had been predicted by Calphad. As a result, any subsequent ageing treatment (even at temperatures of 1250 $^\circ$ for 100 hours) did not produce the single-phase bcc structure expected. In Chapter 6, A Ti-Fe-Mo bcc-superalloy comprising a bcc A2 γ Ti matrix reinforced by an ordered bcc B2 TiFe γ' intermetallic precipitate was investigated. This alloy exhibits an unusual recrystallization phenomenon, whereby ageing with no externally applied deformation results in substantial grain refinement, which we have. In Chapter 7, the work on the recrystallization was extended into the W-Cr system.

In Final Conclusion, there is great scope for developing novel tungsten alloys. It has been shown that either alloying additions or exploiting the miscibility gap can control the microstructure of tungsten and its alloys. However, there are still challenges with manufacturing from a top-down approach. Further investigation into the production of tungsten alloys through powder metallurgy must be conducted to see if alloys can be produced with better densities. The alloys created have shown improvements in strength, yet the ability to ductilise a tungsten alloy to room temperature still remains a major challenge. Grain size control through the second-phase formation and recrystallization has demonstrated new ways in which to refine the grain structure. This benefited both strength and ductility. Future work to further optimise compositions and microstructure either to reduce or enhance the second phases and to investigate what compositions give the optimal mechanical properties, particularly what microstructure is needed in a tungsten-based alloy to promote ductility. Once this is known, the next assessment will be what can be done with the microstructure to give the best irradiation performance.

10 Future work

10.1 Future work - W-Cr

- The next stage of the process has to be to try and iterate a composition of tungsten-chromium that can be HIPped into a fully dense (or near dense alloy). Once an alloy can be manufactured to a satisfactory density, the obvious next step is to try and roll the sample to see what effect this will have on the mechanical properties of the alloy. This should produce enough material that can be manufactured in tensile and Charpy impact bars to access the true DBTT of the alloy.

- Once a homogenous material can be produced, the next step will be to nanostructure the alloy and test its properties following neutron irradiation. This will determine if the hypothesis of nanostructuring the alloy into the two-phase lamellar microstructure affects the irradiation properties.

- Assuming that a fully dense (or near-dense) alloy can be manufactured. A full assessment of the effects of the nanostructuring via decomposition needs to be assessed. To identify what ageing treatment gives the finest grain size to mechanical property ratio. Once this can be determined, the next step is to look at the radiation performance of the alloy and how this nanostructuring affects the ability of the alloy to perform under such conditions.

10.2 Future Work W-Ti, W-Mn

- For each of the four alloys created, the major problem associated with each of them was the macrosegregation and/or porosity. To bulk manufacture these alloys, optimal conditions will need to be sorted, as well as compositional variations. It has been shown in this project that despite different manufacturing routes and suppliers, tungsten alloys produced from conventional arc melting (of either metal fragments

or powder) are insufficient to create an alloy without the segregation of elements or pores.

- Despite various heat treatments (solution heat treating and ageing), the above deficiencies still existed. It may, therefore, be necessary to change tact and look at alternate routes for manufacturing these alloys, such as Spark Plasma Sintering or HIPping. Both techniques may provide the means to fuse tungsten with their binary.

- Both W-Cr and W-Ti produced lamellar precipitates by exploiting the miscibility gap. However, in both alloys, the precipitation was not entirely homogenous throughout the alloy (but for different reasons). For W-Ti following ageing at 1000 °C, the titanium-rich matrix is entirely covered by the decomposed tungsten-rich lamellar. However, the problem remains with the prior tungsten powder particles that have not dissolved into the titanium matrix following solution heat treatment. Despite 100h hours at 1400 °C, considerable macrosegregation is present. Therefore, improving this, as with the other alloys, additive manufacturing of a W-Ti sample seems sensible. Following adequate blending of powders, there should be better homogeneity after manufacture.

- Although 3-point bending has been performed on the W-Ti rolled samples, little mechanical work could be done on the other alloys. Scaling up the manufacture of these alloys through additive manufacturing would give enough material to produce tensile and Chapry impact bars. This would allow the DBTT of the alloys to be determined with greater accuracy. Larger samples would also better clarify the exact values of the yield stresses, ultimate tensile stresses, and elongation to failure. It would also gather information on the effects of macroscopic defects (if any) in the sample on their potential uses in fusion reactors.

- As these alloys are to be used in high-temperature applications, an investigation of their mechanical properties and oxidation potential will need to be conducted to see if they can be suitable materials for use within a fusion reactor.

- As these alloys are intended to be used in fusion reactors, creep tests are one of the biggest questions to answer after successful manufacture. To see how the mechanical properties of these alloys change at operating temperatures.

- The ultimate goal of any nanostructured alloy following bulk manufacture is to irradiate any samples in a cyclotron. This will determine whether the nanostructuring through decomposition leads to a better performance than current tungsten alloys.

10.3 Future Work - HEA

- Figures 8.18 and 8.19 both show compositions of single-phase HEAs. It would therefore be reasonable to suggest that the next step would be to try and bulk cast alloys with these compositions when both alloys were homogenized at 1400 °C and observed under SEM, considerable macrosegregation of elements was still seen even after 4 days. In addition, the second bcc (WVCr) phase is probably present due to the slow decomposition of the tungsten-rich dendrite phase. To confirm this and the actual presence of the other two phases in the alloy homogenization at higher temperatures needs to be done to determine if the phases observed in this study accurately represent the stable phases or result from incomplete diffusion of elements. The inability to solution heat treat these alloys above 1400 °C has been the biggest stumbling block. I believe that solution heat treating these alloys at higher temperatures may produce an alloy with a single-phase bcc structure, eliminating the hard and brittle C14 Laves phase identified in both alloys.

- Although we have shown that a tungsten-based HEA can be cast in a bulk manner, the primary issue has been the melting of the tungsten metal. One way to get around this stumbling block may be using additive manufacturing. This would mean creating the 4 and 5 HEA from powders and using manufacturing methods such as HIPping or SPS. This would potentially prevent the inhomogeneous microstructure in the as-cast samples that permeated through the solution heat-treated and aged

samples. It may be that starting from a mechanically alloyed or blended powder base may reduce the need to do higher temperatures for homogenization. So far, only thin films of these alloys have been tested for their potential uses as materials for fusion reactors. Even though the alloys created here are incredibly brittle, their microstructure and mechanical properties would be worth trying following neutron irradiation. Thin films of tungsten HEAs have shown promise under irradiation, even demonstrating self-annealing behaviour. Although it must be noted that those films are of a different composition, It would be interesting to see if the presence of the Laves phase has any detrimental or beneficial effect on the irradiation properties.

10.4 Further Work - Ti-Fe-Mo

- The next step is to try and modify the composition to control the B2 precipitates. This will allow the optimisation of the ratio of B2 precipitates to give the best mechanical properties. In addition, as the alloy was observed to be extremely brittle at room temperature, the alloying with other elements, such as aluminium, may help to improve its mechanical properties.

- Once modifications are made the next step will be to look at ductilising the alloy with the addition of elements to the matrix to reduce the brittleness of the alloy with BCC alloys such as vanadium. Once all of these parameters have been accessed the final step will be to look at additive manufacturing such as HIPping or laser bed technology to bulk manufacture larger pieces.

11 References

Bibliography

Administration, U. E. I. (2023), 'The international energy outlook 2016 (ieo2016)', *https://www.eia.gov/outlooks/ieo/* **DOE/EIA-0484(2016)**.

Aguirre M, Martin A Pastor J LLorca J Monge M Pareja, R. (2009), 'Mechanical behavior of w-y2o3 and w-ti alloys from 25 ℃ to 1000c,', *Metal. Mater. Trans. A* **40A**, 2283–2290.

Aguirre M, Martin A Pastor J LLorca J Monge M Pareja, R. (2010), 'Mechanical properties of y2o3-doped w-ti alloys', *J. Nucl. Mater.* **404**, 203–209.

Angqvist M, Rahm JM Gharaee L Erhart, P. (2019), 'Structurally driven asymmetric miscibility in the phase diagram of w-ti', *PHYSICAL REVIEW MATERIALS.* **3**, 073605.

Armstrong DEJ, Edmondson PD Roberts, S. (2013), 'Effects of sequential tungsten and helium ion implantation on nano-indentation hardness of tungsten', *Appl. Phys. Lett.* **102 (25)**, 251901.

Armstrong, DEJ Edmondson PD Roberts, S. (2013*a*), 'Effects of sequential tungsten and helium ion implantation on nano-indentation hardness of tungsten', *Applied Physics Letters* **102**(25), 251901.

Armstrong, DEJ Wilkinson AJ Roberts, S. (2011), 'Mechanical properties of ion-implanted tungsten–5 wt% tantalum', *Physica Scripta* **2011**(T145), 014076.

Armstrong, DEJ Wilkinson YI X AJ Roberts, S. (2013*b*), 'Hardening of self ion implanted tungsten and tungsten 5-wt% rhenium', *Journal of Nuclear Materials* **432**(1), 428–436.

Atwani O El, Li N Li M Devaraj A Baldwin J Schneider MM Sobieraj D Wrobel JS Nguyen-Manh D Maloy S Martinez, E. (2019), 'Outstanding radiation resistance of tungsten-based high-entropy alloys', *Science Advances* **5**.

Backer, AD Sand AE Nordlund K Luneville L Simeone D Dudarev, S. (2016), 'Subcascade formation and defect cluster size scaling in high-energy collision events in metals', *Europhysics Letters* **115**(2), 26001.

Bai, XM Voter AF Hoagland RG Nastasi M Uberuaga, B. (2010), 'Efficient annealing of radiation damage near grain boundaries via interstitial emission', *Science* **327**, 1631–1634.

Baldwin, MJ Doerner, R. (2008), 'Helium induced nanoscopic morphology on tungsten under fusion relevant plasma conditions', *Nuclear Fusion* **48**(3), 035001.

Baldwin MJ, Doerner, R. (2010), 'Formation of helium induced nanostructure fuzz on various tungsten grades', *J. Nucl. Mater.* **404**, 165–173.

Bampton CC, Jones IP Loretto, M. (1978), 'Stacking fault energy measurements in some austenitic stainless steels', *Acta Metall* **26**, 39–51.

Barbour, J., Charbonnier, F., Dolan, W., Dyke, W., Martin, E. & Trolan, J. (1960), 'Determination of the surface tension and surface migration constants for tungsten', *Physical Review* **117**(6), 1452 – 1459.

Barton, JL Buchenauer DA Wampler WR Rudakov DL Fang ZZ Lasnier CJ Whaley JA Watkins JG Unterberg EA Kolasinski RD Guo, H. (2019), 'Retention properties in displacement damaged ultra-fine grain tungsten exposed to divertor plasma', *Nucl. Mater. Energy* **20**, Article 100689.

Basinski ZS, Christian, J. (1954), 'A pressurized high-temperature debye-scherrer camera, and its use to determine the structures and coefficients of expansion of γ- and δ-manganese', *Proc. R. Soc. Lond. A* **223A (1155)**, 554–560.

Beck, CE Hofmann F EliasonJK Maznev AA Nelson KA Armstrong, D. (2017), 'Correcting for contact area changes in nanoindentation using surface acoustic waves', *Scripta Materialia* **128**, 83–86.

Becquart, CS Domain, C. (2012), 'Solute–point defect interactions in bcc systems: Focus on first principles modelling in w and rpv steels', *Current Opinion in Solid State and Materials Science* **16**(3), 115–125.

Beer AG, Barnett, M. (2007), 'Microstructural development during hot working of mg-3al-1zn', *Metall Mater Trans A* **38A**, 1856–1867.

Benjamin JS, . (1992), 'Mechanical alloying – history and future potential', *Advances in Powder Metallurgy and Particulate Materials, JM Capus, and RM German, Eds.,* **Metal Powder Industries Federation, Princeton, NJ, USA, vol. 7**, 155–168.

Bingert JF, L. V. & Cerreta, E. (2009), 'Characterization of shear localization and shock damage with ebsd. in electron backscatter diffraction in materials science', *(eds. A. J. Schwartz, M. Kumar, B.L. Adams, D.P. Fields)* **Chapter 12, Springer Science and Business Media, New York**, 301–315.

Birringer R, Herr U Gleiter, Y. (1986), 'Nanocrystalline materials—a first report, trans. jpn.', *Inst. Metals* **27**, 43–52.

Bodine G, . (1963), 'Tungsten sheet rolling program', *Final Report, Fasteel Metallurgical Corp.,* **North Chicago, Illinois**.

Bolt H, Barabash V Krauss W Linke J Neu R Suzuki S Yoshida, N. (2004), 'Materials for the plasma-facing components of fusion reactors', *J. Nucl. Mater* **329–333**, 66–73.

Bonnekoh C, Hoffmann A Reiser, J. (2018), 'The brittle-to-ductile transition in cold rolled tungsten: On the decrease of the brittle-to-ductile transition by 600 k to 65°c', *Int. J. Refract. Met. Hard Mater.* **71**, 181–189.

Bracq G, Laurent-Brocq M Perri'ere L Pir'es R Joubert JM Guillot, I. (2017), 'The fcc solid solution stability in the co-cr-fe-mn-ni multi-component system', *Acta Materialia* **128**, 327–336.

Brewer L, Field DP Merriman, C. (2009), 'Mapping and assessing plastic deformation using ebsd. in electron backscatter diffraction in materials science', *eds. A. J. Schwartz, M. Kumar, B.L. Adams, D.P. Fields),* **Chapter 18, Springer Science and Business Media, New York**, 251–262.

Briant C, Hall, E. (1989), 'The microstructure of rolled and annealed tungsten rod', *Metall. Mater. Trans. A* **20**, 1669–1686.

Broeder FJA, . (1972), 'Interface reaction and a special form of grain boundary diffusion in the cr-w system', *Acta Metallurgica* **20, 3**, 319–332.

Broglie, I Beck CE Liu W Hofmann, F. (2015), 'Temperature dependence of helium-implantation-induced lattice swelling in polycrystalline tungsten: X-ray micro-diffraction and eigenstrain modelling', *Scripta Materialia* **107**.

Brown, AM Ashby, M. (1980), 'Correlations for diffusion constants', *Acta Metallurgica* **28**(8), 1085–1101.

Budagovskiy S, Bykov V Gavrilyuk M Pod Yachev, V. (1973), 'Some electron structure characteristics of w-re solid solutions', *NASA Technical Translation Report NASA TT F-15* p. 214.

Burgers, W. (1934), 'On the process of transition of the cubic-body-centered modification into the hexagonal-close-packed modification of zirconium', *Physica* **1**(7-12), 561–586.

Calcagnotto M, Ponge D Demir E Raabe, D. (2010), 'Orientation gradients and geometrically necessary dislocations in ultrafine grained dual-phase steels studied by 2d and 3d ebsd', *Mater. Sci. Eng. A* **527**, 2738–2746.

Calvo-Dahlborg, M Brown, S. (2017), 'Hume-rothery for hea classification and self-organizing map for phases and properties prediction', *Journal of Alloys and Compounds* **724**, 353–364.

Carruthers, AW Li BS Rigby M Raquet LC Mythili R Ghosh C Dasgupta A Armstrong DEJ Gandy AS Pickering, E. (2021), 'Novel reduced-activation tivcrfe based high entropy alloys', *Journal of Alloys and Compounds* **856**, 157399.

Cerný R, e. a. (2013), 'Trimetallic borohydride li3mzn5(bh4) 15 (m ¼ mg, mn) containing two weakly interconnected frameworks', *Inorg. Chem.* **52 (17)**, 9941–9947.

Charifi Z, Reshak AH Baaziz, H. (2009), 'Electronic band structures of av 2 (a = ta,ti, hf and nb) laves phase compounds', *J. Phys. Condens. Matter* **21**, 25502.

Chen KC, Allen S M Livingston, J. (1997), 'Microstructures of two-phase ti-cr alloys containing the ticr2 laves phase intermetallic.', *J. Mater. Res* **12**, 1472–1480.

Chen KC, Allen S M Livingston, J. (1998), 'Factors affecting the room-temperature mechanical properties of ticr2-base laves phase alloys', *J. . Mater. Sci. Eng. A* **242**, 162–173.

Chen X, Wolf W Podloucky R Rogl, P. (2005), 'Ab initio study of ground state properties of the laves phase compounds ticr2 , zrcr2 , and hfcr2.', *Phy. Rev. B* **71**, 174101.

Chena, SM Mac Z-Y Qiud S Zhange LJ Zhangf SZ Yanga R Hu, Q. (2021), 'Phase decomposition and strengthening in hfnbtatizr high entropy alloy from first-principles calculations', *AMI: Acta Materialia* **pre-print**.

Cheng G, Jian W Xu W Yuan H Millett P Zhu, Y. (2013), 'Grain size effect on deformation mechanisms of nanocrystalline bcc metals', *Mater. Res. Lett.* **1**, 26–31.

Cheng W, Jian W Yuan H Tsai M Zhu, Y. (2013), 'Dislocations with edge components in nanocrystalline bcc mo', *J. Mater. Res.* **28**, 1820–1826.

Cheng Y, Mrovec M Gumbsch, P. (2008), 'Atomistic simulations of interactions between the 1/2<111> edge dislocation and symmetric tilt grain boundaries in tungsten', *Philos. Mag.* **88**, 547–560.

Choe HJ, Won JW Hyun YT Lim KR Yoon, S. (2018), 'Tife precipitation behavior and its effect on strengthening in solution heat-treated ti-5al-3.5fe during isothermal aging', *Metals* **8**, 875–822.

Cizek, P. (2016), 'The microstructure evolution and softening processes during high-temperature deformation of a 21cr–10ni–3mo duplex stainless steel', *Acta Mater* **106**, 129–143.

Coenen J, Philipps V Brezinsek S Pintsuk G Uytdenhouwen I Wirtz M Kreter A Sugiyama K Kurishita H Torikai Y Ueda Y Samm, U. (2011), 'The textorteam, melt-layer ejection and material changes of three different tungsten materials under high heat-flux conditions in the tokamak edge plasma of textor', *Nuclear Fusion* **51**, 113020.

Coolidge W, . (1910), 'Ductile tungsten', *249th meeting of the american institute of electrical engineers, A.I.E.E* p. 961–965.

Cotton, J. D., Briggs, R. D., Boyer, R. R., Tamirisakandala, S., Russo, P., Shchetnikov, N. & Fanning, J. C. (2015), 'State of the art in beta titanium alloys for airframe applications', *Jom* **67**(6), 1281–1303.

Cram DG, Zurob HS Brechet YJM Hutchinson, C. (2009), 'Modelling discontinuous dynamic recrystallization using a physically based model for nucleation', *Acta Mater 57* pp. 5218–5228.

D, S. (2019), 'Recent advances in characterising irradiation damage in tungsten for fusion power', *Applied Sciences* **1**, 1614.

Danon CA, Servant, C. (2004), 'A thermodynamic evaluation of the ta-v system', *J. Alloys Compd.* **366**, 191–200.

Derby, B. (1991), 'An overview of the thermomechanical processing of α/β titanium alloys: Current status and future research opportunities', *Acta Metall Mater* **39**, 955–62.

Derby B, Ashby, M. (1987), 'On dynamic recrystallization', *Scripta Metall* **21**, 879–884.

Dewald, M Curtin, W. (2011), 'Multiscale modeling of dislocation/grain-boundary interactions: Iii. 60 degrees dislocations impinging on sigma 3, sigma 9 and sigma 11 tilt boundaries in al', *Model. Simul. Mater. Sci. Eng.* **19 (5)**.

Dieter G, . (1961), 'Mechanical metallurg,', *McGraw-Hill, New York,* .

Dine S, Elodie B Herlin N Grisolia C Tingaud D Vrel, D. (2021), 'Shs synthesis, sps densification and mechanical properties of nanometric tungsten', *Metals* **11**(2).
URL: *https://www.mdpi.com/2075-4701/11/2/252*

Dodds R, Knowles, A. (2018), 'Nanostructured tungsten alloys for fusion reactor applications', *MEng Materials Science and Engineering thesis* .

Doherty RD, Szpunar, J. (1984), 'Kinetics of subgrain coalescence—a reconsideration of the theory', *Acta Metallurgica* **32**, 1789–1798.

Dong R, Li J Kou H Fan J Tang B Sun, M. (2018), 'Precipitation behavior of α phase during aging treatment in a β-quenched ti-7333', *Mater. Charact.* **140**, 275–280.

Donovan, P. (1989), 'A yield criterion for $pd_{40}ni_{40}p_{20}$ metallic glass', *Acta Metall* **37:**, 445.

El-Guebaly L, Kurtz R Rieth M Kurishita H Robinson, A. (2011), 'W-based alloys for advanced divertor designs: options and environmental impact of state-of-the-art alloys', *Fusion Sci. Technol* **60**, 185–189.

Elsebaie O, Jaansalu, K. (2018), 'A study of the manganese–tungsten binary phase diagram', *International Journal of Refractory Metals and Hard Materials* **72**, 332–340.

Enqvist H, Uhrenius, B. (2003), 'Determination of the average grain size of cemented carbides', *Int J Refract Met Hard Mater* **21**, 31–35.

Ericsson, T. (1966), 'The temperature and concentration dependence of the stacking fault energy in the co-ni system', *Acta Metall* **14**, 853–865.

Evans, J. (1977), 'An interbubble fracture mechanism of blister formation on helium-irradiated metals', *Journal of Nuclear Materials* **68**(2), 129–140.

Faleschini M, Kreuzer H Kiener D Pippan, R. (2007), 'Fracture toughness investigations of tungsten alloys and spd tungsten alloys', *J. Nucl. Mater.* **367–370**, 800–805.

Fan L, Yang T Luan JH Jiao, Z. (2020), 'Control of discontinuous and continuous precipitation of $\gamma\prime$ strengthened high-entropy alloys through nanoscale nb segregation and partitioning', *Journal of Alloys and Compounds* **832**, 154903.

Fang, X Kreter A Rasinski M Kirchlechner C Brinckmann S Linsmeier C Dehm, G. (2018), 'Hydrogen embrittlement of tungsten induced by deuterium plasma: Insights from nanoindentation tests', *Journal of Materials Research* **33**(20), 3530 –3536.

Fleming, M Sublet JC Gilbert, M. (2018), 'High-energy activation simulation coupling tendl and spacs with fispact-ii', *J. Phys.: Conf. Ser.Article 012002* **1046**, 1046.

Franke P, Neuschütz, D. (2006), 'Thermodynamic properties of inorganic materials · binary systems. part 4: Binary systems from mn-mo to y-zr', *Group IV Physical Chemistry* **19B4**.

Fujita, T Chen, M. (2008), 'Characteristic length scale of bicontinuous nanoporous structure by fast fourier transform', *Japanese Journal of Applied Physics* **47**, 1161.

Funkenbusch, A., Bacon, F. & Lee, D. (1979), 'The influence of microstructure on fracture of drawn tungsten wire', *Metallurgical Transactions A* **10**(8), 1085 – 1091.

Gaffet E, Louison C Harmelin M Faudot, F. (1991), 'Metastable phase transformations induced by ball-milling in the cu w system,', *Mater. Sci. Eng. A* **134**, 1380–1384.

Galiyev A, Kaibyshev R Gottstein, G. (2001), 'Correlation of plastic deformation and dynamic recrystallization in magnesium alloy zk60', *Acta Mater* **49**, 1199–1207.

Garfinkle M, . (1966), 'Room-temperature tensile behavior of<100>oriented tungsten single crystals with rhenium in dilute solid solution,', *NASA TN D-3190* **1**.

Garner, F. H. H. S. R. M. F. (1990), 'Implications of neutron spectrum and flux differences on fission-fusion correlations at high neutron fluence', *Radiation Effects and Defects in Solids* **113**(1-3), 229–255.

Geach G, Hughes, J. (1955), 'The alloys of rhenium with molybdenum or with tungsten and having good high temperature properties', *Plansee Proceedings Sintered High-temperature and Corrosion-resistant Materials: Papers Presented at the Second Plansee Seminar* p. 245–253.

German, R. (2010), 1 - thermodynamics of sintering, *in* Z. Z. Fang, ed., 'Sintering of Advanced Materials', Woodhead Publishing Series in Metals and Surface Engineering, Woodhead Publishing, pp. 3–32.
URL: *https://www.sciencedirect.com/science/article/pii/B9781845695620500017*

Ghosh C, Basu J Ramachandran D Mohandas, E. (2015), 'Alloy design and microstructural evolution in v-ti-cr alloys.', *Mater. Charact.* **106**, 292–301.

Ghosh G, Olson, G. (2007), 'Integrated design of nb-based superalloys: Ab initio calculations, computational thermodynamics and kinetics, and experimental results', *Acta Materialia* **55**, 3281–3303.

Giannattasio A, Yao Z Tarleton E Roberts, S. (2007), 'An empirical correlation between temperature and activation energy for brittle-to-ductile transitions in single-phase materials', *Philosophical Magazine* **87**, 2589.

Giannattasio A, Yao Z Tarleton E Roberts, S. (2010), 'Brittle–ductile transitions in polycrystalline tungsten', *Philosophical Magazine* **30**, 3947–3959.

Gibala R, Mitchell, T. (1973), 'Solid solution softening and hardening', *Scr. Metall* **7**, 1143–1148.

Gibson, J Armstrong D Roberts, S. (2014), 'The micro-mechanical properties of ion irradiated tungsten', *Physica Scripta* **2014**(T159), 014056.

Gibson JSK, . (2015), 'Fusion power (phd thesis, small)', phd thesis,', *Oxford, University of Oxford* .

Gil Sevillano J, van Houtte P Aernoudt, E. (1980), 'Large strain work hardening and textures', *Prog Mater Sci* **25**, 69–134.

Gilbert A, . (1966), 'A fractographic study of tungsten and dilute tungsten-rhenium alloys', *, J. Less Common Met* **10**, 328–343.

Gilbert, MR Dudarev SL Zheng S Packer WL Sublet, J. (2012), 'An integrated model for materials in a fusion power plant: transmutation, gas production, and helium embrittlement under neutron irradiation', *Nuclear Fusion* **52**(8), 083019.

Gilbert, MR Eade T Rey T Vale1 R Bachmann C Fischer U Taylor, N. (2019), 'Waste implications from minor impurities in european demo materials', *Nucl. Fusion* **59**, 1–15.

Gilbert, MR Fleming M Sublet, J. (2017), 'Automated inventory and material science scoping calculations under fission and fusion conditions', *Nuclear Engineering and Technology* **49**, 1346–1353.

Gilbert, MR Sublet, J. (2011), 'Neutron-induced transmutation effects in w and w-alloys in a fusion environment', *Nuclear Fusion* **51**(4), 043005.

Gilbert MR, Sublet, J. (2011), 'Neutron-induced transmutation effects in w and w-alloys in a fusion environment', *Nucl. Fusion,* **51**, 043005.

Gleiter H, Hansen N Horswell A Leffers T Lidholt, H. E. (1981), 'Proc. 2nd riso int. symp.', *Metallurgy and Materials Science, Riso National Laboratory, Roskilde, Denmark,* p. 15–21.

Gludovatz B, Wurster S Hoffmann A Pippan, R. (2010), 'Fracture toughness of polycrystalline tungsten alloys', *, Int. J. Refract. Met. Hard Mater.* **28**, 674–678.

Gludovatz, B., Wurster, S., Weingärtner, T., Hoffmann, A. & Pippan, R. (2011), 'Influence of impurities on the fracture behaviour of tungsten', *Philosophical Magazine* **91**(22), 3006–3020.

Gonderman S, Tripathi JK Novakowski TJ Sizyuk T Hassanein, A. (2016), 'Effect of dual ion beam irradiation (helium and deuterium) on tungsten-tantalum alloys under fusion relevant conditions', *Nucl. Mater. Energy* **12**, 346–352.
URL: *https://doi.org/10.1016/j.nme.2017.02.011*

Gorsse, S Bellanger P Brechet Y Sellier E Umarji A Ail U Decourt, R. (2011), 'Nanostructuration via solid state transformation as a strategy for improving the thermoelectric efficiency of pbte alloys', *Acta Mater* **59**, 7425–7437.

Groger A, Vitek, V. (2008), 'Multiscale modeling of plastic deformation of molybdenum and tungsten: I. atomistic studies of the core structure and glide of 1/2(111) screw dislocations at 0k', *Acta Mater* **56**, 5401–5411.

Gröger, R., Bailey, A. & Vitek, V. (2008), 'Multiscale modeling of plastic deformation of molybdenum and tungsten: I. atomistic studies of the core structure and glide of 1/2 <111> screw dislocations at 0k', *Acta Materialia* **56**(19), 5401–5411.

Guan L, Liu X Gao J Ma L Wynne B Rainforth, W. (2019), 'Effect of deformation twinning on crystallographic texture evolution in a mg-6.6zn-0.2ca (zx70) alloy during recrystallisation', *Journal of Alloys and Compounds* **774**, 556–564.

GUMBSCH, P RIEDLE J HARTMAIER A FISCHMEISTER, H. (1998), 'Factors for the brittle-to-ductile transition in tungsten single crystal', *SCIENCE* **282**, 1293–1295.

Gupta, V. K., Yoon, D.-H., Meyer III, H. M. & Luo, J. (2007), 'Thin intergranular films and solid-state activated sintering in nickel-doped tungsten', *Acta Materialia* **55**(9), 3131 – 3142.

Han ZD, Chen N Zhao SF Fan LW Yang GN Shao Y Yao, K. (2017), 'Effect of ti additions

on mechanical properties of nbmotaw and vnbmotaw refractory high entropy alloys', *Intermetallics* **84**, 153–157.

Hasegawa A, Tanno T Nogami S Satou, M. (2011), 'Property change mechanism in tungsten under neutron irradiation in various reactors', *J. Nucl. Mater* **417**, 491–494.

Hashimoto, N Hunn JD Parikh N Gilliam S Gidcumb S Patnaik B Snead, L. (2005), 'Microstructural analysis on helium retention of ion-irradiated and annealed tungsten foils', *Journal of Nuclear Materials* **347**(3), 307–313.

He J, G. Tang G Hasegawa A Abe, K. (2006), 'Microstructural development and irradiation hardening of w and w-(3–26) wt% re alloys after high-temperature neutron irradiation to 0.15 dpa', *Nucl. Fusion* **46**, 877–883.

He JY, Wang H Huang HL Xu XD Chen MW Wu YX Liu XY Nieh TG An K Lu, Z. (2016), 'A precipitation-hardened high-entropy alloy with outstanding tensile properties', *Acta Mater.* **102**, 187–196.

He JY Zhu C Zhou DQ Liu WH Nieh TW Lu, Z. (2014), 'Steady state flow of the feconicrmn high entropy alloy at elevated temperatures', *Intermetallics* **55**, 9–14.

Herbstein, FH Borie BS Averbach, B. (1956), 'Local atomic displacements in solid solutions', *Acta Crystallographica* **9**(5), 466–471.

Hirata A, Fujita T Wen YR Schneibel JH Liu C Chen, M. (2011), 'Atomic structure of nanoclusters in oxide-dispersion strengthened steels', *Nature Materials* **vol. 10, no. 12**, 922–926.

Hofmann, F Mason DR Eliason JK Maznev AA Nelson KA Dudarev, S. (2015*a*), 'Non-Contact Measurement of Thermal Diffusivity in Ion-Implanted Nuclear Materials', *Sci Rep* **3**(5), 16042.

Hofmann, F Nguyen-Manh D Gilbert MR Beck CE Eliason JK Maznev AA Liu W Armstrong DEJ Nelson KA Dudarev, S. (2015*b*), 'Lattice swelling and modulus change in

a helium-implanted tungsten alloy: X-ray micro-diffraction, surface acoustic wave measurements, and multiscale modelling', *Acta Materialia* **89**, 352–363.

Hofmann, f Nguyen-Manh D Gilbert MR Beck CE Eliason JK Maznev AA Liu W Armstrong DEJ Nelson WK Dudarev, S. (2015*c*), 'Lattice swelling and modulus change in a helium-implanted tungsten alloy: X-ray micro-diffraction, surface acoustic wave measurements, and multiscale modelling', *Acta Materialia* **89**, 352–363.

Hu YJ, Fellinger MR Butler BG Wang Y Darling KA Kecskes LJ D Trinkle DR Liu, Z. (2017), 'Solute-induced solid-solution softening and hardening in bcc tungsten', *Acta Materialia* **141**, 304–316.

Hull D, Bacon, D. (2001), 'Introduction to dislocations,', *Oxford: ButterworthHeinemann* .

Hull, D Bacon, D. (2011), 'Introduction to dislocations', *Elsevier Ltd.* **fifth edition,**.

Hull, D Bacon, D. (Oxford (2001)), Introduction to dislocations, *in* 'Sintering of Advanced Materials', Butterworth-Heinemann,).

Hume-Rothery, W. (1969), 'The structure of metals and alloys', *Indian Journal of Physics* **11**, 74–74.

Humphreys FJ, Hatherly, M. (Pergamon UK), 'Recrystallization and related annealing phenomena', *2nd edition* **: Pergamon**, 2004.

Huot J, Ravnsbæk DB Zhang J Cuevas F Latroche M Jensen, M. ((Jan. 01, 2013)), 'Mechanochemical synthesis of hydrogen storage materials', *Prog. Mater. Sci.* **58 (1)**, 30–75.

Iguchi Y, Katona G Cserh'ati C Langer G Csík A Erd'elyi, Z. (2017), 'Nanolayered diffusion couple technique for the reconsidering of the miscibility gap', *Materials Science* .

ITER (2019*a*), 'https://www.iter.org/proj/inafewlines, what will iter do?, webpage. (2019)'.

ITER (2019*b*), 'https://www.iter.org/sci/whatisfusion, what is fusion?, webpage.'.

Iwakiri, H Morishita K Yoshida, N. (2002), 'Effects of helium bombardment on the deuterium behaviour in tungsten', *Journal of Nuclear Materials* **307-311**, 135–138.

Jaffee R, Sims, C. (1958), 'The effect of rhenium on the fabricability and ductility of molybdenum and tungsten,', *Battelle Memorial Institute* .

Jiang, L Lu YP Jiang H Wang HM Wei BM Cao ZQ Li, T. (2016), 'Formation rules of single phase solid solution in high entropy alloys,', *Materials Science and Technology* **32:6**, 588–592.

Jin ZP, Qiu, C. (1993), 'Thermodynamic evaluation of ti–w system', *Mater. Sci. Technol.* **9**, 378.

Jones AR, Ralph B Hansen, N. (1979), 'The interaction between particles and low angle boundaries during recovery of aluminium-alumina alloys', *Proc R. Soc* **A368**, 345–357.

Jonsson S, Metallkd, Z. (1996), 'Reevaluation of the ti-w system and prediction of the ti-w-n phase diagram', *International Journal of Materials Research.* **87**, 784.

Joshi, A. & Stein, D. (1970), 'Intergranular brittleness studies in tungsten using auger spectroscopy', *Metallurgical Transactions* **1**(9), 2543 – 2546.

Karamched, PS Wilkinson, K. (2011), 'High resolution electron back-scatter diffraction analysis of thermally and mechanically induced strains near carbide inclusions in a superalloy', *Acta Materialia* **59**, 263–272.

Kevskes L, Cho K Dowding R Schuster B Valiev R Wei, Q. (2007), 'Grain size engineering of bcc refractory metals: top-down and bottom-up application to tungsten,', *Mater. Sci. Eng. A* **467**, 33–34.

Keys LK, Moteff, J. (1970), 'Neutron irradiation and defect recovery of tungsten', *J. Nucl. Mater* **34**, 260–280.

Kim Y, Lee K Kim E Cheong D Hong, S. (2009), 'Fabrication of high temperature oxides dispersion strengthened tungsten composites by spark plasma sintering process', *Int. J. Refract. Met. Hard Mater.* **27**, 842–846.

KL, M. (1975), 'Chapter 3. radiation damage.', *Fundam Asp Nucl React Elem* **59**, 1–6.

Klopp W, . (1968), 'Review of ductilizing of group via elements by rhenium and other solutes', *Lewis Research Center report NASA TN D-4955* .

Klopp W, Witzke W Raffo, P. (1966), 'Mechanical properties of dilute tungsten-rhenium alloys.', *NASA Technical Note* **NASA TN D-3483**.

Knowles, A. J., Dye, D., Dodds, R. J., Watson, A., Hardie, C. D. & Humphry-Baker, S. A. (2021), 'Tungsten-based bcc-superalloys', *Applied Materials Today* **23**, 101014.

Knowles A, Jones A Messe OMDM Barnard JS Jones CN Stone, H. (2016), 'Phase equilibria in the fe-mo-ti ternary system at 1000 °c', *MEng Materials Science and Engineering thesis* **60**, 160–168.

Knowles A, Jun TS Bhowmik A Jones NG Britton TB Giuliani F Stone HJ Dye, D. (2017), 'A new beta titanium alloy system reinforced with superlattice intermetallic precipitates', *Scripta Materialia* **139**, 71–75.

Krautwasser P, Derz H Kny, E. (1995), 'Influence of fast neutron fluence on the dbtt of w, w10re and w3.4ni1.6fe', *(OEFZS-A–3304)* **77**, 673.

Kuhn B, . (2011), 'Effect of laves phase strengthening on the mechanical properties of high cr ferritic steels for solid oxide fuel cell interconnect application', *Mater. Sci. Eng. A* **528**, 5888–5899.

Kumar, A., Singh, A. & Suhane, A. (2022), 'A critical review on mechanically alloyed high entropy alloys: processing challenges and properties', *Materials Research Express* **9**(5), 052001.

Kumar, M Gurao NP Upadhyaya, A. (2022), 'Evolution of microstructure and crystallographic texture during cold rolling of liquid phase sintered tungsten heavy alloy', *International Journal of Refractory Metals and Hard Materials* **105**, 105849.

Kuo, K. (1953), 'Ternary laves and sigma-phases of transition metlas', *Acta Metall.* **1**, 720–724.

Lang S, Yan Q Sun N Zhang X Deng L Wang Y Ge, C. (2016), 'Microstructure, basic thermal-mechanical and charpy impact properties of w-0.1 wt.% tic alloy via chemical method', *J. Alloys Compd.* **660**, 184–192.

Larrouy B, Villechaise P Cormier J Berteaux, J. (2015), 'Grain boundary,Äìslip bands interactions: Impact on the fatigue crack initiation in a polycrystalline forged ni-based superalloy', *Acta Materialia* **99**, 325–336.

Lassner E, Schubert, W. (1999), 'Tungsten—properties, chemistry, technology of the element, alloys, and chemical compounds,', *Springer, Berlin* .

Laurent-Brocq, M Perri'ere L Pir'es R Champion, Y. (2016), 'From high entropy alloys to diluted multicomponent alloys: Range of existence of a solid-solution', *Materials & Design* **103**, 84–89.

Lee, H. & Tomar, V. (2013), 'An examination of nickel doping effect on the mechanical strength of a tungsten grain boundary', *Computational Materials Science* **77**, 131 – 138.

Lee, SW Kim K.M Park C.H Hong JK Yeom JT Shih, D. (2017), 'Effects of tife intermetallic compounds on the tensile behavior of ti-4al-4fe-0.25si alloy', *Metall Mater. Trans. A* **48**, 561–567.

Leonhardt T, . (2009), 'Properties of tungsten–rhenium and tungsten–rhenium with hafnium carbide', *JOM* **61**, 68–71.

Lesker, K. (2022), 'https://www.lesker.com/newweb/faqs/question.cfm?id=290'.

Ley, MB Ravnsbæk DB Filinchuk Y Lee YS Janot R Cho YW Skibsted J Jensen, T. ((May 2012)), 'Lice(bh4)3cl, a new lithium-ion conductor and hydrogen storage material with isolated tetranuclear anionic clusters', *Chem. Mater.* **24 (9)**, 1654–1663.

Li, H., Wurster, S., Motz, C., Romaner, L., Ambrosch-Draxl, C. & Pippan, R. (2012), 'Dislocation-core symmetry and slip planes in tungsten alloys: Ab initio calculations and microcantilever bending experiments', *Acta Materialia* **60**(2), 748–758.

Lim LC, Watanabe, T. (1990), 'Fracture toughness and brittle-ductile transition controlled by grain boundary character distribution (gbcd) in polycrystals', *Acta Metall. Mater.* **38**, 2507–2516.

Liu CT, Heatherly L Easton DS Carmichael CA Schneibel JH Chen CH Wright JL Yoo MH Horton JA Inoue, A. (1998), 'Test environments and mechanical properties of zr-base bulk amorphous alloys.', *Metall Mater Trans* **A29**, 1811.

Liu, G Li J Chen K He G Yang Z Guoa, S. (2016), 'High-gravity combustion synthesis of w-cr alloys with improved hardness', *Materials Chemistry and Physics* **182**, 6–9.

Liu, J. M. & Shen, B.-W. (1982), 'Grain boundary fracture in tungsten bi-crystals', *Acta Metallurgica* **30**(6), 1197 – 1202.

Liu R, Zhou Y Hao T Zhang T Wang X Liu C Fang, Q. (2012), 'Microwave synthesis and properties of fine-grained oxides dispersion strengthened tungsten,', *J. Nucl. Mater.* **424**, 171–175.

Loewenhoff T, Buger A Linke J Pintsuk G Schmidt A Singheiser L Thomser, C. (2011), 'Evolution of tungsten degradation under combined high cycle edgelocalized mode and steady-state heat loads', *Phys. Scr* **T145**, 014057.

Lowhaphandu P, Montgomery SL Lewandowski, J. (1999), 'Effects of superimposed hydrostatic pressure on flow and fracture of a zr-ti-ni-cu-be bulk amorphous alloy', *Scripta Mater* **41:.**, 19.

Lu HH, Guo HK Liang W Li JC Zhang GW Li, T. (2020), 'High temperature laves precipitation and its effects on recrystallisation behaviour and luders deformation in super ferritic stainless steels', *Materials and Design* **188**, 108477.

Luo A, Jacobson D Shin, K. (1991), 'Solution softening mechanism of iridium and rhenium in tungsten at room temperature,', *Int. J. Refract. Met. Hard Mater.* **10**, 107–114.

Lutjering G, Williams, J. (2007), *Titanium,(2nd. ed.)*, Springer-Verlag Berlin, Heidelberg New York.

Ma D, Grabowski B Kormann FNeugebauer J Raabe, D. (2015), 'Ab initio thermodynamics of the cocrfemnni high entropy alloy: Importance of entropy contributions beyond the configurational one', *Acta Materialia* **100**, 90–97.

Manikandan R, R. A. A. (2022), 'Tungsten heavy alloys processing via microwave sintering, spark plasma sintering, and additive manufacturing: A review', *Processes.* **10(11)**, 2352.

Matolich J, Nahm H Moteff, J. (1974), 'Swelling in neutron irradiated tungsten and tungsten-25 percent rhenium', *Scr. Metall* **8**, 837–841.

Maykuth D, . (1964), 'The production of powder-metallurgy tungsten sheet and plate', *DMIC Memorandum, Battelle Memorial Institute,* .

McQueen, H. (2004), 'Development of dynamic recrystallization theory', *Mater Sci Eng A* **387-389**, 203–208.

Miller, MK Parish CM Li, Q. (2013), 'Advanced oxide dispersion strengthened and nanostructured ferritic alloys', *Materials Science and Technology (United Kingdom)* **vol. 29, no. 10,**, 1174–1178.

Millett PC, Aidhy DS Desai T Phillpot SR Wolf, D. (2009), 'Grain-boundary source/sink behavior for point defects: an atomistic simulation study.', *Int J Mater Res* **100**, 550–555.

Miracle DB Senkov, O. (2017), 'A critical review of high entropy alloys and related concepts', *Acta Materialia* **122**, 448–511.

Miyamoto M, Watanabe T Nagashima H Nishijima D Doerner RP Krasheninnikov SI Sagara A Yoshida, N. (2014), 'In situ transmission electron microscope observation of the formation of fuzzy structures on tungsten', *Phys. Scr.* **T159**, 014028.

Monge M, Auger M Leguey T Ortega Y Bolzoni L Gordo E Pareja, R. (2009), 'Characterization of novel w alloys produced by hip,', *J. Nucl. Mater.* **386–388**, 613–617.

Moosakazemi F, Tavakoli Mohammadi MR Mohseni M Karamoozian M Zakeri, M. ((Aug. 2017)), 'Effect of design and operational parameters on particle morphology in ball mills', *Int. J. Miner. Process* **165**, 41–49.

Morris DG, . (2011), 11 - strengthening mechanisms in nanocrystalline metals, *in* 'Nanostructured Metals and Alloys', Woodhead Publishing, pp. 299–328.

Murphy, T. (2021), 'Energy and human ambitions on a finite planet', *eScholarship* **Open Access Publications from the University of California**.

Murray, J. (1981), 'The fe-ti (iron-titanium) system', *Bulletin of Alloy Phase Diagrams* **2**, 320–334.

Musalimov R, Valiev, R. (1992), 'Dilatometric analysis of aluminum alloy with submicrometer grained structure', *Scr. Metall. Mater.* **27**, 1685–1690.

Mutoh Y, Ichikawa K Nagata K Takeuchi, M. (1995), 'Effect of rhenium addition on fracture toughness of tungsten at elevated temperatures', *J. Mater. Sci.* **30**, 770–775.

Muzyk M, Nguyen-Manh D Kurzydłowski K Baluc N Dudarev, S. (2011), 'Phase stability, point defects, and elastic properties of w-v and w-ta alloys', *Phys. Rev. B* **84**, 104115.

Naidu, S Sriramamurthy A Rao, P. (1984), 'The cr-w (chromium-tungsten) system', *Bull. Alloy Phase Diagrams* **5**, 289–292.

Nemoto YY Hasegawa A Satou M Abe, K. (2000), 'Microstructural development of neutron irradiated w-re alloys', *J. Nucl. Mater.* **283–287**, 1144–1147.

Nes, E. (1998), 'Current pattern of plastic deformation stages', *Prog Mater Sci* **41**, 129–193.

Nieh, T. (1984), 'Grain boundary segregation of ni in w', *Scripta Metallurgica* **18**(11), 1279 – 1282.

Nishijima D, Baldwin MJ Doerner RP Yu, J. (2011), 'Sputtering properties of tungsten fuzzy surfaces', *J. Nucl. Mater.* **415**, S96–S99.

Nogamia S, Hasegawa A Fukuda M Watana S Reiser J Rieth, M. (2020), 'Tungsten modified by potassium doping and rhenium addition for fusion reactor applications', *Fusion Engineering and Design* **152**, 111445.

Nye, J. (1953), 'Some geometrical relations in dislocated crystals', *Acta Metallurgica* **1**, 153–162.

Nygren R, Raffray R Whyte D Urickson M Baldwin M Snead, L. (2011), 'Making tungsten work,', *J. Nucl. Mater.* **417**, 451–456.

Nygren, R., Raffray, R., Whyte, D., Urickson, M., Baldwin, M. & Snead, L. (2011), 'Making tungsten work–icfrm-14 session t26 paper 501 nygren et al. making tungsten work', *Journal of Nuclear Materials* **417**(1-3), 451–456.

Oliver Cc, Schuh, C. (2021), 'The structural evolution and densification mechanisms of nanophase separation sintering', *Metall Mater Trans A* **52**, 4946–4956.

Oono N, Tang QX Ukai, S. (2016), 'Oxide particle refinement in ni-based ods alloy', *Materials Science and Engineering: A Structural Materials: Properties, Microstructure, and Processing* **vol. 649**, 250–253.

Otto, F Yang Y Bei H George, E. (2013), 'Relative effects of enthalpy and entropy on the phase stability of equiatomic high-entropy alloys', *Acta Materialia* **61**(7), 2628–2638.

Otto F, Yang Y Bei H George, E. (2013), 'Relative effects of enthalpy and entropy on the phase stability of equiatomic high-entropy alloys', *Acta Materialia* **61,7**, 2628–2638.

Oya, Y Shimada M Kobayashi M Oda T Hara M Watanabe H Hatano Y Calderoni P Okuno, K. (2011), 'Comparison of deuterium retention for ion-irradiated and neutron-irradiated tungsten', *Physica Scripta* **2011**(T145), 014050.

Park M, Alexander KC Schuh, C. (2014), 'Diffusion of tungsten in chromium: Experiments and atomistic modeling', *Journal of Alloys and Compounds* **611**, 433–439.

Park, M. & Schuh, C. A. (2015), 'Accelerated sintering in phase-separating nanostructured alloys', *Nature Communications* **6**(1), 6858.

Parkes N, Dodds R Watson A Dye D Hardie C Humphry-Baker SA Knowles, A. (2023), 'Tungsten-based bcc-superalloys: Thermal stability and ageing behaviour', *International Journal of Refractory Metals and Hard Materials* **113**, 106209.

Pavlu J, Vrest'al J Chen X Q Rogl, P. (2011), 'Thermodynamic modeling of laves phases in the tav system: Reassessment using first-principles results. calphad comput.', *Coupling Phase Diagrams Thermochem.* **35**, 103–108.

Pavlu J, Vrest'al J Sob, M. (2009), 'Re-modeling of laves phases in the cr-nb and cr-ta systems using first-principles results. calphad comput.', *Coupling Phase Diagrams Thermochem* **33**, 179–186.

Phaniraj, MP Kim DI Shim JH Cho, Y. (2009), 'Microstructure development in mechanically alloyed yttria dispersed austenitic steels', *Acta Materialia* **vol. 57, no. 6**, 1856–1864.

Pickering, EJ Jones, N. (2016), 'High-entropy alloys: a critical assessment of their founding principles and future prospects', *International Materials Reviews* **61**(3), 183–202.

Pierce DT, Jimenez JA Bentley J Raabe D Wittig, J. (2015), 'The influence of stacking fault energy on the microstructural and strain-hardening evolution of fe–mn–al–si steels during tensile deformation', *Acta Mater* **100**, 178–190.

Piotter V, Zeep B Norajitra P Ruprecht R von der Weth A Hausselt, J. (2008), 'Development of a powder metallurgy process for tungsten components,', *Fusion Eng. Des* **83**, 1517–1520.

Porter, D. (1967), 'The decomposition of tungsten chromium solid solution', **15, (5)**, 721–726.
URL: *https://doi.org/10.1016/0001-6160(67)90352-5.*

Raffo P, . (1969), 'Yielding and fracture in tungsten and tungsten-rhenium alloys,', *J. Less Common Met.* **17**, 133–149.

Raghu T, Sundaresan R Ramakrishnan P Mohan, T. (2001), 'Synthesis of nanocrystalline copper–tungsten alloys by mechanical alloying,', *Mater. Sci. Eng. A* **304**, 438–441.

Rahaman, N. (2010), 2 - kinetics and mechanisms of densification, *in* 'Sintering of Advanced Materials', Woodhead Publishing Series in Metals and Surface Engineering, Woodhead Publishing, pp. 33–64.
URL: *https://www.sciencedirect.com/science/article/pii/B9781845695620500029*

Ramalingam M, Jacobson, D. (1986), 'Elevated temperature softening of progressively annealed and sintered w-re alloys', *J. Less Common Met* **123**, 153–161.

Ravnsbæk DB, e. a. ((Oct. 2013)), 'Novel alkali earth borohydride sr(bh4)2 and borohydride-chloride sr(bh4)cl', *Inorg. Chem* **52 (19)**, 10877–10885.

Ravnsbœk, DB Sørensen LH Filinchuk Y Besenbacher F Jensen, Y. ((Apr. 2012)), 'Screening of metal borohydrides by mechanochemistry and diffraction', *Angew. Chem. Int. Ed* **51 (15)**, 3582–3586.

Reiser J, Hoffmann J Jantsch U Kilmenkov M Bonk S Bonnekoh C Rieth M Hoffmann A Mrotzek, T. (2016), 'Ductilisation of tungsten (w): On the shift of the brittleto- ductile transition (bdt) to lower temperatures through cold rolling,', *Int. J. Refract. Met. Hard Mater.* **54**, 351–369.

Reiser J, Rieth M Dafferner B Hoffmann A Yi X Armstrong, D. (2012), 'Tungsten foil laminate for structural divertor applications – analyses and characterisation of tungsten foil,.', *J. Nucl. Mater* **424**, 197–203.

Ren, C., Fang, Z., Koopman, M., Butler, B., Paramore, J. & Middlemas, S. (2018), 'Methods for improving ductility of tungsten - a review', *International Journal of Refractory Metals and Hard Materials* **75**, 170–183.

Rieth, M Dudarev SL Gonzalez de Vicente, S. (2013), 'Recent progress in research on tungsten materials for nuclear fusion applications in europe', *Journal of Nuclear Materials* **432**(1), 482–500.

Rieth M, Reiser J Dafferner B Baumgartner, S. (2012), 'The impact of refractory material properties on the helium cooled divertor design', *Trans. Fusion Sci. Technol* **61**, 381–384.

Roberts S, Hirsch P Booth A Ellis M Serbena, F. (1993), 'Dislocations, cracks and brittleness in single crystals', *Physica Scripta* **T49B**, 420.

Romaner L, Ambrosch-Draxl C Pippan, R. (2010), 'Effect of rhenium on the dislocation core structure in tungsten', *Phys. Rev. Lett* **104**, 195503.

Rupp D, Monig R Gruber P Weygand, S. (2010), 'Fracture toughness and microstructural characterization of polycrystalline rolled tungsten', *Int. J. Refract. Met. Hard Mater.* **28**, 669–673.

Ryazanov, AI Metelkin EV Semenov, E. (2009), 'Modeling of cascade and sub-cascade formation at high pka energies in irradiated fusion structural materials', *Journal of Nuclear Materials* **386-388**, 132–134.

Ryazanov, AI Semenov, E. (2011), 'Radiation damage formation in fusion structural materials due to elastic and inelastic processes', *Journal of Nuclear Materials* **417**(1), 1074–1077.

Saito Y, Tsuji N Utsunomiya H Sakai T Hong, R. (1998), 'Ultra-fine grained bulk aluminum produced by accumulative roll-bonding (arb) process', *Scr. Mater.* **39**, 1221–1227.

Saito Y, Utsunomiya H Tsui TY Sakai, T. (1999), 'Novel ultra-high straining process for bulk materials - development of the accumulative roll-bonding process', *Acta Mater.* **47**, 579–583.

Sal, E. (2023), 'Self-passivating w-cr-y alloys as plasma-facing materials: Effect of zr addition on fusion relevant properties; study of hydrogen retention, neutron irradiation and joining feasibility to steel doctoral dissertation'.

Salishchev G, Valiahmetov O Galeev, R. (1993), 'Formation of submicrocrystalline structure in the titanium alloy vt8 and its influence on mechanical properties,', *J. Mater. Sci.* **28**, 2898–2902.

Sawan, M. (2012), 'Damage parameters of structural materials in fusion environment compared to fission reactor irradiation', *Fusion Engineering and Design* **87**(5), 551–555.

Schade, P. (2010), '100 years of doped tungsten wire', *Int. J. Refract. Metals Hard Mater.* **28**, 648–660.

Schirra JJ, Caless RH Hatala, R. (1991), 'The effect of laves phases on the mechanical properties of wrought and cast+hip inconel 718 superalloys 718, 625 and various derivatives (ed. loria, e. a.)', *(The Minerals, Metals and Materials Society, 1991)* p. 375–388.

Sefta F, Hammond KD Juslin N Wirth, B. (2013), 'Tungsten surface evolution by helium bubble nucleation, growth and rupture', *Nucl. Fusion, Jul.* **53**, 073015.

Segal V, . (1977), 'Patent of the ussr, no. 575892'.

Segal V, . (1995), 'Materials processing by simple shear,', *Mater. Sci. Eng. A* **197**, 157–164.

Sekimura, N. (1996), 'Primary knock-on atom energy dependence of cascade damage formation and interaction', *Journal of Nuclear Materials* **233-237**, 1080–1084.

Senkov, O. (2010), 'Refractory high-entropy alloys', *Intermetallics* **18**, 1758–1765.

Senkov, ON Miller JD Miracle D Woodward, C. (2015), 'Accelerated exploration of multi-principal element alloys with solid solution phases', *Nat Commun* **6**, 6529.

Setyawan W, Kurtz, R. (2012), 'Effects of transition metals on the grain boundary cohesion in tungsten', *Scr. Mater.* **66**, 558–561.

Setyawan, W. & Kurtz, R. J. (2012), 'Effects of transition metals on the grain boundary cohesion in tungsten', *Scripta Materialia* **66**(8), 558–561.

Sharafat, S Takahashi S Nagasawa K Ghoniem, N. (2009), 'A description of stress driven bubble growth of helium implanted tungsten', *Journal of Nuclear Materials* **389**(2), 203–212. Particle Beam Induced Radiation Effects in Materials.

Sharma G, Ramanujan R.V Tiwari, G. (1999), 'Interphase precipitation in γ-tial alloy', *Mater. Sci. Eng. A* **269**, 21–25.

Shen T, Dai Y Lee, Y. (2016), 'Microstructure and tensile properties of tungsten at elevated temperatures', *J. Nucl. Mater.* **468**, 348–354.

Shen, T., Dai, Y. & Lee, Y. (2016), 'Microstructure and tensile properties of tungsten at elevated temperatures', *Journal of Nuclear Materials* **468**, 348 – 354.

Sims, T Hagel William, C. (1923-), 'The superalloys', *edited by Chester T. Sims [and] William C. Hagel* **New York : Wiley-Interscience, [1972]**.

Smallman RE, Ngan, A. (2007), 'Physical metallurgy and advanced materials engineering', **Elsevier, Oxford, U.K**.

Smirnova N, Levit V Pilyugin V Kuznetsov R Davydova LSazonova, V. (1986), 'Evolution of the structure of f.c.c. single crystal subjected to strong plastic deformation,', *Fiz. Met. Metalloved* **61**, 1170–1177.

Smiti E, Jouffrey P Kobylanski, A. (1984*a*), 'The influence of carbon and oxygen in the grain boundary on the brittle-ductile transition temperature of tungsten bi-crystals', *Scr. Metall.* **18**, 673–676.

Smiti E, Jouffrey PKobylanski, A. (1984*b*), 'The influence of carbon and oxygen in the grain boundary on the brittle-ductile transition temperature of tungsten bi-crystals', *Scr. Metall.* **18**, 673–676.

Snow, D. (1979), 'The recrystallization of commercially pure and doped tungsten wire drawn to high strain', *Metall. Trans. A,* **10**, 815–821.

Sobieraj D, Wróbel JS Rygier T Kurzydłowski KJ Atwani O Devaraj A Saez EM Nguyen-Manh, D. (2020), 'Chemical short-range order in derivative cr–ta–ti–v–w high entropy alloys from the first-principles thermodynamic study', *Phys. Chem. Chem. Phys* **22**, 23929–23951.

Steichen JM, . (1976), 'Tensile properties of neutron irradiated tzm and tungsten', *J. Nucl. Mater.* **60**, 13.

Stephens J, . (1970), 'Dislocation structures in single-crystal tungsten and tungsten alloys', *Metall. Mater. Trans. B* **1**, 1293–1301.

Stephenson R, . (1971), 'Comparative creep-rupture properties of tungsten-25and powder-metallurgy techniques', *J. Less Common Met.* **24**, 173–182.

Stolyarov V, Zhu Y Alexandrov I Lowe T Valiev, R. (2001), 'Influence of ecap routes on the microstructure and properties of pure ti,', *Mater. Sci. Eng.* **A299**, 59–67.

Sun S, Adams BL King, W. (2000), 'Observations of lattice curvature near the interface of a deformed aluminium bicrystal', *Philos. Mag. A* **80**, 9–25.

Takamura S, Ohno N Nishijima D Kajita, S. (2006), 'Formation of nanostructured tungsten with arborescent shape due to helium plasma irradiation', *Plasma Fusion Res.* **1**, 051–051.

TAKAMURA, S OHNO N NISHIJIMA D KAJITA, S. (2006), 'Formation of nanostructured tungsten with arborescent shape due to helium plasma irradiation', *Plasma and Fusion Research* **1**, 051–051.

Takeuchi A, Inoue, A. (2005), 'Classification of bulk metallic glasses by atomic size difference, heat of mixing and period of constituent elements and its application to characterization of the main alloying element', *Materials Transactions, Vol. , () pp.* **46, No. 12**, 2817 – 2829.

Takigawa Y, Honda M Uesugi T Higashi, K. (2008), 'Effect of initial grain size on dynamically recrystallized grain size in az31 magnesium alloy', *Mater Trans* **49**, 1979–1982.

Tanno T, Hasegawa A Fujiwara M He JC Nogami S Satou M Shishido T Abe, K. (2008*a*), 'Precipitation of solid transmutation elements in irradiated tungsten alloys', *Mater. Trans* **49, (10)**, 2259–2264.

Tanno T, Hasegawa A He JC Fujiwara M Nogami S Satou M Shishido T Abe, K. (2007), 'Effects of transmutation elements on neutron irradiation hardening of tungsten', *Mater. Trans.* **48, (9)**, 2399–2402.

Tanno T, Hasegawa A He JC Fujiwara M Nogami S Satou M Shishido T Abe, K. (2008*b*), 'Precipitation of solid transmutation elements in irradiated tungsten alloys', *Mater. Trans.,* **49, (10),**, 2259–2264.

Tarleton E, Roberts, S. (2009), 'Dislocation dynamic modelling of the brittle-ductile transition in tungsten', *Philosophical Magazine* **89**, 2759–2769.

Terentyev, D Bakaeva A Pardoen T Favache A Zhurkin, E. (2016), 'Surface hardening induced by high flux plasma in tungsten revealed by nano-indentation', *Journal of Nuclear Materials* **476**, 1–4.

Terentyev D, Xiao X Dubinko A Bakaeva A Duan, H. (2015), 'Dislocation-mediated strain hardening in tungsten: Thermo-mechanical plasticity theory and experimental validation', *J. Mech. Phys. Solids* **85**, 1–15.

Tran-Huu-Loi, Morniroli, J., Gantois, M. & Lahaye, M. (1985), 'Brittle fracture of polycrystalline tungsten', *Journal of Materials Science* **20**(1), 199 – 206.

Troparevsky, M. (2015), 'Criteria for predicting the formation of single-phase high-entropy alloys', *Physical review.* **5**, 011041–011041–6.

Tsai, CW Chen YL Tsai MH Yeh JW Shun TT Chen, S. (2009), 'Deformation and annealing behaviors of high-entropy alloy al0.5cocrcufeni', *Journal of Alloys and Compounds* **486**(1), 427–435.

Tsai, KY Tsai HF Yeh, J. (2013), 'Sluggish diffusion in co–cr–fe–mn–ni high-entropy alloys', *Acta Materialia* **61**(13), 4887–4897.

Tsai, MH Yeh, J. (2014), 'High-entropy alloys: A critical review', *Materials Research Letters* **2**(3), 107–123.

Urcola JJ, Sellars, C. (1987), 'Effect of changing strain rate on stress-strain behaviour during high temperature deformation', *Acta Metall* **35**, 2637–2647.

Valiev R, Kaibyshev O Kuznetsov R Musalimov R Tsenev, N. (1988), 'Low-temperature superplasticity of metallic materials', *Proc. USSR Acad. Sci.* **301**, 864–866.

Valiev R, Korznikov A Mulyukov, R. (1993), 'Structure and properties of ultrafinegrained materials produced by severe plastic deformation,', *Mater. Sci. Eng.* **A168**, 141–148.

Valiev R, Krasilnikov N Tsenev, N. (1991), 'Plastic deformation of alloys with submicron-grained structure', *Mater. Sci. Eng* **A137**, 35–40.

Valiev R, Mulyukov R Ovchinnikov, V. (1990), 'Direction of a grain-boundary phase in submicrometre-grained iron,', *Philos. Mag. Lett.* **62**, 253–256.

Valitov V, Salishchev G Muhtarov, Z. (1994), 'Superplasticity of heat-resistant nickel superalloy with submicrocrystalline structure', *Metally* **3**, 127–133.

Vashi, UK Armstrong RW Zima, G. (1970), 'The hardness and grain size of consolidated fine tungsten powder', *Metall Mater Trans B 1* p. 1769–1771.

Veverka J, Vilémová M Lukáč FKądzielawa AP Legut D Vontorová J Kozlík J Chráska, T. (2023), 'Decreasing the w-cr solid solution decomposition rate: Theory, modelling and experimental verification', *Journal of Nuclear Materials* **576**, 154288.

Volodin, VN Tuleushev YZ Zhakanbaev, E. (2014), 'Structure of β-tantalum-tungsten alloy films produced by the codeposition of sputtered metals', *Journal of Surface Investigation. X-ray, Synchrotron and Neutron Techniques* **8**(1), 169–174.

Wang K, Liu G Zhao J Wang J Yuan, S. (2016), 'Formability and microstructure evolution for hot gas forming of laser-welded ta15 titanium alloy tubes', *Mater Des* **91**, 269–277.

Wang, K Yan Y Xiong Y Zhao S Chen D Woller, K. (2024), 'Enhanced radiation resistance of w-based hea under helium-ion irradiation conditions', *Journal of Nuclear Materials* **588**, 154761.

Wang WR Wang WL Wang SC Tsai YC Lai CH Yeh, J. (2012), 'Effects of al addition on the microstructure and mechanical property of alxcocrfeni high-entropy alloys', *Intermetallics* **26**, 44–51.

Wang, Y. (2020), 'Applying 2d fft to analyze patterns of spinodal decomposition in matlab um-sjtu joint institute'. https://sites.ji.sjtu.edu.cn/yanming-wang/2020/12/03/2d-fft/.

Waseem O, Lee J Lee HM Ryu, H. (2018), 'The effect of ti on the sintering and mechanical properties of refractory high-entropy alloy tixwtavcr fabricated via spark plasma sintering for fusion plasma-facing materials', *Materials Chemistry and Physics* **210**, 87–94.

Watanabe T, Tsurekawa, S. (2004), 'Toughening of brittle materials by grain boundary engineering', *Mater. Sci. Eng. A,* **387–389**, 447–455.

Wei Q, . (2007), 'Microstructure and mechanical properties at different length scales and strain rates of nanocrystalline tantalum produced by high-pressure torsion', *Acta Mater* **42**, 1709–1727.

Wei Q, Cheng S Ramesh K Ma, E. (2004), 'Effect of nanocrystalline and ultrafine grain sizes on the strain rate sensitivity and activation volume: fcc versus bcc metals', *Mater. Sci. Eng. A* **381**, 71–79.

Wei Q, Kecskes, L. (2008), 'Effect of low-temperature rolling on the tensile behavior of commercially pure tungsten,', *Mater. Sci. Eng. A* **491**.

Wei Q, Pan Z Wu X Schuster B Kecskes L Valiev, R. (2011), 'Microstructure and mechanical properties at different length scales and strain rates of nanocrystalline tantalum produced by high-pressure torsion', *Acta Mater* **59**, 2433–2436.

Wei Q, Zhang H Schuster B Ramesh KValiev R Kecskes L Dowding R Magness L Cho, K. (2006), 'Microstructure and mechanical properties of super-strong nanocrystalline tungsten processed by high-pressure torsion', *Acta Mater.* **54**, 4079–4089.

Wenwang, W Schaublin, R. (2018), 'Simulations of weak-beam diffraction contrast images of dislocation loops by the many-beam schaeublin–stadelmann equations', *Journal of Materials Science* **53**, 15694 – 15702.

Williams, D. B., Carter, C. B., Williams, D. B. & Carter, C. B. (1996), *The transmission electron microscope*, Springer.

Williams, DB Butler, E. (1981), 'Grain boundary discontinuous precipitation reactions', *Int. Met. Rev* **26**, 153–183.

Williams RK, Wiffen FW Bentley J Stiegler, J. (1983), "irradiation induced precipitation in tungsten based,w-re alloys", *Metall. Trans. A,* **14A**, 655–666.

Wright WJ, Saha R Nix, W. (2001), 'Deformation mechanisms of the zr40ti14ni10cu12be24 bulk metallic glass', *Mater Trans ;.* **42**, 642.

Wu, YD Cai YH. Chen XH Wang T Si JJ Wang L Wang YD Hui, X. (2015), 'Phase composition and solid solution strengthening effect in tizrnbmov high-entropy alloys', *Materials & Design* **83**, 651–660.

Wurster S, Baluc N Battabyal M Crosby T Du J Garcia-Rosales C Hasegawa A Hoffmann A Kimura A Kurishita H Kurtz R Li H Noh S Reiser J Riesch J Rieth M Setyanwan W Walter M You J Pippan, R. (2013), 'Recent progress in r&d on tungsten alloys for divertor structural and plasma facing materials', *J. Nucl. Mater.* **442**, S181–S189.

Wurster S, Gludovatz B Hoffmann A Pippan, R. (2011), 'Fracture behavior of tungsten vanadium and tungsten-tantalum alloys and composites,', *J. Nucl. Mater.* **413**, 166–176.

Wurster S, Gludovatz B. Pippan, R. (2010), 'High temperature fracture experiments on tungsten-rhenium alloys', *Int. J. Refract. Met. Hard Mater* **28**, 692–697.

Xie Z, Liu R Miao S Yang X Zhang T Wang, X. (2015), 'Extraordinary high ductility/strength of the interface designed bulk w-zrc alloy plate at relatively low temperature', *Sci. Rep.* **5**, 16014.

Xie, ZM Liu R Miao S Yang XD Zhang T Wang XP Fang QF Liu CS Luo GN Lian YY Liu, X. (2015), 'Extraordinary high ductility/strength of the interface designed bulk w-zrc alloy plate at relatively low temperature', *Sci. Rep.* **5**, 1–11.

Yamagata H, Ohuchida Y Saito N Otsuka, M. (2001), 'Nucleation of new grains during discontinuous dynamic recrystallization of 99.998 mass % aluminum at 453 k', *Scri Mate* **45**, 1055–1061.

Yamamoto Y, . (2007), 'Alumina-forming austenitic stainless steels strengthened by laves phase and mc carbide precipitates', *Metall. Mater. Trans. A Phys. Metall. Mater. Sci.* **38 A**, 2737–2746.

Yamashita A, Horita Z Langdon, T. (2001), 'Improving the mechanical properties of magnesium and a magnesium alloy through severe plastic deformation', *Mater. Sci. Eng.* **A300**, 142–147.

Yan q, Zhang X Wang T Yang C Ge, C. (2013), 'Effect of hot working process on the mechanical properties of tungsten materials,', *J. Nucl. Mater.* **442**, S233–S236.

YANG, LI HANKUI LU XIAOTAO, Z. (2009), 'First-principles study of the migration of helium in tungsten', *International Journal of Modern Physics B* **23**(08), 2077–2082.

Yang X, Zhang, Y. (2012), 'Prediction of high-entropy stabilized solid-solution in multi-component alloys', *Materials Chemistry and Physics* **132 Issues 2–3**, 233–238.

Yeh, J. (2014), 'Alloy design strategies and future trends in high-entropy alloys', *Journal of Materials* **65**(12), 1759–1771.

Yeh JW, . (2006), 'Recent progress in high-entropy alloys', *Ann. Chim. Sci. des Mater* **31**, 633–648.

Yeh JW, Chen SK Lin SJ Gan JY Chin TS Shun TT Tsau CH Chang, S. (2004), 'Nanostructured high-entropy alloys with multiple principal elements: Novel alloy design concepts and outcomes', *Adv. Eng. Mater* **6**, 299–303.

Yi, X Jenkins ML Briceno M Roberts SG Zhou Z Kirk, M. (2013), 'In situ study of self-ion irradiation damage in w and w–5re at 500c', *Philosophical Magazine* **93**(14), 1715–1738.

Yi, X Jenkins ML Kirk MA Zhou Z Roberts, S. (2016), 'In-situ tem studies of 150 kev w+ ion irradiated w and w-alloys: Damage production and microstructural evolution', *Acta Materialia* **112**, 105–120.

Yih S, Wang, C. (1979), 'Tungsten: Sources, metallurgy, properties, and applications.', *Plenum Press, New York* .

Yin C, Terentyev D Zhang T Nogami S Antusch S Chang CC Petrov RH Pardoen, T. (2021), 'Ductile to brittle transition temperature of advanced tungsten alloys for nuclear fusion applications deduced by miniaturized three-point bending tests', *International Journal of Refractory Metals and Hard Materials* **vol. 95**, 105464.

Yoshida N, . (1999), 'Review of recent works in development and evaluation of high-z plasma facing materials', *J. Nucl. Mater* **266-269**, 197–206.

Yoshida, N Iwakiri H Tokunaga K Baba, T. (2005), 'Impact of low energy helium irradiation on plasma facing metals', *Journal of Nuclear Materials* **337-339**, 946–950.

Yu, JH Tanigawa H Hamaguchi D Nozawa, T. (2020), 'Mechanical properties of three kinds of iter-grade pure tungsten with different manufacturing processes', *Fusion Engineering and Design* **157**, 111679.

Yvell K, Grehk TM Hedstrom P Borgenstam A Engberg, G. (2018), 'Microstructure development in a high-nickel austenitic stainless steel using ebsd during in situ tensile deformation', *Materials Characterization* **135**, 228–237.

Zang L, . (2004), 'Department of materials science & engineering', *https://my.eng.utah.edu/lzang/images/lecture-23.pdf* .

Zang L, . (2015), 'Lecture 22: Spinodal decomposition: Part 1: general description and practical implications'. Accessed: 08/09/2019.
URL: *https://my.eng.utah.edu/ lzang/images/lecture-22.pdf*

Zayachuk, Y Armstrong DEJ Bystrov K Van-Boxel S Morgan T Roberts, S. (2017), 'Nanoindentation study of the combined effects of crystallography, heat treatment and exposure to high-flux deuterium plasma in tungsten', *Journal of Nuclear Materials* **486**, 183–190.

Zeng ZR, Zhu YM Xu SW Bian MZ Davies CHJ Birbilis N Nie, J. (2016), 'Texture evolution during static recrystallization of cold-rolled magnesium alloys', *Acta Materialia* **105**, 479–494.

Zenobia, SJ Garrison LM Kulcinski, G. (2012), 'The response of polycrystalline tungsten to 30kev helium ion implantation at normal incidence and high temperatures', *Journal of Nuclear Materials* **425**(1), 83–92.

Zeumert B, Sauthoff, G. (1997), 'Intermetallic nialta alloys with strengthening laves phase for high-temperature applications. i. basic properties', *Intermetallics 5* p. 563–577.

Zhang, D Jin C Tian H Xiong Y Zhang H Qiao P Fan J Zhang Z Li ZY Li, J. (2017), 'An in situ tem study of the surface oxidation of palladium nanocrystals assisted by electron irradiation', *Nanoscale* **9**, 6327.

Zhang D, Qui D Gibson M Zheng Y Fraser H Prasad A StJohn D Easton, M. (2020), 'Refining prior-β grains of ti–6al–4v alloy through yttrium addition', *Journal of Alloys and Compounds* **841**, 1–7.

Zhang X, Yan Q Lang S Xia Y Ge, M. (2016), 'Texture evolution and basic thermalmechanical properties of pure tungsten under various rolling reductions,', *J. Nucl. Mater.* **468**, 339–347.

Zhang, Z Armstrong DEJ Grant, P. (2022), 'The effects of irradiation on crmnfeconi high-entropy alloy and its derivatives', *Progress in Materials Science* **123**, 100807.

Zhao YL, Yang T Tong Y Wang J Luan JH Jiao ZB Che D Yang Y Hu A Liu CT Kai, J. (2017), 'Heterogeneous precipitation behavior and stacking-fault mediated deformation in a cocrni-based medium-entropy alloy', *Acta Mater* **138**, 72–82.

Zhi D, Zongqing M Yu L Liu, Y. (2021), 'Achieving high strength and ductility in ods-w alloy by employing oxide@w core-shell nanopowder as precursor', *Nature Communications* **12**, 5052.

Zhilyaev A, Langdon, T. (2008), 'Using high-pressure torsion for metal processing: fundamentals and applications', *Prog. Mater. Sci.* **53**, 893–979.

Zhilyaev A, Nurislamova G Kim B Baro M Szpunar J Langdon, T. (2003), 'Experimental parameters influencing grain refinement and microstructural evolution during high-pressure torsion', *Acta Mater* **51**, 753–765.

Zinkle SJ, Busby J, T. (2009), 'Structural materials for fission and fusion energy', *Mater. Today* **12**, 12–19.

Zinkle, SJ Ghoniemb, N. (2000), 'Operating temperature windows for fusion reactor structural materials', *Fusion Engineering and Design* **51–52**, 55–71.

Zinkle, SJ Snead, L. (2014), 'Designing radiation resistance in materials for fusion energy', *Annual Review of Materials Research* **44:1**, 241–267.

12 Appendices

Table 45: **XRD of TiFeMo** 2θ angle as calculated from XRD of TiFeMo and lattice parameter of each phase present

Sample	2 θ angle	θ angle	d= λ/2sin(θ)	1/d^2	H	K	L	Lattice parameter
TiFeMo as cast	42.72	21.36	2.12	0.22	1	1	0	2.99
	58.17	31.03	1.49	0.45	2	0	0	3.167$\pm$0.002
	72.88	36.44	1.30	0.60	2	1	1	
	86.67	43.34	1.12	0.92	2	2	0	
	94.96	47.48	1.05	0.92	3	1	0	
	100.12	50.06	1.01	0.99	2	2	2	
	55.19	27.59	1.66	0.36	0	0	2	3.324$\pm$0.002
	62.06	31.03	1.49	0.45	2	1	0	
	76.14	38.07	1.25	0.64	2	1	1	
TiFeMo heat treated 1170C 16 hours	42.96	21.48	2.10	0.22	1	1	0	2.98
	40.20	20.10	2.24	0.20	1	1	0	3.141$\pm$0.006
	59.07	29.54	1.56	0.41	2	0	0	
	73.96	36.98	1.28	0.61	2	1	1	
	87.85	43.92	1.11	0.81	2	2	0	
	95.11	47.56	1.04	0.92	3	1	0	
	101.63	50.81	0.99	1.01	2	2	2	
	36.98	18.49	2.43	0.17	1	1	0	3.335$\pm$0.084
	62.06	31.03	1.49	0.45	2	1	0	
	78.26	39.13	1.22	0.67	2	1	1	
TiFeMo heat treated and aged 750C 72 hours	41.88	20.94	2.16	0.22	1	1	0	2.99$\pm$0.002
	40.66	20.33	2.21	0.20	1	1	0	3.150$\pm$0.011
	58.66	29.33	1.57	0.40	2	0	0	
	73.47	36.74	1.29	0.60	2	1	1	
	87.12	43.56	1.12	0.80	2	2	0	
	100.66	50.33	1.00	1.00	3	1	0	
	43.37	21.68	2.08	0.23	1	1	0	2.98$\pm$0.086
	62.73	31.37	1.48	0.46	2	0	0	
	78.98	39.49	1.21	0.68	2	1	1	
	94.82	47.41	1.05	0.91	2	2	0	
	109.24	54.62	0.94	1.12	3	1	0	

ACI Alloys, Inc.

1458 Seareel Place
San Jose, CA 95131
Phone (408) 259-7337
Fax (408) 729-0277

Certificate Of Analysis

W/Mn 50/50 at% 99.95%

Ag: ND	F: ND	Na: ND	Sn: ND
Al: ND	Fe: 0.0005	Nb: ND	Sr: ND
As: ND	Ga: ND	Nd: ND	Ta: 0.0004
Au: ND	Gd: ND	Ni: ND	Tb: ND
B: ND	Ge: ND	O: 0.023	Te: ND
Ba: ND	H: 0.0046	Os: ND	Ti: ND
Be: ND	Hf: ND	P: 0.0002	Tl: ND
Bi: ND	Hg: ND	Pb: ND	Tm: ND
Br: ND	Ho: ND	Pd: ND	V: ND
C: 0.0002	I: ND	Pr: ND	W: 76.9919
Ca: ND	In: ND	Pt: ND	Y: ND
Cd: ND	Ir: ND	Re: ND	Yb: ND
Ce: ND	K: ND	Rh: ND	Zn: ND
Cl: ND	La: ND	Ru: ND	Zr: ND
Co: ND	Li: ND	S: 0.006	
Cr: 0.0003	Lu: ND	Sb: ND	
Cu: ND	Mg: ND	Sc: ND	
Dy: ND	Mn: 22.9999	Se: ND	
Er: ND	Mo: 0.0049	Si: 0.0005	
Eu: ND	N: 0.0005	Sm: ND	

*Above values are theoretical based on the lots below:

*Results in wt%

W: TRZ1403 -: -
Mn: SAX4425 -: -
-: - -: -
-: - -: -
-: - -: -

Charles Albert, PhD
ACI Alloys, Inc.

Figure 12.1: WMn Data sheet

ACI Alloys, Inc.

1458 Seareel Place
San Jose, CA 95131
Phone (408) 259-7337
Fax (408) 729-0277

Certificate Of Analysis

W/Cr/V/Ta 25/25/25/25 at% 99.95%

Ag:	ND	F:	ND	Na:	ND	Sn:	ND
Al:	ND	Fe:	0.0006	Nb:	0.0091	Sr:	ND
As:	ND	Ga:	ND	Nd:	ND	Ta:	38.6566
Au:	ND	Gd:	ND	Ni:	0.0002	Tb:	ND
B:	ND	Ge:	ND	O:	0.0016	Te:	ND
Ba:	ND	H:	ND	Os:	ND	Ti:	ND
Be:	ND	Hf:	ND	P:	ND	Tl:	ND
Bi:	ND	Hg:	ND	Pb:	ND	Tm:	ND
Br:	ND	Ho:	ND	Pd:	ND	V:	10.8853
C:	0.0008	I:	ND	Pr:	ND	W:	39.3156
Ca:	ND	In:	ND	Pt:	ND	Y:	ND
Cd:	ND	Ir:	ND	Re:	ND	Yb:	ND
Ce:	ND	K:	ND	Rh:	ND	Zn:	ND
Cl:	ND	La:	ND	Ru:	ND	Zr:	ND
Co:	ND	Li:	ND	S:	0.0002		
Cr:	11.1145	Lu:	ND	Sb:	ND		
Cu:	ND	Mg:	ND	Sc:	ND		
Dy:	ND	Mn:	ND	Se:	ND		
Er:	ND	Mo:	0.0031	Si:	0.003		
Eu:	ND	N:	0.0005	Sm:	ND		

*Above values are theoretical based on the lots below:

*Results in wt%

W: TRZ1403 -: -
Cr: GMP0102 -: -
V: ASM1041 -: -
Ta: TCB2112 -: -
-: - -: -

Charles Albert, PhD
ACI Alloys, Inc.

Figure 12.2: 4Hea Data sheet

ACI Alloys, Inc.

1458 Seareel Place
San Jose, CA 95131
Phone (408) 259-7337
Fax (408) 729-0277

Certificate Of Analysis

W/Cr/V/Ta/Ti 20/20/20/20/20 at% 99.95%

Ag: ND	F: ND	Na: ND	Sn: ND
Al: ND	Fe: 0.0006	Nb: 0.0083	Sr: ND
As: ND	Ga: ND	Nd: ND	Ta: 35.0657
Au: ND	Gd: ND	Ni: 0.0002	Tb: ND
B: ND	Ge: ND	O: 0.0031	Te: ND
Ba: ND	H: ND	Os: ND	Ti: 9.2891
Be: ND	Hf: ND	P: ND	Tl: ND
Bi: ND	Hg: ND	Pb: ND	Tm: ND
Br: ND	Ho: ND	Pd: ND	V: 9.8741
C: 0.0009	I: ND	Pr: ND	W: 35.6634
Ca: ND	In: ND	Pt: ND	Y: ND
Cd: ND	Ir: ND	Re: ND	Yb: ND
Ce: ND	K: ND	Rh: ND	Zn: ND
Cl: ND	La: ND	Ru: ND	Zr: ND
Co: ND	Li: ND	S: 0.0002	
Cr: 10.0821	Lu: ND	Sb: ND	
Cu: ND	Mg: ND	Sc: ND	
Dy: ND	Mn: ND	Se: ND	
Er: ND	Mo: 0.0028	Si: 0.0027	
Eu: ND	N: 0.0006	Sm: ND	

*Above values are theoretical based on the lots below:

*Results in wt%

W: TRZ1403 -: -
Cr: GMP0102 -: -
V: ASM1041 -: -
Ta: TCB2112 -: -
Ti: FMX8112 -: -

Charles J Albert

Charles Albert, PhD
ACI Alloys, Inc.

Figure 12.3: WMn Data sheet